SETTLEMENT OF THE KANSAI INTERNATIONAL AIRPORT ISLANDS

BY

JASON R. FUNK

DISSERTATION

Submitted in partial fulfillment of the requirements
for the degree of Doctor of Philosophy in Civil Engineering
in the Graduate College of the
University of Illinois at Urbana-Champaign, 2013

Urbana, Illinois

Doctoral Committee:

Professor Gholamreza Mesri, Chair
Professor Youssef Hashash
Professor Emeritus James H. Long
Professor and Director Stephen Marshak
Associate Professor Scott M. Olson

ABSTRACT

The Kansai International Airport was constructed 5km off the coast of Senshu in 18m to 20m deep sea water to avoid noise pollution, and land acquisition disputes that had been experienced at Itami and Narita Airports. Construction of Island I began in 1987 and the Island I runway began operation in 1994. Construction of Island II began in 1999 and the Island II runway began operation in 2007. Utilizing over 2 million vertical sand drains and 400 million cubic meters of reclamation fill material for construction of two airport islands, the project is viewed as an engineering marvel. In fact, the American Society of Civil Engineers named the airport one of the "Civil Engineering Monuments of the Millennium". As part of the original design considerations, the surface elevation of the airport islands were to remain above +4m Chart Datum Level (CDL) to avoid the erosive action of waves overtopping the seawall (Arai, 1991). However, as of December 2012, the average seabed settlement has exceeded 12.9m and 14.2m, respectively, for Airport Islands I and II (NKIAC, 2012). Much of the surface elevation of Island I is already below +4m CDL, and the surface elevation of part of Island II is predicted to be at +4m CDL in September 2023. Furthermore, Island I is predicted to be at sea level in June 2067, and part of Island II is expected to be at sea level in January 2056.

The Kansai Airport project has received considerable attention in geotechnical engineering literature in part because of the scale of the project; Island I is 511ha in approximately 18m deep seawater and Island II is 545ha in approximately 20m deep seawater. The project is also significant because of the sufficiently detailed subseabed information as well as observations of settlement and porewater pressure reaching depths up to 350m below the seabed. The projected or observed consolidation behavior of the subseabed has been arrogated in an ongoing debate on the uniqueness of the end-of-primary void ratio – effective vertical stress relationship of clay and silt deposits. Some have explicity argued against application of the uniqueness principle to settlement and porewater pressure predictions at the Kansai Airport site (Hight and Leroueil, 2003; Mimura and Jang, 2005; Rocchi et al., 2006), while others have made settlement calculations for the Kansai International Airport using rheological models that assume separate and independent effective stress and time compressiblities (Imai et al., 2005; Oda et al., 2005; Tanaka, 2005). Additionally, in connection to secondary compression behavior of Osaka

Bay clays, potentially misleading interpretations have been published as a result of possible misinterpretation of laboratory oedometer tests as well as settlement observations at the airport site.

This study includes a review of the geologic history of Osaka Bay as well as a careful evaluation of the available subseabed data for 14 marine clay layers, 8 non-marine clay layers, and 20 sand layers that are contained within the up to 350m depth below seabed contributing to settlement of the Kansai Airport islands. Additionally, the reclamation process used to construct the airport islands and the instrumentation installed for settlement and porewater pressure observations were carefully examined as part of this study. Explicit finite difference techniques were developed within the ILLICON framework (Mesri and Rokhsar, 1974; Choi, 1982; Lo, 1991; Mesri et al., 1994) to facilitate settlement and porewater pressure calculations at the Kansai International Airport site. Settlement and porewater pressure calculations were performed at the Kansai International Airport Island I and Island II based on the assumption of uniqueness of end-of-primary void ratio – effective vertical stress relationship, together with the C_α/C_c law of compressibility to compute secondary compression.

Settlement calculations for the Holocene marine clay layer (Ma13), which is fully penetrated by forty centimeter diameter displacement type vertical sand drains at the Kansai Airport site, are in good agreement with observations. Therefore, the uniqueness principle satisfactorily explains the magnitude of vertical compression of Ma13 at Kansai Airport. End-of-primary compression for the 17m to 24m Ma13 clay layer ranges from 6.2m to 8.3m at the airport site. End-of-primary compression for Ma13 was reached soon after reclamation was completed for Airport Island I and Airport Island II. Therefore, the majority of the post-construction seabed settlement for the Kansai Airport Islands will result from compression of the Pleistocene clay layers underlying Ma13.

The ILLICON program was used together with settlement and porewater pressure observations to back-calculate equivalent permeabilities (k_{eq}) for the Pleistocene sand layers to compute the post-construction settlement projections of the Pleistocene layers. The permeability values used in the ILLICON analysis are comparable to values reported by Nakase (1987) and values used by Mimura and Jang (2005) and Shibata and Karube (2005) in their settlement analysis for Kansai Airport. Calculated settlements and excess porewater pressures for the Pleistocene layers are in good agreement with observations that are available up to 2011. Seabed

settlement, including contributions from the Holocene clay layer and the Pleistocene clay layers, is expected to be 15.7m at Island I and 24.9m at Island II in the year 2100.

The uniqueness principle together with the C_α/C_c law of compressibility sufficiently explains settlement and porewater pressure observations reported for the Kansai International Airport project.

This work is dedicated to my parents Linda and David, and to my wife Michelle, with love and gratitude.

ACKNOWLEDGEMENTS

I would like to start by thanking Mr. Naoshi Nishimura for providing earth pressure cell, porewater pressure, and settlement observations for the Island II monitoring point MP2-II.

A special thanks to Charles Robert Ullrich who inspired me to pursue geotechnical engineering while I was an undergraduate and graduate student at the University of Louisville, and who continued to encourage me while I was at the University of Illinois.

Throughout my time at the University of Illinois, I have had the opportunity to work next to many fantastic geotechnical graduate students. I would like to extend a special thanks to Nejan Huvaj – Sarihan, Mark Muszynski, Andrew Anderson, Kamran Akhtar, Brett Zitny, Kashif Muhammad, Abdul Qudoos Khan, Pouyan Assem, Weichu Lee, Byungmin Kim, Dave Hall, and Seung Jae Lee.

I would like to extend a special thanks to the students of CEE 483 who gave me many great memories from Fall 2009 to Spring 2013 that I will take with me for the rest of my life.

I would like to extend special thanks to Michael Musgrove for guidance and for many fruitful discussions regarding programming with Microsoft Visual Studio©.

I would like to thank Professor Jim Long, Professor Scott Olson, Professor Stephen Marshak, and Professor Youssef Hashash for their willingness to serve on my dissertation committee and for their useful contributions to this research.

This work would not have been possible without the dedicated supervision of Professor Gholamreza Mesri, who at all times exemplified what it means to be a great teacher and advisor and whose lessons I hope to keep with me for the rest of my life.

This dissertation would not have been possible without the support of my family. I would like to extend my sincere thanks to my parents Linda and David, my sister Carla, my grandmother Effie, and my wife Michelle. A special thanks to Michelle for reading this manuscript in its entirety.

TABLE OF CONTENTS

LIST OF SYMBOLS

A_c	Activity
β	Degree of compression
C_α	Secondary compression index
C_c	Compression index
C_c'	Secant compression index
CDL	Chart Datum Level
CF	Clay-size fraction
C_k	Change-in-permeability-index
C_r	Recompression index
C_s	Swelling index
CT	Connecting taxiway for the Kansai International Airport
c_h	Coefficient of consolidation in the horizontal direction
c_v	Coefficient of consolidation in the vertical direction
c_{vo}	Coefficient of consolidation in the vertical direction corresponding to initial conditions
D	Degree of excess porewater pressure dissipation
D_{10}	Grain size corresponding to 10% finer
Ds	Diluvial sand layer
DS	Drain spacing
$\Delta\sigma_v$	Increase in vertical stress
e	Void ratio
e_o	Initial or preconstruction void ratio
e_p	End-of-primary void ratio
e_{pp}	End-of-primary void ratio at the preconsolidation pressure
EOP	End-of-primary
G_s	Specific gravity of solids
γ	Unit weight
γ_w	Unit weight of water
I_p	Plasticity index

k	Coefficient of permeability
k_{vo}	Initial or preconstruction coefficient of permeability
K-I	Point K of the Island I pilot section
KALD	Kansai International Airport Land Development Company
KIAC	Kansai International Airport Company
L_o	Initial layer thickness
Ma	Marine clay layer
MOT	Ministry of Transportation
MP1-I	Monitoring Point 1 of Island I
MP1-II	Monitoring Point 1 of Island II
MP2-II	Monitoring Point 2 of Island II
NKIAC	New Kansai International Airport Company
OP	Osaka Peil
r_e	Radius of the soil cylinder influenced by the vertical drain
r_s	External radius of smear zone
r_w	Radius of the vertical drain
σ'_p	Preconsolidation pressure
σ'_v	Effective vertical stress
σ'_{vo}	Initial or preconstruction effective vertical stress
t	Elapsed time
t_p	Time to end-of-primary consolidation
u'	Excess porewater pressure
u'_s	Excess porewater pressure within incompressible impeded drainage layer
w_ℓ	Liquid limit
w_o	Natural or preconstruction water content
w_p	Plastic limit

CHAPTER 1 INTRODUCTION

1.1 Problem statement

Japan's extensive reclamation history stems from a need for additional land in coastal areas away from uninhabitable mountain terrain (Vadus, 1991). Reclamation has taken place in Osaka Bay at least as early as the Edo Era (1600 to 1867) when it was used for rice cultivation (Mikasa and Ohnishi, 1981; Sasaki et al., 1987). Reclamation projects in Osaka Bay that were completed in the latter half of the 20th century and into the 21st century incorporate residential, commercial, recreational, educational, and transportation facilities with industrial, distribution, and harbor centers as part of an effort to make the Kansai Region the center of its own international economic activities. Construction of a 24 hour international airport was intended to be an important step towards the globalization of the Kansai Region and the decentralization of the Japanese economy from Tokyo (Sasaki et al., 1987; Rai, 1990; Takahashi and Kaneko, 1991).

The Kansai International Airport was constructed 5km off the coast of Senshu in 18 to 20m deep water to avoid land acquisition disputes as well as noise related issues (KALD, 2005). Utilizing over 2 million vertical sand drains and 400 million cubic meters of fill material for construction of two airport islands, the project is viewed as an engineering marvel. In fact, the American Society of Civil Engineers named Kansai International Airport one of the "Civil Engineering Monuments of the Millennium". However, as of December 2012, the average seabed settlements have exceeded 12.9m and 14.2m, respectively, for Airport Islands I and II (NKIAC, 2012). If settlements are too large the airport facilities will be out of service when waves overtop the seawall surrounding the islands. Eventually the islands could settle below sea level.

The Kansai International Airport has received a lot of attention in geotechnical literature in part because of the scale of the project (Island I is 511ha and the seabed is approximately 18m below sea level and Island II is 545ha and the seabed is approximately 20m below sea level) and because of the availability of subsurface data as well as observations from settlement and porewater pressure instrumentation. At the forefront of the discussion regarding interpretation of field observations at the Kansai Airport site is whether or not the uniqueness principle (Mesri and Choi, 1985b) can be applied to make settlement and porewater pressure predictions.

The discussion related to uniqueness of the end-of-primary (EOP) void ratio – effective vertical stress relationship is not a recent development. The uniqueness debate began in 1972 when G. A. Leonards posed the following question to L. Bjerrum at a 1972 ASCE Conference:

> "The question is, at the time the excess pore pressure has dissipated … will the clay layer in the field have compressed much more than that measured in the laboratory test…? "

Leonards (1972) observed that if the answer to his question was affirmative, then there would be cases where settlement observations in the field were substantially greater than settlement predictions based on laboratory oedometer tests. However, Leonards (1972) continued:

> "To date, no such cases have come to the writer's attention."

Ladd et al. (1977) stated the question in terms of Figure 1-1 which "shows two extremes for the effect of sample thickness," concluding that "Little definitive data exists to show which of the two hypotheses is more nearly correct for the majority of cohesive soils (though the General Reporter is obviously biased toward curve A)." The extreme demonstrated by curve A for a thick sample is consistent with the uniqueness principle, whereas the extreme demonstrated by curve B implies significantly larger EOP strain for the thick sample. Additionally, Mesri (1977) recognizing that hypothesis B had originated from a theoretical analysis of consolidation proposed:

> "If a model of soil structure is assumed in which separate and independent elements represent effective stress and time compressibilities, then the simplistic conclusion inevitably follows that the longer the duration of primary consolidation, the lower the end-of-primary void ratio… However, this conclusion need not be true, if in fact during primary consolidation, the incremental compressibilities with respect to effective stress and with respect to time are interrelated."

Since that time, evidence has been presented supporting the uniqueness principle (Mesri and Choi, 1979; Mesri and Choi, 1985a; Mesri and Choi, 1985b; Mesri and Lo, 1989; Lo, 1991;

Mesri et al., 1994; Mesri et al., 1995; Mesri and Feng, 2009, 2013; Mesri and Khan, 2012) while some continue to argue against uniqueness (e.g. Leroueil, 1988, 1994, 1995; Degago et al., 2009, 2011).

The applicability of the uniqueness principle to settlement and porewater pressure predictions at Kansai Airport is particularly important because the profile contains marine and non-marine Pleistocene clay layers, some of which are more than 20m thick, separated by sand layers with relatively high fines content. Additionally, no vertical sand drains were installed in the Pleistocene layers to accelerate primary consolidation. Therefore, the time compressibility component of consolidation is expected to act over many decades before some of the Pleistocene clay layers reach end-of-primary consolidation.

Hight and Leroueil (2003), who are among those that discount the uniqueness principle, made the following statement regarding the Kansai Airport project:

> "The Kansai reclamation project confirms, therefore, that under a given effective stress, the in situ strain, and thus settlement is larger than that deduced from laboratory tests, and this is mostly attributed to the viscosity of clayey soils… These results confirm the conclusion reached by Leroueil (1988, 1996) that, in highly compressible clays or for embankments of special importance (embankments for which the magnitude of settlements may have important consequences), the viscous component of settlements can be significant and should be considered."

Hight and Leroueil (2003) indicate that the assumption of uniqueness will lead to an underestimate of settlement resulting from primary consolidation.

Other investigators who have made settlement calculations for the Kansai Airport Islands have also argued against the uniqueness principle. Rocchi et al. (2006) made the following statement regarding settlement and porewater pressure observations and laboratory oedometer tests associated with the Kansai Airport project:

> "The 'field' behavior of Osaka clays at these two sites demonstrates that 'primary compression' settlements predicted by elastoplastic models and conventional interpretation of oedometer tests may be substantially lower than observed, casting doubt

on the uniqueness of the 'end-of-primary' (EOP) void ratio – effective stress relationship, which is found to provide reliable predictions only under special circumstances."

Additionally, Mimura and Jang (2005) wrote:

"The phenomenon taking place due to the reclamation is far from the conventional concept of consolidation in which deformation advances associated with the dissipation of excess pore water pressure."

In addition to statements arguing against the uniqueness principle, a group of researchers (Mimura et al., 2003; Imai et al., 2005; Mimura and Jang, 2005; Oda et al., 2005, Tanaka, 2005) have made settlement calculations for the Kansai International Airport using rheological models that inherently assume that the compressibilities with respect to effective stress and with respect to time are separate independent mechanisms contributing to consolidation.

Potentially misleading conclusions regarding the secondary compression behavior of Osaka Bay clays have also been reached as a result of possible misinterpretation of laboratory oedometer tests as well as settlement observations at Kansai Airport. For example, the following statement by Imai et al. (2005) highlights confusion related to the secondary compression behavior of Osaka Bay Pleistocene clays:

"The most shocking finding is that a large compression endlessly takes place for long time even when an applied load is smaller than p_c [preconsolidation pressure]. Why does such an abnormal behavior take place?"

The C_α/C_c law of compressibility has been used to successfully explain relatively large compression resulting from application of stress leading to a final effective vertical stress near the preconsolidation pressure (Mesri and Godlewski, 1977).

In summary, the inability to explain the settlement and porewater pressure observations for the Kansai International Airport project together with a misunderstanding of the secondary compression behavior of soft clays has led researchers involved with the project to discount the uniqueness principle which has been successfully applied to laboratory and field interpretation of

consolidation explicitly by Mesri and co-workers and implicitly by experienced engineers such as G. A. Leondards, C. C. Ladd, and many others. Perhaps no quotation summarizes the confusion better than the following statement by Duncan et al. (2005):

> "The compressibility of clay increases as rates of loading decrease, and secondary compression continues after all excess porewater pressures have dissipated. It is unclear how these important effects should be included in predictions of settlements of thick clay deposits."

1.2 Research objectives

This study is intended to meet the following research objectives:

- Review the geologic history of Osaka Bay to determine the depositional environment, lateral variation of thickness, and age for geologic layers that make up the subseabed profile.
- Evaluate all available subseabed data to determine the compressibility and permeability of each geologic layer at the Kansai International Airport site.
- Examine the procedures required to construct two man-made islands with a combined area exceeding 1000ha in 18 to 20m deep water, and determine the reclamation load at the seabed for the Kansai Airport Islands.
- Examine the instrumentation used for settlement and porewater pressure observation at the Kansai International Airport site.
- Within the ILLICON framework, develop a finite difference technique that includes the contribution of horizontal flow to the dissipation of excess porewater pressure within compressible clay layers.
- Develop a finite difference technique to account for excess porewater pressure buildup in sand layers adjacent to compressible clay layers, and horizontal flow of porewater in the sand layers for the case of (a) two-dimensional flow, and (b) axi-symmetric flow.
- Perform settlement and porewater pressure calculations at the Kansai International Airport Island I and Island II based on the assumption of uniqueness of end-of-primary void ratio – effective vertical stress relationship, together with the C_α/C_c law to compute secondary compression.

1.3 Scope

The study is presented in 10 chapters.

Chapter 1 describes the need for research and the objectives of the investigation.

Chapter 2 describes the geology of Osaka Bay. Emphasis is placed on formation of Osaka Basin as well as deposition as a result of the rise and fall of sea level over geologic time.

Chapter 3 describes the history of reclamation projects in Osaka Bay, emphasizing the more recent reclamation projects.

Chapter 4 presents the subseabed data used for settlement and porewater pressure analyses at the Kansai Airport site.

Chapter 5 describes the reclamation process for the Kansai International Airport Islands.

Chapter 6 describes the instruments used for settlement and porewater pressure observation at the Kansai International Airport site and presents the observations.

Chapter 7 describes ILLICON; software developed at the University of Illinois at Urbana Champaign that uses an explicit finite difference solution technique for settlement analysis. Emphasis is placed on additions made to ILLICON as they relate to the research objectives listed above.

Chapter 8 details the settlement analyses performed for the Kansai International Airport site.

Chapter 9 summarizes the major conclusions from this study.

Appendix 1 presents the details of settlement analyses performed for the Osaka Port Reclaimed Islands. Appendix 2 presents two proposed methods to back-calculate horizontal coefficient of consolidation (c_h) for time-dependent loading with vertical drains. Appendix 3 describes calculation of the compression of Pleistocene sand layers for the Kansai Airport site.

1.4 Figures

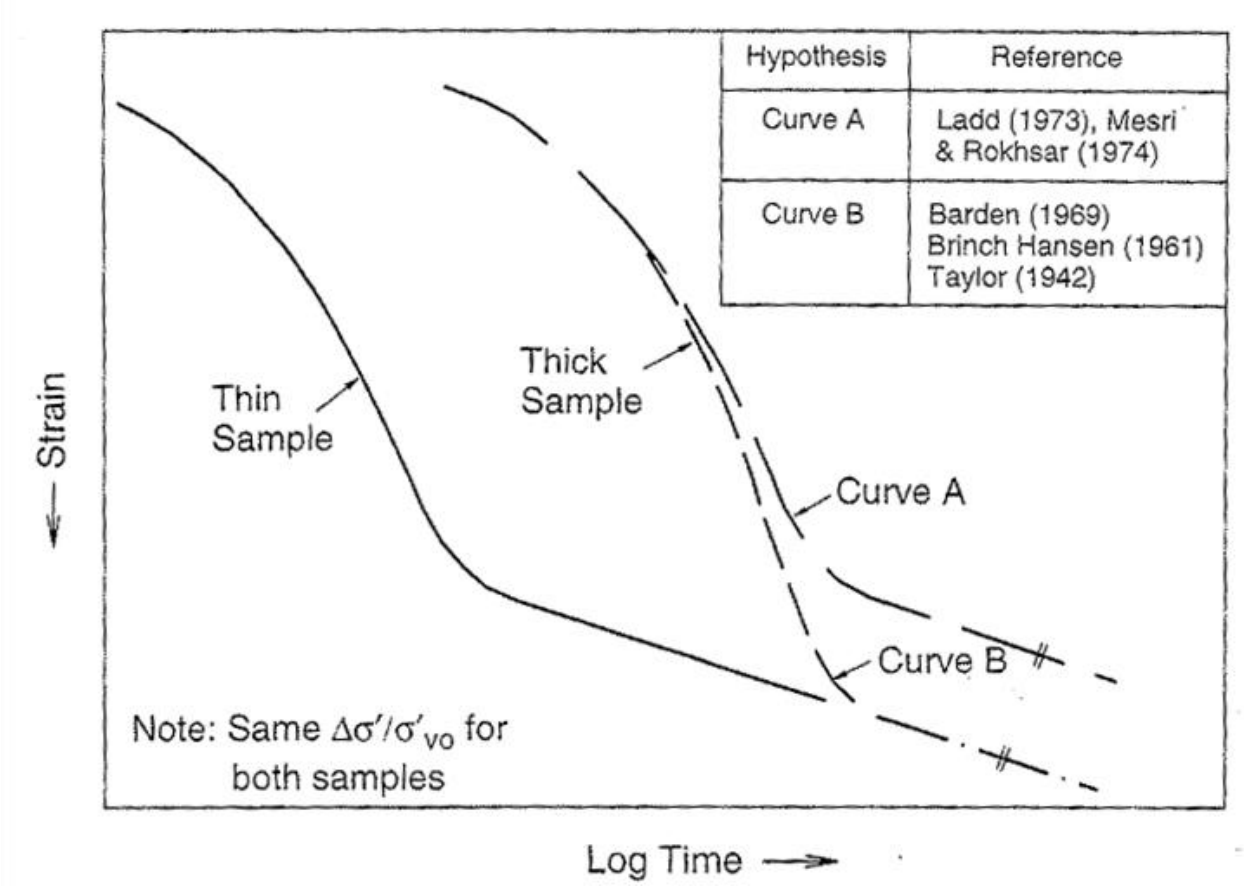

Figure 1-1 Two extremes for the effect of sample thickness (Ladd et al., 1977).

CHAPTER 2 GEOLOGIC HISTORY OF OSAKA BAY

2.1 Introduction

Osaka Bay, located in the western part of Osaka Basin at the eastern end of the Seto Inland Sea in Southwest Japan, is bordered by the Rokko Mountains to the north, the Ikoma and the Kongo Mountains to the east, and the Izumi Mountains to the south (Figure 2-1). Osaka Basin is one of several ellipsoidal basins in Southwest Japan that formed as a result of crustal stresses caused by the oblique subduction of the Philippine Sea Plate beneath the Eurasian Plate (Huzita, 1962; Yamasaki and Nakada, 1996; Itoh et al., 2000; Inoue et al., 2003). The subseabed profile and the lateral variation of thickness for individual layer formations within Osaka Bay are a result of tectonic activity and changes of relative sea level that have occurred during the late Cenezoic Era.

2.2 Formation of Osaka Basin

The formation of sedimentary basins in Southwest Japan began as a result of crustal movements that started in the middle Miocene Epoch. Initially, movements were primarily in a north-south direction as evidenced by uplifted and depressed provinces including the Setouti Province of Depression where the Osaka Basin is located (Figure 2-2). Relative movement between the subducting Philippine Sea Plate and the Eurasian Plate shifted to the northwest-southeast beginning in the Pliocene Epoch. This shift in movement has had a significant impact on crustal deformation since the middle Pleistocene Epoch at the culmination of the Rokko Movement when the anticlinal part of foundation folding fractured, many thrusts appeared as shear planes, and wedge-shaped rock bodies were pushed up (see Rokko Mountains in Figure 2-1). The cumulating effect of these movements was formation of ellipsoidal basins bordered by short and narrow mountain ranges (Huzita, 1962).

The Rokko Movement is responsible for much of the topography within the Kinki Triangle Tectonic Region. The Kinki Triangle is located in the central part of the Setouti Province of Depression and is bordered by Wakasa Bay, Osaka Bay, and Ise Bay. There are four main fault trends within the region. Three sets are parallel to the respective sides of the triangle and the fourth set is perpendicular to the base which coincides with the Median Tectonic Line (Huzita, 1962). Locally, Osaka Basin is surrounded by the Median Tectonic Line, the

Awaji-Rokko Fault System, the Arima-Takatsuki Tectonic Line, the Ikoma Fault, and the Kongo Fault (Figure 2-3). The Awaji-Rokko Fault System, Arima-Takatsuki Tectonic Line and Median Tectonic Line are right-lateral strike slip fault systems. The Kongo Fault and Ikoma Fault are thrust faults. Part of the Awaji-Rokko Fault system caused the Hyogo-ken Nanbu Earthquake in 1995 (Itoh et al., 2000).

2.3 Basement rock and stratigraphy

Itihara et al. (1975) reported the results of a geologic survey area extending from Sakai City southwestward to Misaki Town and from Osaka Bay southward to the Izumi Ranges (Figure 2-4). Basement rocks crop out in the surveyed area and include Ryoke Granite (Paleozoic to Mesozoic), Sennan Acidic Pyroclasts (early to late Cretaceous), the Izumi Group (latest Cretaceous), the Kannabi Formation (Miocene), and Nabeyama basalt (Miocene to Pliocene). Figure 2-5 (a, b, c, and d) shows the distribution of the basement rocks within the surveyed area. In addition to the basement rocks south of Osaka Bay, Mesozoic Ryoke granodiorites are well exposed in the Ikoma Range east of Osaka and in Awaji Island to the west (Ikebe et al., 1970).

The maximum depth to bedrock in Osaka Bay is more than 3000m near the Osaka-Wan Fault towards the center of the bay as shown in Figure 2-6 (Kagawa et al., 2004).

Bedrock is overlain unconformably by freshwater sediments in nearly all parts of Osaka Basin. Figure 2-7 shows subsurface profiles for borings OD-1 and OD-2 located just east of Osaka Bay (see Figure 2-6 for location). Boring OD-2 shows decomposed and disintergrated diorite at a depth of 656m overlain by the Kobe Group, Infra-Osaka Group, Osaka Group, Upper Pleistocene, and recent Alluvium (Ikebe et al., 1970).

The Kobe Group (440 to 656m depth in boring OD-2) is exposed in Kobe north of Osaka Bay, and consists of conglomerates, sandstones, mudstones, and vitric tuffites. The vitric tuffites contain abundant plant fossils that are middle Miocene age.

The Infra-Osaka Group, also refered to as the upper Nijo Group, is evident in borings OD-1 and OD-2 and consists of sands interbedded with consolidated claystones (Ikebe et al., 1970).

The Osaka Group contains freshwater gravel, sand, silt, and clay deposits interbedded with marine clay deposits (designated Ma0 to Ma10) as well as volcanic ash beds. Osaka Basin began to subside and accumulate the lower part of the Osaka Group at the close of the Pliocene.

The lowermost portion of the Osaka Group is dominated by freshwater deposits (Huzita, 1962; Ikebe et al., 1970; Itihara et al., 1975) and overlays Mesozoic basement rock unconformably in nearly all parts of the marginal areas of Osaka Basin (Ikebe et al., 1970). This has been confirmed in the area south of Osaka Bay (Itihara et al., 1975).

Upper Pleistocene deposits include marine clay layers with designation Ma11 and Ma12 as well as sand and gravel deposits (Ikebe et al., 1970). Upper Pleistocene deposits are overlain by Holocene deposits. The Holocene marine clay layer Ma13 is currently being deposited in Osaka Bay.

2.4 Subseabed profile at the Kansai International Airport site

Figure 2-8 shows the subseabed profile at the Kansai International Airport site located in the southern portion of Osaka Bay (see Figure 2-6 for location of the Kansai Airport Islands). The profile includes Pleistocene marine clay layers from the Osaka Group (Ma0 to Ma10) as well as the Upper Pleistocene (Ma11L to Ma12) and recent Holocene (Ma13) marine deposits. Marine clay layers alternate with sand (Ds) and non-marine clay (Doc and NMC) layers as well as very thin volcanic ash deposits (not shown in Figure 2-8). Marine clay layers are distinguishable from non-marine clay layers because of the presence of nannoplankton and foraminifera calcareous fossils. The layer Dtc was determined to be a shallow marine clay layer because it lacks these nannofossils (Itoh et al., 2001). Freshwater clays contain fossils of the same mollusca that currently live in Lake Biwa which is located just to the northeast of Osaka Bay (Ikebe et al., 1970). The non-marine clay layer Doc5 was deposited in a lacustrine environment, known as paleo-Lake Senshu, 0.5 to 0.4 million years before present when sediments were dammed as a result of crustal warping in the southern portion of Osaka Basin (Itoh et al., 2001).

Depositional environments for the sand layers present at the Kansai Airport site include river floor and flood plain environments (Ds1, Ds3, Ds5, Ds6, Ds7, Ds8, Ds9, and Ds10) as well as marine sand bar environments at low sea level (Ds2). Sand layers Ds1 and Ds10 are widely distributed throughout Osaka Bay (Takemura and Nakaseko, 2005).

The alternating sequence of marine clay and freshwater deposits is a result of a lateral migration of depositional environment caused by changes in sea level. Marine clay layers correspond to warm global climates when sea levels were relatively high while non-marine clay

and sand layers correspond to cold global climates when sea levels were relatively low. Cold climates correspond to sea level lows because large volumes of water are stored as glacial ice on the continents (Ikebe et al., 1970; Itihara et al., 1975; Takatsugi and Hyodo, 1995; Yamasaki and Nakada, 1996; Biswas et al., 1999; Itoh et al., 2000, 2001; Takemura and Nakaseko, 2005). The correlation of marine and non-marine layers to climate has been confirmed by pollen analyses. Marine clay layers contain larger amounts of broad-leaf tree pollen (Quercus and Fagus) indicating a warm climate while freshwater sediments contain larger amounts of coniferous pollen (Picea and Tsuga) indicating a cold climate (Takatsugi and Hyodo, 1995).

The correlation of marine and non-marine layers to climate and sea level has also been confirmed by oxygen isotope records. The ratios of oxygen isotopes ^{18}O and ^{16}O give an indication of ancient water temperature because large amounts of ^{16}O are stored in ice during glacial episodes and are therefore diminished in freshwater soil layers (Harmon, 1961; Takatsugi and Hyodo, 1995; Itoh et al., 2000; Inoue et al., 2003).

The water-holding capacity, as evidenced by liquid limit, within individual marine clay layers provides additional evidence for the rise and fall of sea level. Many of the marine clay layers (e.g. Ma10, Ma9, Ma8, and Ma7) have lower reported liquid limit values near their upper and lower boundaries with the highest liquid limit values near the center of the layer. For example, Figure 2-9 shows the plastic limit (w_p), liquid limit (w_l), and natural water content (w_o) with respect to the ratio of depth into the layer (z) divided by layer thickness (L_o) for marine clay layer Ma10 at the Kansai Airport site. Prior to deposition of Ma10, the sand layer Ds6 was deposited in a floodplain environment at low sea level. As sea level rose, eventually covering the area currently occupied by the Kansai Airport Islands, marine clay was deposited. However, the sediment-carrying rivers and estuaries remained relatively close so that very small, clay particles were deposited with coarser materials. As sea level continued to rise, the distance from the Kansai Airport site to the mouth of the sediment-carrying rivers increased and only small clay particles were deposited (i.e. only small clay particles can travel a significant distance in relatively calm waters). When the sea level fell again, the process was reversed until eventually a floodplain environment existed and deposition of the sand layer Ds5 commenced.

2.5 Lateral correlation of geologic layers

Lateral continuity of each Pleistocene layer from different boreholes was established

using a combination of tephrochronology, magnetostratigraphy, and micropaleontology as well as oxygen isotope and pollen analyses previously described.

Tephrochronology uses layers of volcanic ash to create a chronological framework. The age of the Osaka Group sediments is constrained by more than 50 volcanic ash layers (Inoue et al., 2003). At the Kansai Airport site, the Pink volcanic ash layer ($1.0x10^6$ years before present found between Ma1 and Ma2), Azuki volcanic ash layer ($8.5x10^5$ years before present found in the lower portion of Ma3), Kkt ($3x10^5$ years before present found in Ma10), Ata-Th ($2.3x10^5$ to $2.5x10^5$ years before present found in Ma11), At ($2.0x10^4$ to $2.5x10^4$ years before present found in Ds1), and K-Ah ($6.3x10^3$ years before present found in Ma13) were used to correlate stratigraphy. The location of the volcanic ash deposits within the subseabed profile as well as the geologic age before present is shown in Figure 2-10 (Nakaseko et al., 1984; Itoh et al., 2001). The Azuki volcanic ash layer was particularly useful. The dominant heavy minerals within the Azuki layer include orthorhombic pyroxene and clinopyroxene (Itihara et al., 1975).

The earth's magnetic field fluctuates directionally. At times, the geomagnetic field can reverse completely while at other times it can exhibit rapid and extreme deviations known as geomagnetic excursions without complete global polarity reversals. During or soon after deposition, magnetic grains in sediments align with the earth's magnetic field. The technique that correlates magnetic direction of sedimented deposits to known geomagnetic reversals and excursions is known as magnetostratigraphy or paleomagnetism. At Osaka Bay, measurements were mainly performed on volcanic ash, fluvial, and lacustrine samples, and the primary magnetic mineral was greigite (Ishida et al., 1969; Takatsugi and Hyodo, 1995; Biswas et al., 1999; Itoh et al., 2000, 2001).

Micropaleontological data is used to determine depositional environment in addition to correlating strata from different boreholes. Microfossils including foraminifer, radiolarian, ostracoda, scale, diatom, sea urchin, sponge spicule, and nannoplankton, were analyzed in the area near the Kansai Airport site. Nannoplanktons, which are marine phytoplankton, were particularly useful. The layers were correlated based on known information regarding the abundance and type of nannoplankton present. For example, 440,000 years before present Pseduomiliana lacunose became extinct and Gephyrocapsa occeanica emerged, and Emiliana huxleyi emerged 270,000 years before present and became prosperous 70,000 years before present (Kanda et al., 1991).

2.6 Lateral distribution of geologic layers in Osaka Bay

The lateral distribution of Pliocene and Pleistocene deposits in Osaka Bay is a direct result of crustal movements driven by interaction of the Eurasian and Philippine Sea Plates. In general, the thickness of individual layer formations increases from the margins of the basin towards the central part of Osaka Bay where the depth to bedrock is nearly 3000m (see Figure 2-6). The depth to bedrock is maximum near the center of Osaka Bay primarily because of subsidence of the footwall of the Osaka-wan Fault (Inoue et al., 2003).

The subsurface structure of the basement rock in the northern part of Osaka Basin is controlled by active faults including the Awaji-Rokko Fault System, the Wada-Misaka Fault, and the Osaka-Wan Fault (Figure 2-3), and layer thicknesses have been controlled by differential subsidence of fault bounded blocks (Itoh et al., 2000; Inoue et al., 2003).

In the southern portion of Osaka Basin, including the Kansai International Airport site, the layer thicknesses follow a northwest homoclinal structure as a result of vertical movements of the Osaka-Wan Fault, and the thicknesses are augmented by crustal warping (Itoh et al., 2001). North-south trending folds developed slowly from 1.0 to 0.4 million years before present; however, there are no major faults near the Kansai Airport site (Inoue et al., 2003).

2.7 Concluding remarks

A combination of north – south crustal movements that began in the middle Miocene Epoch and northwest – southeast crustal movements that began in the Pliocene Epoch were responsible for producing a chain of ellipsoidal basins, including Osaka Basin, in Southwest Japan. The rise and fall of sea level over geologic time in conjunction with these crustal movements and associated basin formation are responsible for the subseabed profile and the lateral variation of thickness for individual layer formations within Osaka Bay.

2.8 Figures

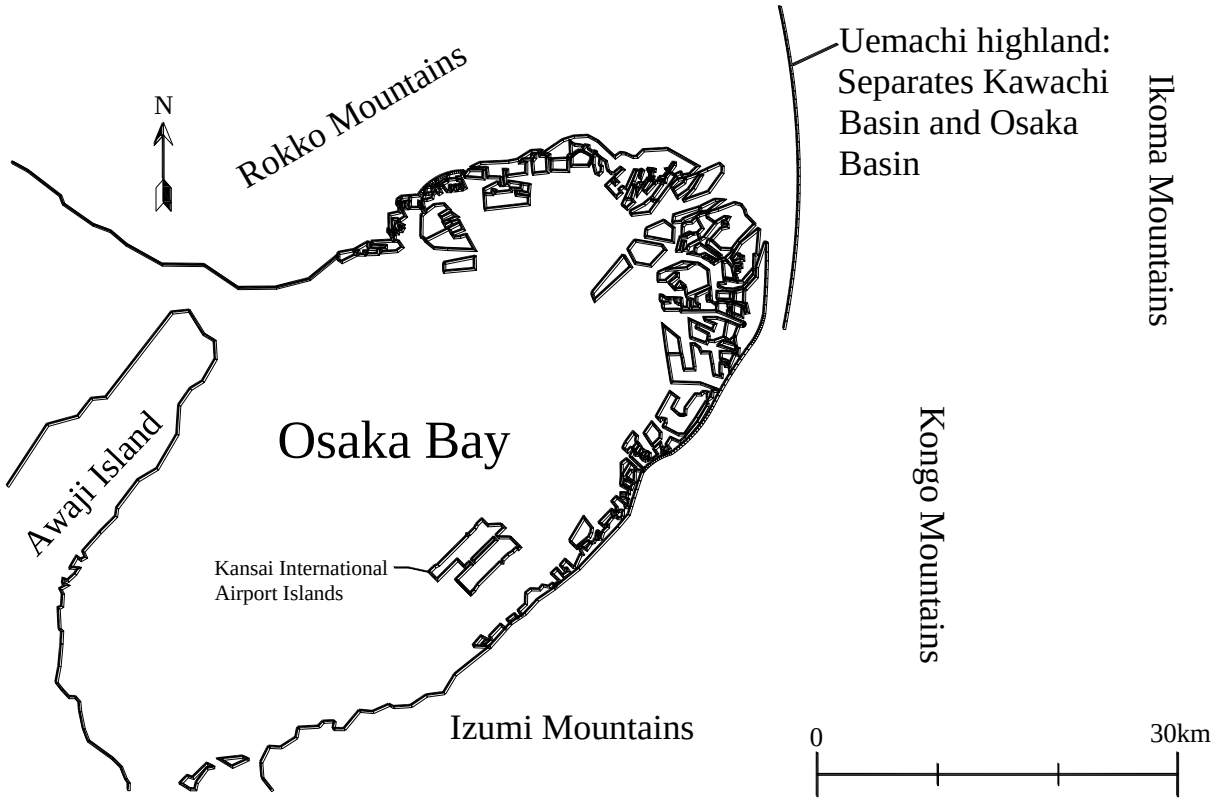

Figure 2-1 Osaka Bay Southwest Japan (Yamasaki and Nakada, 1996).

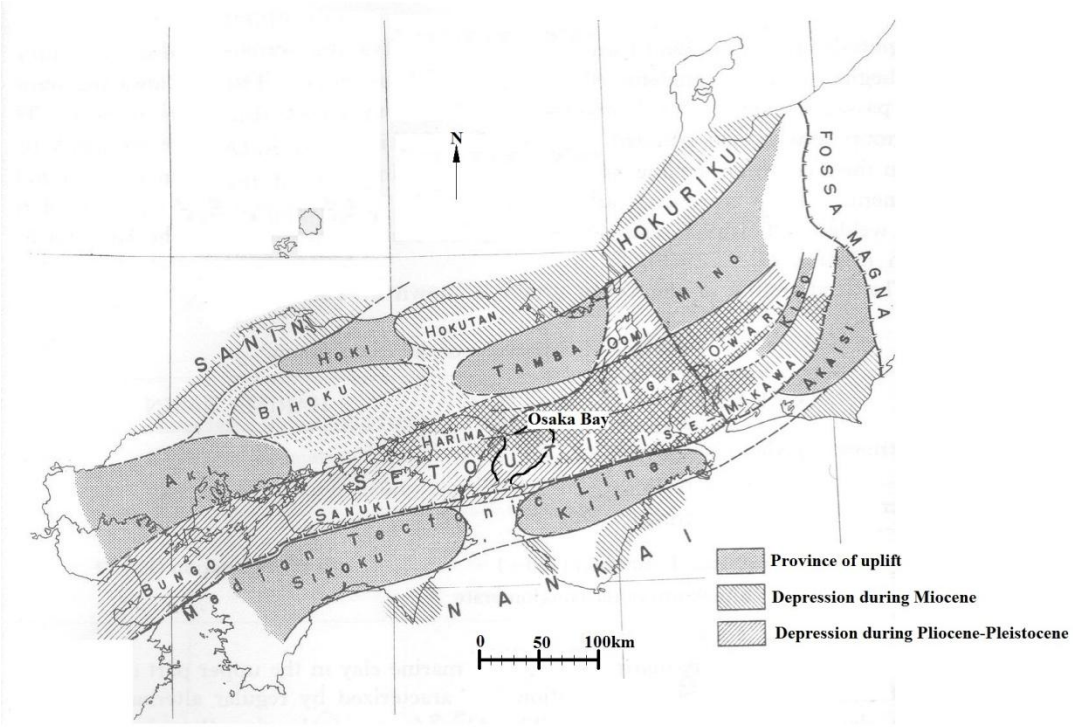

Figure 2-2 Geologic provinces of Japan (Huzita, 1962).

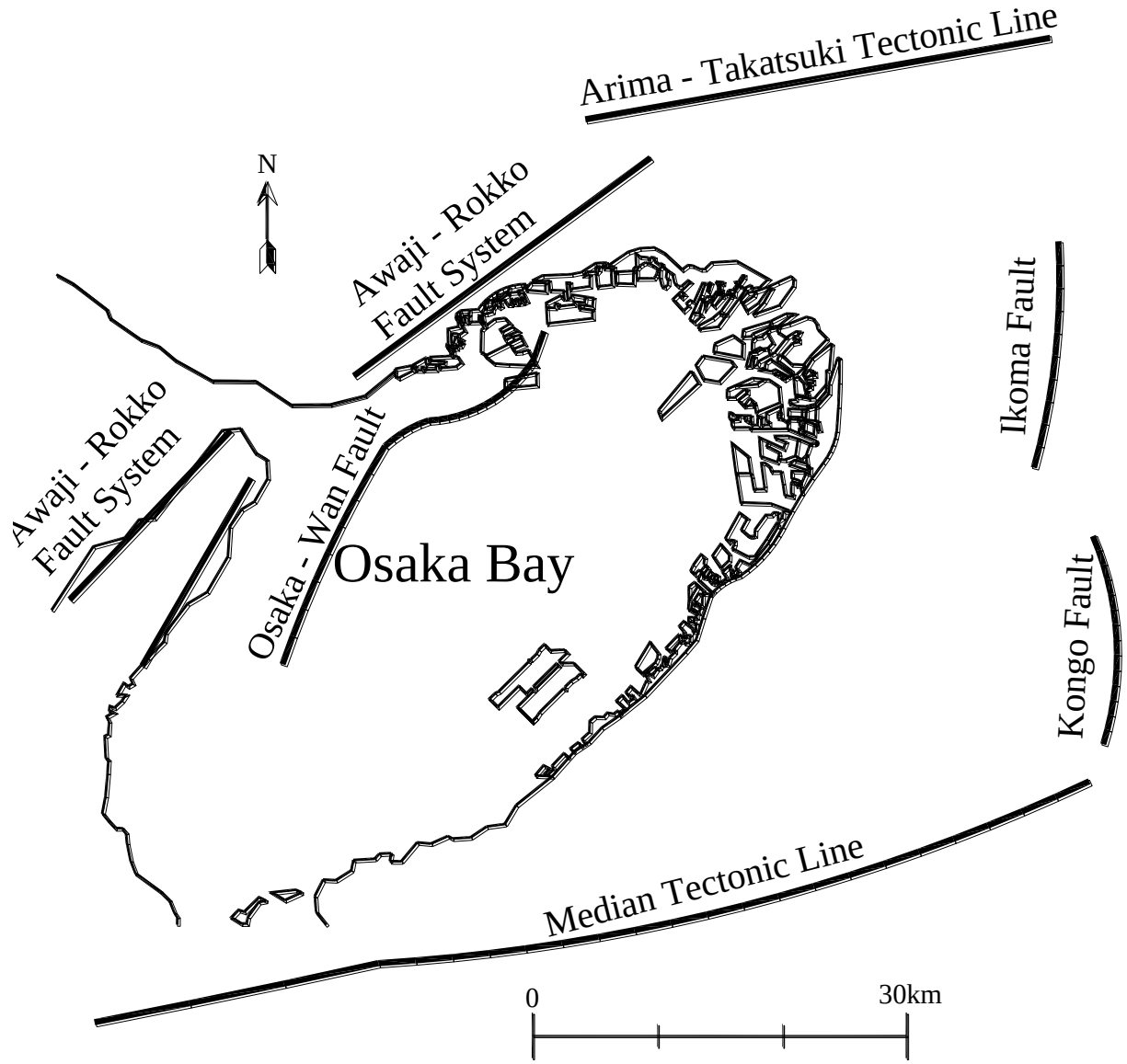

Figure 2-3 Fault systems near Osaka Bay (Itoh et al., 2000).

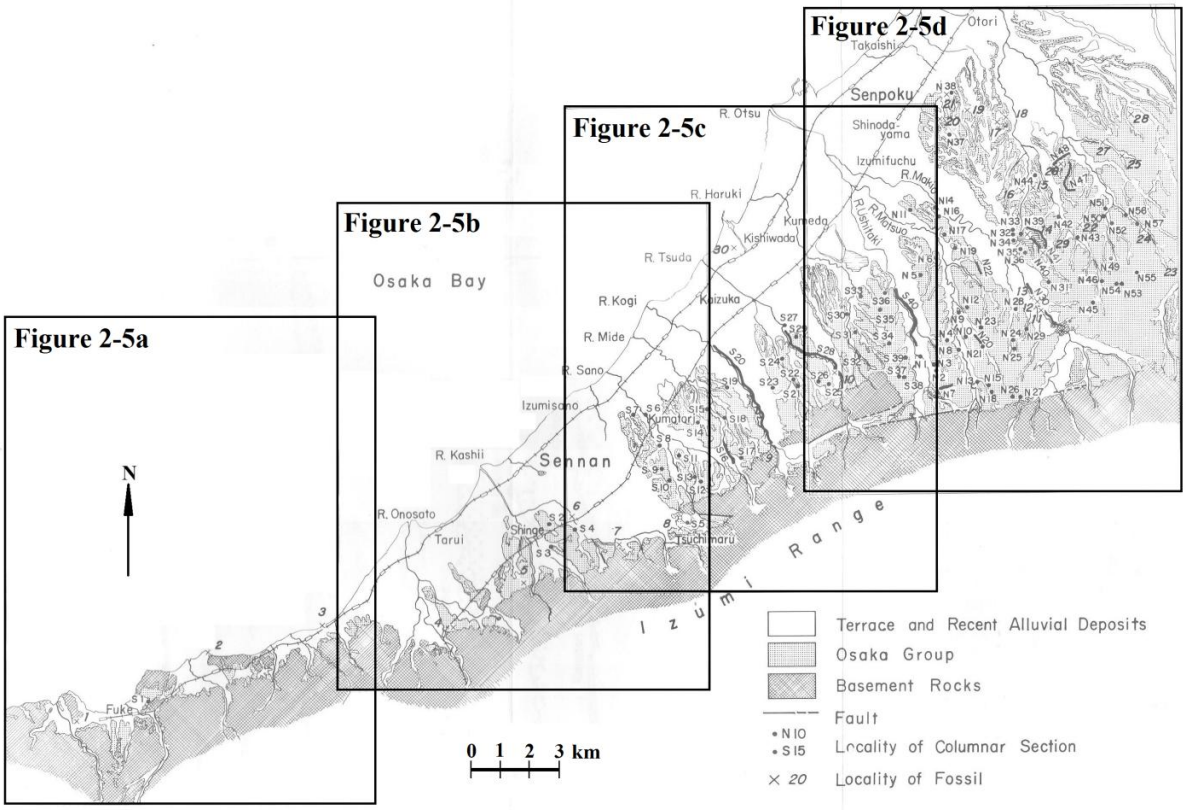

Figure 2-4 Survey area (Itihara et al., 1975).

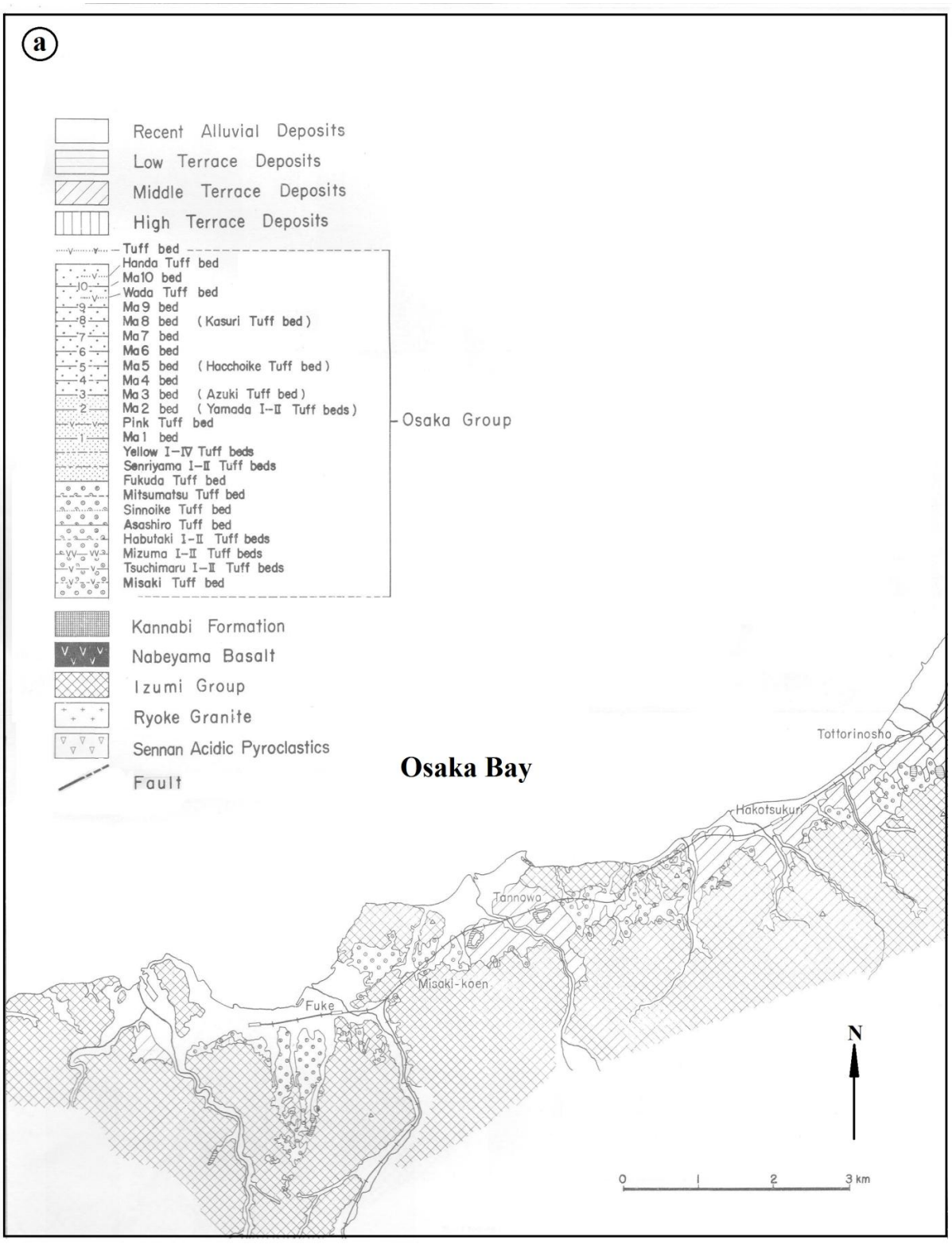

Figure 2-5 Bedrock in area south of Osaka Bay (Itihara et al., 1975).

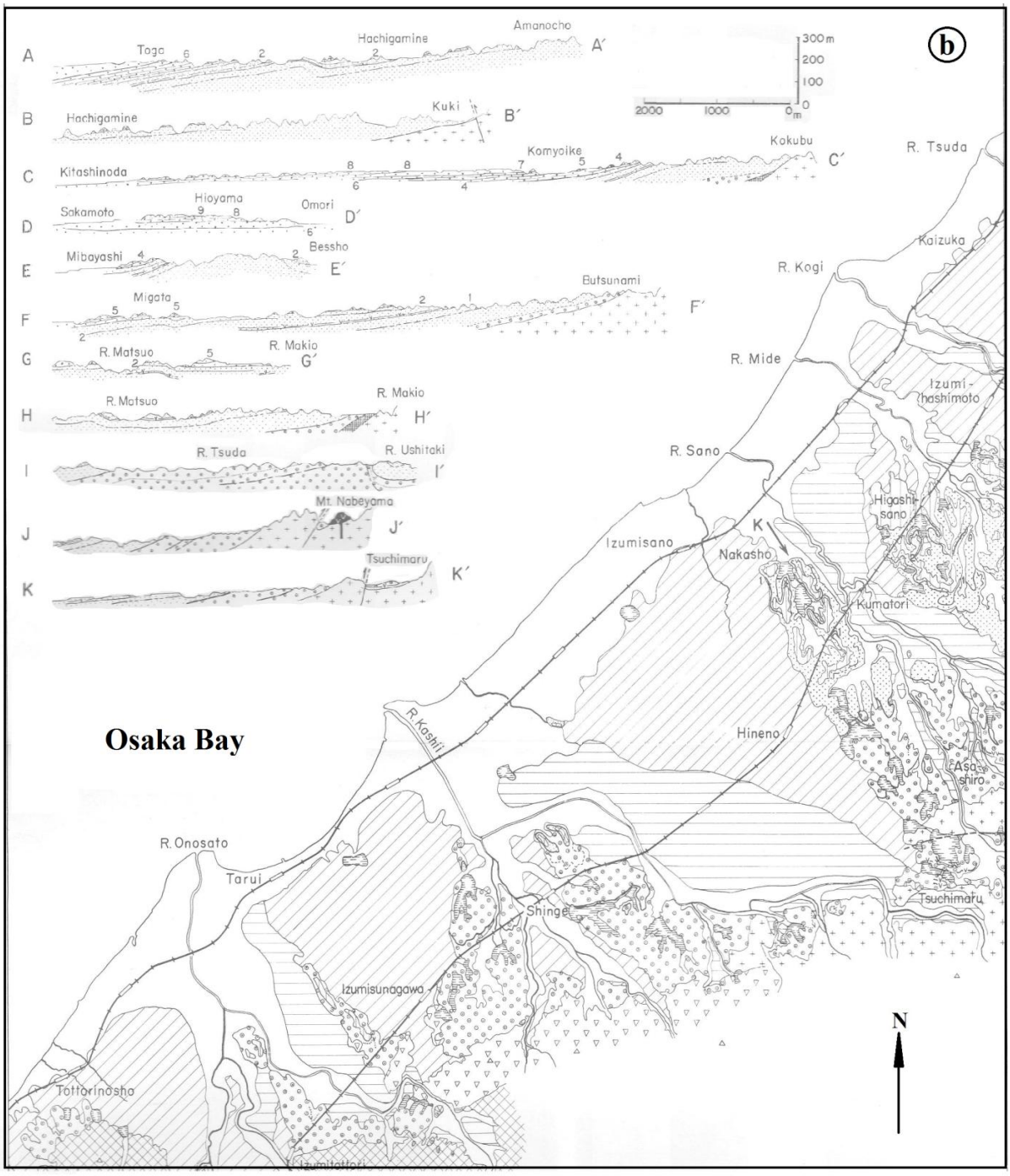

Figure 2-5 cont. Bedrock in area south of Osaka Bay (Itihara et al., 1975).

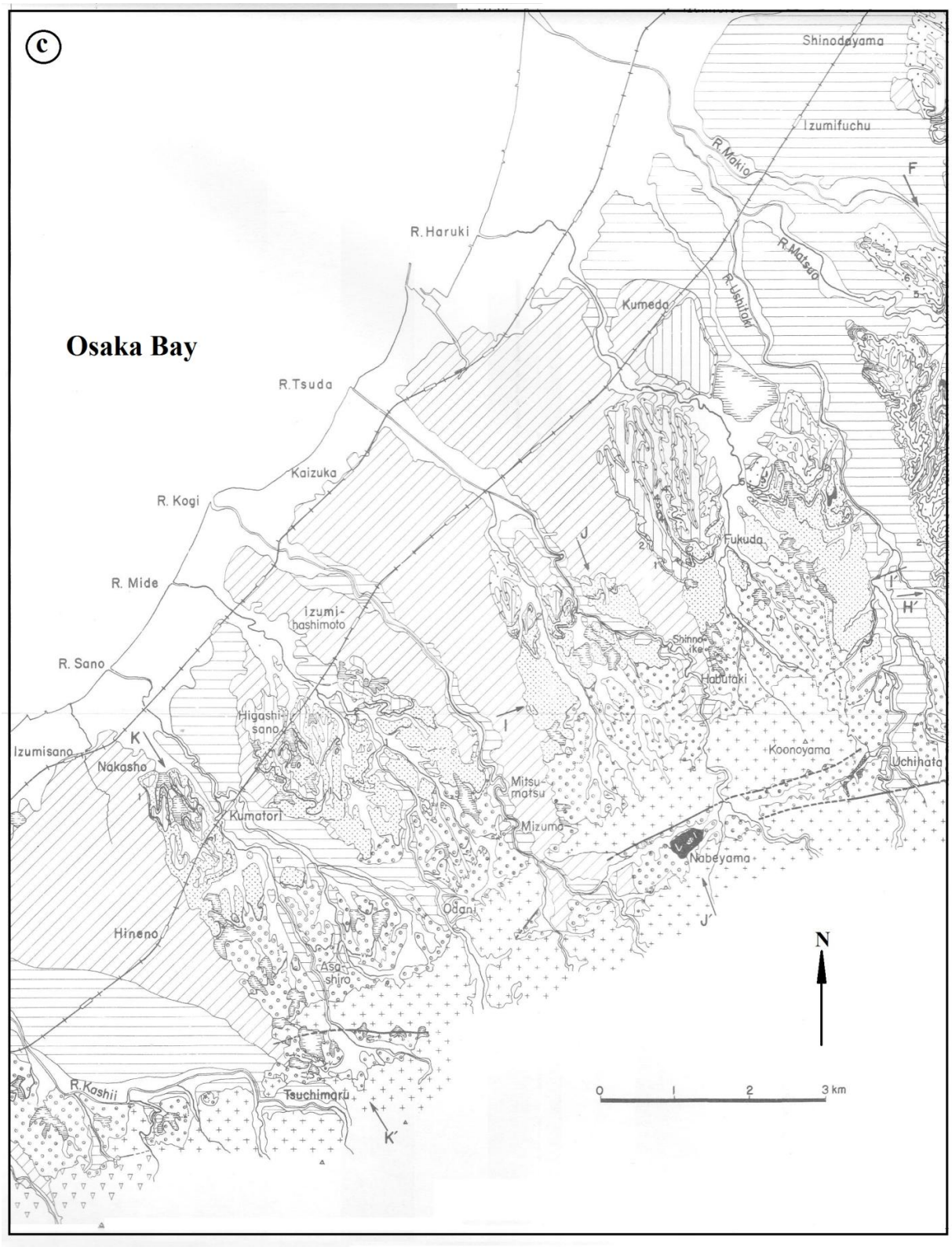

Figure 2-5 cont. Bedrock in area south of Osaka Bay (Itihara et al., 1975).

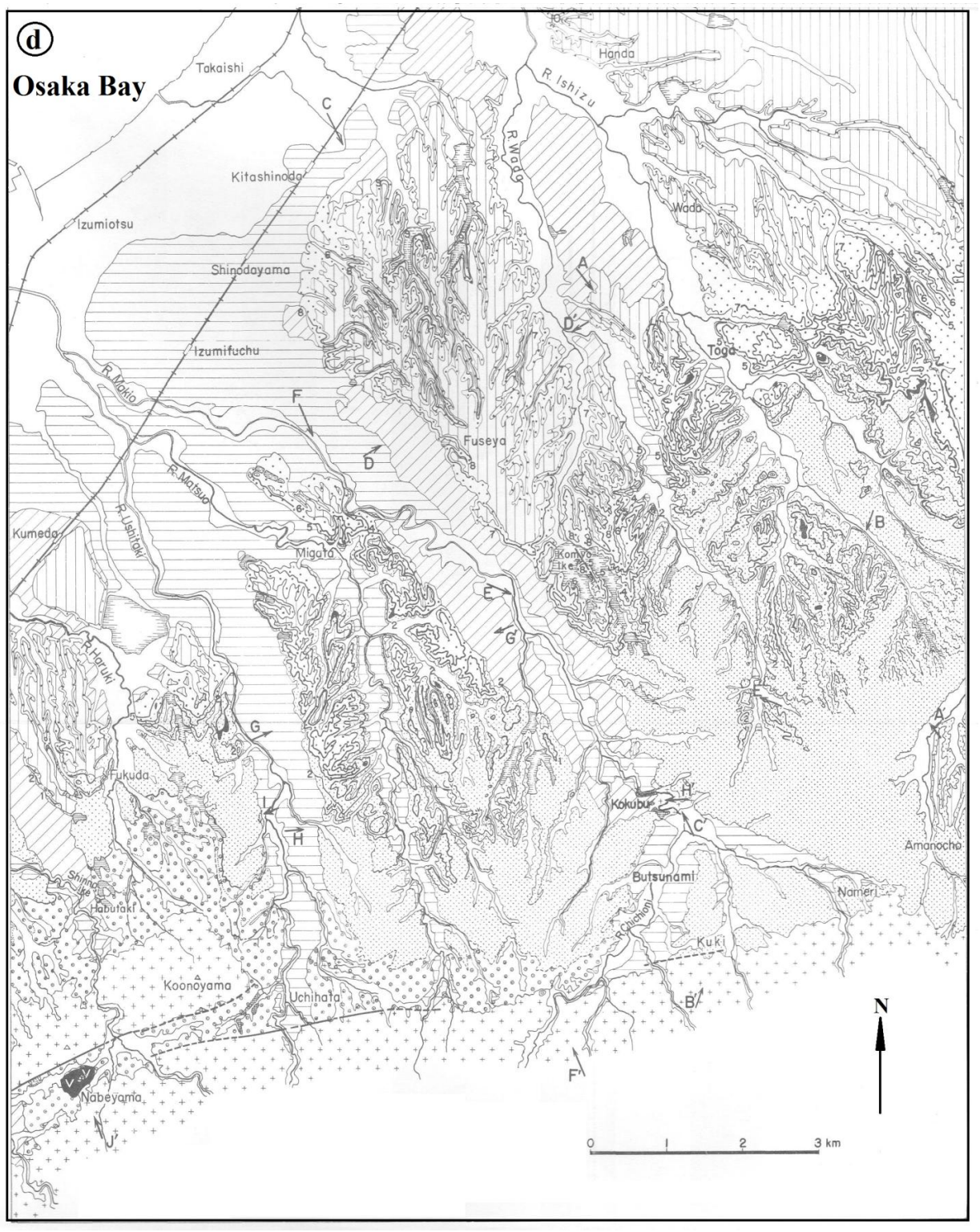

Figure 2-5 cont. Bedrock in area south of Osaka Bay (Itihara et al., 1975).

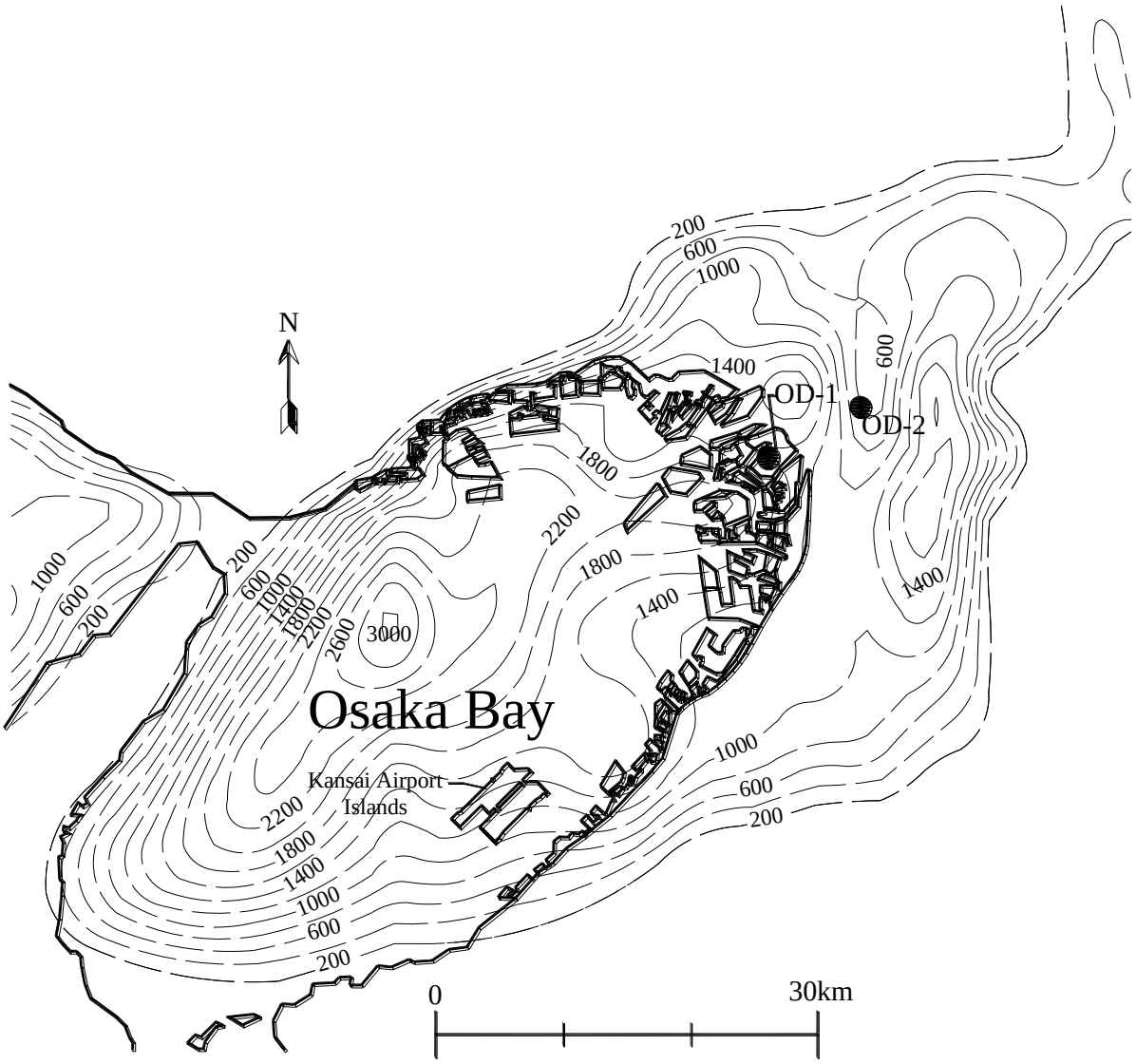

Figure 2-6 Osaka Bay (Mikasa and Ohnishi, 1981; Yamasaki and Nakada, 1996; Sekiguchi and Aksornkoae, 2008) together with depth to bedrock contours in meters (Kagawa et al., 2004).

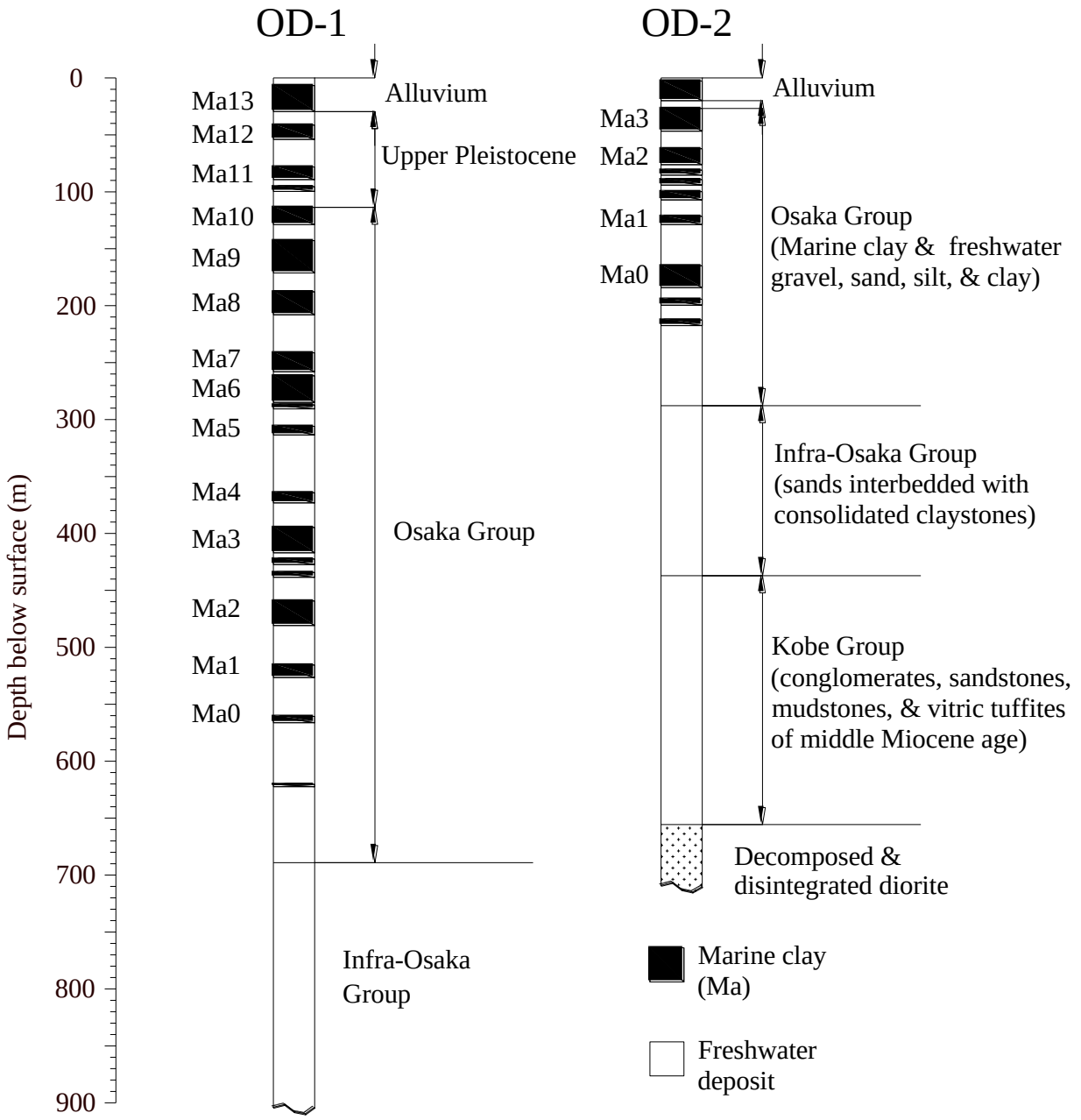

Figure 2-7 Subsurface profiles for borings OD-1 and OD-2 (Boring OD-2 is onshore) (Ikebe et al., 1970).

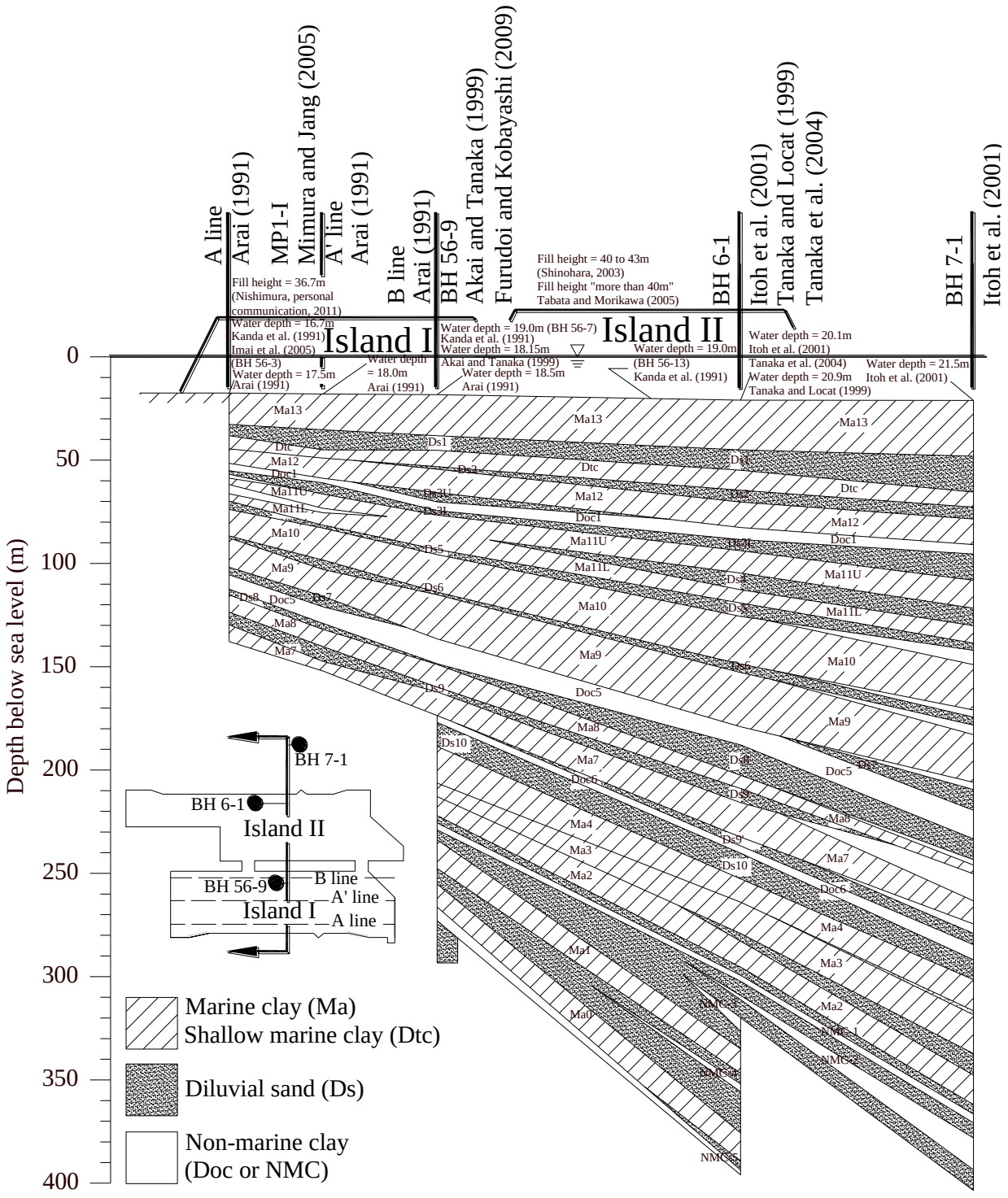

Figure 2-8 Subseabed profile at the Kansai International Airport site (10 to 1 vertical to horizontal exaggeration).

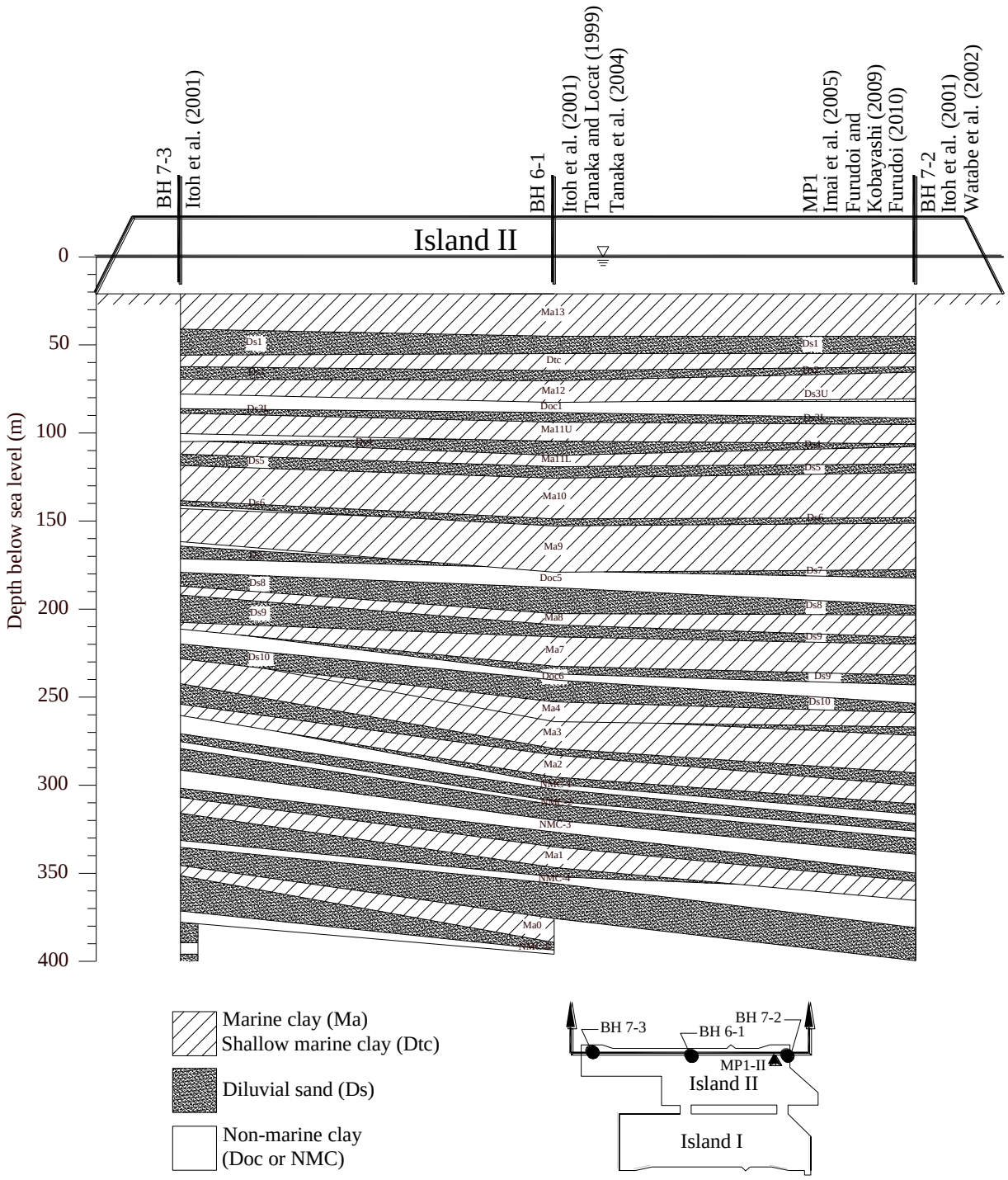

Figure 2-8 cont. Subseabed profile at the Kansai International Airport site (10 to 1 vertical to horizontal exaggeration).

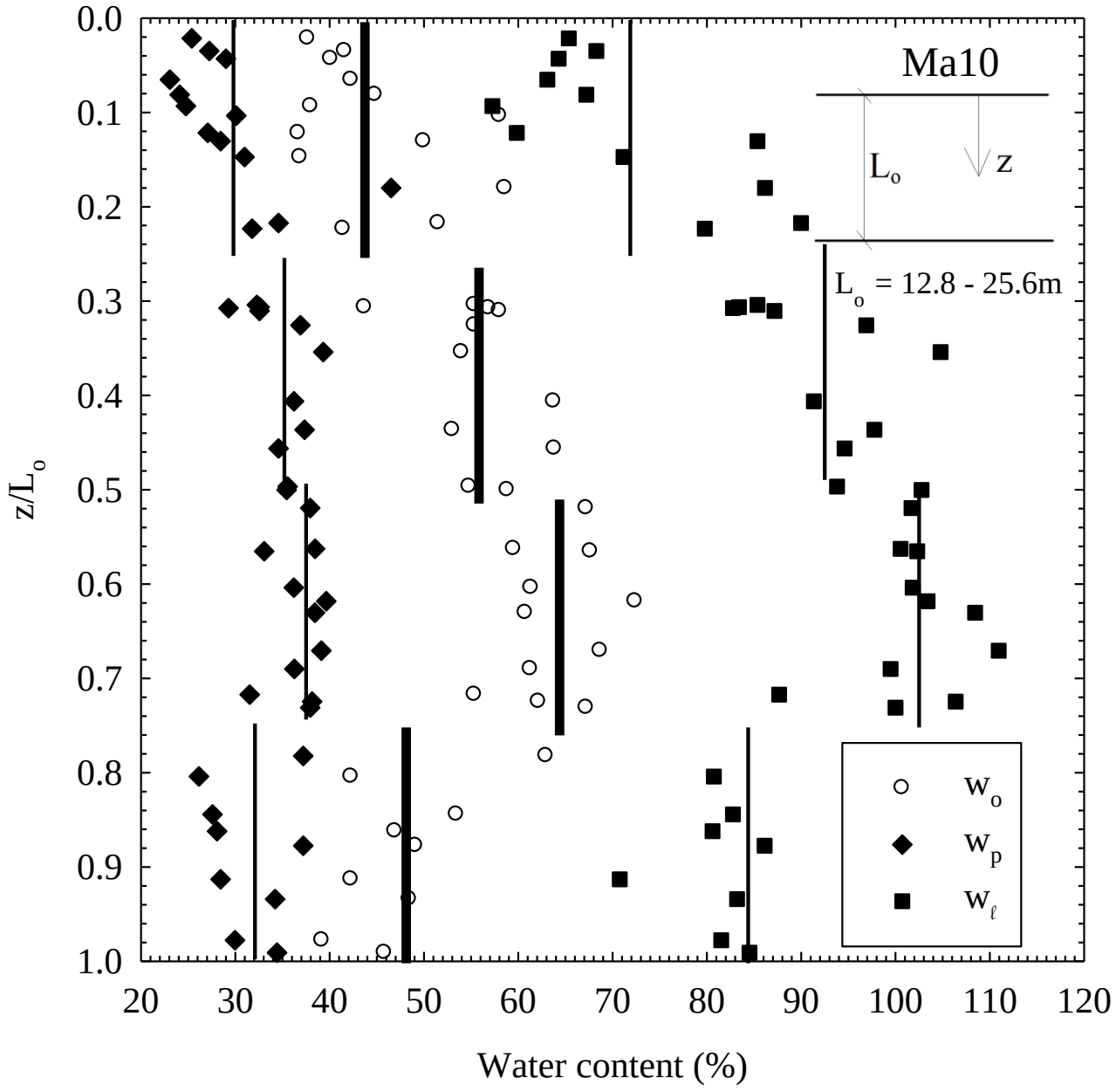

Figure 2-9 Plastic limit (w_p), liquid limit (w_l), and natural water content (w_o) for marine clay layer Ma10 at the Kansai Airport site. Data from Akai and Tanaka (1999), Tanaka and Locat (1999), Watabe et al. (2002), Tanaka et al. (2004), and Imai et al. (2005).

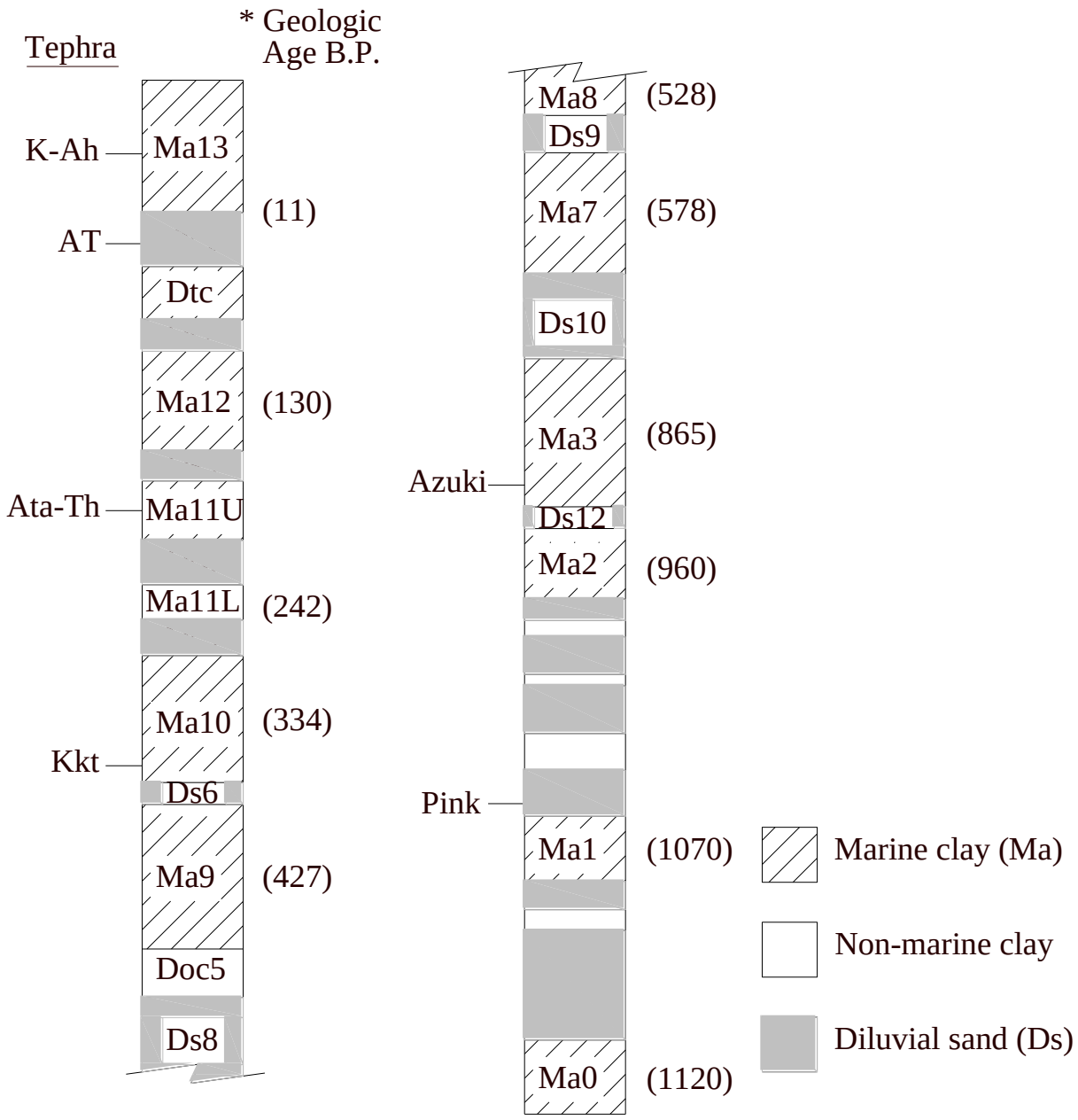

Figure 2-10 Location of volcanic ash deposits (tephra) and age of deposits (Values in parentheses represent geologic age in 1000's of years before present).

CHAPTER 3 RECLAMATION PROJECTS IN OSAKA BAY

3.1 Introduction

Only about 30% of Japan's land area is available for human activity and the rest consists of uninhabitable mountain terrain. Much of the habitable area consists of flood plains with low-lying marshland and shallow inland seas. In fact, approximately 70% of the population lives within 50 miles of the coast. Therefore, the extensive history of reclamation in Japan stems from a need for additional land in low-lying coastal areas (Sasaki et al., 1987; Vadus, 1991).

Figure 3-1 shows the progression of land reclamation in Osaka Bay. Reclamation began as early as the Edo Era (1600 to 1867) in the Osaka Bay area when reclamation fill was made available as a result of the excavation of canals. The earliest reclaimed lands were constructed adjacent to the Yodo River and Yamato River deltas and were primarily used for rice cultivation (Mikasa and Ohnishi, 1981; Sasaki et al., 1987).

During the Meiji Era (1868 to 1912), Japan adopted modern industry from western cultures. The scarcity of domestic natural resources lead Japanese industries to develop in coastal areas in order to minimize transportation costs. In this context, reclamation was used to increase space for industrial activities and ports and harbors (Sasaki et al., 1987; Rai, 1990).

Large tracts of land were reclaimed in Japan as relatively inexpensive industrial and residential areas after World War II (1939-1945). The increase in reclamation was part of an effort for Japan to be more self-sufficient after the war (Araki and Hoes, 2008).

3.2 Recent developments in Osaka Bay

Two oil crises in the 1970's prompted the economic downturn of heavy industry in the Osaka Bay area. These crises in conjunction with a desire for more residential, commercial, recreational, transportation and communication infrastructure highlighted the need for a shift in future planning of the Osaka Bay area. In response to these changes, the Ports and Harbors Bureau of the Ministry of Transportation of Japan promoted the "Osaka Bay Area Development Project" which emphasized incorporation of people-oriented functions along with improvements in distribution and industry, development of research and technology, improvements in transportation, and promotion of growth in rural areas. Additionally, the Osaka Bay Area

Development Project focused on the decentralization of economic power in Tokyo as well as creating a master plan for the Osaka Bay area while meeting specific needs of local governments (Sasaki et al., 1987; Rai, 1990; Takahashi and Kaneko, 1991).

The Kansai International Airport was constructed to help meet the goals of the Osaka Bay Area Development Project and to make the Kansai Region, which includes cities of Osaka, Kobe, Kyoto, Nara, and Wakayama, a self dependent and international metropolis (Rai, 1990).

3.3 Reclamation projects in Osaka Bay

Many of the reclamation projects in Osaka Bay, excluding the Kansai Airport Islands, are directly associated with ports. Ports in Osaka Bay include: Osaka Port, Kobe Port, Hannan Port, Saakaiizumikita Port, and Amagasaki Nishinomiya Port as shown in Figure 3-1 (Mikasa and Ohnishi, 1981; Sekiguchi and Aksornkoae, 2008). A description of more recent man-made islands constructed in Osaka Port and Kobe Port is provided below. The Izumiotsu and Amagasaki Phoenix Projects sites as well as the Kansai International Airport Islands are also briefly described.

3.3.1 Osaka Port

Excavation of canals and reclamation of sea areas in the Osaka Port area began in the Edo Era after the construction of Osaka Castle in 1583 (Sasaki et al., 1987). As mentioned previously, the earliest reclaimed lands constructed near the Yodo and Yamato Rivers were used for rice cultivation (Mikasa and Ohnishi, 1981). During the 17th and 18th centuries, Osaka Port was already a bustling port serving as the entrance to the rapidly developing City of Osaka. However, it wasn't until 1868 that Osaka Port opened as an international trading port (PHRI, 1994).

Some reclaimed lands in Osaka Port that were originally developed in the 19th century for harbor functions, were transformed into urban areas, and more recent reclamation projects (after World War II) were constructed for urban facilities like residential areas, commercial areas, sites for research and development, and business centers. However, reclaimed land continued to serve port related functions as well (Matsui, 1994; Araki and Hoes, 2008). The four most recent reclaimed islands that make up Osaka Port are: Sakashima, Maishima, Yumeshima, as well as a relatively new island development on the offshore side of Yumeshima (Figure 3-2).

Sakishima, also known as the South Port, is a 1002ha reclamation and its construction began in 1958 (Matsui, 1994; Osaka Municipal Government, 2000; Mimura and Jang, 2005). South Port contains advanced port and distribution facilities as well as an urban environment known as Port Town that includes residential, commercial, and recreational areas (Sasaki et al, 1987).

The North Port includes the 224ha Maishima and the 391ha Yumeshima as well as a 300ha island offshore from Yumeshima. Construction of Maishima and Yumeshima began in 1972 and 1977, respectively (Matsui, 1994; Osaka Municipal Government, 2000; Mimura and Jang, 2005). The reclaimed islands of North Port together with 160ha of South Port known as Cosmosquare make up what is known as Technoport Osaka. Technoport Osaka was meant for facilities related to technological development, international exchange and trade, and information and telecommunications in addition to providing space for residential, commercial, and recreational areas (Sasaki et al., 1987; Rai, 1990; Champion, 1991; Matsui, 1994; PHRI, 1994; Osaka Municipal Government, 2000; Ikeda et al., 2003).

The reclaimed islands in Osaka Port provide a site for final waste disposal in addition to providing additional usable land space. Waste disposal, including clays dredged for moorings and waterways, began in Sakashima in 1958 and continued to 1972, when disposal at the north port began (Sasaki et al., 1987; Matsui, 1994, 2001). Figure 3-2 shows that Maishima and Yumeshima are divided into four main sections that are separated by partition dikes. Section 1 of both islands consists of residues of incinerated domestic waste as well as waste generated from public water and sewerage system facilities. Sections 2 and 3 consist of left over soil from construction work sites as well as dredged soil from rivers and harbor areas. Section 4 of each island was constructed using soil fill and surplus soil from construction work sites. Pump dredgers were used to transport dredged material directly to the site or dredged soil was loaded onto a barge, brought to the site, and then unloaded using ships with discharge pipes (Osaka Municipal Government, 2000).

The new island was constructed primarily because Yumeshima had reached capacity and additional space was required for waste disposal. Osaka Municipal Government (2000) projected that at least part of the island would be set aside for disposal of dredged seabed material.

3.3.2 Kobe Port

Kobe Port has developed from an ancient harbor to a major international port in Japan. It took its first step towards becoming a modern port in 1907 when plans were finalized to construct Shinko Piers 1 through 4 (Figure 3-3). An increase in trade volume brought about by post World War II economic growth lead to construction of the Shinko Higashi and Hyogo Wharves. Construction of the Maya Wharf began in 1959 and continued to 1967 to facilitate exporting with larger vessels and more cargo (Matsui, 1994; Kobe Ports and Harbors Office, 2004).

Construction of the 436ha Port Island Phase 1 began in 1966 and continued to 1981. It was constructed to serve harbor and urban related functions (Iwatani et al., 1991; Koushige et al., 2003; Shigeno et al., 2003; Kobe Ports and Harbors Office, 2004).

Rokko Island was constructed in response to the Port Development Plan for fiscal years 1971 to 1975 which expressed a desire for more modern port facilities integrated with residential areas, offices, business centers, and education facilities (Kobe Ports and Harbors Office, 2004). Construction of the 580ha Rokko Island began in 1972 and reclamation was completed in 1992 (Iwatani, 1991; Matsui, 1994).

Additional port and urban facilities were added through construction of Port Island Phase 2. Construction of the 390ha addition to Port Island began in 1987 and was interrupted by the Hyogoken Nanbu Earthquake in 1995 which caused significant damage to Kobe Port. Much of the reclaimed land at Kobe port suffered liquefaction related failures and there was significant damage to bridge foundation elements and superstructure (Hayashi et al, 2000; Shigeno et al., 2003; Kobe Ports and Harbors Office, 2004; Fujino et al., 2005). The national government conducted restoration works at Kobe Port that lasted two years. Earthquake resistant wharves were constructed at Port Island Phase 2 after the 1995 event (Kobe Ports and Harbors Office, 2004).

Construction of Kobe Airport began in 1999 and was completed in 2006. It has a single runway and handles only domestic flights. There is also a new island development under construction just to the south of Rokko Island (Kobe Ports and Harbors Office, 2004).

Fill material used for construction of the man-made islands in Kobe Port consist primarily of weathered granite derived from the Rokko Mountains (sometimes referred to as masa-do). Other materials used for reclamation include soil derived from the Kobe Group, waste

soil from within the city, and slag (Matsui, 1994; Koushige et al., 2003; Shigeno et al., 2003).

3.3.3 Izumiotsu and Amagasaki Phoenix Project Sites

The Phoenix Project sites were named for the Egyptian myth about a bird that lives for several hundred years, burns itself on a funeral pile, and then rises again for another long life. They were also named after a subtropical plant that belongs to the palm family. The project was started by the Ministry of Health and Welfare and the Ministry of Transportation to provide a final disposal site at sea while producing land to be used for port and urban facilities (Rai, 1990; Iwatani, 1991; Matsui, 1994). Garbage was collected from the greater Osaka Metropolitan area which includes six prefectures (149 cities and towns) and brought to one of two locations: off of Izumiotsu or off of Amagasaki (Figure 3-1) (Rai, 1990; Iwatani, 1991).

The Regional Offshore Improvement Center is responsible for reclamation activities related to the Phoenix Project. Figure 3-4 and Figure 3-5 show the 113ha Amagasaki and 203ha Izumiotsu sites, respectively. Construction of the Amagasaki site began in 1987 and construction of the Izumiotsu site began in 1989 (Matsui, 1994). Each site has two types of disposal area. Cinder, sludge, slag, and domestic waste were disposed in an impermeable area intended to seal and minimize leakage of leachate to the outside. Plastic, rubber, metal, glass, and ceramic are among the materials that were disposed in a solid fill area. Both sites include a wastewater treatment facility (Iwatani, 1991).

The Phoenix Project sites are used for port and urban facilities. A portion of each island was set aside specifically for green space (Iwatani, 1991; Kobe Ports and Harbors Office, 2004).

3.3.4 Kansai International Airport Islands

The Kansai International Airport (Figure 3-6) was constructed as part of an effort to improve the economy of the Kansai Region and to decentralize the economic power of Japan from Tokyo. It was constructed at sea to avoid the type of noise pollution and land acquisition disputes that had been experienced at Itami Airport and Narita Airport (Vadose, 1991; KALD, 2005).

The airport consists of two Islands. Construction of the 511ha Island I began in 1987 and the Island I runway began operation in 1994. Construction of the 545ha Island II began in 1999

and the Island II runway began operation in 2007. Approximately 400 million cubic meters of fill material taken from earth collection sites on Awaji Island as well as Kada and Misaki just south of Osaka Bay was used to construct the airport islands (Nakase, 1987; Arai, 1991; Tabata and Morikawa, 2005; Watabe et al., 2008).

3.4 Concluding remarks

Osaka Bay has an extensive history of reclamation beginning in the Edo Era (1600 to 1867). More recent developments including reclamation projects in Osaka Bay have focused on the incorporation of residential, commercial, recreational, and education facilities with new and existing industrial, distribution, and harbor centers. The Kansai International Airport was constructed as part of a national effort to improve the economy of the Kansai Region and to decentralize the economic power of Japan from the Tokyo area.

3.5 Figures

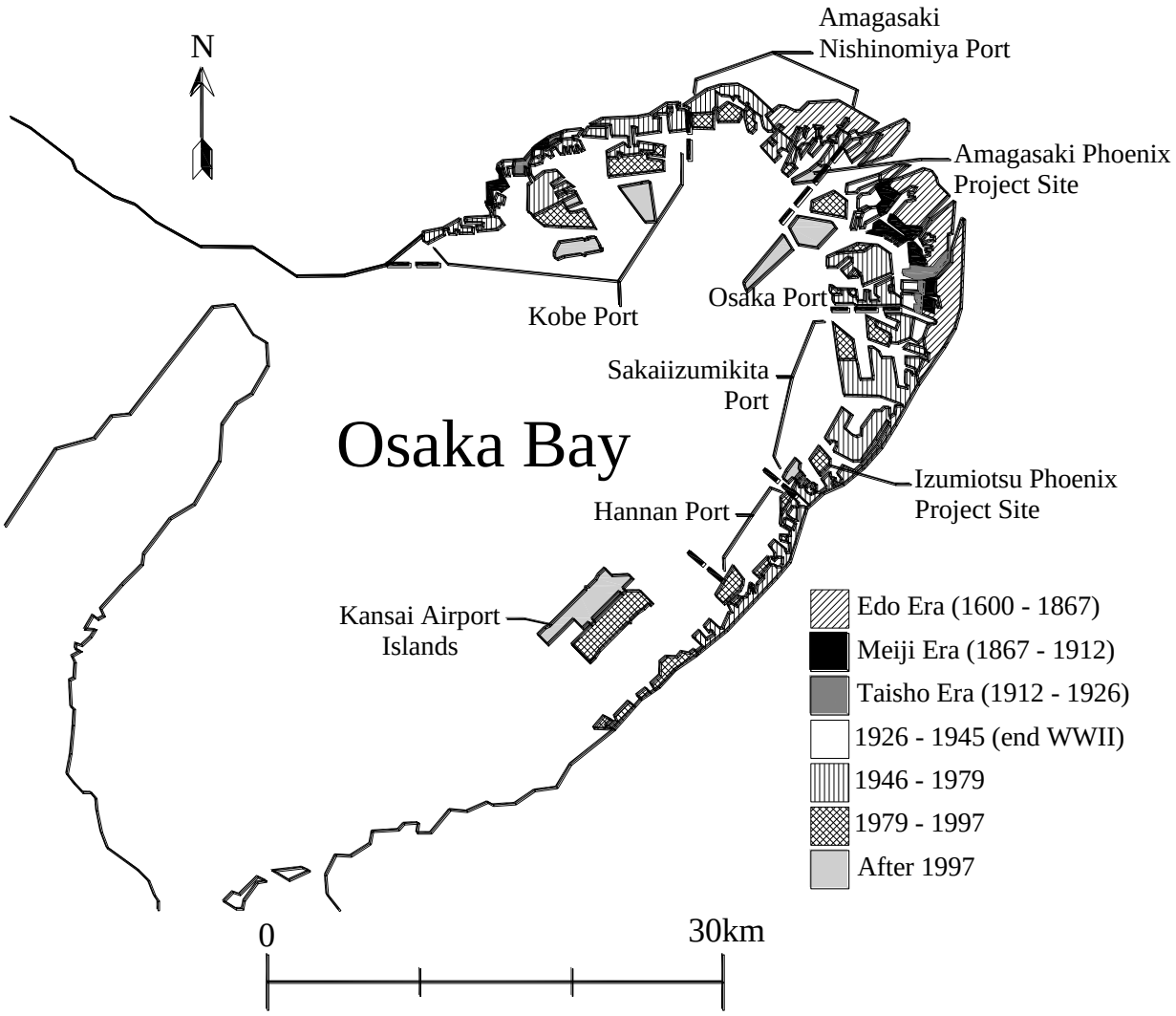

Figure 3-1 History of reclamation in Osaka Bay (Mikasa and Ohnishi, 1981; Sekiguchi and Aksornkoae, 2008).

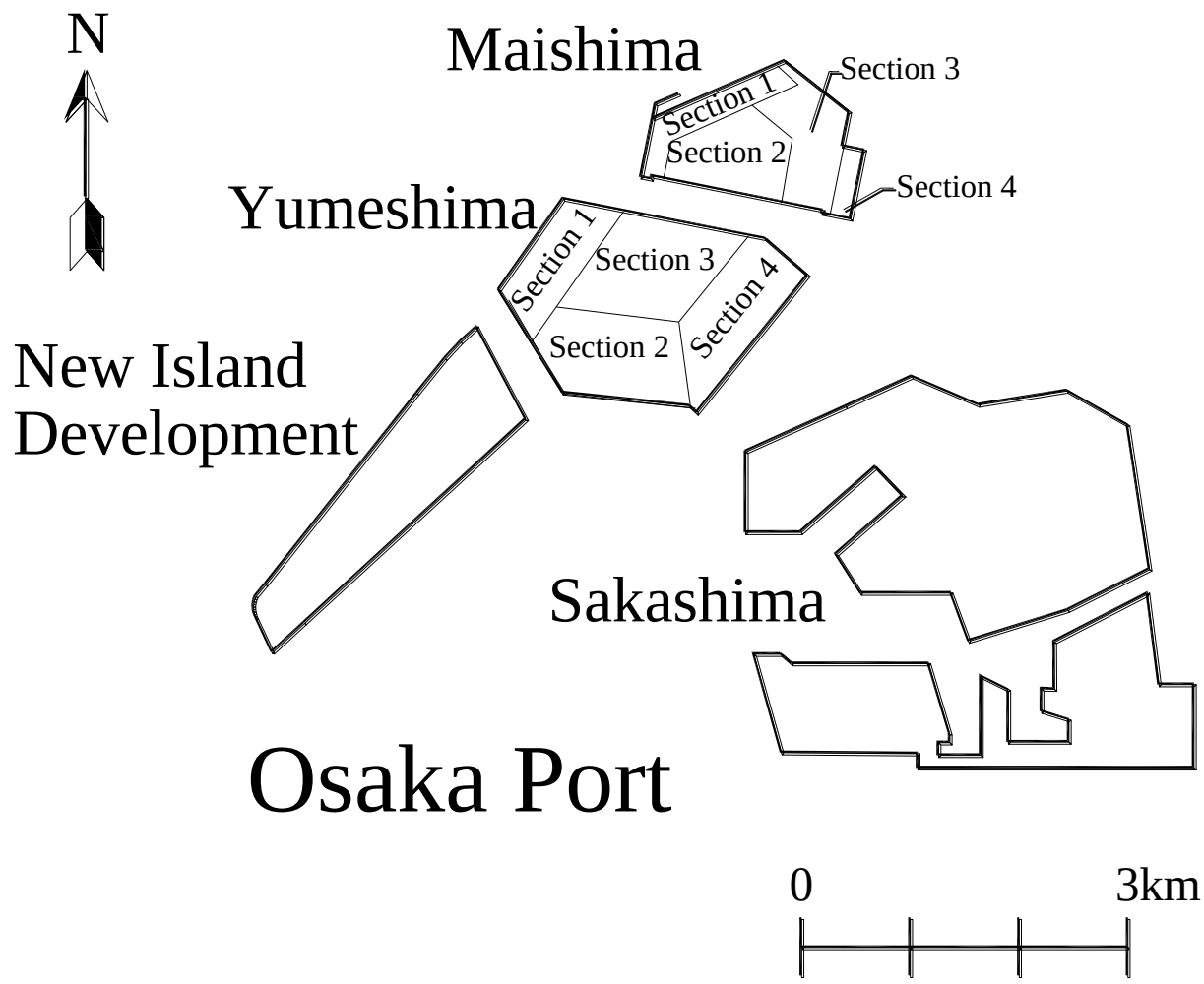

Figure 3-2 Reclaimed islands in Osaka Port.

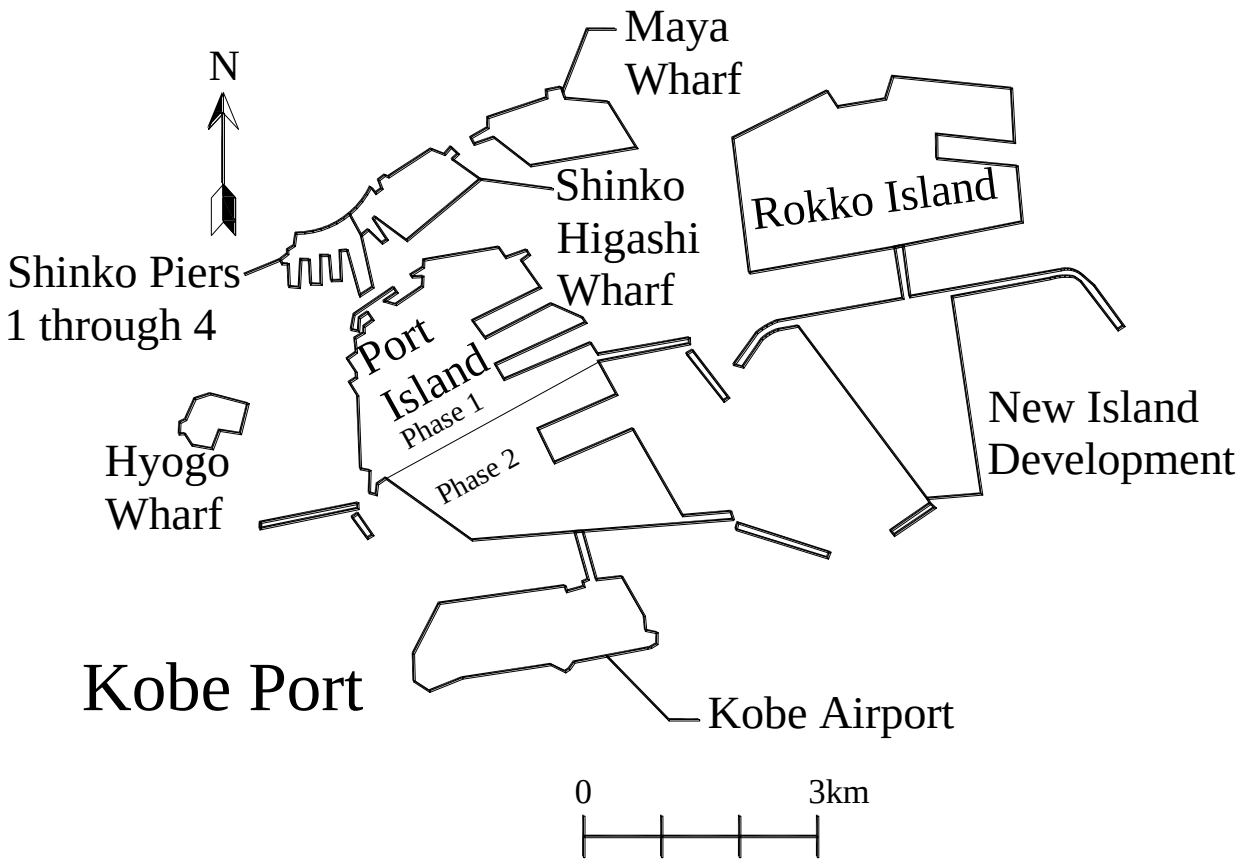

Figure 3-3 Reclaimed islands in Kobe Port.

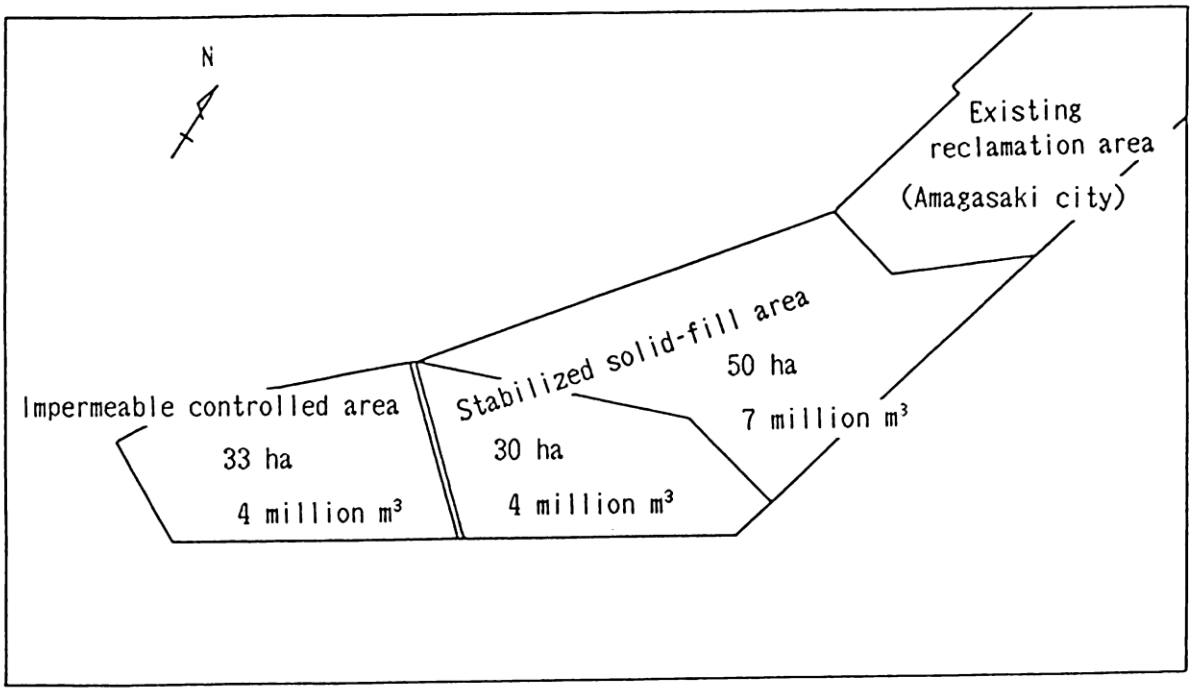

Figure 3-4 Phoenix Project Site off of Amagasaki City (Iwatani, 1991) .

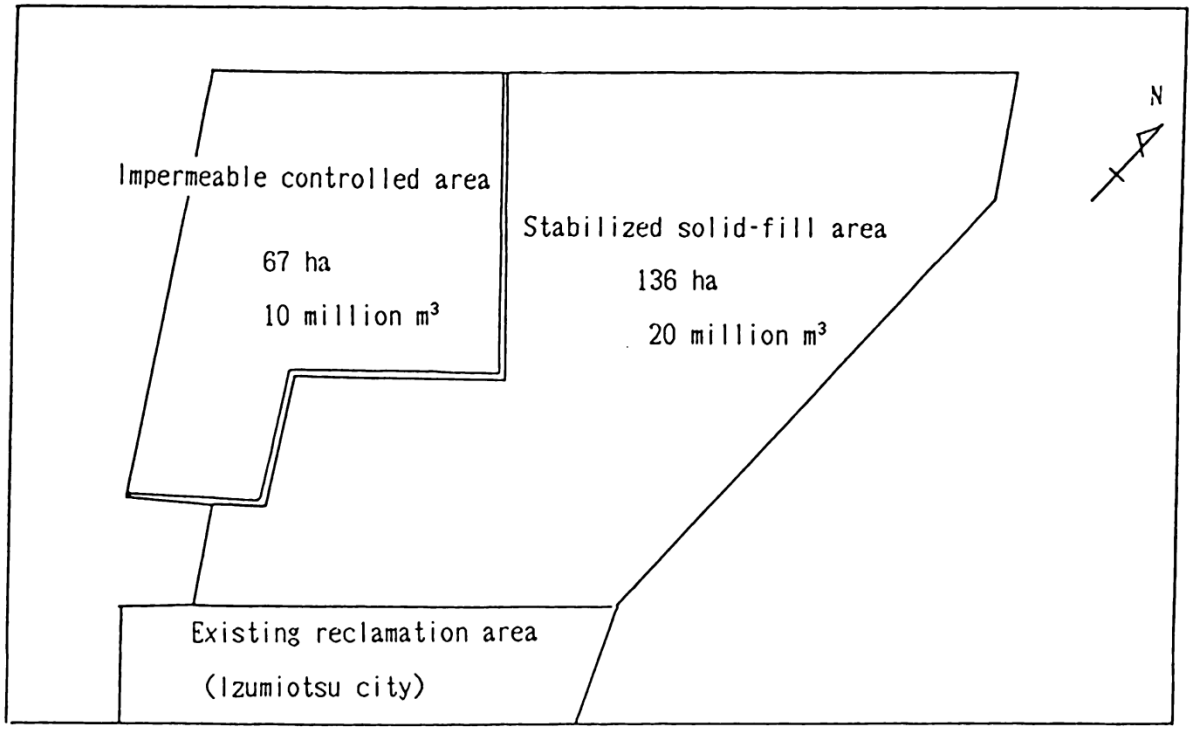

Figure 3-5 Phoenix Project Site off of Izumiotsu City (Iwatani, 1991).

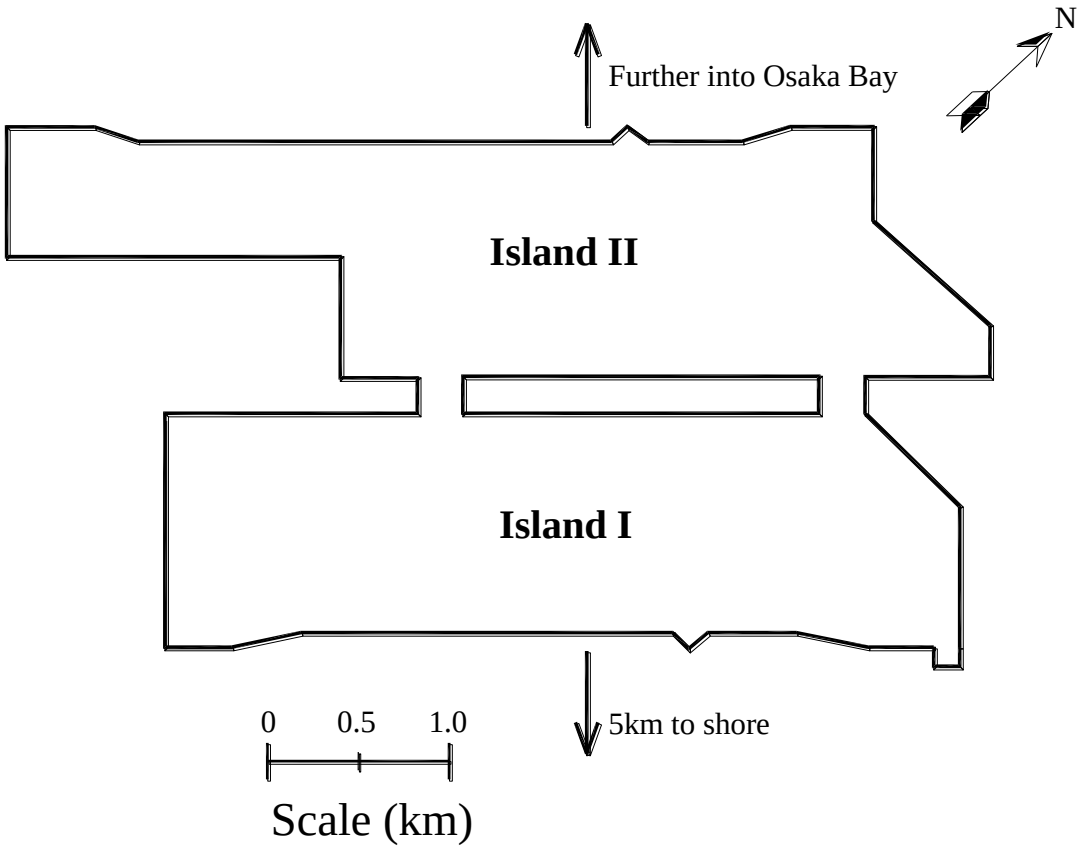

Figure 3-6 Plan view of the Kansai International Airport Islands.

CHAPTER 4 COMPRESSIBILITY AND PERMEABILITY OF THE SUBSEABED AT KANSAI INTERNATIONAL AIRPORT

4.1 Introduction

The initial subseabed investigation for the Kansai International Airport project began in 1977 and continued through 1982. Sixty-three borings were made to depths varying from 100 to 200m and two borings (borehole 56-9 on the offshore side of Island I and borehole 57-30 further into Osaka Bay) were made to a depth of 400m below seabed. Four additional 400m deep borings (boreholes 6-1, 7-1, 7-2, and 7-3) were made in 1994 and 1995. Figure 4-1 shows the locations of the boreholes at the Kansai Airport site (Nakase, 1987; Kanda et al., 1991; Tabata and Morikawa, 2005; Furudoi and Kobayashi, 2009).

All available subseabed data, including vertical profiles of natural water content, Atterberg limits, particle size distribution, specific gravity of solids, and unit weight, as well as oedometer data were evaluated as part of the ILLICON procedure for the settlement analyses of Kansai Airport Island I and Island II. These data were used to subdivide each geologic layer. Then, permeability and compressibility relationships were assigned to each sublayer based on the available data.

4.2 Subseabed profile

Figure 4-2 and Figure 4-3 show subseabed stratigraphy across the Kansai Airport site (the vertical scale is 10 times the horizontal scale). Figure 4-2 and Figure 4-3 were constructed based on profile drawings of boreholes reported in the literature (Arai, 1991; Kanda et al., 1991; Akai and Tanaka, 1999; Tanaka and Locat, 1999; Itoh et al., 2001; Watabe et al., 2002; Tanaka et al., 2004; Imai et al., 2005; Mimura and Jang, 2005; Furudoi and Kobayashi, 2009; Furudoi, 2010). The water depth to the seabed, referenced from Chart Datum Level (CDL), increases gradually with distance from the shoreline and is approximately 17m at the onshore side of Island I, approximately 20m at the offshore side of Island II, and approximately 21.5m further into Osaka Bay at the Borehole 7-1 location approximately, 950m from the offshore side of Island II (Arai, 1991; Kanda et al., 1991; Akai and Tanaka, 1999; Tanaka and Locat, 1999; Itoh et al., 2001; Tanaka et al., 2004; Imai et al., 2005).

The subseabed consists of marine clay layers (Ma), including the upper Holocene marine clay layer (Ma13), that were deposited when the sea level was relatively high as well as sand (Ds), and non-marine clay layers (Doc or NMC) that were deposited when sea level was relatively low. The layer designated Dtc is a shallow marine clay layer that is missing the nannofossils found in other marine clay layers (Takemura and Nakaseko, 2005). Figure 4-2 and Figure 4-3 show that while some sand layers (Ds1 and Ds10) are thick and continuous across the Kansai Airport construction site, others are thin and sometimes discontinuous.

4.3 Sampling and sample disturbance at the Kansai International Airport site

Soil samples were obtained from depths up to 400m below the seabed at Kansai Airport site. The wire-line system was employed as a relatively quick and efficient means to obtain relatively undisturbed samples. This system uses a double tube sampling technique where the outer tube transmits rotational power while the inner tube protects the sample from torsion, swelling, and contamination from drilling fluid. The inner tube is attached to a wire that facilitates retrieval of the sample (Peck et al., 1974; Kanda et al., 1991).

At Kansai Airport, the wire-line rod weighed as much as 12 tons because of the great sampling depths. Therefore, the largest boring machines together with a very large fixed steel platform that rested on the sea bottom were utilized (Kanda et al., 1991).

4.3.1 Samplers

Water-pressure fixed piston samplers (Figure 4-4) were used to sample soft to slightly hard cohesive soils for depths less than 130m, Denison samplers (Figure 4-5) were used to sample hard cohesive soils and sandy soils, and double core tube type samplers were used to sample sand and gravel (Kanda et al., 1991; Tanaka et al., 2002).

Two millimeter and 4mm thick sampling tubes were used for the water-pressure fixed piston samplers for soft cohesive soils exhibiting unconfined compressive strengths less than 200kPa and for hard cohesive soils exhibiting an unconfined compressive strength between 200 and 2000kPa, respectively. Up to 2000kPa water pressure was required to sample soft cohesive soils, and 2000 to 7000kPa water pressure was required to sample hard cohesive soils (Kanda et al. 1991).

The Denison sampler contains a core barrel within a larger barrel. Drilling mud flows down between the barrels and then up between the outer barrel and the borehole. The sampler is equipped with a spring core catcher (Terzaghi et al., 1996). The inner diameter of the Denison sampler used at the Kansai International Airport site was 80mm (Watabe and Tsuchida, 2001).

4.3.2 Sample disturbance

Andresen and Kolstad (1979) suggested a method for quantifying sample disturbance using the volumetric strain (ε_{vo}) of an oedometer specimen when subjected to in-situ effective overburden pressure or the volumetric strain of a triaxial specimen when subjected to in situ effective vertical and effective horizontal stress. The volumetric strains obtained from these laboratory tests may be used to assign a Specimen Quality Designation (SQD) from Table 4-1 (Terzaghi et al., 1996).

Figure 4-6 shows ε_{vo} with depth for Osaka Bay Pleistocene clay samples (Tanaka et al., 2002). It might be expected that sample disturbance would increase with depth as a result of distortion of the soil fabric caused by removing the in situ effective vertical and horizontal stresses. However, Figure 4-6 shows that sample disturbance remains more or less constant for depths reaching 400m. The measured volumetric strains are between 2 and 4% for the majority of samples; therefore, the samples are SQD-C, according to Table 4-1.

4.4 Soil Mineralogy

Tanaka and Locat (1999) reported results from physicochemical tests on Osaka Bay Pleistocene clays, including values of specific surface area (S), cation exchange capacity (CEC), and organic matter content. X-ray diffraction analyses were also performed to determine mineralogy, and scanning electron microscope (SEM) photographs were taken of undisturbed samples. The samples were obtained from Borehole 6-1 (see Figure 4-1). Table 4-2 shows the results of the physicochemical tests.

Table 4-2 shows that the specific surface area ranges from 83 to 201 m^2/g, the cation exchange capacity ranges from 12 to 27 mequiv./100g, and the organic content ranges from 1.4 to 3.6% for the Osaka Bay Pleistocene clays tested by Tanaka and Locat (1999). The X-ray diffraction analyses indicated that the clay minerals within the Pleistocene clays consist of

smectite, chlorite, kaolinite, illite, possibly smectite-vermiculite, and significant amounts of other mixed layered minerals. The bulk samples also contained quartz and feldspar minerals, microfossils, as well as less than 3% calcium carbonate (Figure 4-7) (Tanaka and Locat, 1999; Imai et al., 2005).

Scanning electron microscope images (SEM) shown in Figure 4-8 were taken after samples were freeze dried in nitrogen. The images show microfossils including diatoms present within the soil. Diatom skeletons can be either centric or elongate and they can be as large as 0.1 mm. They have a large internal porosity and their porous skeleton resembles a series of closely spaced chambers (Tanaka and Locat, 1999).

Although microfossils are present in many of the SEM photographs in Figure 4-8, Tanaka and Locat (1999) reported plastic limits in the range of 20 to 45%. The plastic limit is expected to be high if there are a significant number of microfossils because water held within the porous skeleton does not contribute to the consistency of the surrounding soil particles during the rolling process. For reference, Mexico City Clay contains 5 to 10% sand-sized particles mostly made of calcareous ooliths, 55 to 65% microfossils (mostly diatoms), 20 to 30% clay minerals, and 5 to 10% organic matter. The plastic limit of this material is approximately 150% (Mesri et al., 1975) whereas the plastic limit of sodium montmorillonite is only 47% (Mesri and Olson, 1971).

Figure 4-9 shows the chloride content with depth below sea level for Osaka Bay clays. One possible explanation for the abrupt decrease in chloride content with depth is that leaching or diffusion has taken place throughout the geologic history of the deposits. Leaching and diffusion are forms of chemical alteration aging of soil that result in a decrease in salt concentration in free porewater and possible cation exchange (Mesri, 1997).

4.5 Natural water content, Atterberg limits, clay-size fraction, and specific gravity of solids

Natural water content (w_o) and specific gravity of solids (G_s) used to obtain initial void ratio (e_o) assuming degree of saturation equal to 100%. Plastic limit (w_p), liquid limit (w_l), clay-size fraction (CF), and e_o together with an empirical relationship presented in Mesri et al. (1994) are used to estimate preconstruction vertical permeability (k_{vo}).

Figure 4-10 summarizes the Atterberg limit data on the Casagrande plasticity chart for the fine grained soils underlying Kansai Airport (Maeda et al., 1990; Akai and Tanaka, 1999;

Tanaka and Locat, 1999; Watabe et al., 2002; Tanaka et al., 2003; Tanaka et al., 2004; Imai et al., 2005). Most of the data in Figure 4-10 plot above the A-line and have w_ℓ greater than 50%. Therefore, according to the Unified Soil Classification System, the majority of the fine grained soils are clays of high plasticity (CH).

Natural water content, w_p, w_ℓ, CF, and G_s data collected for each layer are displayed in Figure 4-11 through Figure 4-32, together with vertical lines showing the values used for subsequent settlement analyses. For each layer, data are shown with respect to the depth into the layer (z) divided by the preconstruction layer thickness (L_o) so that comparisons can be made at various boreholes at the Kansai Airport site. The natural water content and Atterberg limit data demonstrate that there is a change in mineralogical composition throughout the thickness of many of the marine clay layers. The variation in water-holding capacity, as indicated by w_ℓ, with depth is at least partly a result of changes in depositional environment driven by the rise and fall of sea level over geologic time.

4.6 k_{vo}, e – log k_v, and k_h/k_v

In the absence of reported direct measurements of permeability, the values of k_{vo} used for each sublayer of the Pleistocene clay layers in subsequent settlement analyses were computed from the following empirical equation (Mesri et al., 1994):

$$k_{vo}(m/s) = C\left(\frac{e_o / CF}{A_c + 1}\right)^4 \qquad (4-1)$$

where the constant C is equal to 6.5e-11 (for k_{vo} in m/s) and $A_c = I_p/CF$ is activity. The constant (C) was selected based on data from natural soft clay and silt deposits (Batiscan, Berthierville, St. Hilaire, Vasby, and Boston Blue). The clay-size fraction for these soils was defined as the percentage of particles with an equivalent spherical diameter less than 2μm. Akai and Tanaka (1999) and Watabe et al. (2002) report the percentage of particles with an equivalent spherical diameter less than 5μm and Tanaka and Locat (1999) report the percentage of particles with an equivalent spherical diameter less than 2μm. Therefore, the values reported in Tanaka and Locat (1999) were used together with Atterberg limit data and Equation 4-1 to calculate k_{vo}.

The initial vertical permeabilities for the Ma13 sublayers were assigned based on values

reported in Tanaka et al. (2003). The values reported in Tanaka et al. (2003) were obtained from rate of compression observed in incremental loading oedometer tests interpreted according to the Terzaghi theory of consolidation (Figure 4-33). Values of permeability that are computed this way are often smaller than directly measured values by a factor of 2 (Mesri et al., 1994). The difference in computed and measured values is due, in part, to the changes in compressibility and permeability of clay during a pressure increment that are not taken into account in the Terzaghi theory of consolidation. Computed and measured values are also different because the Terzaghi theory of consolidation does not consider compressibility with respect to time at a constant effective stress. Therefore, values of k_{vo} delineated in Figure 4-33 were increased by a factor of 2.

Permeability is commonly expressed as a function of void ratio. A widely-used permeability - void ratio relationship that is employed for settlement analyses is based on $C_k = \Delta e/\Delta \log k$ = constant, where C_k is the change-in-permeability-index (Raymond, 1969; Mesri and Rokhsar, 1974; Burghignoly and Vestroni, 1975; Tavenas et al., 1983b). The change-in-permeability-index (C_k) can be determined from routine oedometer tests or through direct permeability measurements. There were not sufficient oedometer test data or direct permeability measurements available at the Kansai International Airport site to determine C_k; therefore, the empirical relationship $C_k = 0.5e_o$ was employed for subsequent settlement analyses (Tavenas et al., 1983b; Mesri et al., 1994).

Clay and silt deposits of marine origin generally have a flocculated random fabric and, therefore, permeability anisotropy (k_h/k_v), especially at low values of effective overburden pressure, rarely exceeds 1.5 and is often near 1.0 (Mesri et al. 1994). Although permeability anisotropy can be important for Pleistocene clays that are deep in the profile, the water flow due to consolidation of these layers at the Kansai Airprt Site is primarily in the vertical direction. However, vertical sand drains were installed in Ma13; therefore, the time rate of compression is sensitive to k_h/k_v for the Holocene marine clay layer. In the absence of direct information, subsequent settlement analyses use k_h/k_v equal to 1 for all clay layers.

Table 4-3 summarizes representative values of w_o, w_p, w_l, I_p, CF, G_s, e_o, k_{vo}, and C_k for each sublayer.

4.7 Vertical profiles of preconstruction porewater pressure, σ'_{vo}, and σ'_p

Figure 4-34 shows porewater pressure measured at Monitoring Point 2 of Island II (MP2-II) in November 2001, relatively soon after reclamation began at that location. The calculated preconstruction porewater pressure is also shown assuming hydrostatic porewater pressure from sea level with unit weight of water (γ_w) equal to 10.04kN/m^3 above the top of sand layer Ds1 and γ_w equal to 9.80 kN/m^3 below the top of sand layer Ds1(Nishimura, personal communication, 2011). The November 2001 porewater pressure measurements include a relatively small contribution of excess porewater pressure generated from reclamation fill applied at the seabed surface whereas the calculated porewater pressures do not include any construction related porewater pressure. Figure 4-34 demonstrates that it is reasonable to assume that the preconstruction porewater pressure distribution is hydrostatic from sea level and, therefore, this assumption is employed for subsequent settlement analyses and porewater pressure interpretation at the Kansai Airport Island site.

The preconstruction effective vertical stress (σ'_{vo}) is calculated based on the preconstruction porewater pressures and unit weight (γ) of each sublayer. Figure 4-35 shows γ data together with vertical lines indicating the values used for subsequent settlement analyses for clay layers. Figure 4-36 shows γ data together with vertical lines indicating the values used for subsequent settlement analyses for sand layers.

Profiles of $\sigma'_p/\ \sigma'_{vo}$ with depth were obtained at the Kansai International Airport site from incremental loading (IL) and constant rate of strain (CRS) oedometer test data on undisturbed specimens.

It is well established that the e-log σ'_v relationship obtained from the CRS test is strain-rate dependent (Taylor, 1942; Crawford, 1964, 1965, 1988; Bjerrum, 1967; Sallfors, 1975; Tavenas and Leroueil, 1977; Vaid et al., 1979, 1980; Leroueil and Tavenas, 1979; Mesri and Choi, 1979; Leonards, 1980; Graham et al., 1983; Leroueil et al., 1983; Morin et al., 1983; Mesri and Choi, 1984; Jamiolkowski et al., 1985; Leroueil et al., 1985; Larsson and Sallfors, 1986; Mesri and Feng, 1986; Leroueil, 1988; Feng, 1991). Mesri and Feng (1986) recommended an equation to compute the end-of-primary strain rate ($\dot{\varepsilon}_p$):

$$\dot{\varepsilon}_p = \frac{k_{vo}}{2^{C_c/C_k} H^2} \frac{\sigma'_p}{\gamma_w} \frac{C_\alpha}{C_c} \qquad (4-2)$$

where C_c is the compression index, H is the maximum drainage distance, and C_α is the secondary compression index. The end-of-primary (EOP) strain rate induces near-zero excess porewater pressure within the sample throughout the recompression and compression ranges, and it produces a void ratio – effective vertical stress relationship that is nearly identical to the end-of-primary relationship obtained from an incremental loading oedometer test. The end-of-primary strain rate is equal to the secondary compression rate immediately after the completion of primary consolidation (Feng, 1991).

In a discussion of Vaid et al. (1979), Mesri and Choi (1979) showed that the effect of strain rate on σ'_p can be predicted using the C_α/C_c law of compressibility with the following equation:

$$\frac{\left[\sigma'_p\right]_{\dot{\varepsilon}_p}}{\left[\sigma'_p\right]_{\dot{\varepsilon}_I}} = \left(\frac{\dot{\varepsilon}_p}{\dot{\varepsilon}_I}\right)^{\frac{C\alpha}{Cc}} \qquad (4-3)$$

where $\dot{\varepsilon}_I$ is the imposed strain rate for a given CRS test.

For a typical soft clay or silt deposit $\dot{\varepsilon}_p$ is approximately equal to 2.7e-7s^{-1}. The $\sigma'_p/\ \sigma'_{vo}$ data collected for the Osaka Bay clays include CRS oedometer tests with imposed strain rates equal to 3.3e-6s^{-1} (Tanaka et al., 2003; Tanaka, 2005) and 1.67e-6s^{-1} (Watabe et al., 2002). Therefore, $\sigma'_p/\ \sigma'_{vo}$ obtained from those tests were multiplied by 0.90 and 0.93, respectively, according to Equation 4-3.

Figure 4-37 and Figure 4-38 displays $\sigma'_p/\ \sigma'_{vo}$ data for the Holocene clay layer and the Pleistocene clay layers, respectively. The figures also show vertical lines indicating values used for subsequent settlement analyses. Values larger than the average of the data are used for the settlement analyses because sample disturbance tends to decrease $\sigma'_p/\ \sigma'_{vo}$.

Table 4-4 summarizes γ and $\sigma'_p/\ \sigma'_{vo}$ values selected for each layer. The ratio of preconsolidation pressure to preconstruction effective vertical stress used in subsequent settlement analyses range from 1.50 to 2.10 for the Holocene clay layer and from 1.28 to 1.50 for the Pleistocene clay layers.

The magnitude of $\sigma'_p/\ \sigma'_{vo}$ for the Osaka Bay Pleistocene clays can be explained by aging processes alone. Mechanisms associated with aging are explained in detail by Mesri (1997) and include: secondary compression, thixotropic hardening, and chemical alteration.

Thixotropic hardening occurs under conditions of constant composition and volume. The result of this process is increased interparticle interaction often through particle rotations. Secondary compression results from particle rearrangement into a more efficient packing and is associated with a decrease in the volume of voids. The C_α/C_c law of compressibility completely explains the secondary compression behavior of soils (Mesri and Godlewski 1977, 1979; Mesri, 2001). Chemical alterations could include chemical changes in soil particles or free pore water and may result in a change in void volume.

If $\sigma'_p/\ \sigma'_{vo}$ is a result of secondary compression, then the following equation can be used to estimate $\sigma'_p/\ \sigma'_{vo}$ (Mesri and Choi, 1979, 1984):

$$\frac{\sigma'_p}{\sigma'_{vo}} = \left[\frac{t}{t_p}\right]^{\frac{C\alpha/Cc}{1-Cr/Cc}} \qquad (4-4)$$

where t_p is the time to end-of-primary consolidation.

The last increment of loading prior to deposition of Ma13 may be considered when calculating $\sigma'_p/\ \sigma'_{vo}$ due to secondary compression. According to Itoh et al. (2001), deposition of Ma13 commenced approximately 11,000 years ago. Therefore, if the time (t) is 11,000 years, t_p is approximated as 10 years, C_α/C_c is approximately 0.04, and C_r/C_c is approximately 0.1 (Ladd 1971, Mesri and Rokhsar, 1974) then $\sigma'_p/\ \sigma'_{vo}$ is equal to 1.37, according to Equation 4-4.

Mesri (1997) recommended the following equation to incorporate the effects of thixotropic hardening:

$$\frac{\sigma'_p}{\sigma'_{v0}} = \left[\frac{t}{t_p}\right]^{\frac{C\alpha/Cc}{1-Cr/Cc}+\beta} \qquad (4-5)$$

where β ranges from 0.015 to 0.025 and is a parameter that defines the magnitude of thixotropic hardening during secondary compression. If β is approximately 0.02 and the previous assumptions apply then $\sigma'_p/\ \sigma'_{vo}$ is equal to 1.57, according to Equation 4-5.

The computed $\sigma'_p/\ \sigma'_{vo}$ from aging considerations alone are very reasonable compared to the values reported for the subseabed underlying the Kansai Airport Islands.

4.8 The ratio of recompression index to compression index

It is difficult to accurately determine the recompression index from oedometer test results because sample disturbance may significantly increase the value of this parameter. Therefore, an empirical database from high quality test data has been previously used to estimate the ratio of recompression index to compression index (C_r/C_c) for soft clay and silt deposits (Mesri and Rokhsar, 1974). Additionally, Ladd (1971) has suggested C_r/C_c values in the range of 0.1 to 0.2. Based on these recommendations, the EOP e – log σ'_v relationships for subsequent settlement analysis were constructed using C_r/C_c' equal to 0.1 where C_c' is the secant compression index defined at σ'_{vf} / σ'_p equal to 2.

4.9 Secant compression indices for Osaka Bay Holocene and Pleistocene clay layers

To construct the EOP e – log σ'_v relationships, first the point (σ'_{vo}, e_o) was defined. Then, the recompression curve from σ'_{vo} to σ'_p was constructed assuming C_r/C_c' equal to 0.1 where C_c' is the secant compression index defined at σ'_{vf} / σ'_p equal to 2. The compression curve beyond σ'_p was defined using the following equation:

$$e = e_{pp} - C_c^{'} \times \log\left(\frac{\sigma_v^{'}}{\sigma_p^{'}}\right) \qquad (4-6)$$

e_{pp} is the end-of-primary void ratio at the intersection of the recompression curve and the preconsolidation pressure.

To obtain C_c' values for Ma13, a compression curve was drawn based on 8 oedometer tests that were available in the literature (Figure 4-39). Then, secant lines were drawn for void ratios in the range of 1.6 to 3.0 from the compression curve (Figure 4-40). Figure 4-41 summarizes the C_c' values obtained from this procedure.

Differential settlement gauge observations as well as CRS test data suggest that the shallow marine clay layer Dtc is less compressible than the other Pleistocene clay layers. Therefore, the procedure described above for Ma13 was also applied to this layer (Figure 4-42 and Figure 4-43). Secant compression indices for the other Pleistocene marine clay layers were obtained from Figure 4-44 which was prepared from published data for 34 oedometer tests. Four to seven (σ'_v / σ'_p, C_c') data points were obtained from Figure 4-41, Figure 4-43, or Figure 4-44 together with Equation 4-6 to construct compression curves beyond σ'_p.

4.10 Secondary Compression behavior of Osaka Bay clays

The secondary compression behavior of any geotechnical material is explained by the C_α/C_c law of compressibility which states that there is a unique interrelationship between the time compressibility and the effective stress compressibility that holds true throughout the secondary consolidation stage. It is well established that C_α/C_c is a constant for any soil where the (C_α, C_c) data pair correspond to the same point (e, σ'_v, t) during secondary compression, and that the values of C_α/C_c for all geotechnical materials are in the range of 0.01 to 0.07 (Mesri and Godlewski, 1977, 1979; Mesri and Choi, 1984; Mesri, 1987; Mesri and Castro, 1987; Mesri et al., 1997).

Figure 4-45 through Figure 4-51 show vertical strain (ε_v) versus log t and ε_v versus log σ'_v for Osaka Bay clays (Imai et al., 2005; Tanaka, 2005; Watabe et al., 2008). For the CRS tests, the vertical stresses correspond to a strain rate equal to 3.3e-6s^{-1}; therefore, the vertical stresses were reduced by 10% according to Equation 4-3 to obtain the EOP relationship.

For cases where σ'_{vf} was less than σ'_p in the long term consolidation tests, the load increment ratio was apparently not large enough for an inflection point (Mesri and Godlewski, 1977) to be visible in the ε_v – log t curve (e.g. applied load equal to 98kPa for Ma13). Therefore, the maximum slope of the ε_v – lot t curve is a result of secondary compression and was paired with the maximum slope of the ε_v – log σ'_v curve to determine C_α/C_c for the point (ε_v, σ'_v, t).

Figure 4-52 and

Figure 4-53 show $C_\alpha/(1+e_o)$ versus $C_c/(1+e_o)$ for Ma13 and the Pleistocene clay layers, respectively. Figure 4-52 indicates that C_α/C_c is 0.043 for Ma13 and

Figure 4-53 indicates that C_α/C_c is 0.032 for the Pleistocene clay layers. The d value of 0.032 is also obtained as the average of values computed for 11 layers, from Dtc to Ma2, with a range of 0.024 to 0.042 (Mesri, personal communication, 2005).

4.11 Permeability of Pleistocene sand layers

When sea levels receded intermittently throughout the Pleistocene Epoch subaerially exposing the ground where Kansai Airport is currently located, a flood plain environment existed and it is likely that the southern portion of Osaka Bay remained relatively far from fast flowing rivers and estuaries capable of transporting sand-size particles. Therefore, in many instances throughout geologic history, little to no clean sand was deposited at the location currently

occupied by the Kansai Airport Islands. As a result, many of the sand layers that underlie Kansai Airport are high in fines content.

Nakase (1987) listed the range of measured permeabilities for the Pleistocene sand layers as 10^{-8} to 10^{-5} m/s. Nakase went on to say that the measured permeabilities were very small and that the small values could be a result of the difficulty of sampling sand from great depths. The small permeability measurements would be expected to produce significant excess porewater pressures within some of the Pleistocene sand layers. This complication was commented on by Mimura and Jang (2005):

> "The most serious problem originating from sandy deposits is permeability that controls the rate of consolidation of the sandwiched Pleistocene clays … The effect of the existence of excess porewater pressure in the permeable Pleistocene sand gravel layers on the subsequent advance in settlement of the Pleistocene deposits is of great concern for predicting the long-term settlement of the offshore-reclaimed marine foundations."

Mimura and Jang (2005) go on to make the following statement regarding the permeability of sand layers Ds6 and Ds7:

> "Because of the poor quality of mass permeability of the sand gravel layers (Ds6, Ds7) Ma10, Ma9, and Doc 5 behave as if they are one continuous clay layer … Here, Ds6 and Ds7 [do] not function as permeable layers at all."

Later in the same paper, Mimura and Jang (2005) make the following statement:

> "Pleistocene sand gravel layers in the foundation of KIA have insufficient thickness, continuity, and sufficient fine components in them, which results in the storage of undissipated excess porewater pressure in the permeable sand gravel layers for a long time… The above-mentioned problem still remains unsolved."

Table 4-5 lists the permeabilities used by Mimura and Jang (2005) for their analysis at Monitoring Point 1 of Island I (MP1-I, near the center of Island I). Mimura and Jang (2005) do

not describe how they arrived at the permeabilities they assumed for their analysis. The sand layer Ds2 is not mentioned presumably because the authors ignored any drainage contribution that Ds2 may have had for the surrounding clay layers (Dtc and Ma12). The Pleistocene sand layer Ds10 was assumed to be freely draining, Ds1 was assigned a relatively high permeability (1e-2 m/s), and the permeability values used in their analysis for the remaining sand layers ranged from 2.5×10^{-7} m/s to 4.5×10^{-5} m/s.

Shibata and Karube (2005) performed a finite element analysis that included both Island I and Island II of Kansai Airport. Table 4-6 lists the permeabilities they assumed for the Pleistocene sand layers in their analysis. As with Mimura and Jang (2005), Shibata and Karube do not describe how they obtained the permeabilities for their analysis. The permeability values listed in Table 4-6 range from 1×10^{-5} m/s to 8.5×10^{-5} m/s.

Kobayashi et al. (2005) made the following statement regarding the Pleistocene sand layers:

> "There was an additional concern about the thickness of sand layers that alternated with clay layers which suggested that these sand layers might not function sufficiently as drainage layers… most of the sand [layers] are very thin. Only Ds1 and Ds10, which exist under Ma13 and Ma7, respectively, can function as drainage layers in terms of the thickness and area. Other sand layers, particularly those that could drain water from Ma10 and Ma9, are quite thin; the layer thickness is almost zero at some locations."

The lack of specific published data for the permeability of the Pleistocene sand layers has led the author to rely on layer by layer settlement and excess porewater pressure observations to back-calculate an equivalent permeability for each of the Pleistocene sand layers. Then, the back-calculated permeabilities are used to forecast long-term settlement at various locations for the Airport Islands. The back-calculated permeability of the sand layers, however, are comparable to those reported by Nakase (1987), Mimura and Jang (2005), and Shibata and Karube (2005).

4.12 Tables

Table 4-1 Specimen quality designation (SQD) (Terzaghi et al. 1996).

Volumetric Strain (%)	Specimen Quality Designation (SQD)
< 1	A
1-2	B
2-4	C
4-8	D
> 8	E

Table 4-2 Results of physicochemical tests reported by Tanaka and Locat (1999). The designation TT indicates that a hydraulic fixed piston sampler was used for sampling and the designation D indicates that a Denison double tube sampler was used for sampling.

Layer	Sample No.	Depth below seabed (m)	S (m^2/g)	CEC (meq./ 100g)	Organic Content (%)
Ma12	TT-19	49.8	110	16.5	2.4
Ma11U	TT-44	78.3	119	22.4	2.3
Ma10	D-8	108.0	125	15.6	2.6
Ma10	TT-62	112.0	94	12.3	2.0
Ma10	TT-70	119.3	126	16.4	1.7
Ma10	TT-74	123.2	90	13.9	2.3
Ma9	TT-85	134.5	87	12.1	2.5
Ma9	TT-90	141.5	83	14.5	2.2
Ma9	TT-92	149.5	119	16.7	2.2
Ma9	D-18	150.5	120	15.1	2.4
Doc5	D-22	160.5	150	18.7	1.4
Ma7	D-71	198.5	101	14.5	2.7
Ma4	D-109	236.5	201	18.8	3.6
Ma3	D-117	243.8	166	20.7	2.0
Ma3	D-119	245.6	164	20.6	3.3
Ma3	D-129	254.0	130	15.6	2.7
Ma0	D-207	362.8	120	27.2	1.5

Table 4-3 Representative values of w_o, w_p, w_l, I_p, CF, G_s, e_o, k_{vo}, and C_k for each sublayer.

Layer	Sublayer	w_o (%)	w_p (%)	w_l (%)	I_p (%)	CF (%)	G_s	e_o	k_{vo} (m/s)	C_k
Ma13	1	110	35	102	67	-	2.67	2.933	2.3E-08	1.5
	2	96	35	99	64	-	2.67	2.560	1.1E-08	1.3
	3	86	32	90	58	-	2.67	2.293	5.0E-09	1.1
	4	74	30	78	48	-	2.67	1.973	2.2E-09	1.0
	5	66	30	66	36	-	2.67	1.760	1.0E-09	0.9
Dtc	1	44	25	55	30	17	2.70	1.195	2.6E-09	0.6
	2	48	25	61	36	30	2.70	1.297	9.8E-10	0.6
	3	40	24	58	33	32	2.70	1.070	4.6E-10	0.5
Ma12	1	79	38	104	65	35	2.66	2.101	1.2E-09	1.1
	2	55	29	76	47	39	2.66	1.453	5.4E-10	0.7
Doc1	1	47	22	71	48	29*	2.68*	1.259	4.6E-10	0.6
Ma11U	1	56	30	79	49	38	2.71	1.510	5.8E-10	0.8
	2	41	26	62	36	40	2.71	1.112	3.1E-10	0.6
Ma11L	1	49	28	70	42	29	2.69	1.328	8.2E-10	0.7
Ma10	1	43	30	72	42	30	2.69	1.171	4.5E-10	0.6
	2	56	35	92	57	23	2.69	1.499	8.0E-10	0.7
	3	64	37	102	65	27	2.69	1.731	8.1E-10	0.9
	4	48	32	84	52	29	2.69	1.292	4.2E-10	0.6
Ma9	1	55	35	91	57	28	2.69	1.480	6.1E-10	0.7
	2	51	34	90	56	39	2.69	1.383	3.0E-10	0.7
Doc5	1	63	39	105	66	36	2.63	1.645	4.4E-10	0.8
	4	52	36	84	47	52	2.63	1.378	2.4E-10	0.7
Ma8	1	44	31	83	51	33	2.70	1.174	2.4E-10	0.6
	2	54	36	91	56	33	2.70	1.448	4.6E-10	0.7
	3	46	32	60	28	33	2.70	1.241	1.1E-09	0.6
Ma7	1	48	33	80	46	28	2.68	1.280	5.6E-10	0.6
	2	54	37	96	59	29	2.68	1.460	4.9E-10	0.7
	3	46	33	83	50	45	2.68	1.231	1.8E-10	0.6
Doc6	1	46	34	89	54	36	2.68*	1.242	2.3E-10	0.6
Ma4	1	49	34	87	53	30	2.68*	1.302	3.8E-10	0.7
Ma3	1	50	35	86	50	29	2.68*	1.330	5.2E-10	0.7
Ma2	1	41	31	82	51	28	2.68*	1.096	2.4E-10	0.5
NMC-1	1	35	29	78	50	26	2.68*	0.927	1.5E-10	0.5
NMC-2	1	29	23	57	34	30	2.68*	0.774	1.3E-10	0.4
NMC-3	1	32	24	63	38	21	2.68*	0.864	3.0E-10	0.4
Ma1	1	39	32	84	51	26	2.68*	1.036	2.1E-10	0.5
NMC-4	1	25	18	35	16	6	2.68*	0.659	4.6E-09	0.3
Ma0	1	32	25	63	38	14	2.68*	0.861	4.8E-10	0.4
NMC-5	1	19	25	62	37	12	2.68*	0.515	7.8E-11	0.3

*Value assigned based on average of available data for other clay layers.

Table 4-4 Representative values of γ and σ'_p/σ'_{vo} for each layer.

Layer	γ (kN/m^3)	σ'_p/σ'_{vo}
Ma13	14.5	2.10
	14.7	1.60
	15.0	1.50
	15.4	1.50
	15.8	1.50
Dtc	16.7	1.50
Ma12	15.1	1.40
Doc1	16.4[a]	1.40
Ma11U	16.5	1.40
Ma11L	16.7	1.40
Ma10	16.5	1.50
Ma9	16.4	1.30
Doc5	15.8	1.35
Ma8	17.1	1.30
Ma7	16.8	1.28
Doc6	16.4[a]	1.28[b]
Ma4	16.4[a]	1.30
Ma3	17.2	1.40
Ma2	16.4[a]	1.35
NMC-1	16.4[a]	1.35[b]
NMC-2	16.4[a]	1.35[b]
NMC-3	16.4[a]	1.35[b]
Ma1	16.4[a]	1.30
NMC-4	16.4[a]	1.30[b]
Ma0	16.4[a]	1.40
NMC-5	16.4[a]	1.40[b]

a. Value assigned based on average of available data for other clay layers.
b. Value assigned based on overlying clay layer.

Table 4-5 Permeability of Pleistocene sand layers used by Mimura and Jang (2005) for their analysis at MP1-I.

Pleistocene sand layer	kvo (m/s)
Ds1	1.0E-02
Ds3	4.0E-05
Ds4	1.2E-05
Ds5	4.5E-05
Ds6	2.5E-07
Ds7	2.5E-07
Ds8	2.0E-05
Ds9	2.5E-07
Ds10	Freely draining

Table 4-6 Permeability of Pleistocene sand layers used by Shibata and Karube (2005) in their analysis.

Pleistocene sand layer	kvo (m/s)
Ds1	8.5E-05
Ds2	8.5E-05
Ds3	4.0E-05
Ds4	3.5E-05
Ds5	4.5E-05
Ds6	2.5E-05
Ds7	1.5E-05
Ds8	not listed
Ds9	2.5E-05
Ds10	4.0E-05
Ds12	4.0E-05
Fill	1.0E-05

4.13 Figures

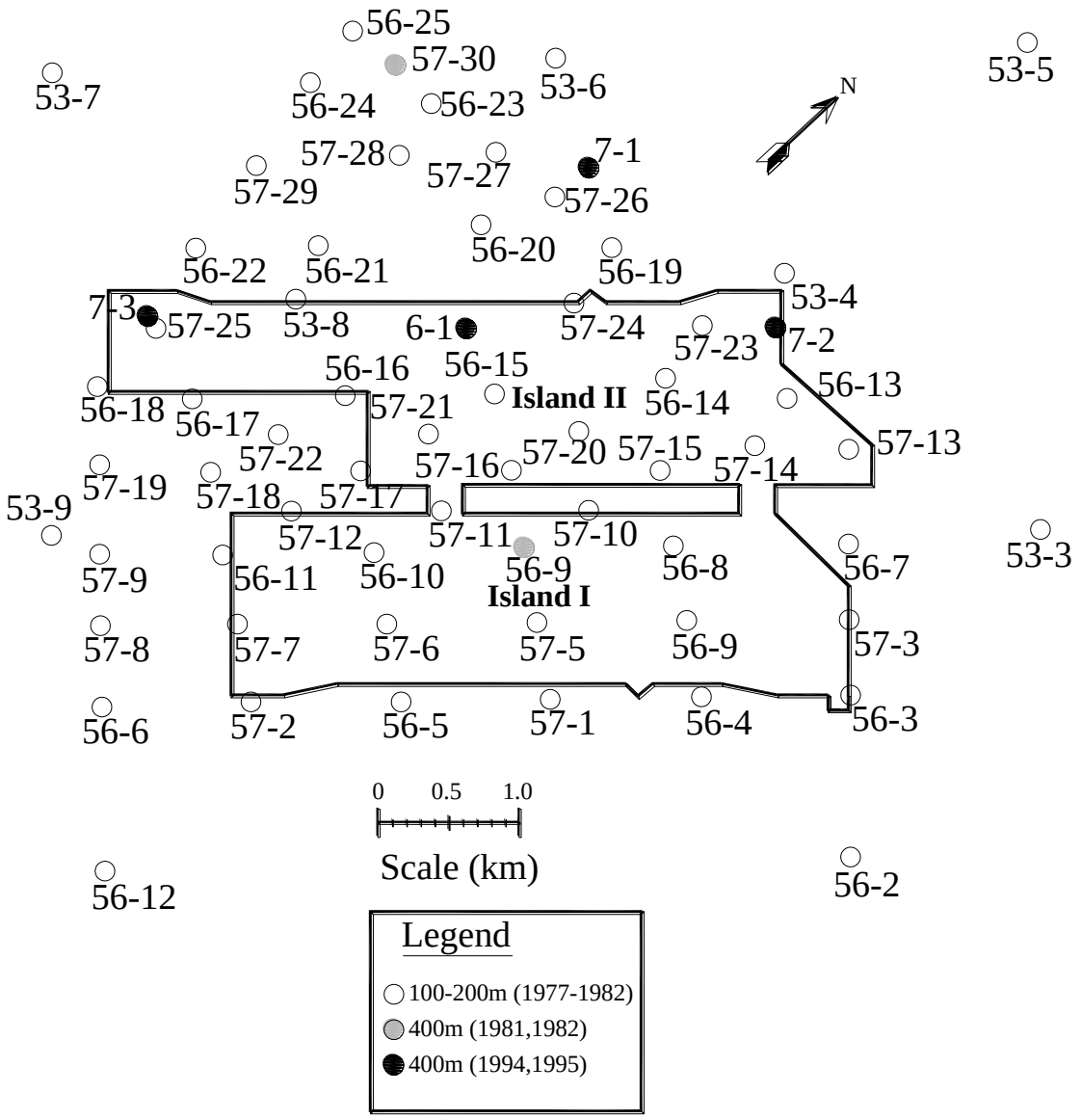

Figure 4-1 Locations of borings at the Kansai International Airport (Nakase, 1987; Kanda et al., 1991; Tabata and Morikawa, 2005; Furudoi and Kobayashi, 2009).

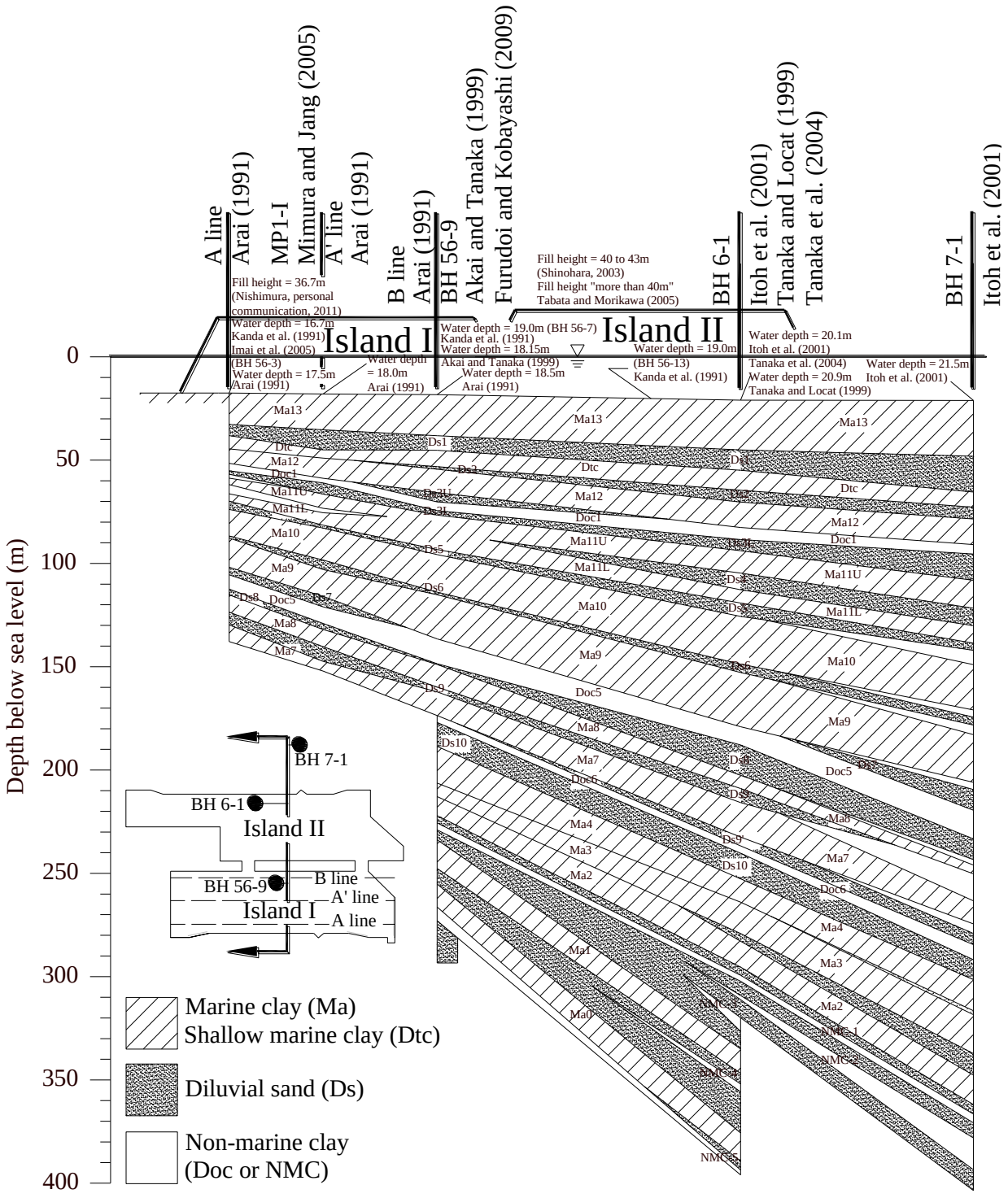

Figure 4-2 Subseabed stratigraphy at Kansai International Airport.

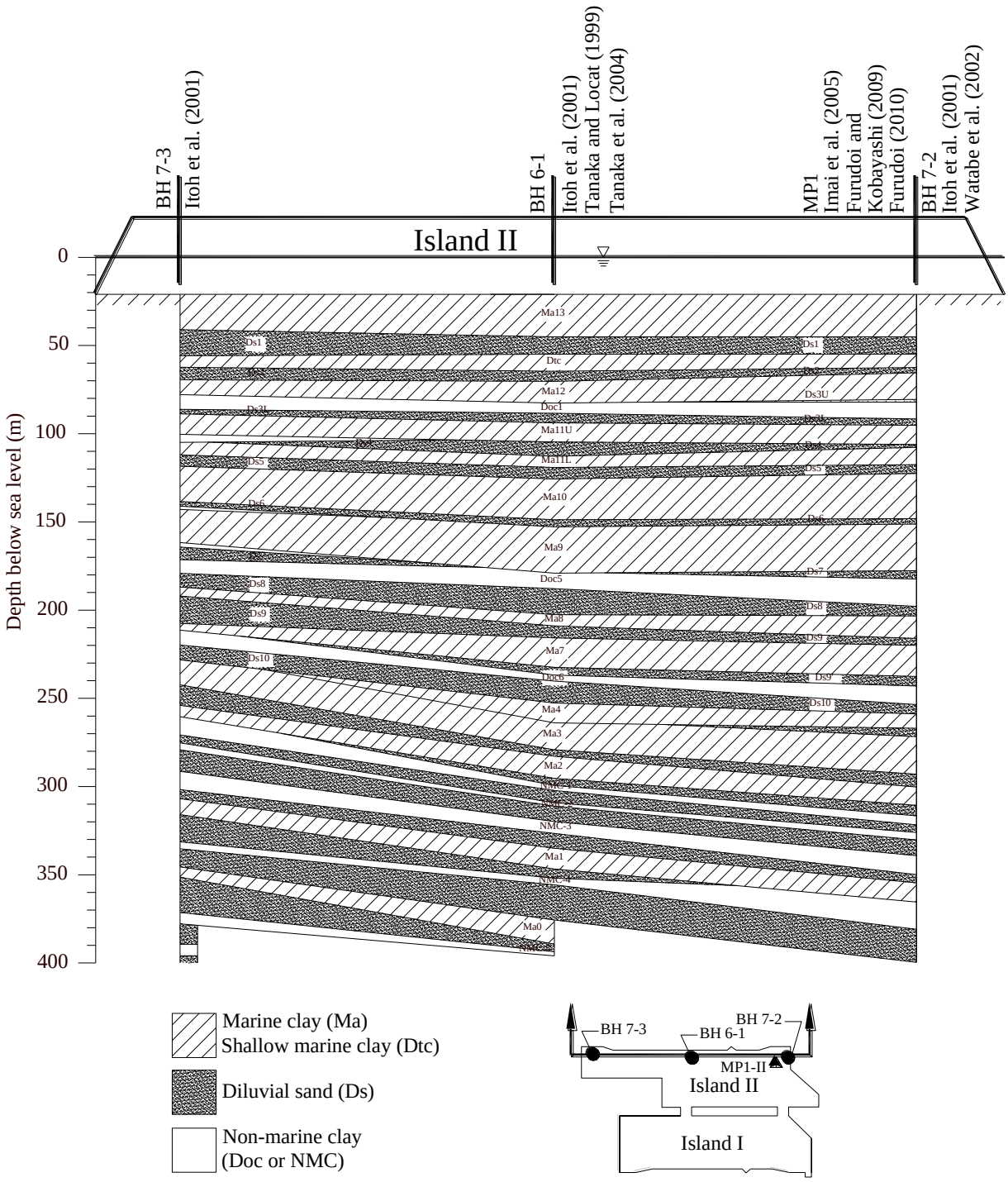

Figure 4-3 Subseabed stratigraphy at Kansai International Airport.

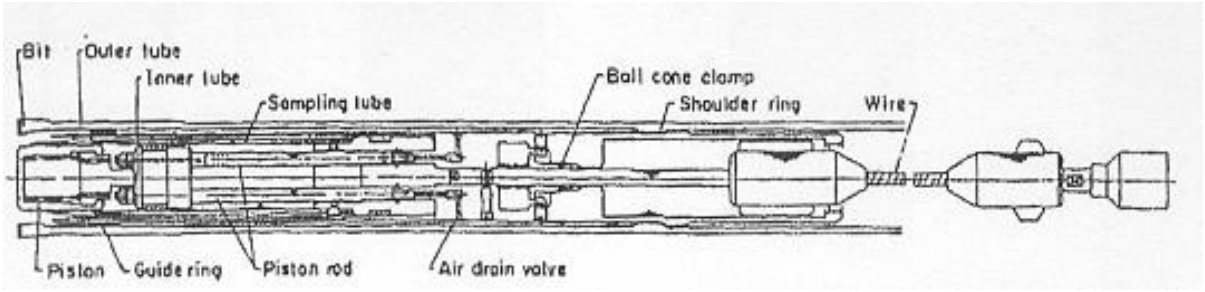

Figure 4-4 Typical fixed piston type sampler used for soft to slightly hard cohesive soils at the Kansai International Airport site (Kanda et al. 1991).

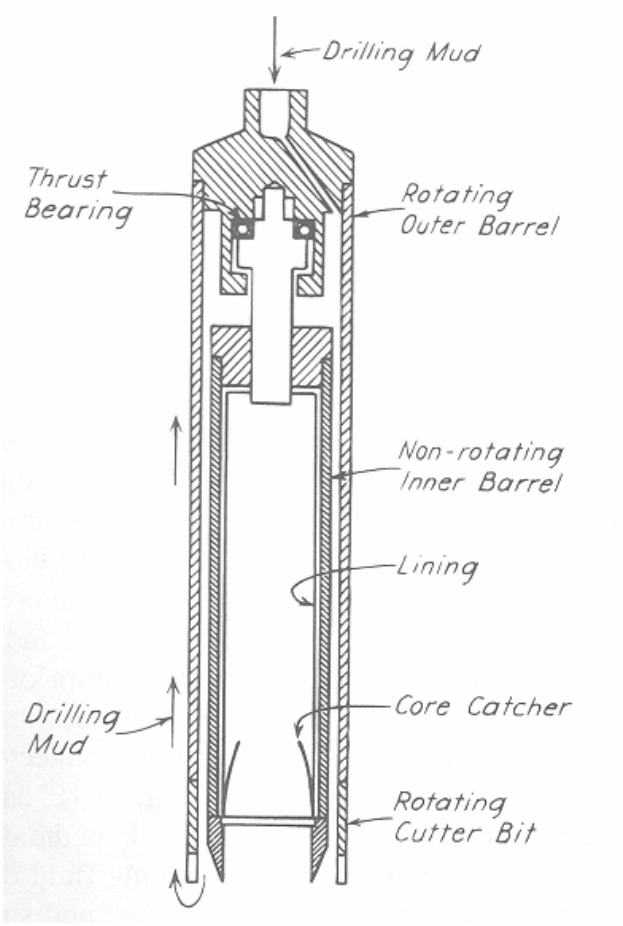

Figure 4-5 Sketch showing the principal features of a Denison sampler (Terzaghi et al. 1996).

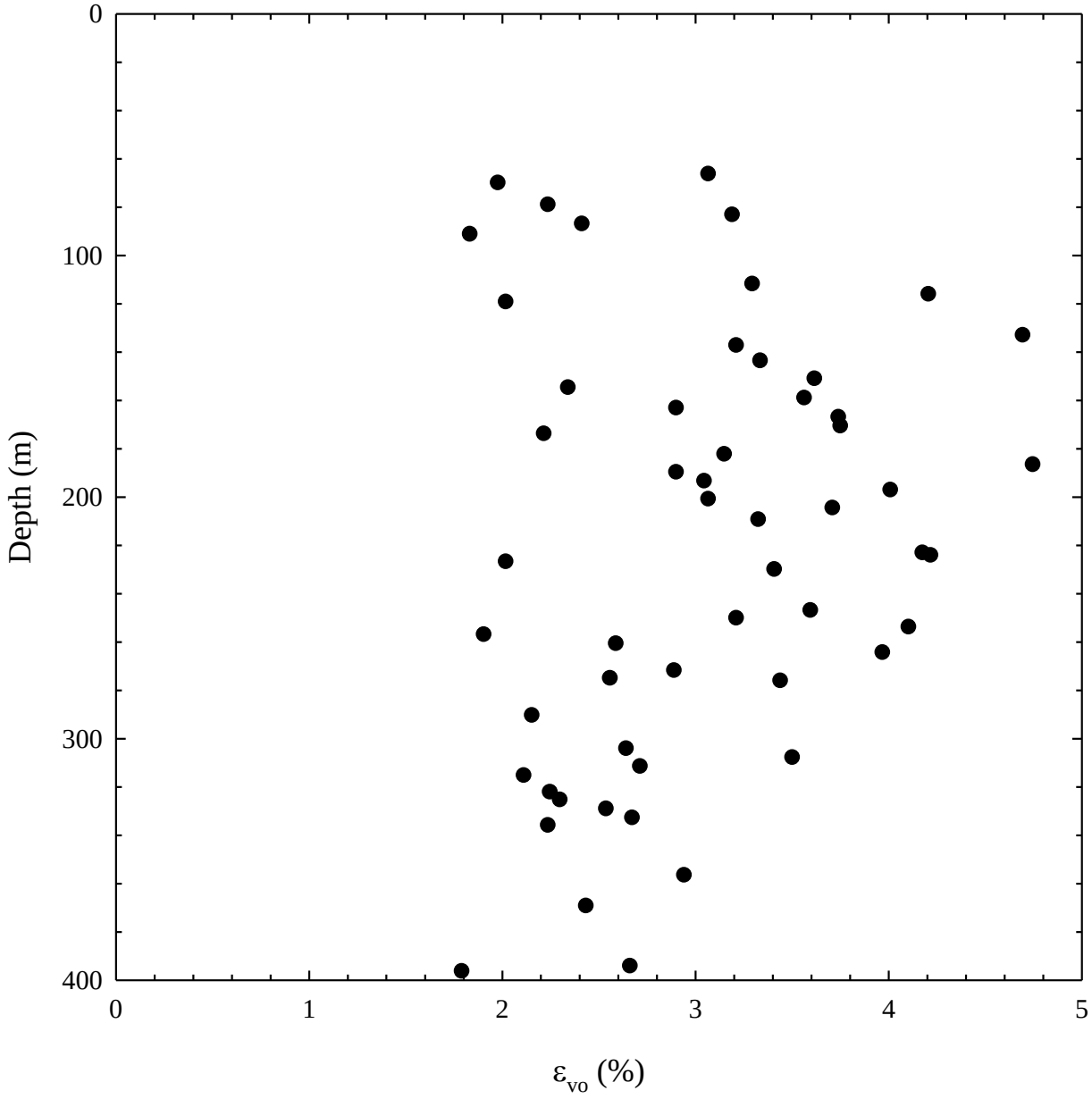

Figure 4-6 Volumetric strain (ε_{vo}) caused by applying in situ effective stress condition (Tanaka et al., 2002).

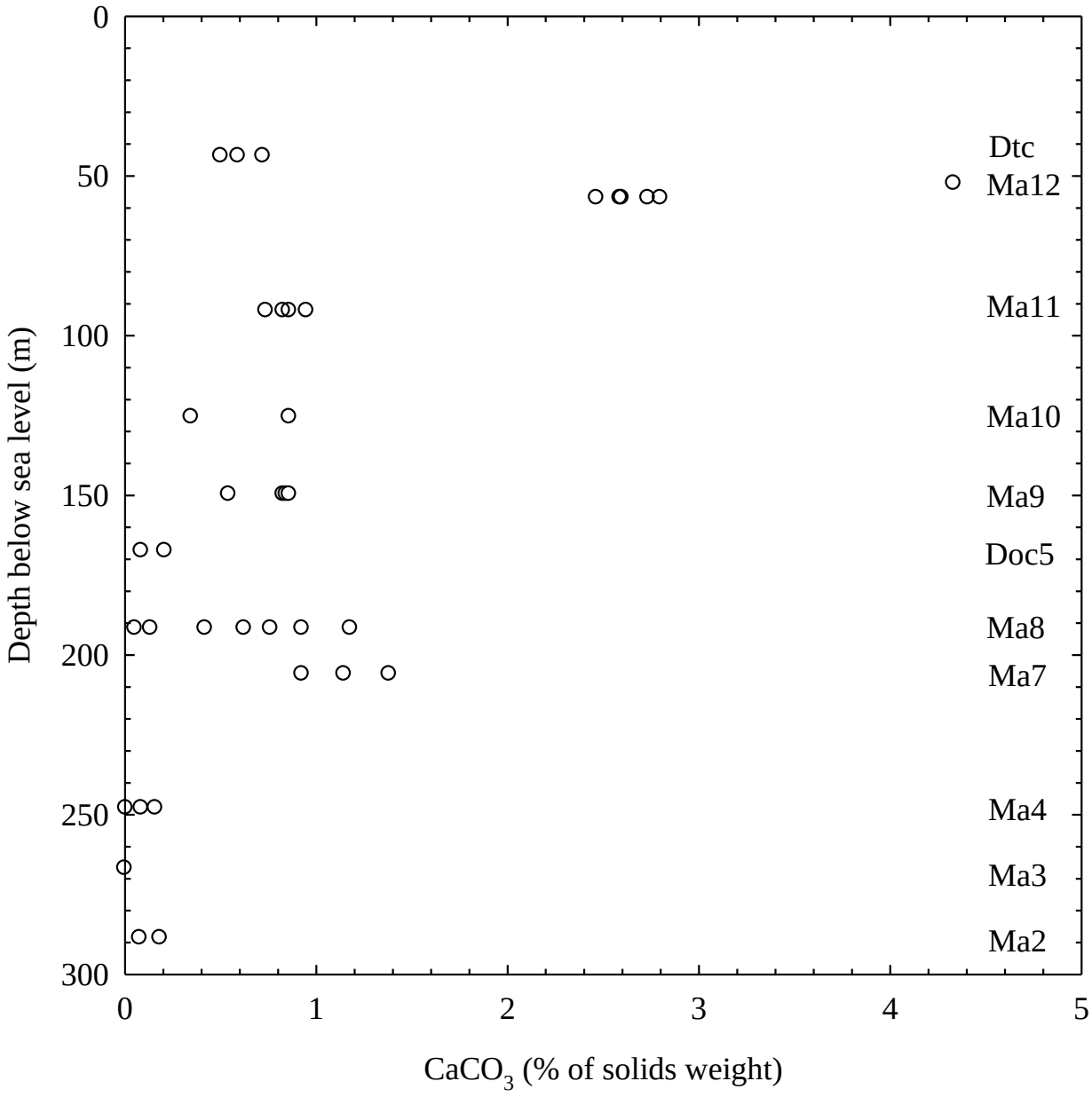

Figure 4-7 Calcium carbonate content with depth. Data from Imai et al. (2005).

Figure 4-8 SEM images of Osaka Bay clays from Borehole 6-1 (Tanaka and Locat, 1999).

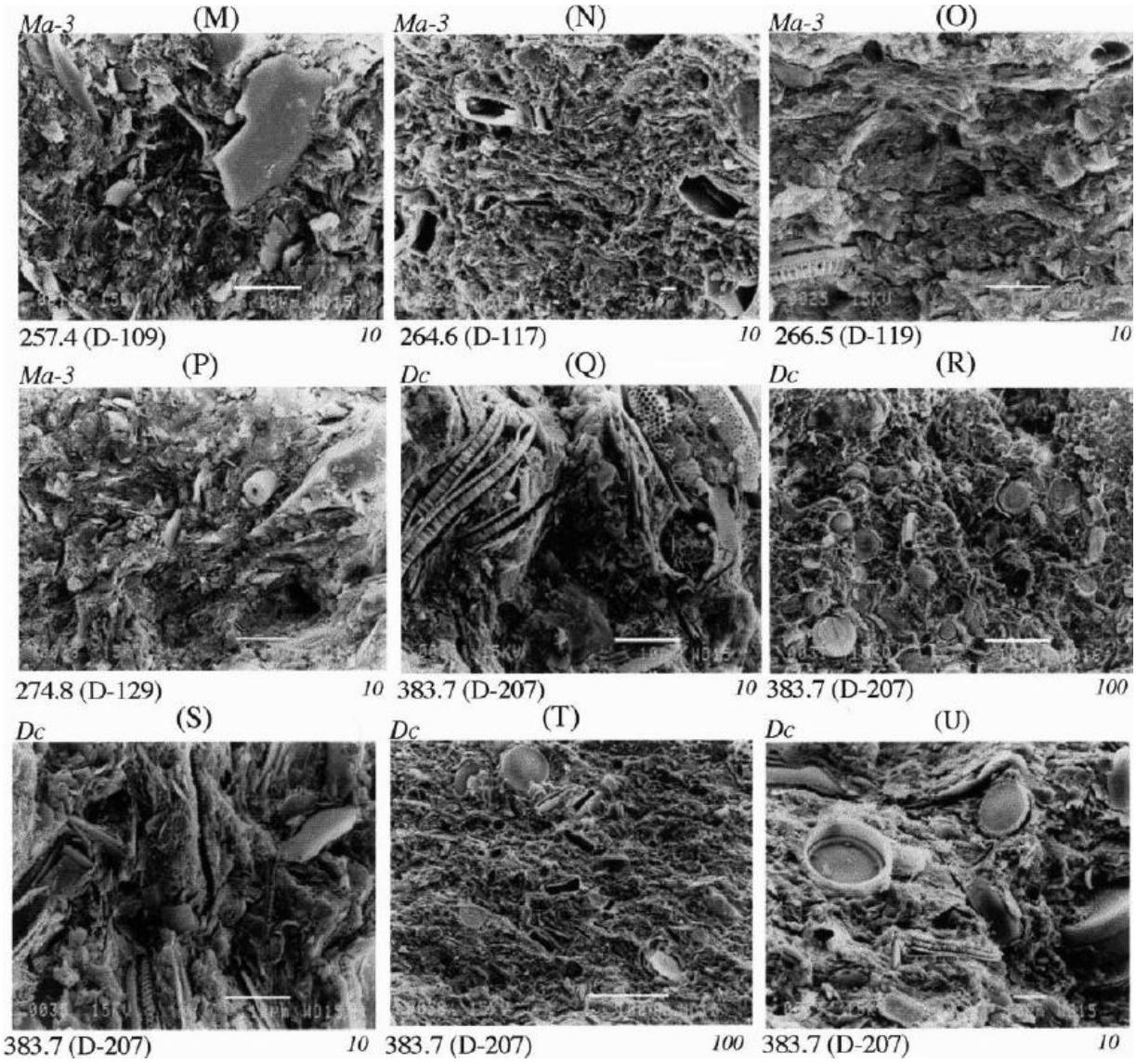

Figure 4-8 cont. SEM images of Osaka Bay clays from Borehole 6-1 (Tanaka and Locat, 1999).

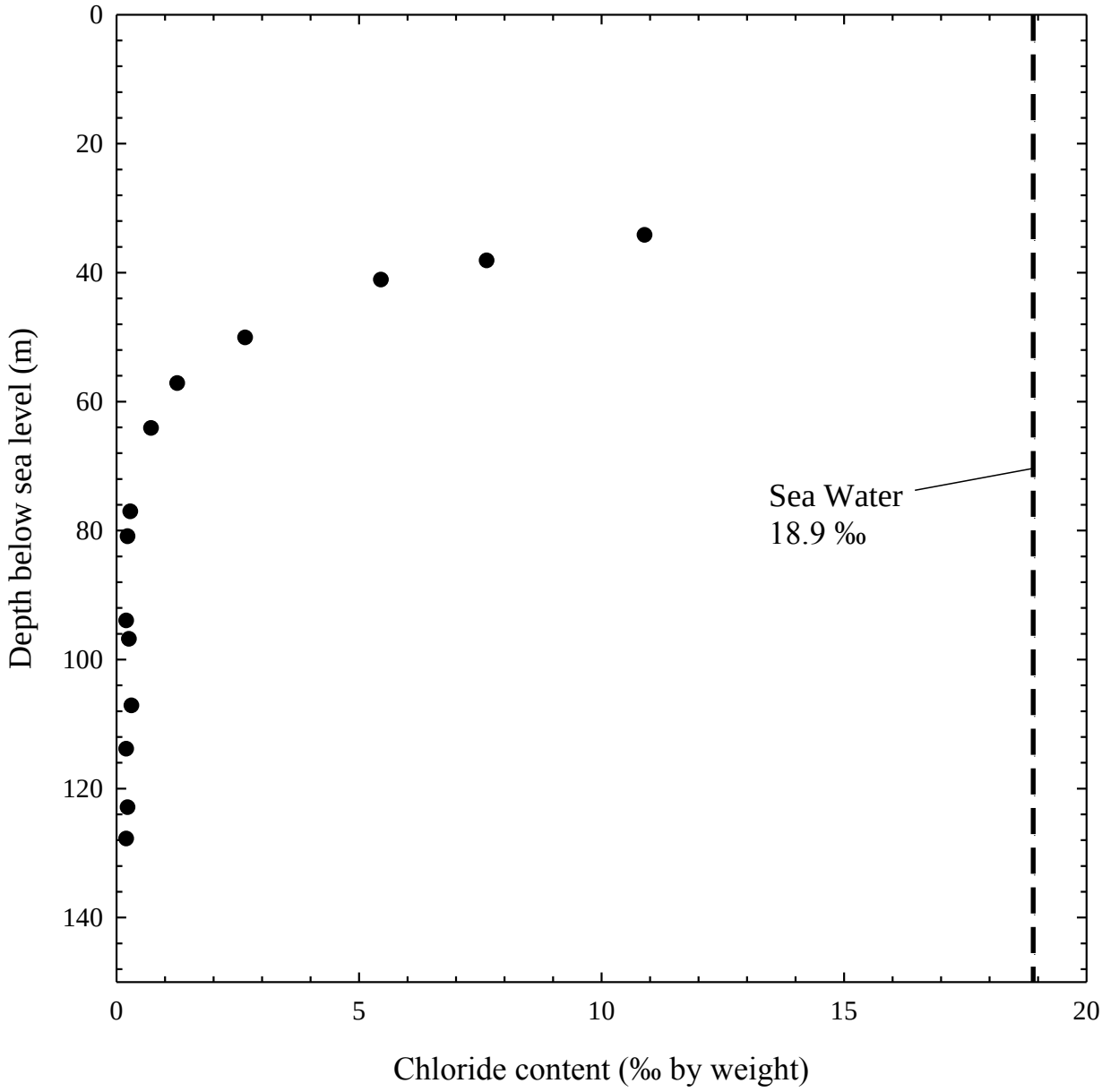

Figure 4-9 Chloride content with depth. Data from Tanaka et al. (2003).

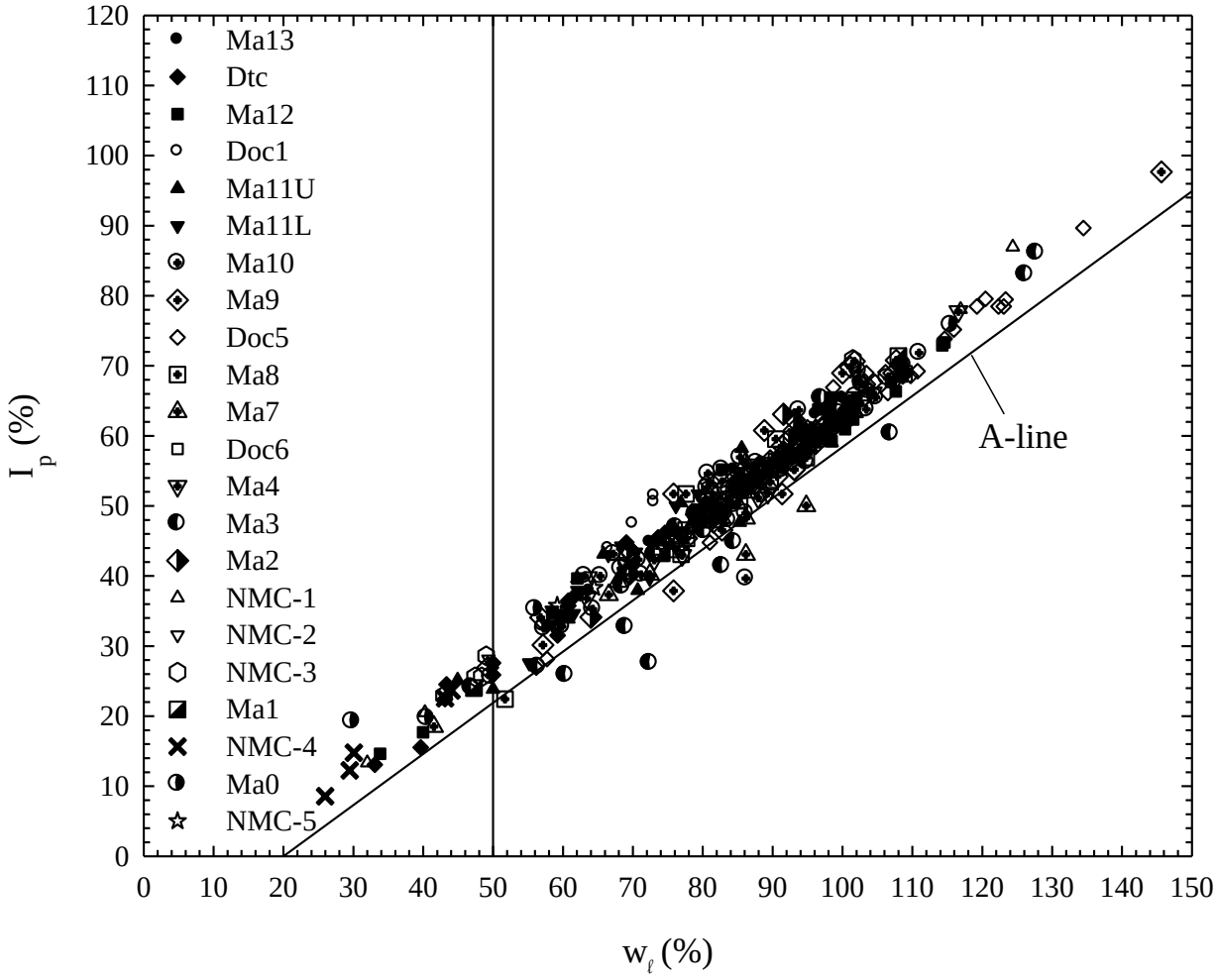

Figure 4-10 Summary of Atterberg limits for clay layers underlying Kansai Airport (Maeda et al., 1990; Akai and Tanaka, 1999; Tanaka and Locat, 1999; Watabe et al., 2002; Tanaka et al., 2003; Tanaka et al., 2004; Imai et al., 2005).

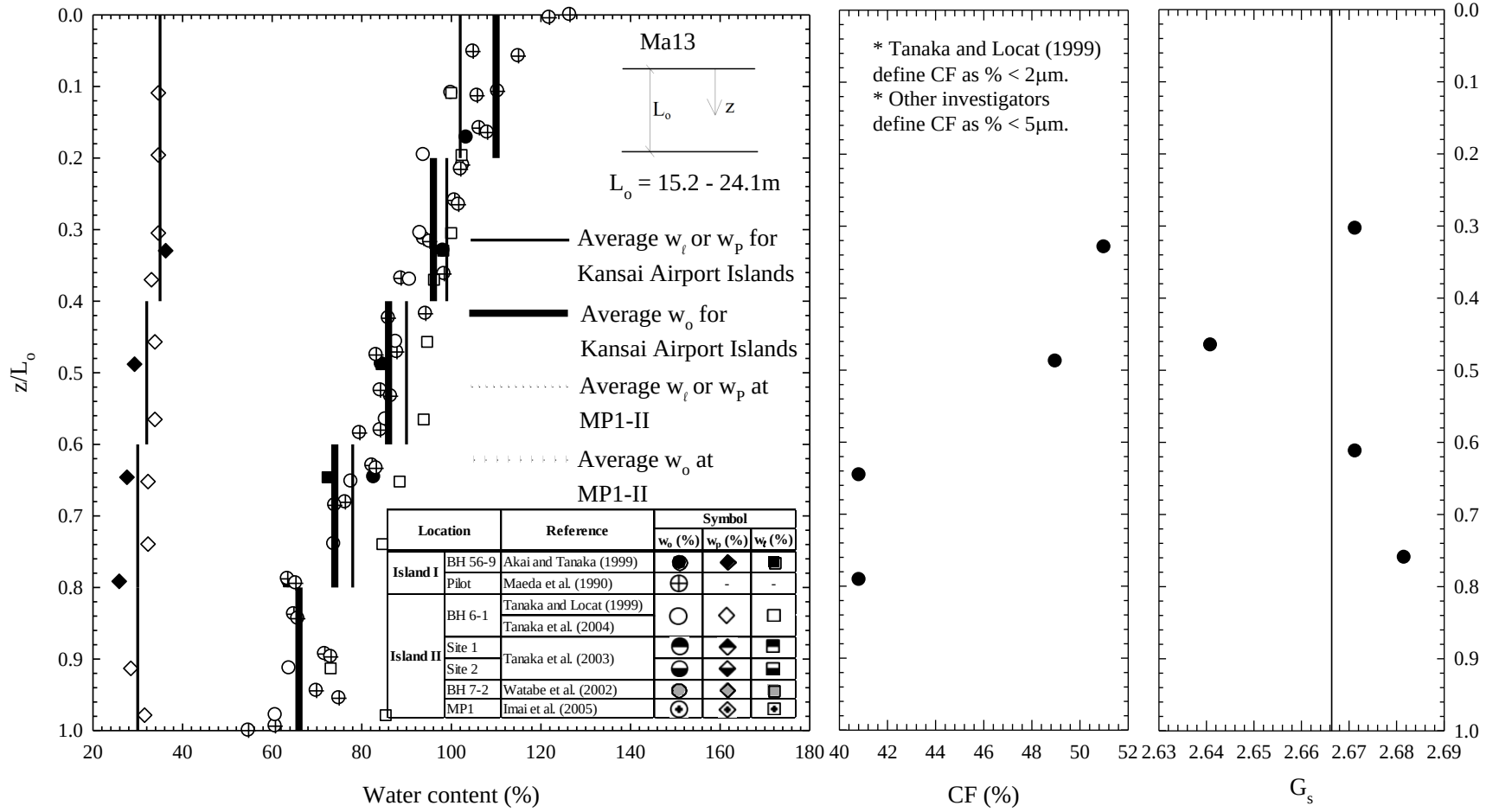

Figure 4-11 Atterberg limits and natural water content, clay-size fraction, and specific gravity for Ma13.

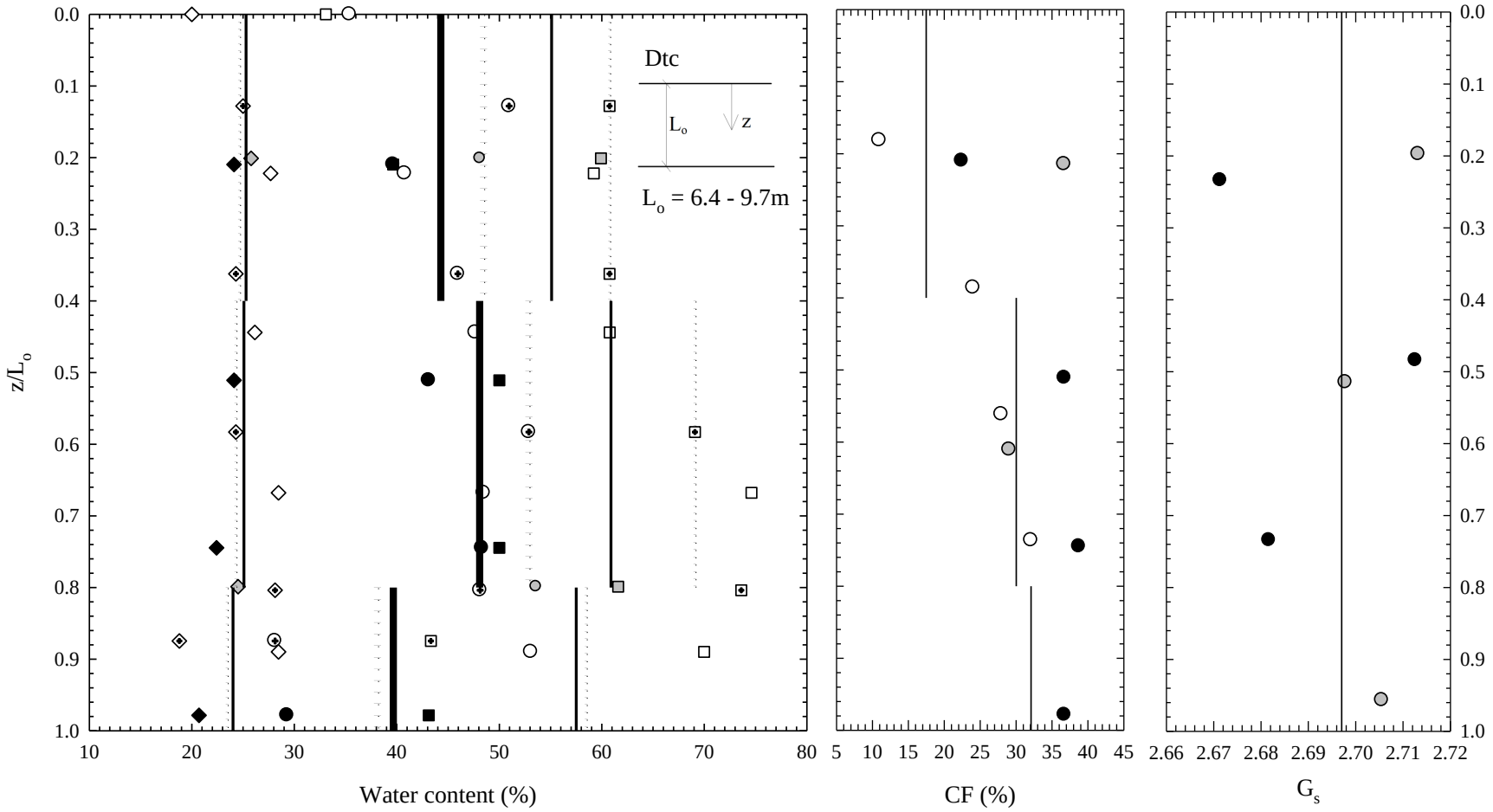

Figure 4-12 Atterberg limits and natural water content, clay-size fraction, and specific gravity for Dtc. Average of clay size fraction data representing % < 2μm used to calculate vertical permeability (Tanaka and Locat, 1999; Mesri et al., 1994). See Figure 4-11 for symbol meanings.

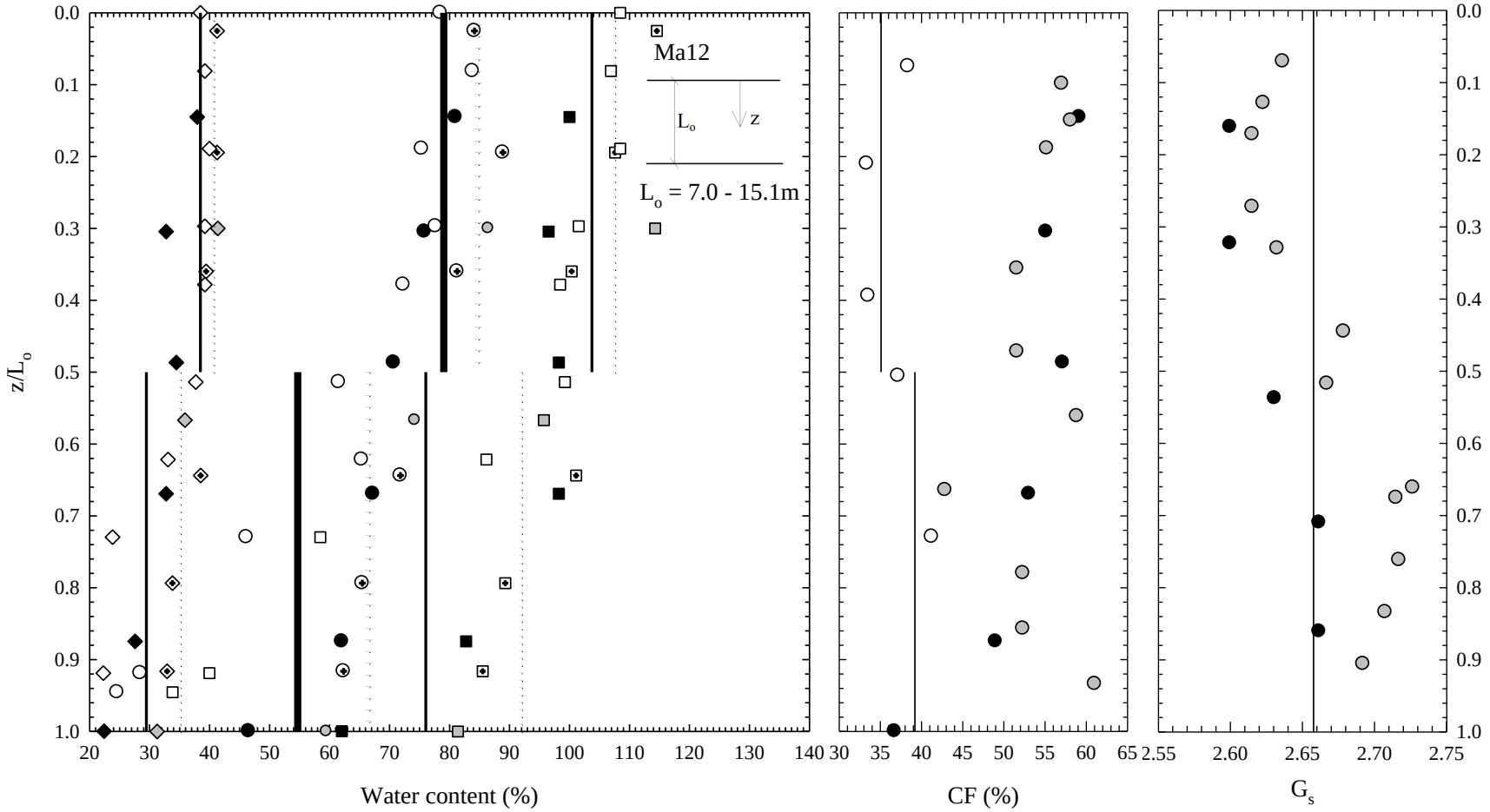

Figure 4-13 Atterberg limits and natural water content, clay-size fraction, and specific gravity for Ma12. Average of clay size fraction data representing % < 2μm used to calculate vertical permeability (Tanaka and Locat, 1999; Mesri et al., 1994). See Figure 4-11 for symbol meanings.

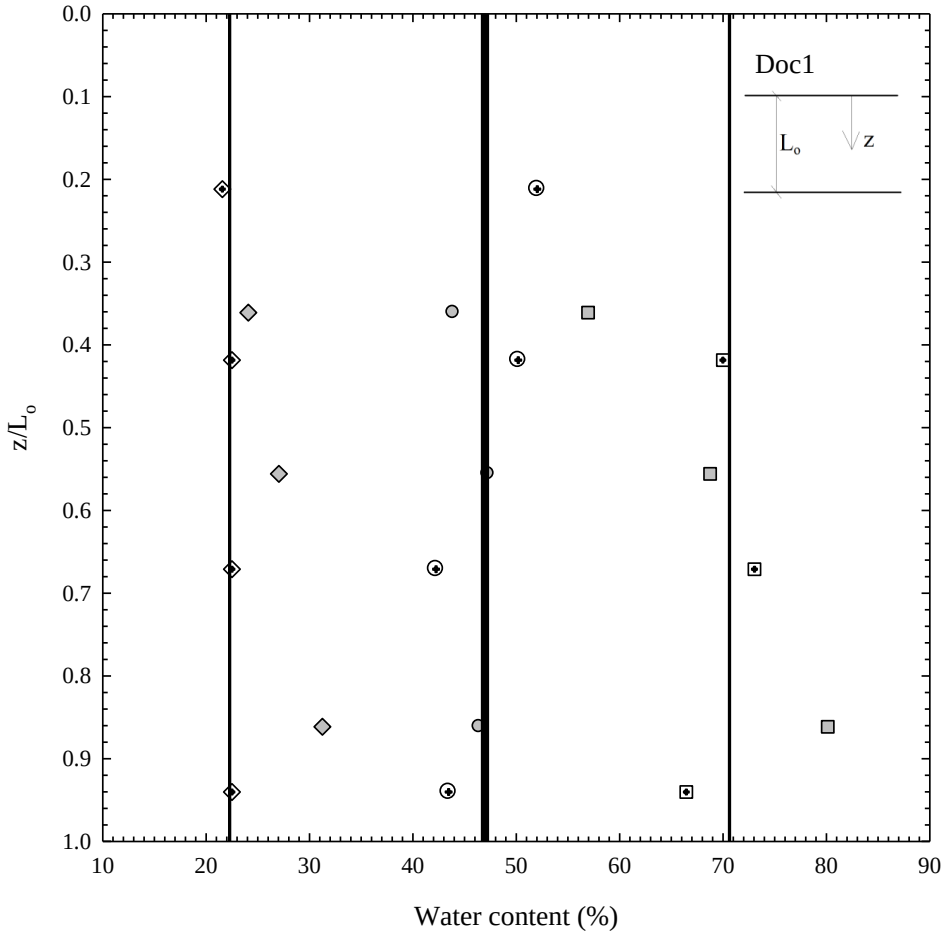

Figure 4-14 Atterberg limits and natural water content for Doc1. See Figure 4-11 for symbol meanings.

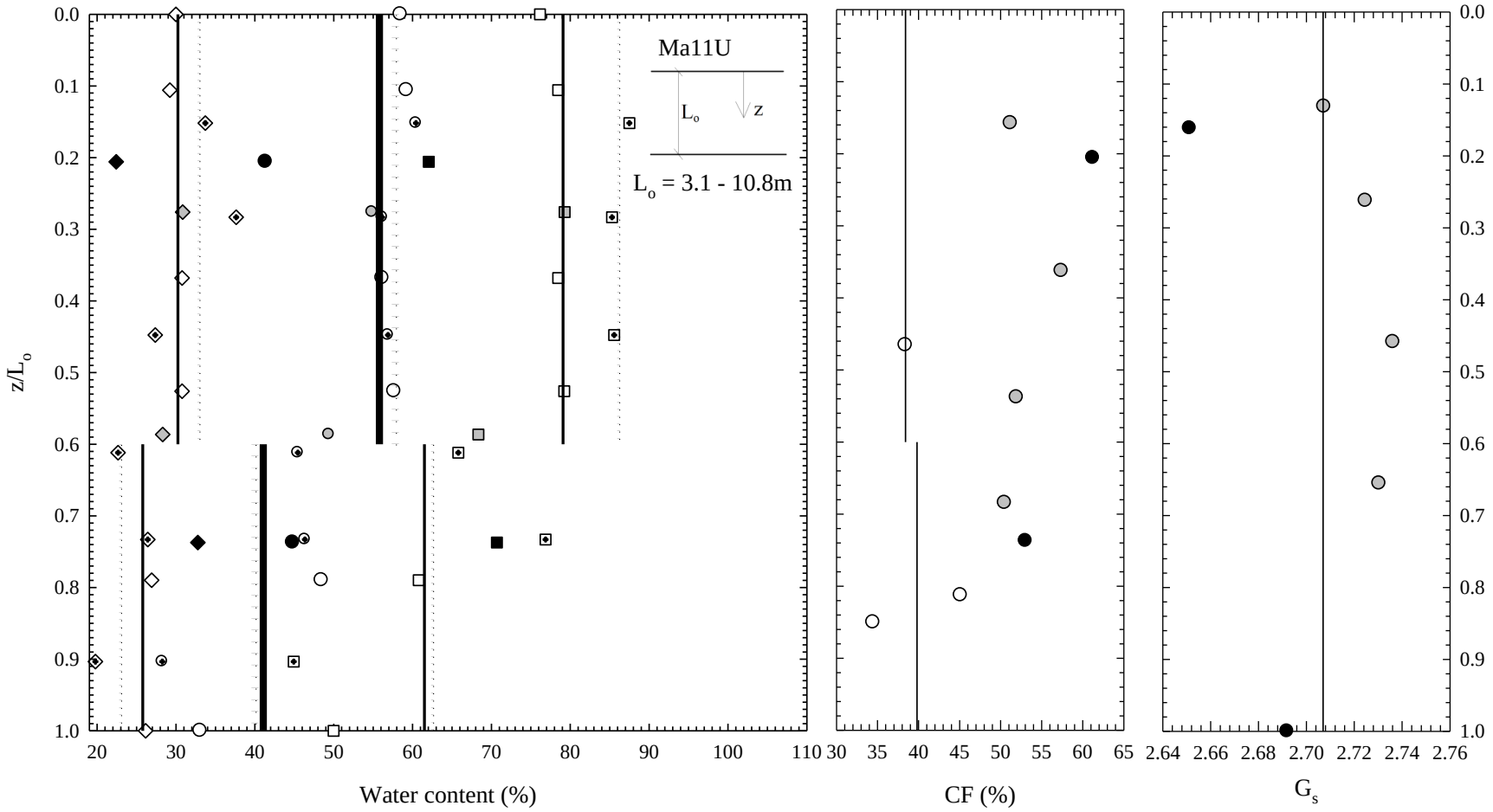

Figure 4-15 Atterberg limits and natural water content, clay-size fraction, and specific gravity for Ma11U. Average of clay size fraction data representing % < 2μm used to calculate vertical permeability (Tanaka and Locat, 1999; Mesri et al., 1994). See Figure 4-11 for symbol meanings.

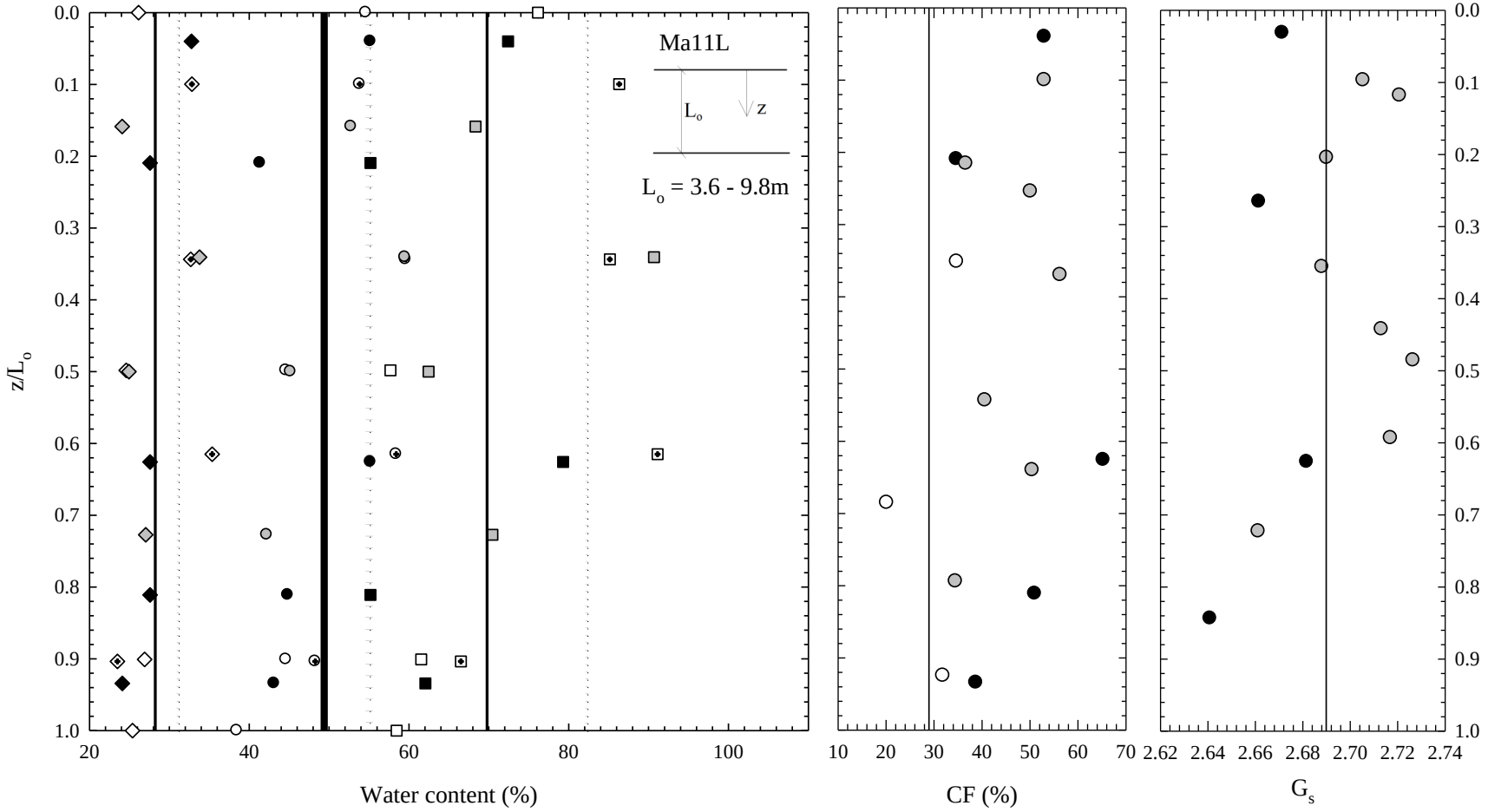

Figure 4-16 Atterberg limits and natural water content, clay-size fraction, and specific gravity for Ma11L. Average of clay size fraction data representing % < 2μm used to calculate vertical permeability (Tanaka and Locat, 1999; Mesri et al., 1994). See Figure 4-11for symbol meanings.

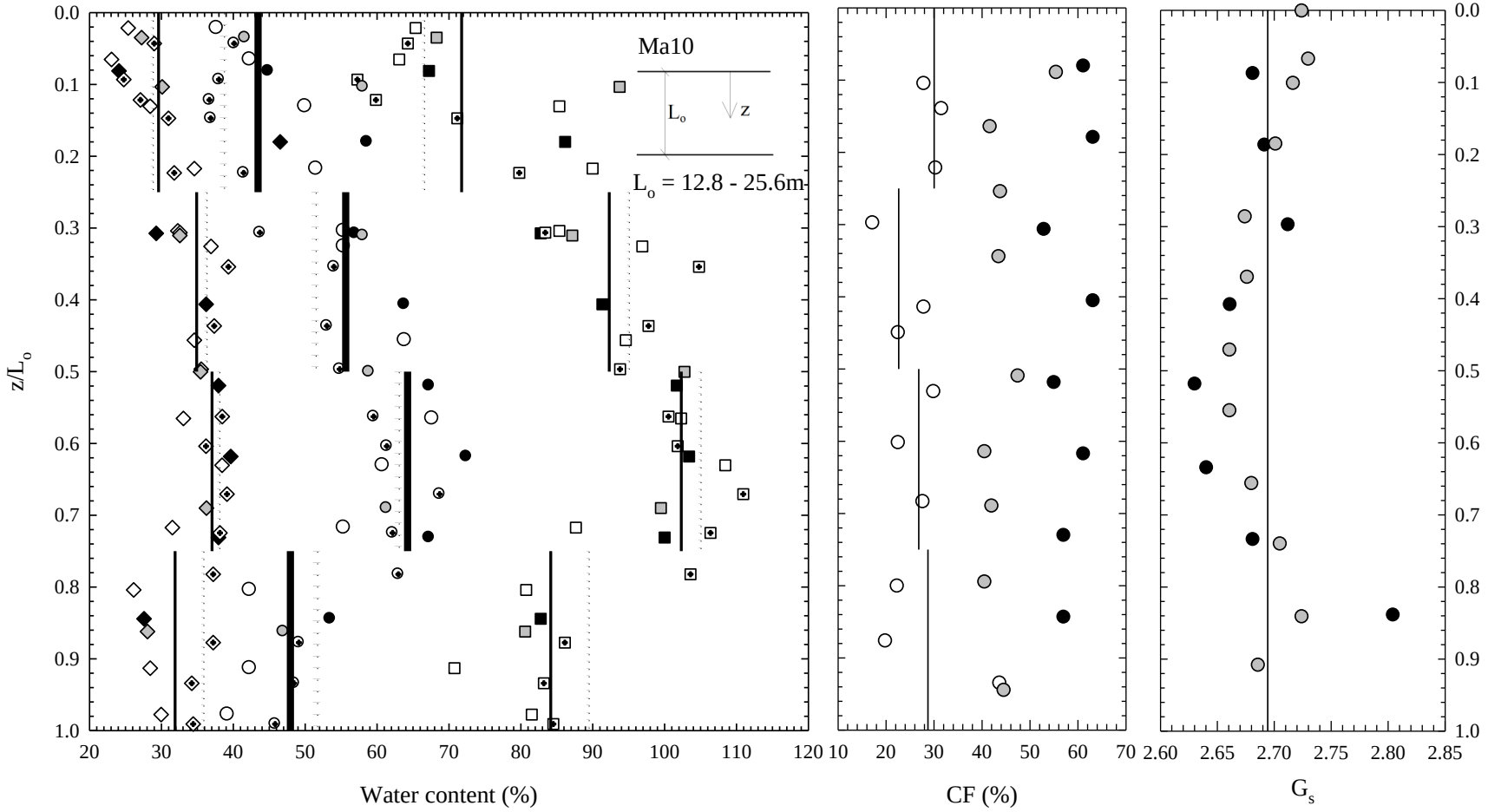

Figure 4-17 Atterberg limits and natural water content, clay-size fraction, and specific gravity for Ma10. Average of clay size fraction data representing % < 2μm used to calculate vertical permeability (Tanaka and Locat, 1999; Mesri et al., 1994). See Figure 4-11 for symbol meanings.

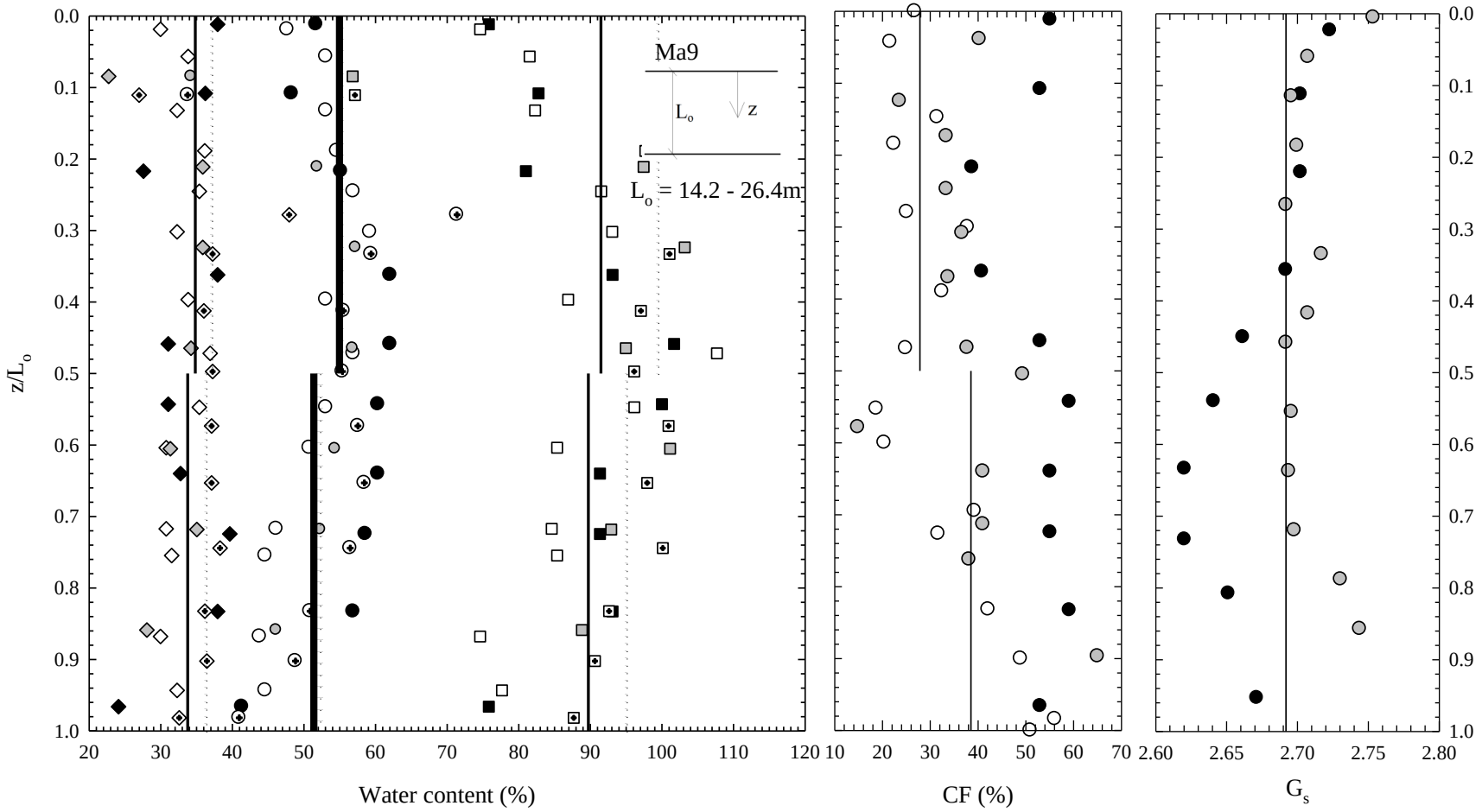

Figure 4-18 Atterberg limits and natural water content, clay-size fraction, and specific gravity for Ma9. Average of clay size fraction data representing % < 2μm used to calculate vertical permeability (Tanaka and Locat, 1999; Mesri et al., 1994). See Figure 4-11 for symbol meanings.

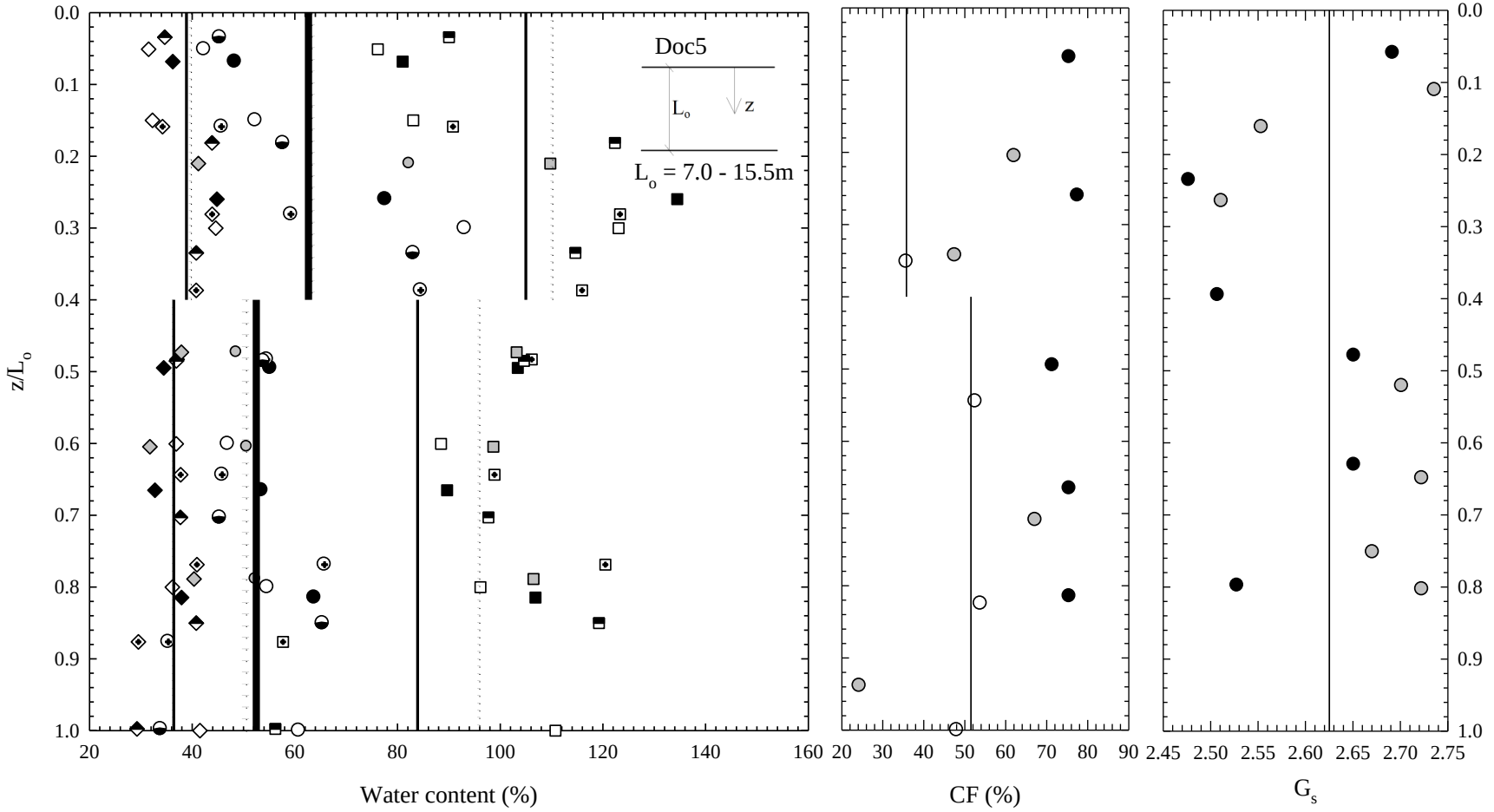

Figure 4-19 Atterberg limits and natural water content, clay-size fraction, and specific gravity for Doc5. Average of clay size fraction data representing % < 2μm used to calculate vertical permeability (Tanaka and Locat, 1999; Mesri et al., 1994). See Figure 4-11 for symbol meanings.

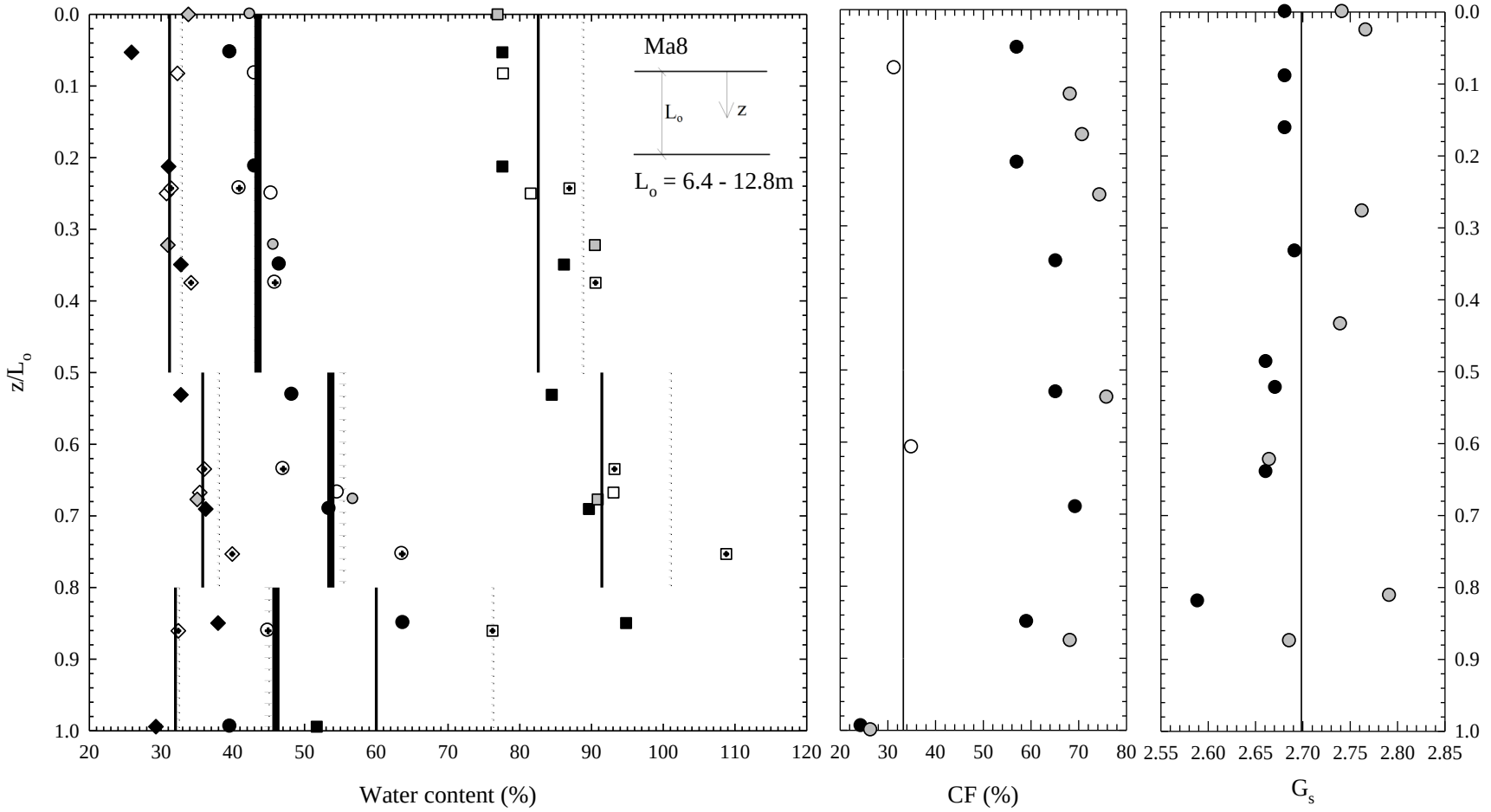

Figure 4-20 Atterberg limits and natural water content, clay-size fraction, and specific gravity for Ma8. Average of clay size fraction data representing % < 2μm used to calculate vertical permeability (Tanaka and Locat, 1999; Mesri et al., 1994). See Figure 4-11 for symbol meanings.

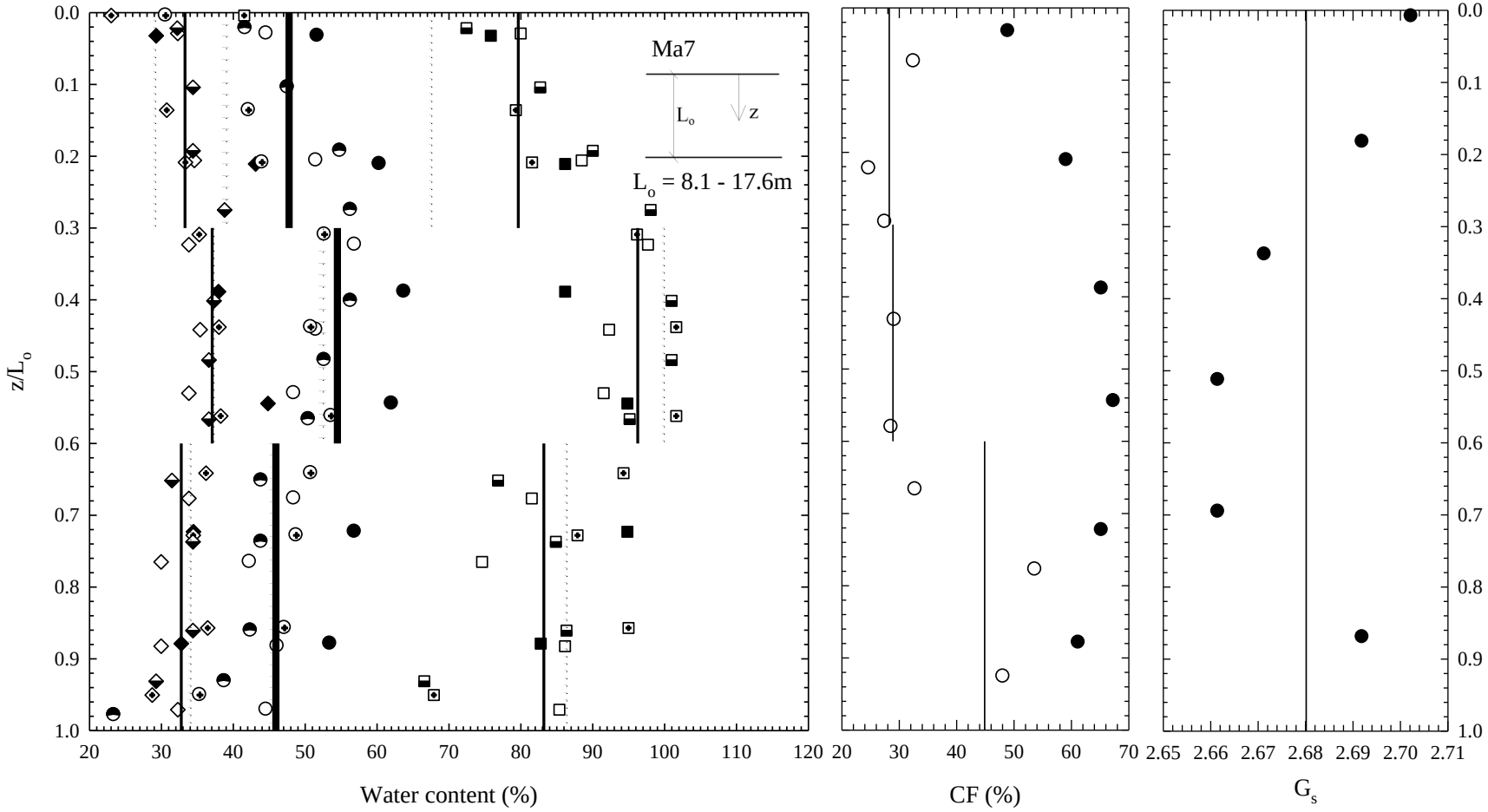

Figure 4-21 Atterberg limits and natural water content, clay-size fraction, and specific gravity for Ma7. Average of clay size fraction data representing % < 2μm used to calculate vertical permeability (Tanaka and Locat, 1999; Mesri et al., 1994). See Figure 4-11 for symbol meanings.

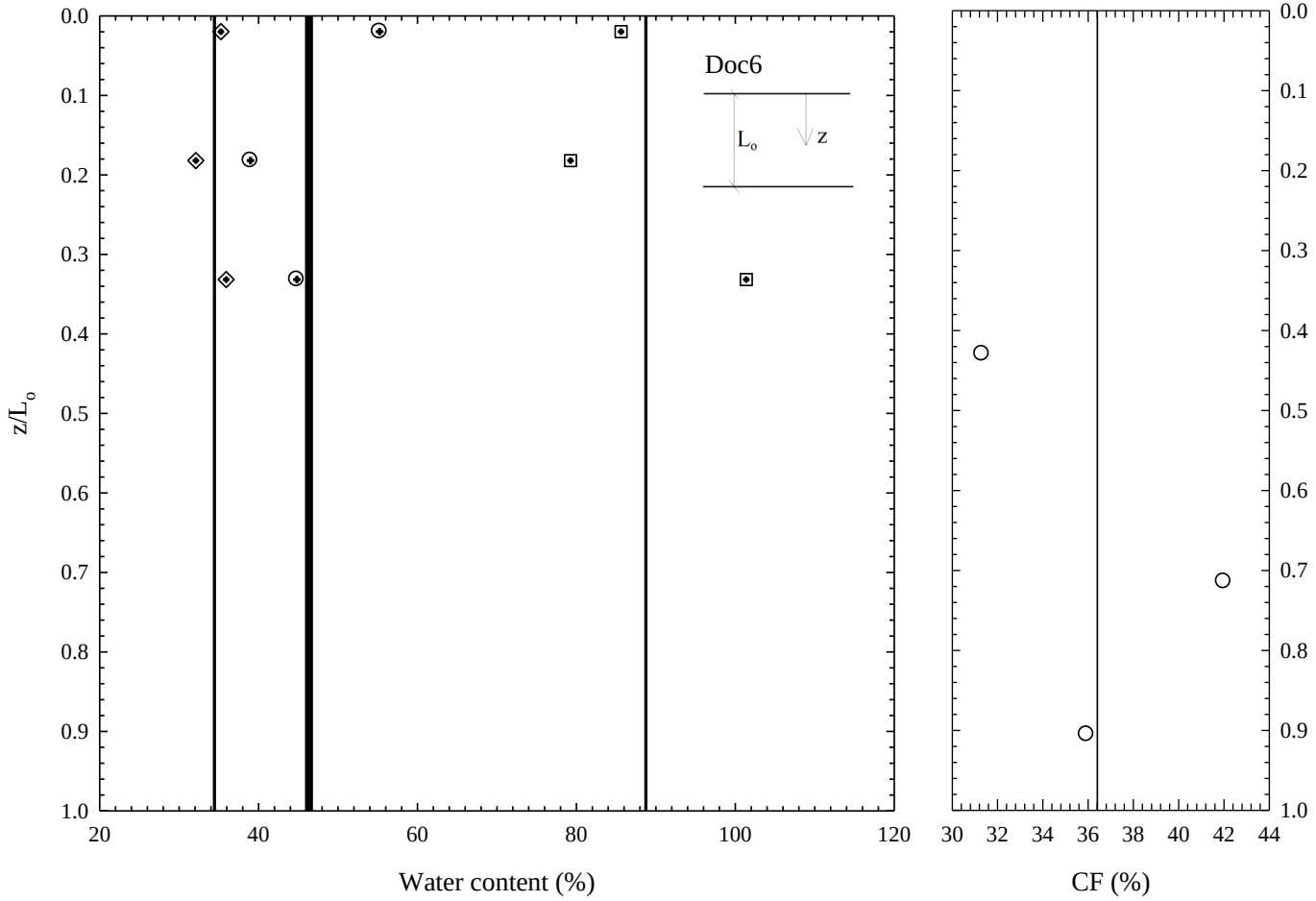

Figure 4-22 Atterberg limits and natural water content and clay-size fraction for Doc6. Average of clay size fraction data representing % < 2μm used to calculate vertical permeability (Tanaka and Locat, 1999; Mesri et al., 1994). See Figure 4-11 for symbol meanings.

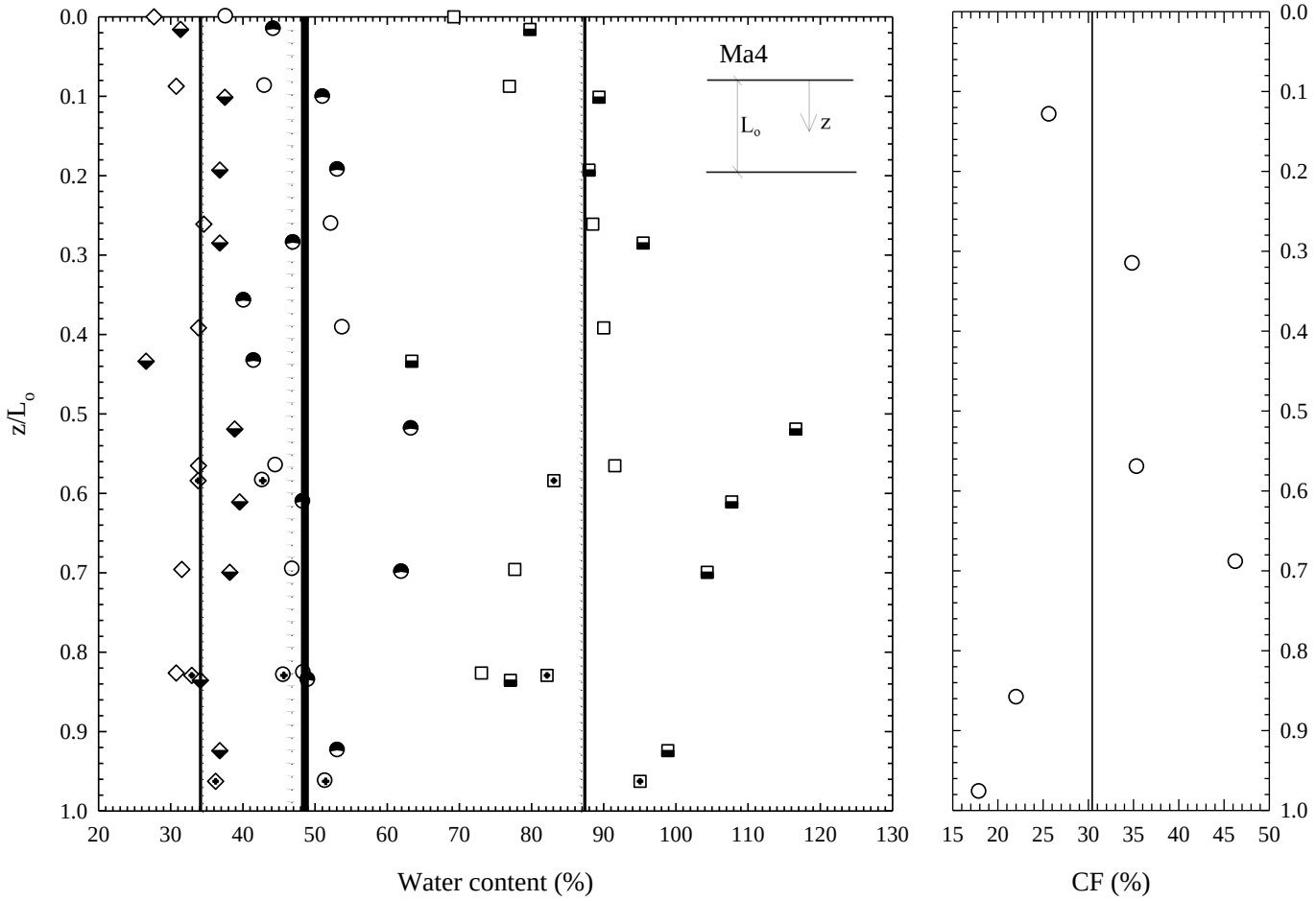

Figure 4-23 Atterberg limits and natural water content and clay-size fraction for Ma4. Average of clay size fraction data representing % < 2μm used to calculate vertical permeability (Tanaka and Locat, 1999; Mesri et al., 1994). See Figure 4-11 for symbol meanings.

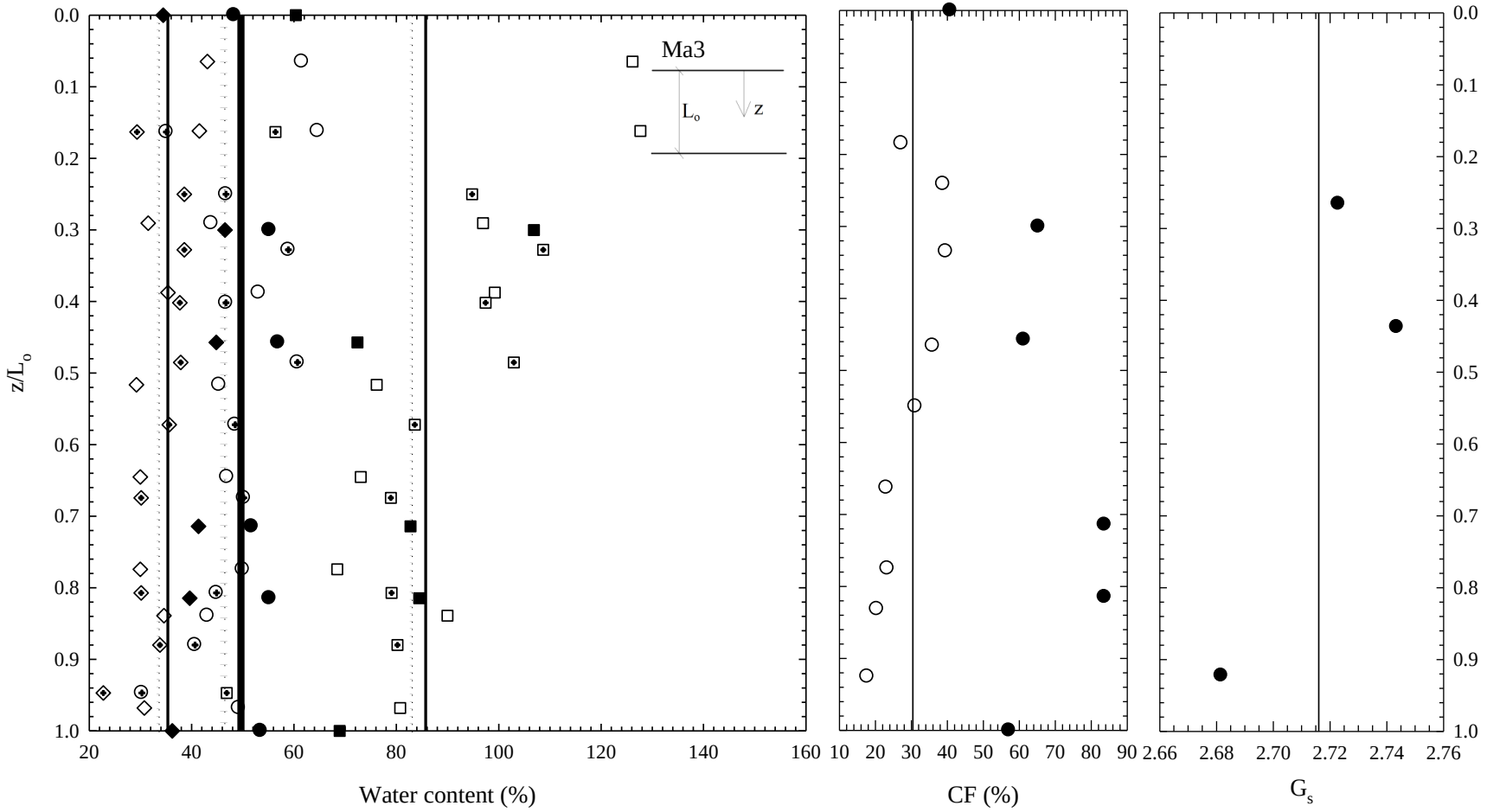

Figure 4-24 Atterberg limits and natural water content and clay-size fraction for Ma3. Average of clay size fraction data representing % < 2μm used to calculate vertical permeability (Tanaka and Locat, 1999; Mesri et al., 1994). See Figure 4-11 for symbol meanings.

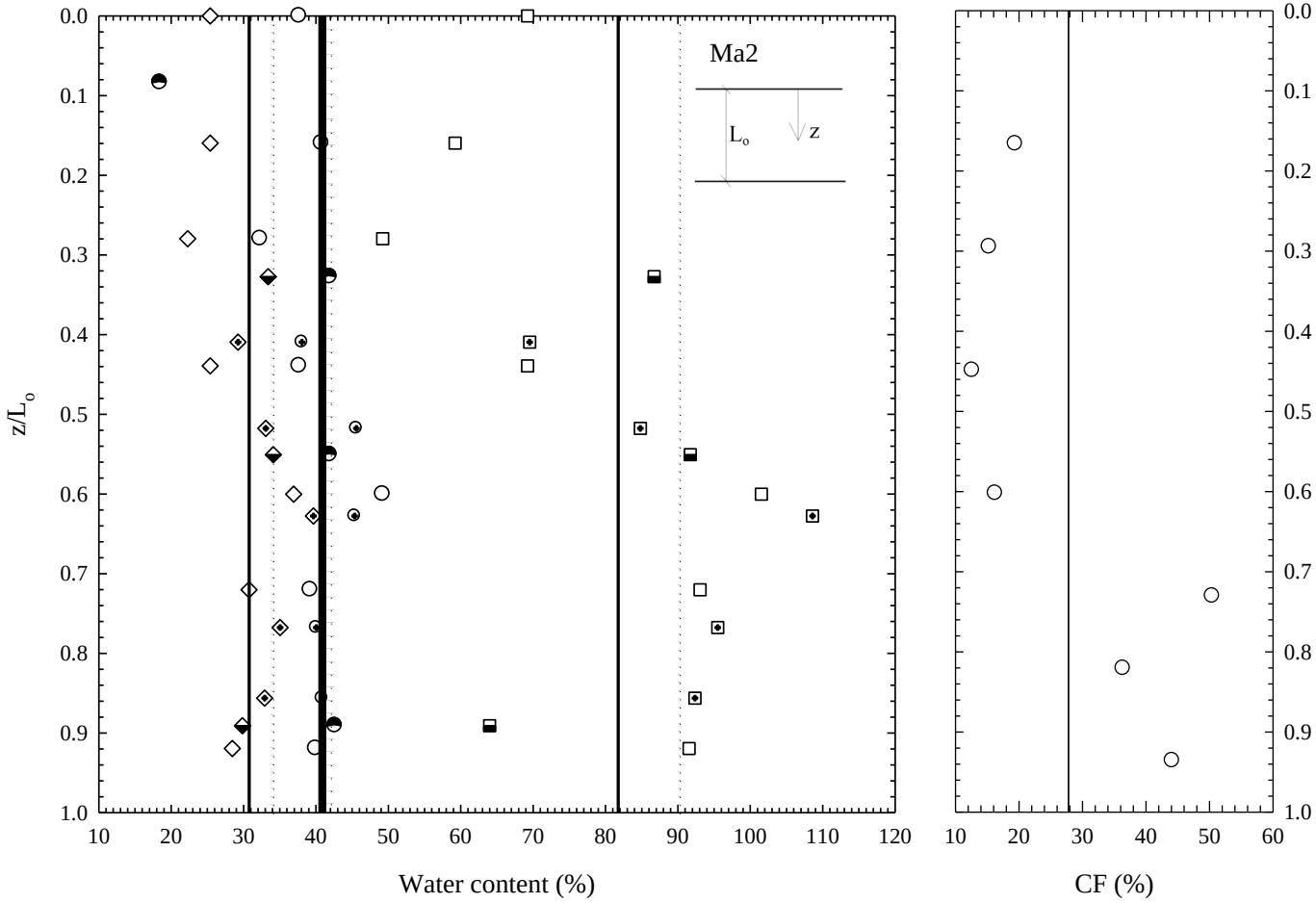

Figure 4-25 Atterberg limits and natural water content and clay-size fraction for Ma2. Average of clay size fraction data representing % < 2μm used to calculate vertical permeability (Tanaka and Locat, 1999; Mesri et al., 1994). See Figure 4-11 for symbol meanings.

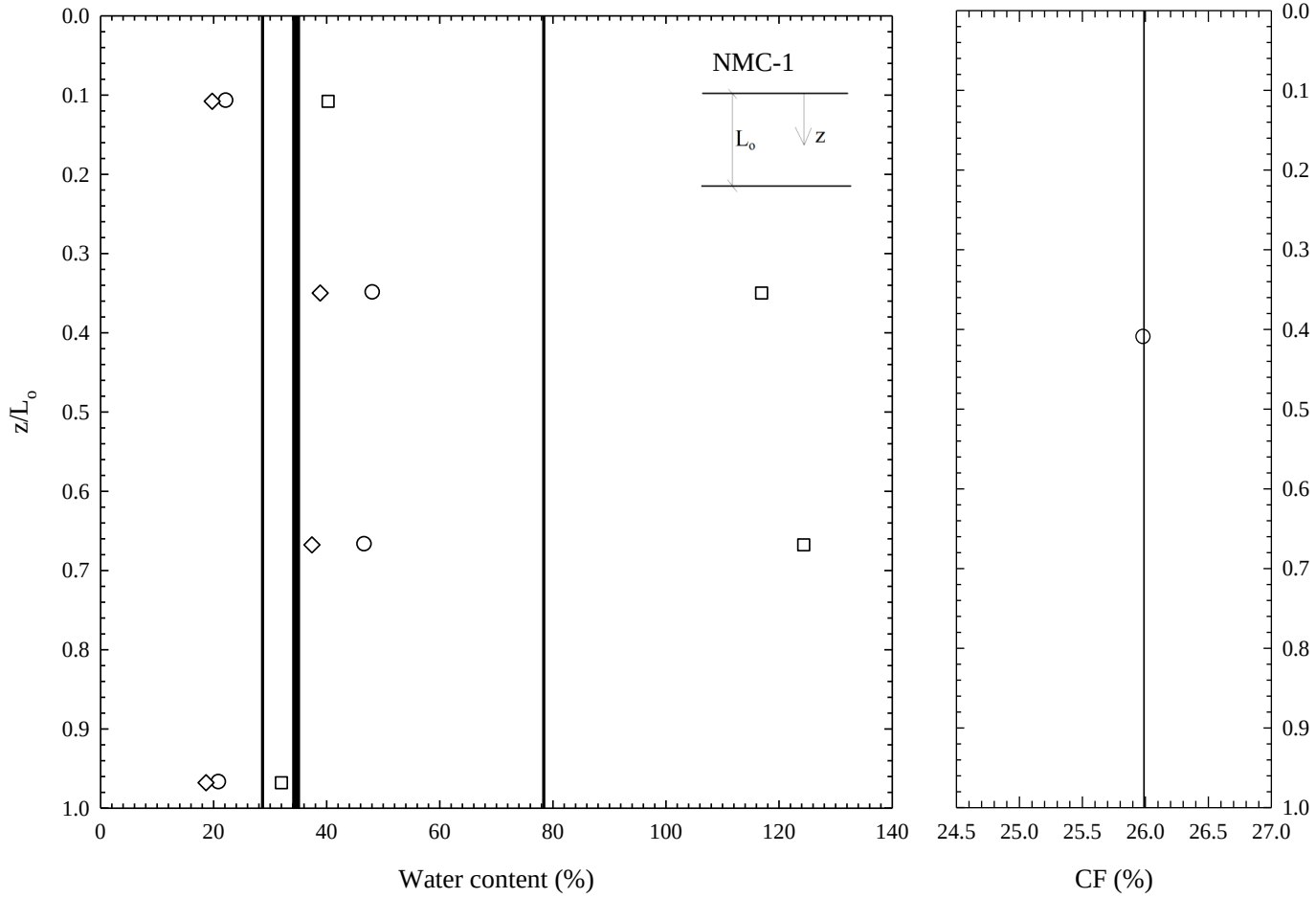

Figure 4-26 Atterberg limits and natural water content and clay-size fraction for NMC-1. Average of clay size fraction data representing % < 2μm used to calculate vertical permeability (Tanaka and Locat, 1999; Mesri et al., 1994). See Figure 4-11 for symbol meanings.

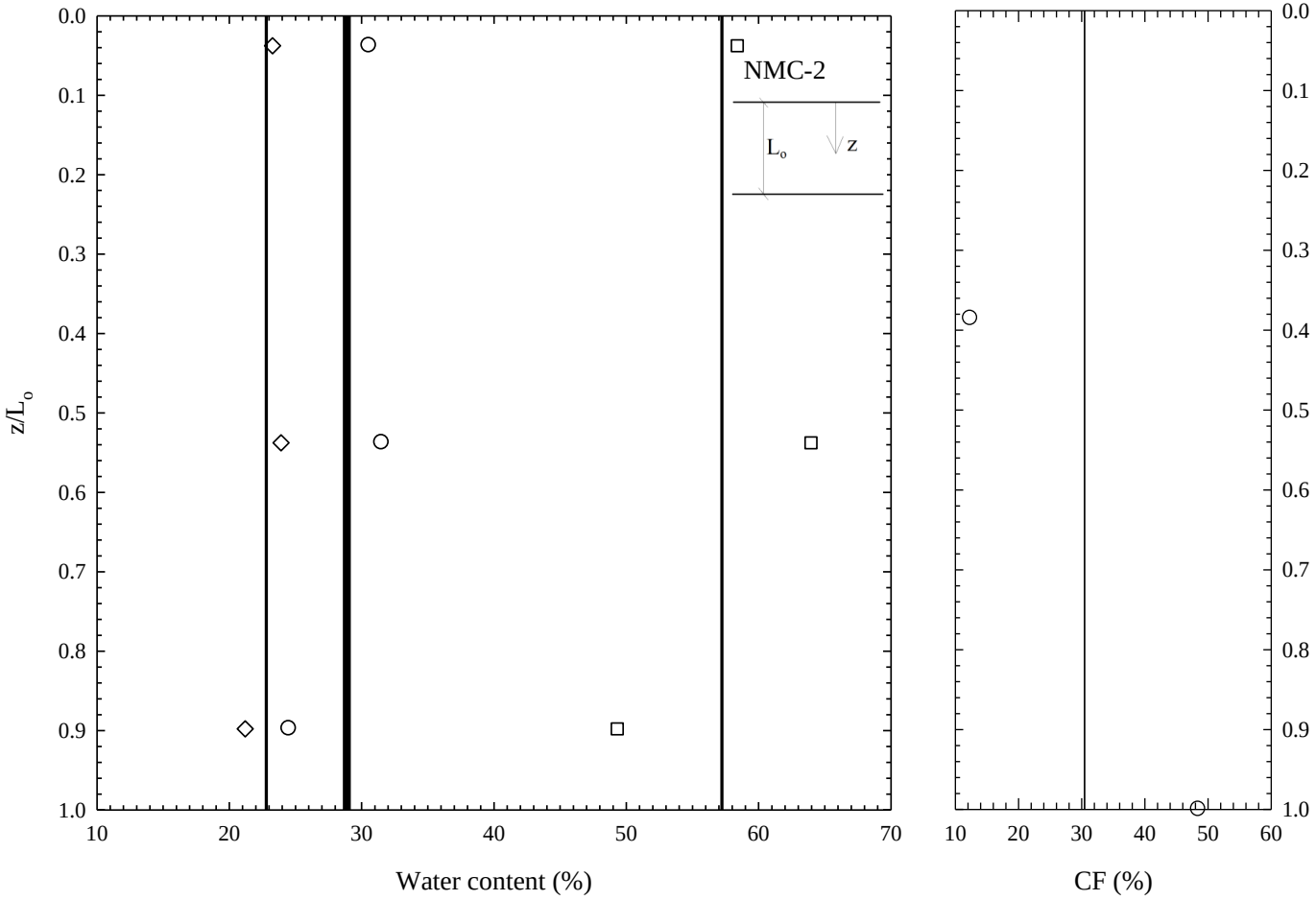

Figure 4-27 Atterberg limits and natural water content and clay-size fraction for NMC-2. Average of clay size fraction data representing % < 2μm used to calculate vertical permeability (Tanaka and Locat, 1999; Mesri et al., 1994). See Figure 4-11 for symbol meanings.

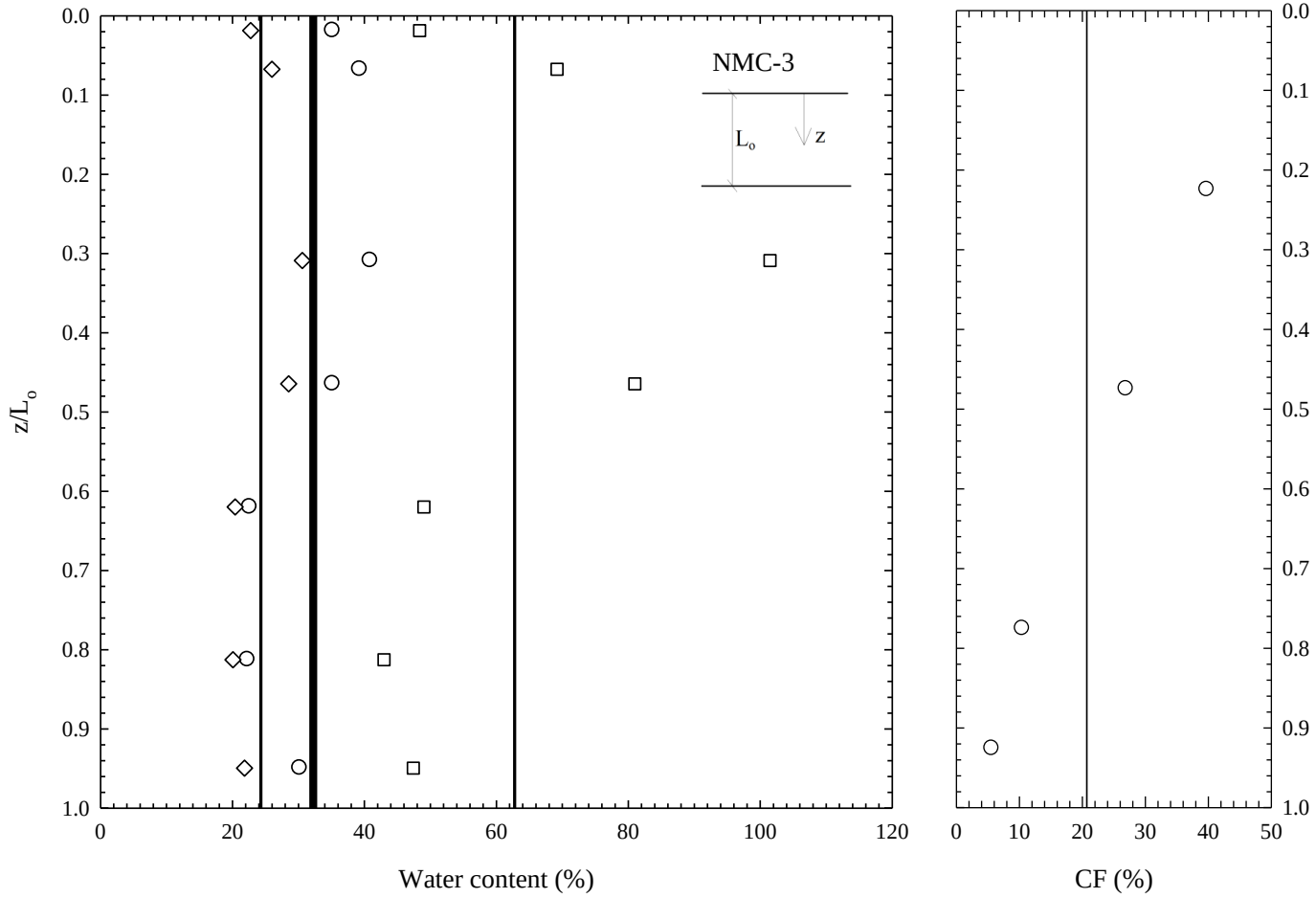

Figure 4-28 Atterberg limits and natural water content and clay-size fraction for NMC-3. Average of clay size fraction data representing % < 2μm used to calculate vertical permeability (Tanaka and Locat, 1999; Mesri et al., 1994). See Figure 4-11 for symbol meanings.

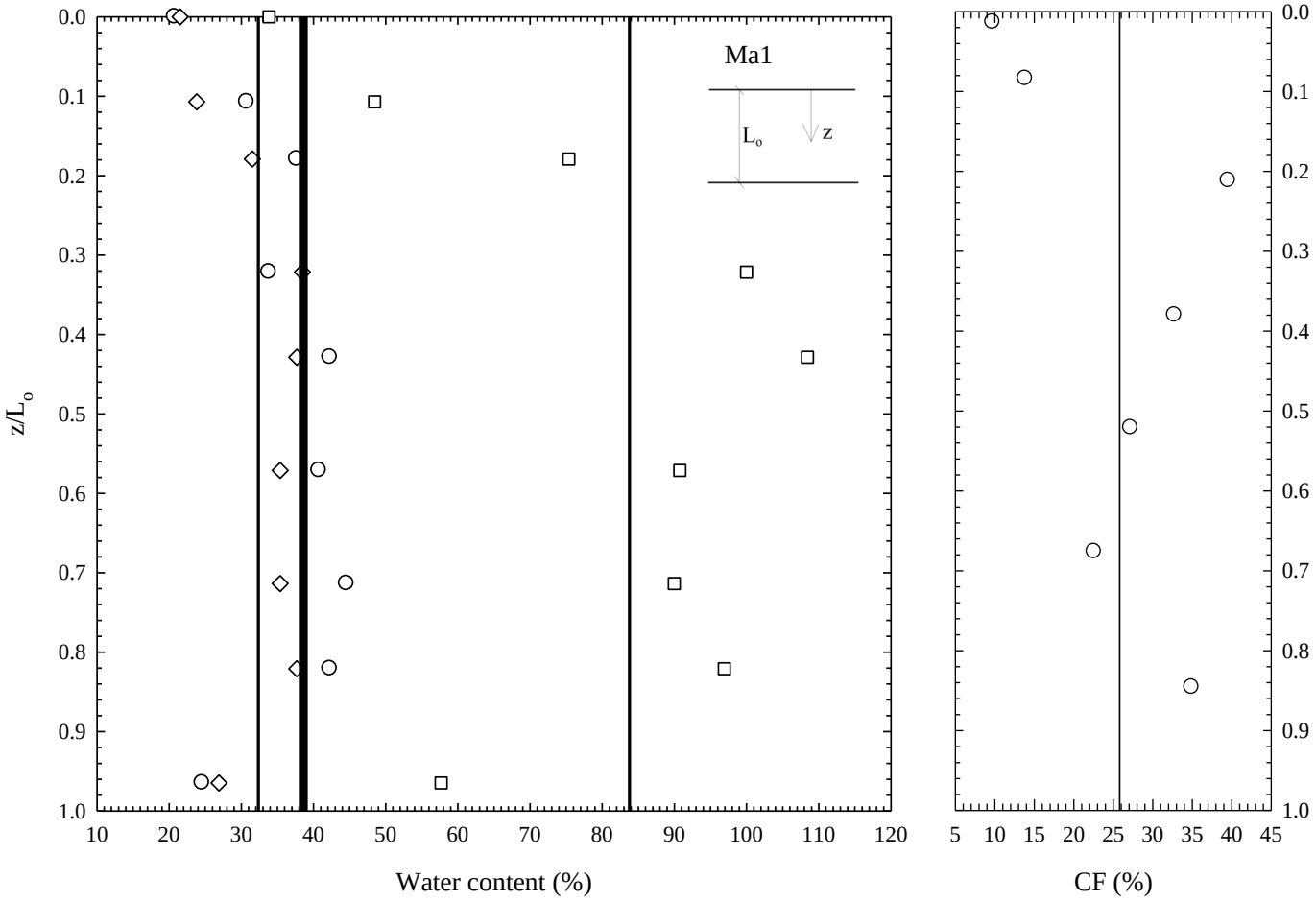

Figure 4-29 Atterberg limits and natural water content and clay-size fraction for Ma1. Average of clay size fraction data representing % < 2μm used to calculate vertical permeability (Tanaka and Locat, 1999; Mesri et al., 1994). See Figure 4-11 for symbol meanings.

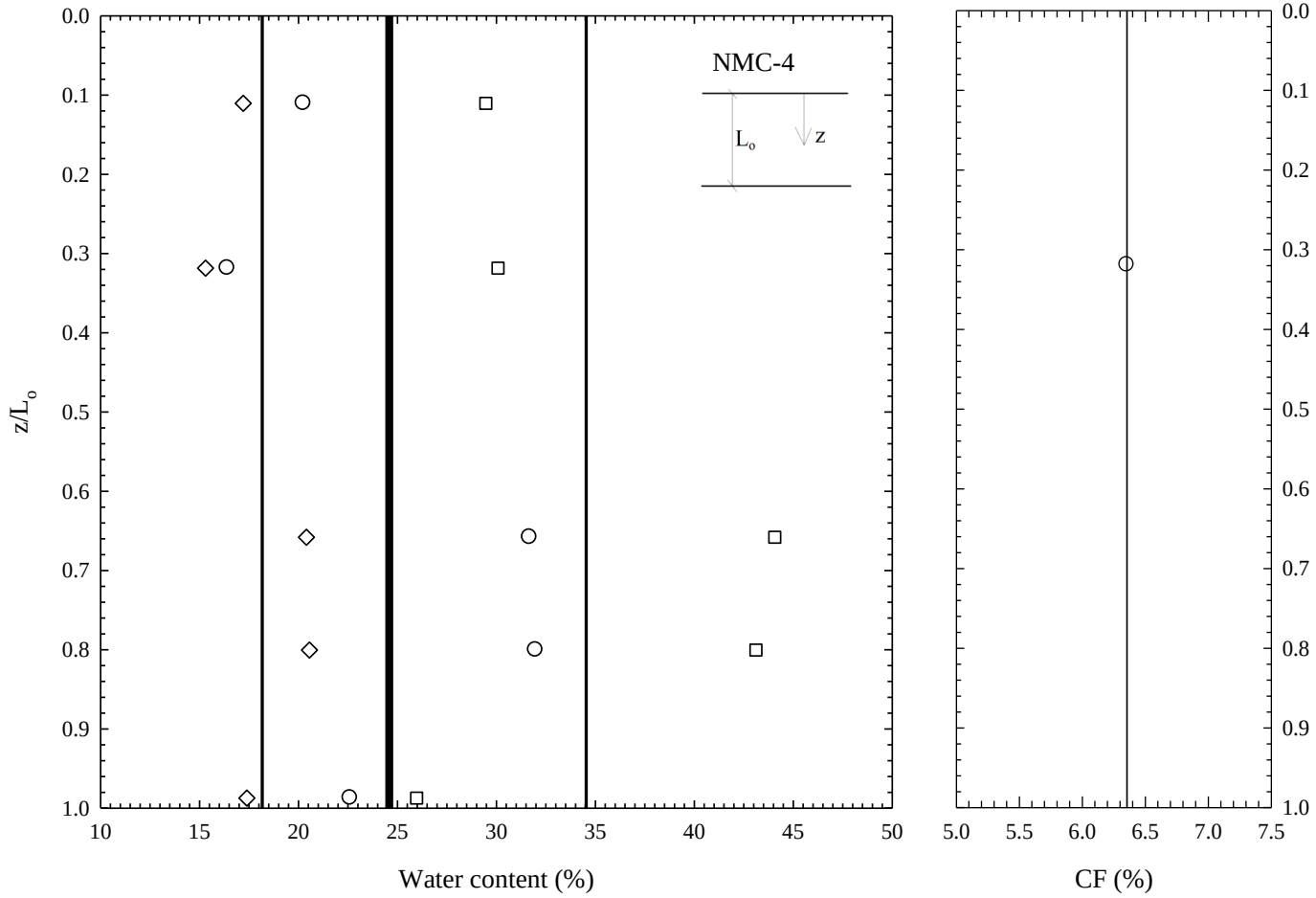

Figure 4-30 Atterberg limits and natural water content and clay-size fraction for NMC-4. Average of clay size fraction data representing % < 2μm used to calculate vertical permeability (Tanaka and Locat, 1999; Mesri et al., 1994). See Figure 4-11 for symbol meanings.

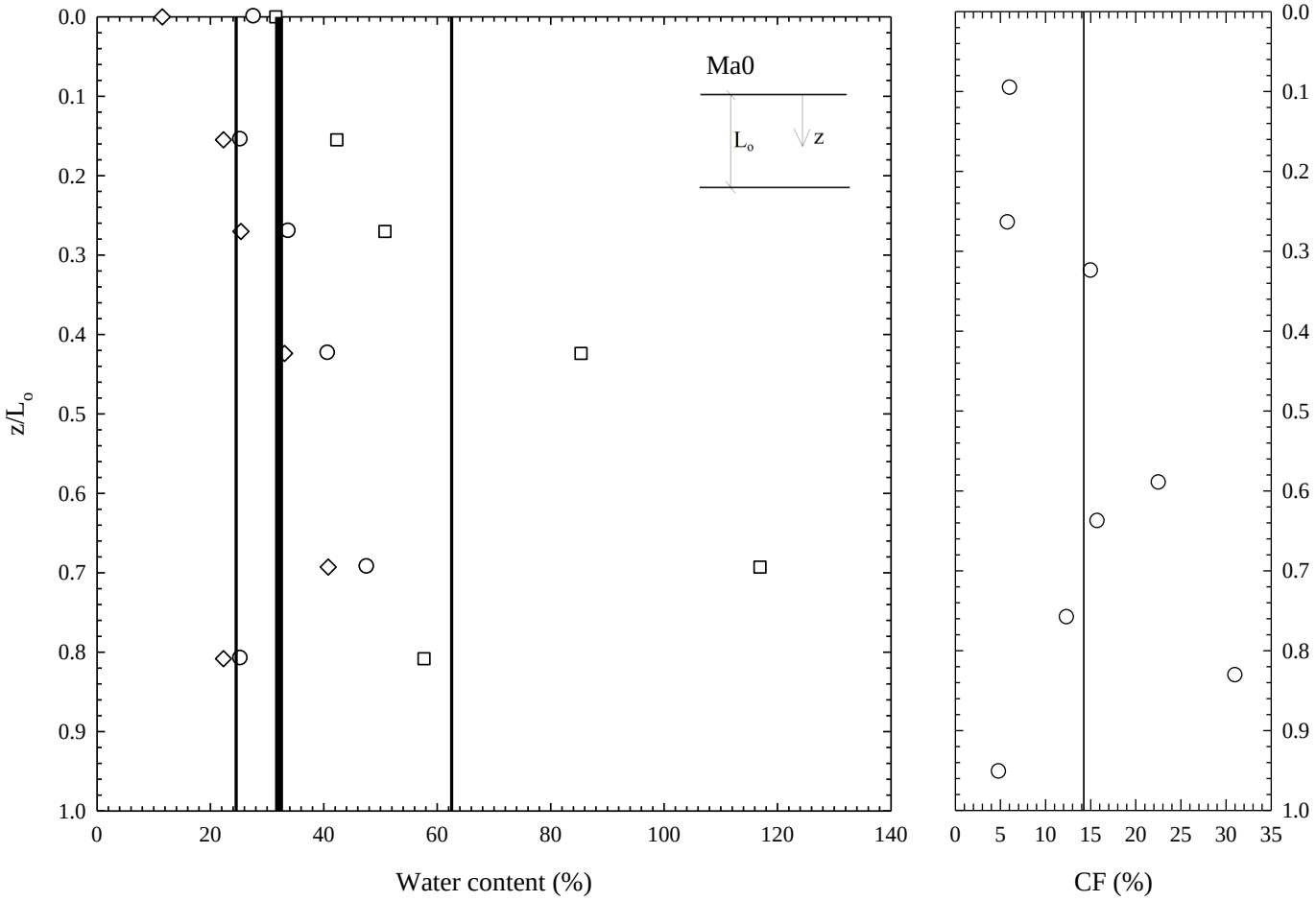

Figure 4-31 Atterberg limits and natural water content and clay-size fraction for Ma0. Average of clay size fraction data representing % < 2μm used to calculate vertical permeability (Tanaka and Locat, 1999; Mesri et al., 1994). See Figure 4-11 for symbol meanings.

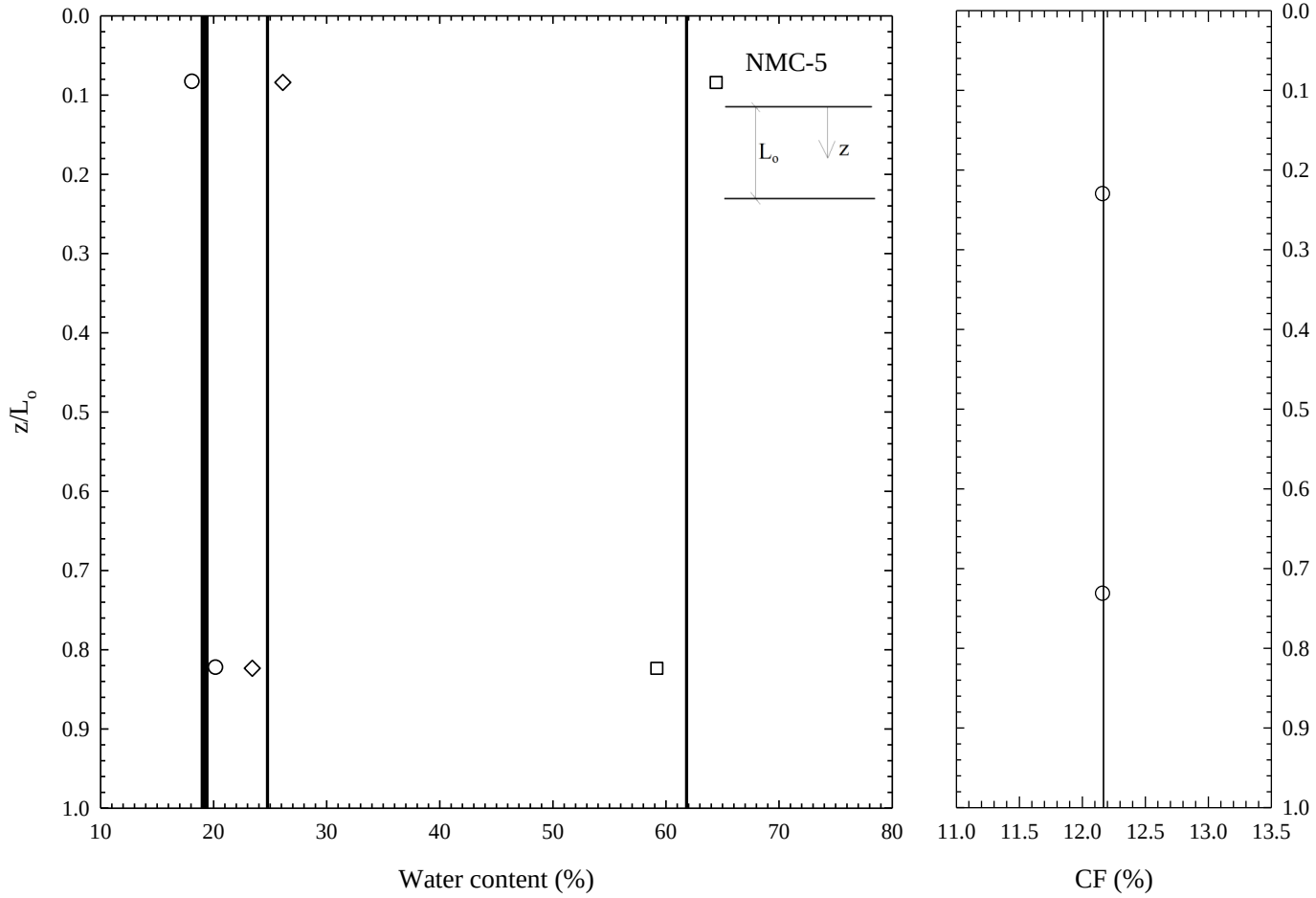

Figure 4-32 Atterberg limits and natural water content and clay-size fraction for NMC-5. Average of clay size fraction data representing % < 2μm used to calculate vertical permeability (Tanaka and Locat, 1999; Mesri et al., 1994). See Figure 4-11 for symbol meanings.

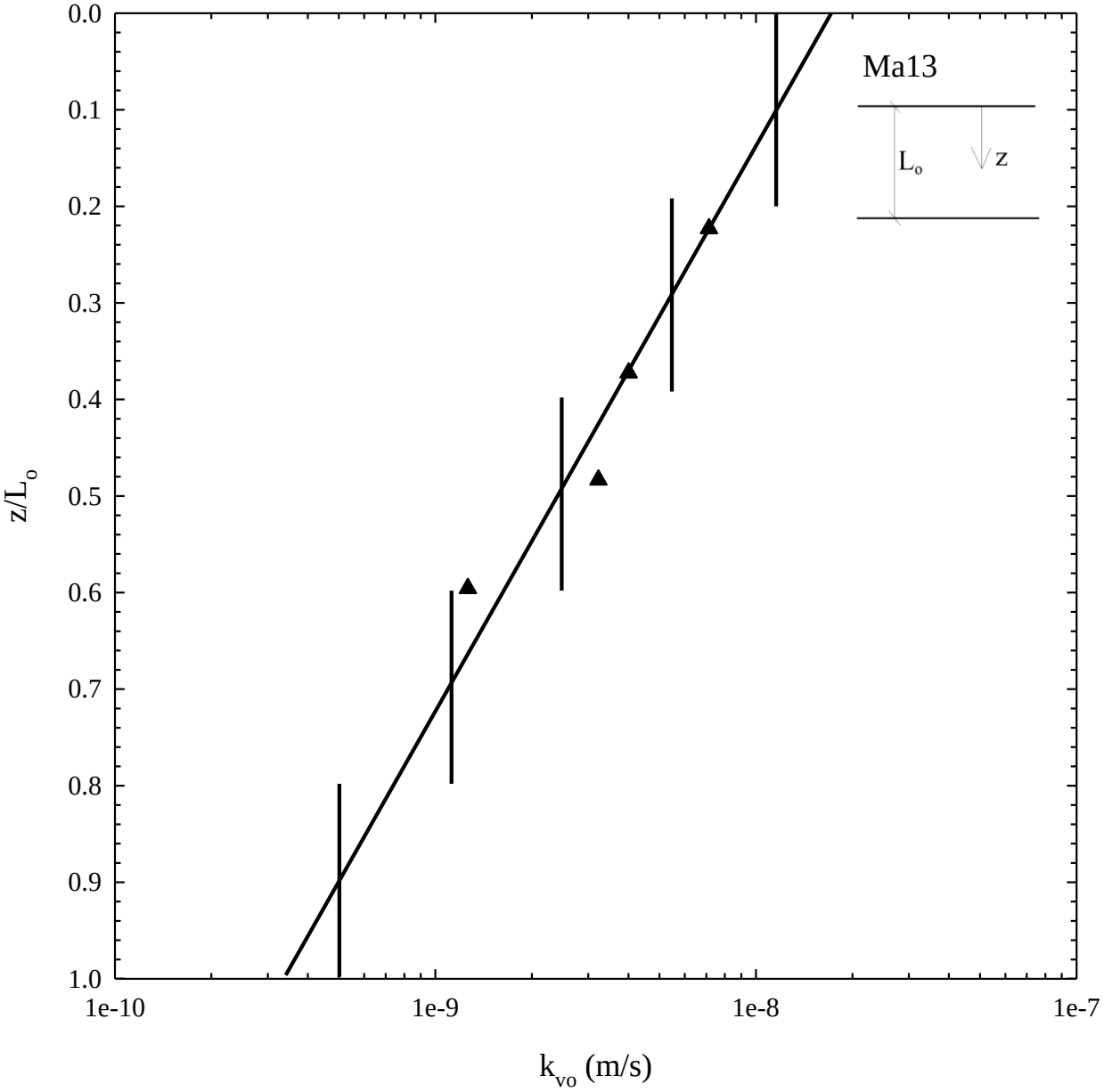

Figure 4-33 k_{vo} values (indicated by solid triangles) estimated from rate of compression observed in incremental loading oedometer tests interpreted using the Terzaghi theory of consolidation (Tanaka et al., 2003), and values considered for subsequent settlement analyses (indicated by vertical lines). Values delineated with vertical lines were increased by a factor of 2 for ILLICON analyses because values of k_v computed from rate of compression data together with the Terzaghi theory of consolidation generally underestimate permeability by a factor of 2 (Mesri et al., 1994).

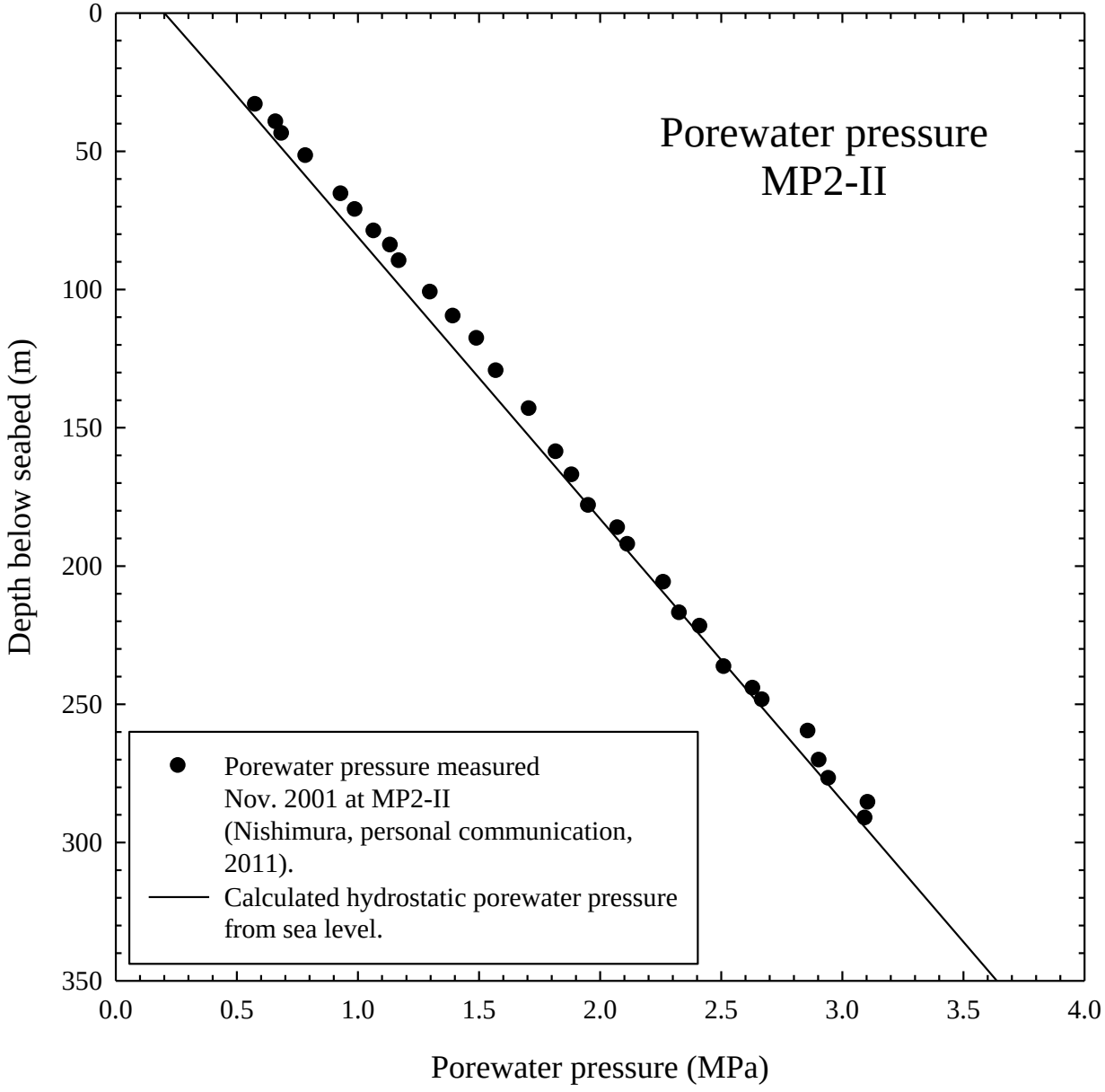

Figure 4-34 Porewater pressure measurements at MP2-II in November 2001 and calculated preconstruction porewater pressure assuming hydrostatic porewater pressure from sea level with unit weight of water (γ_w) equal to 10.04kN/m^3 above the top of sand layer Ds1 and γ_w equal to 9.80 kN/m^3 below the top of sand layer Ds1 (Nishimura, personal communication, 2011).

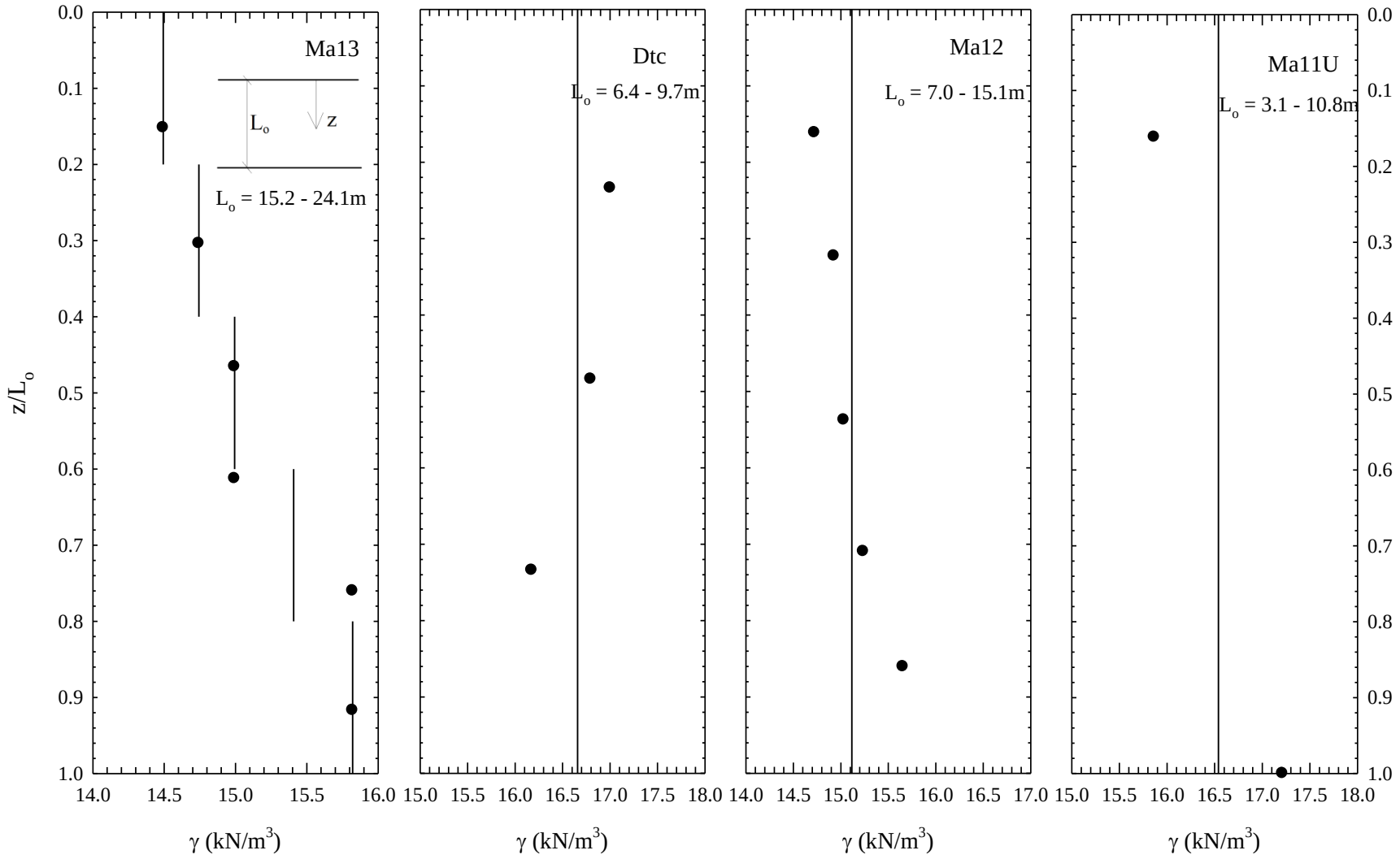

Figure 4-35 Unit weight of clay layers (Akai and Tanaka, 1999).

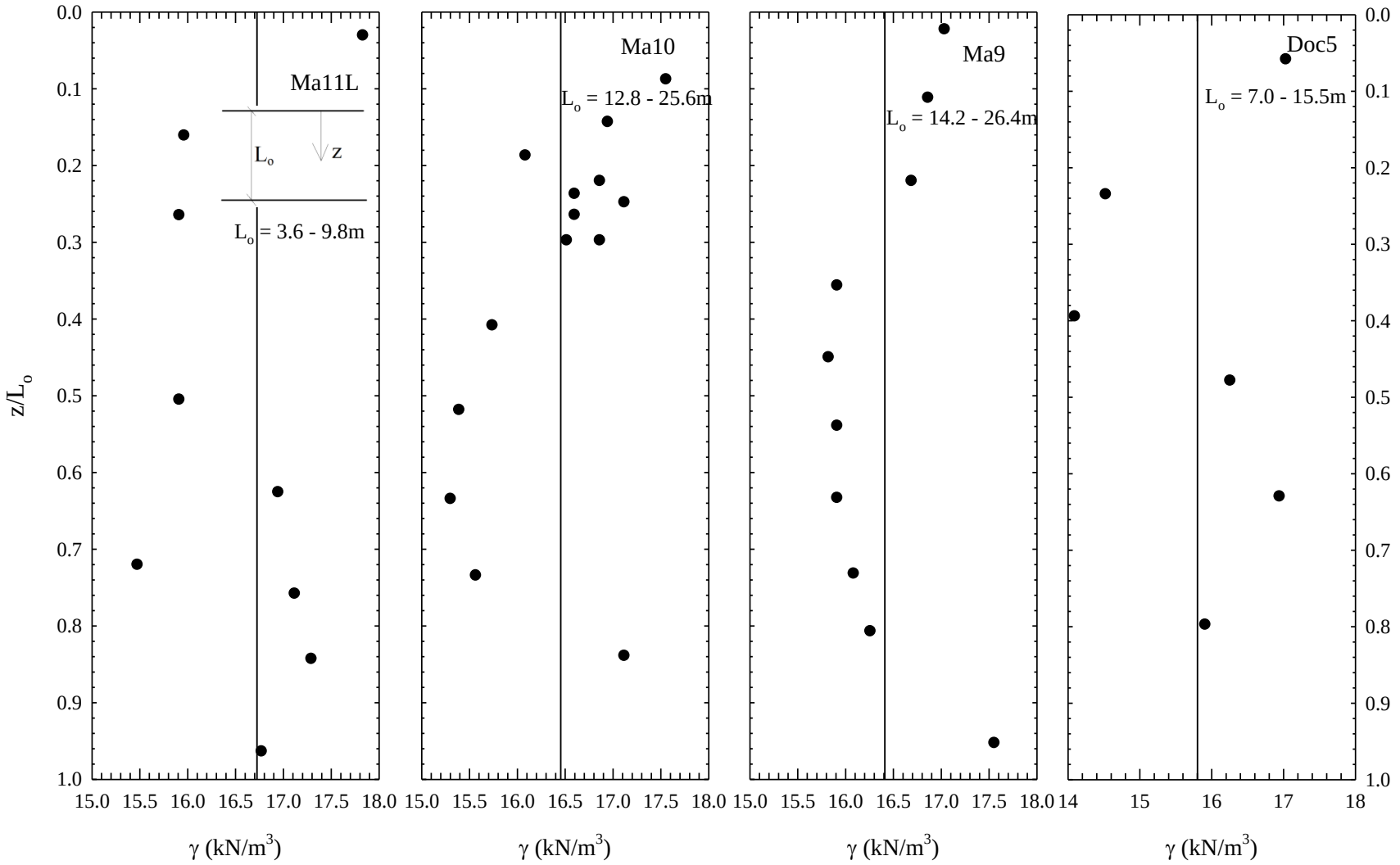

Figure 4-35 cont. Unit weight of clay layers (Akai and Tanaka, 1999).

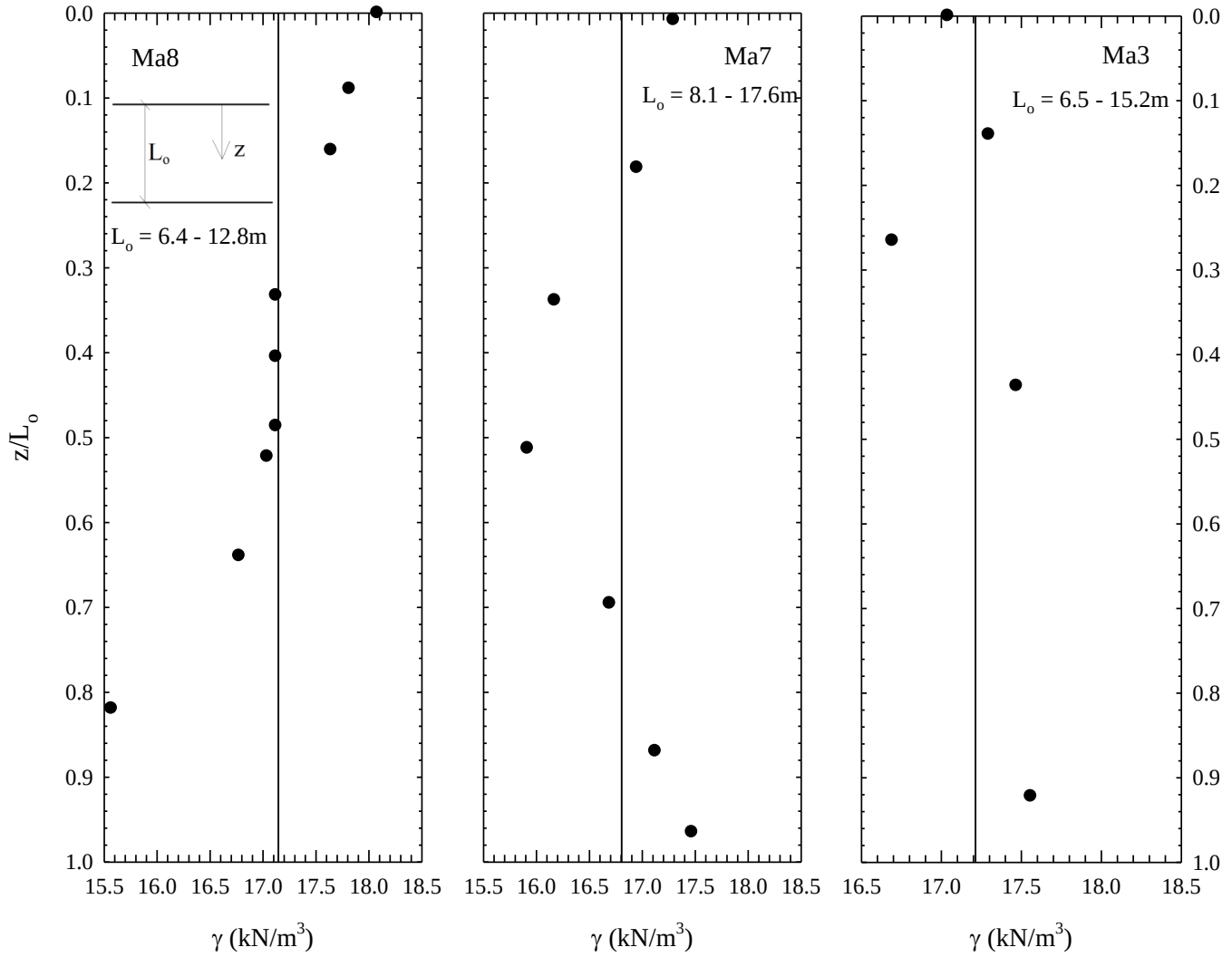

Figure 4-35 cont. Unit weight of clay layers (Akai and Tanaka, 1999).

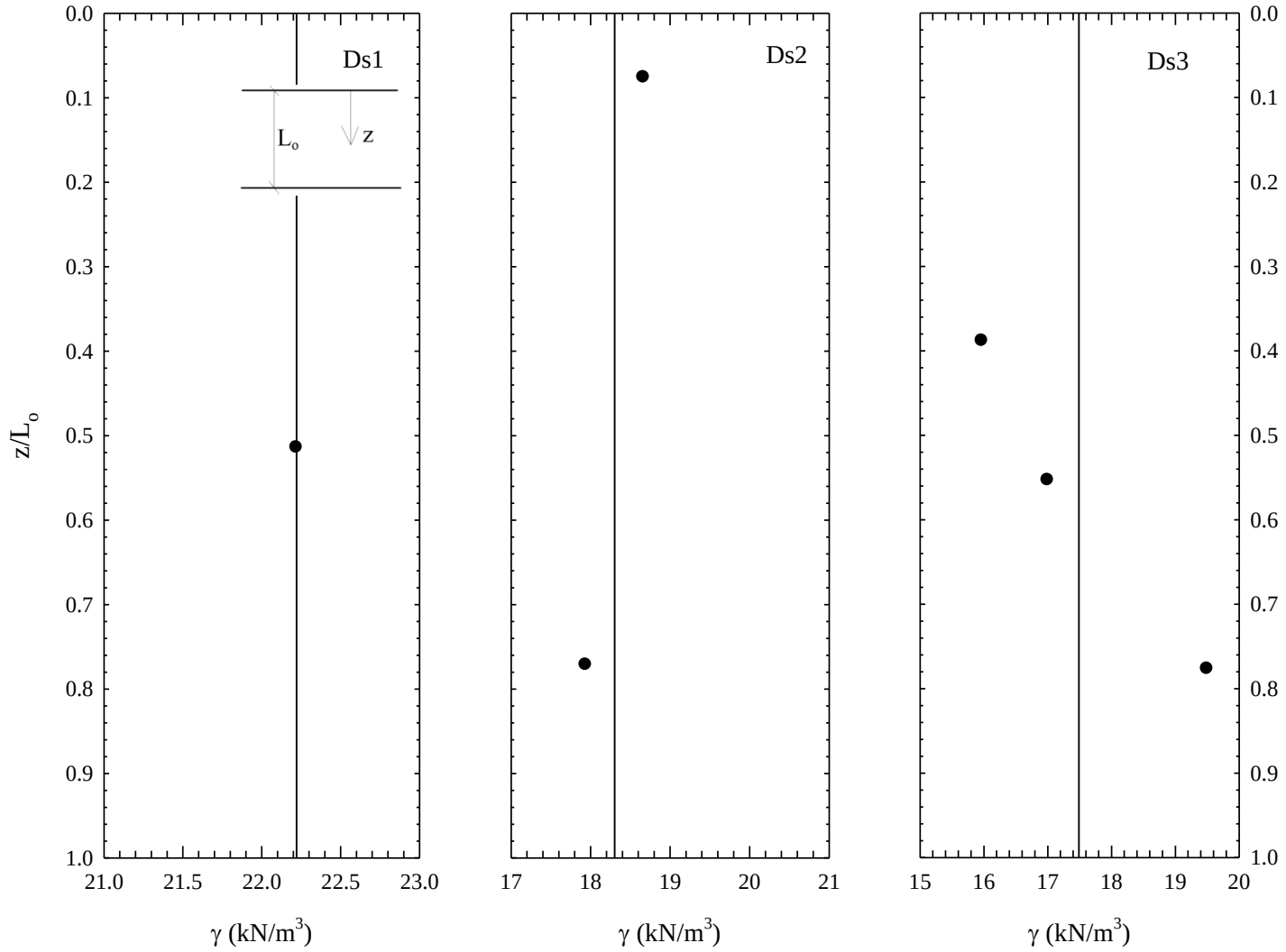

Figure 4-36 Unit weight of sand layers (Akai and Tanaka, 1999).

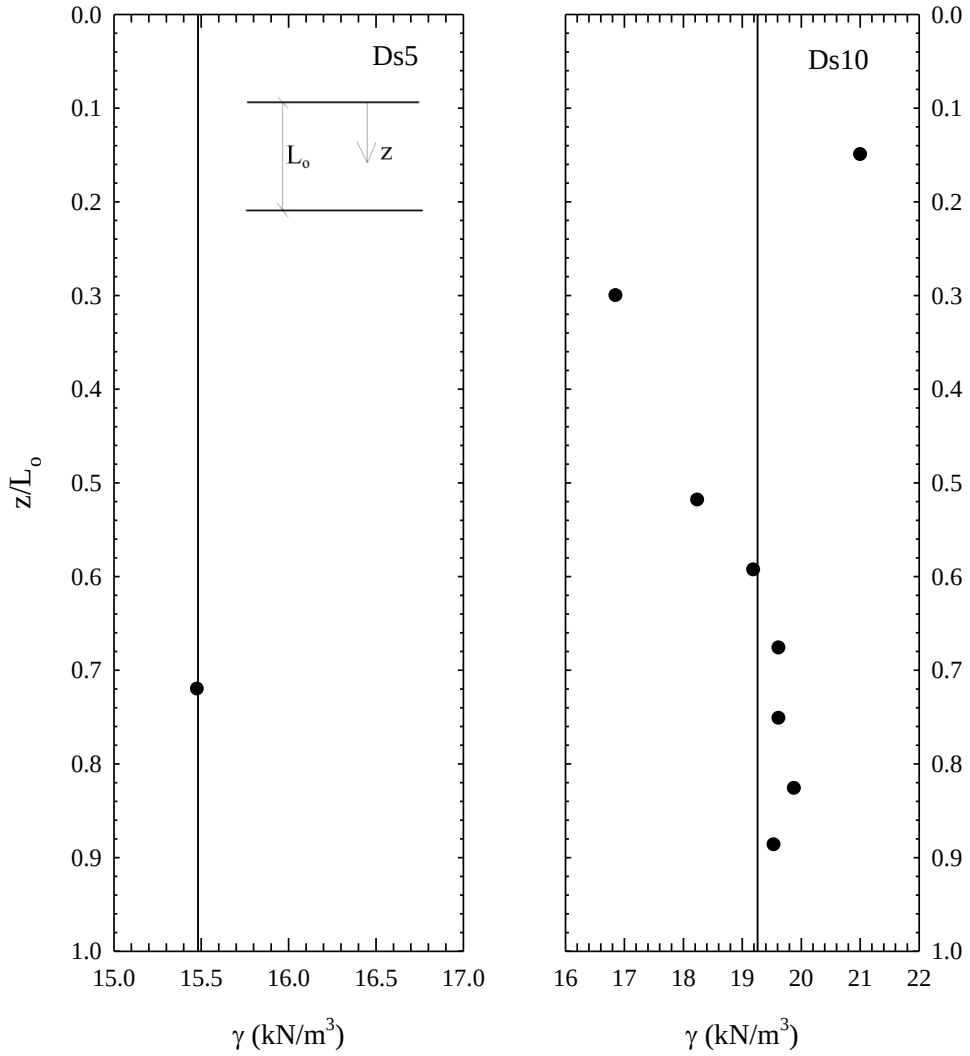

Figure 4-36 cont. Unit weight of sand layers (Akai and Tanaka, 1999).

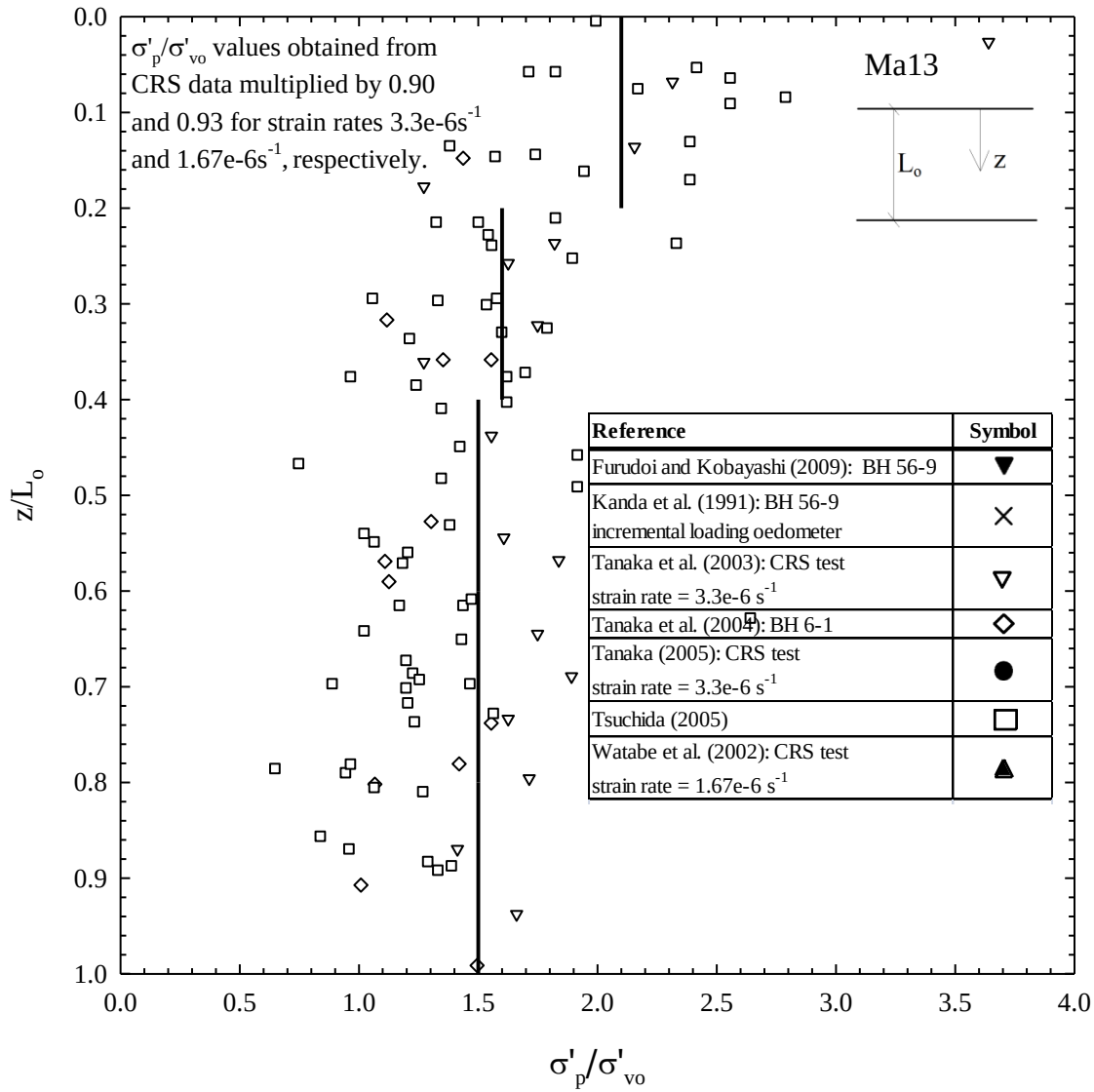

Figure 4-37 σ'_p/σ'_{vo} for Ma13.

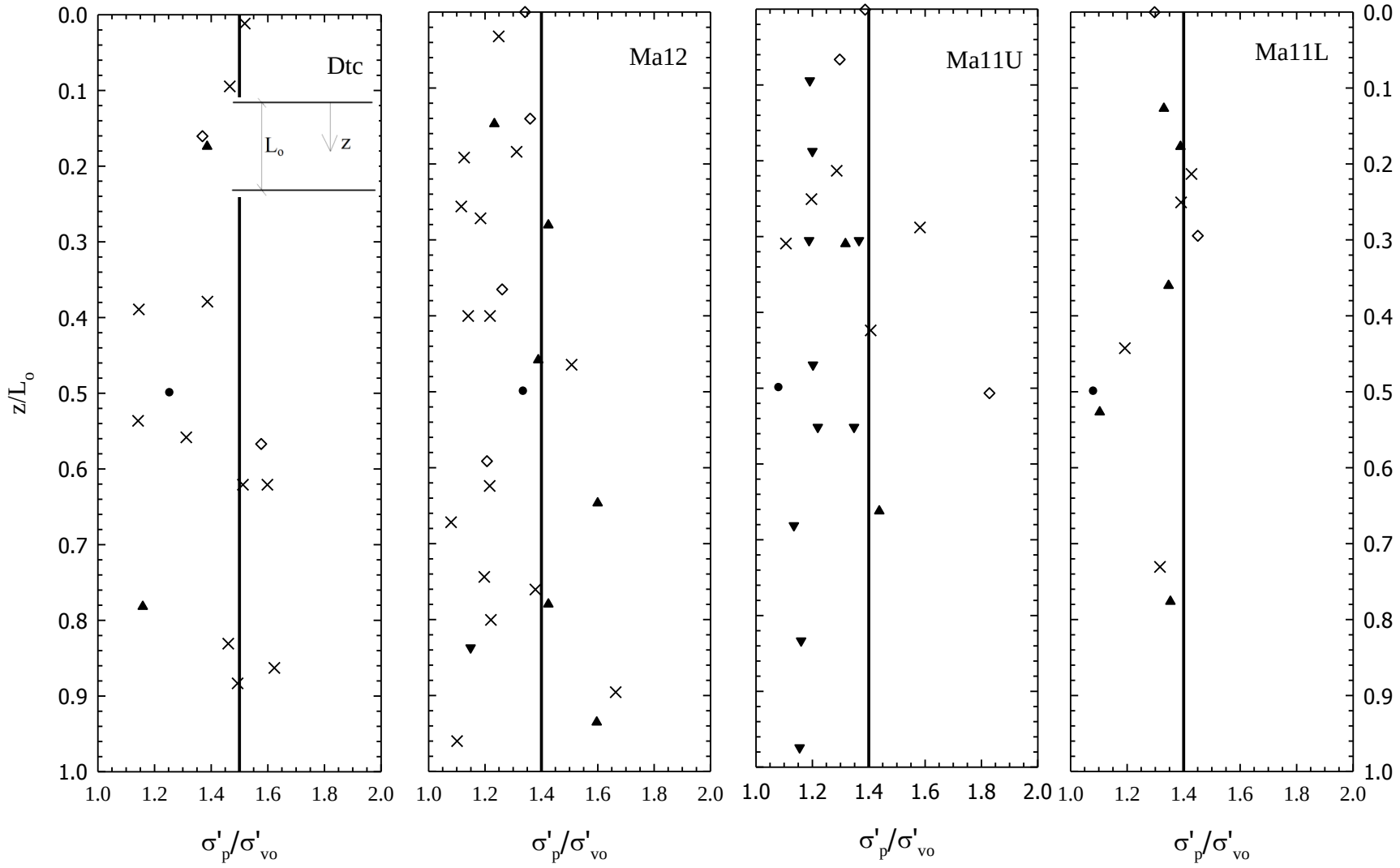

Figure 4-38 cont. σ'_p/σ'_{vo} for Pleistocene clay layers.

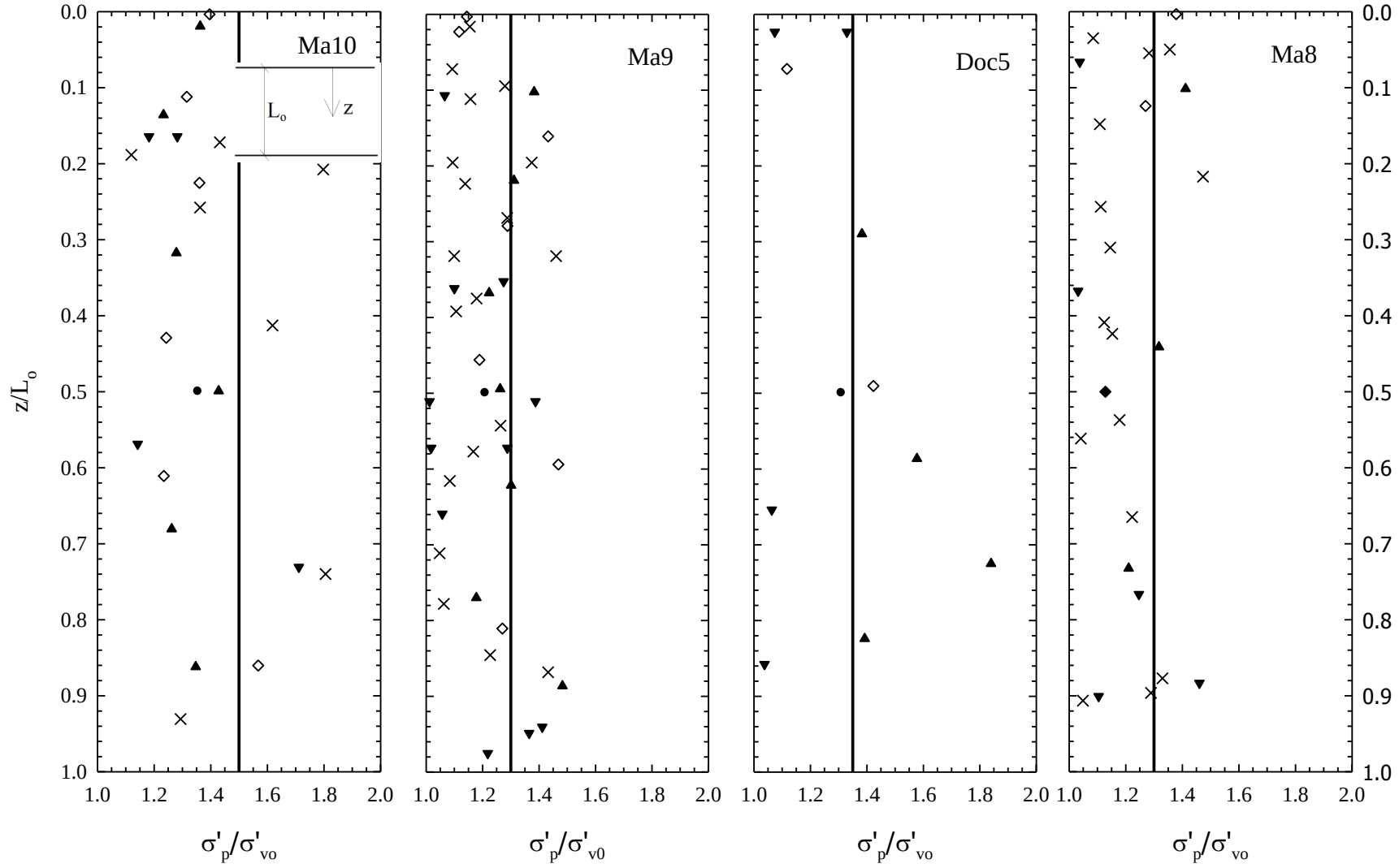

Figure 4-38 cont. σ'_p/σ'_{vo} for Pleistocene clay layers.

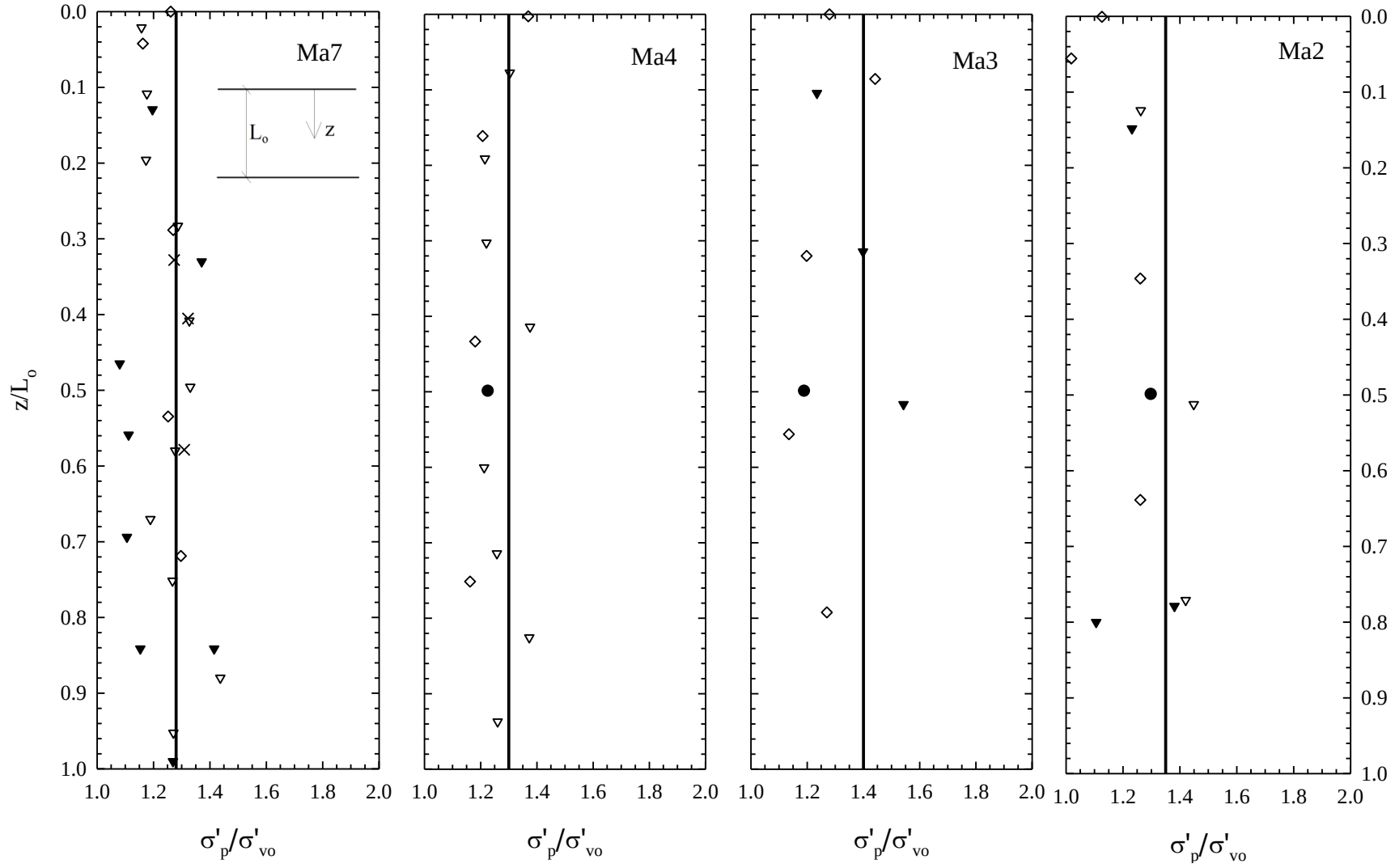

Figure 4-38 cont. σ'_p/σ'_{vo} for Pleistocene clay layers.

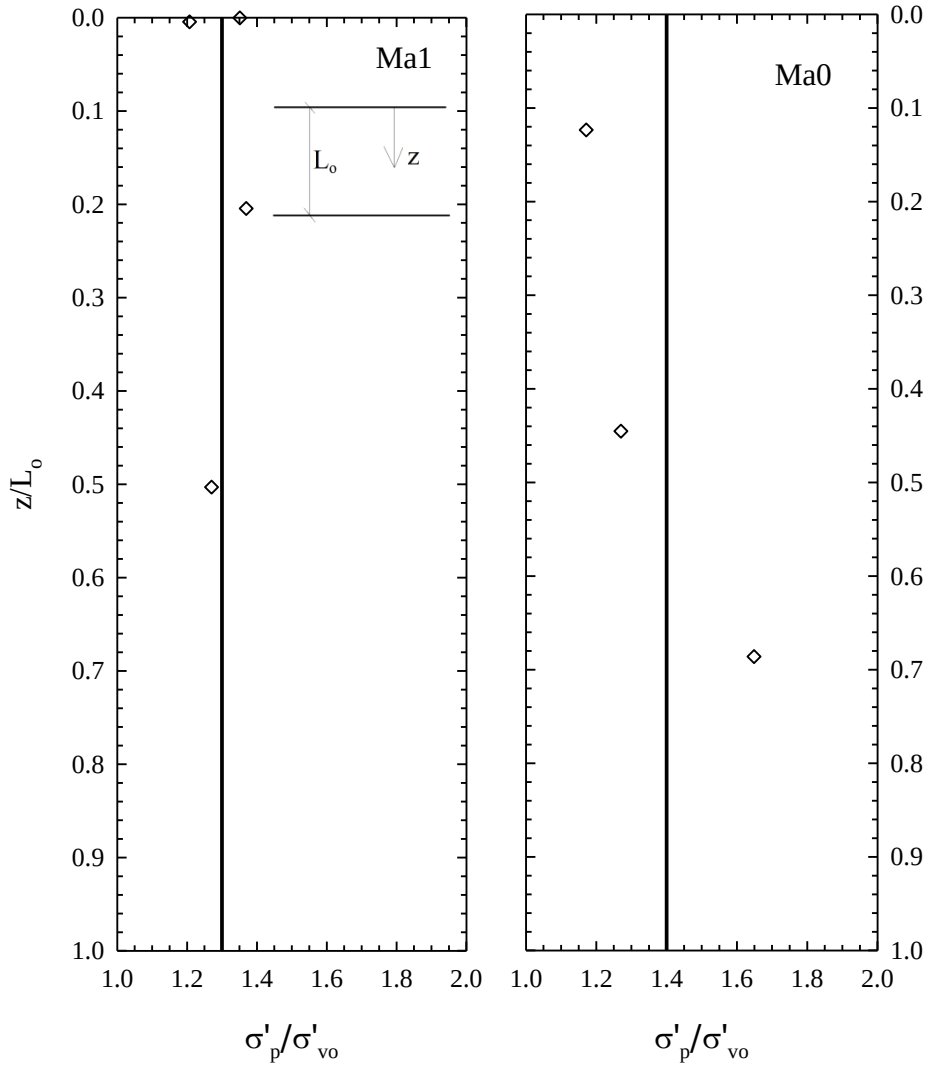

Figure 4-38 cont. σ'_p/σ'_{vo} for Pleistocene clay layers.

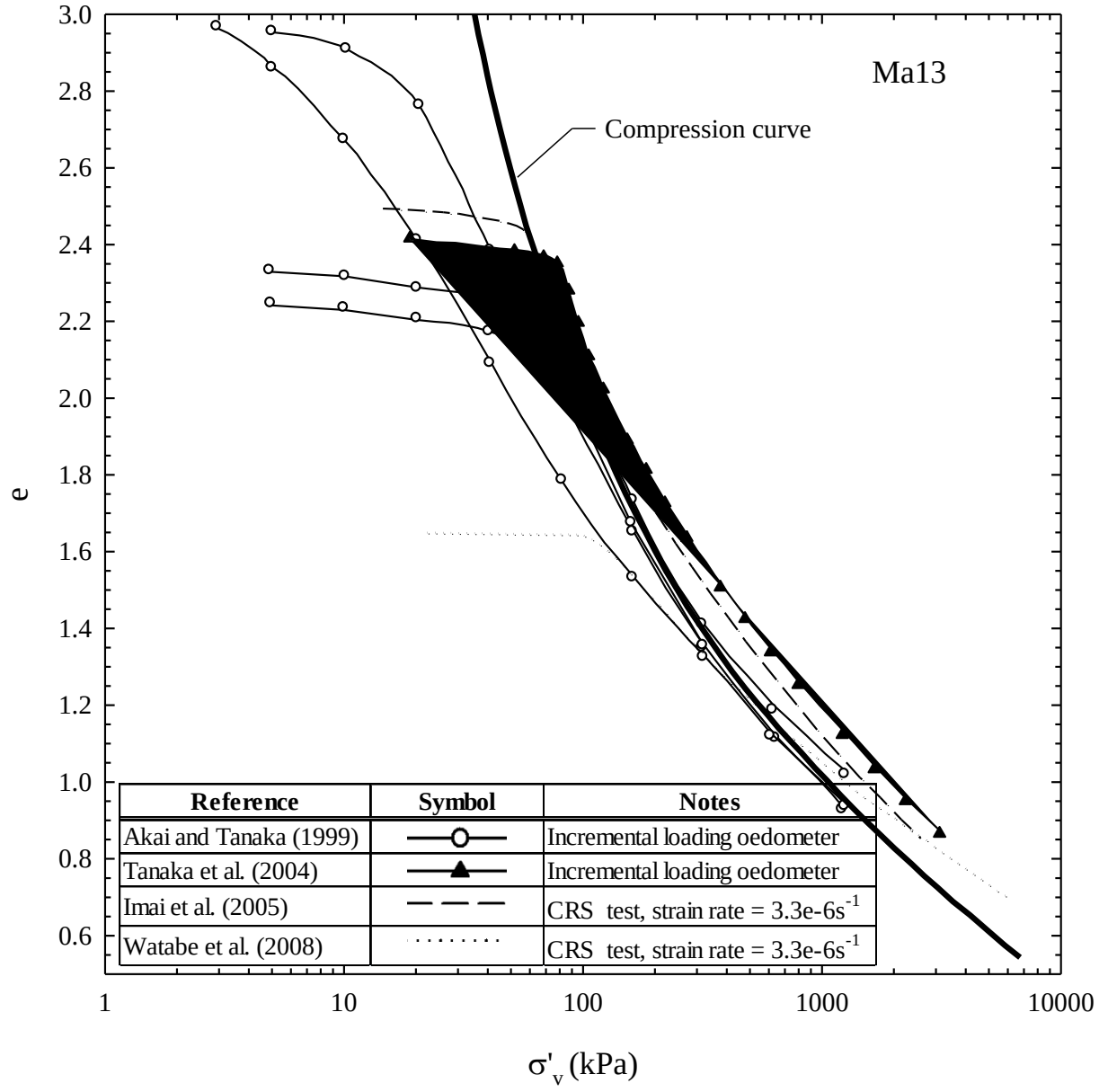

Figure 4-39 Compression curve for Ma13.

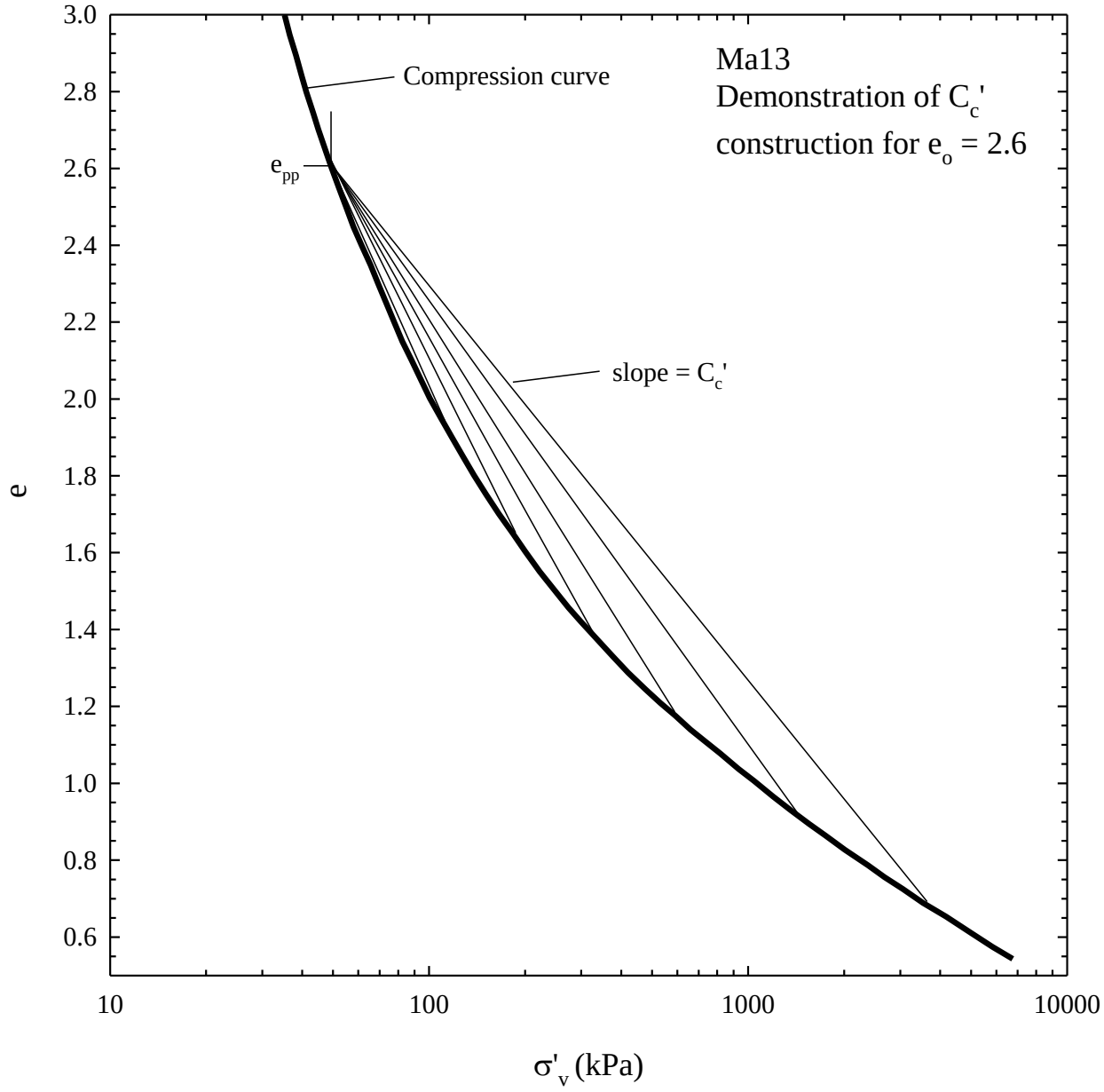

Figure 4-40 Secant compression indices for Ma13 (e_o equal to 2.6).

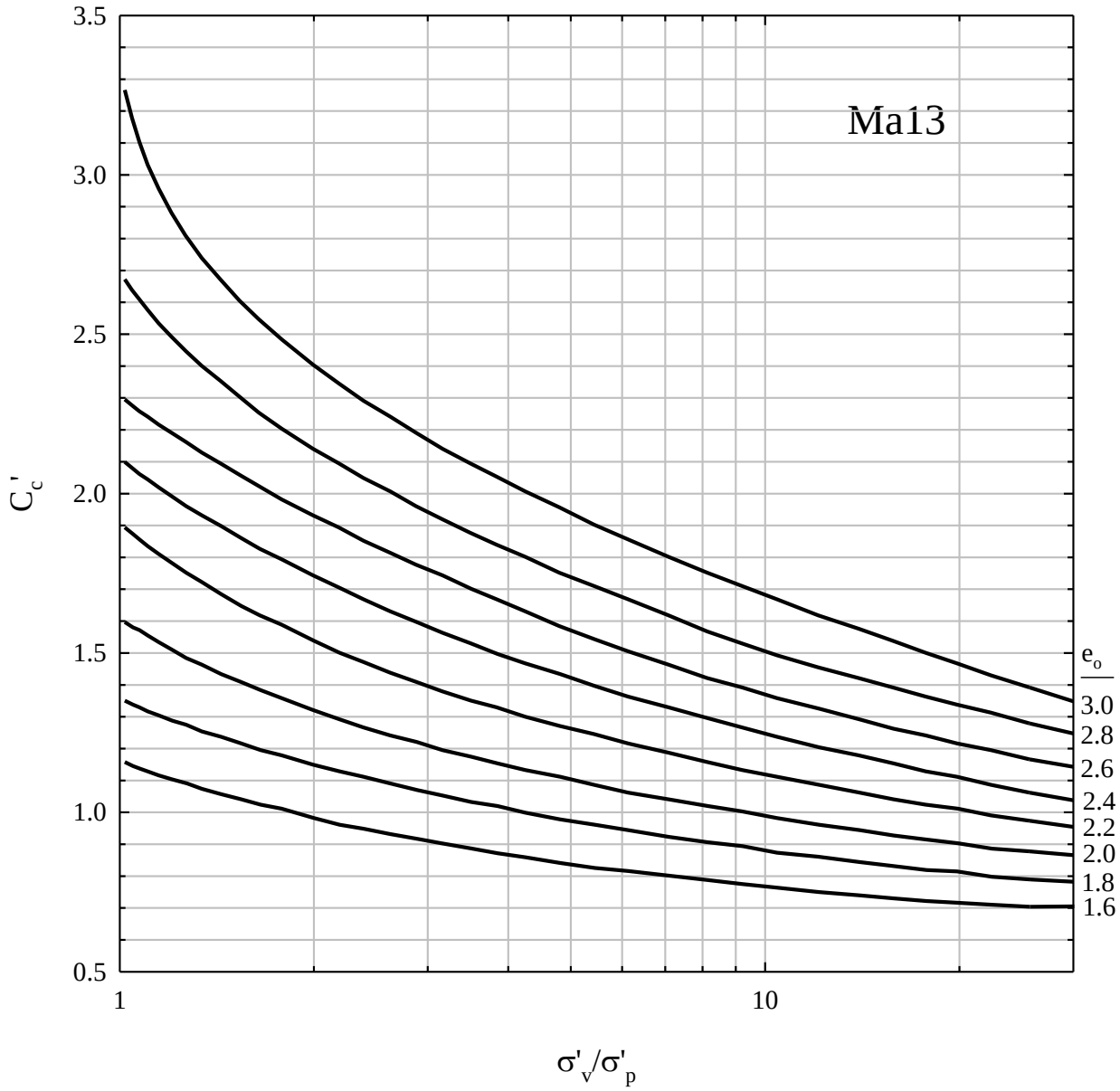

Figure 4-41 Secant compression indices for Ma13.

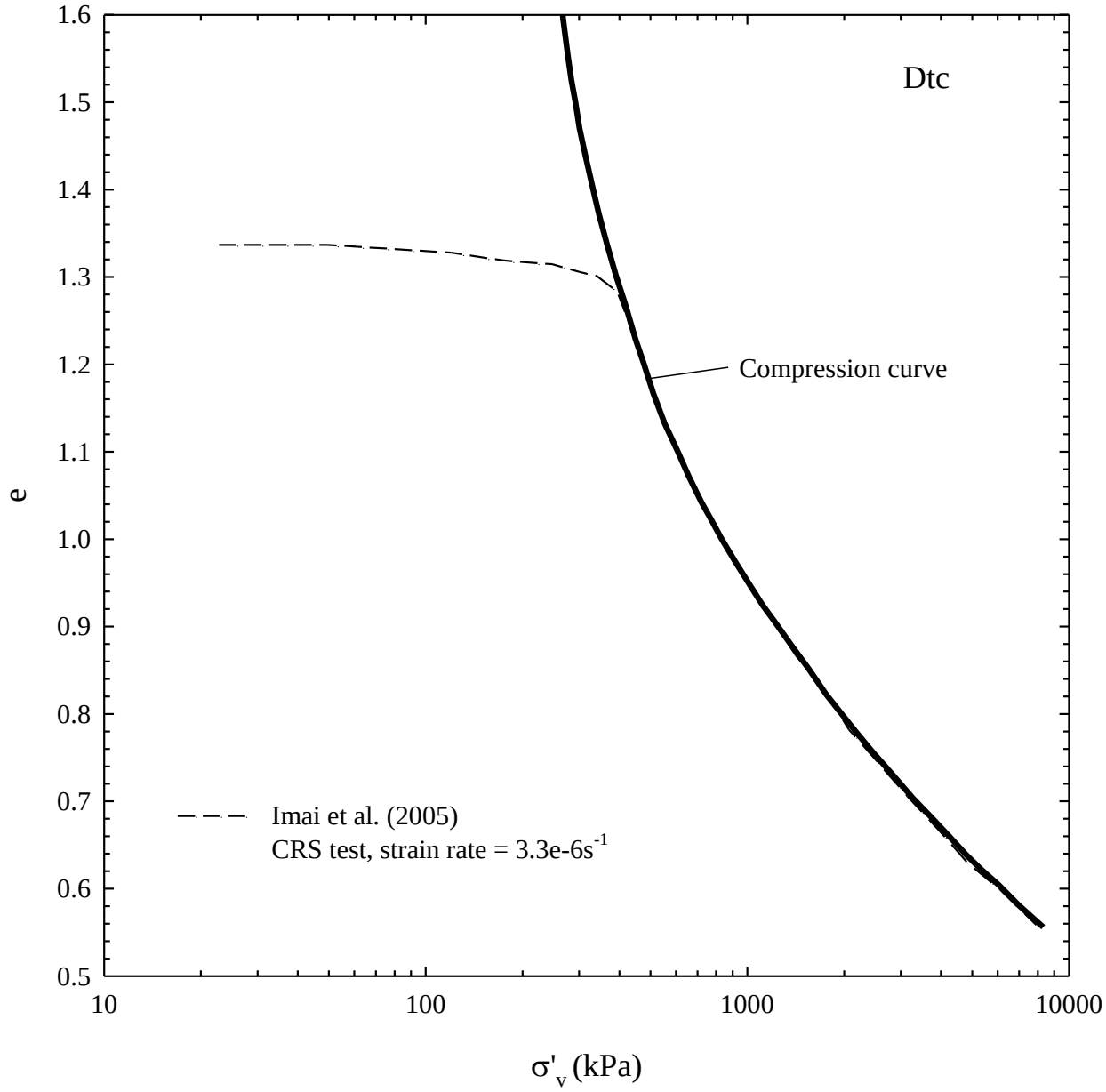

Figure 4-42 Compression curve for Dtc.

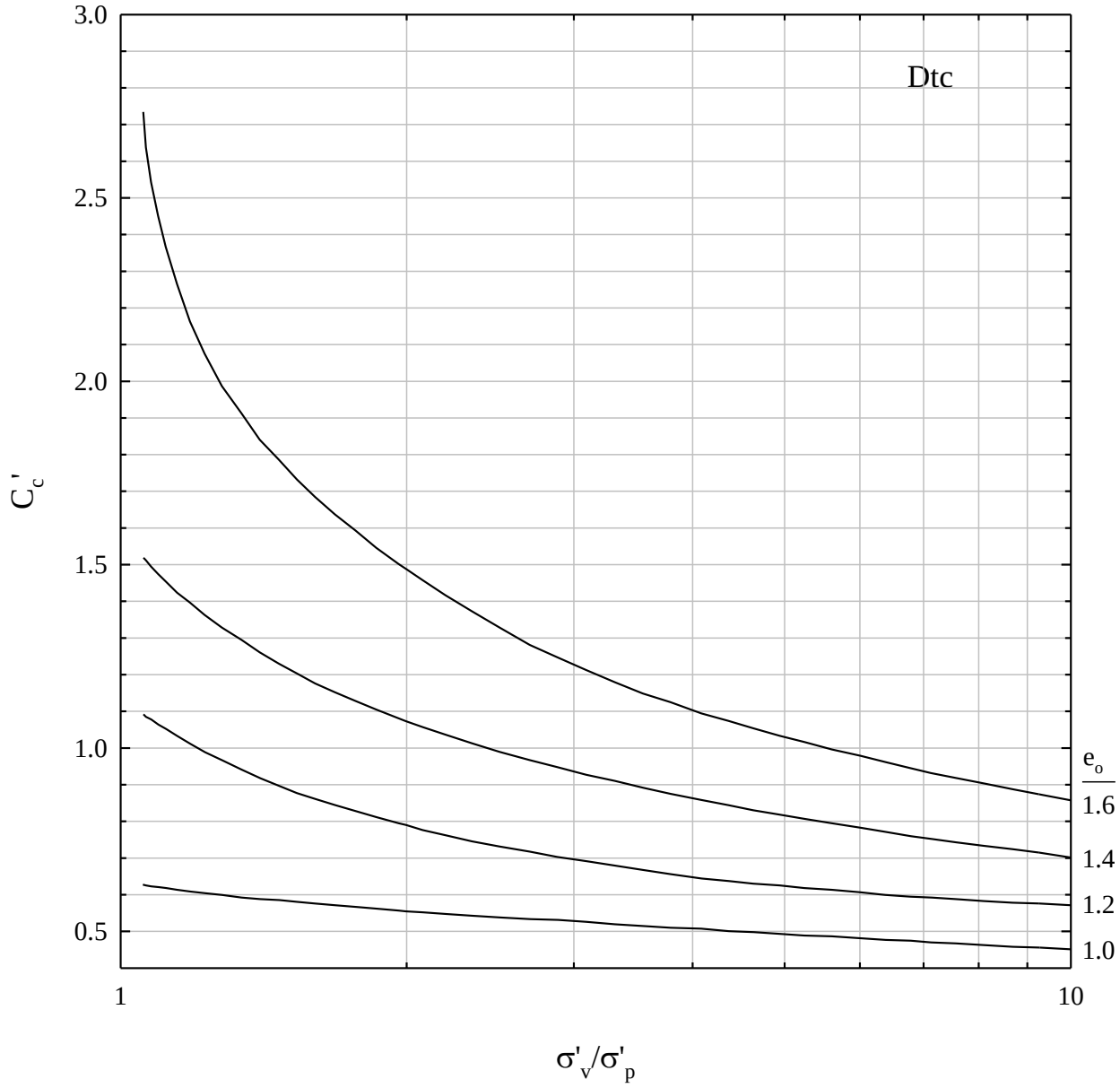

Figure 4-43 Secant compression indices for Dtc.

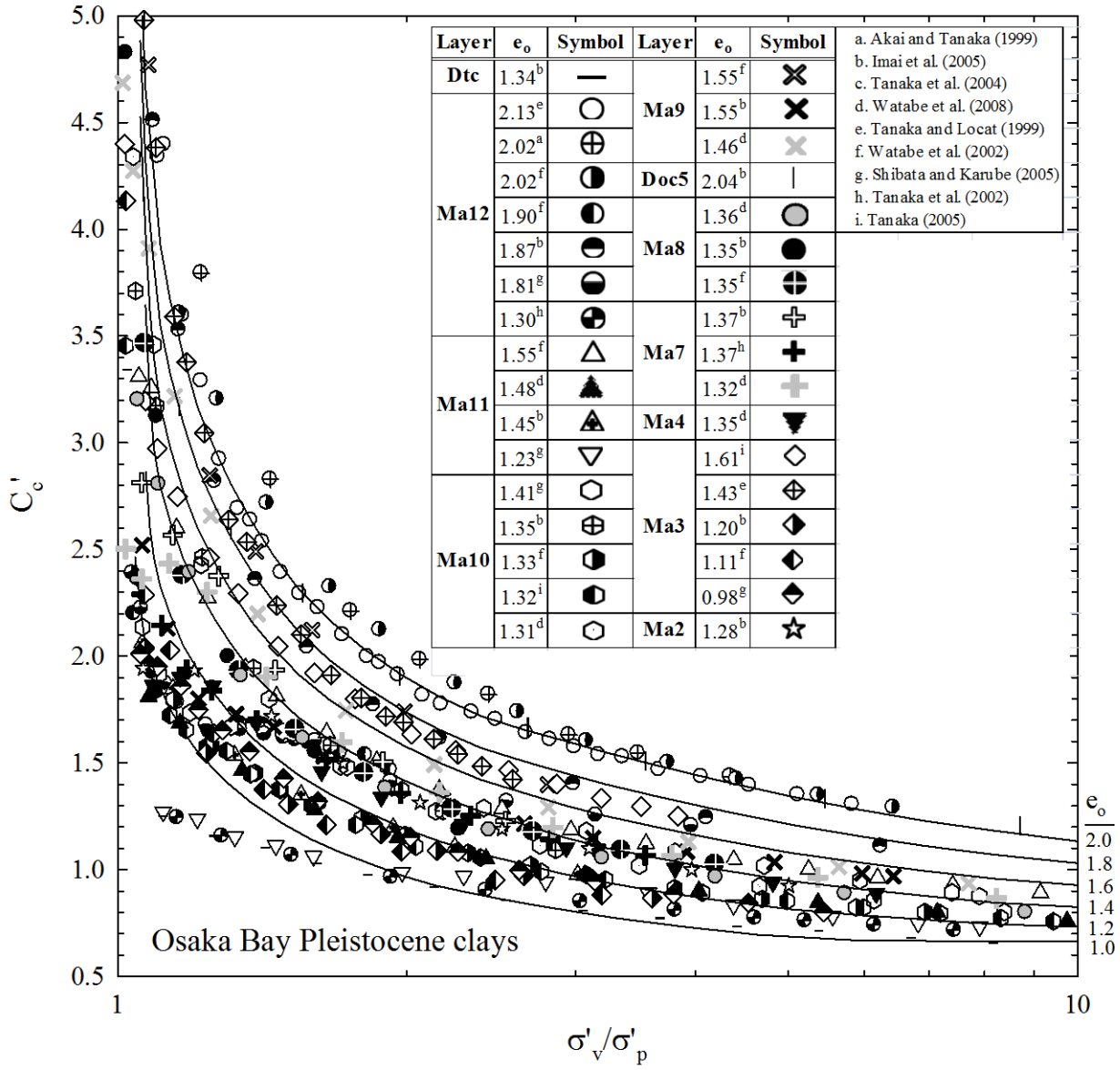

Figure 4-44 Secant compression indices for Pleistocene clay layers.

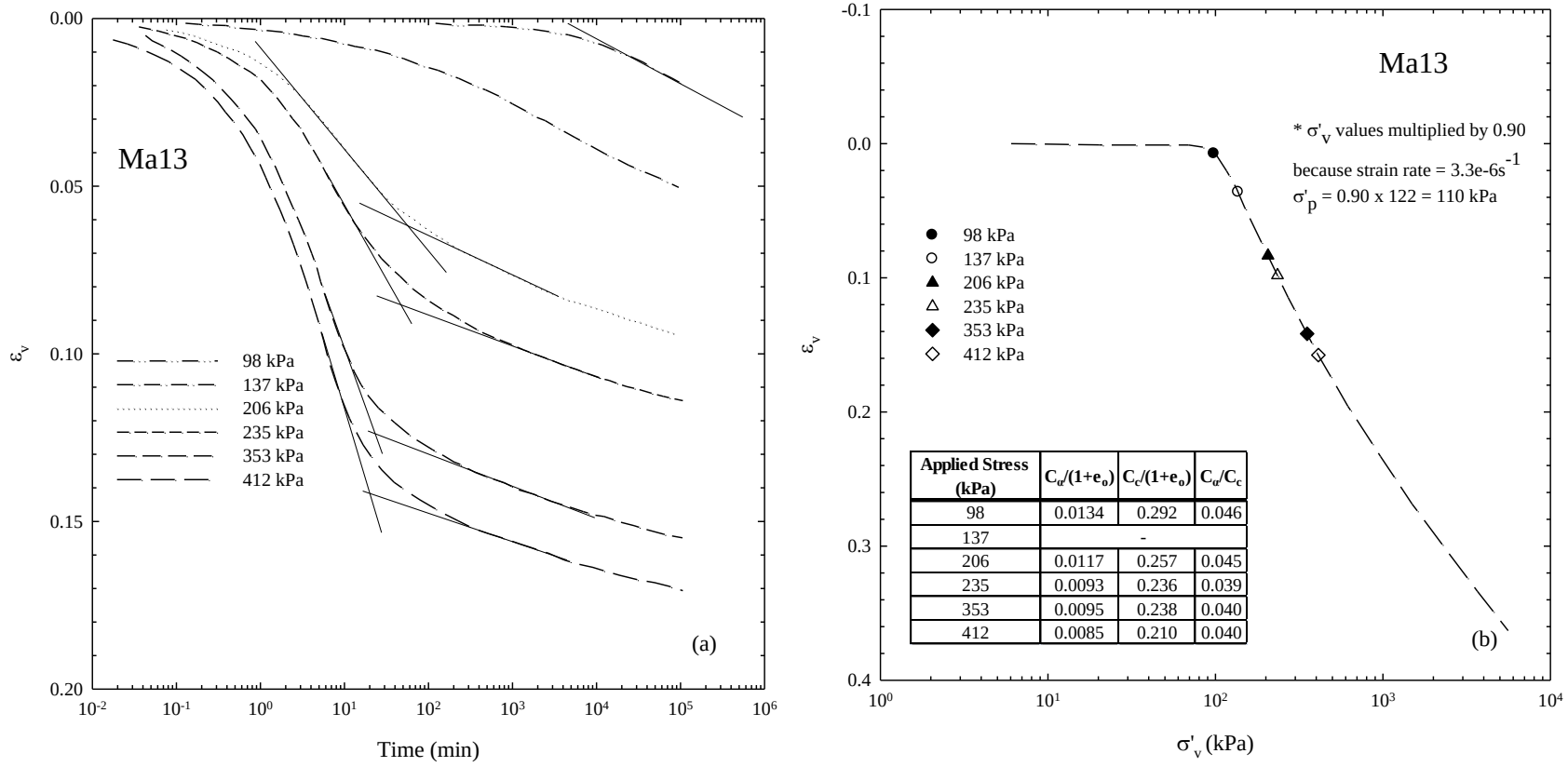

Applied Stress (kPa)	$C_\alpha/(1+e_o)$	$C_c/(1+e_o)$	C_α/C_c
98	0.0134	0.292	0.046
137	-		
206	0.0117	0.257	0.045
235	0.0093	0.236	0.039
353	0.0095	0.238	0.040
412	0.0085	0.210	0.040

Figure 4-45 Vertical strain versus log of time (a) and EOP vertical strain versus log of effective vertical stress (b) for a specimen from the Ma13 layer(Watabe et al., 2008).

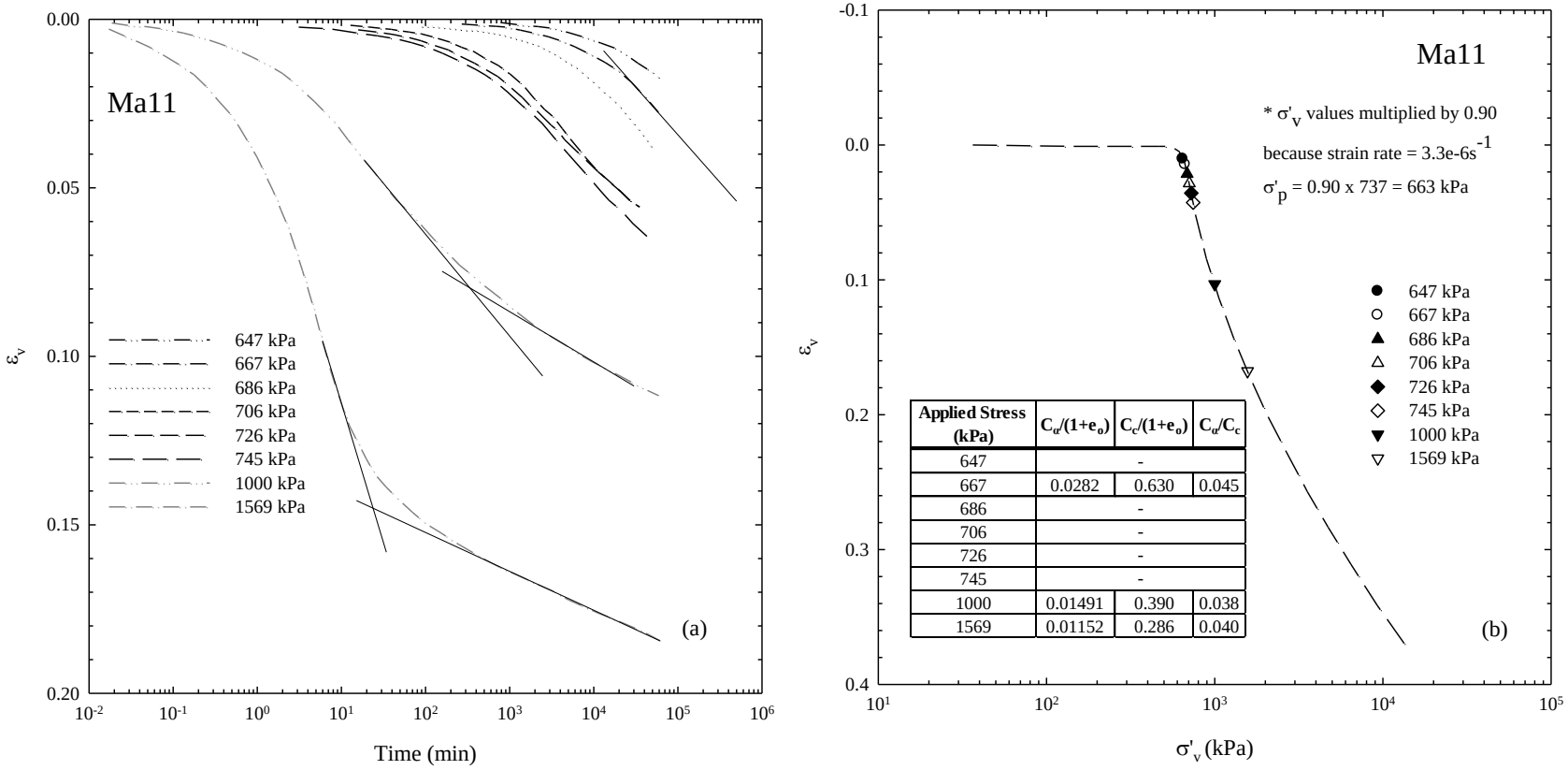

Applied Stress (kPa)	$C_\alpha/(1+e_o)$	$C_c/(1+e_o)$	C_α/C_c
647	-		
667	0.0282	0.630	0.045
686	-		
706	-		
726	-		
745	-		
1000	0.01491	0.390	0.038
1569	0.01152	0.286	0.040

Figure 4-46 Vertical strain versus log of time (a) and EOP vertical strain versus log of effective vertical stress (b) for a specimen from the Ma11 layer (Watabe et al., 2008).

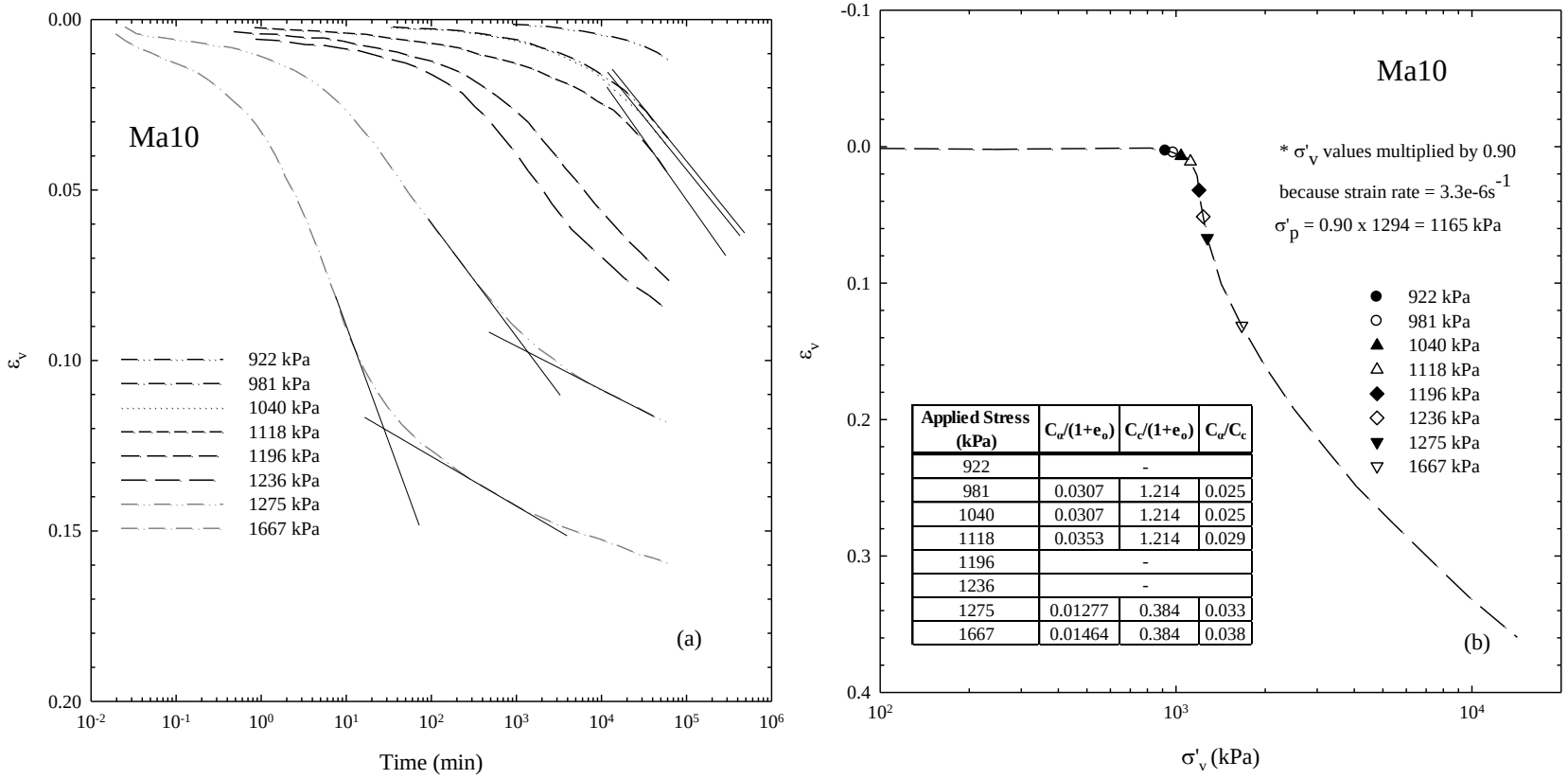

Applied Stress (kPa)	$C_\alpha/(1+e_o)$	$C_c/(1+e_o)$	C_α/C_c
922	-		
981	0.0307	1.214	0.025
1040	0.0307	1.214	0.025
1118	0.0353	1.214	0.029
1196	-		
1236	-		
1275	0.01277	0.384	0.033
1667	0.01464	0.384	0.038

Figure 4-47 Vertical strain versus log of time (a) and EOP vertical strain versus log of effective vertical stress (b) for a specimen from the Ma10 layer (Watabe et al., 2008).

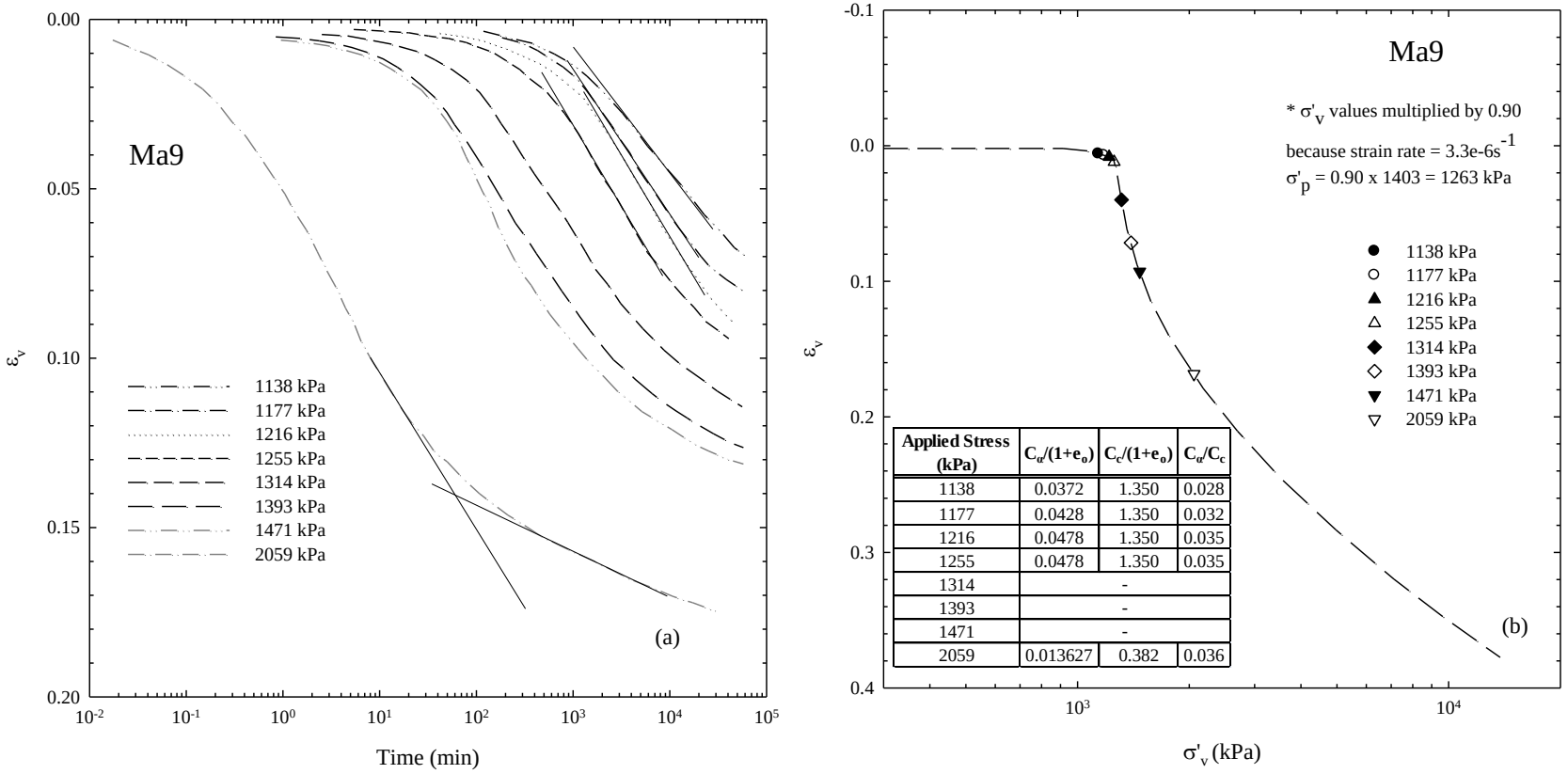

Applied Stress (kPa)	$C_\alpha/(1+e_o)$	$C_c/(1+e_o)$	C_α/C_c
1138	0.0372	1.350	0.028
1177	0.0428	1.350	0.032
1216	0.0478	1.350	0.035
1255	0.0478	1.350	0.035
1314	-		
1393	-		
1471	-		
2059	0.013627	0.382	0.036

Figure 4-48 Vertical strain versus log of time (a) and EOP vertical strain versus log of effective vertical stress (b) for a specimen from the Ma9 layer (Watabe et al., 2008).

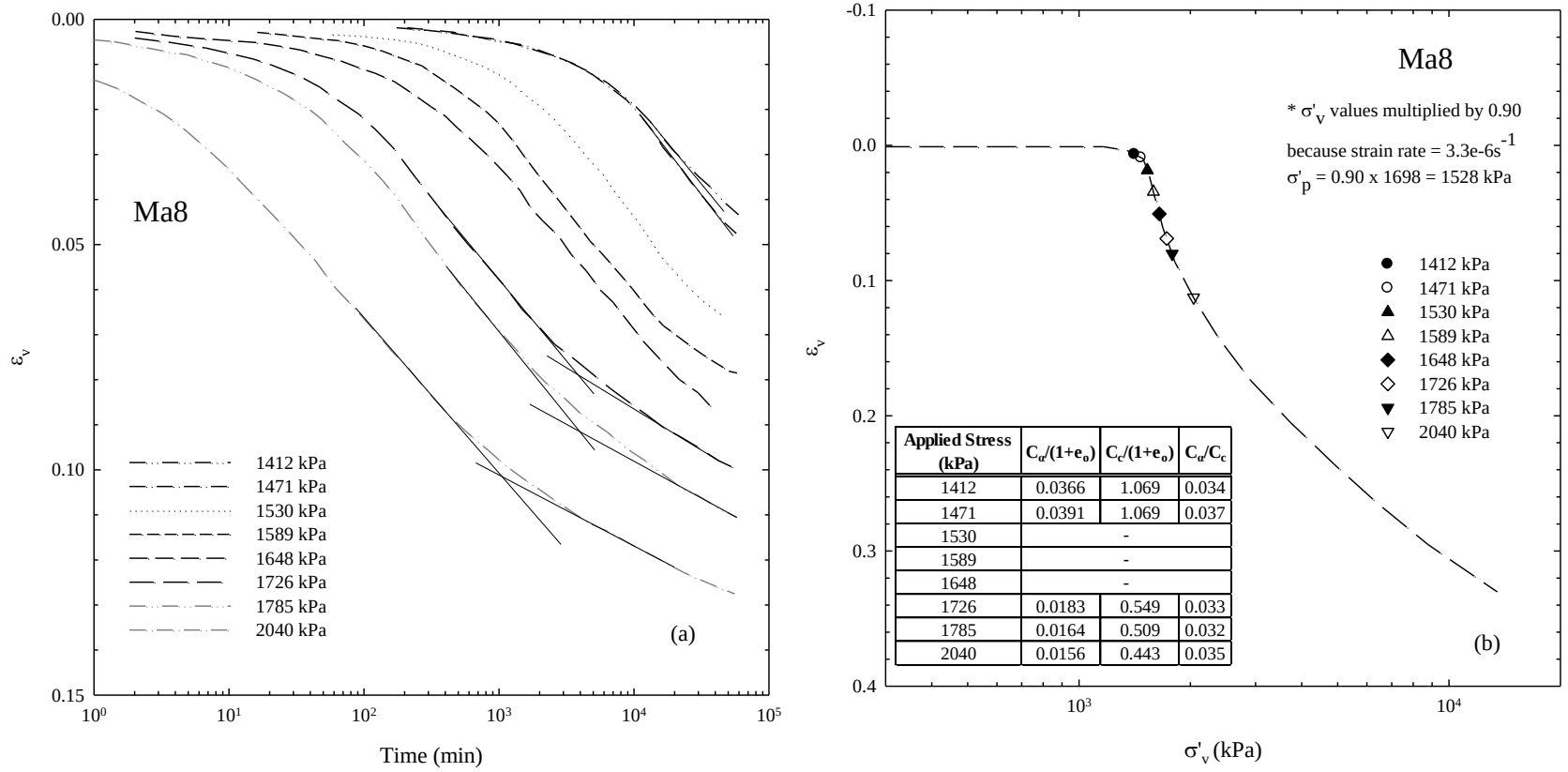

Applied Stress (kPa)	$C_\alpha/(1+e_o)$	$C_c/(1+e_o)$	C_α/C_c
1412	0.0366	1.069	0.034
1471	0.0391	1.069	0.037
1530	-		
1589	-		
1648	-		
1726	0.0183	0.549	0.033
1785	0.0164	0.509	0.032
2040	0.0156	0.443	0.035

Figure 4-49 Vertical strain versus log of time (a) and EOP vertical strain versus log of effective vertical stress (b) for a specimen from the Ma8 layer (Watabe et al., 2008).

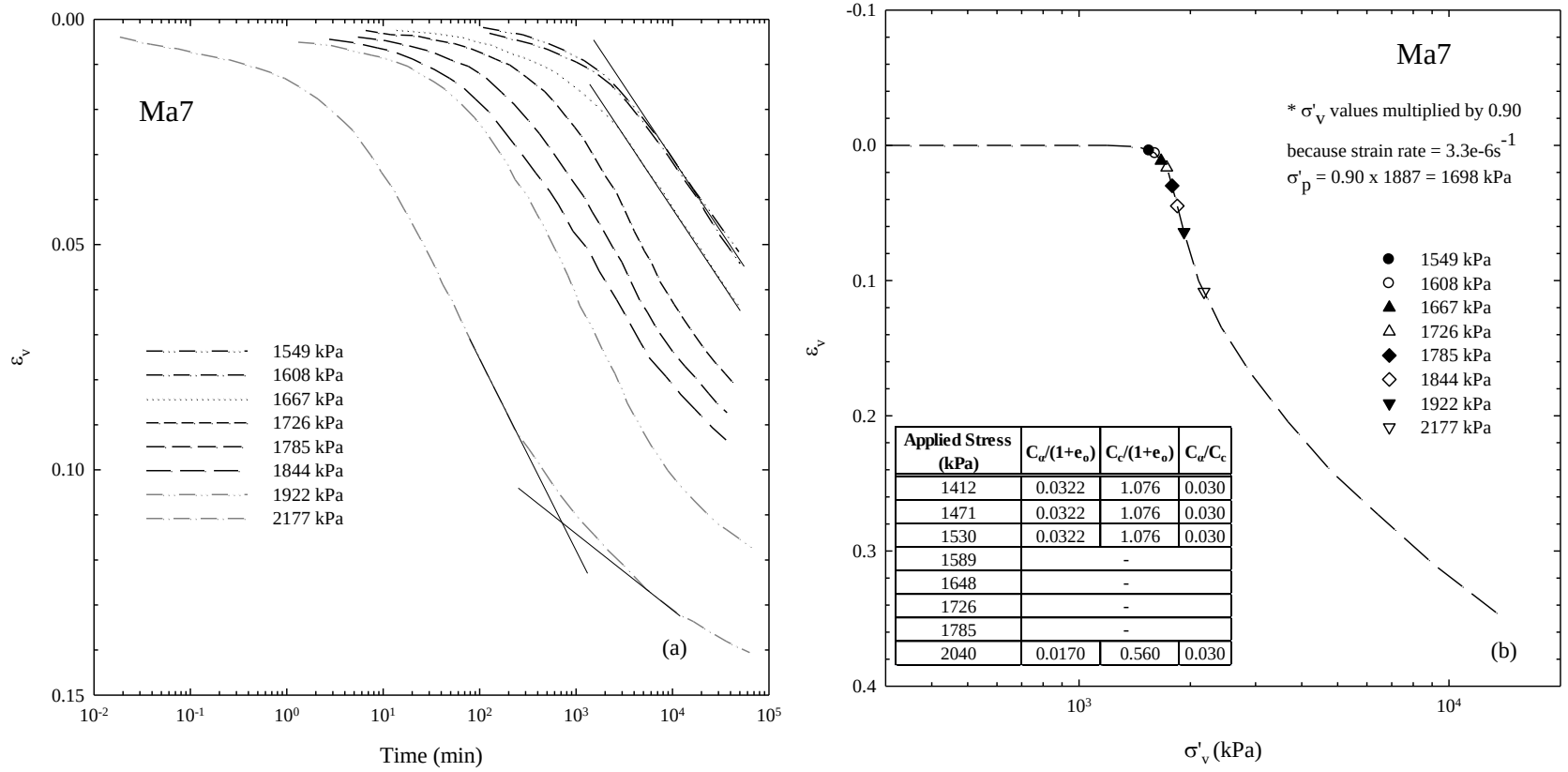

Applied Stress (kPa)	$C_\alpha/(1+e_o)$	$C_c/(1+e_o)$	C_α/C_c
1412	0.0322	1.076	0.030
1471	0.0322	1.076	0.030
1530	0.0322	1.076	0.030
1589	-		
1648	-		
1726	-		
1785	-		
2040	0.0170	0.560	0.030

Figure 4-50 Vertical strain versus log of time (a) and EOP vertical strain versus log of effective vertical stress (b) for a specimen from the Ma7 layer (Watabe et al., 2008).

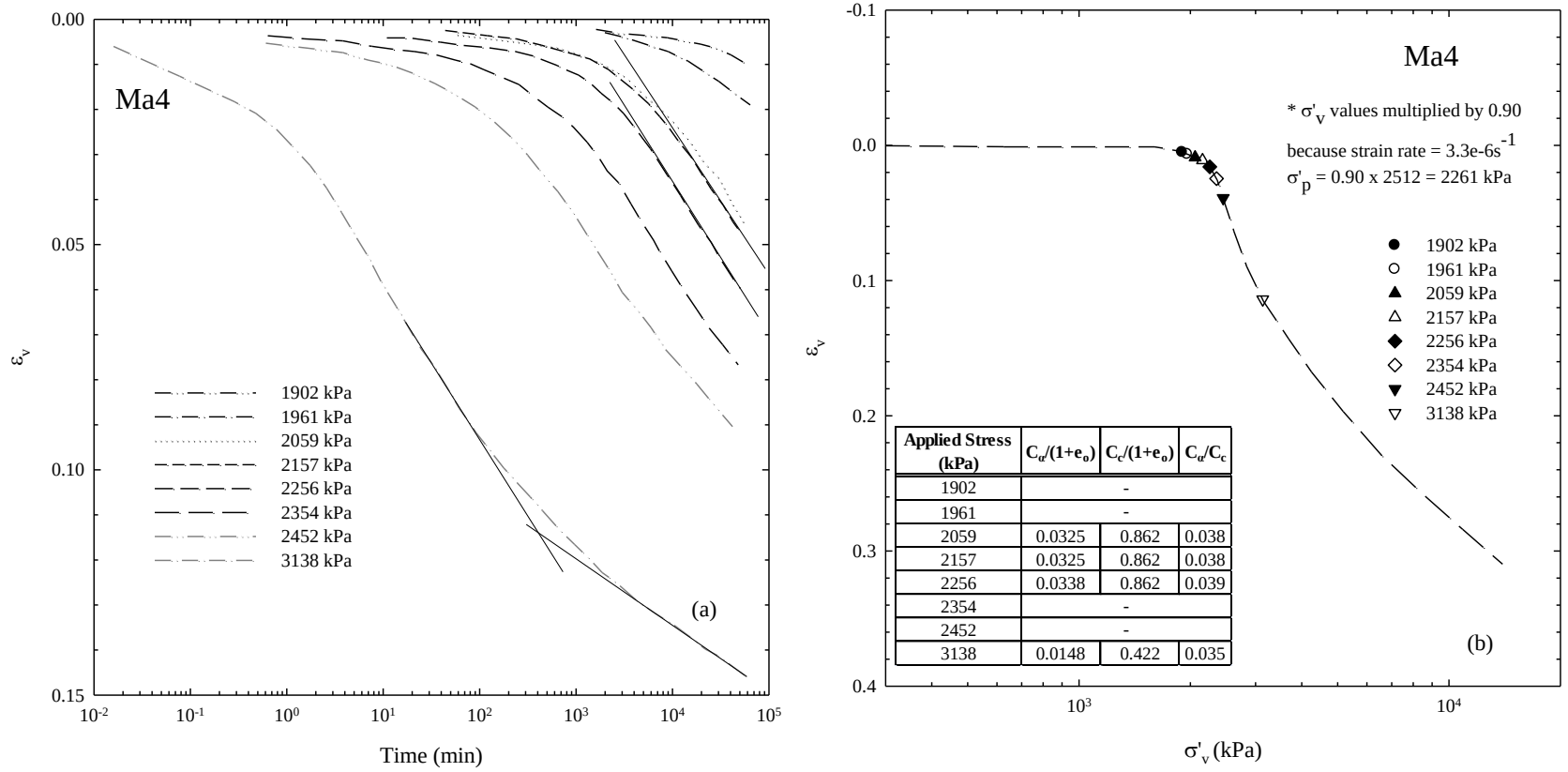

Applied Stress (kPa)	$C_\alpha/(1+e_o)$	$C_c/(1+e_o)$	C_α/C_c
1902	-		
1961	-		
2059	0.0325	0.862	0.038
2157	0.0325	0.862	0.038
2256	0.0338	0.862	0.039
2354	-		
2452	-		
3138	0.0148	0.422	0.035

Figure 4-51 Vertical strain versus log of time (a) and EOP vertical strain versus log of effective vertical stress (b) for a specimen from the Ma4 layer (Watabe et al., 2008).

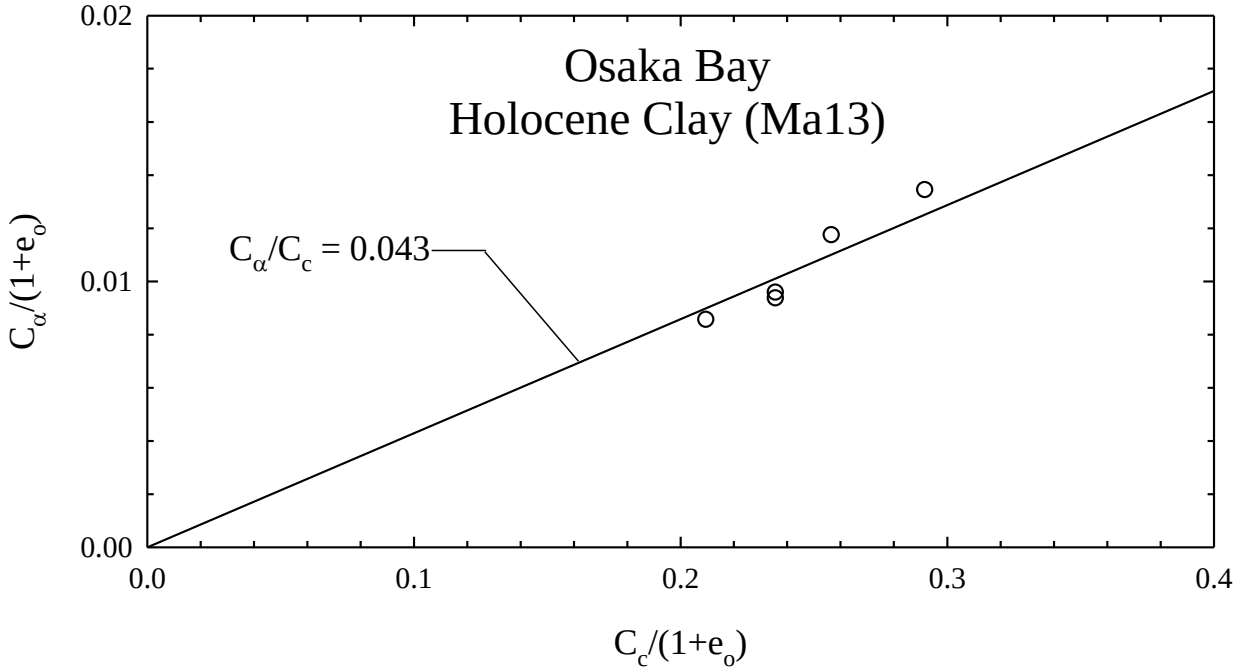

Figure 4-52 C_α/C_c for Ma13. Data from Watabe et al. (2008).

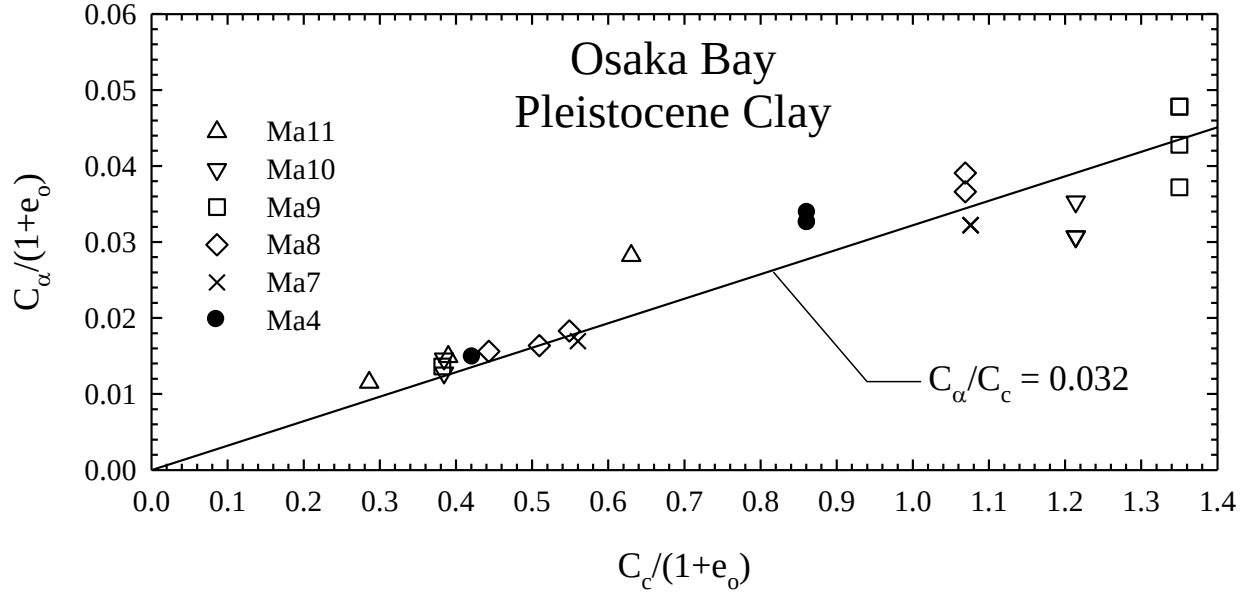

Figure 4-53 C_α/C_c for Pleistocene clay layers. Data from Watabe et al. (2008).

CHAPTER 5 CONSTRUCTION OF THE KANSAI INTERNATIONAL AIRPORT ISLANDS

5.1 Introduction

The Kansai International Airport was proposed as part of an effort to improve the economy of the Kansai Region and to decentralize the economic power of Japan from Tokyo (Rai, 1990; Vadose, 1991; KALD, 2005). However, the Ministry of Transportation had had a history of problems related to airport expansion and construction. The Osaka International Airport, also known as Itami Airport (opened in 1939), was the only international airport serving the Kansai Region before Kansai Airport was constructed. Locals began to protest when jet airplanes began using Osaka International Airport in 1964 and lawsuits were filed in 1967 based on the Environmental Pollution Control Law and the Airport Noise Prevention Law. The Itami City Council passed a resolution in 1973 to abolish Itami Airport, and in 1981 the Supreme Court of Japan awarded compensation for past damages in the Itami Airport Lawsuits (KALD, 2005).

In addition to the noise-related issues at Osaka International Airport, the Japanese government also dealt with land acquisition disputes with farmers for the International Airport constructed in the Narita Suburb of Tokyo. Construction of Narita Airport began in 1969. The Japanese government confiscated farmland from locals and major protests ensued. Thousands of activists were arrested, lives were lost, and construction was delayed for a decade (Talley et al., 2000; KALD, 2005).

In April 1968, the Ministry of Transportation began surveying eight possible sites including two sites on land (on the Osaka-Wakayama prefectural border and on Awaji Island) and six sites at sea (off the shores of Kishiwada, Nishinomiya, Akashi, and Senshu as well as Port Island and Rokko Island) for airport construction (NKIAC, 2012). It was decided that an international airport at sea would allow for continued growth of the Kansai economy while avoiding noise-related problems and land acquisition disputes similar to those at Itami and Narita, and eventually the location 5km off the coast of Senshu was selected (Nakase, 1987; Arai, 1991; KALD, 2005).

Various complications, however, have arisen as a result of construction of Kansai Airport. The Japanese government was forced to give Osaka fisherman significant compensation

because it was determined that airport construction would alter fish routes in the bay. Additionally, protestors disrupted construction with mortar attacks and fires at the quarries where reclamation fill material was obtained (Nakase, 1987; Talley et al., 2000).

The Japanese government has also had some financial trouble as a result of construction of Kansai Airport. Unforeseen settlement helped to cause the cost of construction of Island I to reach $15 billion (40% over budget), and despite charging some of the world's highest landing fees, high food prices, and high office rent, the airport managed to lose $1.28 billion in 2000 (Sterngold, 1993; Talley et al., 2000; Sims, 2001). Additionally, the United States threatened to impose trade sanctions on Japan for not opening its public sector construction market for international competition (Bradsher, 1993). Despite the financial troubles of Kansai Airport, the decision was made to construct Island II which would house a second runway (4000m length). Island II was constructed to increase international traffic and provide additional repair and maintenance time for the existing Island I runway (KALD, 2005; Tabata and Morikawa, 2005).

The events related to construction of Kansai Airport are outlined in Table 5-1.

5.2 Construction of the Kansai International Airport

Construction of the Kansai Airport Islands was an enormous undertaking. Approximately, 180 million cubic meters of reclamation fill material was used to construct the 511ha Island I and approximately 250 million cubic meters of reclamation fill material was used to construct the 545ha Island II. Construction of Island I began in January 1987 and the airport opened in September 1994. Island II construction began July 1999 and operation of the second runway commenced August 2007 (Nakase, 1987; Arai, 1991; Tabata and Morikawa, 2005; Watabe et al., 2008). Figure 5-1 shows the airport islands in plan view.

The construction of each airport island can generally be divided into four stages: installation of vertical drains in the Ma13 clay layer following placement of a sand blanket on the seabed, construction of the seawall, reclamation, and construction of airport facilities. Table 5-2 shows the construction schedule for Island I and Island II of Kansai International Airport.

5.2.1 Installation of vertical drains in Ma13

Before installation of vertical sand drains, a 1.5m thick sand blanket was placed on the

seabed. Two methods were used to place the sand blanket. In one method, a pump located on a sand spreading barge is used to remove sand from a stock barge and spray it on the sea floor in a fan shape (Figure 5-2). In the second method, material is retrieved from a hopper barge by a sand spreading barge with backhoes. The material is put in a hopper and carried to the sea floor with a tremie pipe (Figure 5-3) (KALD, 2005; KIAC, 2005).

Forty centimeter diameter displacement-type vertical sand drains were installed such that they fully penetrate the upper Holocene marine clay layer (Ma13) and form a drainage connection to the overlying 1.5m sand blanket and to the underlying diluvial sand layer Ds1. The vertical drains were installed on a 1.6m by 2.5m rectangular pattern beneath the seawall and a 2.5m square pattern beneath the reclamation area for both Island I and Island II (Nakase, 1987; Maeda et al., 1990; Arai, 1991, Yamakawa and Tsuruoka, 1996; Shinohara, 2003; Suzuki et al., 2003; Tabata and Morikawa, 2005). A steel pipe casing fitted with a lid was advanced through Ma13 into the underlying sand layer Ds1 using a vibrating pile driver. After the steel pipe was filled with sand, a withdrawal winch gradually vibrated the pipe, removing it from Ma13 and leaving a sand column (Yamakawa and Tsuruoka 1996). Figure 5-4 shows the sand drain barges used to install the vertical sand drains in Ma13. Approximately 1 million sand drains were placed for Island I construction (Yamakawa and Tsuruoka, 1996) and approximately 1.2 million sand drains were placed for Island II construction (Tabata and Morikawa, 2005).

Sand compaction piles and deep cement-soil mixing were also used to improve Ma13 under portions of the Island I and Island II seawalls (Nakase, 1987; Arai 1991; KIAC, 2005).

5.2.2 Seawall construction

Approximately 80% of the Island I seawall (Nakase, 1987) and approximately 90% of the Island II seawall (Shinohara, 2003) consist of a gently-sloping rubble mound (Figure 5-5). Yamane et al. (2003) describe the construction of the rubble-mound seawall for Island II. After placement of the 1.5m sand blanket and installation of vertical drains as described in the previous section, a 16m thick sand fill was placed by direct dumping with a barge. Next, rubble material was placed with a grab bucket attached to a barge (Figure 5-6a). Armor stones were placed on the seaward side of the rubble mound at locations along the seawall where wave action was considered a potential concern. The armor blocks were leveled with a backhoe above the water surface (Figure 5-6b) and by divers below the water surface. Concrete blocks were then formed

on land, transported to the airport site with crane barges, and placed on top of the rubble stone (Figure 5-6c). Wave dissipating blocks were placed at locations where wave-action was a concern. Finally, concrete was placed to form an earth retaining wall for the reclamation material (Figure 5-6d). The rubble-mound seawall was used extensively at both airport islands because it was believed to be environmentally friendly to marine habitats, structurally flexible, and relatively low cost (Shinohara, 2003). The wave dissipating rubble mound seawall was designed to withstand a 50 year storm event producing 3.5m high waves with a period of 6 seconds in a West-Southwest direction (Arai, 1991).

Steel cellular bulkheads and caissons were also used for portions of the Kansai Airport seawall. The concrete caissons contain slits in certain areas to help dissipate wave energy (Nakase, 1987; Shinohara, 2003; KIAC, 2005). Figure 5-7 shows the locations for the different types of seawall construction along the perimeter of the Kansai Airport Islands.

5.2.3 Reclamation

A portion of the seawall was left open so that hopper barges could enter and begin the reclamation process. Large quantities of fill material were required to complete the reclamation. Island I required approximately 180 million cubic meters of material and Island II required approximately 250 million cubic meters of material (Nakase, 1987; Tabata and Morikawa, 2005). Fill material was taken from the locations shown in Figure 5-8. Figure 5-9 shows an earth collection site.

The reclamation process was similar for both airport islands. After placement of the 1.5m sand blanket and installation of vertical sand drains into Ma13 as described previously, large hopper barges (Figure 5-10), each capable of transporting 3000 cubic meters of material, placed reclamation material to elevation -6m Chart Datum Level (CDL). Once the elevation of the reclamation material reached -6m CDL, smaller hopper barges were used to place reclamation fill to -3m CDL. Next, box barges were used to carry the fill to the site and reclaimer barges fitted with conveyors (Figure 5-11) were used to place the reclamation fill above sea level to +7 to +9.5m CDL. Shovel and dump trucks were used to reach the final reclamation height (Figure 5-12) (Arai, 1991; Tabata and Morikawa, 2005). Tabata and Morikawa (2005) and Furudoi (2010) reported that the final reclamation height was reached by placing reclamation material in 60cm lifts with 8 passes of the vibratory roller for each lift at Island II.

Reclamation generally proceeded from the offshore side to the onshore side for Island I (Nakase, 1987). Nakase (1987) reported that the height of reclamation fill above the seabed was expected to reach approximately 30m for Island I. Arai (1991) reported that the height of reclamation fill above the seabed was initially going to be 29.5m, but that it was increased to 33m due to settlement forecasts. Nishimura (personal communication, 2011) reported the final height of reclamation fill above the seabed to be 36.7m.

The Island II site was divided into 200m by 200m blocks to minimize the difference in loading history between adjacent blocks. The 200m by 200m blocks were further divided into 40m by 40m blocks to avoid potential stability issues during above water placement with conveyors. This direct soil heaping process was started at key locations like the runway and access taxiway to avoid future large differential settlements in these areas (Tabata and Morikawa, 2005). The height of reclamation fill above the seabed at Island II was reported as 40 to 43m by Shinohara (2003) and as "more than 40m" by Tabata and Morikawa (2005) and Furudoi (2010).

Table 5-3 summarizes the unit weight of fill material reported in the literature for Kansai Airport Island I and Island II. Tabata and Morikawa (2005) and Furudoi (2010) reported the maximum grain size of the fill material to be approximately 300mm.

5.3 Quality control

Twenty-two surveying scaffolds located 500m apart were used to position the vertical sand drain vessels for Island I. Light beams emitted from the vessels were reflected off of the surveying scaffolds so that their position could be determined (Arai, 1991). An automatic recording instrument gathered data on the position of the ends of the pipe casings from the penetration and withdrawal record, data on the level of the sand within the pipe, and data on the amount of time from the beginning of pipe penetration to the end of pipe withdrawal (Yamakawa and Tsuruoka, 1996). GPS systems were used to guide vertical sand drain barges to the correct location for Island II construction (KALD, 2005).

Prior to reclamation, GPS guided boats performed bathymetric surveys of the existing seabed. The surveys were performed by boats containing a narrow multi-beam echo sounder. Each echo sounder device uses 60 beams that fan out over 90 degrees (Yamane et al., 2003). Then, GPS guided barges placed soil according to the reclamation plan and a post-dumping

bathymetric survey was performed to obtain the thickness of the fill. Bathymetric surveys were taken periodically after each dumping interval to monitor settlement (Shinohara, 2003). Data from the bathymetric survey together with a database including each sand barge's name, fill dumping position, fill volume, and fill source location was used to control the reclamation task as construction proceeded. An optical beam system calculated the volume of soil placed on each sand barge by measuring the height of the surface of the fill as it was loaded onto the barge (Arai, 1991).

The quality of above water placement and compaction was monitored using density and water content measured using radioisotope devices, density measured by the water replacement technique, modulus of subgrade reaction determined from plate load tests, and stiffness of the compacted fill obtained from accelerometers placed on the vibratory rollers. Bulldozers and vibratory rollers were also controlled with GPS equipment (Tabata and Morikawa, 2005).

5.4 Reclamation load at the seabed

Construction of Airport Island I and Airport Island II generated load on the surface of the seabed throughout the island building process. The increase in stress on marine and non-marine clay layers underlying the Kansai Airport site resulting from the applied reclamation load at the seabed surface caused vertical compression of these layers that has continued to present day. Settlement observations exceeded forecasts for Island I and the height of reclamation was increased as a result; the original design called for height of reclamation above seabed equal to approximately 30m (Nakase, 1987; Arai, 1991), then the reclamation height was increased to 33m (Arai, 1991), and it was subsequently increased to approximately 37m (Nishimura, personal communication, 2011).

Settlement analyses for Kansai Airport presented in Chapter 8 are performed at five locations: Monitoring Point 1 of Island II (MP1-II), Monitoring Point 2 of Island II (MP2-II), the Connecting Taxiway (CT), Point K of Island I (K-I), and Monitoring Point 1 of Island I (MP1-I) (Figure 5-13). Figure 5-14 through Figure 5-18 show reclamation load at seabed for the locations shown in Figure 5-13. The reclamation loads increase from Island I to the Connecting Taxiway and to Island II.

The load at seabed versus time relationships displayed in Figure 5-14 through Figure

5-18 include calculated values reported by others (Kobayashi et al., 2005; Shibata and Karube, 2005; Tabata and Morikawa, 2005; Furudoi and Kobayashi, 2009; Furudoi, 2010; Nishimura, personal communication, 2011) as well as reported load cell measurements (Kobayashi et al., 2005; Tabata and Morikawa, 2005; Furudoi, 2010; Nishimura, personal communication, 2011). Load cell measurements were reported for MP1-II and MP2-II only. Figure 5-17 and Figure 5-18 show that while the load cell measurements reported for MP2-II are relatively consistent, reaching a maximum value approximately equal to 535kPa to 540kPa, the load cell measurements reported for MP1-II are different by as much as 140kPa (maximum load reported for load cell 1 is approximately equal to 500kPa and the maximum load reported for load cell 2 is approximately equal to 640). However, the variation of load cell 1 and load cell 2 measurements as a function of time is nearly identical after May 2003 for MP1-II.

If the average value of the load cell measurements for a specific date at MP1-II is considered, then the average unit weight of the fill material can be back-calculated and checked against values reported in Table 5-3. In 2010, the average of the load cell readings is approximately 550kPa and the seabed settlement is approximately 15m (NKIAC, 2012). If the height of reclamation above the seabed at Island II is assumed to be 43m (Shinohara, 2003; Tabata and Morikawa, 2005) and the water depth 20m (Tanaka and Locat, 1999; Itoh et al., 2001; Tanaka et al., 2004) then the average unit weight is computed to be approximately equal to 21.0kN/m^3 (for unit weight of water equal to 10.0kN/m^3). This is reasonable based on the values reported in Table 5-3. Therefore, the average of the load cell readings was used for subsequent settlement analyses at MP1-II.

The same procedure can be used to check the reclamation load at seabed versus time reported near MP1-I by Kobayashi et al. (2005) and Shibata and Karube (2005). The maximum applied load reported by Kobayashi et al. (2005) and Shibata and Karube (2005) is approximately equal to 455kPa and the seabed settlement reported in December 2011 is 12.88m (NKIAC, 2012). If the height of reclamation above the seabed at Island I is assumed to be 36.7m (Nishimura, personal communication, 2011) and the water depth 18m (Arai, 1991) then the average unit weight is approximately equal to 20.8kN/m^3 (assuming unit weight of water equal to 10.0kN/m^3). Again, this is reasonable based on the values reported in Table 5-3.

The decrease in applied stress associated with settlement and the resulting submergence of reclamation fill below sea level is an important consideration for settlement analyses of

Kansai Airport primarily because the seabed settlements are very large. For example, average seabed settlement in December 2012 was 12.92 and 14.25 for Island I and Island II, respectively (NKIAC, 2012). However, the relationships presented in Figure 5-14 through Figure 5-18 reach relatively constant values of reclamation load. Kobayashi (personal communication, 2007) has explained that this is because reclamation fill was added in small steps even after the majority of the reclamation was completed. This is evidenced by the load cell measurements between July 2004 and January 2010 shown in Figure 5-18. Figure 5-14 shows the calculated reduction in reclamation load after January 1992 for MP1-I, if no additional fill material was added. The additional reclamation fill in meters required to maintain a constant load is also shown in Figure 5-14, assuming the unit weight of reclamation fill is 21kN/m^3.

Calculated reclamation load at seabed versus time relationships reported by Furudoi and Kobayashi (2009), Furudoi (2010), and Shibata and Karube (2005) were used directly for subsequent settlement analyses at CT, K-I, and MP1-I, respectively. The average of reported load cell measurements at the seabed are used for subsequent settlement analyses at MP1-II and MP2-II.

5.5 Tables

Table 5-1 Timeline of events for Kansai International Airport (Nakase, 2003; NKIAC, 2012).

Date		Description
1968	**April**	MOT began surveying eight proposed airport sites.
1971	**Nov.**	MOT conducted noise pollution surveys at 3 candidate sites.
1973	**Aug.**	MOT conducted air pollution surveys at 3 candidate sites.
1974	**Aug.**	The Council for Civil Aviation submitted to MOT a report recommending the site off the coast of Senshu as the best option.
1977		Subseabed investigation began for Kansai Airport site.
1979	**May**	MOT carried out aircraft flight study.
1983	**Dec.**	MOT started seabed improvement experiments off the coast of Senshu.
1984	**Oct.**	Kansai International Airport Co., Ltd (KIAC) was founded.
1985	**Oct.**	KIAC submitted a preliminary report assessing environmental impact. Meetings were held to explain the project to local residents.
	Dec.	Cabinet Council approved general plan for airport construction.
1986	**April**	KIAC entered in compensation agreement with Federation of Fishermen Associations in Osaka Prefecture.
	Nov.	KIAC entered in compensation agreement with Hyogo and Wakayama Federation of Fishermen Associations as well as Izumisano Fisherman's Cooperative Association.
1987	**Jan.**	Governor of Osaka Prefecture licensed KIAC to carry out reclamation of public waters.
	June	Start of work for airport access bridge.
	Aug.	Installation of silt protection sheets.
1991	**May**	Construction of the Passenger Terminal Building began.
1994	**March**	Kansai Airport access bridge completed.
	Sept.	September 4, Kansai International Airport was opened.
1996	**June**	Kansai International Airport Land Development Co. (KALD), Ltd. was founded.
1998	**Feb.**	KALD submitted preliminary report assessing the environmental impact of Phase II construction.
1999	**July**	Governor of Osaka Prefecture licensed KALD to carry out reclamation work for Phase II. Installation of silt protection sheets.
2001	**Jan.**	Kansai Airport was awarded "Monument of the Millenium" by ASCE.
2007	**Aug.**	August 2, opening of 2nd runway.
2008	**Aug.**	Renewal of 1st runway was completed.
2012	**April**	Establishment of New Kansai International Airport Co., Ltd
	July	Kansai International Airport and Osaka International Airport merge.

Table 5-2 Construction schedule for Kansai International Airport (Arai, 1991; Tabata and Morikawa, 2005; Furudoi and Kobayashi, 2009; Furudoi, 2010).

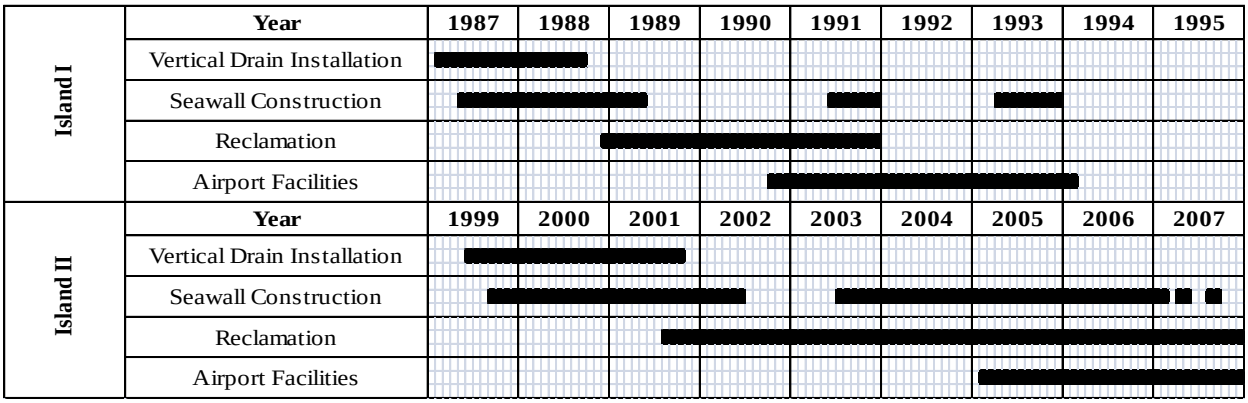

Table 5-3 Unit weight of fill material from available literature (Arai, 1991; Endo et al., 1991; Shiraishi and Suzuki, 1995; Yamane, 2003; Tabata and Morikawa, 2005).

	Reference	Unit Weight of Reclamation Fill (kN/m^3)	Notes
Island I	Arai (1991)	19.6 (above water) 11.8 (submerged unit weight below water)	Back calculated from settlement analysis on Ma13.
	Endo et al. (1991)	18 to 21 (average 19.6)	Unit weight measured using water replacement technique.
	Shiraishi and Suzuki (1995)	19.6 (above water) 11.8 (submerged unit weight below water)	Unit weight assumed by authors for settlement calculation.
Island II	Tabata and Morikawa (2005)	22.8	Unit weight equal to average of radioisotope measurements for soil placed above water.
	Yamane et al. (2003)	12.4	Average submerged unit weight based on data from bathymetric survey.

5.6 Figures

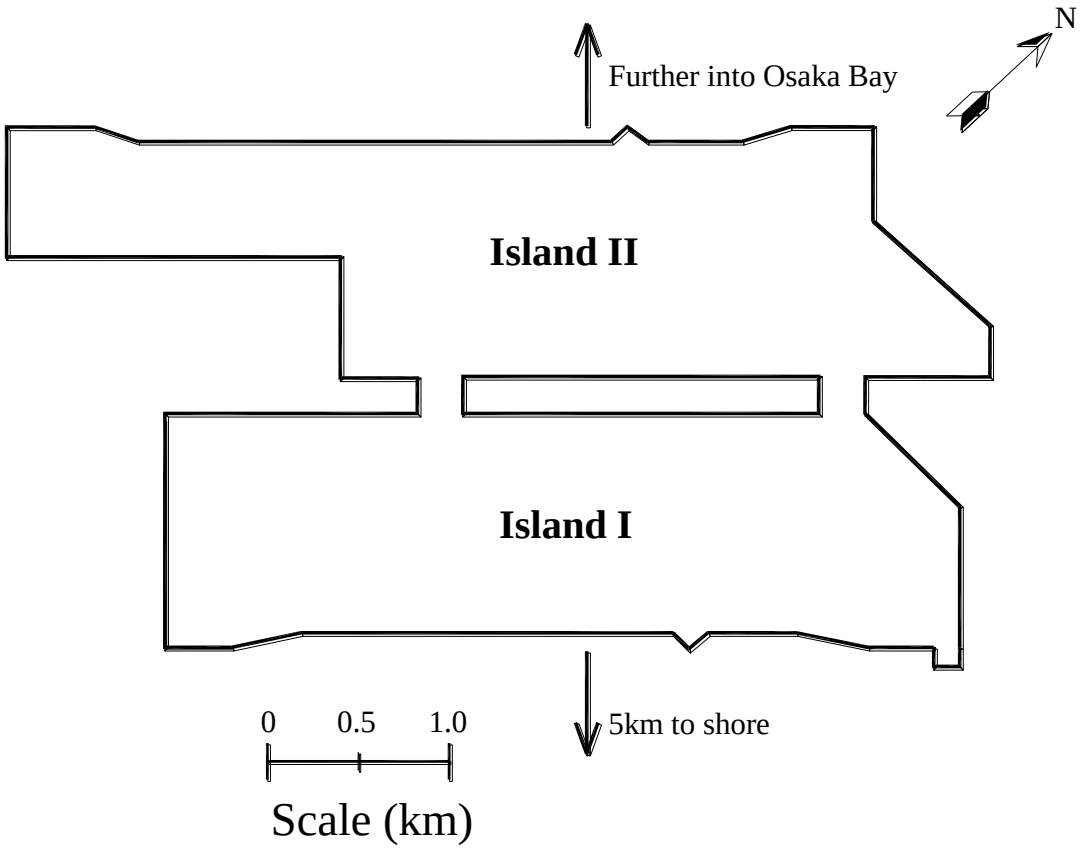

Figure 5-1 Plan view of the Kansai International Airport Islands.

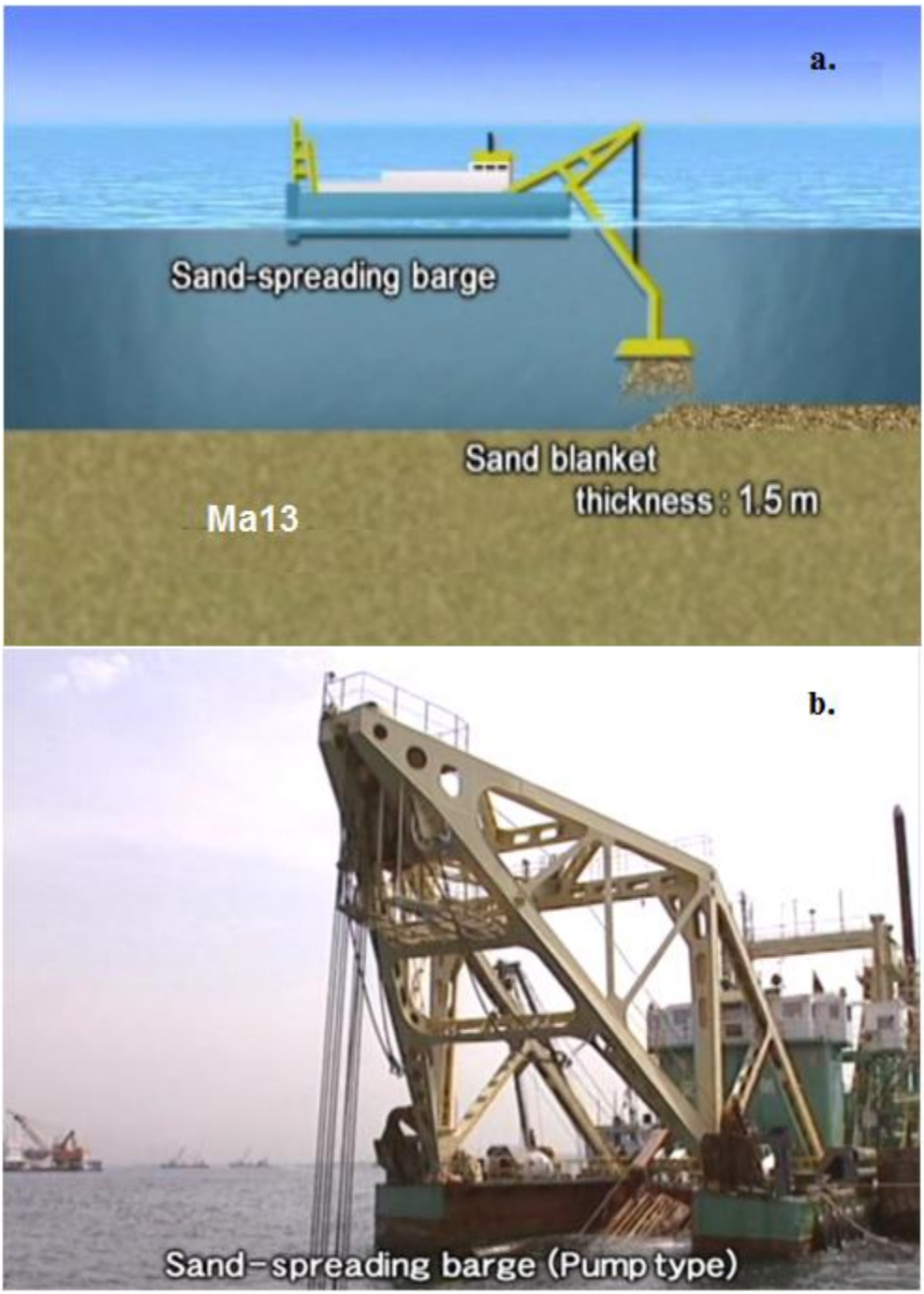

Figure 5-2 a. Diagram and b. photo showing the pump method for placement of 1.5m sand blanket (KALD, 2005).

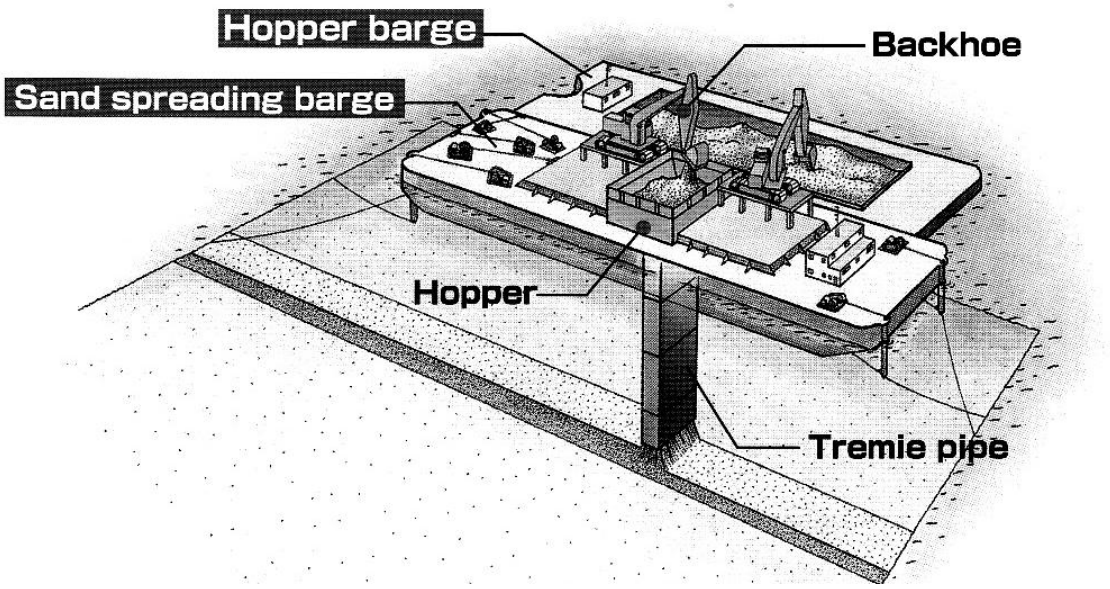

Figure 5-3 Diagram showing the tremie method for placement of 1.5m sand blanket (KIAC, 2005).

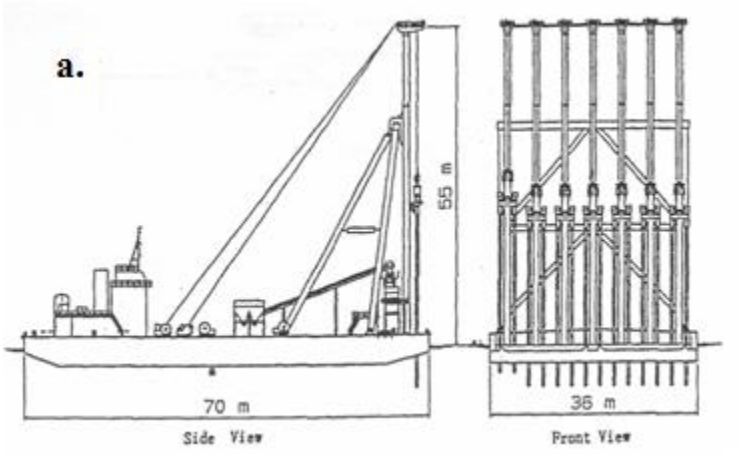

Figure 5-4 a. Diagram and b. photo of vertical sand drain barge used at Kansai International Airport site. (Yamakawa and Tsuruoka, 1996; KALD, 2005).

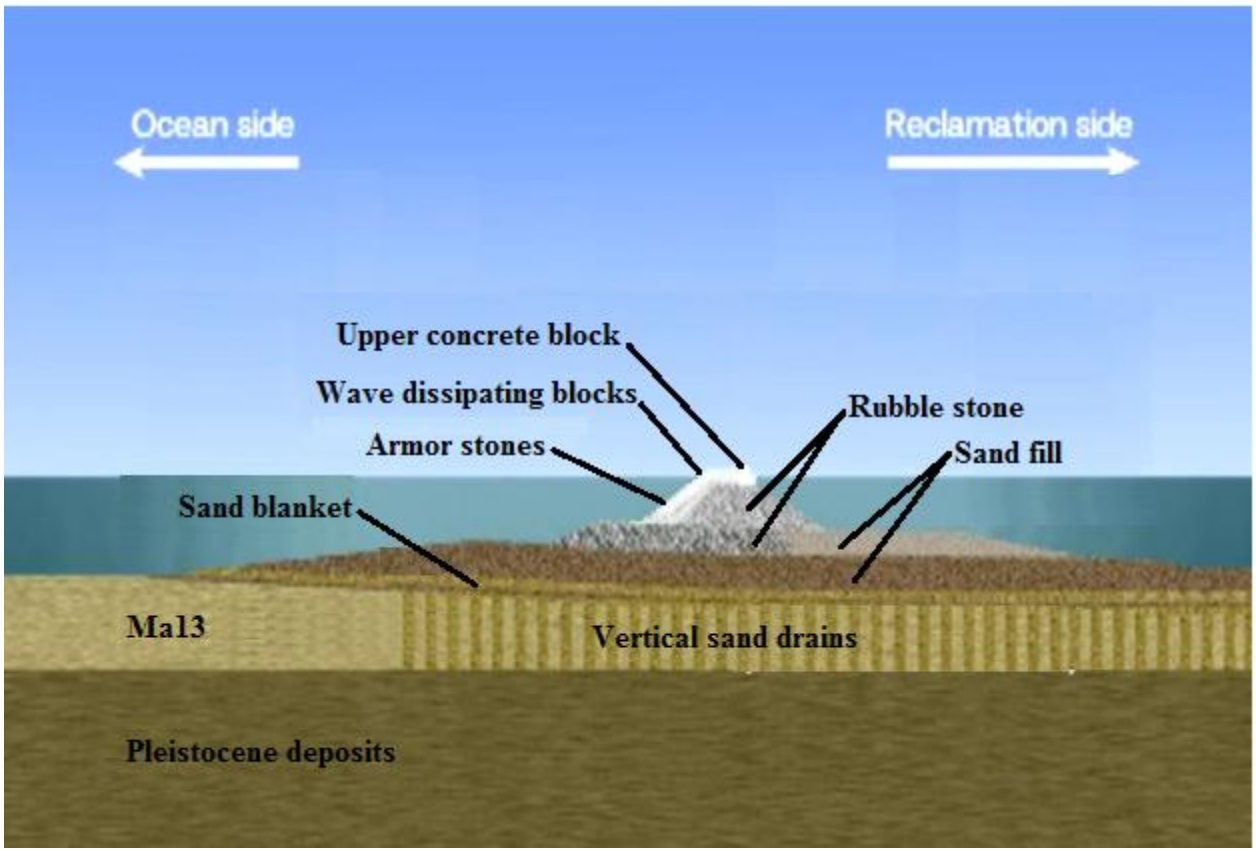

Figure 5-5 Diagram of gently sloping rubble mound seawall with armor stones and wave dissipating blocks (KALD, 2005)

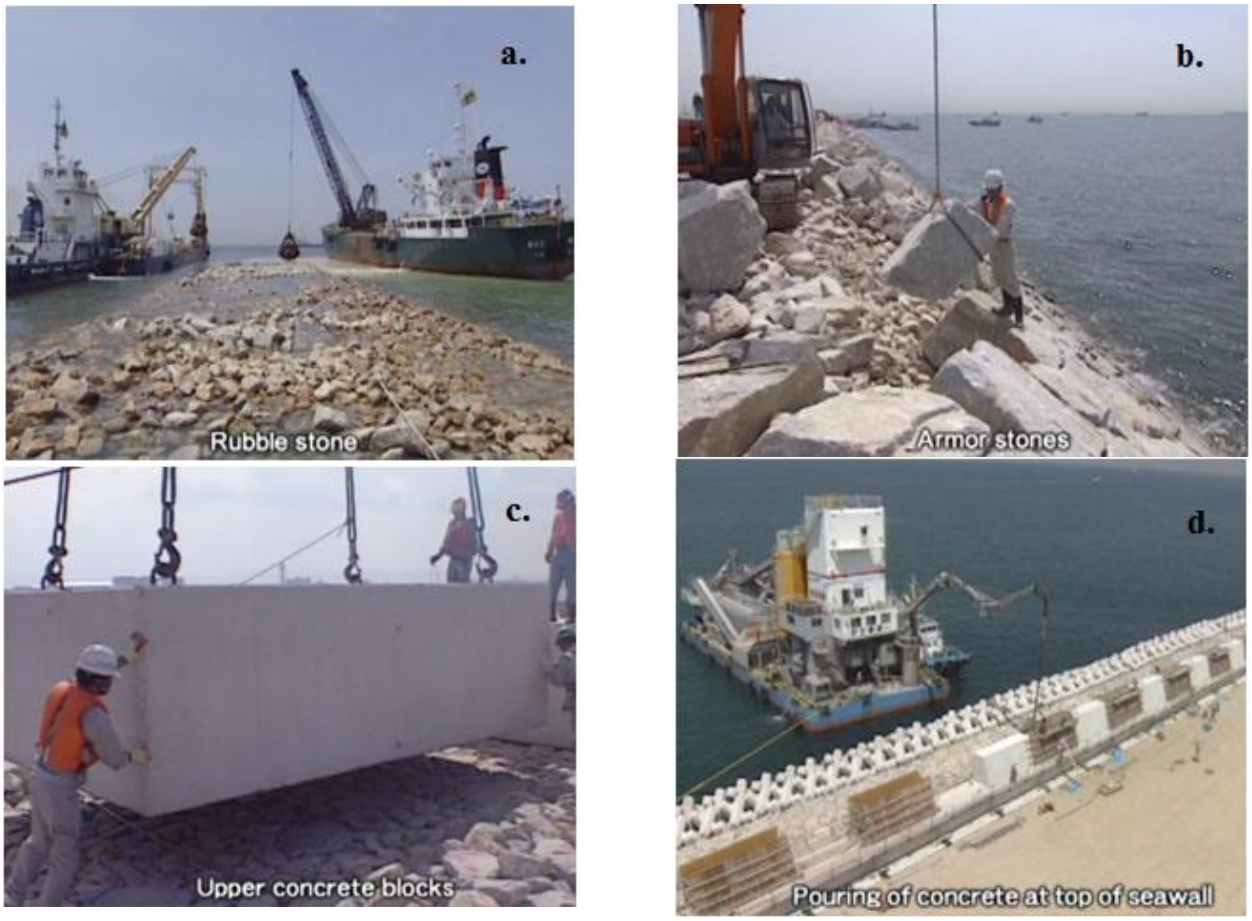

Figure 5-6 a. Placement of rubble material. b. Placement of armor stones. c. Placement of concrete blocks. d. Pouring of concrete at top of seawall (KALD, 2005).

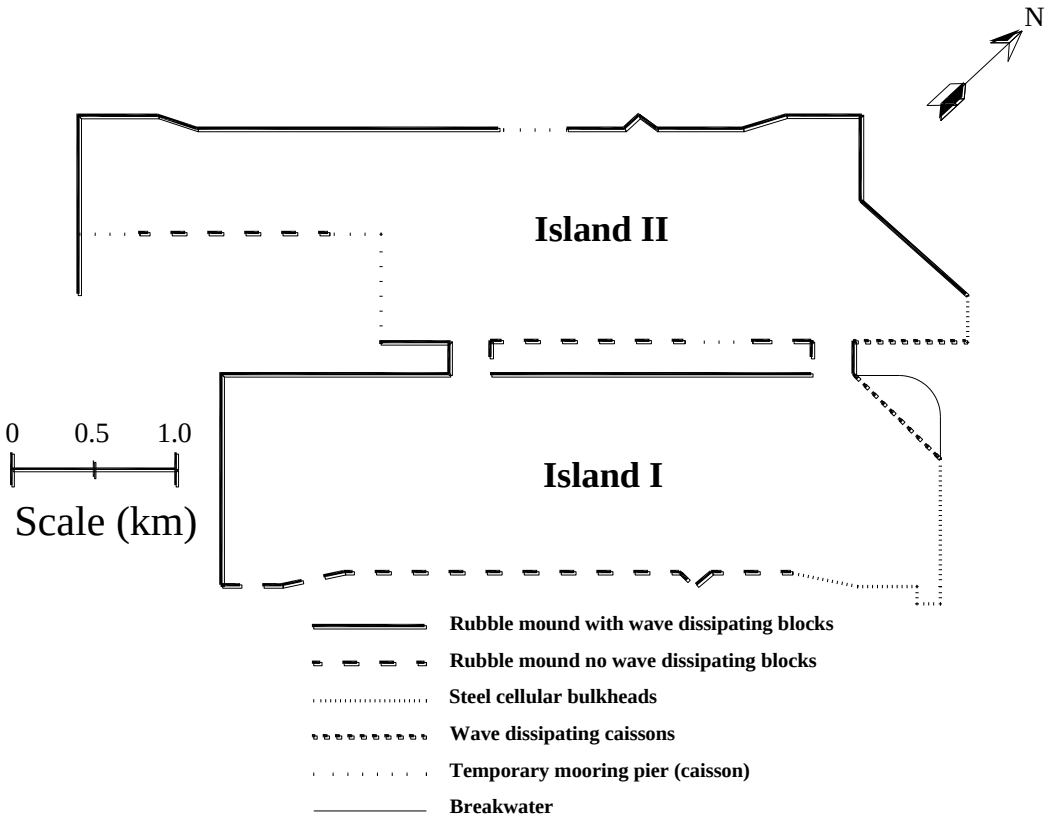

Figure 5-7 Location of different types of seawall construction along the perimeter of the Kansai Airport Islands (Maeda et al., 1990; KIAC, 2005).

Figure 5-8 Locations where reclamation fill material was obtained (KALD, 2005).

Figure 5-9 Earth collection site for reclamation fill material (KALD, 2005).

Figure 5-10 Large hopper barge used for soil dumping (KALD, 2005).

Figure 5-11 Reclaimer barge fitted with conveyor used for above water placement (KALD, 2005).

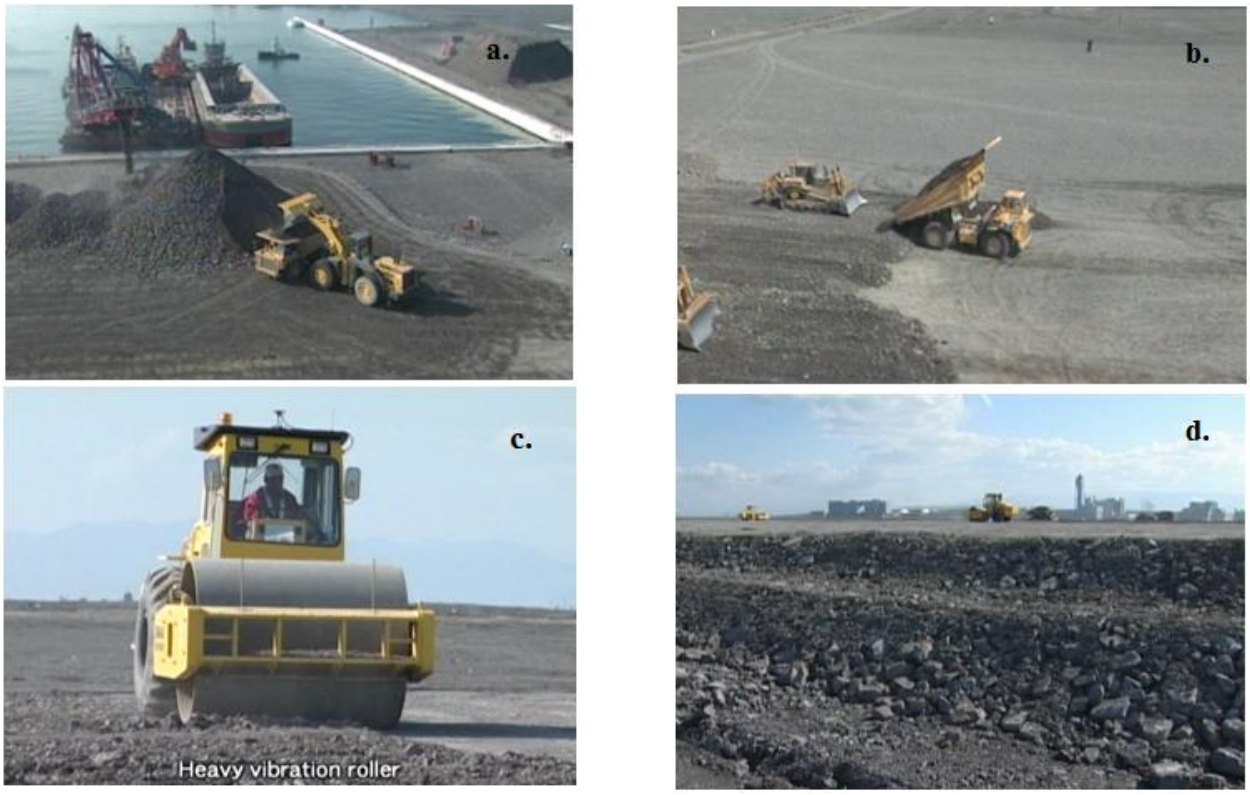

Figure 5-12 a. and b. Shovel and dump trucks used to place fill. c. Heavy vibratory roller used for compaction. d. Photo indicating lift thickness (60cm) and grain size for Island II construction (KALD, 2005).

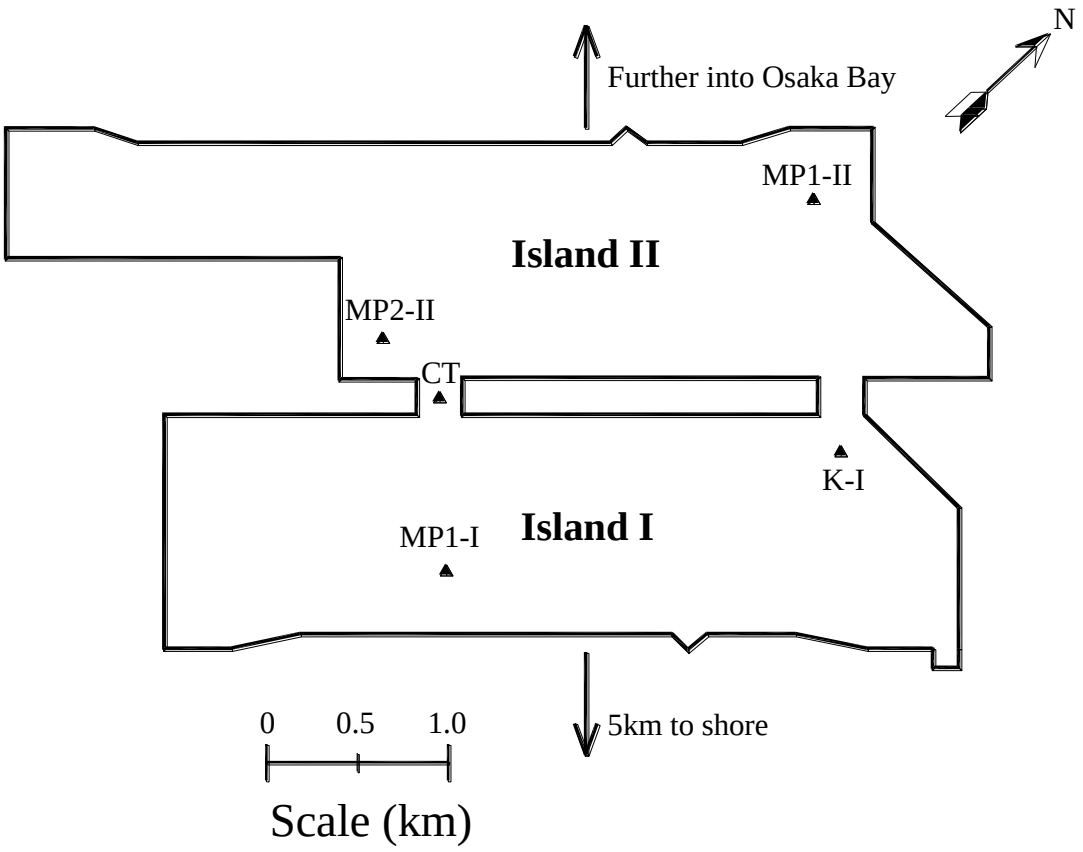

Figure 5-13 Locations where subsequent settlements analyses performed (see Chapter 8).

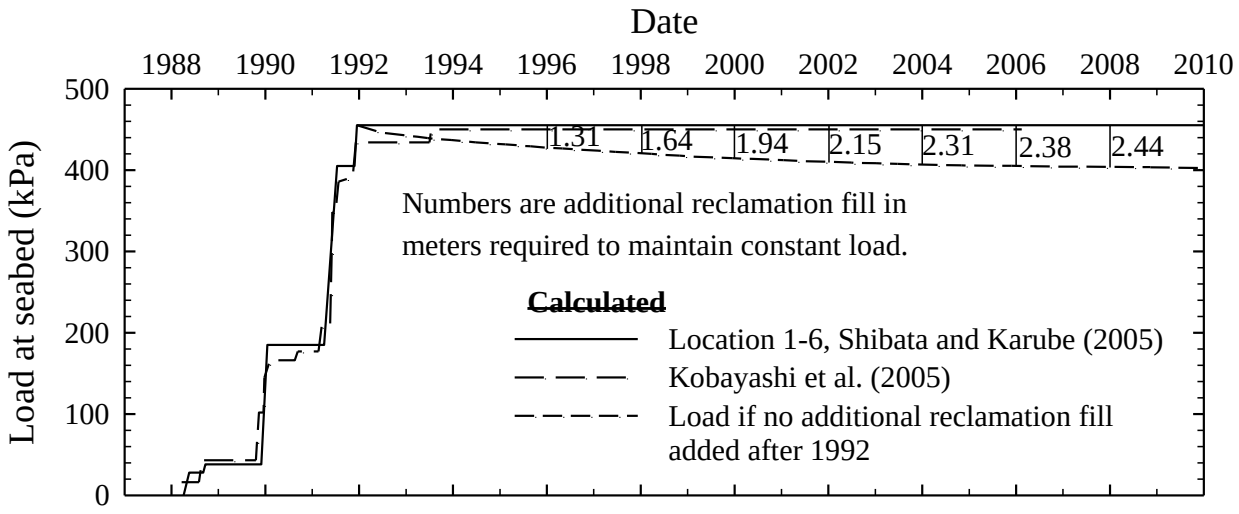

Figure 5-14 Applied reclamation load at seabed reported for MP1-I.

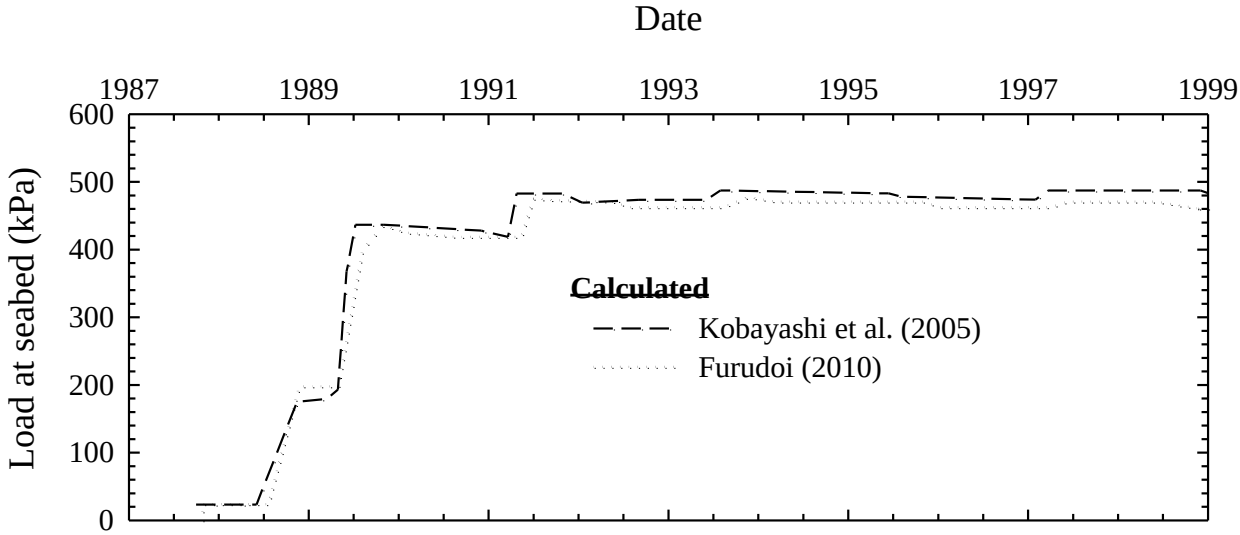

Figure 5-15 Applied reclamation load at seabed reported for K-I.

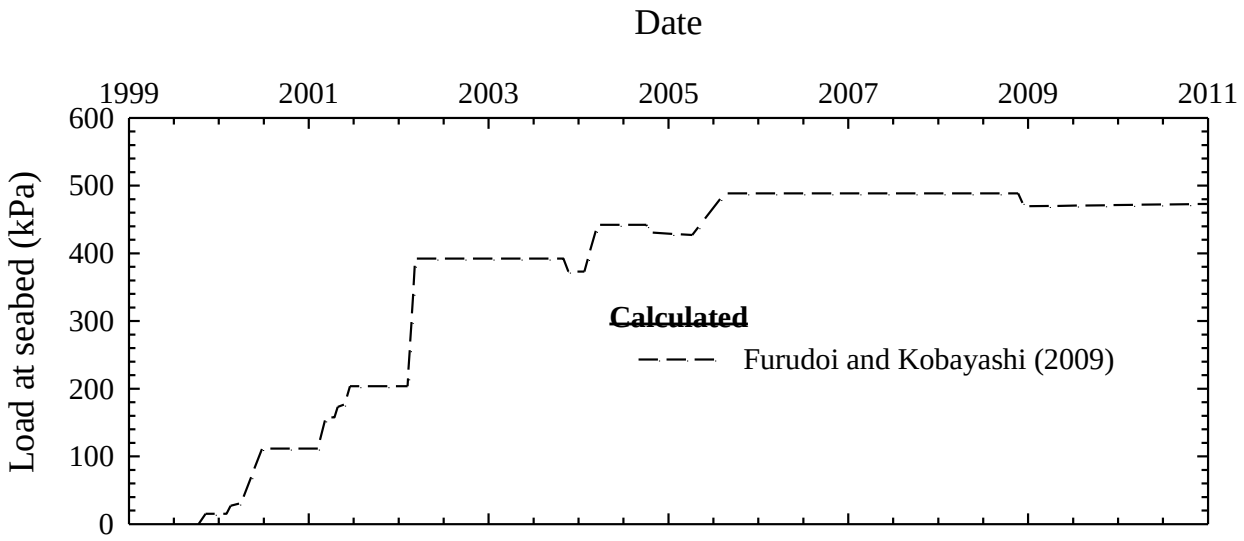

Figure 5-16 Applied reclamation load at seabed reported for CT.

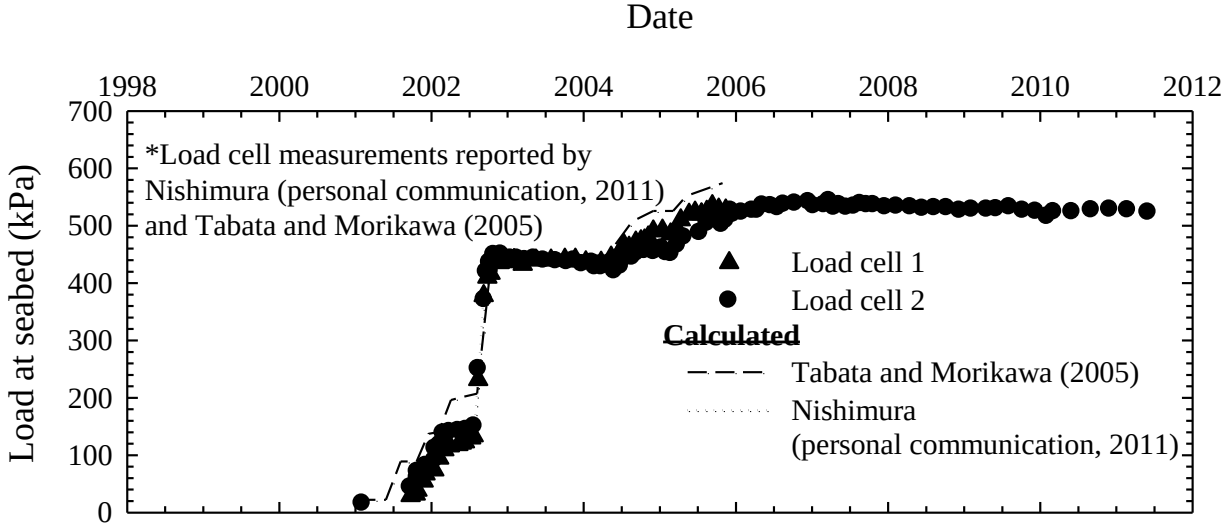

Figure 5-17 Applied reclamation load at seabed reported for MP2-II.

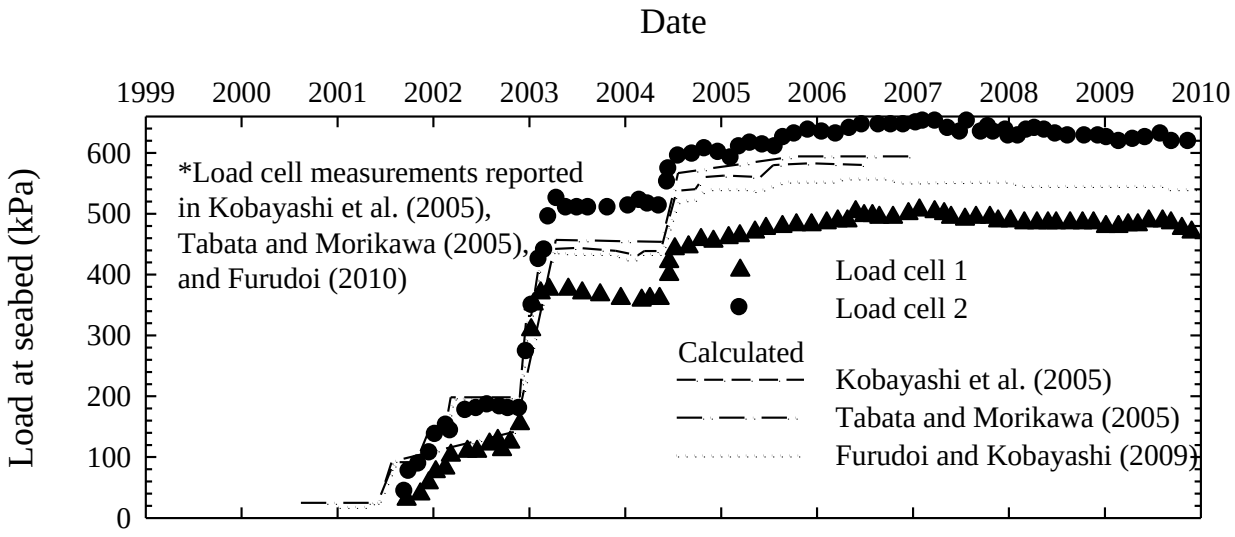

Figure 5-18 Applied reclamation load at seabed reported for MP1-II.

CHAPTER 6 INSTRUMENTATION AT KANSAI INTERNATIONAL AIRPORT

6.1 Introduction

A variety of instruments were installed in the seabed underlying the Kansai Airport Islands to monitor load on the seabed, porewater pressure, settlement, and lateral displacement resulting from construction of the seawall and placement of the reclamation fill. Instrument observations provided a check for assumptions and calculations used in the design of the airport islands (Maeda et al., 1990; Arai et al., 1991; Kobayashi et al., 2005). Instrumentation used for the Kansai Airport project can generally be divided into three groups: instruments installed beneath the pilot work section of Island I, instruments installed at specific monitoring point locations at Island I and Island II, and instruments installed beneath the seawall and reclamation areas throughout the Kansai International Airport site.

The settlement and porewater pressure instrumentation used at the Kansai International Airport site is described first. Then, settlement and porewater pressure observations are presented for the pilot work section of Island I, the monitoring point locations at Island I and Island II, and the seawall and reclamation areas, respectively. Finally, vertical compression data for Ma13, which was determined by subtracting settlement of the Pleistocene layers from seabed settlement, is presented.

6.2 Settlement and porewater pressure instrumentation

At least five types of settlement measurement devices were used at the Kansai Airport site: the settlement plate (Figure 6-1), the anchor-rod settlement gauge (Figure 6-2), the double-tube settlement gauge (Figure 6-3), the magnetic transmission water pressure gauge, and the magnetic differential settlement gauge (Figure 6-4).

The settlement plates consist of a plate with upright cylinders (Figure 6-1). They were placed on the sand blanket immediately following installation of vertical drains. The water pressure at the top of the cylinders was measured by a diver with a portable gauge. The measured water pressure gives depth below sea level to the cylinder which is used to determine the elevation of the top of the cylinder. Measurements were taken weekly, except when prohibited by inclement weather. The main disadvantage of the settlement plates is that they were obstacles

for barges and other work vessels during construction (Shinohara, 2003; KALD, 2005; Tabata and Morikawa, 2005).

The anchor-rod settlement gauge consists of an anchor that is embedded in a lower soil layer, an inner rod connected to the anchor, and a pipe to isolate the inner rod from the surrounding soil (Figure 6-2). The elevation of the inner rod can be used to determine settlement of the ground below the anchor installation point. Inclinometer measurements were used to compensate for inclination of the rod (Maeda et al., 1990; Shinohara, 2003; Tabata and Morikawa, 2005).

The double-tube settlement gauge consists of an outer tube that rests on the sand blanket above Ma13 and an inner tube that is embedded in sand layer Ds1 underlying Ma13 (Figure 6-3). The elevation of the outer pipe is used to determine seabed settlement, and the elevation of the inner pipe is used to determine settlement of the Pleistocene layers below Ma13 (Arai, 1991; Endo et al., 1991).

The magnetic transmission water pressure gauge measures the water pressure on the seabed every two hours and converts the pressure to seabed settlement. The data are transmitted to a boat equipped with a magnetic data receiver. The advantage of the magnetic transmission water pressure gauge is that it is not a construction obstacle and it provides continuous measurement of seabed settlement (Shinohara, 2003; KALD, 2005; Tabata and Morikawa, 2005; NKIAC, 2012).

The magnetic differential settlement gauge consists of a probe and a number of magnetic elements positioned along the length of an access pipe (Figure 6-4). The probe is lowered through the access pipe to detect the depth of the magnetic elements which move with the surrounding ground (Shinohara, 2003; Tabata and Morikawa, 2005).

Pneumatic piezometers were also installed at the Kansai International Airport site to measure porewater pressure. The pneumatic piezometer balances, through a gas pressure, the water pressure applied externally to the device (Figure 6-5) (Shinohara, 2003; Tabata and Morikawa, 2005). Pneumatic piezometers can malfunction if water enters the pressure lines (Dunnicliff, 1993). Excess porewater pressure was calculated from the porewater pressure observations by assuming a hydrostatic reference porewater pressure condition from sea level (Shinohara, 2003; Kobayashi et al., 2005; Tabata and Morikawa, 2005; Furudoi, 2010; Nishimura, personal communication, 2011; Jeon et al., 2012).

6.3 Pilot work section

In November 1986, two months prior to the start of construction of Island I, work began on the pilot work section (Maeda et al., 1990). The purpose of the pilot work section was to improve settlement prediction and to improve predictions for the rate of undrained strength gain in Ma13. The pilot section was deemed necessary because Airport Island I was constructed further offshore and in deeper water than previous reclamation projects in Osaka Bay. Results of the instrument observations were used by the designers to adjust parameters for settlement prediction and to modify the amount of time provided for consolidation of Ma13 between construction stages (Maeda et al., 1990; Arai, 1991; Kobayashi et al., 2005).

The pilot work section consisted of a seawall section and a 6ha reclamation section as shown in Figure 6-6. The 500m long pilot seawall section was constructed as a gently sloping rubble mound (see Figure 5-5). Seabed settlement and settlement of the Pleistocene layers were monitored at both the seawall and reclamation pilot sections. Undisturbed samples of Ma13 were taken intermittently during construction to monitor increase in undrained strength (Maeda et al., 1990; Endo et al., 1991).

The settlement plate (Figure 6-1), the anchor-rod settlement gauge (Figure 6-2), and the double-tube settlement gauge (Figure 6-3) were used at the pilot work section (Arai, 1991). The settlement plate was used to determined seabed settlement. The anchor rod settlement gauge was used to determine settlement of the Pleistocene layers (Maeda et al., 1990; Shinohara, 2003; Tabata and Morikawa, 2005). The elevation of the outer pipe of the double-tube settlement gauge was used to determine seabed settlement, and the elevation of the inner pipe was used to determine settlement of the Pleistocene layers (Arai, 1991; Endo et al., 1991). Figure 6-7 shows seabed settlement and settlement of Pleistocene layers for Point K (designated K-I) at the reclamation pilot section.

6.4 Monitoring points

Platforms were constructed in the reclamation area for Island I and Island II to monitor the progress of consolidation of the Pleistocene clay layers. Figure 6-8 shows the location of Monitoring Points 1 and 2 of Island II (MP1-II and MP2-II) and Monitoring Point 1 of Island I

(MP1-I). Magnetic differential settlement gauges and pneumatic piezometers were installed at each of the monitoring points. Magnetic elements for the differential settlement gauge and pneumatic piezometers were installed as deep as 350m below the seabed (Shinohara, 2003; Tabata and Morikawa, 2005). Earth pressure gauges were also installed at MP1-II and MP2-II in the sand blanket that was placed above Ma13.

Figure 6-9, Figure 6-10, and Figure 6-11 show reclamation load on the seabed and magnetic differential settlement gauge observations at MP1-II, MP2-II, and MP1-I, respectively.

Figure 6-12, Figure 6-13, and Figure 6-14 show excess porewater pressure determined from pneumatic piezometer observations in the Pleistocene sand layers for locations MP1-II, MP2-II, and MP1-I, respectively. Excess porewater pressure was calculated by assuming a hydrostatic reference porewater pressure condition from sea level (Shinohara, 2003; Kobayashi et al., 2005; Tabata and Morikawa, 2005; Furudoi, 2010; Nishimura, personal communication, 2011; Jeon et al., 2012).

The observed excess porewater pressure doesn't appear to be dissipating in some of the Pleistocene sand layers (e.g. Ds6 and Ds9 at MP1-II and Ds9 at MP2-II). As mentioned previously it is possible for pneumatic piezometers to become damaged if water enters the pressure lines (Dunnicliff, 1993). Akai and Tanaka (1999) made the following statement regarding porewater pressure observations for the Kansai Airport Project:

> "The progress of consolidation within these Pleistocene clays have been monitored by pore pressure sensors and a vertical array of settlement gauges in bore holes to obtain the local compressions along the hole. Several of such instrumented bore holes are located on KIA, but only few gave a good set of both pore pressure and local compression measurements because of the difficulty of installing many instruments in such a deep hole."

This comment by Akai and Tanaka (1999) indicates that the authors had some doubt about the reliability of the deeper instruments installed at the Kansai Airport site.

6.5 Instrumentation installed beneath the seawall and reclamation areas

Additional instrumentation was installed below the seawall and reclamation areas throughout the Kansai Airport site. Figure 6-15 and Figure 6-16 show the location of instruments installed at Island I and Island II, respectively (not all of instrument observation points are shown in Figure 6-15 and Figure 6-16). Twenty settlement gauges were installed beneath the seawall and 17 settlement gauges were installed beneath the reclamation area for Island I. Thirty-six settlement plates and 7 magnetic transmission water pressure gauges were installed beneath the seawall for Island II. Additionally, 17 settlement plates and 37 magnetic transmission water pressure gauges were installed beneath the reclamation area for Island II. The magnetic transmission water pressure gauges were installed on a 350m by 250m rectangular grid at Island II (Shinohara, 2003; KALD, 2005; Tabata and Morikawa, 2005; NKIAC, 2012).

Table 6-1 gives seabed settlement for the 17 points identified in Figure 6-15 as well as the average seabed settlement for Island I. The observed seabed settlements at Island I range from 9.73m to 15.38m in December 2012, and the average seabed settlement for Island I was 12.92m in December 2012. Table 6-2 gives seabed settlement for 54 points specified in Figure 6-16 as well as the average seabed settlement for Island II. The observed seabed settlements for Island II range from 11.31m to 16.49m in December 2012, and the average seabed settlement for Island II was 14.25m in December 2012 (NKIAC, 2012).

6.6 Vertical compression of Ma13

Vertical compression of the Holocene marine clay layer (Ma13) is determined by subtracting settlement of the Pleistocene layers from seabed settlement. Observed vertical compression of Ma13 at MP1-II, MP2-II, CT, K-I, and MP1-I is shown in Figure 6-17, Figure 6-18, Figure 6-19, Figure 6-20, and Figure 6-21, respectively.

6.7 Concluding remarks

The majority of the instrumentation installed at the Kansai International Airport site was intended to monitor the progress of seabed settlement. Construction and associated instrumentation of the pilot section was intended to improve settlement prediction for Ma13. Monitoring points at Airport Islands I and II were constructed to monitor the progress of consolidation of the Pleistocene clay layers using magnetic differential settlement gauges, and

pneumatic piezometers. Finally, settlement plates and magnetic transmission water pressure gauges were used to monitor seabed settlement beneath the seawall and beneath the reclamation area throughout the Kansai International Airport site.

6.8 Tables

Table 6-1 Seabed settlement (m) at Island I for the points identified in Figure 6-15 (NKIAC, 2012).

Measurement Date		Location identification number (see Figure 6-15)								
Year	**Month**	**1**	**2**	**3**	**4**	**5**	**6**	**7**	**8**	**9**
Reclamation began Sept. 1987		0.00	0.00	0.00	0.00	0.00	0.00	0.00	0.00	0.00
1994	**Dec.**	8.76	7.88	10.78	10.31	9.69	8.82	9.00	10.98	10.46
1995	**Nov.**	9.11	8.25	11.17	10.71	10.06	9.22	9.34	11.38	10.88
1996	**Nov.**	9.44	8.59	11.54	11.09	10.43	9.59	9.63	11.74	11.28
1997	**Nov.**	9.74	8.87	11.88	11.43	10.79	9.89	9.88	12.08	11.63
1999	**Feb.**	10.11	9.23	12.29	11.85	11.19	10.28	10.21	12.49	12.02
1999	**Dec.**	10.33	9.44	12.51	12.08	11.43	10.49	10.37	12.73	12.26
2000	**Dec.**	10.57	9.67	12.76	12.33	11.67	10.71	10.55	12.99	12.49
2001	**Dec.**	10.78	9.87	13.00	12.57	11.89	10.89	10.69	13.20	12.70
2002	**Dec.**	10.97	10.04	13.19	12.77	12.06	11.04	10.82	13.42	12.87
2003	**Dec.**	11.13	10.19	13.36	12.91	12.21	11.17	10.90	13.54	13.02
2004	**Dec.**	11.26	10.30	13.49	13.04	12.32	11.27	10.98	13.66	13.12
2005	**Dec.**	11.38	10.41	13.60	13.14	12.42	11.35	11.05	13.73	13.21
2006	**Dec.**	11.48	10.50	13.73	13.26	12.51	11.42	11.12	13.81	13.30
2007	**Dec.**	11.58	10.59	13.83	13.34	12.59	11.49	11.16	13.87	13.36
2008	**Dec.**	11.68	10.68	13.93	13.43	12.67	11.55	11.23	13.93	13.42
2009	**Dec.**	11.77	10.76	14.02	13.52	12.74	11.62	11.28	13.99	13.49
2010	**Dec.**	11.87	10.84	14.12	13.60	12.81	11.69	11.33	14.05	13.55
2011	**Dec.**	11.95	10.90	14.21	13.68	12.88	11.75	11.38	14.11	13.62
2012	**Dec.**	12.05	10.98	14.30	13.77	12.96	11.82	11.44	14.17	13.68

Table 6-1 cont. Seabed settlement (m) at Island I for the points identified in Figure 6-15 (NKIAC, 2012).

Measurement Date		**Location identification number (see Figure 6-15)**								
Year	**Month**	**10**	**11**	**12**	**13**	**14**	**15**	**16**	**17**	**Avg.**
Reclamation began Sept. 1987		0.00	0.00	0.00	0.00	0.00	0.00	0.00	0.00	**0.00**
1994	**Dec.**	9.85	8.79	10.50	10.38	9.95	10.82	8.13	11.87	**9.82**
1995	**Nov.**	10.22	9.15	10.95	10.87	10.47	11.20	8.33	12.32	**10.21**
1996	**Nov.**	10.55	9.44	11.35	11.29	10.91	11.52	8.51	12.70	**10.56**
1997	**Nov.**	10.85	9.69	11.71	11.63	11.25	11.80	8.65	13.10	**10.87**
1999	**Feb.**	11.20	9.99	12.14	12.04	11.66	12.11	8.84	13.53	**11.25**
1999	**Dec.**	11.40	10.15	12.39	12.26	11.89	12.30	8.93	13.78	**11.46**
2000	**Dec.**	11.60	10.32	12.65	12.48	12.13	12.50	9.04	14.05	**11.68**
2001	**Dec.**	11.79	10.46	12.89	12.68	12.34	12.68	9.13	14.28	**11.87**
2002	**Dec.**	11.94	10.59	13.07	12.86	12.52	12.83	9.22	14.46	**12.04**
2003	**Dec.**	12.08	10.71	13.25	13.02	12.69	12.98	9.29	14.64	**12.18**
2004	**Dec.**	12.18	10.80	13.40	13.17	12.84	13.12	9.38	14.78	**12.30**
2005	**Dec.**	12.28	10.88	13.50	13.28	12.97	13.22	9.43	14.87	**12.40**
2006	**Dec.**	12.35	10.95	13.59	13.39	13.08	13.33	9.49	14.95	**12.49**
2007	**Dec.**	12.44	11.01	13.67	13.47	13.19	13.41	9.53	15.04	**12.56**
2008	**Dec.**	12.50	11.06	13.74	13.52	13.26	13.48	9.57	15.10	**12.63**
2009	**Dec.**	12.57	11.12	13.81	13.59	13.35	13.56	9.61	15.17	**12.70**
2010	**Dec.**	12.64	11.18	13.87	13.68	13.45	13.65	9.66	15.24	**12.78**
2011	**Dec.**	12.71	11.24	13.94	13.77	13.54	13.72	9.69	15.31	**12.85**
2012	**Dec.**	12.79	11.31	14.01	13.85	13.64	13.79	9.73	15.38	**12.92**

Table 6-2 Seabed settlement (m) at Island II for the points identified in Figure 6-16.

Measurement Date		Location identification number (see Figure 6-16)								
Year	**Month**	**1**	**2**	**3**	**4**	**5**	**6**	**7**	**8**	**9**
1999	**Dec.**	0.00	0.00	0.00	0.00	0.00	0.00	0.00	0.00	0.00
2000	**Dec.**	2.78	3.54	0.62	1.78	0.68	2.00	2.48	0.72	0.80
2001	**Dec.**	5.48	5.11	3.45	4.82	3.16	5.09	4.75	3.05	3.28
2002	**Dec.**	7.64	5.91	5.90	5.63	5.64	6.04	6.79	5.67	5.68
2003	**Dec.**	8.85	7.76	9.12	7.55	8.69	7.69	7.76	8.50	8.66
2004	**Dec.**	9.76	8.39	10.56	8.24	10.05	8.52	8.92	9.75	10.06
2005	**Dec.**	10.68	9.17	11.75	9.01	11.15	9.50	10.09	10.85	11.25
2006	**Dec.**	11.45	9.70	12.71	9.47	12.05	10.13	10.89	11.71	12.18
2007	**Dec.**	11.96	10.25	13.47	10.00	12.79	10.72	11.48	12.41	12.91
2008	**Dec.**	12.35	10.64	14.07	10.40	13.39	11.19	11.94	12.99	13.51
2009	**Dec.**	12.70	11.02	14.62	10.78	13.93	11.59	12.38	13.55	14.09
2010	**Dec.**	13.02	11.38	15.12	11.14	14.44	11.98	12.79	14.07	14.62
2011	**Dec.**	13.27	11.68	15.53	11.46	14.90	12.34	13.14	14.51	15.03
2012	**Dec.**	13.48	12.11	15.87	11.86	15.35	12.66	13.46	14.99	15.47
Year	**Month**	**10**	**11**	**12**	**13**	**14**	**15**	**16**	**17**	**18**
1999	**Dec.**	0.00	0.00	0.00	0.00	0.00	0.00	0.00	0.00	0.00
2000	**Dec.**	2.11	0.65	2.90	4.11	0.53	0.71	0.73	0.69	0.35
2001	**Dec.**	4.83	3.13	4.92	5.46	3.10	3.03	3.38	2.83	3.37
2002	**Dec.**	5.64	6.29	5.77	7.59	6.00	5.02	5.42	7.01	6.48
2003	**Dec.**	5.97	8.58	7.53	8.90	8.55	8.18	8.30	8.29	8.65
2004	**Dec.**	8.03	9.92	8.13	10.24	9.87	9.77	9.64	9.26	9.82
2005	**Dec.**	8.96	11.13	8.74	11.64	11.13	10.75	10.79	10.23	11.00
2006	**Dec.**	9.68	12.07	9.33	12.47	12.08	11.52	11.55	10.93	11.90
2007	**Dec.**	10.31	12.85	10.35	13.10	12.82	12.22	12.21	11.53	12.56
2008	**Dec.**	10.81	13.48	11.00	13.59	13.45	12.79	12.80	12.05	13.16
2009	**Dec.**	11.22	14.06	11.57	14.07	13.99	13.33	13.37	12.56	13.68
2010	**Dec.**	11.61	14.63	12.04	14.47	14.49	13.84	13.89	13.04	14.03
2011	**Dec.**	11.92	15.09	12.45	14.83	14.94	14.28	14.33	13.40	14.48
2012	**Dec.**	12.28	15.57	12.84	15.16	15.38	14.71	14.83	13.83	14.88

Table 6-2 cont. Seabed settlement (m) at Island II for the points identified in Figure 6-16.

Measurement Date		Location identification number (see Figure 6-16)								
Year	**Month**	**19**	**20**	**21**	**22**	**23**	**24**	**25**	**26**	**27**
1999	**Dec.**	0.00	0.00	0.00	0.00	0.00	0.00	0.00	0.00	0.00
2000	**Dec.**	0.62	0.36	0.40	0.39	0.64	0.73	0.61	1.18	0.53
2001	**Dec.**	3.06	3.02	2.67	3.39	3.25	3.06	3.05	4.19	3.50
2002	**Dec.**	5.22	5.07	6.47	5.92	4.97	5.05	6.17	6.69	6.10
2003	**Dec.**	8.21	7.75	7.82	8.42	7.62	7.71	7.86	7.42	8.32
2004	**Dec.**	9.64	8.99	8.65	9.78	9.31	9.48	9.02	7.84	9.62
2005	**Dec.**	10.83	10.26	9.63	10.85	10.37	10.56	9.92	8.43	10.68
2006	**Dec.**	11.75	11.15	10.36	11.74	11.18	11.45	10.79	8.88	11.54
2007	**Dec.**	12.46	11.83	10.96	12.50	11.90	12.24	11.59	9.55	12.25
2008	**Dec.**	13.06	12.40	11.46	13.12	12.52	12.88	12.22	10.08	12.83
2009	**Dec.**	13.56	12.92	11.89	13.69	13.04	13.45	12.77	10.49	13.41
2010	**Dec.**	14.07	13.37	12.33	14.21	13.55	13.98	13.27	10.87	13.92
2011	**Dec.**	14.51	13.83	12.73	14.66	-	14.43	13.69	11.19	14.38
2012	**Dec.**	14.91	14.24	13.07	15.07	-	-	-	-	14.79
Year	**Month**	**28**	**29**	**30**	**31**	**32**	**33**	**34**	**35**	**36**
1999	**Dec.**	0.00	0.00	0.00	0.00	0.00	0.00	0.00	0.00	0.00
2000	**Dec.**	0.53	0.66	0.62	2.73	0.47	0.79	0.54	0.59	0.76
2001	**Dec.**	2.94	3.10	2.91	5.17	3.23	2.82	2.71	2.64	3.14
2002	**Dec.**	5.02	4.98	5.75	7.24	6.10	5.04	4.70	4.55	5.76
2003	**Dec.**	7.20	6.17	7.59	8.27	8.62	7.86	4.97	6.52	8.98
2004	**Dec.**	8.75	8.52	8.22	9.49	10.13	9.21	8.06	8.01	10.57
2005	**Dec.**	9.89	9.91	9.60	10.61	11.24	10.47	9.58	9.10	11.76
2006	**Dec.**	10.72	10.77	10.44	11.37	12.11	11.34	10.48	9.88	12.66
2007	**Dec.**	11.46	11.52	11.19	11.96	12.82	12.11	11.24	10.58	13.38
2008	**Dec.**	12.08	12.15	11.83	12.41	13.40	12.75	11.88	11.18	13.97
2009	**Dec.**	12.66	12.73	12.40	12.86	13.96	13.35	12.46	11.72	14.52
2010	**Dec.**	13.19	13.27	12.91	13.26	14.47	13.90	13.00	12.22	15.03
2011	**Dec.**	13.65	13.73	13.34	13.58	14.92	14.36	13.46	12.64	15.47
2012	**Dec.**	14.15	14.17	13.73	13.93	15.36	14.82	13.88	13.06	15.88

Table 6-2 cont. Seabed settlement (m) at Island II for the points identified inFigure 6-16.

Measurement Date		Location identification number (see Figure 6-16)								
Year	**Month**	**37**	**38**	**39**	**40**	**41**	**42**	**43**	**44**	**45**
1999	**Dec.**	0.00	0.00	0.00	0.00	0.00	0.00	0.00	0.00	0.00
2000	**Dec.**	0.71	0.25	0.64	1.31	3.42	0.78	0.64	0.74	0.58
2001	**Dec.**	2.88	2.42	2.60	3.93	5.41	3.12	2.97	2.54	2.67
2002	**Dec.**	5.02	4.60	4.67	5.27	7.24	5.97	5.01	4.81	4.65
2003	**Dec.**	7.84	4.84	4.95	6.56	8.37	9.04	7.90	5.14	4.85
2004	**Dec.**	9.18	7.35	8.01	7.08	9.43	10.83	9.13	5.44	7.35
2005	**Dec.**	10.63	9.22	9.12	7.66	10.99	12.15	10.71	9.08	8.53
2006	**Dec.**	11.63	10.56	10.34	8.37	11.89	13.12	11.72	10.48	9.82
2007	**Dec.**	12.50	11.52	11.34	9.01	12.51	13.87	12.59	11.43	10.88
2008	**Dec.**	13.20	12.25	12.07	9.65	13.01	14.47	13.28	12.16	11.67
2009	**Dec.**	13.83	12.89	12.71	10.78	13.45	15.03	13.90	12.81	12.35
2010	**Dec.**	14.39	13.47	13.29	11.37	13.86	15.54	14.46	13.40	12.98
2011	**Dec.**	14.89	13.97	13.78	11.87	14.21	15.98	14.95	13.91	13.50
2012	**Dec.**	15.32	14.48	14.27	12.38	14.56	16.38	15.40	14.39	13.99
Year	**Month**	**46**	**47**	**48**	**49**	**50**	**51**	**52**	**53**	**54**
1999	**Dec.**	0.00	0.00	0.00	0.00	0.00	0.00	0.00	0.00	0.00
2000	**Dec.**	2.81	0.85	0.66	0.68	0.62	1.31	2.69	3.12	2.66
2001	**Dec.**	5.10	2.77	2.92	2.62	2.62	4.28	5.36	5.36	4.87
2002	**Dec.**	7.13	5.48	5.02	4.82	4.76	5.21	7.08	6.11	5.29
2003	**Dec.**	8.34	8.76	7.62	5.08	5.04	6.22	8.44	7.89	5.49
2004	**Dec.**	9.25	10.59	9.08	5.24	7.37	7.02	9.23	8.68	5.56
2005	**Dec.**	10.96	11.96	10.71	8.38	8.40	7.45	10.45	9.69	6.74
2006	**Dec.**	11.90	12.95	11.71	10.24	9.63	8.39	11.33	10.41	7.62
2007	**Dec.**	12.57	13.78	12.60	11.32	10.66	8.86	11.91	11.10	8.40
2008	**Dec.**	13.10	14.43	13.32	12.08	11.38	9.35	12.41	11.64	10.11
2009	**Dec.**	13.54	15.00	13.96	12.74	12.02	9.93	12.82	12.12	10.93
2010	**Dec.**	13.97	15.56	14.55	13.35	12.59	10.49	13.18	12.57	11.55
2011	**Dec.**	14.33	16.05	15.06	13.88	13.08	10.94	13.55	12.96	12.02
2012	**Dec.**	14.69	16.49	15.56	14.41	13.57	11.31	13.89	13.34	12.47

Table 6-2 cont. Seabed settlement (m) at Island II for the points identified in Figure 6-16.

Measurement Date		Avg.
Year	**Month**	
1999	**Dec.**	0.00
2000	**Dec.**	1.22
2001	**Dec.**	3.60
2002	**Dec.**	5.72
2003	**Dec.**	7.54
2004	**Dec.**	8.85
2005	**Dec.**	10.08
2006	**Dec.**	10.97
2007	**Dec.**	11.71
2008	**Dec.**	12.32
2009	**Dec.**	12.87
2010	**Dec.**	13.37
2011	**Dec.**	13.79
2012	**Dec.**	14.25

6.9 Figures

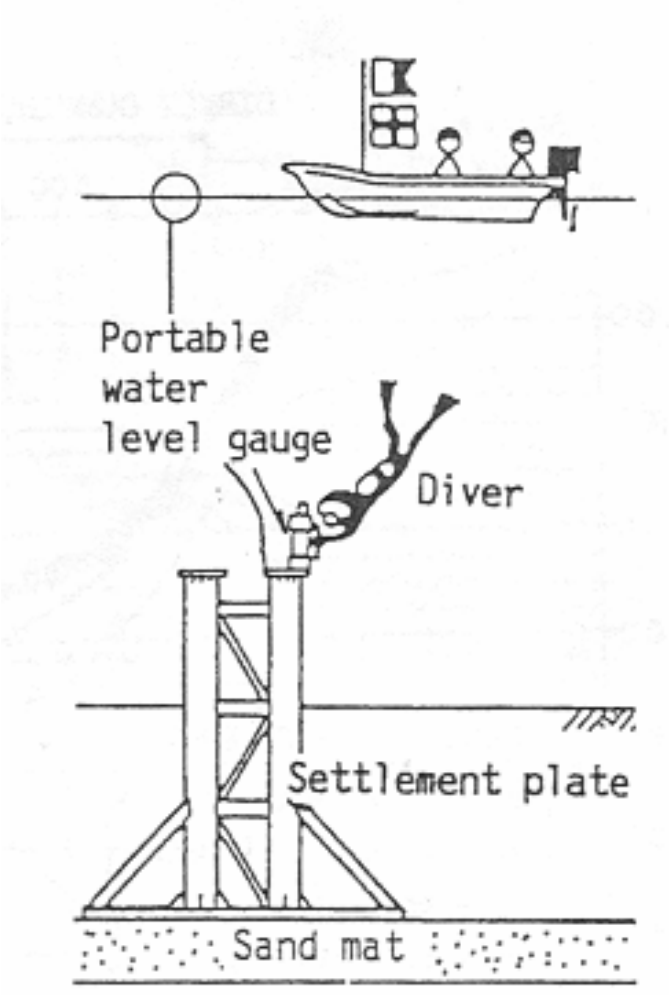

Figure 6-1 Diagram of settlement plate (Arai, 1991).

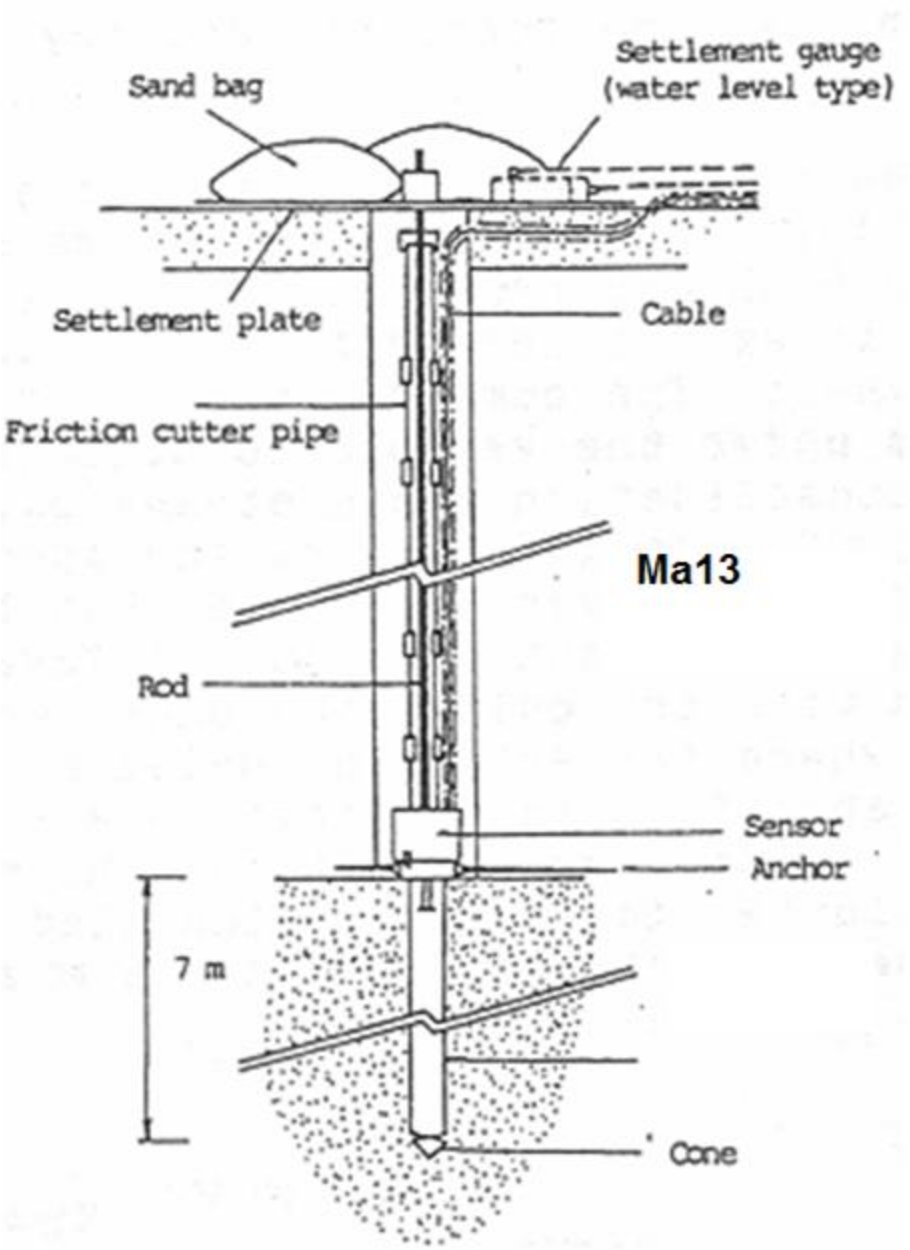

Figure 6-2 Diagram of anchor-rod settlement gauge (Arai, 1991).

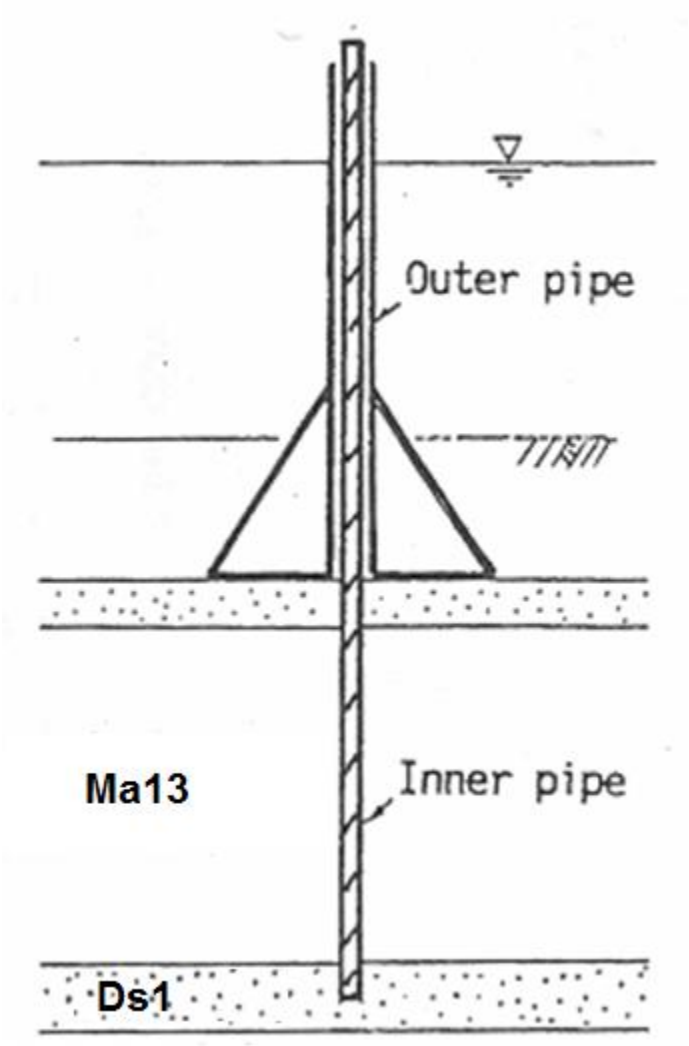

Figure 6-3 Diagram of double-tube settlement gauge (Arai, 1991).

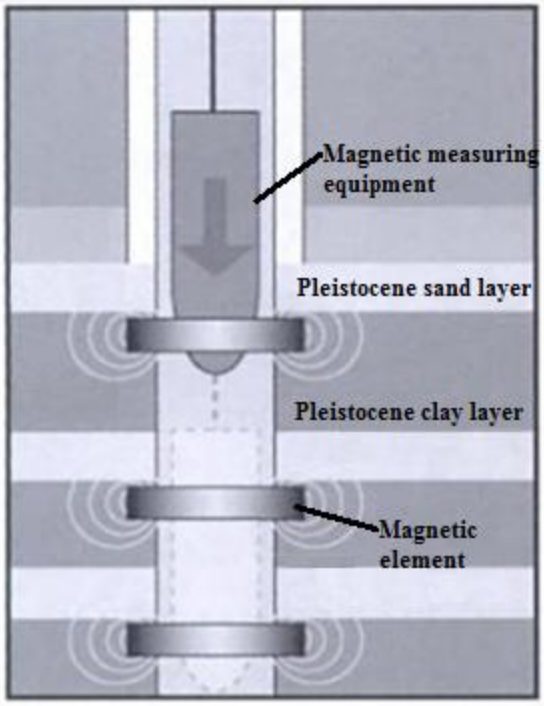

Figure 6-4 Diagram of magnetic differential settlement gauge (Shinohara, 2003; Tabata and Morikawa, 2005).

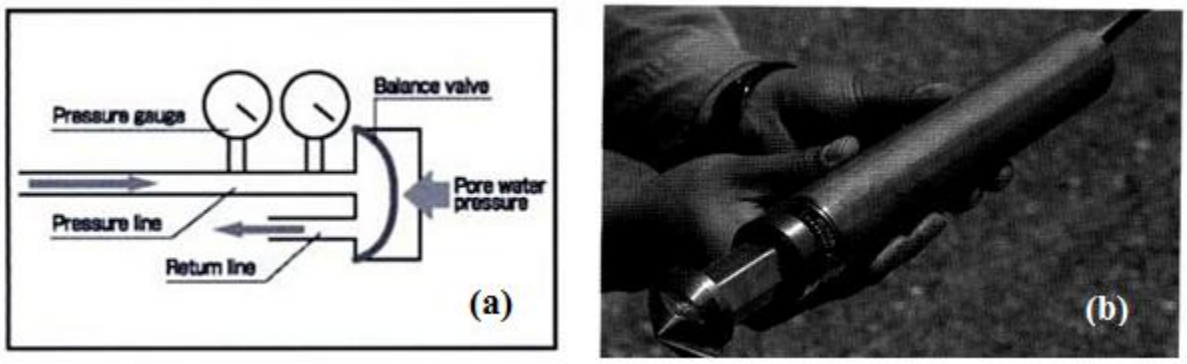

Figure 6-5 (a) Diagram and (b) photo of pneumatic piezometer (Shinohara, 2003; Tabata and Morikawa, 2005; KALD, 2005).

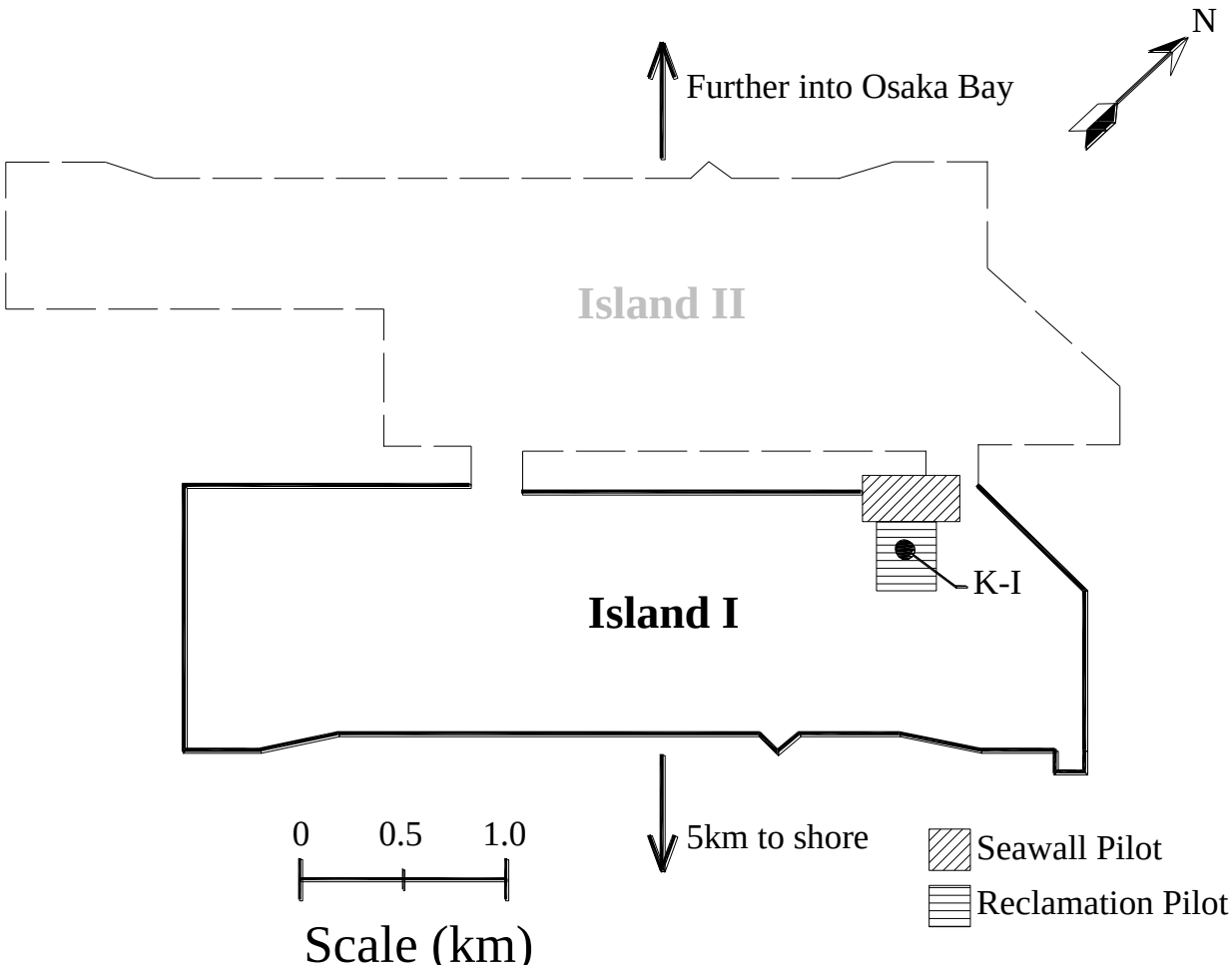

Figure 6-6 Location of Island I Seawall and Reclamation Pilot Sections (Maeda et al., 1990; Endo et al., 1991; Arai et al., 1991).

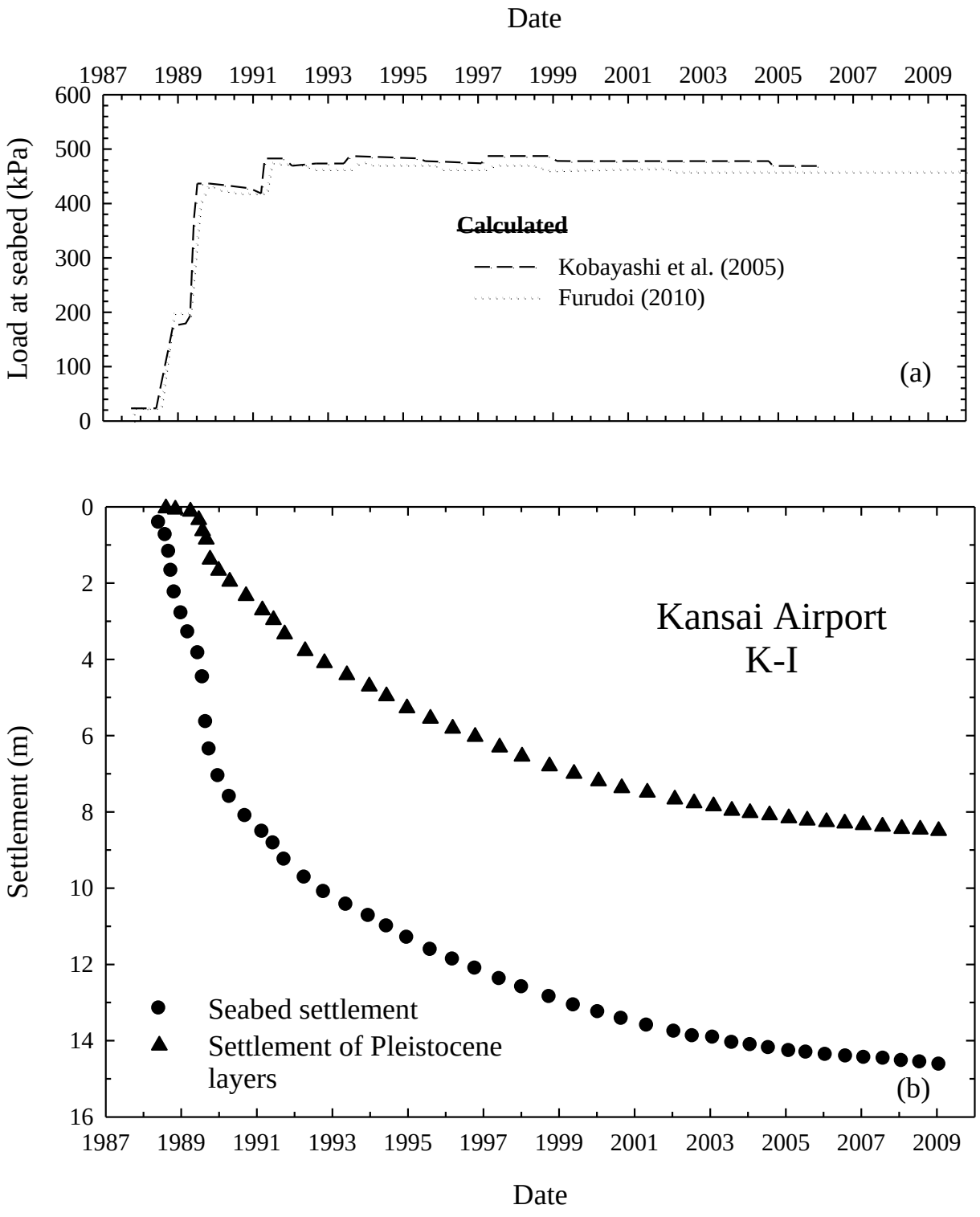

Figure 6-7 (a) Load ast seabed and (b) seabed settlement and settlement of Pleistocene layers at K-I of the pilot section (Endo et al., 1991; Arai, 1991; Kobayashi et al., 2005; Furudoi, 2010).

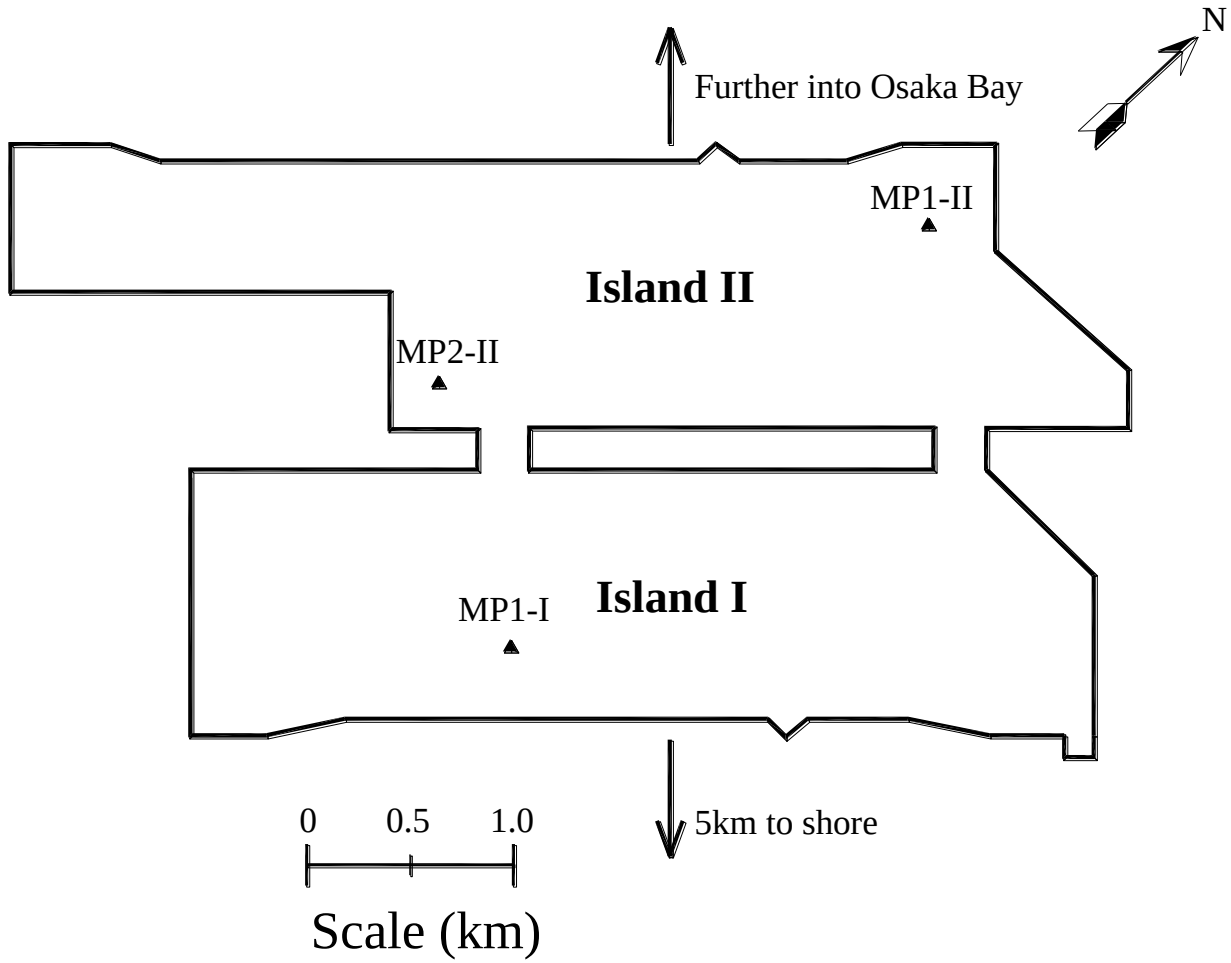

Figure 6-8 Location of monitoring points at Kansai International Airport.

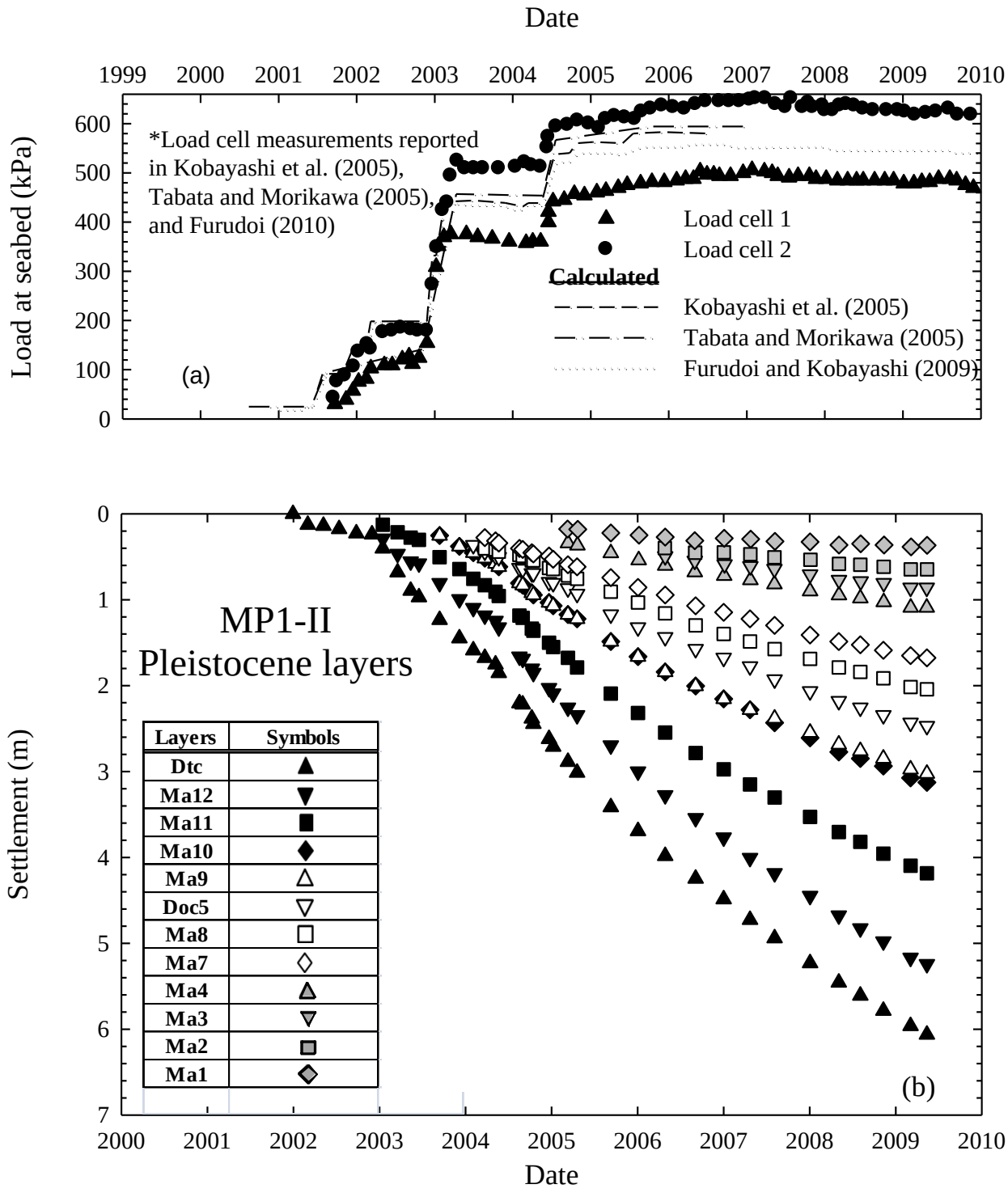

Figure 6-9 (a) Load at seabed and (b) magnetic differential settlement gauge observations (Furudoi and Kobayashi, 2009) for MP1-II.

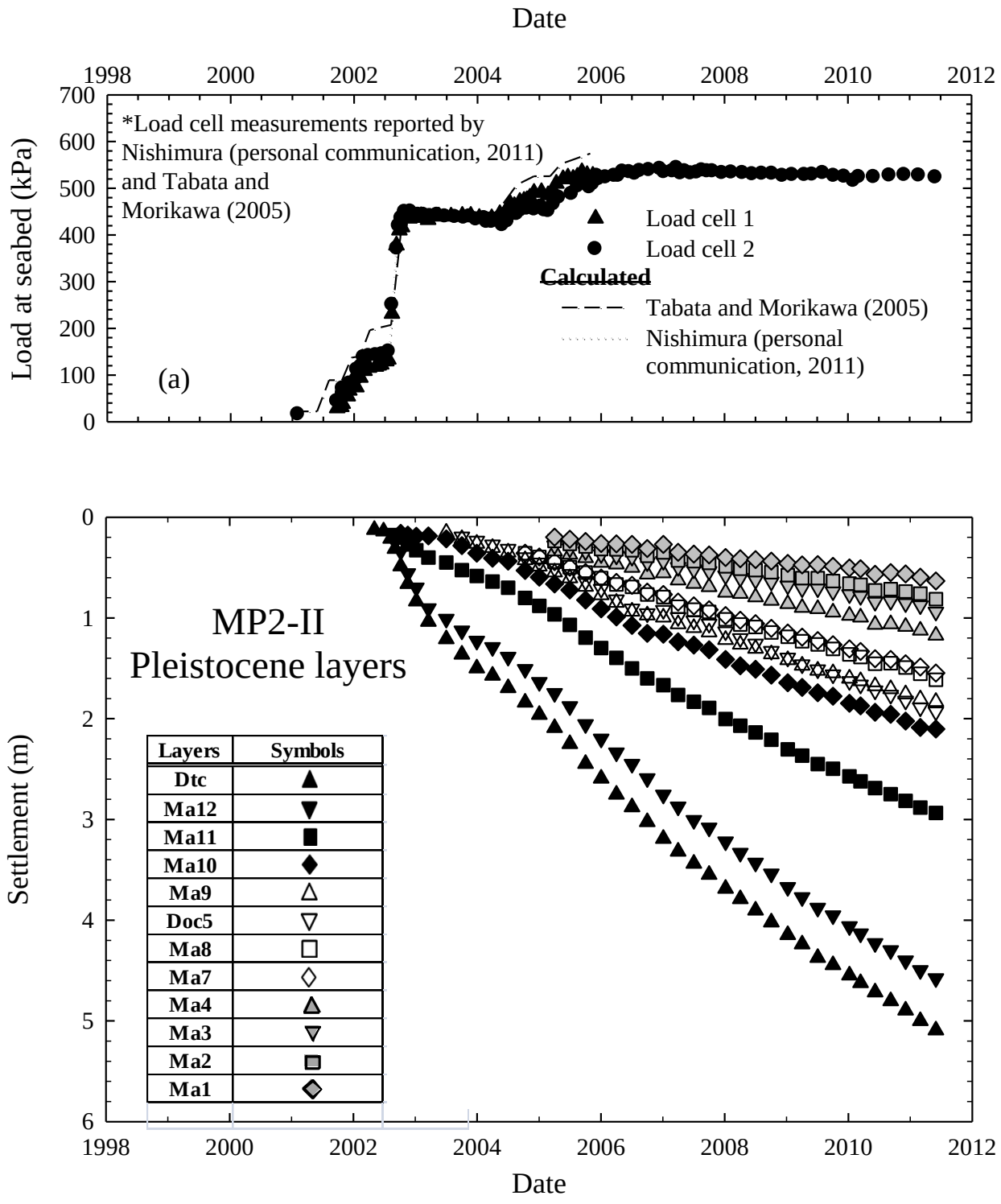

Figure 6-10 (a) Load at seabed and (b) magnetic differential settlement gauge observations (Nishimura, personal communication, 2011) for MP2-II.

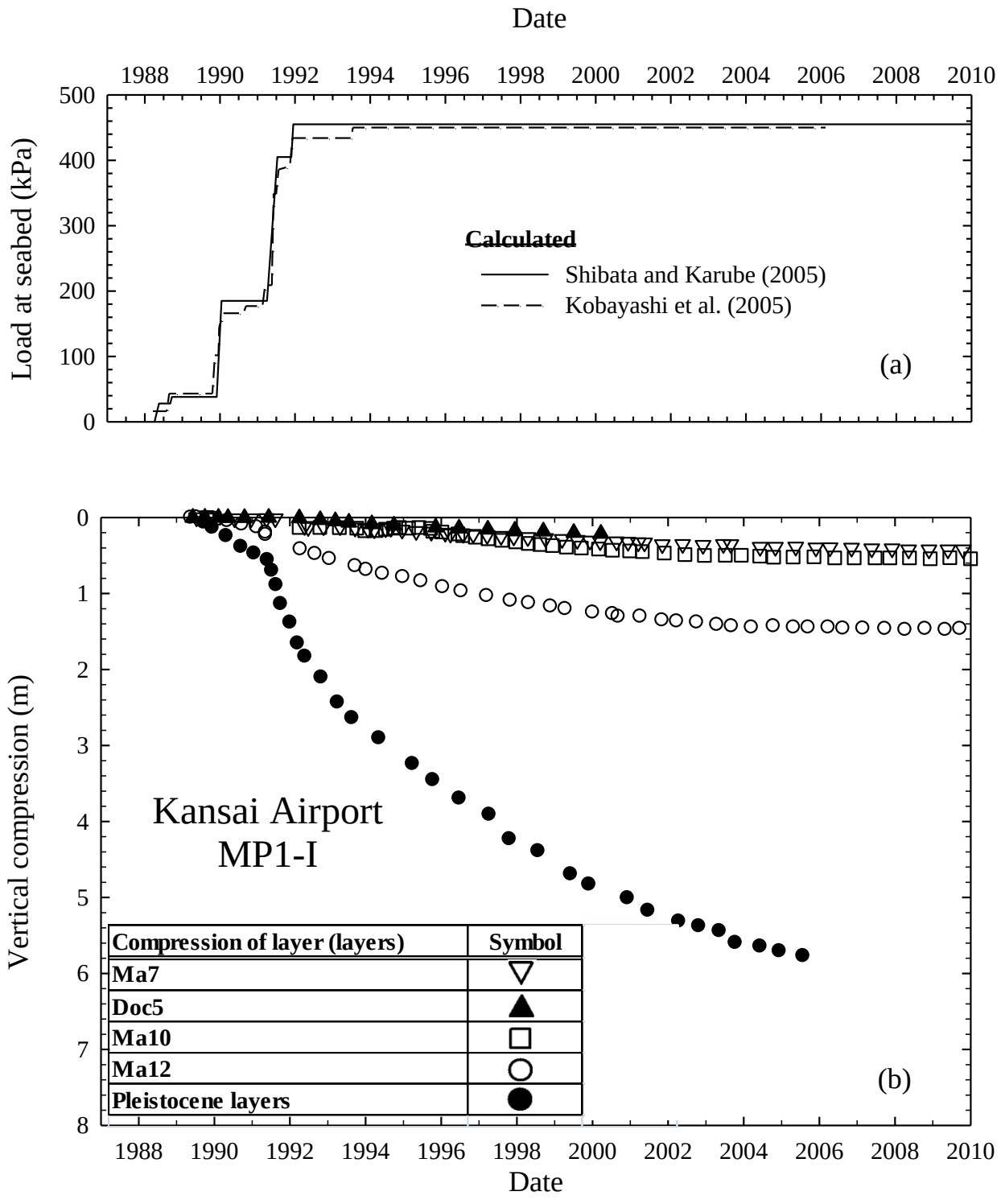

Figure 6-11 (a) Load at seabed and (b) magnetic differential settlement gauge observations (Kobayashi et al., 2005; Rocchi et al., 2007; Jeon et al., 2012) for MP1-I.

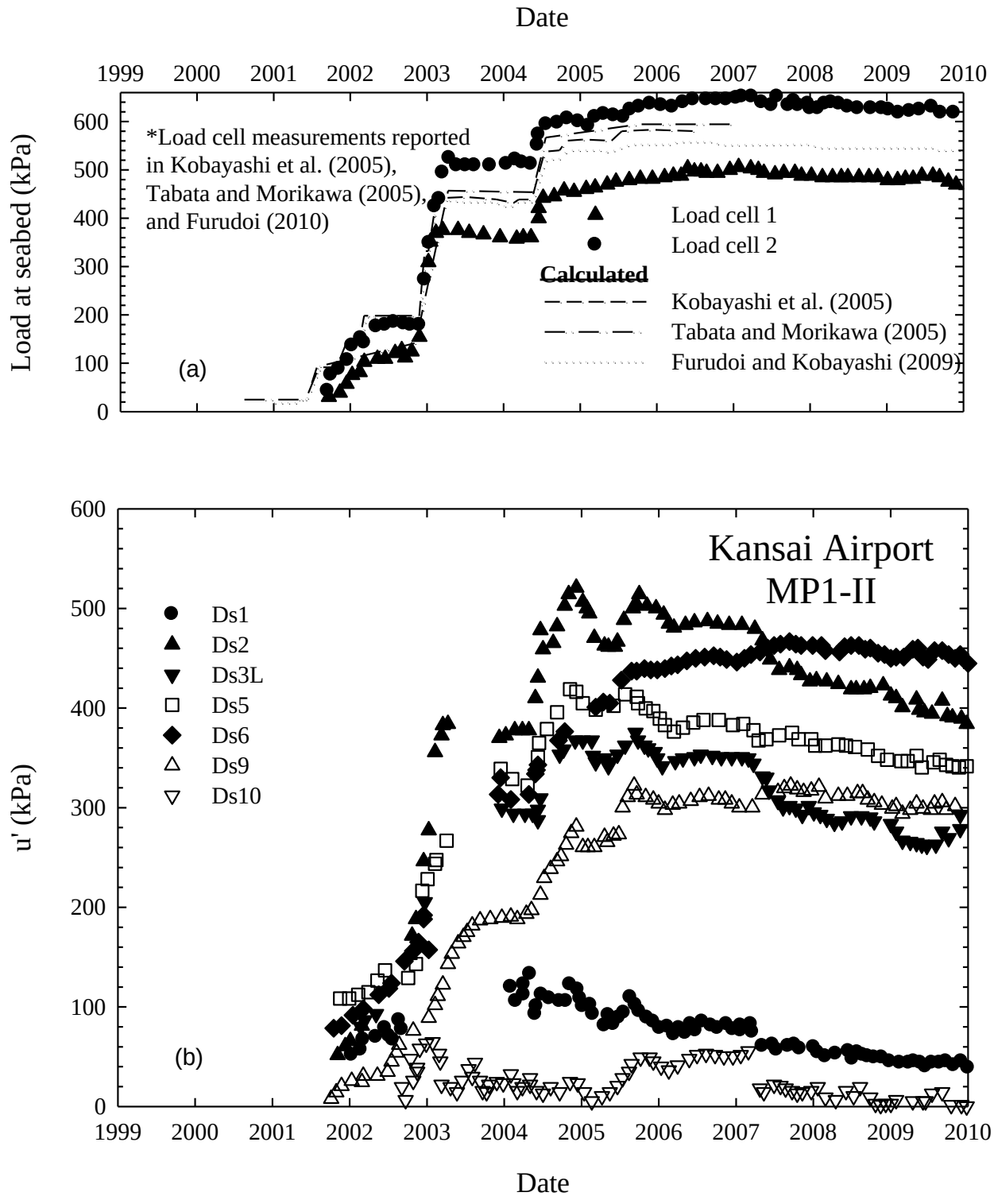

Figure 6-12 (a) Load at seabed and (b) pneumatic piezometer observations in Pleistocene sand layers at MP1-II (Furudoi, 2010).

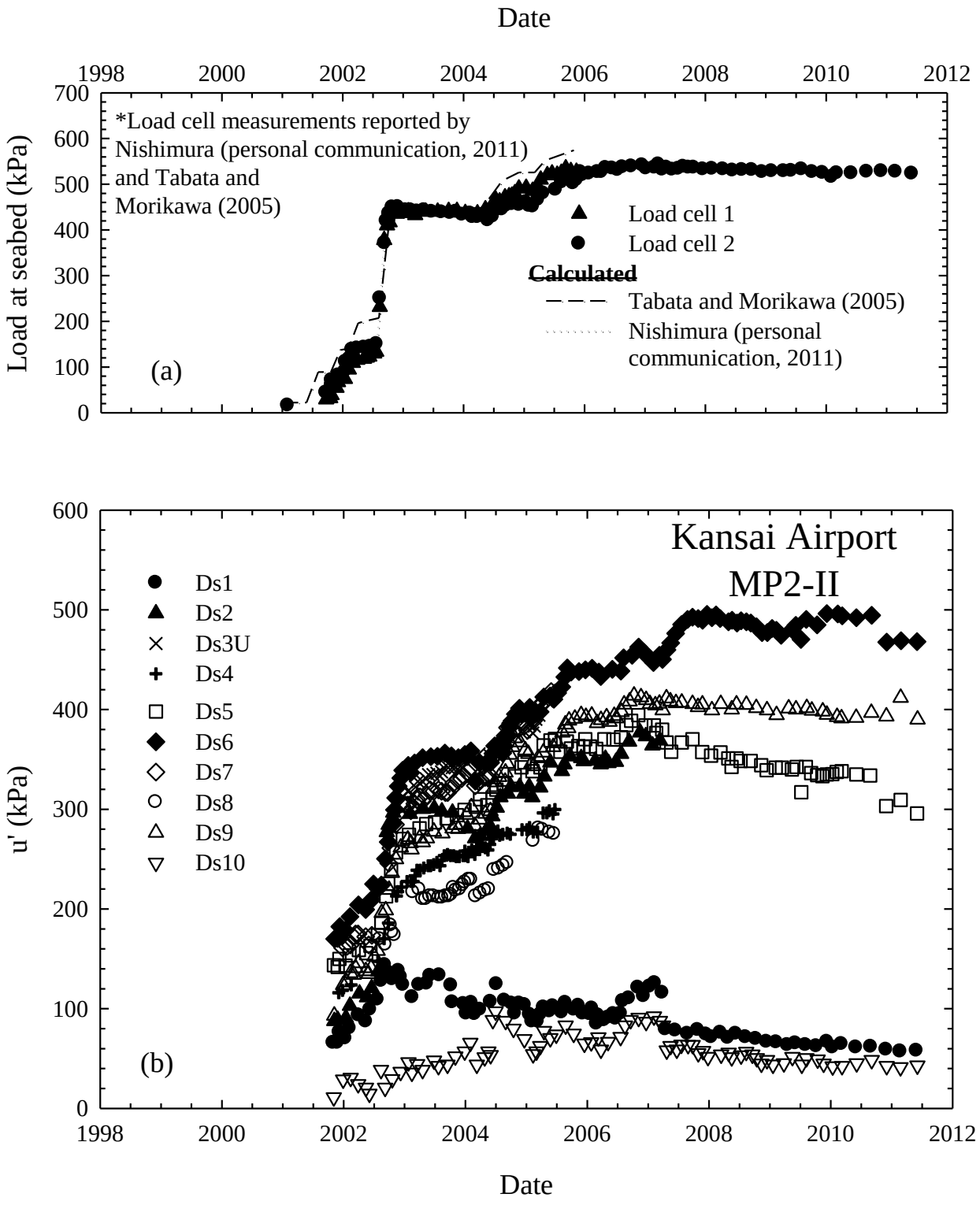

Figure 6-13 (a) Load at seabed and (b) pneumatic piezometer observations in Pleistocene sand layers at MP1-II (Tabata and Morikawa, 2005).

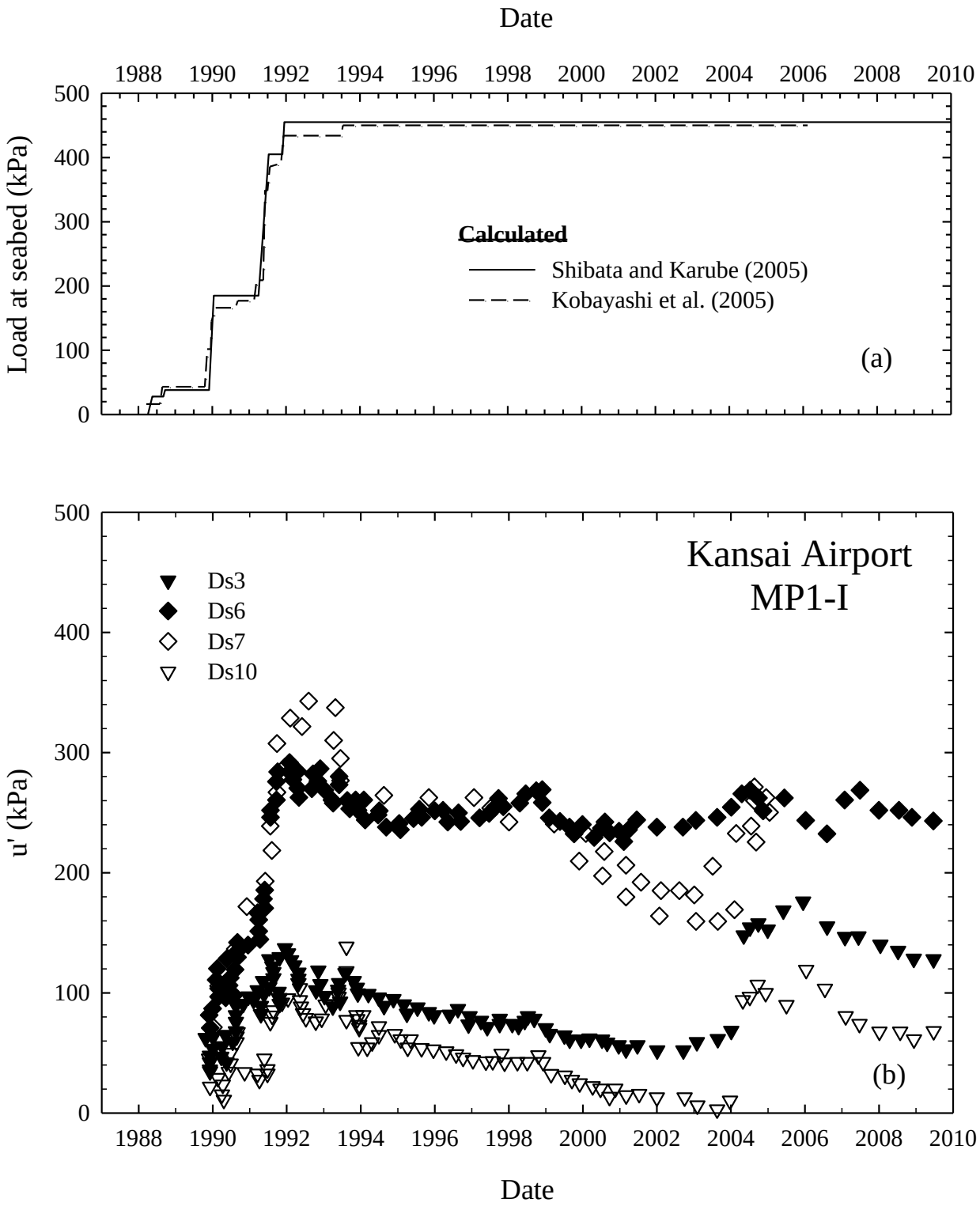

Figure 6-14 (a) Load at seabed and (b) pneumatic piezometer observations in Pleistocene sand layers at MP1-I (Kobayashi et al., 2005; Jeon et al., 2012).

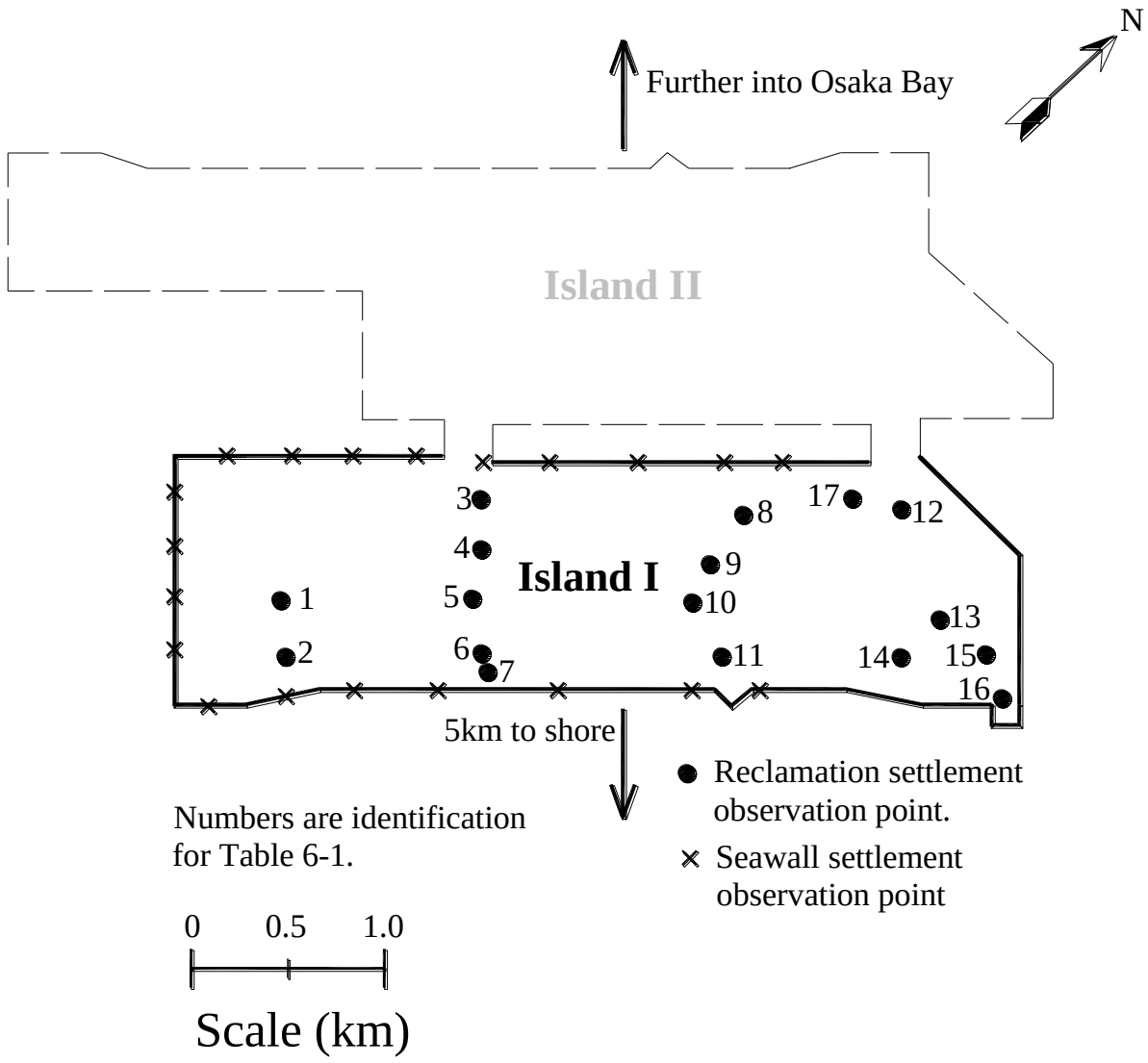

Figure 6-15 Settlement observation points at Island I (Maeda et al., 1990; Arai et al., 1991).

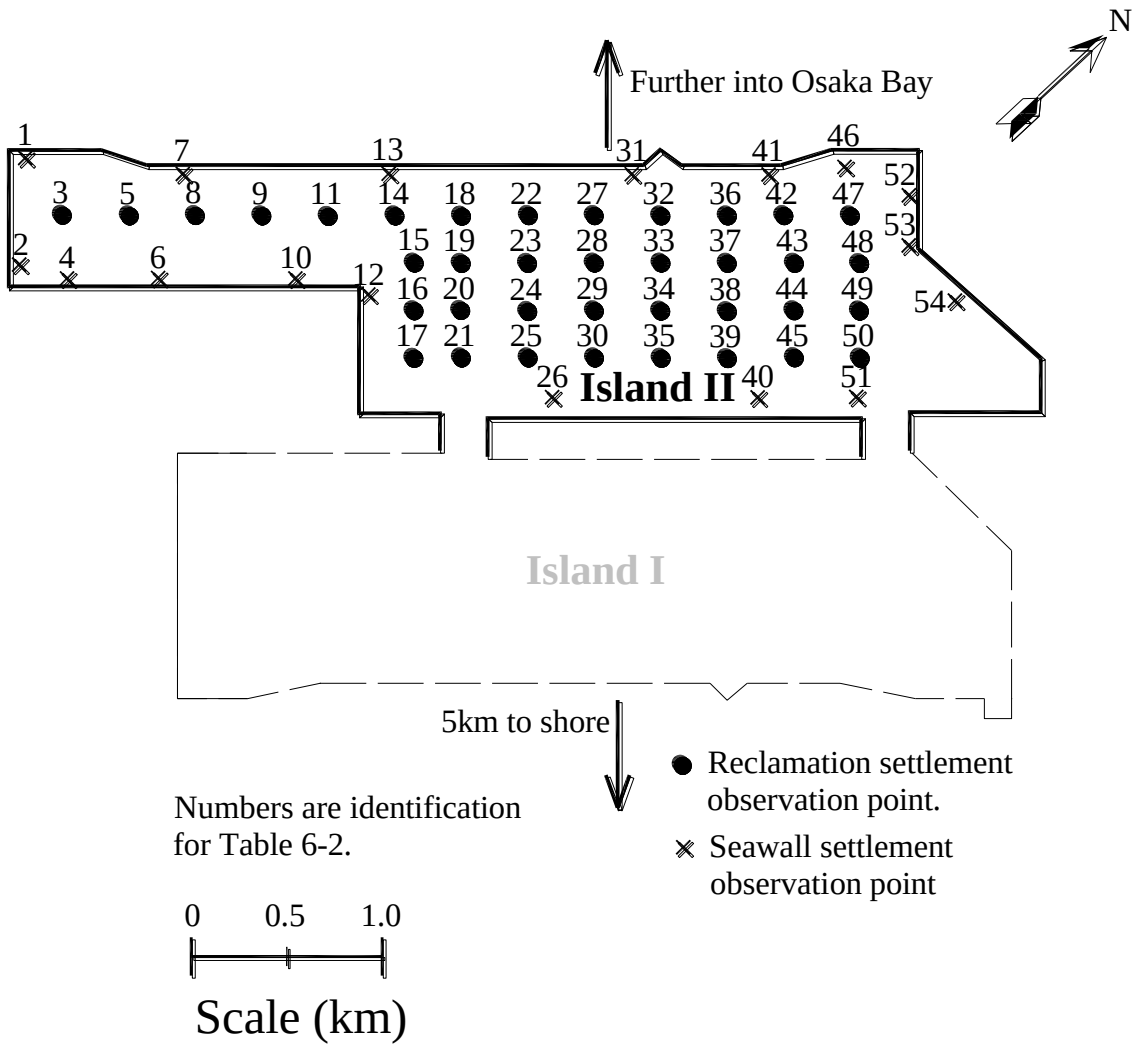

Figure 6-16 Settlement observation points at Island II (KALD, 2005; Tabata and Morikawa, 2005; NKIAC, 2012)

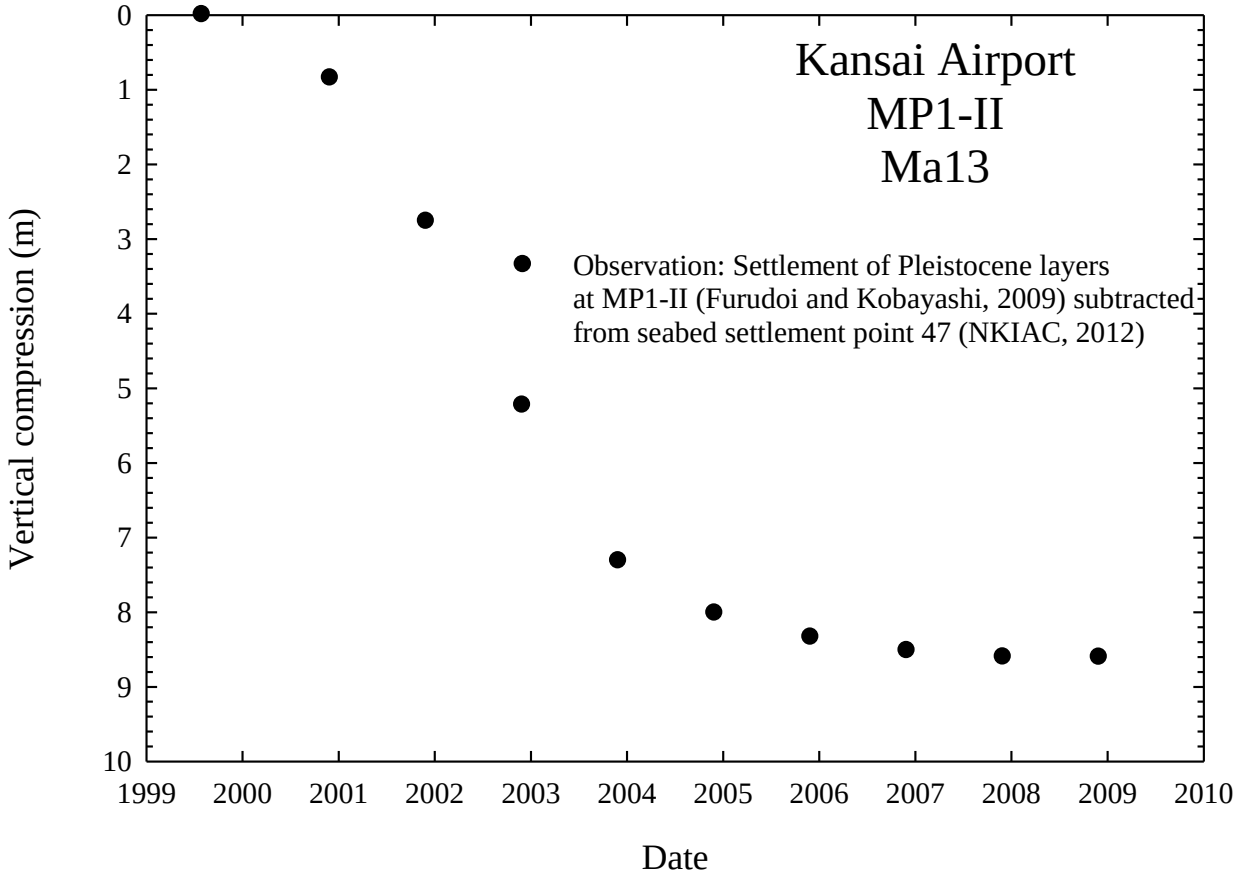

Figure 6-17 Observed compression of Ma13 at MP1-II.

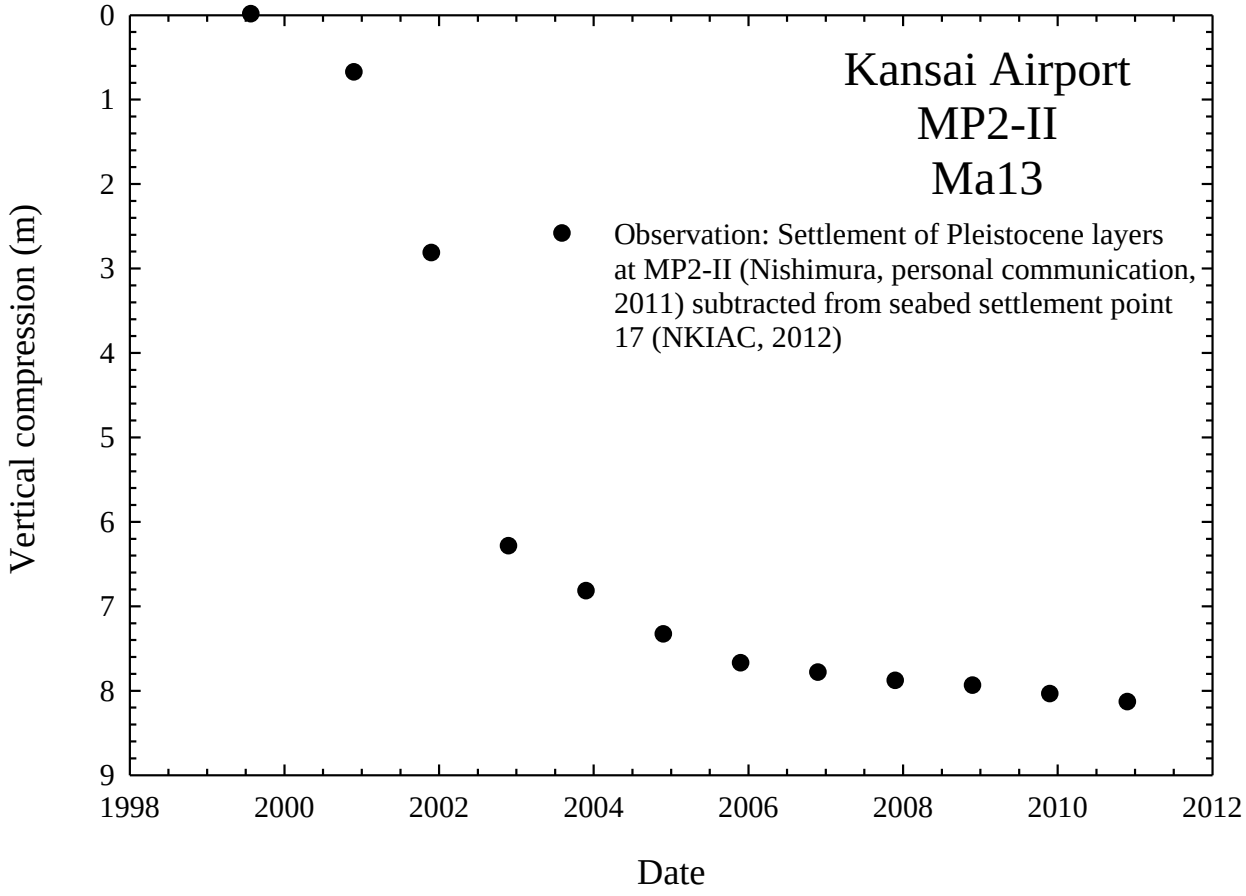

Figure 6-18 Observed compression of Ma13 at MP2-II.

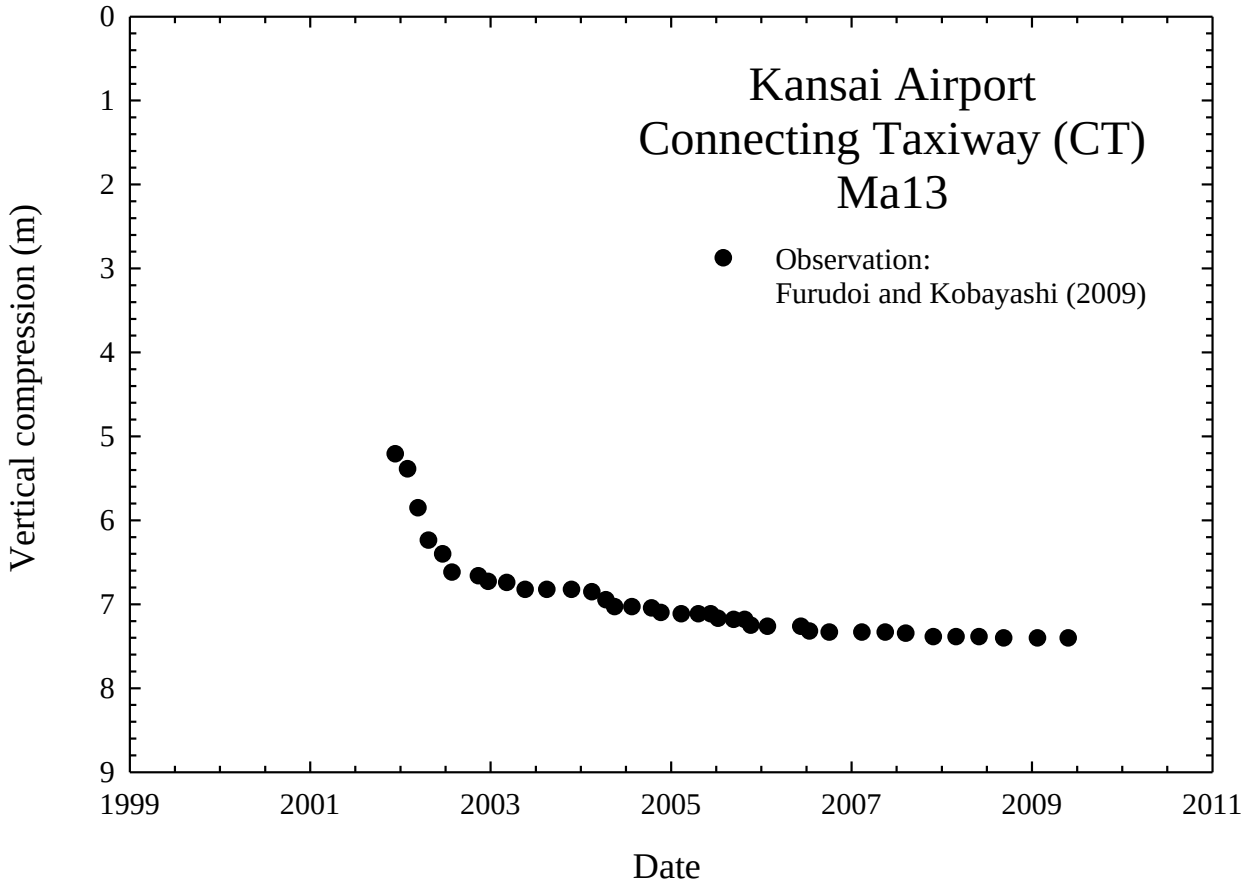

Figure 6-19 Observed compression of Ma13 at CT.

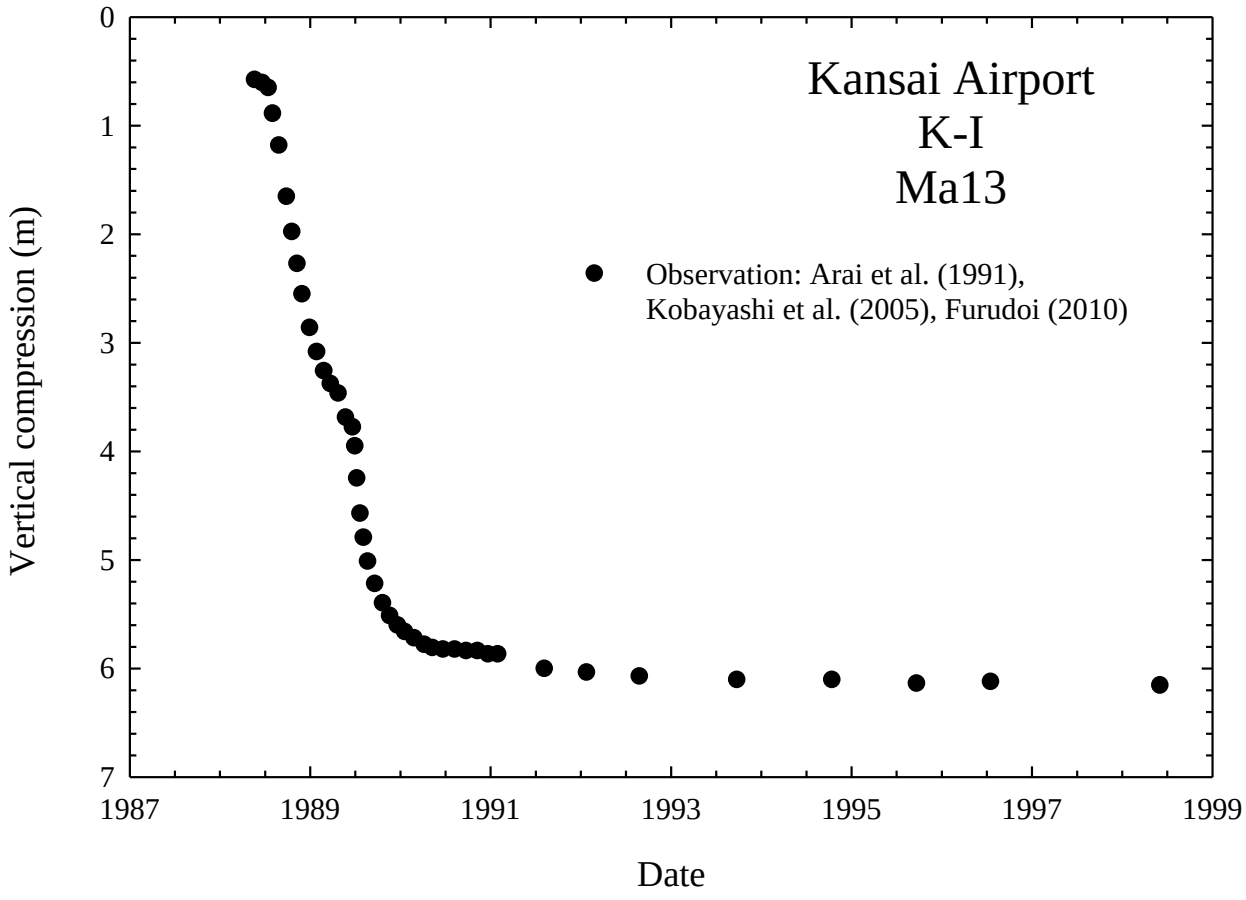

Figure 6-20 Observed compression of Ma13 at K-I.

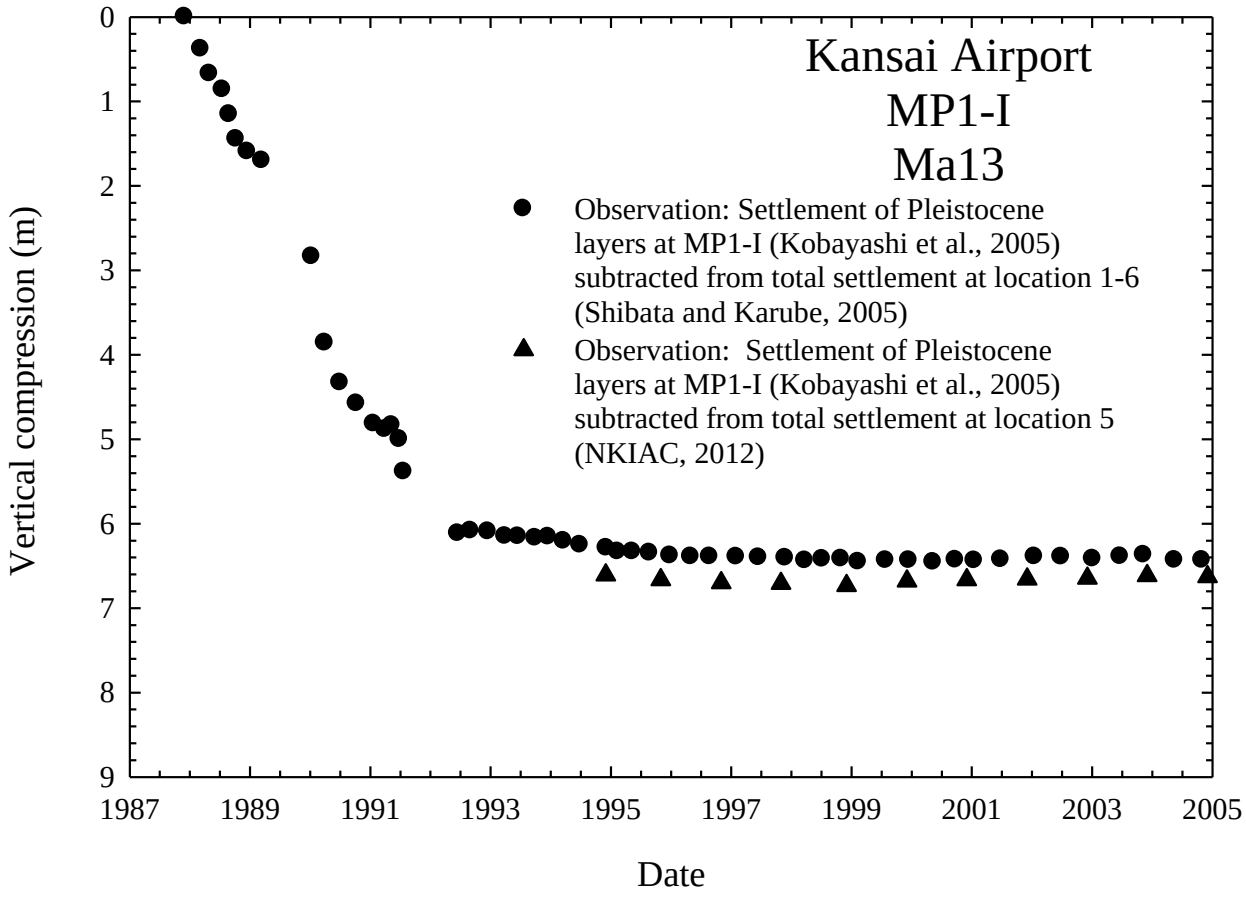

Figure 6-21 Observed compression of Ma13 at MP1-I.

CHAPTER 7 NUMERICAL MODELING WITH ILLICON

7.1 Introduction

Mesri and Rokhsar (1974) developed a theory of one-dimensional consolidation for clays that modified the Terzaghi theory by including the variation of compressibility and permeability during primary consolidation. The finite strain theory, as it was presented in 1974, made use of a bilinear EOP e – log σ'_v relationship and a linear e – log k_v relationship. Choi (1982) revised the theory so that any shape of EOP e – log σ'_v relationship could be used.

The computer program ILLICON was created based on the theory developed by Mesri and Rokhsar (1974) with modifications introduced by Choi (1982). S. Greenbaum contributed to ILLICON by giving the program the capability to analyze multiple sublayers. Y. K. Choi, S. Greenbaum, W. A. Kitch, G. A. Sraders, and D. O. K. Lo expanded the program to accommodate fully or partially penetrating vertical drains. D. O. K. Lo incorporated well resistance and a smear zone around the vertical drain as well as a non-linear e – log k_v relationship.

Excellent agreement between computed behavior and field observations was achieved for cases where compression and water flow took place primarily in the vertical direction such as Olga B test embankment in Matagami Quebec and Vasby test fill in Stockholm (Mesri and Choi, 1985a) as well as Ska-Edeby Area IV (Lo, 1991). Additionally, excellent agreement between computed behavior and field observations was achieved for cases where vertical drains were used such as the Ska Edeby test fills in Sweden, the Changi Airport in Singapore, and the Chek Lap Kok Airport in Hong Kong (Lo, 1991). ILLICON has also been used successfully to analyze cases such as the road construction project in Saga, Japan and the East Pier project at the Port of Tianjin, China where vacuum preloading together with prefabricated vertical drains were used to expedite the consolidation process (Khan, 2010).

The current version of the program is capable of performing three types of analyses: one-dimensional consolidation, consolidation with vertical drains (including vacuum loading), and consolidation with incompressible impeded drainage layers.

The following assumptions apply to all three types of analyses within ILLICON:

- the soil is saturated,
- the soil solids and porewater are incompressible

- each sublayer is homogeneous
- the Darcy flow equation is valid
- compression takes place only in the vertical direction
- there is no immediate or undrained settlement
- there is a unique EOP e – log σ'_v relationship for each sublayer
- the relative contributions of compressibility with respect to time and compressibility with respect to effective vertical stress to the decrease in void ratio during primary consolidation are a function of the degree of compression
- permeability is a function of void ratio

7.2 The uniqueness of the EOP e – log σ'_v relationship

ILLICON assumes a unique EOP e – log σ'_v relationship for each compressible sublayer. During consolidation, the void ratio is a function of effective vertical stress and time. Therefore, the rate of change of void ratio with respect to time is defined as (Taylor and Merchant, 1940; Mesri and Choi, 1979; Mesri et al., 1995):

$$\frac{de}{dt} = \left(\frac{\partial e}{\partial \sigma'_v}\right)_t \frac{d\sigma'_v}{dt} + \left(\frac{\partial e}{\partial t}\right)_{\sigma'_v} \qquad (7-1)$$

Equation 7-1 indicates that there are two fundamental compressibility parameters that contribute to the one-dimensional compression of voids within soil: the compressibility with respect to effective vertical stress at any time $\left(\frac{\partial e}{\partial \sigma'_v}\right)_t$ and the compressibility with respect to time at any effective vertical stress $\left(\frac{\partial e}{\partial t}\right)_{\sigma'_v}$. Equation 7-1 can be integrated to obtain Δe and divided into primary and secondary compression, leading to the following equation (Mesri and Choi, 1985a):

$$\Delta e = \int_0^{t_p} \left[\left(\frac{\partial e}{\partial \sigma'_v}\right)_t \frac{d\sigma'_v}{dt} + \left(\frac{\partial e}{\partial t}\right)_{\sigma'_v} \right] dt + \int_{t_p}^{t} \left(\frac{\partial e}{\partial t}\right)_{\sigma'_v} dt \qquad (7-2)$$

where t_p is the time to end-of-primary consolidation. Equation 7-2 shows that primary compression includes both the compressibility with respect to effective stress and

compressibility with respect to time, and that secondary compression includes only compressibility with respect to time. By definition, the uniqueness of the EOP void ratio - effective stress relationship implies that the change in void ratio during primary consolidation in Equation 7-2 is independent of the duration of primary consolidation (t_p). In order for this condition to be met, there must be an interrelationship between compressibility with respect to effective stress and compressibility with respect to time in which both parameters depend on the rate of change in effective stress with respect to time and, therefore, the duration of primary consolidation (Mesri et al., 1995). The C_α/C_c law of compressibility has demonstrated that there is an interrelationship between C_α and C_c during secondary compression (Mesri and Godlewski, 1977, 1979; Mesri, 1978, 2001; Mesri and Ajlouni, 2007) and there is much evidence to support that there is an interrelationship between compressibility parameters throughout primary compression (Mesri and Choi 1985a; Mesri and Choi 1985b; Mesri and Lo 1989; Mesri et al. 1994; Mesri et al. 1995; Mesri, 2001). This interrelationship allows for a unique EOP void ratio - effective vertical stress relationship.

7.3 Hydrodynamic equation

The hydrodynamic equation that describes one-dimensional consolidation of a soil element is presented in Mesri and Rokhsar (1974). A detailed derivation of the continuity equation for the hydrodynamic consolidation process with vertical drains can be found in Lo (1991).

Because the length to width ratio for the Kansai Airport Island I and Island II is approximately equal to 3.5, it was decided to develop a hydrodynamic equation that takes into account vertical flow as well as horizontal flow that is unidirectional and perpendicular to the long-dimension of each airport island. Figure 7-1 shows the rectangular soil element that is used to derive the hydrodynamic equation for the case of two-dimensional flow (in the x and z directions) with compression in the z direction only.

In Figure 7-1, ds is the height of solids, $d\xi$ is the height of the element during consolidation, dz is the height of the element prior to consolidation, dx is the length of the element in the direction of horizontal flow, dy is the width of the element, v_ξ is the velocity of

water entering the element in the z direction, $v_\xi + \frac{\partial v_\xi}{\partial \xi}\partial\xi$ is the velocity of water leaving the element in the z direction, v_x is the velocity of water entering the element in the x direction, and $v_x + \frac{\partial v_x}{\partial x}\partial x$ is the velocity of water leaving the element in the x direction.

For a unit volume of solids at any time (t) the volume of water in the element is:

$$\frac{e}{1+e}\,dx\,dy\,d\xi \qquad (7-3)$$

where e is the void ratio at time t.

The rate of decrease of the volume of voids with respect to time is:

$$-\frac{d}{dt}\left(\frac{e}{1+e}\,dx\,dy\,d\xi\right) \qquad (7-4)$$

which can be simplified to:

$$-\frac{1}{1+e}\frac{de}{dt}\,dx\,dy\,d\xi \qquad (7-5)$$

because $(dx\,dy\,d\xi)/(1+e)$ is a constant.

Assuming flow of porewater in the z and x directions, the net flow into or out of the element (q_{net}) is:

$$q_{net} = \frac{dq_\xi}{d\xi}d\xi + \frac{dq_x}{dx}dx \qquad (7-6)$$

where $dq_\xi/d\xi * d\xi$ is the net flow in the z direction and $dq_x/dx * dx$ is the net flow in the x direction. Applying the Darcy flow equation gives:

$$q_\xi = -k_z\frac{\partial h}{\partial \xi}\,dx\,dy \qquad (7-7)$$

and

$$q_x = -k_x\frac{\partial h}{\partial x}\,dy\,d\xi \qquad (7-8)$$

where k_z and k_x are the coefficient of permeabilities in the z and x directions, respectively, and h is the total head. The minus sign indicates positive flow in the direction of decreasing total head. Differentiation is with respect to ξ rather than z since application of the Darcy flow equation requires an unchanging assemblage of particles. The net flow into or out of the element becomes:

$$q_{net} = -\frac{\partial}{\partial \xi}\left(k_z \frac{\partial h}{\partial \xi}\right) dx dy d\xi - \frac{\partial}{\partial x}\left(k_x \frac{\partial h}{\partial x}\right) dx dy d\xi \qquad (7-9)$$

Equating the rate of volume change to the net flow into or out of the element yields:

$$-\frac{1}{1+e}\frac{de}{dt} dx dy d\xi = -\frac{\partial}{\partial \xi}\left(k_z \frac{\partial h}{\partial \xi}\right) dx dy d\xi - \frac{\partial}{\partial x}\left(k_x \frac{\partial h}{\partial x}\right) dx dy d\xi \qquad (7-10)$$

which simplifies to:

$$\frac{1}{1+e}\frac{de}{dt} = \frac{\partial}{\partial \xi}\left(k_z \frac{\partial h}{\partial \xi}\right) + \frac{\partial}{\partial x}\left(k_x \frac{\partial h}{\partial x}\right) \qquad (7-11)$$

For consolidation and swelling, we are interested in the flow into or out of the element due to a gradient in excess porewater pressure (u′). Therefore, total head is defined as:

$$h = \frac{u'}{\gamma_w} \qquad (7-12)$$

where γ_w is the unit weight of water. Applying:

$$d\xi = \frac{1+e}{1+e_0} dz \qquad (7-13)$$

where e_0 is the initial void ratio yields:

$$\frac{1}{1+e}\frac{de}{dt} = \frac{1+e_0}{1+e}\frac{\partial}{\partial z}\left(\frac{k_z}{\gamma_w}\frac{1+e_0}{1+e}\frac{\partial u'}{\partial z}\right) + \frac{\partial}{\partial x}\left(\frac{k_x}{\gamma_w}\frac{\partial u'}{\partial x}\right) \qquad (7-14)$$

Taking partial derivitives with respect to z and x and solving for de/dt yields:

$$\frac{de}{dt} = \frac{1}{\gamma_w}\left(\frac{1+e_0}{1+e}\right)^2\left[(1+e)\left(k_z \frac{\partial^2 u'}{\partial z^2} + \frac{\partial k_z}{\partial z}\frac{\partial u'}{\partial z}\right) - k_z \frac{\partial u'}{\partial z}\frac{\partial e}{\partial z}\right]$$

$$+ \frac{1+e}{\gamma_w}\left[k_x \frac{\partial^2 u'}{\partial x} + \frac{\partial k_x}{\partial x}\frac{\partial u'}{\partial x}\right] \qquad (7-15)$$

Equation 7-15 is the hydrodynamic equation for a saturated soil element with incompressible solids and pore fluid, that is subjected to compression in the z direction and allows flow of water in the z and x directions. Equation 7-15 is ideal for analyzing consolidation as a result of a uniform load over a strip area or uniform load over a rectangular area where one dimension of the rectangle is significantly longer than the other. In both cases, water flow will

take place in the vertical direction and in the horizontal direction perpendicular to the long dimension of the uniform strip load or uniform rectangular load. As mentioned previously, Equation 7-15 was developed as part of this project because the length to width ratio of Kansai Airport Island I and Island II is approximately equal to 3.5. However, further inspection of the subseabed profile and the airport site revealed that the thickness of individual clay layers is small compared to the dimensions of the airport islands; therefore, within the Pleistocene clay layers at the Kansai Airport site, water flow resulting from consolidation is primarily in the vertical direction towards adjacent sand layers.

The hydrodynamic equation presented in Lo (1991) for vertical drains can also be used to describe a consolidating cylindrical disk subjected to a uniform load over a circular area that allows drainage in the vertical (z) and radial (r) directions and compression in the z direction (Figure 7-2).

$$\frac{de}{dt} = \frac{1}{\gamma_w}\left(\frac{1+e_0}{1+e}\right)^2\left[(1+e)\left(k_z\frac{\partial^2 u'}{\partial z^2}+\frac{\partial k_z}{\partial z}\frac{\partial u'}{\partial z}\right)-k_z\frac{\partial u'}{\partial z}\frac{\partial e}{\partial z}\right]$$

$$+\frac{1+e}{\gamma_w}\left[k_r\left(\frac{1}{r}\frac{\partial u'}{\partial r}+\frac{\partial^2 u'}{\partial r^2}\right)+\frac{\partial k_r}{\partial r}\frac{\partial u'}{\partial r}\right] \qquad (7-16)$$

7.4 Constitutive equation

The constitutive equation described in this section is a slight modification of the constitutive equation presented in Mesri and Rokhsar (1974) and the constitutive equation presented in Choi (1982) and Mesri and Choi (1985a). The assumptions regarding the relative contribution of the time compressibility and effective vertical stress compressibility terms during primary consolidation are required to meet two conditions:

1. To satisfy the uniqueness principle, the void ratio must equal the EOP void ratio when EOP consolidation is reached.
2. To satisfy the C_α/C_c law of compressibility, $\Delta e = C_c\frac{C_\alpha}{C_c}\Delta\log t$ following EOP consolidation, where C_c is the compression index at the current void ratio.

The decrease in void ratio during one-dimensional compression is a function of effective vertical stress and time as described by Equation 7-1. The compressibility with respect to effective vertical stress at any time $(\partial e/\partial \sigma'_v)_t$ is evaluated by:

$$\left(\frac{\partial e}{\partial \sigma'_v}\right)_t = \frac{-0.434 C_c^*}{\sigma'_v} \qquad (7-17)$$

where C_c^* is the ratio of the change in void ratio due to the change in effective vertical stress (i.e. excluding the contribution from the compressibility with respect to time at a constant effective vertical stress) to the change in log of effective vertical stress. C_c^* is computed using:

$$C_c^* = C_c\left(1-\beta\frac{C_\alpha}{C_c}\frac{\Delta \log t}{\Delta \log \sigma'_v}\right) \qquad (7-18)$$

β is the degree of compression and is defined by:

$$\beta = \frac{e_0 - e}{e_0 - e_P} \qquad (7-19)$$

where e_P is the EOP void ratio for the applied stress increment at any time.

The compressibility with respect to time at any effective stress during primary consolidation is evaluated by:

$$\left(\frac{\partial e}{\partial t}\right)_{\sigma'_v} = \frac{-0.434\frac{C_\alpha}{C_c}\beta C_c}{t} \qquad (7-20)$$

For a constant applied load, $d\sigma'_v/dt$ is equal to $-du'/dt$. Equations 7-17 and 7-20 are substituted into Equation 7-1, together with the appropriate hydrodynamic equation to solve for du'/dt.

$$\frac{du'}{dt} = -\frac{\frac{de}{dt} - \left(\frac{\partial e}{\partial t}\right)_{\sigma'_v}}{\left(\frac{\partial e}{\partial \sigma'_v}\right)_t} \qquad (7-21)$$

7.5 Finite difference solution technique

ILLICON is an explicit finite difference consolidation program. The previous version of ILLICON was coded in Fortran 77 and had the capability of running two types of analyses:

one-dimensional consolidation and consolidation with vertical drains (Mesri and Rokhsar, 1974; Choi, 1982; Lo, 1991). The previous version took the following into account:

- Any variation with depth of initial void ratio, initial coefficient of permeability, and initial or preconstruction effective vertical stress.
- For each sublayer, any shape for the EOP e – log σ'_v relationship.
- For each sublayer, any shape for the e – log k_v relationship.
- For each sublayer, the ratio of horizontal to vertical permeability (consolidation with vertical drains only).
- Compressibility with respect to time during the primary consolidation stage.
- Any variation with depth and time of total vertical stress increase.
- Fully or partially penetrating vertical drains.
- Finite permeability (or well resistance) for vertical drains.
- Variable installation time for vertical drains.
- Smear zone adjacent to the vertical drain with EOP e – log σ'_v relationship for each sublayer different from EOP e – log σ'_v relationship of undisturbed soil ($k_h/k_v = 1$ assumed within smear zone).

ILLICON was rebuilt using Microsoft Visual Studio 2010© to facilitate the settlement and porewater pressure calculations for the Kansai International Airport. A user-interface that provides graphical output was created as a Windows© Form Application and the computational core was coded using Microsoft Visual C++©. The current version of ILLICON retains the capabilities listed above with the following additions:

- Capability to analyze consolidation with incompressible impeded drainage layers for the two-dimensional flow case and the axi-symmetric flow case.
- Capability to account for the decrease in load at the original ground surface resulting from settlement and associated submergence of fill material below sea level.
- Capability to analyze cases involving vacuum consolidation.

The assumptions related specifically to the portion of ILLICON that includes

consolidation with impeded drainage layers include:

- the impeded drainage layers are incompressible.
- the thickness, EOP e – log σ'_v relationship, e – log k_v relationship, and k_h/k_v for each compressible sublayer are uniform throughout the numerical model
- the permeability and thickness of each impeded drainage layer are uniform throughout the numerical model
- water flows either radially or in one horizontal direction with no vertical component of flow within the impeded drainage layers
- water flows either vertically and radially or vertically and in one horizontal direction within the compressible layers

7.5.1 Consolidation of clay with incompressible impeded drainage layers

For the present purpose, incompressible impeded drainage layers (sand layers at the Kansai Airport site) are layers that have a higher permeability than adjacent compressible layers and are continuous at least to the horizontal or radial boundary of the elastic vertical stress distribution that approximates the increase in vertical stress at any depth resulting from reclamation load. An excess porewater pressure gradient forces water to flow, according to the Darcy flow equation, from adjacent compressible layers into the impeded drainage layer and to the horizontal or radial boundary where the excess porewater pressure is small.

Two possible scenarios have been considered: two-dimensional flow (in the z and x directions) and axi-symmetric flow (in the z and r directions).

For the case of two-dimensional flow, compression in the vertical direction and flow of water in the vertical and one horizontal direction, are considered within the clay layers. Water entering the sand layers flows horizontally in one direction to the horizontal boundary of the vertical stress increase. The two-dimensional flow case is ideal for analyzing consolidation due to application of a uniform strip load. However, it may also be used to approximate consolidation resulting from a uniform load over a rectangular area that has one dimension considerably longer than the other dimension.

For the case of axi-symmetric flow, compression is in the vertical direction, and water flow is vertical and radial within the clay layers. Radial flow is considered within the sand layers.

The axi-symmetric flow case is ideal for analyzing consolidation due to application of a uniform load over a circular area. However, it may also be used to approximate a uniform load over an irregularly-shaped area.

Figure 7-3 shows the general setup for the explicit finite difference approximation. The top and bottom boundaries in Figure 7-3 may be impervious or freely draining. The vertical line directly under the center of the applied load is an impervious boundary. The horizontal or radial edge of the applied vertical stress increase is a freely draining boundary. Layers are separated by incompressible impeded drainage layers. Each layer consists of sublayers and each sublayer has its own EOP e – log σ'_v relationship, e – log k_v relationship, C_α/C_c, and k_h/k_v. Each sublayer consists of rows that contain a calculation node to facilitate the finite difference solution.

7.5.1.1 Internal nodes

Internal nodes are all nodes not lying on the top or bottom boundary, at a layer interface, at a sublayer interface, under the center of the applied load, or at the horizontal or radial edge of the applied vertical stress increase. The partial derivatives with respect to z for all internal nodes are approximated by the following finite difference equations (see Figure 7-3 for definition of layer i, sublayer j, row k, and column ℓ):

$$\left(\frac{\partial u'}{\partial z}\right)_{i,j,k,\ell} = \frac{u'_{i,j,k+1,\ell} - u'_{i,j,k-1,\ell}}{2\Delta z_{i,j}} \qquad (7-22)$$

$$\left(\frac{\partial^2 u'}{\partial z^2}\right)_{i,j,k,\ell} = \frac{u'_{i,j,k+1,\ell} - 2u'_{i,j,k,\ell} + u'_{i,j,k-1,\ell}}{\left(\Delta z_{i,j}\right)^2} \qquad (7-23)$$

$$\left(\frac{\partial e}{\partial z}\right)_{i,j,k,\ell} = \frac{e_{i,j,k+1,\ell} - e_{i,j,k-1,\ell}}{2\Delta z_{i,j}} \qquad (7-24)$$

$$\left(\frac{\partial k_z}{\partial z}\right)_{i,j,k,\ell} = \frac{\left(k_z\right)_{i,j,k+1,\ell} - \left(k_z\right)_{i,j,k-1,\ell}}{2\Delta z_{i,j}} \qquad (7-25)$$

For the two-dimensional flow case, the partial derivatives with respect to the x direction are approximated by:

$$\left(\frac{\partial u'}{\partial x}\right)_{i,j,k,\ell} = \frac{u'_{i,j,k,\ell+1} - u'_{i,j,k,\ell-1}}{2\Delta x} \qquad (7-26)$$

$$\left(\frac{\partial^2 u'}{\partial x^2}\right)_{i,j,k,\ell} = \frac{u'_{i,j,k,\ell+1} - 2u'_{i,j,k,\ell} + u'_{i,j,k,\ell-1}}{(\Delta x)^2} \qquad (7-27)$$

$$\left(\frac{\partial e}{\partial x}\right)_{i,j,k,\ell} = \frac{e_{i,j,k,\ell+1} - e_{i,j,k,\ell-1}}{2\Delta x} \qquad (7-28)$$

$$\left(\frac{\partial k_x}{\partial x}\right)_{i,j,k,\ell} = \frac{\left(\frac{k_x}{k_z}\right)_{i,j}\left[(k_z)_{i,j,k,\ell+1} - (k_z)_{i,j,k,\ell-1}\right]}{2\Delta x} \qquad (7-29)$$

For the axi-symmetric flow case, the partial derivatives with respect to r are approximated by:

$$\left(\frac{\partial u'}{\partial r}\right)_{i,j,k,\ell} = \frac{u'_{i,j,k,\ell+1} - u'_{i,j,k,\ell-1}}{2\Delta r} \qquad (7-30)$$

$$\left(\frac{\partial^2 u'}{\partial r^2}\right)_{i,j,k,\ell} = \frac{u'_{i,j,k,\ell+1} - 2u'_{i,j,k,\ell} + u'_{i,j,k,\ell-1}}{(\Delta r)^2} \qquad (7-31)$$

$$\left(\frac{\partial e}{\partial r}\right)_{i,j,k,\ell} = \frac{e_{i,j,k,\ell+1} - e_{i,j,k,\ell-1}}{2\Delta r} \qquad (7-32)$$

$$\left(\frac{\partial k_r}{\partial r}\right)_{i,j,k,\ell} = \frac{\left(\frac{k_r}{k_z}\right)_{i,j}\left[(k_z)_{i,j,k,\ell+1} - (k_z)_{i,j,k,\ell-1}\right]}{2\Delta r} \qquad (7-33)$$

7.5.1.2 Nodes at sublayer boundaries

The excess porewater pressure at the bottom of sublayer j must be equal to the excess porewater pressure at the top of sublayer j+1.

$$u'_{i,j,k,\ell} = u'_{i,j+1,1,\ell} \qquad (7-34)$$

Additionally, the following equation must apply to satisfy the continuity of water flow across the sublayers (Choi, 1982):

$$(1+e_0)_{i,j}\left[\frac{k_z}{1+e}\frac{\partial u'}{\partial z}\right]_{i,j,k,\ell} = (1+e_0)_{i,j+1}\left[\frac{k_z}{1+e}\frac{\partial u'}{\partial z}\right]_{i,j+1,1,\ell} \qquad (7-35)$$

Equations 7-34 and 7-35 are used to calculate the excess porewater pressure at the sublayer boundaries from the excess porewater pressures calculated at the adjacent internal nodes.

7.5.1.3 Nodes at layer boundaries

Layers are separated by incompressible impeded drainage layers. The magnitude of excess porewater pressure within the impeded drainage layers is a function of the thickness and permeability of the impeded drainage layer, the compressibility and permeability of the compressible layers above and below the impeded drainage layer, and the distance to the horizontal or radial boundary of the applied vertical stress increase where $\Delta\sigma_v$ and u′ are small.

7.5.1.3.1 Two – dimensional flow

Figure 7-4 illustrates the coupling of flow from two compressible layers into one horizontally draining incompressible impeded drainage layer for the case of two-dimensional flow.

The equation of continuity is given by:

$$q_{zi} + q_{z(i+1)} = \frac{\partial q_x}{\partial x}dx \qquad (7-36)$$

Applying the Darcy flow equation and substituting equation 7-13 into equation 7-36 yields:

$$\left[\frac{k_z}{\gamma_w}\frac{\partial u'}{\partial z}\left(\frac{1+e_0}{1+e}\right)\right]_i dxdy + \left[\frac{k_z}{\gamma_w}\frac{\partial u'}{\partial z}\left(\frac{1+e_0}{1+e}\right)\right]_{i+1} dxdy = -\frac{\partial}{\partial x}\left(\frac{(k_s)_i L_i}{\gamma_w}\frac{\partial u'}{\partial x}dy\right)dx \qquad (7-37)$$

where $(k_s)_i$ and L_i, respectively, are the permeability and thickness of the i^{th} impeded drainage layer. Equation 7-37 simplifies to:

$$\left[\frac{k_z}{\gamma_w}\frac{\partial u'}{\partial z}\left(\frac{1+e_0}{1+e}\right)\right]_i dxdy + \left[\frac{k_z}{\gamma_w}\frac{\partial u'}{\partial z}\left(\frac{1+e_0}{1+e}\right)\right]_{i+1} dxdy = -\frac{(k_s)_i L_i}{\gamma_w}\frac{\partial^2 u'}{\partial x^2}dxdy \qquad (7-38)$$

Further simplifying and putting into finite difference form gives:

$$\left[\frac{k_z}{\Delta z}\left(\frac{1+e_0}{1+e}\right)\right]_{i,j}\left(u'_{i,j,k,\ell} - \left(u'_s\right)_{i,\ell}\right) + \left[\frac{k_z}{\Delta z}\left(\frac{1+e_0}{1+e}\right)\right]_{i+1,1}\left(u'_{i+1,1,2,\ell} - \left(u'_s\right)_{i,\ell}\right)$$

$$= -\frac{(k_s)_i L_i}{\Delta x^2}\left[(u'_s)_{i,\ell-1} - 2(u'_s)_{i,\ell} + (u'_s)_{i,\ell+1}\right] \qquad (7-39)$$

where $(u'_s)_{i,\ell\text{-}1}$, $(u'_s)_{i,\ell}$, and $(u'_s)_{i,\ell+1}$, are the excess porewater pressures in the i^{th} impeded drainage layer at column ℓ-1, ℓ, and ℓ+1 respectively, $u'_{i,j,k,\ell}$ is the excess porewater pressure at the second to last node in the overlying compressible layer at column ℓ, and $u'_{i+1,1,2,\ell}$ is the excess porewater pressure at the second node in the underlying compressible layer at column ℓ. Further rearranging leads to:

$$\left[-\frac{(k_s)_i L_i}{\Delta x^2}\right](u'_s)_{i,\ell-1} + \left[\left[\frac{k_z}{\Delta z}\left(\frac{1+e_0}{1+e}\right)\right]_{i,j} + \left[\frac{k_z}{\Delta z}\left(\frac{1+e_0}{1+e}\right)\right]_{i+1,1} + \frac{2(k_s)_i L_i}{\Delta x^2}\right](u'_s)_{i,\ell} - \left[\frac{(k_s)_i L_i}{\Delta x^2}\right](u'_s)_{i,\ell+1}$$

$$= \left[\frac{k_z}{\Delta z}\left(\frac{1+e_0}{1+e}\right)\right]_{i,j} u'_{i,j,k,\ell} + \left[\frac{k_z}{\Delta z}\left(\frac{1+e_0}{1+e}\right)\right]_{i+1,1} u'_{i+1,1,2,\ell} \qquad (7-40)$$

Equation 7-40 can be rewritten in the following form for any impeded drainage layer:

$$A(u'_s)_{\ell-1} + B_\ell(u'_s)_\ell + A(u'_s)_{\ell+1} = C_\ell \qquad (7-41)$$

where A and B_ℓ have replaced the coefficients in front of the excess porewater pressure terms in the impeded drainage layer on the left hand side of Equation 7-40 and C_ℓ has replaced the right hand side of Equation 7-40.

Equation 7-40 applies for all nodes within the impeded drainage layer except the node directly under the center of the loaded area. The two-node form of the equation is:

$$\left[\left[\frac{k_z}{\Delta z}\left(\frac{1+e_0}{1+e}\right)\right]_{i,j} + \left[\frac{k_z}{\Delta z}\left(\frac{1+e_0}{1+e}\right)\right]_{i+1,1} + \frac{4(k_s)_i L_i}{\Delta x^2}\right](u'_s)_{i,1} - \left[\frac{4(k_s)_i L_i}{\Delta x^2}\right](u'_s)_{i,2}$$

$$= \left[\frac{k_z}{\Delta z}\left(\frac{1+e_0}{1+e}\right)\right]_{i,j} u'_{i,j,k,1} + \left[\frac{k_z}{\Delta z}\left(\frac{1+e_0}{1+e}\right)\right]_{i+1,1} u'_{i+1,1,2,1} \qquad (7-42)$$

which can be rewritten for any impeded drainage layer as:

$$D(u'_s)_1 + E(u'_s)_2 = C_1 \qquad (7-43)$$

Equations 7-41 and 7-43 can be combined into matrix form for n columns of nodes.

$$\begin{bmatrix} D & E & 0 & 0 & 0 & ... & 0 \\ A & B_2 & A & 0 & 0 & ... & 0 \\ 0 & A & B_3 & A & 0 & ... & 0 \\ . & . & . & . & . & . & . \\ . & . & . & . & . & . & . \\ . & . & . & . & . & . & . \\ 0 & 0 & 0 & 0 & 0 & A & B_{n-1} \end{bmatrix} \begin{bmatrix} \left(u_s'\right)_1 \\ \left(u_s'\right)_2 \\ \left(u_s'\right)_3 \\ . \\ . \\ . \\ \left(u_s'\right)_{n-1} \end{bmatrix} = \begin{bmatrix} C_1 \\ C_2 \\ C_3 \\ . \\ . \\ . \\ C_{n-1} \end{bmatrix} \qquad (7-44)$$

Equation 7-44 is used to solve for the excess porewater pressures in any incompressible impeded drainage layer for the two-dimensional flow case. The excess porewater pressure at the n^{th} node is equal to 0. Excess porewater pressures in the compressible layers computed during the previous time step are used.

7.5.1.3.2 Axi-symmetric flow

Figure 7-5 illustrates the coupling of flow from two compressible layers into one radially draining incompressible impeded drainage layer for the case of axi-symmetric flow.

The equation of continuity is given by:

$$q_{zi} + q_{z(i+1)} = \frac{\partial q_r}{\partial r} dr \qquad (7-45)$$

Applying the Darcy flow equation and substituting equation 7-13 into equation 7-45 yields:

$$\left[\frac{k_z}{\gamma_w}\frac{\partial u'}{\partial z}\left(\frac{1+e_0}{1+e}\right)\right]_i r d\theta dr + \left[\frac{k_z}{\gamma_w}\frac{\partial u'}{\partial z}\left(\frac{1+e_0}{1+e}\right)\right]_{i+1} r d\theta dr$$

$$= -\frac{\partial}{\partial r}\left(\frac{(k_s)_i L_i}{\gamma_w}\frac{\partial u'}{\partial r} r d\theta\right) dr \qquad (7-46)$$

Equation 7-46 simplifies to:

$$\left[\frac{k_z}{\gamma_w}\frac{\partial u'}{\partial z}\left(\frac{1+e_0}{1+e}\right)\right]_i r d\theta dr + \left[\frac{k_z}{\gamma_w}\frac{\partial u'}{\partial z}\left(\frac{1+e_0}{1+e}\right)\right]_{i+1} r d\theta dr$$

$$= -\frac{(k_s)_i L_i r}{\gamma_w}\left(\frac{\partial^2 u'}{\partial r^2} + \frac{1}{r}\frac{\partial u'}{\partial r}\right) d\theta dr \qquad (7-47)$$

Further simplifying and putting into finite difference form gives:

$$\left[\frac{k_z}{\Delta z}\left(\frac{1+e_0}{1+e}\right)\right]_{i,j}\left(u'_{i,j,k,\ell}-\left(u'_s\right)_{i,\ell}\right)+\left[\frac{k_z}{\Delta z}\left(\frac{1+e_0}{1+e}\right)\right]_{i+1,1}\left(u'_{i+1,1,2,\ell}-\left(u'_s\right)_{i,\ell}\right)$$

$$=-\frac{(k_s)_i L_i}{\Delta r}\left[\frac{\left(u'_s\right)_{i,\ell-1}-2\left(u'_s\right)_{i,\ell}+\left(u'_s\right)_{i,\ell+1}}{\Delta r}+\frac{\left(u'_s\right)_{i,\ell-1}-\left(u'_s\right)_{i,\ell+1}}{2r}\right] \qquad (7-48)$$

where $(u'_s)_{i,\ell-1}$, $(u'_s)_{i,\ell}$, and $(u'_s)_{i,\ell+1}$, are the excess porewater pressures in the i^{th} impeded drainage layer at column ℓ-1, ℓ, and ℓ+1, respectively, $u'_{i,j,k,\ell}$ is the excess porewater pressure at the second to last node in the overlying compressible layer at column ℓ, and $u'_{i+1,1,2,\ell}$ is the excess porewater pressure at the second node in the underlying compressible layer at column ℓ. Further rearranging leads to:

$$\left[\frac{(k_s)_i L_i}{\Delta r}\left(\frac{1}{2r}-\frac{1}{\Delta r}\right)\right]\left(u'_s\right)_{i,\ell-1}+\left[\left[\frac{k_z}{\Delta z}\left(\frac{1+e_0}{1+e}\right)\right]_{i,j}+\left[\frac{k_z}{\Delta z}\left(\frac{1+e_0}{1+e}\right)\right]_{i+1,1}+\frac{2(k_s)_i L_i}{\Delta r^2}\right]\left(u'_s\right)_{i,\ell}$$

$$-\left[\frac{(k_s)_i L_i}{\Delta r}\left(\frac{1}{2r}+\frac{1}{\Delta r}\right)\right]\left(u'_s\right)_{i,\ell+1}=\left[\frac{k_z}{\Delta z}\left(\frac{1+e_0}{1+e}\right)\right]_{i,j}u'_{i,j,k,\ell}+\left[\frac{k_z}{\Delta z}\left(\frac{1+e_0}{1+e}\right)\right]_{i+1,1}u'_{i+1,1,2,\ell} \qquad (7-49)$$

Equation 7-49 can be rewritten in the following form for any impeded drainage layer:

$$A_\ell\left(u'_s\right)_{\ell-1}+B_\ell\left(u'_s\right)_\ell+C_\ell\left(u'_s\right)_{\ell+1}=D_\ell \qquad (7-50)$$

where A_ℓ and B_ℓ, and C_ℓ have replaced the coefficients in front of the excess porewater pressure terms in the impeded drainage layer on the left hand side of Equation 7-49, and D_ℓ has replaced the right hand side of Equation 7-49.

Equation 7-49 applies for all nodes within the impeded drainage layer except the node directly under the center of the loaded area. The two-node form of the equation is:

$$\left[\left[\frac{k_z}{\Delta z}\left(\frac{1+e_0}{1+e}\right)\right]_{i,j}+\left[\frac{k_z}{\Delta z}\left(\frac{1+e_0}{1+e}\right)\right]_{i+1,1}+\frac{8(k_s)_i L_i}{\Delta r^2}\right]\left(u'_s\right)_{i,1}-\left[\frac{8(k_s)_i L_i}{\Delta r^2}\right]\left(u'_s\right)_{i,2}$$

$$=\left[\frac{k_z}{\Delta z}\left(\frac{1+e_0}{1+e}\right)\right]_{i,j}u'_{i,j,k,1}+\left[\frac{k_z}{\Delta z}\left(\frac{1+e_0}{1+e}\right)\right]_{i+1,1}u'_{i+1,1,2,2} \qquad (7-51)$$

which can be rewritten for any impeded drainage layer as:

$$E\left(u'_s\right)_1+F\left(u'_s\right)_2=D_1 \qquad (7-52)$$

Equations 7-50 and 7-52 can be combined into matrix form for n columns of nodes.

$$\begin{bmatrix} E & F & 0 & 0 & 0 & \dots & 0 \\ A_2 & B_2 & C_2 & 0 & 0 & \dots & 0 \\ 0 & A_3 & B_3 & C_3 & 0 & \dots & 0 \\ . & . & . & . & . & . & . \\ . & . & . & . & . & . & . \\ . & . & . & . & . & . & . \\ 0 & 0 & 0 & 0 & 0 & A_{n-1} & B_{n-1} \end{bmatrix} \begin{bmatrix} \left(u_s^{'}\right)_1 \\ \left(u_s^{'}\right)_2 \\ \left(u_s^{'}\right)_3 \\ . \\ . \\ . \\ \left(u_s^{'}\right)_{n-1} \end{bmatrix} = \begin{bmatrix} D_1 \\ D_2 \\ D_3 \\ . \\ . \\ . \\ D_{n-1} \end{bmatrix} \qquad (7-53)$$

Equation 7-53 is used to solve for the excess porewater pressures in any incompressible impeded drainage layer for the axi-symmetric flow case. The excess porewater pressure at the n^{th} node is equal to 0. Excess porewater pressures in the compressible layers computed during the previous time step are used.

7.5.1.4 Nodes at the top and bottom boundaries

The top and bottom boundaries of the profile may be freely draining or impermeable. If the top or bottom boundary is freely draining then the excess porewater pressure is equal to zero, the void ratio is equal to the end-of-primary void ratio, and the vertical permeability is equal to the vertical permeability at end-of-primary consolidation.

If the top or bottom boundaries are impermeable then for t > 0 (Lo, 1991):

$$\frac{\partial u'}{\partial z} = 0 \qquad (7-54)$$

$$\left(\frac{\partial^2 u'}{\partial z^2}\right)_{i,j,k,l} = \frac{2u^{'}_{i,j,k+1,l} - 2u^{'}_{i,j,k,l}}{\left(\Delta z_{i,j}\right)^2} \qquad (7-55)$$

$$\left(\frac{\partial k_z}{\partial z}\right)_{i,j,k,l} = \frac{\left(k_z\right)_{i,j,k+1,l} - \left(k_z\right)_{i,j,k,l}}{\Delta z_{i,j}} \qquad (7-56)$$

7.5.1.5 Nodes at the horizontal or radial edge of the applied vertical stress increase

The horizontal boundary of the applied vertical stress increase is a freely draining boundary. Therefore, the excess porewater pressure is equal to zero, the void ratio is equal to the end-of-primary void ratio, and the vertical permeability is equal to the vertical permeability at the end-of-primary consolidation.

7.5.1.6 Nodes under the center of the applied load

The vertical boundary directly under the center of the loaded area is impermeable as a consequence of symmetry. The assumptions for the two-dimensional flow and axi-symmetric flow cases within the clay layers are listed below.

7.5.1.6.1 Two-dimensional flow

The finite difference approximations for nodes lying directly under the center of the applied load for the case of two-dimensional flow include:

$$\frac{\partial u'}{\partial x} = 0 \qquad (7-57)$$

$$\left(\frac{\partial^2 u'}{\partial x^2}\right)_{i,j,k,\ell} = \frac{u'_{i,j,k,\ell+1} - 2u'_{i,j,k,\ell}}{(\Delta x)^2} \qquad (7-58)$$

$$\left(\frac{\partial k_x}{\partial x}\right)_{i,j,k,\ell} = \frac{\left(\frac{k_x}{k_z}\right)_{i,j}\left[(k_z)_{i,j,k,\ell+1} - (k_z)_{i,j,k,\ell}\right]}{\Delta x} \qquad (7-59)$$

7.5.1.6.2 Axi-symmetric flow

The finite difference approximations for nodes lying directly under the center of the applied load for the case of two-dimensional flow include:

$$\frac{\partial u'}{\partial r} = 0 \qquad (7-60)$$

$$\left(\frac{\partial^2 u'}{\partial r^2}\right)_{i,j,k,\ell} = \frac{u'_{i,j,k,\ell+1} - 2u'_{i,j,k,\ell}}{(\Delta r)^2} \qquad (7-61)$$

$$\left(\frac{\partial k_r}{\partial r}\right)_{i,j,k,\ell} = \frac{\left(\frac{k_r}{k_z}\right)_{i,j}\left[(k_z)_{i,j,k,\ell+1} - (k_z)_{i,j,k,\ell}\right]}{\Delta r} \qquad (7-62)$$

7.5.1.7 Finite difference solution process

The solution process for each time step during the explicit finite difference solution is:

1. Determine the vertical stress increase at each node from the applied load at the surface for the current time.
2. Determine the final effective vertical stress, end-of-primary void ratio, permeability, and excess porewater pressure at each node.
3. If the top and/or bottom boundaries are freely draining, then set the excess porewater pressure to 0, the void ratio and permeability equal the end-of-primary void ratio (Mesri and Godlewski, 1977, 1979) and permeability, respectively, and the effective vertical stress equal to the final effective vertical stress, or if the top and/or bottom boundaries are impermeable, then apply Equations 7-54 through 7-56.
4. Apply Equations 7-44 or 7-53 to determine the excess porewater pressures within the incompressible impeded drainage layers for the two-dimensional flow case or the axi-symmetric flow case, respectively.
5. Compute the finite difference approximations for partial derivatives of excess porewater pressure, void ratio, and permeability with respect the z and x or r directions.
6. Compute de/dt for all internal nodes and for nodes at impermeable boundaries using Equation 7-15 (two-dimensional flow) or 7-16 (axi-symmetric flow).
7. Calculate C_c*, $(de/d\sigma'_v)_t$, and $(de/dt)_{\sigma'v}$ for all internal nodes and for nodes at impermeable boundaries using Equations 7-18, 7-17, and 7-20, respectively.
8. Solve for du'/dt for all internal nodes and for nodes at impermeable boundaries using Equation 7-21.
9. Calculate the new excess porewater pressure ($u' = u'_{old} + du'/dt*(\Delta t)$) for all internal nodes and for nodes at impermeable boundaries.
10. Calculate the new excess porewater pressures at sublayer boundaries using Equation 7-35.
11. Calculate the new effective vertical stress ($\sigma'_v = \sigma'_{v0} + \Delta\sigma_v - u'$) and obtain the void ratio from the EOP e – log σ'_v relationship and the vertical permeability from the e – log k_v relationship for all internal nodes and for nodes at impermeable boundaries.
12. Calculate compression and degree of compression at each node.

7.5.2 Submergence of fill material below sea level

For cases involving reclamation, as settlement progresses fill material will become

submerged below the water level causing a decrease in the vertical stress increase. This effect can be significant when settlements are very large. Therefore, ILLICON has been updated to take the effect of submergence into account. The user inputs the loading schedule without submergence together with the time when the fill height reaches the level of the water. Thereafter, the vertical stress increase with submergence at any time $(\Delta\sigma_{applied})_t$ is calculated by:

$$\left(\Delta\sigma_{applied}\right)_t = \left(\Delta\sigma_{applied}\right)_{t-\Delta t} + \left[\left(\Delta\sigma_{ws}\right)_t - \left(\Delta\sigma_{ws}\right)_{t-\Delta t}\right] - \Delta S \times \gamma_w \qquad (7-63)$$

where $(\Delta\sigma_{applied})_{t-\Delta t}$ is the vertical stress increase at time t - Δt, $(\Delta\sigma_{ws})_t$ is the vertical stress increase without submergence at time t, $(\Delta\sigma_{ws})_{t-\Delta t}$ is the vertical stress increase without submergence at time t-Δt, and ΔS is the increment of settlement during Δt.

If the user incorporates the submergence effect as a part of the load – time relationship directly, then there is no need to use Equation 7-63 to compute the vertical stress increase.

7.6 The C_α/C_c law of compressibility to compute secondary settlement

The secondary compression behavior of any geotechnical material is explained by the C_α/C_c law of compressibility which states that there is a unique interrelationship between the time compressibility and the effective stress compressibility that holds true throughout the secondary consolidation stage. It is well established that C_α/C_c is a constant for any soil where the (C_α, C_c) data pair correspond to the same point (e, σ'_v, t) during secondary compression, and that the values of C_α/C_c for all geotechnical materials are in the range of 0.01 to 0.07 (Mesri and Godlewski, 1977, 1979; Mesri and Choi, 1984; Mesri, 1987; Mesri and Castro, 1987; Mesri et al., 1997).

The ILLICON computer program uses the C_α/C_c law of compressibility (Mesri and Godlewski, 1977, 1979) to compute secondary compression after the final vertical stress increase specified by the user has been applied to the soil profile and after the average degree of compression for the layer reaches 95%. ILLICON computes the void ratio at any time step, $e^{(t)}$, resulting from secondary compression using the following equation:

$$e^{(t)} = e^{(t-\Delta t)} + \left(\frac{\partial e}{\partial t}\right)^{(t)}_{\sigma'v} \Delta t \qquad (7-64)$$

where $e^{(t-\Delta t)}$ is the void ratio from the previous time step, Δt is the calculation time step, and

$\left(\frac{\partial e}{\partial t}\right)_{\sigma'v}^{(t)}$ is defined as:

$$\left(\frac{\partial e}{\partial t}\right)_{\sigma'v}^{(t)} = \frac{-0.434}{t}\frac{C_\alpha}{C_c} \times C_c \qquad (7-65)$$

The superscripts (t) and (t-Δt) are not exponents. They indicate when the variables are evaluated by ILLICON. The C_c term in Equation 7-65 is set equal to the value of C_c at $e^{(t-\Delta t)}$ for the EOP e – log σ'_v relationship specified for the sublayer.

7.7 Error for finite difference approximation

Replacing an exact mathematical model with a numerical finite difference model introduces error into the solution. The error introduced is a result of using a space - time mesh with finite distance between calculation nodes and finite time increments, as well as the loss of information caused by rounding of numbers to fit a finite computer word length. Discretization error is the difference between the exact solution of the finite difference equations (i.e. without loss of information resulting from rounding of numbers) and the exact solution of the non-discretized equations. Round-off error is the difference between the numerical solution of the finite difference equations from a computer with finite precision and the exact solution of the finite difference equations. Manipulation errors are introduced as equations containing numbers with finite precision are processed during the solution process. Numerical error is the combined error resulting from round-off and manipulation error (Jaluria and Torrance, 1986; Cook et al., 2002).

7.7.1 Discretization error

Richardson's extrapolation formula (Cook et al., 2002) was used to quantify discretization error associated with the ILLICON solution for settlement analyses at Kansai Airport. First, excess porewater pressure (u′) is plotted against node spacing (Δz or Δx) or time increment (Δt), to the power n. The exponent, n, is selected such that the data fall on a straight line. Richardson's extrapolation formula is then used to estimate the value of the quantity of interest at zero node spacing or zero time increment. As an example, the following equation was

used to estimate the value of excess porewater pressure at zero node spacing in the z direction (u'_∞) :

$$u'_\infty = \frac{u'_1 \Delta z_2^n - u'_2 \Delta z_1^n}{\Delta z_2^n - \Delta z_1^n} \qquad (7-66)$$

where Δz_1 and Δz_2 are values of node spacing in the z direction used for two separate analyses, and u'_1 and u'_2 are the calculated excess porewater pressures corresponding to node spacing Δz_1 and Δz_2, respectively. The calculated values obtained from separate runs of the finite difference solution must be compared at the same location in the model and at the same model time. Additionally, in order to apply Equation 7-66, the mesh must be refined such that nodes of the coarser mesh are preserved while new nodes are added. At least three different mesh sizes are required to distinguish a curve from a straight line (Cook et al., 2002).

It is preferred to use the procedure outlined above to estimate the error associated with using a particular node spacing (e.g. Δz_2 from the above example) or time increment (Δt) rather than applying Equation 7-66 directly to determine excess porewater pressure. Therefore, an estimate of the percentage error (% error) of u'_2 is given by:

$$\%\ \text{error} = \frac{u'_2 - u'_\infty}{u'_\infty} \times 100\% \qquad (7-67)$$

Regular mesh refinement was used to systematically decrease the node spacing in the vertical (z) direction, then the horizontal (x) direction, followed by a decrease in time increment (Δt) for a settlement analysis at Kansai Airport. Equation 7-67 was applied to estimate the percentage error for each mesh. This procedure was used to estimate discretization errors for excess porewater pressures at the top of each sublayer.

Figure 7-6 shows excess porewater pressure at the top of sublayer 2 for marine clay layer Ma12 as a function of node spacing in the z direction (Δz). The power, n, in Equation 7-66 was determined graphically to be 1 in every case. Based on the straight line drawn through the data points the value of excess porewater pressure at zero node spacing is equal to 423.8kPa. As an example, applying Equation 7-67 gives an estimated percentage error associated with using Δz equal to 0.54m of -2.8%.

Table 7-1 summarizes the estimated percentage error for excess porewater pressure for various node spacing in the z direction. Node spacing in the x direction and time increment were held constant to calculate the percent errors in Table 7-1. Table 7-1 indicates that node spacing in

the z direction can have a significant impact on the solution. The node spacing in the z direction used for each sublayer at MP1-II is shown in Table 7-2.

Table 7-3 summarizes the estimated percentage error for excess porewater pressure for various node spacing in the x direction. Node spacing in the z direction and time increment were held constant to calculate the percent errors in Table 7-3. Table 7-3 indicates that node spacing in the x direction has very little influence on the solution for the case analyzed. Node spacing in the x direction was set equal to 29.1m for subsequent settlement analyses at MP1-II.

Table 7-4 summarizes the estimated percentage error for excess porewater pressure for various time increments. Node spacing in the x and z direction were held constant to calculate the percent errors in Table 7-4. Table 7-4 indicates that the time increment has very little influence on the solution for the case analyzed (except for numerical stability described in Section 7.7.2). Time increment was set equal to 0.02 days for subsequent settlement analyses at MP1-II.

7.7.2 Numerical error (round-off and manipulation error)

It is of interest to estimate the minimum time increment required such that the numerical error remains bounded as the solution progresses. For the case of vertical compression and vertical water flow:

$$\frac{de}{dt} = \left(\frac{\partial e}{\partial \sigma_v'}\right)_t \left(\frac{-du'}{dt}\right) + \left(\frac{\partial e}{\partial t}\right)_{\sigma_v'} =$$

$$\frac{1}{\gamma_w}\left(\frac{1+e_0}{1+e}\right)^2 \left[(1+e)\left(k_z \frac{\partial^2 u'}{\partial z^2} + \frac{\partial k_z}{\partial z}\frac{\partial u'}{\partial z}\right) - k_z \frac{\partial u'}{\partial z}\frac{\partial e}{\partial z}\right] \qquad (7-68)$$

Putting into finite difference form, solving for u′, and rearranging yields:

$$(u')_{i,j,k,\ell}^{(t+\Delta t)} =$$

$$\left(\frac{(1+e_0)^2}{\gamma_w \Delta z^2 (1+e)^2}\right)_{i,j,k,\ell}^{(t)} \left[(k_z(1+e))_{i,j,k,\ell}^{(t)} - \left(\frac{1+e}{4}\right)_{i,j,k,\ell}^{(t)} \left((k_z)_{i,j,k+1,\ell}^{(t)} - (k_z)_{i,j,k-1,\ell}^{(t)}\right) +\right.$$

$$\left.\left(\frac{k_z}{4}\right)_{i,j,k,\ell}^{(t)} \left((e)_{i,j,k+1,\ell}^{(t)} - (e)_{i,j,k-1,\ell}^{(t)}\right)\right] \times \frac{\ln(10)(\sigma_v')_{i,j,k,\ell}^{(t)} \Delta t}{(C_c^*)_{i,j,k,\ell}^{(t)}} \times (u')_{i,j,k-1,\ell}^{(t)} +$$

$$\left(\frac{(1+e_0)^2}{\gamma_w \Delta z^2 (1+e)^2}\right)_{i,j,k,\ell}^{(t)} \left[1-\left(\frac{\ln(10)\sigma_v' k_z (1+e)}{C_c^*}\right)_{i,j,k,\ell}^{(t)} \Delta t\right] \times (u')_{i,j,k,\ell}^{(t)} +$$

$$\left(\frac{(1+e_0)^2}{\gamma_w \Delta z^2 (1+e)^2}\right)_{i,j,k,\ell}^{(t)} [(k_z(1+e))_{i,j,k,\ell}^{(t)} + \left(\frac{1+e}{4}\right)_{i,j,k,\ell}^{(t)} \left((k_z)_{i,j,k+1,\ell}^{(t)} - (k_z)_{i,j,k-1,\ell}^{(t)}\right) -$$

$$\left(\frac{k_z}{4}\right)_{i,j,k,\ell}^{(t)} \left((e)_{i,j,k+1,\ell}^{(t)} - (e)_{i,j,k-1,\ell}^{(t)}\right)] \times \frac{\ln(10)\left(\sigma_v'\right)_{i,j,k,\ell}^{(t)} \Delta t}{\left(C_c^*\right)_{i,j,k,\ell}^{(t)}} \times (u')_{i,j,k+1,\ell}^{(t)} +$$

$$\left(\frac{C_\alpha}{C_c}\beta\sigma_v'\right)_{i,j,k,\ell}^{(t)} \frac{\Delta t}{t} \qquad (7-69)$$

where (t) and (t+Δt) indicate the previous time and current time in the model, respecively. The (t) and (t+Δt) terms shown in Equation 7-69 are not exponents but indicate when the parameters were evaluated during the solution process. Equation 7-69 can be simplified to the following form:

$$(u')_{i,j,k,\ell}^{(t+\Delta t)} = A(u')_{i,j,k-1,\ell}^{(t)} + B(u')_{i,j,k,\ell}^{(t)} + C(u')_{i,j,k+1,\ell}^{(t)} + D \qquad (7-70)$$

Equation 7-70 describes both the exact solution of the finite difference equation and the numerical solution from a computer with finite precision. Therefore, if the exact solution of the finite difference equation is subtracted from the numerical solution of the finite difference equation, then the round-off error (ε) remains:

$$(\varepsilon)_{i,j,k,\ell}^{(t+\Delta t)} = A(\varepsilon)_{i,j,k-1,\ell}^{(t)} + B(\varepsilon)_{i,j,k,\ell}^{(t)} + C(\varepsilon)_{i,j,k+1,\ell}^{(t)} + D \qquad (7-71)$$

To ensure that the error remains bounded, the sum of the absolute value of the coefficient terms must be less than or equal to 1 (Jaluria and Torrance, 1986).

$$|A| + |B| + |C| \le 1 \qquad (7-72)$$

If the following condition is satisfied,

$$(k_z)_{i,j,k,\ell}^{(t)} > \left| \pm \frac{\left((k_z)_{i,j,k+1,\ell}^{(t)} - (k_z)_{i,j,k-1,\ell}^{(t)}\right)}{4} \mp \frac{(k_z)_{i,j,k,\ell}^{(t)}}{4(1+e)_{i,j,k,\ell}^{(t)}} \left((e)_{i,j,k+1,\ell}^{(t)} - (e)_{i,j,k-1,\ell}^{(t)}\right) \right| \qquad (7-73)$$

then solving Equation 7-72 for Δt yields:

$$\Delta t \le \frac{\gamma_w}{2\ln(10)}\left(\frac{C_c^*(1+e)(\Delta z)^2}{\sigma_v' k_z (1+e_0)^2}\right)_{i,j,k,\ell}^{(t)} \qquad (7-74)$$

However, C_c^*, σ'_v, (1+e), and k_z vary during consolidation. To get an estimate for the value of Δt required for stability before running the analysis, let C_c^* equal C_{co} (the compression index corresponding to e_o), let σ'_v equal σ'_{vo}, let (1+e) equal $(1+e_o)$, and let k_z equal k_{vo}. Equation 7-74 becomes:

$$\Delta t \le \frac{\gamma_w}{2\ln(10)}\left(\frac{C_{co}(\Delta z)^2}{\sigma_{vo}' k_{vo}(1+e_0)}\right) \qquad (7-75)$$

The coefficient of consolidation corresponding to initial conditions (c_{vo}) is:

$$c_{vo} = \frac{\ln(10) k_{vo}(1+e_0)\sigma_{vo}'}{\gamma_w C_{co}} \qquad (7-76)$$

therefore, Equation 7-75 can be written in the following form:

$$\Delta t \le \frac{\Delta z^2}{2c_{vo}} \qquad (7-77)$$

It's likely that Δt required for stability will be less than that suggested by Equation 7-77 because C_c^* will decrease for a constant C_c during consolidation. Additionally, σ'_v will increase, and (1+e) will become less than $(1+e_o)$ during consolidation (see Equation 7-74). However, Equation 7-77 can be used to estimate the time increment required to produce a stable solution.

The same procedure can be applied to Equation 7-15; the case for compression in the z direction and water flow in the z and x directions. If the condition specified by Equation 7-73 is satisfied in addition to the following condition:

$$(k_x)_{i,j,k,\ell}^{(t)} > \left|\frac{\left((k_x)_{i,j,k,\ell+1}^{(t)} - (k_z)_{i,j,k,\ell-1}^{(t)}\right)}{4}\right| \qquad (7-78)$$

then:

$$\Delta t \le \frac{\gamma_w}{2\ln(10)}\left(\frac{C_c^*(1+e)(\Delta z \Delta x)^2}{\sigma_v'\left(k_z(1+e_0)^2\Delta x^2 + k_x(1+e)^2\Delta z^2\right)}\right)_{i,j,k,\ell}^{(t)} \qquad (7-79)$$

Then applying the same simplifications as before (i.e. let C_c^* equal C_{co}, let σ'_v equal σ'_{vo}, let (1+e) equal $(1+e_o)$, let k_z equal k_{vo}), and substitute Equation 7-76 to obtain:

$$\Delta t \le \frac{(\Delta z)^2}{2c_{vo}\left(1+(k_x/k_z)(\Delta z/\Delta x)^2\right)} \qquad (7-80)$$

Finally, the same procedure can be applied for Equation 7-16; the case for compression in the z direction and water flow in the z and r directions. If the condition specified by Equation 7-73 is satisfied in addition to the following condition:

$$(k_r)^{(t)}_{i,j,k,\ell} > \left| \frac{(k_r)^{(t)}_{i,j,k,\ell}\,\Delta r}{2r} + \frac{\left((k_r)^{(t)}_{i,j,k,\ell+1} - (k_r)^{(t)}_{i,j,k,\ell-1}\right)}{4} \right| \qquad (7-81)$$

then:

$$\Delta t \le \frac{\gamma_w}{2\ln(10)} \left(\frac{C_c^*(1+e)(\Delta z \Delta r)^2}{\sigma'_v\left(k_z(1+e_0)^2\Delta r^2 + k_r(1+e)^2\Delta z^2\right)} \right)^{(t)}_{i,j,k,\ell} \qquad (7-82)$$

Applying the same simplifications as before (i.e. let C_c^* equal C_{co}, let σ'_v equal σ'_{vo}, let (1+e) equal ($1+e_o$), let k_z equal k_{vo}), and substitute Equation 7-73 to obtain:

$$\Delta t \le \frac{(\Delta z)^2}{2c_{vo}\left(1+(k_r/k_z)(\Delta z/\Delta r)^2\right)} \qquad (7-83)$$

As with Equation 7-77, Equations 7-80 and 7-83 are only capable of providing an estimate for the time increment required to produce a stable solution.

Equation 7-80 was used to check stability for subsequent settlement analyses at the Kansai Airport site. The Δt required for stability was calculated for each sublayer in the profile, and Δt used in the analyses was selected to be less than the minimum Δt required for stability for all sublayers. For the settlement analysis of Pleistocene clay layers at MP1-II the minimum Δt required for stability of all sublayers according to Equation 7-80 is equal to 0.10 days (Δt equal to 0.02 days was used for the explicit finite difference approximation).

7.8 Tables

Table 7-1 Estimated percentage error for excess porewater pressure and vertical compression for various node spacing in the z direction.

Layer	Sublayer	Run 1		Run 2		Run 3	
		Δz (m)	u' % error	Δz (m)	u' % error	Δz (m)	u' % error
Dtc	1	1.02	-	0.51	-	0.25	-
	2	1.02	-21.6	0.51	-10.5	0.25	-5.5
	3	0.51	-12.8	0.25	-6.2	0.13	-3.3
Ma12	1	1.08	-5.0	0.54	-2.6	0.27	-1.2
	2	1.08	-5.7	0.54	-2.8	0.27	-1.4
Doc1	1	1.05	-5.0	0.53	-2.4	0.26	-1.3
Ma11U	1	1.09	-16.5	0.54	-8.6	0.27	-3.9
	2	1.09	-1.6	0.54	-0.8	0.27	-0.4
Ma11L	1	1.09	-4.2	0.54	-2.1	0.27	-1.0
Ma10	1	1.07	-4.4	0.53	-2.2	0.27	-1.1
	2	1.07	-4.3	0.53	-2.1	0.27	-1.1
	3	1.07	-4.0	0.53	-2.0	0.27	-1.0
	4	1.07	-3.7	0.53	-1.8	0.27	-0.9
Ma9	1	1.02	-3.1	0.51	-1.6	0.25	-0.7
	2	1.02	-3.8	0.51	-1.9	0.25	-0.9
Doc5	1	1.03	-20.1	0.52	-9.9	0.26	-5.1
	2	1.03	-10.4	0.52	-5.3	0.26	-2.5
Ma8	1	1.06	-24.2	0.53	-12.7	0.27	-5.8
	2	1.28	-3.2	0.64	-1.7	0.32	-0.8
	3	0.85	-3.9	0.43	-1.9	0.21	-1.0
Ma7	1	1.06	-20.0	0.53	-10.2	0.26	-4.9
	2	1.06	-6.0	0.53	-3.4	0.26	-1.3
	3	1.17	-11.1	0.59	-5.9	0.29	-2.6
Doc6	1	1.05	-52.4	0.53	-29.7	0.26	-11.3

Table 7-1 cont. Estimated percentage error for excess porewater pressure and vertical compression for various node spacing in the z direction.

Layer	Sublayer	Run 1		Run 2		Run 3	
		Δz (m)	u' % error	Δz (m)	u' % error	Δz (m)	u' % error
Ma4	**1**	2.72	-	1.36	-	0.68	-
Ma3	**1**	2.13	-15.4	1.06	-7.7	0.53	-3.9
Ma2	**1**	2.60	-15.5	1.30	-7.9	0.65	-3.8
NMC-1	**1**	1.70	-21.1	0.85	-10.6	0.42	-5.3
NMC-2	**1**	1.40	-23.6	0.70	-11.8	0.35	-5.9
NMC-3	**1**	2.67	-24.1	1.34	-12.0	0.67	-6.0
Ma1	**1**	2.71	-23.0	1.36	-11.5	0.68	-5.7
NMC-4	**1**	2.57	-18.0	1.29	-9.1	0.64	-4.4
Ma0	**1**	2.72	-18.2	1.36	-9.2	0.68	-4.5
NMC-5	**1**	0.79	-19.9	0.40	-9.9	0.20	-5.0

Table 7-2 Node spacing in the z direction used for subsequent analysis at MP1-II.

Layer	Sublayer	Sublayer Thickness (m)	No. Nodal Rows	Δz (m)
Dtc	**1**	3.05	13	0.25
	2	3.05	13	0.25
	3	1.53	13	0.13
Ma12	**1**	7.53	29	0.27
	2	7.53	29	0.27
Doc1	**1**	9.49	19	0.53
Ma11U	**1**	6.51	13	0.54
	2	4.34	9	0.54
Ma11L	**1**	9.79	19	0.54
Ma10	**1**	6.39	13	0.53
	2	6.39	13	0.53
	3	6.39	13	0.53
	4	6.39	13	0.53
Ma9	**1**	13.22	14	1.02
	2	13.22	20	0.70
Doc5	**1**	6.20	13	0.52
	2	9.31	19	0.52
Ma8	**1**	6.38	13	0.53
	2	3.83	7	0.64
	3	2.55	7	0.43
Ma7	**1**	5.28	11	0.53
	2	5.28	11	0.53
	3	7.04	13	0.59

Table 7-2 cont. Node spacing in the z direction used for subsequent analysis at MP1-II.

Layer	Sublayer	Sublayer Thickness (m)	No. Nodal Rows	Δz (m)
Doc6	**1**	10.54	41	0.26
Ma4	**1**	8.15	13	0.68
Ma3	**1**	21.27	41	0.53
Ma2	**1**	10.38	17	0.65
NMC-1	**1**	5.09	13	0.42
NMC-2	**1**	4.19	13	0.35
NMC-3	**1**	10.69	17	0.67
Ma1	**1**	10.84	17	0.68
NMC-4	**1**	15.43	25	0.64
Ma0	**1**	13.62	21	0.68
NMC-5	**1**	2.37	13	0.20

Table 7-3 Estimated percentage error for excess porewater pressure and vertical compression for various node spacing in the x direction.

Layer	Sublayer	Run 1		Run 2		Run 3	
		Δx (m)	u' % error	Δx (m)	u' % error	Δx (m)	u' % error
Dtc	1	29.19	-	14.60	-	7.30	-
	2	29.19	0.0	14.60	0.0	7.30	0.0
	3	29.19	0.0	14.60	0.0	7.30	0.0
Ma12	1	29.19	0.0	14.60	0.0	7.30	0.0
	2	29.19	0.0	14.60	0.0	7.30	0.0
Doc1	1	29.19	0.0	14.60	0.0	7.30	0.0
Ma11U	1	29.19	-1.3	14.60	-0.7	7.30	-0.3
	2	29.19	-0.1	14.60	0.0	7.30	0.0
Ma11L	1	29.19	-0.3	14.60	-0.2	7.30	-0.1
Ma10	1	29.19	-0.2	14.60	-0.1	7.30	0.0
	2	29.19	-0.1	14.60	-0.1	7.30	0.0
	3	29.19	-0.2	14.60	-0.1	7.30	0.0
	4	29.19	-0.3	14.60	-0.1	7.30	-0.1
Ma9	1	29.19	-0.6	14.60	-0.3	7.30	-0.2
	2	29.19	-0.2	14.60	-0.1	7.30	-0.1
Doc5	1	29.19	-1.0	14.60	-0.5	7.30	-0.3
	2	29.19	-0.5	14.60	-0.2	7.30	-0.1
Ma8	1	29.19	-0.9	14.60	-0.4	7.30	-0.2
	2	29.19	-0.1	14.60	0.0	7.30	0.0
	3	29.19	0.0	14.60	0.0	7.30	0.0
Ma7	1	29.19	-1.0	14.60	-0.5	7.30	-0.2
	2	29.19	-0.1	14.60	0.0	7.30	0.0
	3	29.19	-0.1	14.60	-0.1	7.30	0.0
Doc6	1	29.19	-2.4	14.60	-1.2	7.30	-0.6

Table 7-3 cont. Estimated percentage error for excess porewater pressure and vertical compression for various node spacing in the x direction.

Layer	Sublayer	Run 1		Run 2		Run 3	
		Δx (m)	u' % error	Δx (m)	u' % error	Δx (m)	u' % error
Ma4	**1**	29.19	-	14.60	-	7.30	-
Ma3	**1**	29.19	-1.0	14.60	-0.5	7.30	-0.2
Ma2	**1**	29.19	-1.3	14.60	-0.7	7.30	-0.3
NMC-1	**1**	29.19	-1.5	14.60	-0.7	7.30	-0.4
NMC-2	**1**	29.19	-1.5	14.60	-0.7	7.30	-0.4
NMC-3	**1**	29.19	-1.5	14.60	-0.8	7.30	-0.4
Ma1	**1**	29.19	-1.3	14.60	-0.7	7.30	-0.3
NMC-4	**1**	29.19	-1.0	14.60	-0.5	7.30	-0.2
Ma0	**1**	29.19	-1.3	14.60	-0.7	7.30	-0.3
NMC-5	**1**	29.19	-1.1	14.60	-0.5	7.30	-0.3

Table 7-4 Estimated percentage error for excess porewater pressure and vertical compression for various time increments.

Layer	Sublayer	Run 1		Run 2		Run 3	
		Δt (days)	u' % error	Δt (days)	u' % error	Δt (days)	u' % error
Dtc	1	0.02	0.1	0.01	0.1	0.005	0.0
	2	0.02	0.0	0.01	0.0	0.005	0.0
	3	0.02	0.0	0.01	0.0	0.005	0.0
Ma12	1	0.02	0.0	0.01	0.0	0.005	0.0
	2	0.02	0.0	0.01	0.0	0.005	0.0
Doc1	1	0.02	0.0	0.01	0.0	0.005	0.0
Ma11U	1	0.02	0.1	0.01	0.0	0.005	0.0
	2	0.02	0.0	0.01	0.0	0.005	0.0
Ma11L	1	0.02	0.0	0.01	0.0	0.005	0.0
Ma10	1	0.02	0.0	0.01	0.0	0.005	0.0
	2	0.02	0.0	0.01	0.0	0.005	0.0
	3	0.02	0.0	0.01	0.0	0.005	0.0
	4	0.02	0.0	0.01	0.0	0.005	0.0
Ma9	1	0.02	0.0	0.01	0.0	0.005	0.0
	2	0.02	0.0	0.01	0.0	0.005	0.0
Doc5	1	0.02	0.0	0.01	0.0	0.005	0.0
	2	0.02	0.1	0.01	0.0	0.005	0.0
Ma8	1	0.02	0.1	0.01	0.0	0.005	0.0
	2	0.02	0.0	0.01	0.0	0.005	0.0
	3	0.02	0.0	0.01	0.0	0.005	0.0
Ma7	1	0.02	0.2	0.01	0.1	0.005	0.0
	2	0.02	0.1	0.01	0.0	0.005	0.0
	3	0.02	0.1	0.01	0.1	0.005	0.0
Doc6	1	0.02	0.3	0.01	0.2	0.005	0.1

Table 7-4 cont. Estimated percentage error for excess porewater pressure and vertical compression for various time increments.

Layer	Sublayer	Run 1		Run 2		Run 3	
		Δt (days)	u' % error	Δt (days)	u' % error	Δt (days)	u' % error
Ma4	**1**	0.04	-	0.02	-	0.01	-
Ma3	**1**	0.04	0.4	0.02	0.2	0.01	0.1
Ma2	**1**	0.04	0.5	0.02	0.2	0.01	0.1
NMC-1	**1**	0.04	0.3	0.02	0.1	0.01	0.1
NMC-2	**1**	0.04	0.2	0.02	0.1	0.01	0.1
NMC-3	**1**	0.04	0.2	0.02	0.1	0.01	0.0
Ma1	**1**	0.04	0.3	0.02	0.1	0.01	0.1
NMC-4	**1**	0.04	0.9	0.02	0.5	0.01	0.2
Ma0	**1**	0.04	0.7	0.02	0.4	0.01	0.2
NMC-5	**1**	0.04	0.4	0.02	0.2	0.01	0.1

7.9 Figures

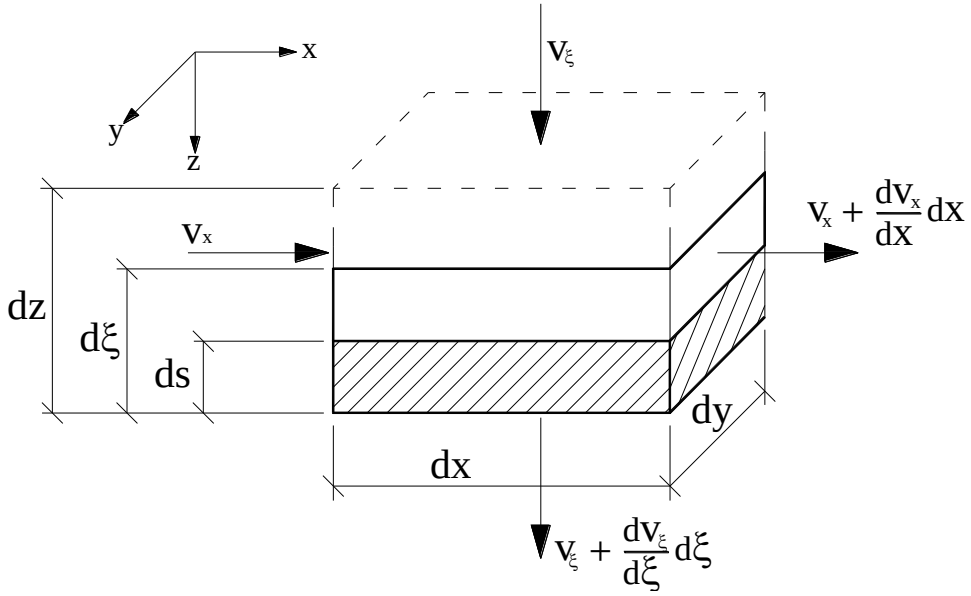

Figure 7-1 Rectangular soil element used for derivation of hydrodynamic equation.

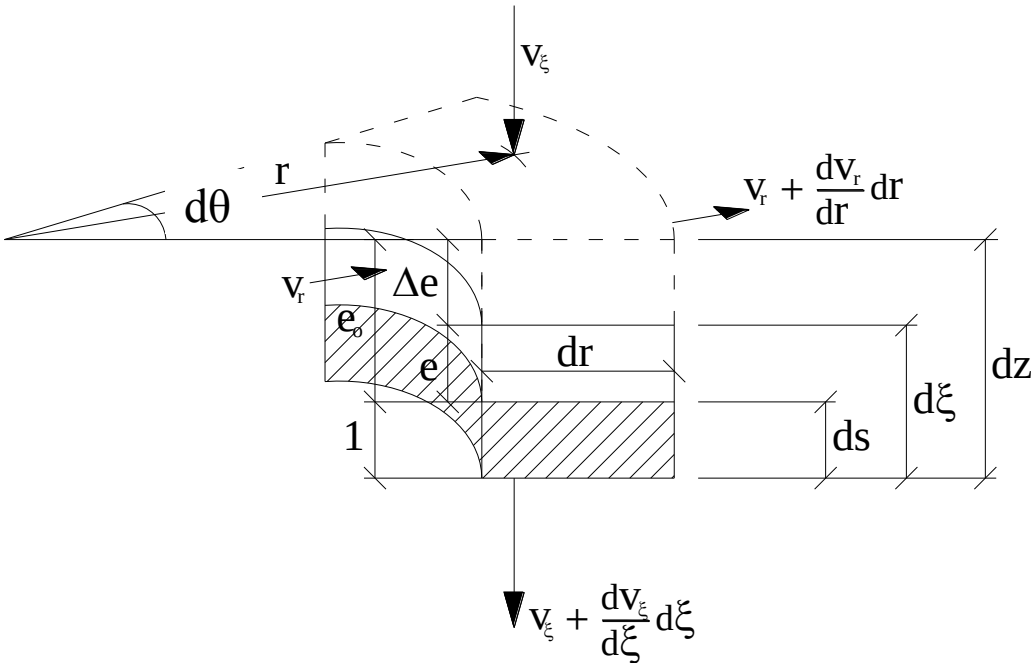

Figure 7-2 Cylindrical soil element used for derivation of hydrodynamic equation.

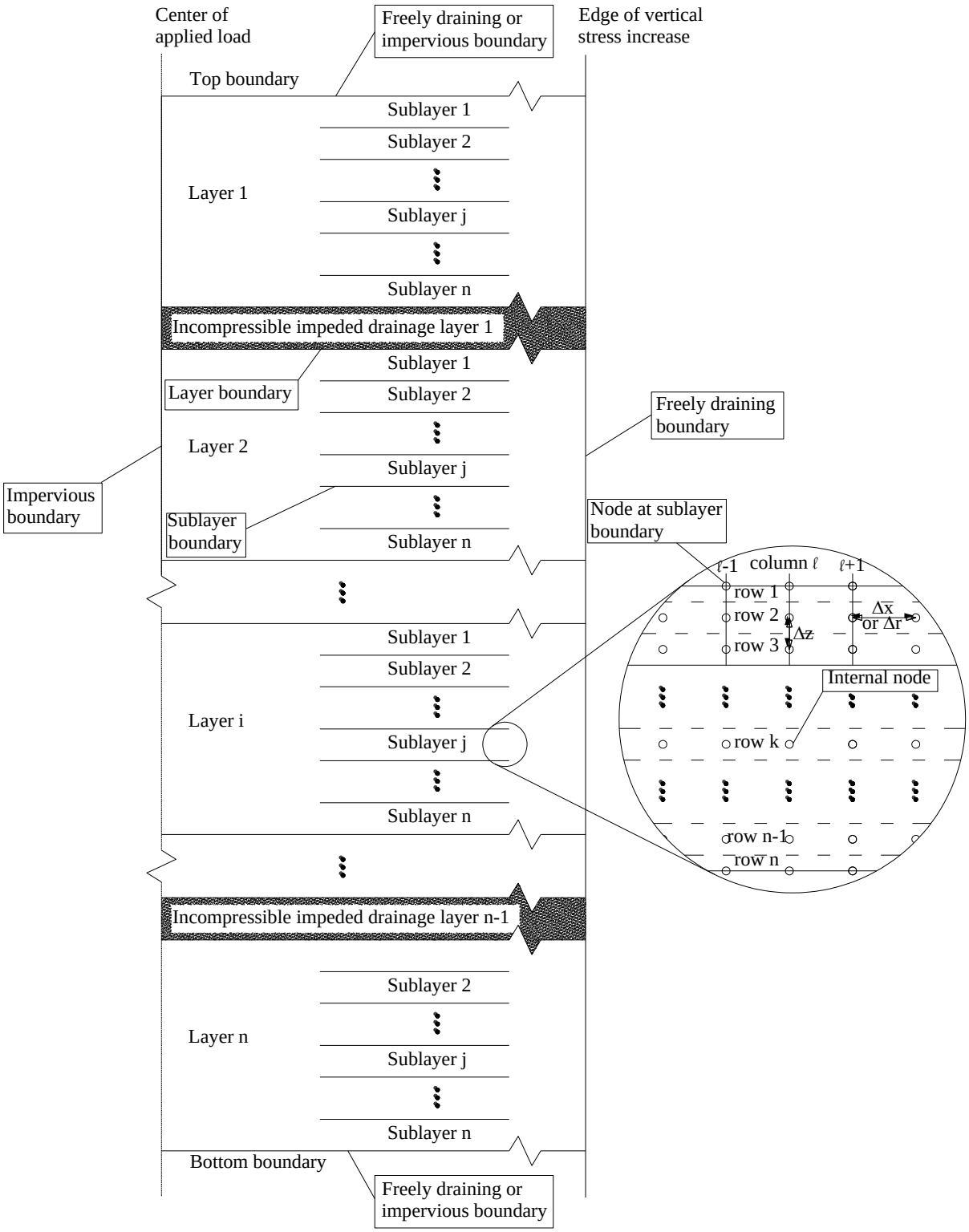

Figure 7-3 General setup for finite difference approximation of consolidation with incompressible impeded drainage layers.

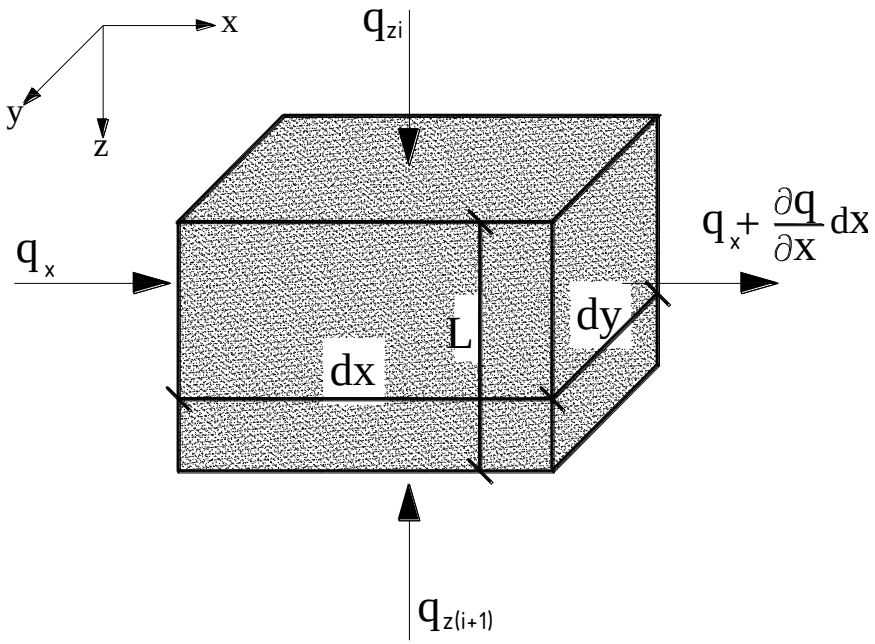

Figure 7-4 Sketch of two-dimensional flow element for impeded drainage layer.

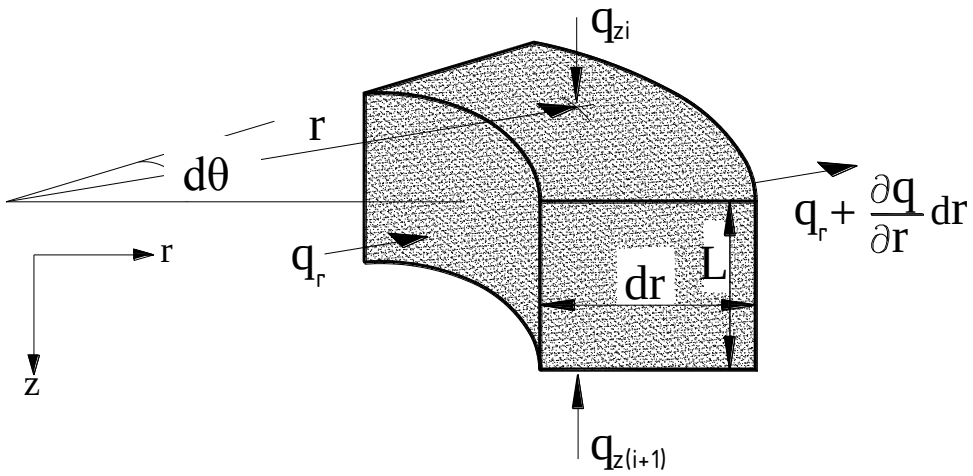

Figure 7-5 Sketch of axi-symmetric flow element for impeded drainage layer.

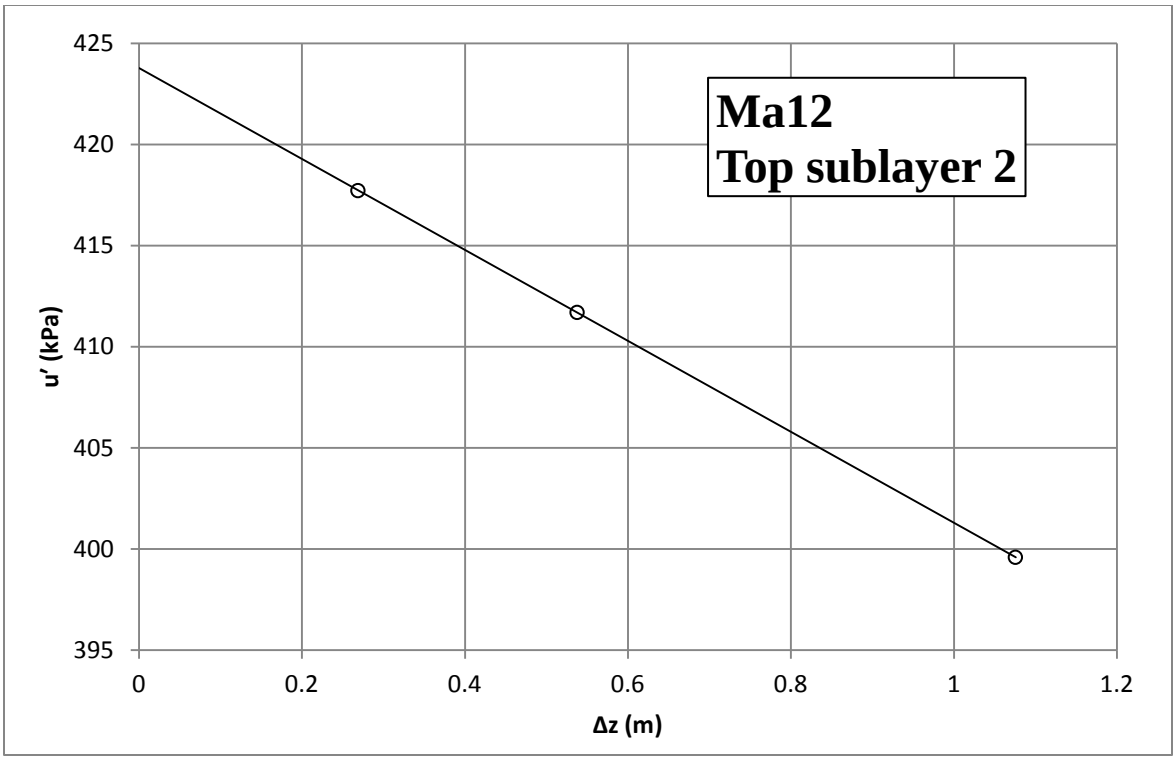

Figure 7-6 Excess porewater pressure at the top of sublayer 2 for marine clay layer Ma12 as a function of node spacing in the z direction (Δz).

CHAPTER 8 SETTLEMENT AND POREWATER PRESSURE PREDICTION AT KANSAI INTERNATIONAL AIRPORT USING THE ILLICON PROCEDURE

8.1 Introduction

The Kansai International Airport Islands are located in the southern portion of Osaka Bay nearly 5km from the Senshu coast. Construction of the 511ha Island I began in January 1987 in approximately 18m deep water (Arai, 1991). Construction of the 545ha Island II began in July 1999 in approximately 20m deep water (Shinohara, 2003; Tabata and Morikawa, 2005). The average seabed settlement in December 2012 was 12.92m and 14.25m for Island I and Island II, respectively (NKIAC, 2012).

Settlement analyses were performed for the five locations shown in Figure 8-1 as part of this study. The vertical compression of Ma13 was computed at Monitoring Point 1 of Island II (MP1-II), Monitoring Point 2 of Island II (MP2-II), the Connecting Taxiway (CT), Point K of Island I (K-I), and Monitoring Point 1 of Island I (MP1-I). Settlement of the Pleistocene layers was calculated for MP1-II, MP2-II, and MP1-I.

8.2 Subseabed condition

The subseabed profile underlying the Kansai Airport Islands consists of a Holocene marine clay layer (Ma13) and alternating sand (Ds), marine clay (Ma), and non-marine clay (Doc or NMC) Pleistocene layers. Figure 8-2 shows the available information on the subseabed profiles for the five locations shown in Figure 8-1. Marine clay layers were deposited in warmer climates when sea levels were relatively high and sand and non-marine clay layers were deposited in colder climates when sea levels were lower (Ikebe et al., 1970; Itihara et al., 1975; Takatsugi and Hyodo, 1995; Yamasaki and Nakada, 1996; Biswas et al., 1999; Itoh et al., 2000, 2001; Takemura and Nakaseko, 2005). Marine clay layers are distinguishable from non-marine clay layers because of the presence of nannoplankton and foraminifera calcareous fossils. Layer Dtc was determined to be a shallow marine clay layer because it lacks these nannofossils (Itoh et al., 2001). Freshwater clays contain fossils of the same mollusca that currently live in Lake Biwa which is located just to the Northeast of Osaka Bay (Ikebe et al., 1970). The non-marine clay layer Doc5 was deposited in a lacustrine environment, known as paleo-Lake Senshu, 0.5 to 0.4 million years before present when sediments were dammed as a result of crustal warping in the

southern portion of Osaka Basin (Itoh et al., 2001).

The rise and fall of sea level over geologic time has had an impact on the change in mineralogical composition with depth within individual clay layers as evidenced by the water-holding capacity of the clay soils. An example of this is seen in Figure 4-11 (Chapter 4) which shows natural water content and Atterberg limit data for Ma13. The water-holding capacity of Ma13 is smallest at the bottom of the layer close to sand layer Ds1 and highest at the top of the layer indicating that the fine particles deposited at the beginning of the Holocene Epoch were larger and less plate-shaped than the fine particles deposited later in the Holocene Epoch. The sea level rise has caused the distance from the Kansai Airport site to the mouth of the sediment-carrying rivers to increase, thereby increasing the distance sediment must travel; only very small, plate-shaped particles are capable of traveling large distances in suspension. Several of the marine clay layers (e.g. Ma10, Ma9, Ma8, and Ma7) have lower reported liquid limit values near their upper and lower boundaries with the highest liquid limit values near the mid-depth of the layer. Again, this indicates the possible influence of the rise and fall of sea level on the relative proportion of clay mineral particles with depth within each of these clay layers.

The Holocene marine clay layer and Pleistocene clay layers were subdivided based on data reported in the literature on w_o, w_p, and w_ℓ (Maeda et al., 1990; Akai and Tanaka, 1999; Tanaka and Locat, 1999; Watabe et al., 2002; Tanaka et al., 2003, 2004; Imai et al., 2005), CF (Akai and Tanaka, 1999; Watabe et al., 2002; Tanaka and Locat, 1999), Gs and γ (Akai and Tanaka, 1999), as well as $\sigma'_p/\ \sigma'_{vo}$ (Kanda et al., 1991; Watabe et al., 2002; Tanaka et al., 2003, 2004; Tanaka, 2005; Tsuchida, 2005; Furudoi and Kobayashi, 2009). Table 8-1 summarizes representative values of these parameters for each sublayer. The natural water content and Atterberg limit values reported in Table 8-1 represent the average of all of the available data from boreholes at the Kansai Airport site for each sublayer, and these values were used for subsequent settlement analyses of Ma13 at MP1-II, MP2-II, CT, K-I, and MP1-I, and the Pleistocene clay layers at MP2-II and MP1-I. Natural water content, Atterberg limits and initial void ratio reported specifically for the Pleistocene clay layers at MP1-II (Imai et al., 2005) were used directly for subsequent settlement analyses at that location (see Table 8-2 for values at MP1-II).

8.3 The Holocene marine clay layer (Ma13) underlying the Kansai Airport Islands

Islands I and II of Kansai Airport were constructed upon the Holocene marine clay layer Ma13. The observed compression of Ma13 is a significant portion of the observed seabed settlement at the Kansai Airport Islands. For example, in January 2009 observed compression of Ma13 was 8.6m and the total observed settlement was 14.4m at MP1-II (Furudoi and Kobayashi, 2009; NKIAC, 2012).

Forty centimeter diameter displacement type vertical sand drains fully penetrate Ma13 and form a drainage connection to the 1.5m thick sand blanket that was placed at the seabed, and to the underlying sand layer Ds1 across the Kansai International Airport site. The sand drains were installed on a 1.6m by 2.5m rectangular grid under the seawalls and a 2.5m by 2.5m square grid under the main reclamation for both islands (Nakase 1987, Maeda et al., 1990, Arai 1991, Yamakawa and Tsuruoka 1996, Shinohara 2003, Suzuki et al. 2003, Tabata and Morikawa 2005).

Seabed settlement was monitored using settlement plates and magnetic transmission hydraulic pressure gauges whereas settlement of the Pleistocene layers was monitored using anchor-rod and magnetic differential settlement gauges. Double tube settlement gauges were used to monitor seabed settlement and settlement of the Pleistocene layers (see Chapter 6). Observed vertical compression of Ma13 was determined by subtracting settlement of the Pleistocene layers from seabed settlement.

8.3.1 EOP e – log σ'_v relationships

Preconstruction effective vertical stress (σ'_{vo}), σ'_p, σ'_{vf}, and σ'_{vf}/σ'_p are summarized in Table 8-3 for all five locations shown in Figure 8-1. The preconstruction porewater pressure is assumed to be hydrostatic from sea level (see Chapter 4). The final effective vertical stresses were computed from the following equation:

$$\sigma'_{vf} = \sigma'_{vo} + \Delta\sigma_v \qquad (8-1)$$

where $\Delta\sigma_v$ is the increase in vertical stress, according to the elastic stress distribution. Because the thickness of Ma13 is relatively small (15m to 24m) compared to the areal extent of the airport islands, there was no reduction in $\Delta\sigma_v$ with depth for Ma13. This assumption was checked by dividing the airport islands into rectangular areas and superimposing the Boussinesq solution

for uniformly loaded rectangular areas. The maximum reclamation load at seabed according to load cell measurements is in the range of 506 to 651 at MP1-II (Kobayashi et al., 2005; Tabata and Morikawa, 2005; Furudoi, 2010) and in the range of 535 to 540 at MP2-II (Tabata and Morikawa, 2005; Nishimura, personal communication, 2011). The maximum calculated reclamation load at seabed was reported as approximately 470kPa at CT (Furudoi and Kobayashi, 2009), 460kPa at K-I (Kobayashi et al., 2005; Furudoi, 2010), and 455kPa at MP1-I (Kobayashi et al., 2005; Shibata and Karube, 2005). Figure 8-2 shows that σ'_{vf} resulting from construction of the Airport Islands is 4 to 25 times σ'_p within Ma13.

To construct the EOP e – log σ'_v relationships, first the point (σ'_{vo}, e_o) was defined. Then, the recompression curve from σ'_{vo} to σ'_p was constructed assuming C_r/C_c' equal to 0.1 where C_c' is the secant compression index defined at σ'_{vf} / σ'_p equal to 2. The compression curve beyond σ'_p was defined using the following equation:

$$e = e_{pp} - C_c' \times \log\left(\frac{\sigma_v'}{\sigma_p'}\right) \qquad (8-2)$$

where e_{pp} is the end-of-primary void ratio at σ'_p. Secant compression indices (C_c') were obtained from Figure 4-41 for Ma13. Seven (σ'_v /σ'_p, C_c') data points were used to construct the compression curve beyond σ'_p for each sublayer.

Figure 8-3 shows the EOP e - log σ'_v relationships constructed for Ma13 at MP1-II, MP2-II, CT, K-I, and MP1-I.

8.3.2 Coefficient of permeability of Ma13

The initial vertical permeability for each sublayer was assigned based on rate of compression from incremental loading oedometer data interpreted according to the Terzaghi theory of consolidation (Figure 4-33) reported in Tanaka et al. (2003). Values of permeability that are computed this way are often smaller than directly measured values by a factor of 2 (Mesri et al., 1994). The difference in computed and measured values is due, in part, to the changes in compressibility and permeability of clay during a pressure increment that are not taken into account in the Terzaghi consolidation theory. Computed and measured values are also different because the Terzaghi consolidation theory does not consider compressibility with respect to time at a constant effective stress. Therefore, k_{vo} values delineated in Figure 4-33 were

increased by a factor of 2.

Permeability is commonly expressed as a function of void ratio. A widely-used permeability - void ratio relationship that is employed for settlement analyses is based on $C_k = \Delta e/\Delta \log k$ = constant, where C_k is the change-in-permeability-index (Raymond, 1969; Mesri and Rokhsar, 1974; Burghignoly and Vestroni, 1975; Tavenas et al., 1983b). The change-in-permeability-index (C_k) can be determined from routine oedometer tests or through direct permeability measurements. There were not sufficient oedometer test data or direct permeability measurements available at the Kansai International Airport site to determine C_k; therefore, the empirical relationship $C_k = 0.5e_o$ was employed for subsequent settlement analyses (Tavenas et al., 1983b; Mesri et al., 1994).

Clay and silt deposits of marine origin generally have a flocculated random fabric and, therefore, permeability anisotropy (k_h/k_v) rarely exceeds 1.5 and is often near 1.0 (Mesri et al. 1994). Therefore, k_h/k_v equal to 1 was used for the Ma13 analyses at Kansai Airport.

Table 8-4 summarizes k_{vo} and C_k for each sublayer of the Holocene marine clay layer. The change-in-permeability-index has been correlated to C_c, and typical values of 0.5 to 2 have been reported (Mesri and Rokhsar, 1974). According to the C_k values reported in Table 8-4 and the C_c' data reported in Figure 4-41, C_k/C_c' ranges from 0.63 to 0.79 for the Osaka Bay Holocene clay where C_c' is the secant compression index defined at σ'_{vf} / σ'_p equal to 2.

8.3.3 Coefficient of permeability of Ds1, vertical sand drains, and sand blanket

Figure 8-4 shows excess porewater pressure observed in the sand layer Ds1 together with load cell measurements at MP1-II. The load cells were installed in the 1.5m sand blanket placed above Ma13. Observed excess porewater pressure was reported as high as 130kPa in sand layer Ds1. Several investigators (Arai, 1991; Endo et al., 1991; Kobayashi et al., 2005; Mimura and Jang, 2005), however, have assumed that Ds1 is freely draining for time rate of settlement calculations. The current version of the ILLICON computer program that was used to perform subsequent settlement analyses requires that the bottom boundary is either impervious or freely draining. Therefore, Ds1 is assumed to be freely draining.

Arai et al. (1991) describe the material used for the vertical sand drains as having an effective grain size equal to 0.3 to 0.4mm and a uniformity coefficient equal to 2 to 3, and Tabata and Morikawa (2005) indicate that the sands used for the vertical drains have a fine-grain

fraction less than 10%. Assuming Arai et al. (1991) were referring to D_{10} as the effective grain size, the following equation proposed by Allen Hazen (1892) for permeability of clean, loose, well rounded, uniform filter sands may be used to approximate the permeability of the vertical sand drains used at the Kansai Airport site:

$$k = C_{10} \times D_{10}^2 \qquad (8-3)$$

Data presented in Terzaghi et al. (1996) indicate an average value of C_{10} equal to 10^{-2} when k is expressed in m/s and D_{10} in mm. The permeability of the vertical sand drains according to Equation 8-3 is approximately equal to 0.0009 to 0.0016m/s for D_{10} equal to 0.3 to 0.4mm, respectively. Therefore, permeability of the vertical sand drains equal to 0.0012m/s is used for subsequent settlement analyses.

As mentioned previously, a sand blanket was placed above Ma13 prior to installation of vertical sand drains. Tabata and Morikawa (2005) describe the material used for the sand blanket as sea sand with a fine-grain fraction less than 10%. Observed porewater pressures presented in Arai et al. (1991) indicate that the excess porewater pressure remains close to zero within the sand blanket during and following application of the reclamation load at K-I. Therefore, the upper boundary of Ma13 is assumed to be freely draining for subsequent settlement analyses.

8.3.4 Smear zone around vertical sand drains

Installation of vertical drains disturbs soil adjacent to the drain. This disturbance increases the compressibility and decreases the permeability of the soil surrounding the drain. Disturbance from drain installation is similar to disturbance resulting from installation of displacement piles. The radial extent of disturbance has been evaluated by porewater pressure measurements, water content, and undrained shear strength. Bjerrum and Johannessen (1960) and Lo and Stermac (1965) reported excess pore water pressures from pile installation observed up to a distance of 15 pile diameters from the installed pile. Holtz and Holm (1973) measured water content at various radial distances from vertical sand drains at Ska-Edeby and found that the water content values reduced for soils sampled closer to the drain. They suggested that the ratio of smear zone radius to drain radius (r_s/r_w) is equal to 2.1 to 2.7. Fellenius and Samson (1976) found that the undrained shear strength of a sensitive soil in Canada was reduced by 10 to 20% at a distance of 2 pile diameters from the center of the installed piled immediately after

installation. Roy et al. (1981) presented vane strength data for St. Alban clay that showed a substantial reduction up to 4 pile diameters away. Mesri and Lo (1991) show data indicating that the smear zone typically extends from one to two times the radius of the mandrel or pipe casing used to install the vertical drain.

After placement of the 1.5m thick sand blanket, a steel pipe casing fitted with a lid was advanced into the ground with a vibrating pile driver into the sand layer Ds1 underlying Ma13. After the steel pipe was filled with sand, a withdrawal winch removed the pipe from Ma13 leaving a sand column (Yamakawa and Tsuruoka, 1996).

The effects of disturbance have been incorporated in subsequent settlement analyses by including a smear zone with a diameter equal to 80cm (two times the diameter of the vertical sand drains). A linear EOP e – log σ'_v relationship is assumed for the soil in the smear zone that is defined by the points (σ'_{vo}, e_o) and (σ'_{vf}, e_p) where e_p is the EOP void ratio corresponding to σ'_{vf}.

Figure 8-5 shows a plan view of the vertical sand drains beneath the reclaimed land at Kansai Airport. The magnitude of EOP compression was computed considering only soil within the undisturbed zone. Time rate of compression calculations were made at the point farthest from the vertical drain. Permeability anisotropy (k_h/k_v) equal to unity within the smear zone is used for subsequent settlement analyses. Including the smear zone in the analysis decreases the calculated time rate of compression for Ma13.

As mentioned previously, the vertical drains were installed on a 2.5m square grid beneath the reclamation; however, the radius of a circular cylinder influenced by the drain (r_e) is required as input for the ILLICON computer program used for subsequent settlement analyses. Therefore, an equivalent radius was calculated using the following equation (Lo, 1991):

$$\pi \times r_e^2 = (DS)^2 \qquad (8-4)$$

where DS is the drain spacing (equal to 2.5m for Kansai Airport). The radius of the soil cylinder influenced by the drain is 0.525(DS) = 1.41m.

8.3.5 Settlement analyses for Ma13

Table 8-5 shows values of e_o, σ'_{vo}, σ'_p / σ'_{vo}, σ'_{vf} / σ'_p, C_c' at σ'_{vf}, and calculated EOP vertical compression for each sublayer of Ma13 at each of the five locations shown in Figure 8-1.

Figure 8-6, Figure 8-7, Figure 8-8, Figure 8-9, and Figure 8-10 show reclamation load at seabed and observed and computed vertical compression of Ma13 at MP1-II, MP2-II, CT, K-I, and MP1-I, respectively.

Only the reclamation load at seabed and the thickness of Ma13 (and therefore σ'_{vo} and σ'_{vf} for each sublayer) changed from location to location for the settlement analyses (i.e. the same values of σ'_p / σ'_{vo}, C_c', and permeability relationships were used at all five locations for the time rate of vertical compression calculations). There is good agreement between observed and computed vertical compression at each location.

The load at seabed versus time relationships include calculated load values (Kobayashi et al., 2005; Shibata and Karube, 2005; Tabata and Morikawa, 2005; Furudoi and Kobayashi, 2009; Furudoi, 2010; Nishimura, personal communication, 2011) as well as reported load cell measurements (Kobayashi et al., 2005; Tabata and Morikawa, 2005; Furudoi, 2010; Nishimura, personal communication, 2011). As mentioned previously, load cell measurements were reported for MP1-II and MP2-II. Figure 8-6a and Figure 8-7a show that while the load cell measurements reported for MP2-II are relatively consistent, reaching a maximum value approximately equal to 535kPa to 540kPa, the load cell measurements reported for MP1-II are different by as much as 140kPa (maximum load reported for load cell 1 is approximately equal to 506kPa and the maximum load reported for load cell 2 is approximately equal to 651). However, the variation of the load cell measurements as a function of time is nearly identical after May 2003 for MP1-II.

Calculated reclamation load at seabed versus time relationships reported by Furudoi and Kobayashi (2009), Furudoi (2010), and Shibata and Karube (2005) were used directly for settlement analyses at CT, K-I, and MP1-I, respectively. The average of reported load cell measurements at the seabed are used for settlement analyses at MP1-II and MP2-II.

8.4 The Pleistocene layers underlying the Kansai Airport Islands

Because Ma13 has reached end-of-primary consolidation from the reclamation loads, the majority of the long-term settlement for the Kansai Airport Islands will be a result of settlement of the Pleistocene clay layers. Magnetic differential settlement gauge observations that indicate the contribution to seabed settlement from individual Pleistocene clay layers, and pneumatic piezometer observations within the Pleistocene sand layers were reported at MP1-II, MP2-II, and MP1-I. Observed settlement of the Pleistocene layers was reported as 6.1m at MP1-II in May

2009 (Furudoi and Kobayashi, 2009), 5.1m at MP2-II in May 2011 (Nishimura, personal communication, 2011), and 5.8m at MP1-I in July 2005 (Rocchi et al., 2007).

Settlement analyses were performed for the Pleistocene layers using the ILLICON procedure at MP1-II, MP2-II, and MP1-I.

8.4.1 EOP e – log σ'_v relationships

Figure 8-11, Figure 8-12, and Figure 8-13 show preconstruction effective vertical stress (σ'_{vo}), preconsolidation pressure (σ'_p), and post-construction final effective vertical stress (σ'_{vf}) with depth at MP1-II, MP2-II, and MP1-I, respectively. The preconstruction porewater pressure is assumed to be hydrostatic from sea level (see chapter 4).

The final effective vertical stresses were computed using Equation 8-1. The increase in vertical stress ($\Delta\sigma_v$) was calculated two ways. In the first method, the airport islands were divided into five rectangular areas (Rectangles A, B, C, D, and E) as shown in Figure 8-14 and the Boussinesq solution for uniformly loaded rectangular areas was used. The contribution to $\Delta\sigma_v$ from each rectangular area was computed for each monitoring point and combined. In the second method, each airport island was treated as a uniformly loaded strip area where the width of the strip was set equal to the short dimension of the island. For this case, $\Delta\sigma_v$ produced by each island was computed separately (e.g. $\Delta\sigma_v$ produced by Island I was not included for the Island II analysis). Both methods were used to compute end-of-primary settlement. The second method was employed for time rate of settlement calculations with the ILLICON program.

To construct the EOP e – log σ'_v relationships, first the point (σ'_{vo}, e_o) was defined. Then, the recompression curve from σ'_{vo} to σ'_p was constructed assuming C_r/C_c' equal to 0.1 where C_c' is the secant compression index defined at σ'_{vf} / σ'_p equal to 2. The compression curve beyond σ'_p was defined using Equation 8-2. Secant compression indices (C_c') for the shallow marine clay layer, Dtc, were obtained from Figure 4-43. Secant compression indices (C_c') for the Pleistocene marine clay layers were obtained from Figure 4-44 which was prepared from published data for 34 oedometer tests. Four (σ'_v / σ'_p, C_c') data points were used to construct the compression curve beyond σ'_p for each sublayer.

Figure 8-15 through Figure 8-35 show the EOP e – log σ'_v relationships constructed for each sublayer at MP1-II, MP2-II, and MP1-I.

8.4.2 Coefficient of permeability of Pleistocene clay layers

Equation 4-1 from Mesri et al. (1994) was used to calculate k_{vo} for each sublayer of the Pleistocene marine clay layers using representative values of e_o, w_p, w_n, and CF. The clay-size fraction data used to develop Equation 4-1 with C equal to 6.5e-11 (for k_v in m/s) was taken as the percentage of particles with an equivalent spherical diameter less than 2μm (Mesri et al., 1994). The clay-size fraction data reported in Akai and Tanaka (1999) and Watabe et al. (2002) represent the percentage of particles with an equivalent spherical diameter less than 5μm (JIS A 1204) and the clay-size fraction data reported in Tanaka and Locat (1999) represent the percentage of particles with an equivalent spherical diameter less than 2μm. Therefore, the data presented in Tanaka and Locat (1999) was used to choose representative values of CF for each sublayer (see Chapter 4).

As with the Holocene marine clay layer (Ma13), the empirical relationship $C_k = 0.5e_o$ was employed for subsequent settlement analyses (Tavenas et al., 1983b; Mesri et al., 1994).

Table 8-5 summarizes k_{vo} and C_k for each sublayer of the Pleistocene marine clay layers. Tanaka et al. (2003) reported k_{vo} values in the range of $6x10^{-11}$ to $4x10^{-9}$ m/s for Pleistocene clay specimens. The k_{vo} values reported in Tanaka et al. (2003) were back-calculated based on rate of compression from incremental loading oedometer data interpreted according to the Terzaghi theory of consolidation. Additionally, Mimura and Jang (2005) used k_{vo} values in the range of $6.7x10^{-11}$ to $5.8x10^{-8}$ m/s for settlement analysis at MP1-1; however, Mimura and Jang (2005) do not describe how they arrived at the permeabilities they assumed for their analysis. Additionally, Shibata and Karube (2005) performed a finite element analysis that included both Island I and Island II of Kansai Airport. They used k_{vo} values ranging from $1.3x10^{-10}$ to $8.8x10^{-10}$ m/s for the Pleistocene clay layers in their analysis without much justification. The k_{vo} values reported in Table 8-5 are comparable to the range of values reported in Tanaka et al. (2003), Mimura and Jang (2005), and Shibata and Karube (2005).

According to the C_k values reported in Table 8-5 and the C_c' data reported in Figure 4-43 and Figure 4-44, C_k/C_c' is approximately equal to 0.8 with a relatively narrow range for the shallow marine clay layer, Dtc, and 0.4 to 0.6 for the other Pleistocene marine clays where C_c' is the secant compression index defined at σ'_{vf} / σ'_p equal to 2.

8.4.3 Settlement analyses for Pleistocene layers at MP1-II

Table 8-7 shows end-of-primary compression for each layer at MP1-II calculated using both methods previously described for determining $\Delta\sigma_v$. The end-of-primary vertical compressions computed for the uniformly loaded rectangular areas assumption are comparable to the end-of-primary vertical compressions computed for the uniformly loaded strip area assumption. This is not surprising because the depth of the deposits considered in the calculation is small compared to the area of the airport islands. According to Table 8-7, calculated end-of-primary settlement of the Pleistocene layers is 15.22m for the uniformly loaded rectangular area assumption and 15.49m for the strip load assumption. The time rate of settlement analysis with ILLICON was performed using the uniformly loaded strip assumption. As mentioned previously, Island II was considered separately from Island I (i.e. $\Delta\sigma_v$ produced by Island I was not included for the Island II analysis).

Figure 8-36 shows the boundary conditions for the ILLICON analysis. The initial thicknesses, compressibility relationships, and permeability relationships are assumed constant in the x direction for each clay sublayer. The distance in the x direction from the centerline of Island II to the freely draining horizontal boundary (2736m) was selected to be twice the short dimension of Island II (1368m). At this value of x, $\Delta\sigma_v$ was less than 2 kPa when the maximum reclamation load at seabed equal to 580kPa was applied. Water flow in the z and x directions within the clay layers was modeled according to Equation 7-15. However, the thickness of the individual clay layers is small compared to the area over which the uniform reclamation load was applied at the seabed, and therefore, the horizontal component of flow within the clay layers does not increase the rate of consolidation for these layers (i.e. water flow resulting from consolidation of the clay layers is primarily in the z direction). Permeability anisotropy was assumed to be equal to unity. Water flow in the x direction within the sand layers was modeled according to Equation 7-53.

The ILLICON program was used to back-calculate equivalent permeabilities (k_{eq}) for the Pleistocene sand layers from settlement and porewater pressure observations so that the long term settlement of the Pleistocene layers could be determined. Table 8-8 shows k_{eq} for the Pleistocene sand layers in the upper portion of the profile at MP1-II. Sand layers Ds1 (below Ma13) and Ds10 (below Doc6) were assumed to be freely draining. For ILLICON to successfully model the sand layers as incompressible impeded drainage layers, the permeability

of those layers must be greater than the permeability of the adjacent clay layers. It was not possible to select a permeability that was low enough for sand layers Ds2 and Ds3U to reasonably explain the observed vertical compression and excess porewater pressure data and to have the computer program run successfully. Therefore, any contribution to horizontal drainage provided by these layers was not modeled. An equivalent permeability equal to 10^{-5} m/s was assigned to the Pleistocene sand layers in the lower part of the profile (below Doc6). The solution was not sensitive to changes in k_{eq} within these lower Pleistocene sand layers because the clay layers below Doc6 remain in the recompression range for post-construction σ'_{vf}. The permeability values reported in Table 8-8 are comparable to values used by Mimura and Jang (2005) and Shibata and Karube (2005) for their analyses at Kansai Airport (see Chapter 4).

Secondary compression of the Pleistocene clay layers was computed based on the C_α/C_c law of compressibility (Mesri and Godlewski, 1977, 1979) using the following equation:

$$S_\alpha = \frac{C_c}{1+e_o}\frac{C_\alpha}{C_c} L_o \log\frac{t}{t_p} \qquad (8-5)$$

where t_p is the time to end-of-primary consolidation. If σ'_{vf} / σ'_p is less than 0.9, then the C_c term in Equation 8-5 was set equal to C_r. If σ'_{vf} / σ'_p is greater than 0.9 but less than 1.0, then the C_c term in Equation 8-5 was set equal to the maximum C_c for the deposit (i.e. C_c just beyond the preconsolidation pressure for the end-of-primary e – log σ'_v relationship). Finally, if σ'_{vf} / σ'_p is greater than 1.0, then the C_c term in Equation 8-5 was set equal to the value of C_c at the current void ratio for the EOP e – log σ'_v relationship.

Figure 8-37 and Figure 8-38 show observed and calculated settlements for the Pleistocene layers through the year 2010 and 2100, respectively. Table 8-9 gives the date when EOP consolidation was reached, σ'_{vf}/σ'_p, end-of-primary compression, compression in December 2012, and secondary compression in the year 2100 for each Pleistocene clay layer at MP1-II. As expected the lower layers reach EOP consolidation relatively quickly (e.g. Ma4 reached end-of-primary 5.6 years after July 1999) because the post-construction σ'_{vf} is less than σ'_p for these layers.

Figure 8-39 shows observed and calculated excess porewater pressure with time in Pleistocene sand layers Ds2, Ds4, Ds5, Ds6, and Ds9. There is relatively good agreement between computed and observed excess porewater pressure for Ds2, Ds4, and Ds5. The computed excess porewater pressure is smaller than the observed values for sand layers Ds6

(located between Ma10 and Ma9) and Ds9 (located between Ma8 and Ma7). In fact, the observed excess porewater pressures show virtually no dissipation for Ds6 and Ds9.

It's possible that some of the pneumatic piezometers malfunctioned at the Kansai Airport site. Akai and Tanka (1999) made the following statement regarding porewater pressure observations for the Kansai Airport Project:

> "The progress of consolidation within these Pleistocene clays have been monitored by pore pressure sensors and a vertical array of settlement gauges in bore holes to obtain the local compressions along the hole. Several of such instrumented bore holes are located on KIA, but only few gave a good set of both pore pressure and local compression measurements because of the difficulty of installing many instruments in such a deep hole."

Pneumatic piezometers have been known to malfunction as a result of water entering the pressure lines (Dunnicliff, 1993).

The observed excess porewater pressures in the Pleistocene sand layers suggest that there will be considerably more primary consolidation in some of the adjacent Pleistocene clay layers.

8.4.4 Settlement analyses for Pleistocene layers at MP2-II

Table 8-10 shows end-of-primary compression for each layer at MP2-II calculated using $\Delta\sigma_v$ for the uniformly loaded rectangular areas assumption and $\Delta\sigma_v$ for the uniformly loaded strip area assumption. Calculated end-of-primary settlement of the Pleistocene layers is 13.1m for the uniformly loaded rectangular area assumption and 12.6m for the strip load assumption.

Table 8-11 shows the back-calculated equivalent permeabilities for the Pleistocene sand layers in the upper portion of the profile at MP2-II. As for the analysis at MP1-II, the equivalent permeabilites of the Pleistocene sand layers were back-calculated from settlement and porewater pressure observations reported for MP2-II so that long-term settlement of the Pleistocene layers could be determined. The computed values of k_{eq} at MP1-II and MP2-II are not identical, partly because of the 2.5km distance of these two locations in a flood plain depositional environment, and also because of the assumed drainage boundary condition for interpretation of compression and water flow at MP1-II and MP2-II. Sand layers Ds1 (below Ma13) and Ds10 (below Doc6)

were assumed to be freely draining. An equivalent permeability equal to 10^{-5} m/s was assigned to the Pleistocene sand layers in the lower part of the profile (below Doc6).

Figure 8-40 and Figure 8-41 show observed and calculated settlements for the Pleistocene layers through the year 2010 and 2100, respectively. Table 8-12 gives the date when EOP consolidation was reached, $\sigma'_{vf}/\ \sigma'_{p}$, end-of-primary compression, compression in December 2012, and secondary compression in the year 2100 for each Pleistocene clay layer at MP2-II.

Figure 8-42 shows observed and calculated excess porewater pressure with time in Pleistocene sand layers Ds2, Ds3U, Ds4, Ds5, Ds6, Ds7, Ds8, and Ds9. There is relatively good agreement between computed and observed excess porewater pressures for each of these Pleistocene sand layers except Ds9. As for MP1-II, the observed excess porewater pressures show virtually no dissipation for Ds9.

8.4.5 Settlement analyses for Pleistocene layers at MP1-I

Table 8-13 shows end-of-primary compression for each Pleistocene clay layer at MP1-I calculated using $\Delta\sigma_v$ for the uniformly loaded rectangular areas assumption and $\Delta\sigma_v$ for the uniformly loaded strip area assumption. Calculated end-of-primary settlement of the Pleistocene layers is 10.5m for the uniformly loaded rectangular area assumption and 10.5m for the strip load assumption because this point is close to the center of Island I.

Table 8-14 shows back-calculated equivalent permeabilities for the Pleistocene sand layers in the upper portion of the profile at MP1-I. As for the analysis at MP1-II and MP2-II, the equivalent permeabilites of the Pleistocene sand layers were back-calculated from settlement and porewater pressure observations reported for MP1-I, so that long-term settlement of the Pleistocene layers could be determined. Sand layers Ds1 (below Ma13) and Ds10 (below Doc6) were assumed to be freely draining. An equivalent permeability equal to 10^{-5} m/s was assigned to the Pleistocene sand layers in the lower part of the profile (below Doc6).

Figure 8-43 and Figure 8-44 show observed and calculated compression for the Pleistocene clay layers Ma7, Doc5, Ma10, and Ma12 as well as compression of all Pleistocene layers through the year 2010 and 2100, respectively. Table 8-15 gives the date when EOP consolidation was reached, $\sigma'_{vf}/\ \sigma'_{p}$, end-of-primary compression, compression in December 2012, and secondary compression in the year 2100 for each Pleistocene clay layer at MP1-I. Because the thicknesses of the Pleistocene clay layers below Ds10 were estimated based on

boring data further offshore, calculated Pleistocene settlement is shown with and without the contribution of those layers. For the case where Pleistocene clay layers below Ds10 are included, the layer thicknesses were estimated by reducing the thicknesses reported at borehole 56-9 (Furudoi and Kobayashi, 2009).

Figure 8-45 shows observed and calculated excess porewater pressure with time in Pleistocene sand layers Ds3, Ds6, and Ds7. There is relatively good agreement between computed and observed excess porewater pressures for the Pleistocene sand layers. Note that observed excess porewater pressures at MP1-I increase in 1999 as a result of Island II reclamation.

8.5 Seabed settlement

As part of the original design considerations, the surface elevation of the airport islands were to remain high enough to avoid the erosive action of waves overtopping the seawall. Arai (1991) made the following statement regarding Island I:

> "The surface elevation of the island is specified to be not lower than [Chart Datum Level] C.D.L. +4m after 50 years from the opening."

According to Figure 8-46 which shows elevations at various points on Island I referenced to CDL in December 2012, much of the surface elevation of Island I is already below +4m CDL.

Figure 8-47 shows seabed settlement for MP1-I. The seabed settlement is calculated both with and without the Pleistocene clay layers below Ds10 included. According to Figure 8-46 and Figure 8-47, Island I MP1 will be at sea level in August 2067.

Figure 8-48 and Figure 8-49 show seabed settlement at MP1-II and MP2-II, respectively. Shinohara (2003) made the following statement regarding the fill height above the seabed for Island II:

> "The total thickness of [reclamation fill] from the seabed up to the final ground surface amounts to 40 to 43m, including the sand blanket."

This statement is consistent with the following statement made by Tabata and Morikawa

(2005):

> "The average thickness of the reclamation layer will amount to more than 40m and the soil required is expected to be around 250 million m^3."

According to the calculated seabed settlements shown in Figure 8-48 and Figure 8-49 and assuming height of reclamation fill above seabed equal to 43m, MP1-II and MP2-II will reach +4m CDL in September 2023 and January 2034, respectively. Additionally, MP1-II will be at sea level in January 2056, and MP2-II will be at sea level in February 2080, according to the time rate of settlement calculation.

8.6 Tables

Table 8-1 Representative subsurface data for the Kansai Airport Site.

Layer	Sublayer	w_o (%)	w_p (%)	w_l (%)	I_p (%)	CF (%)	Gs	e_o	γ (kN/m^3)	σ'_p/σ'_{vo}
Ma13	1	110	35	102	67	45	2.67	2.933	14.5	2.1
	2	96	35	99	64	45	2.67	2.560	14.7	1.6
	3	86	32	90	58	45	2.67	2.293	15.0	1.5
	4	74	30	78	48	45	2.67	1.973	15.4	1.5
	5	66	30	66	36	45	2.67	1.760	15.8	1.5
Dtc	1	44	25	55	30	17	2.70	1.195	16.7	1.5
	2	48	25	61	36	30	2.70	1.297	16.7	1.5
	3	40	24	58	33	32	2.70	1.070	16.7	1.5
Ma12	1	79	38	104	65	35	2.66	2.101	14.8	1.4
	4	55	29	76	47	39	2.66	1.453	15.3	1.4
Doc1	1	47	22	71	48	29*	2.68*	1.260	16.4	1.4
Ma11U	1	56	30	79	49	38	2.71	1.510	16.5	1.4
	2	41	26	62	36	40	2.71	1.112	16.5	1.4
Ma11L	1	49	28	70	42	29	2.69	1.328	16.7	1.4
Ma10	1	43	30	72	42	30	2.69	1.171	16.9	1.5
	2	56	35	92	57	23	2.69	1.499	16.4	1.5
	3	64	37	102	65	27	2.69	1.731	15.4	1.5
	4	48	32	84	52	29	2.69	1.292	17.1	1.5
Ma9	1	55	35	91	57	28	2.69	1.480	16.5	1.3
	2	51	34	90	56	39	2.69	1.383	16.4	1.3
Doc5	1	63	39	105	66	36	2.63	1.645	15.2	1.35
	4	52	36	84	47	52	2.63	1.378	16.4	1.35
Ma8	1	44	31	83	51	33	2.70	1.174	17.5	1.3
	2	54	36	91	56	33	2.70	1.448	16.9	1.3
	3	46	32	60	28	33	2.70	1.241	15.6	1.3
Ma7	1	48	33	80	46	28	2.68	1.280	17.1	1.28
	2	54	37	96	59	29	2.68	1.460	16.0	1.28
	3	46	33	83	50	45	2.68	1.231	17.1	1.28
Doc6	1	46	34	89	54	36	2.68*	1.243	16.4	1.28
Ma4	1	49	34	87	53	30	2.68*	1.303	16.4	1.3
Ma3	1	50	35	86	50	29	2.68*	1.348	17.2	1.35
Ma2	1	41	31	82	51	28	2.68*	1.096	16.4	1.35
NMC-1	1	35	29	78	50	26	2.68*	0.927	16.4	1.35
NMC-2	1	29	23	57	34	30	2.68*	0.774	16.4	1.35
NMC-3	1	32	24	63	38	21	2.68*	0.865	16.4	1.35
Ma1	1	39	32	84	51	26	2.68*	1.036	16.4	1.3
NMC-4	1	25	18	35	16	6	2.68*	0.659	16.4	1.3
Ma0	1	32	25	63	38	14	2.68*	0.861	16.4	1.4
NMC-5	1	19	25	62	37	12	2.68*	0.515	16.4	1.4

*Value assigned based on average of available data.

Table 8-2 Subsurface data for the Kansai Airport Site. Information specific to MP1-II given for w_o, w_p, w_l, I_p, and e_o.

Layer	Sublayer	w_o (%)	w_p (%)	w_l (%)	I_p (%)	CF (%)	Gs	e_o	γ (kN/m^3)	σ'_p/σ'_{vo}
Ma13	1	110	35	102	67	45	2.67	2.933	14.5	2.1
	2	96	35	99	64	45	2.67	2.560	14.7	1.6
	3	86	32	90	58	45	2.67	2.293	15.0	1.5
	4	74	30	78	48	45	2.67	1.973	15.4	1.5
	5	66	30	66	36	45	2.67	1.760	15.8	1.5
Dtc	1	48	25	61	36	17	2.70	1.307	16.7	1.5
	2	53	24	69	45	30	2.70	1.426	16.7	1.5
	3	38	23	58	35	32	2.70	1.028	16.7	1.5
Ma12	1	85	41	108	67	35	2.66	2.253	14.8	1.4
	2	67	35	92	57	39	2.66	1.769	15.3	1.4
Doc1	1	47	22	71	48	29*	2.68*	1.260	16.4	1.4
Ma11U	1	58	33	86	53	38	2.71	1.565	16.5	1.4
	2	40	23	63	40	40	2.71	1.083	16.5	1.4
Ma11L	1	55	31	82	51	29	2.69	1.480	16.7	1.4
Ma10	1	39	29	66	38	30	2.69	1.041	16.9	1.5
	2	51	36	95	59	23	2.69	1.385	16.4	1.5
	3	63	38	105	67	27	2.69	1.696	15.4	1.5
	4	52	36	89	54	29	2.69	1.390	17.1	1.5
Ma9	1	55	37	99	62	28	2.69	1.483	16.5	1.3
	2	52	36	95	59	39	2.69	1.405	16.4	1.3
Doc5	1	63	40	110	70	36	2.63	1.658	15.2	1.35
	2	50	36	96	59	52	2.63	1.323	16.4	1.35
Ma8	1	43	33	89	56	33	2.70	1.172	17.5	1.3
	2	55	38	101	63	33	2.70	1.493	16.9	1.3
	3	45	32	76	44	33	2.70	1.212	15.6	1.3
Ma7	1	39	29	67	38	28	2.68	1.043	17.1	1.28
	2	52	37	100	63	29	2.68	1.404	16.0	1.28
	3	46	34	86	52	45	2.68	1.220	17.1	1.28
Doc6	1	46	34	89	54	36	2.68*	1.243	16.4	1.28
Ma4	1	47	34	87	52	30	2.68*	1.251	16.4	1.3
Ma3	1	46	33	83	49	29	2.68*	1.257	17.2	1.35
Ma2	1	42	34	90	56	28	2.68*	1.125	16.4	1.35
NMC-1	1	35	29	78	50	26	2.68*	0.927	16.4	1.35
NMC-2	1	29	23	57	34	30	2.68*	0.774	16.4	1.35
NMC-3	1	32	24	63	38	21	2.68*	0.865	16.4	1.35
Ma1	1	39	32	84	51	26	2.68*	1.036	16.4	1.3
NMC-4	1	25	18	35	16	6	2.68*	0.659	16.4	1.3
Ma0	1	32	25	63	38	14	2.68*	0.861	16.4	1.4
NMC-5	1	19	25	62	37	12	2.68*	0.515	16.4	1.4

*Value assigned based on average of available data.

Table 8-3 Preconstruction effective vertical stress, σ'_p, σ'_{vf}, and σ'_{vf}/σ'_p for Ma13**.**

Sublayer	Sublayer Thickness (m)	σ'_{vo} (kPa)	σ'_p (kPa)	σ'_{vf} (kPa)	σ'_{vf}/σ'_p
MP1-II					
1	4.82	11	23	571	25
2	4.82	33	52	593	11
3	4.82	56	84	616	7
4	4.82	81	121	641	5
5	4.82	108	162	668	4
MP2-II					
1	4.77	11	22	544	24
2	4.77	32	52	565	11
3	4.77	56	83	589	7
4	4.77	80	120	613	5
5	4.77	107	160	640	4
CT					
1	4.14	9	19	479	25
2	4.14	28	45	498	11
3	4.14	48	72	518	7
4	4.14	69	104	539	5
5	4.14	93	139	563	4
K-I					
1	3.76	8	18	468	25
2	3.76	26	41	486	11
3	3.76	44	66	504	7
4	3.76	63	95	523	5
5	3.76	84	126	544	4
MP1-I					
1	3.46	8	16	463	25
2	3.46	24	38	479	11
3	3.46	40	60	495	7
4	3.46	58	87	513	5
5	3.46	77	116	532	4

Table 8-4 Initial vertical permeability and C_k for Ma13.

Sublayer	**k_{vo} (m/s)**	**C_k**
1	2.3E-08	1.47
2	1.1E-08	1.28
3	5.0E-09	1.15
4	2.2E-09	0.99
5	1.0E-09	0.88

Table 8-5 Summary for end-of-primary vertical compression calculations for Ma13.

Sublayer	Sublayer Thickness (m)	e_o	σ'_{vo} (kPa)	σ'_p/σ'_{vo}	σ'_{vf}/σ'_p	C_c' at σ'_{vf}	EOP Comp. Sublayer (m)	EOP Comp. Total (m)
MP1-II								
1	4.82	2.933	11	2.1	25	1.35	2.41	8.32
2	4.82	2.560	33	1.6	11	1.32	1.93	
3	4.82	2.293	56	1.5	7	1.24	1.61	
4	4.82	1.973	81	1.5	5	1.07	1.30	
5	4.82	1.760	108	1.5	4	0.96	1.07	
MP2-II								
1	4.77	2.933	11	2.1	24	1.35	2.35	8.13
2	4.77	2.560	32	1.6	11	1.32	1.89	
3	4.77	2.293	56	1.5	7	1.25	1.58	
4	4.77	1.973	80	1.5	5	1.08	1.26	
5	4.77	1.760	107	1.5	4	0.97	1.04	
CT								
1	4.14	2.933	9	2.1	25	1.35	2.07	7.10
2	4.14	2.560	28	1.6	11	1.32	1.65	
3	4.14	2.293	48	1.5	7	1.24	1.38	
4	4.14	1.973	69	1.5	5	1.07	1.10	
5	4.14	1.760	93	1.5	4	0.96	0.91	
K-I								
1	3.76	2.933	8	2.1	25	1.34	1.90	6.59
2	3.76	2.560	26	1.6	11	1.31	1.52	
3	3.76	2.293	44	1.5	7	1.23	1.28	
4	3.76	1.973	63	1.5	5	1.07	1.03	
5	3.76	1.760	84	1.5	4	0.96	0.86	
MP1-I								
1	3.46	2.933	8	2.1	25	1.32	1.76	6.17
2	3.46	2.560	24	1.6	11	1.29	1.42	
3	3.46	2.293	40	1.5	7	1.22	1.20	
4	3.46	1.973	58	1.5	5	1.05	0.97	
5	3.46	1.760	77	1.5	4	0.95	0.82	

Table 8-6 Initial vertical permeability and C_k assigned to each Pleistocene sublayer for subsequent settlement analyses.

	MP1-II		MP2-II		MP1-I	
Layer	**k_{vo} (m/s)**	**C_k**	**k_{vo} (m/s)**	**C_k**	**k_{vo} (m/s)**	**C_k**
Dtc	2.3E-09	0.65	2.6E-09	0.60	2.6E-09	0.60
	8.6E-10	0.71	9.8E-10	0.65	9.8E-10	0.65
	3.6E-10	0.51	4.6E-10	0.53	4.6E-10	0.53
Ma12	1.6E-09	1.13	1.2E-09	1.05	1.2E-09	1.05
	7.5E-10	0.88	6.4E-10	0.73	6.4E-10	0.73
Doc1	4.6E-10	0.63	6.4E-10	0.63	6.4E-10	0.63
Ma11U	5.5E-10	0.78	5.8E-10	0.76	5.8E-10	0.76
	2.3E-10	0.54	3.1E-10	0.56	3.1E-10	0.56
Ma11L	7.6E-10	0.74	8.2E-10	0.66	8.2E-10	0.66
Ma10	3.6E-10	0.52	4.5E-10	0.59	4.5E-10	0.59
	5.4E-10	0.69	8.0E-10	0.75	8.0E-10	0.75
	7.0E-10	0.85	8.1E-10	0.87	8.1E-10	0.87
	5.3E-10	0.70	4.2E-10	0.65	4.2E-10	0.65
Ma9	4.8E-10	0.74	6.1E-10	0.74	6.1E-10	0.74
	2.8E-10	0.70	3.0E-10	0.69	3.0E-10	0.69
Doc5	3.9E-10	0.83	4.4E-10	0.82	4.4E-10	0.82
	1.3E-10	0.66	2.4E-10	0.69	2.4E-10	0.69
Ma8	1.9E-10	0.59	2.4E-10	0.59	2.4E-10	0.59
	3.8E-10	0.75	4.6E-10	0.72	4.6E-10	0.72
	4.0E-10	0.61	1.1E-09	0.62	1.1E-09	0.62
Ma7	3.9E-10	0.52	5.6E-10	0.64	5.6E-10	0.64
	3.6E-10	0.70	4.9E-10	0.73	4.9E-10	0.73
	1.6E-10	0.61	1.8E-10	0.62	1.8E-10	0.62
Doc6	2.3E-10	0.62	1.8E-10	0.62	1.8E-10	0.62
Ma4	3.4E-10	0.63	3.8E-10	0.65	3.8E-10	0.65
Ma3	4.4E-10	0.63	5.5E-10	0.67	5.5E-10	0.67
Ma2	2.1E-10	0.56	2.4E-10	0.55	2.4E-10	0.55
NMC-1	1.5E-10	0.46	1.5E-10	0.46	1.5E-10	0.46
NMC-2	1.3E-10	0.39	1.3E-10	0.39	-	-
NMC-3	3.0E-10	0.43	3.0E-10	0.43	-	-
Ma1	2.1E-10	0.52	2.1E-10	0.52	2.1E-10	0.52
NMC-4	4.6E-09	0.33	4.6E-09	0.33	-	-
Ma0	4.8E-10	0.43	4.8E-10	0.43	4.8E-10	0.43
NMC-5	7.8E-11	0.26	7.8E-11	0.26	7.8E-11	0.26

Table 8-7 End-of-primary (EOP) compression corresponding to σ'_{vf} in Figure 8-11 for sublayers at MP1-II calculated using two assumptions for $\Delta\sigma_v$.

Layer	EOP compression rect. (m)	EOP compression strip (m)
Dtc	1.03	1.03
Ma12	2.80	2.80
Doc1	1.36	1.37
Ma11U	1.38	1.38
Ma11L	1.15	1.15
Ma10	1.90	1.92
Ma9	2.32	2.35
Doc5	0.92	0.95
Ma8	0.68	0.71
Ma7	0.82	0.86
Doc6	0.38	0.45
Ma4	0.05	0.06
Ma3	0.13	0.13
Ma2	0.05	0.06
NMC-1	0.02	0.03
NMC-2	0.02	0.02
NMC-3	0.05	0.05
Ma1	0.04	0.05
NMC-4	0.07	0.07
Ma0	0.05	0.05
NMC-5	0.01	0.01
Σ	**15.22**	**15.49**

Table 8-8 Equivalent permeabilities (k_{eq}) back-calculated from settlement and porewater pressure observations at MP1-II.

Layer	**Thickness (m)**	**k_{eq} (m/s)**
Ds2	3.0	-
Ds3U	1.6	-
Ds3L	3.7	8.0E-04
Ds4	1.7	2.0E-05
Ds5	5.0	1.0E-07
Ds6	3.1	1.0E-05
Ds7	4.7	4.0E-04
Ds8	5.4	1.0E-05
Ds9	4.0	7.0E-05
Ds9'	5.4	1.0E-04

Table 8-9 Summary of calculations for compression of Pleistocene clay layes at MP1-II.

Layer	t_p from July 1999 (years)	Date when t_p reached	σ'_{vf}/σ'_p	EOP comp. (β_{avg} = 95%) (m)[a]	Comp. Dec. 2012 (m)	Secondary comp. in 2100 (m)
Dtc	67.9	Jun. 2067	1.97-2.15	0.92	0.82	0.01
Ma12	67.9	Jun. 2067	1.79-1.91	2.40	0.72	0.11
Doc1	67.9	Jun. 2067	1.63	1.16	0.67	0.05
Ma11U	43.5	Feb. 2043	1.44-1.49	1.18	0.95	0.05
Ma11L	β_{avg} = 93% in year 2100		1.36	1.15	0.29	-
Ma10	β_{avg} = 57% in year 2100		1.12-1.20	1.92	0.21	-
Ma9	β_{avg} = 90% in year 2100		1.19-1.23	2.35	0.73	-
Doc5	β_{avg} = 92% in year 2100		1.09-1.11	0.95	0.46	-
Ma8	80.9	Jun. 2080	1.09-1.10	0.49	0.38	0.06
Ma7	93.0	Jul. 2093	1.07-1.09	0.53	0.41	0.03
Doc6	22.3	Nov. 2021	1.05	0.29	0.28	0.34
Ma4	5.6	Mar. 2005	1.01	0.05	0.20	0.50
Ma3	7.7	Mar. 2007	0.92	0.13	0.38	1.19
Ma2	7.4	Dec. 2006	0.93	0.05	0.17	0.52
NMC-1	6.4	Jan. 2006	0.92	0.02	0.08	0.23
NMC-2	6.3	Nov. 2005	0.91	0.02	0.08	0.21
NMC-3	6.6	Feb. 2006	0.90	0.05	0.18	0.51
Ma1	6.6	Feb. 2006	0.92	0.04	0.17	0.50
NMC-4	6.6	Feb. 2006	0.92	0.07	0.28	0.82
Ma0	6.2	Sep. 2005	0.83	0.05	0.06	0.04
NMC-5	5.1	Aug. 2004	0.83	0.01	0.01	0.01
			Σ	**13.81**	**7.52**	**5.18**

a. EOP comp. calculated from EOP void ratio for Ma11L, Ma10, Ma9, and Doc5

Table 8-10 End-of-primary (EOP) compression corresponding to σ'_{vf} in Figure 8-12 for sublayers at MP2-II calculated using two assumptions for $\Delta\sigma_v$.

Layer	EOP compression rect. (m)	EOP compression strip (m)
Dtc	0.69	0.69
Ma12	2.85	2.86
Doc1	1.33	1.33
Ma11U	1.10	1.10
Ma11L	1.10	1.11
Ma10	1.55	1.60
Ma9	1.86	1.93
Doc5	0.68	0.75
Ma8	0.47	0.52
Ma7	0.55	0.70
Doc6	0.08	0.13
Ma4	0.05	0.05
Ma3	0.09	0.10
Ma2	0.03	0.03
NMC-1	0.02	0.02
NMC-2	0.01	0.01
NMC-3	0.03	0.04
Ma1	0.05	0.06
NMC-4	0.02	0.02
Ma0	0.04	0.05
NMC-5	0.01	0.01
Σ	12.61	13.10

Table 8-11 Equivalent permeabilities (k_{eq}) back-calculated from settlement and porewater pressure observations at MP2-II.

Layer	Thickness (m)	k_{eq} (m/s)
Ds2	2.68	-
Ds3U	0.67	-
Ds3L	4.2	1.0E-04
Ds4	0.7	8.0E-07
Ds5	6.6	1.0E-07
Ds6	5.0	1.0E-07
Ds7	4.6	1.0E-07
Ds8	6.4	1.0E-07
Ds9	5.7	1.0E-05
Ds9'	4.9	1.0E-04

Table 8-12 Summary of calculations for compression of Pleistocene clay layes at MP2-II.

Layer	t_p from Jan. 2001 (years)	Date when t_p reached	σ'_{vf}/σ'_p	EOP comp. (β_{avg} = 95%) (m)[a]	Comp. Dec. 2012 (m)	Secondary comp. in 2100 (m)
Dtc	65.7	Sep. 2066	1.85-1.99	0.68	0.60	0.02
Ma12	65.7	Sep. 2066	1.68-1.81	2.70	0.94	0.13
Doc1	65.7	Sep. 2066	1.55	1.27	0.70	0.06
Ma11U	β_{avg} = 92% in year 2100		1.38-1.42	1.10	0.73	-
Ma11L	β_{avg} = 80% in year 2100		1.32	1.11	0.15	-
Ma10	β_{avg} = 23% in year 2100		1.07-1.15	1.60	0.18	-
Ma9	β_{avg} = 55% in year 2100		1.14-1.18	1.93	0.25	-
Doc5	β_{avg} = 18% in year 2100		1.05-1.07	0.75	0.11	-
Ma8	β_{avg} = 64% in year 2100		1.05-1.06	0.52	0.22	-
Ma7	β_{avg} = 76% in year 2100		1.03-1.05	0.70	0.29	-
Doc6	61.7	Sep. 2062	1.01	0.16	0.07	0.06
Ma4	4.9	Dec. 2005	0.97	0.05	0.20	0.40
Ma3	5.1	Jan. 2006	0.87	0.10	0.46	1.01
Ma2	5.6	Aug. 2006	0.89	0.03	0.14	0.34
NMC-1	5.9	Nov. 2006	0.88	0.02	0.06	0.16
NMC-2	5.9	Nov. 2006	0.88	0.01	0.05	0.14
NMC-3	6.2	Feb. 2007	0.87	0.04	0.14	0.44
Ma1	6.4	Jun. 2007	0.9	0.06	0.23	0.76
NMC-4	5.8	Oct. 2006	0.89	0.02	0.09	0.29
Ma0	5.6	Aug. 2006	0.82	0.05	0.06	0.04
NMC-5	4.9	Dec. 2005	0.82	0.01	0.02	0.01
			Σ	**12.89**	**5.71**	**3.85**

a. EOP comp. calculated from EOP void ratio for Ma11U through Ma7

Table 8-13 End-of-primary (EOP) compression corresponding to σ'_{vf} in Figure 8-13 for sublayers at MP1-I calculated using two assumptions for $\Delta\sigma_v$.

Layer	EOP compression rect. (m)	EOP compression strip (m)
Dtc	0.47	0.47
Ma12	1.87	1.87
Doc1	0.36	0.36
Ma11U	0.99	0.99
Ma11L	0.77	0.77
Ma10	1.51	1.51
Ma9	1.37	1.37
Doc5	0.66	0.66
Ma8	0.63	0.63
Ma7	0.32	0.32
Doc6	0.21	0.21
Ma4	0.96	0.96
Ma3	0.03	0.03
Ma2	0.07	0.07
NMC-1	0.02	0.02
Ma1	0.16	0.16
Ma0	0.05	0.05
NMC-5	0.05	0.05
Σ	10.48	10.49

Table 8-14 Equivalent permeabilities (k_{eq}) back-calculated from settlement and porewater pressure observations at MP1-I.

Layer	**Thickness (m)**	**k_{eq} (m/s)**
Ds3L	5.4	1.0E-04
Ds4	2.2	2.0E-05
Ds5	1.5	3.0E-05
Ds6	4.6	5.0E-06
Ds7	5.1	1.0E-06
Ds8	2.9	5.0E-05
Ds9	7.1	1.0E-07

Table 8-15 Summary of calculations for compression of Pleistocene clay layes at MP1-I.

Layer	t_p from Jan. 1987 (years)	Date when t_p reached	σ'_{vf}/σ'_p	EOP comp. (β_{avg} = 95%) (m)[a]	Comp. Dec. 2012 (m)	Secondary comp. in 2100 (m)
Dtc	23.6	Aug. 2010	1.97-2.09	0.46	0.47	0.03
Ma12	23.6	Aug. 2010	1.90-2.03	1.75	1.78	0.16
Doc1	23.6	Aug. 2010	1.82	0.35	0.35	0.02
Ma11U	29.4	May 2016	1.57-1.62	0.95	0.94	0.07
Ma11L	61.3	Apr. 2048	1.47	0.73	0.65	0.04
Ma10	92.1	Jan. 2079	1.22-1.31	1.45	0.57	0.04
Ma9	90.2	Feb. 2077	1.29-1.33	1.31	0.76	0.04
Doc5	90.8	Nov. 2077	1.18-1.19	0.64	0.38	0.03
Ma8	62.9	Nov. 2049	1.17-1.19	0.60	0.52	0.05
Ma7	38.8	Oct. 2025	1.15-1.16	0.30	0.28	0.05
Doc6	38.8	Oct. 2025	1.13	0.21	0.20	0.03
Ma4	β_{avg} = 83% in year 2100		1.07	0.96	0.52	-
Ma3	β_{avg} = 83% in year 2100		0.98	0.03	0.02	-
Ma2	β_{avg} = 83% in year 2100		1.01	0.07	0.04	-
NMC-1	18.4	Jun. 2005	0.99	0.02	0.04	0.11
Ma1	18.4	Jun. 2005	1.02	0.05	0.11	0.27
Ma0	18.4	Jun. 2005	0.94	0.05	0.10	0.26
NMC-5	18.4	Jun. 2005	0.93	0.05	0.10	0.26
			Σ	**9.97**	**7.82**	**1.47**

a. EOP comp. calculated from EOP void ratio for Ma4 through Ma2

8.7 Figures

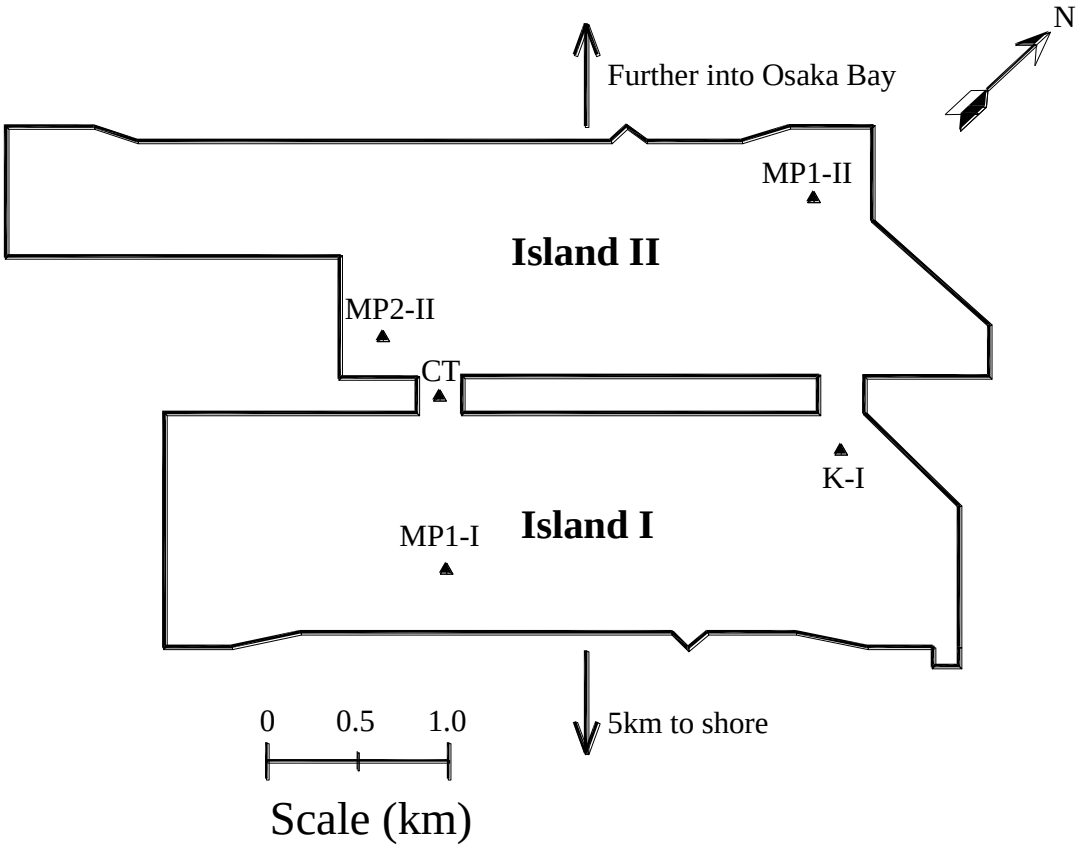

Figure 8-1 Locations where settlement analyses were performed for this study.

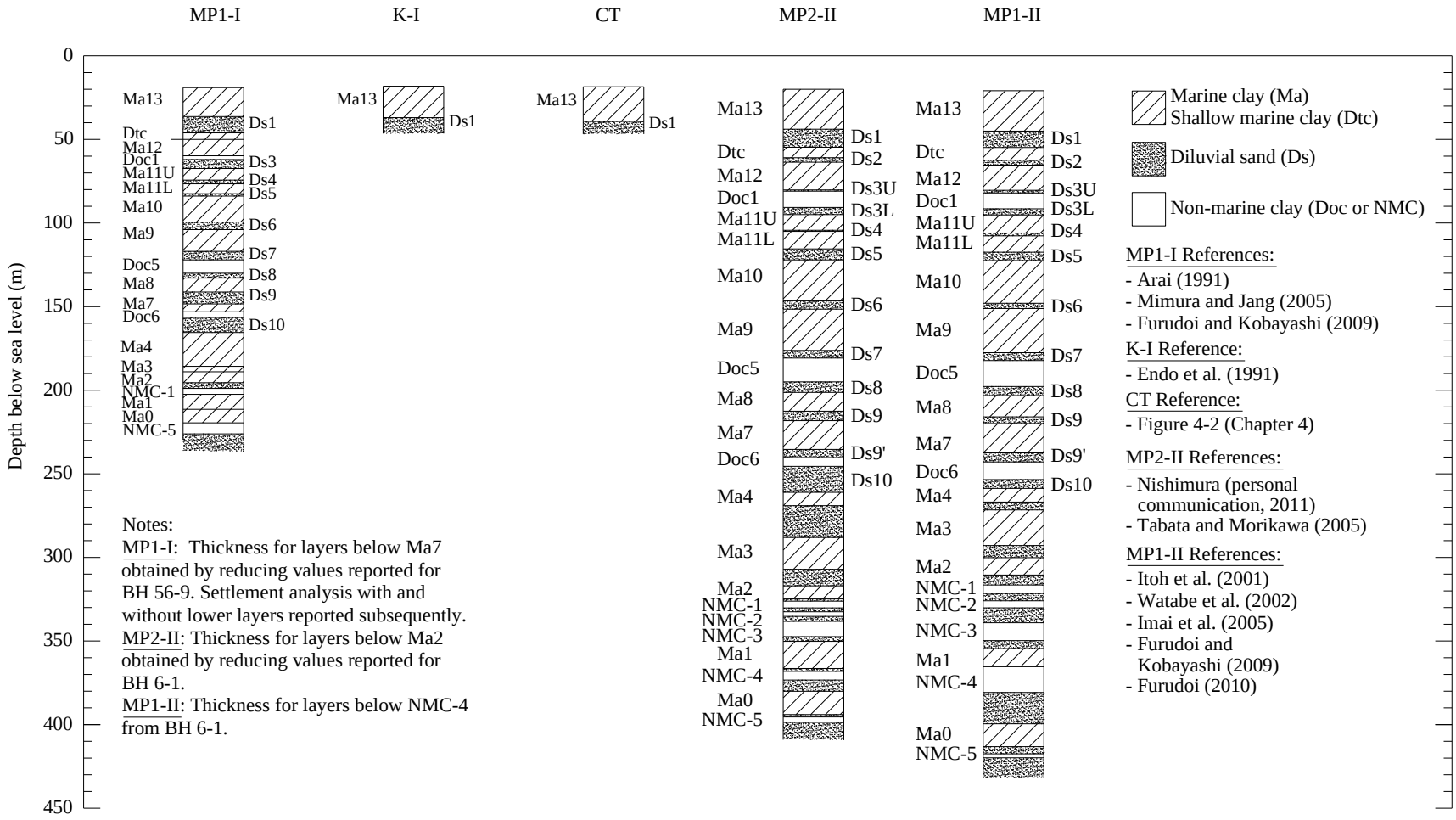

Figure 8-2 Subseabed profiles for 5 locations shown in Figure 8-1.

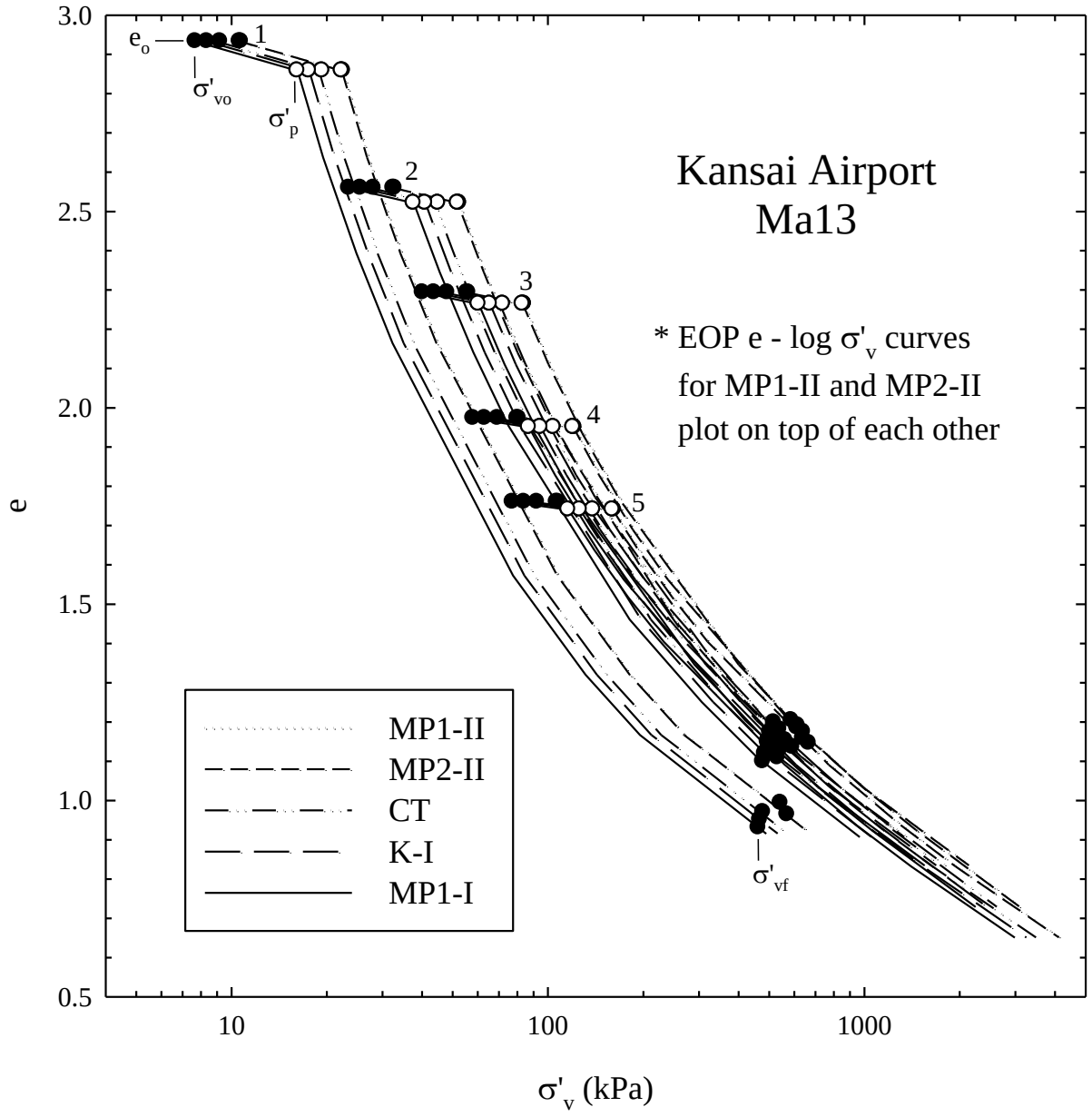

Figure 8-3 EOP e – log σ'_v relationships constructed for Ma13 at MP1-II, MP2-II, CT, K-I, and MP1-I. The numbers identify sublayers.

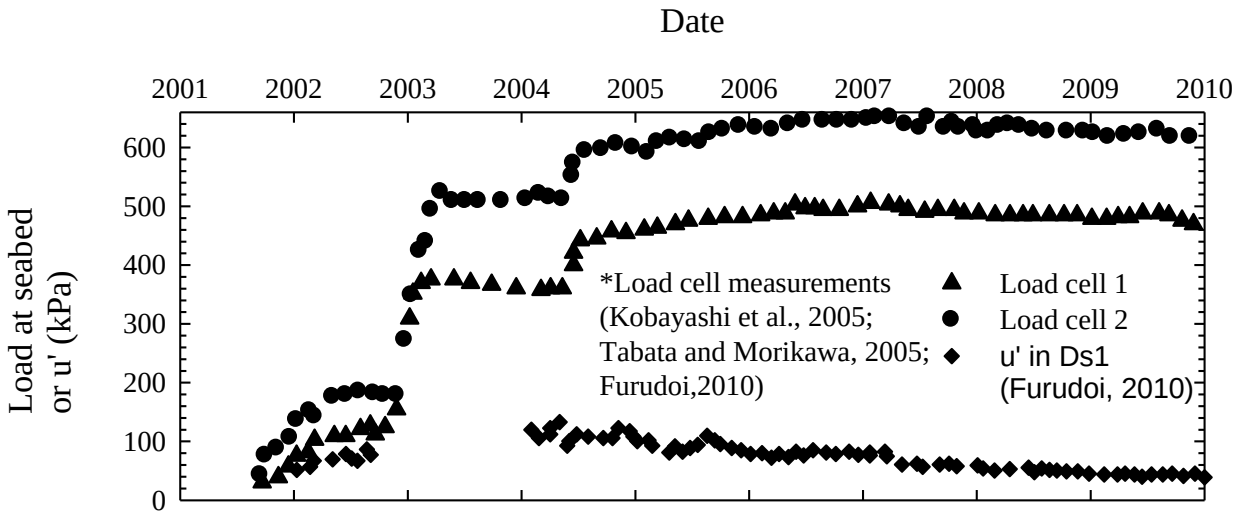

Figure 8-4 Excess porewater pressure within Ds1 together with load cell measurements at MP1-II (Kobayashi et al., 2005; Tabata and Morikawa, 2005; Furudoi, 2010).

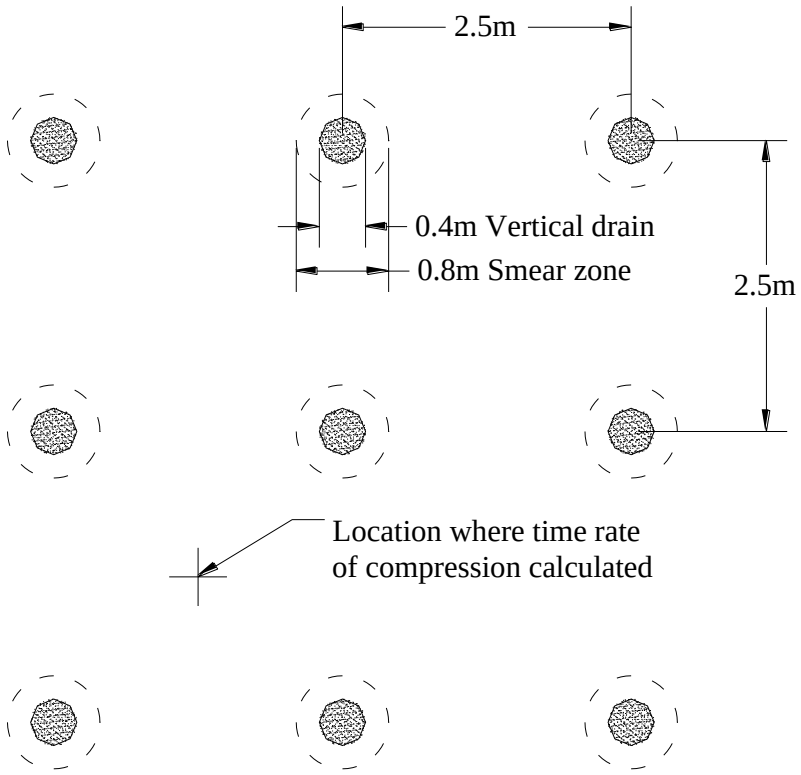

Figure 8-5 Plan view of vertical drains fully penetrating Ma13 at Kansai Airport.

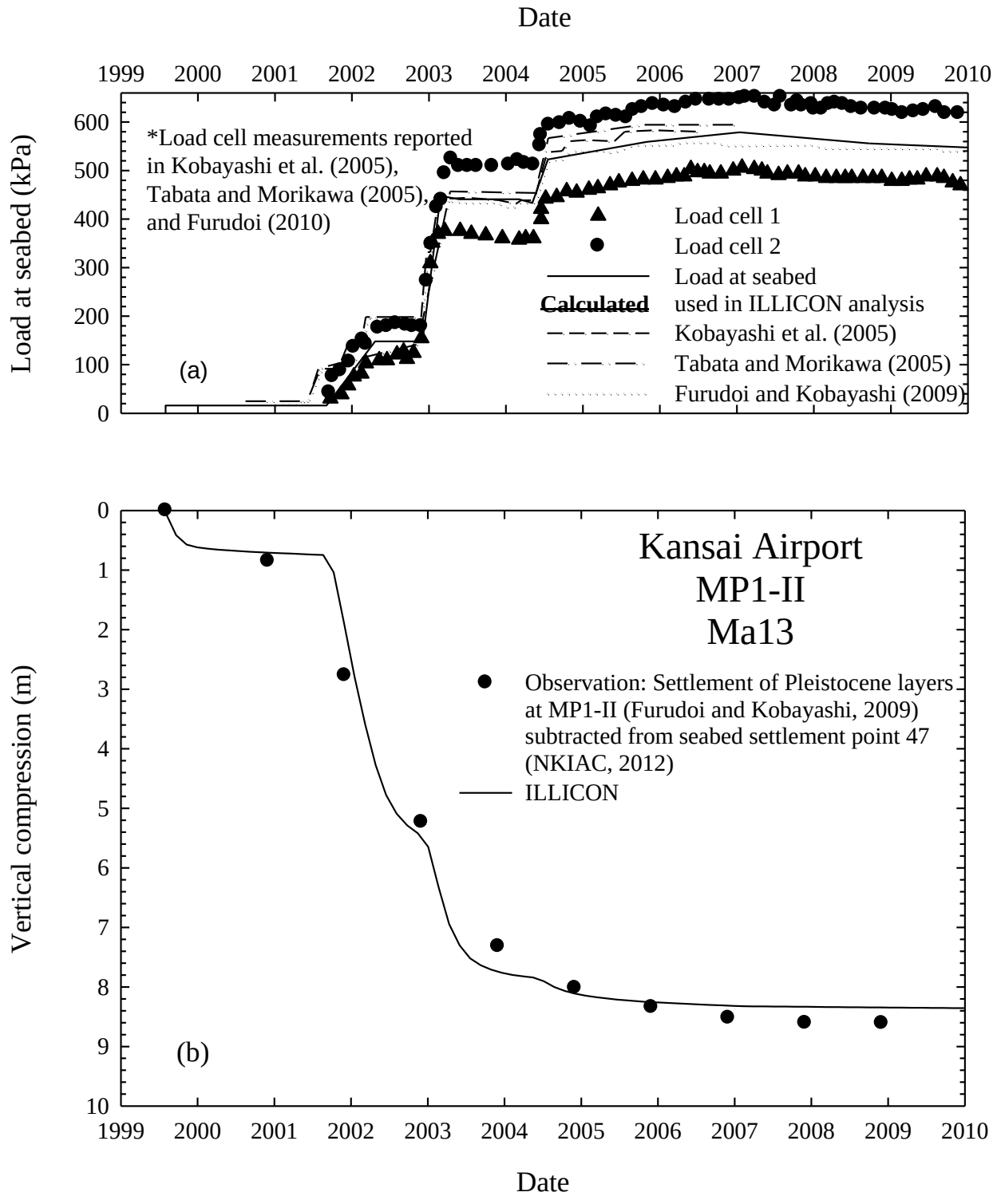

Figure 8-6 (a) Load cell measurements and load at seabed used in analysis. (b) Observed and computed vertical compression for Ma13 at MP1-II.

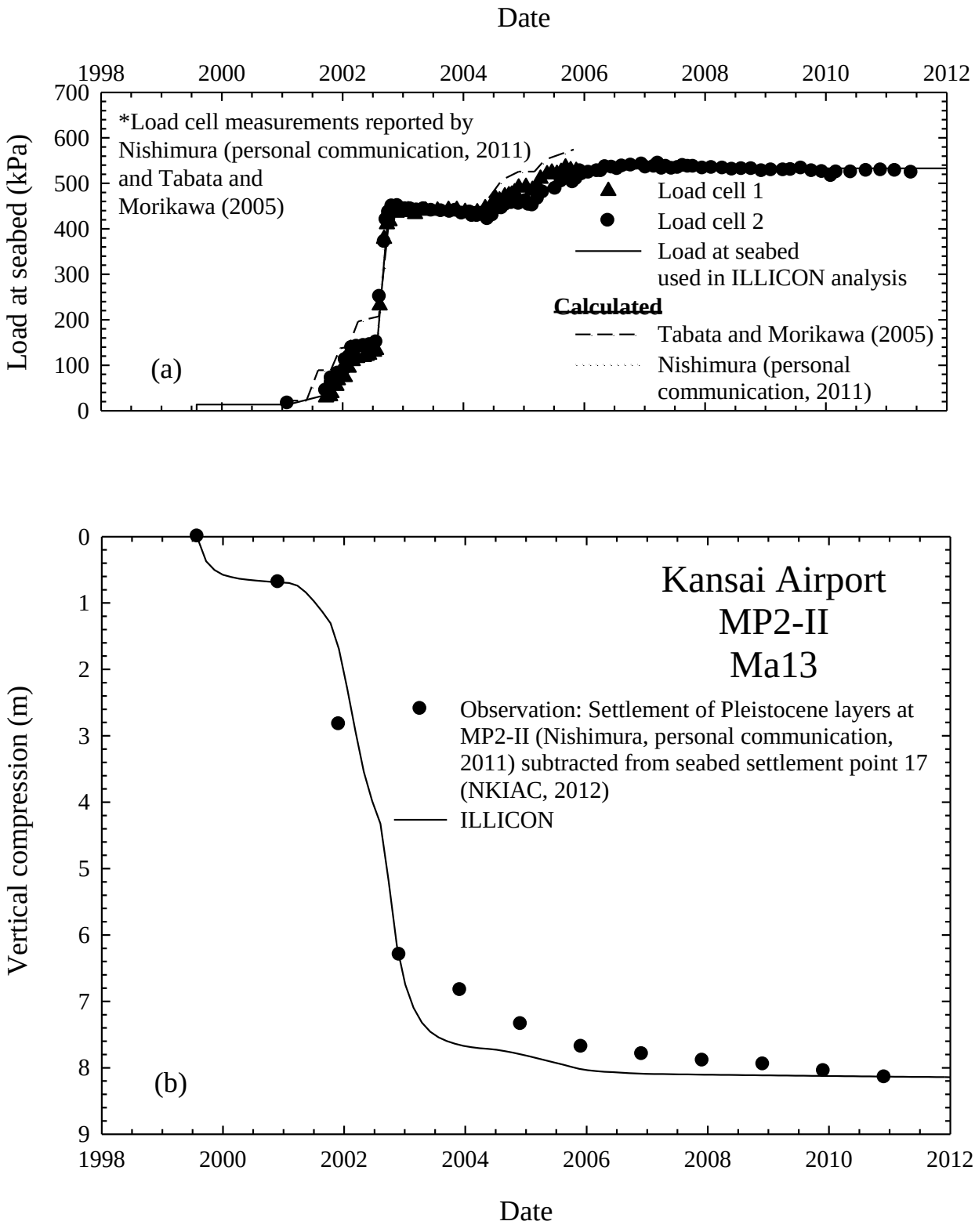

Figure 8-7 (a) Load cell measurements and load at seabed used in analysis. (b) Observed and computed vertical compression for Ma13 at MP2-II.

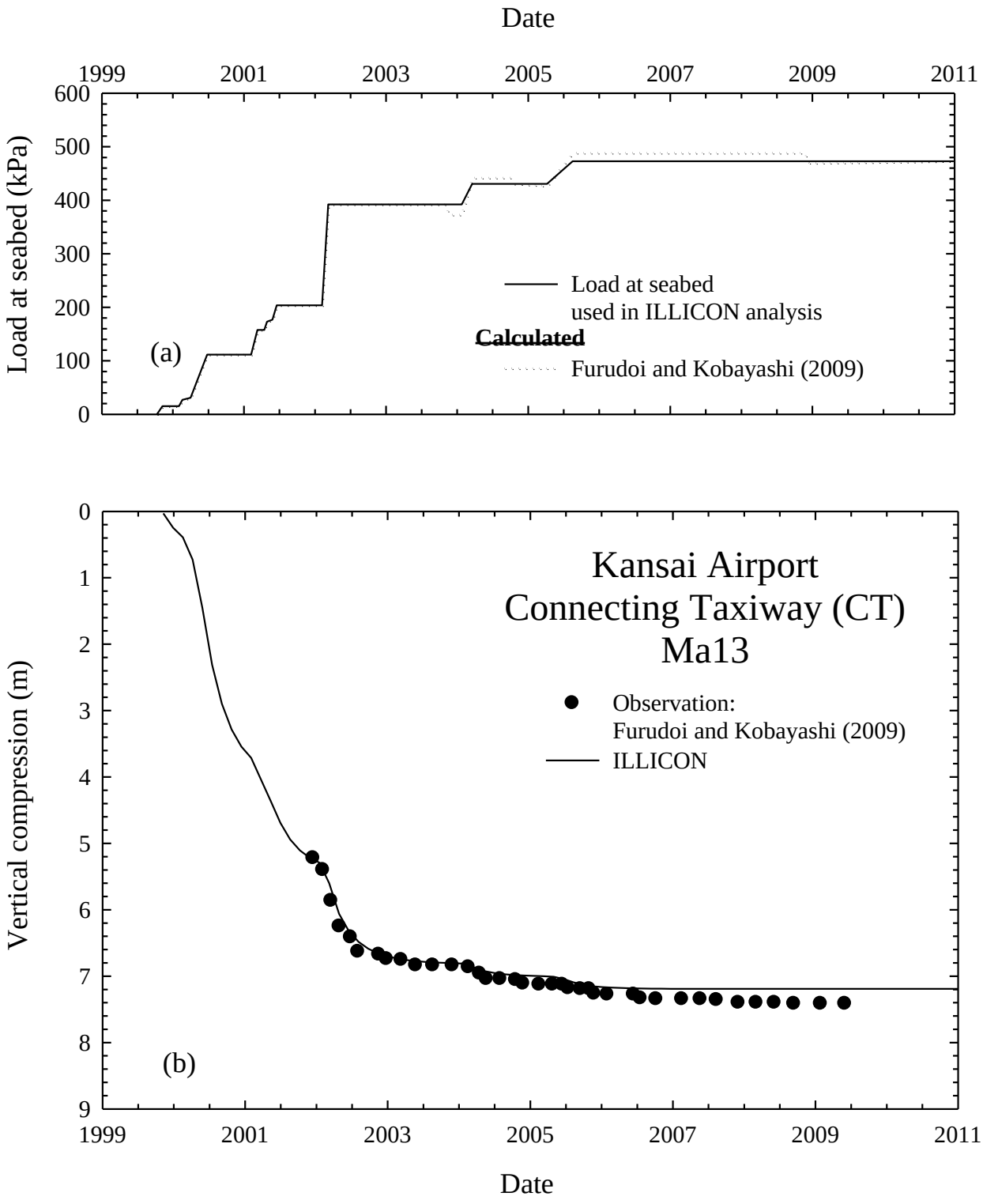

Figure 8-8 (a) Load at seabed used in analysis. (b) Observed and computed vertical compression

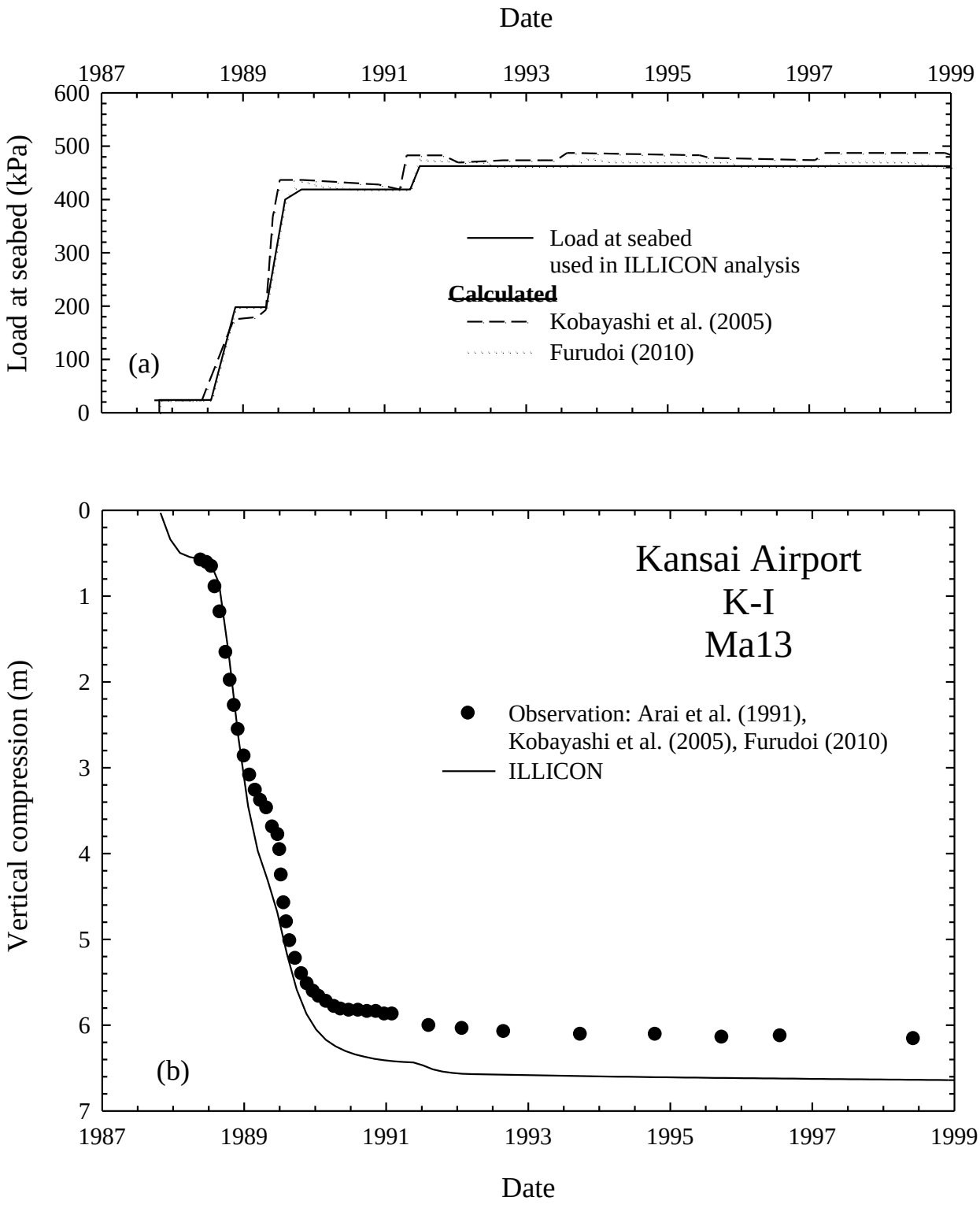

Figure 8-9 (a) Load at seabed used in analysis. (b) Observed and computed vertical compression for Ma13 at K-I.

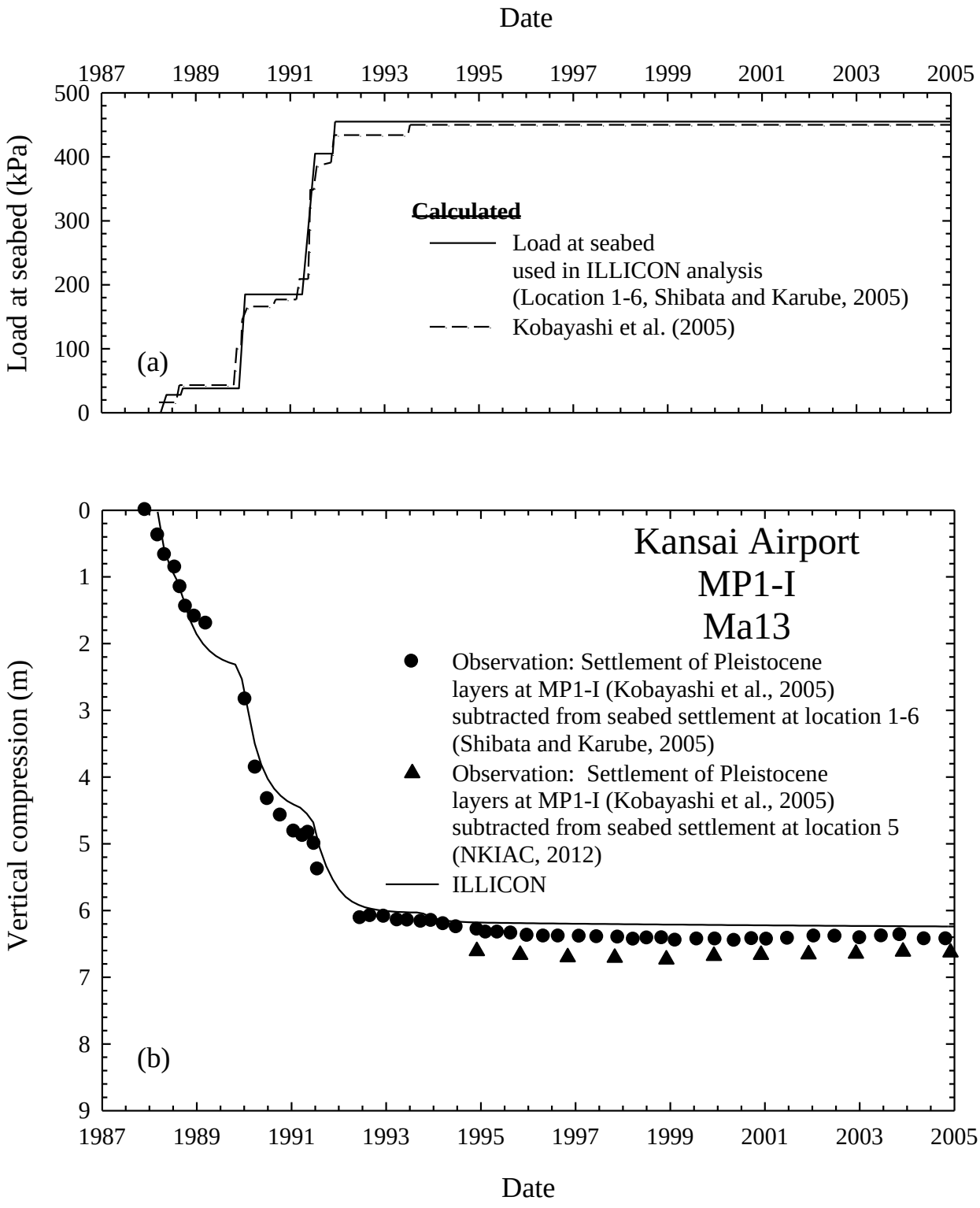

Figure 8-10 (a) Load at seabed used in analysis. (b) Observed and computed vertical compression for Ma13 at MP1-I.

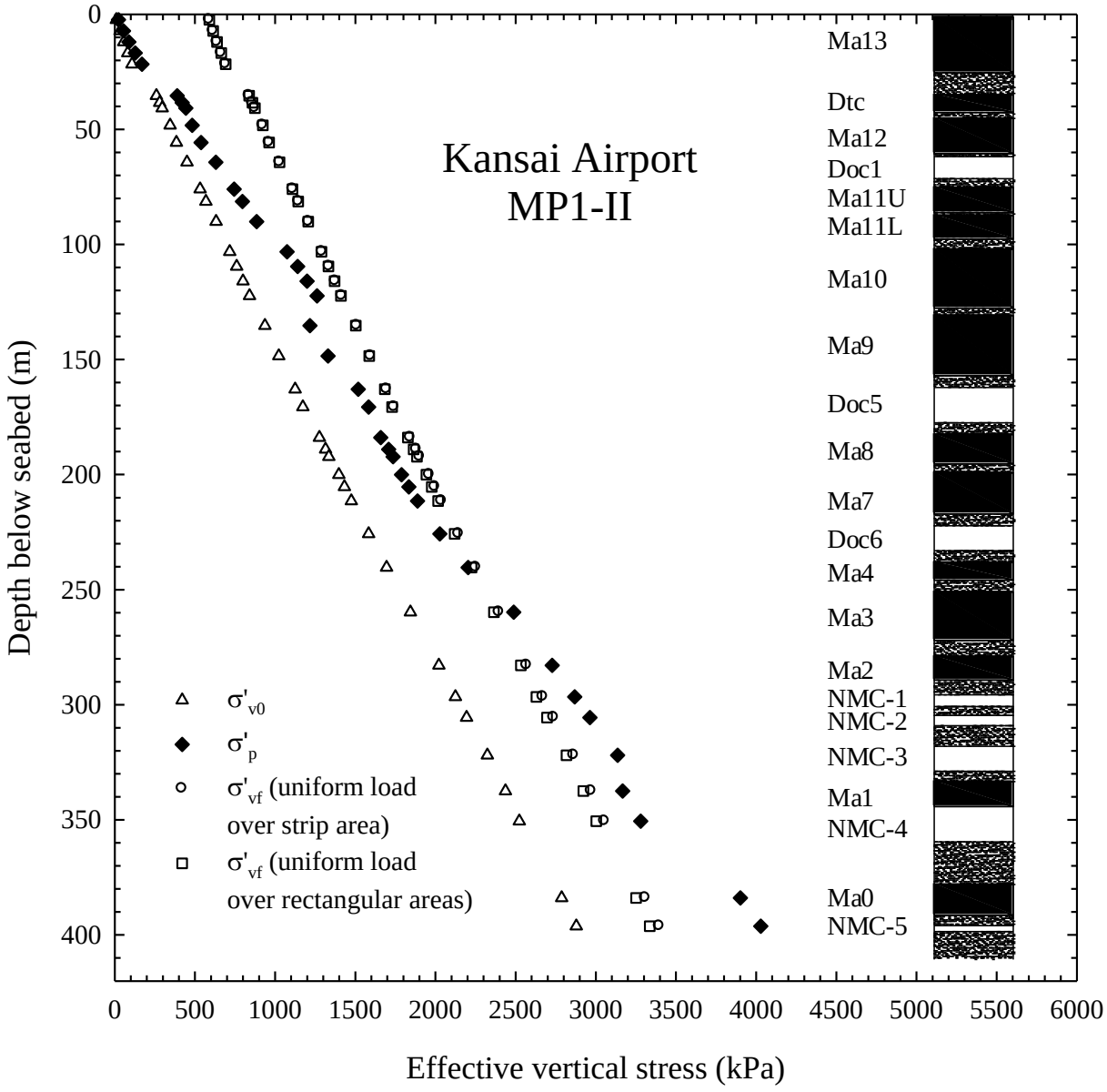

Figure 8-11 Vertical profile of preconstruction effective vertical stress (σ'_{vo}), preconsolidation pressure (σ'_{p}), and post-construction final effective vertical stress (σ'_{vf}) at MP1-II.

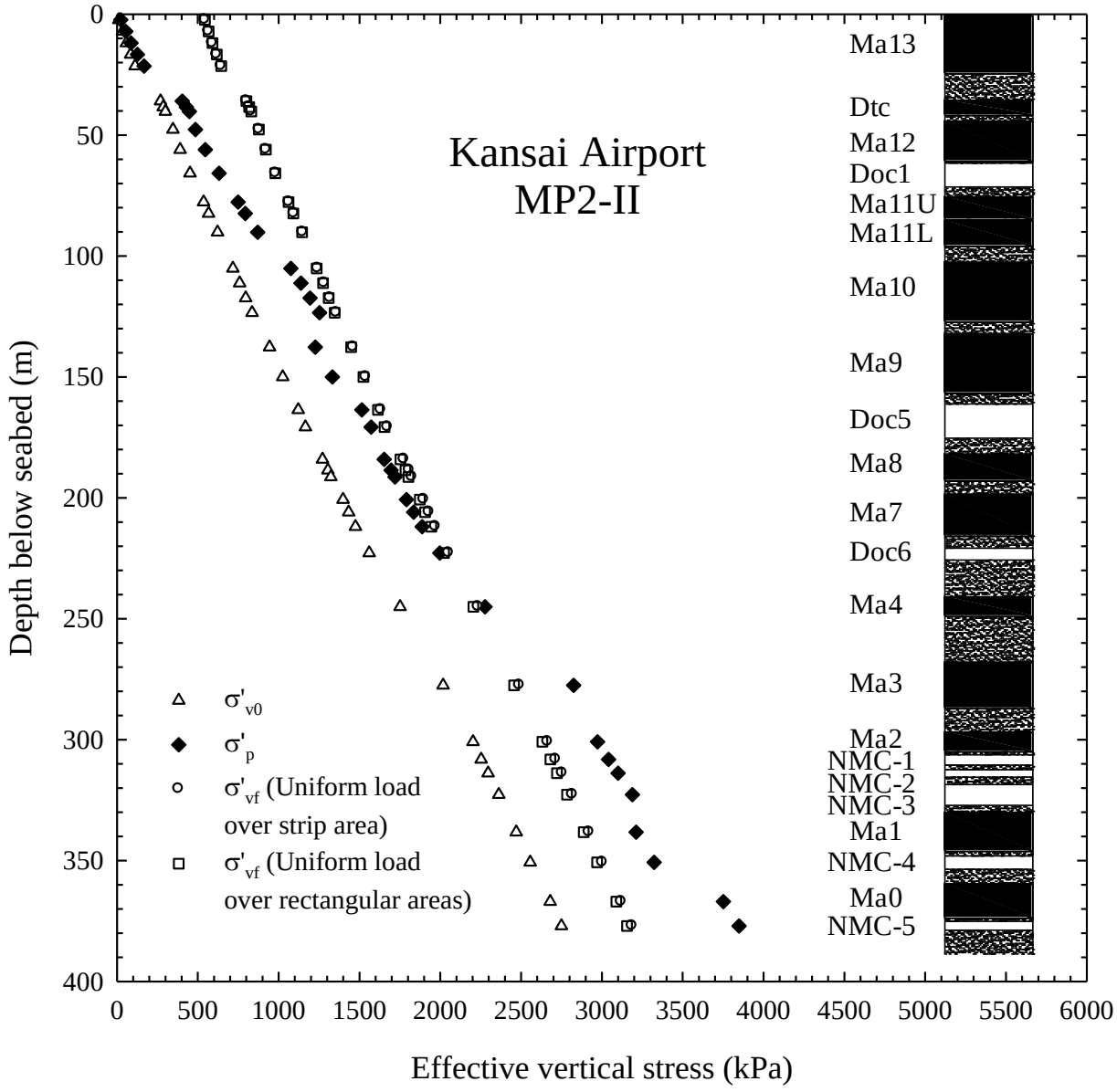

Figure 8-12 Vertical profile of preconstruction effective vertical stress (σ'_{vo}), preconsolidation pressure (σ'_{p}), and post-construction final effective vertical stress (σ'_{vf}) at MP2-II.

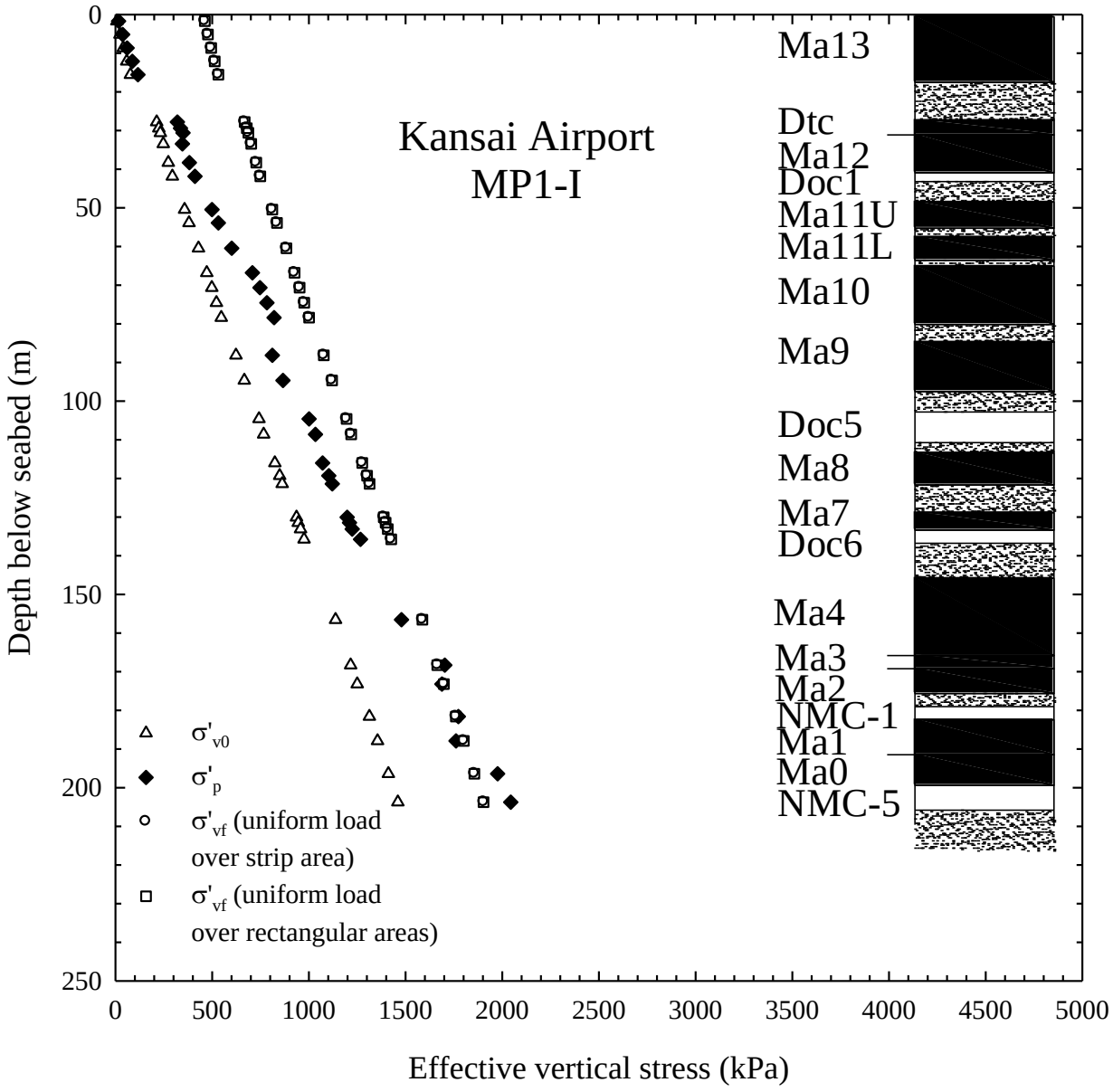

Figure 8-13 Vertical profile of preconstruction effective vertical stress (σ'_{vo}), preconsolidation pressure (σ'_{p}), and post-construction final effective vertical stress (σ'_{vf}) at MP1-I.

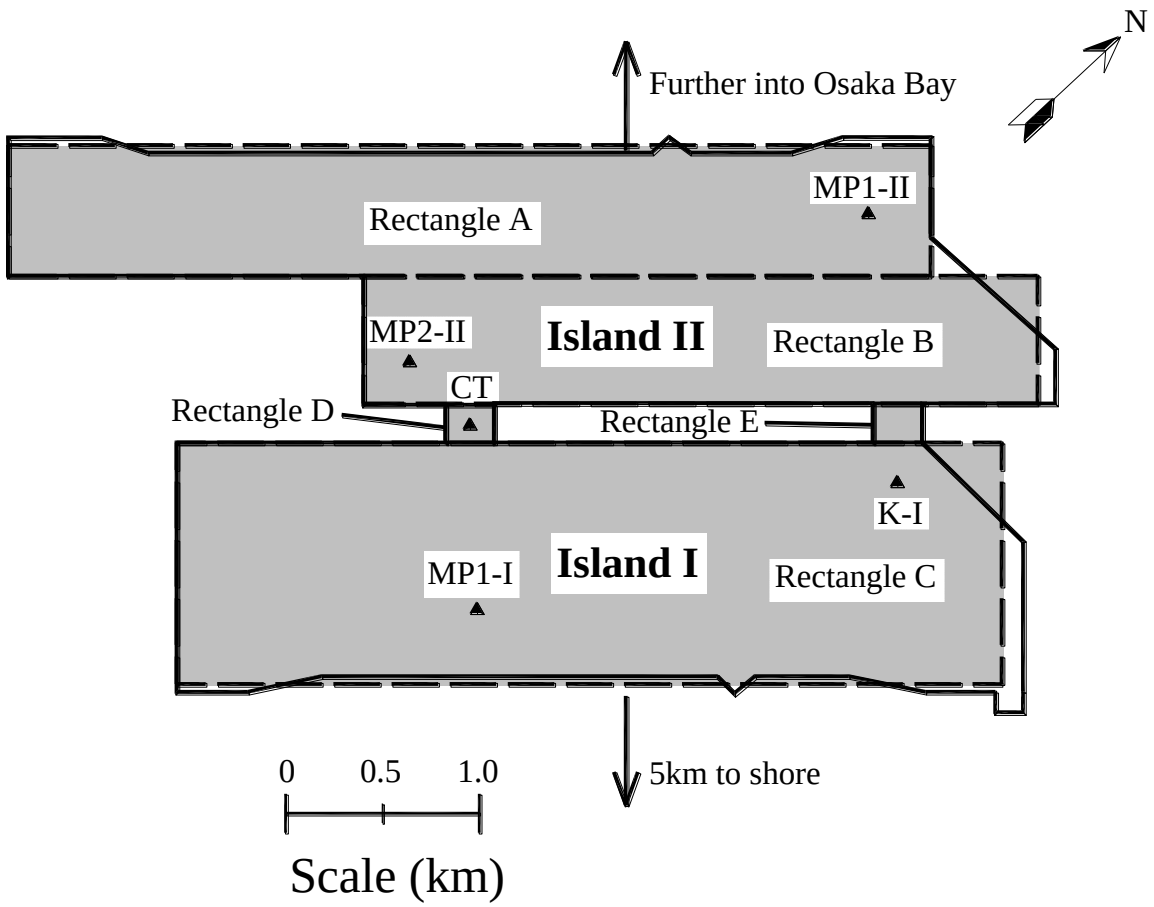

Figure 8-14 Rectangles A, B, C, D, and E used to calculate $\Delta\sigma_v$ for the Kansai Airport Islands.

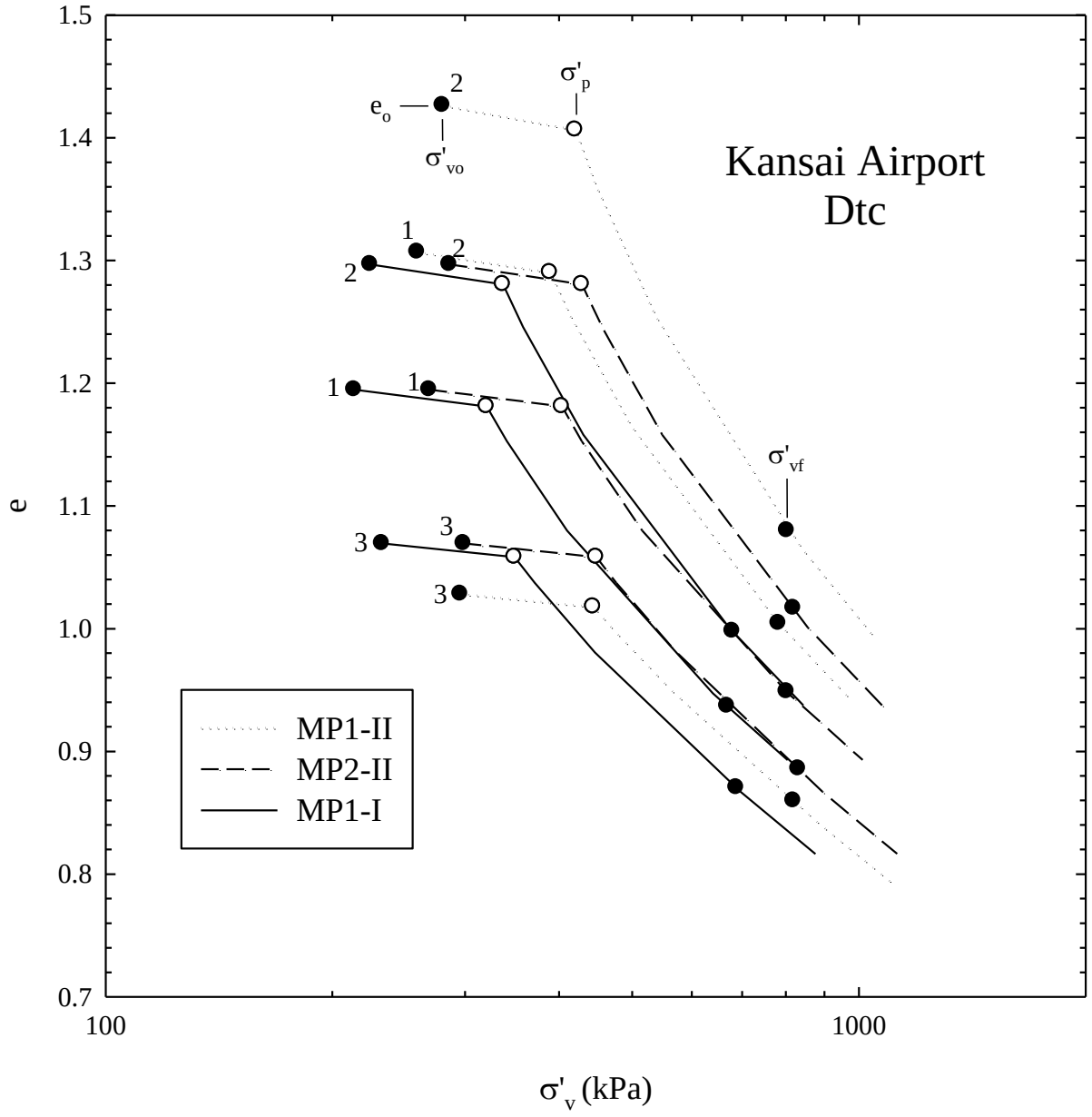

Figure 8-15 EOP e – log σ'_v relationships constructed for Dtc. The numbers identify sublayers.

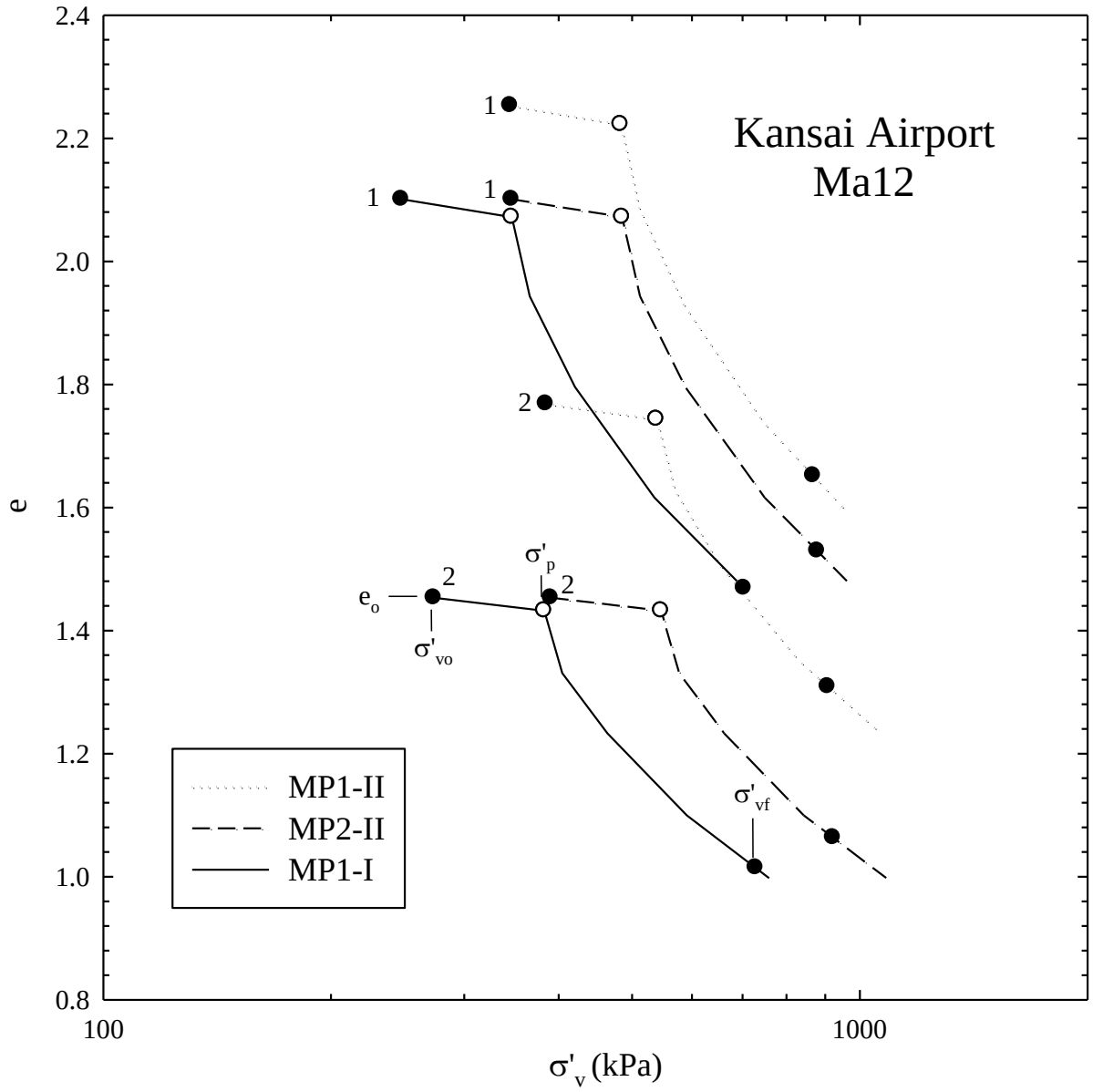

Figure 8-16 EOP e – log σ'_v relationships constructed for Ma12. The numbers identify sublayers.

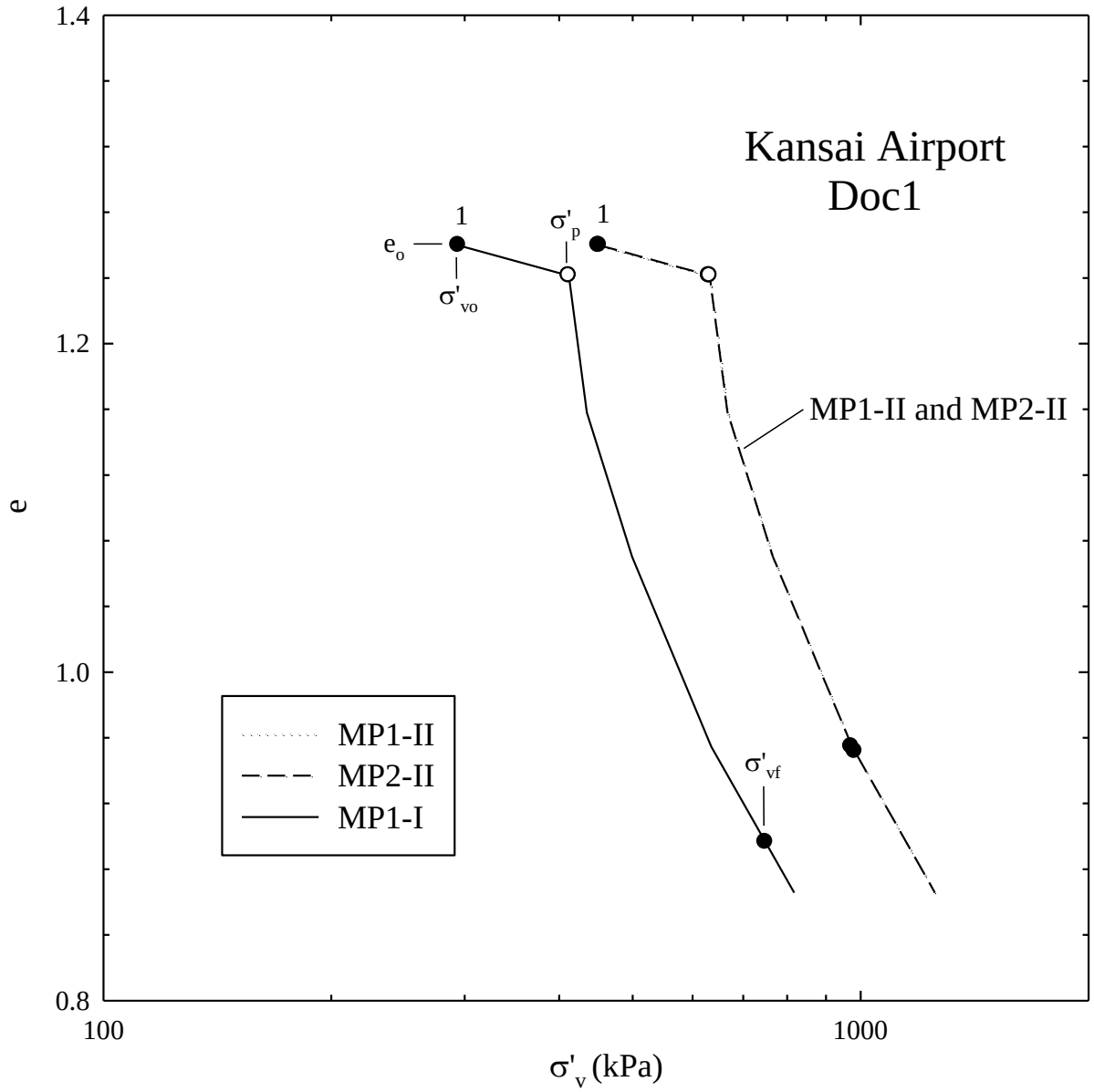

Figure 8-17 EOP e – log σ'_v relationships constructed for Doc1. The numbers identify sublayers.

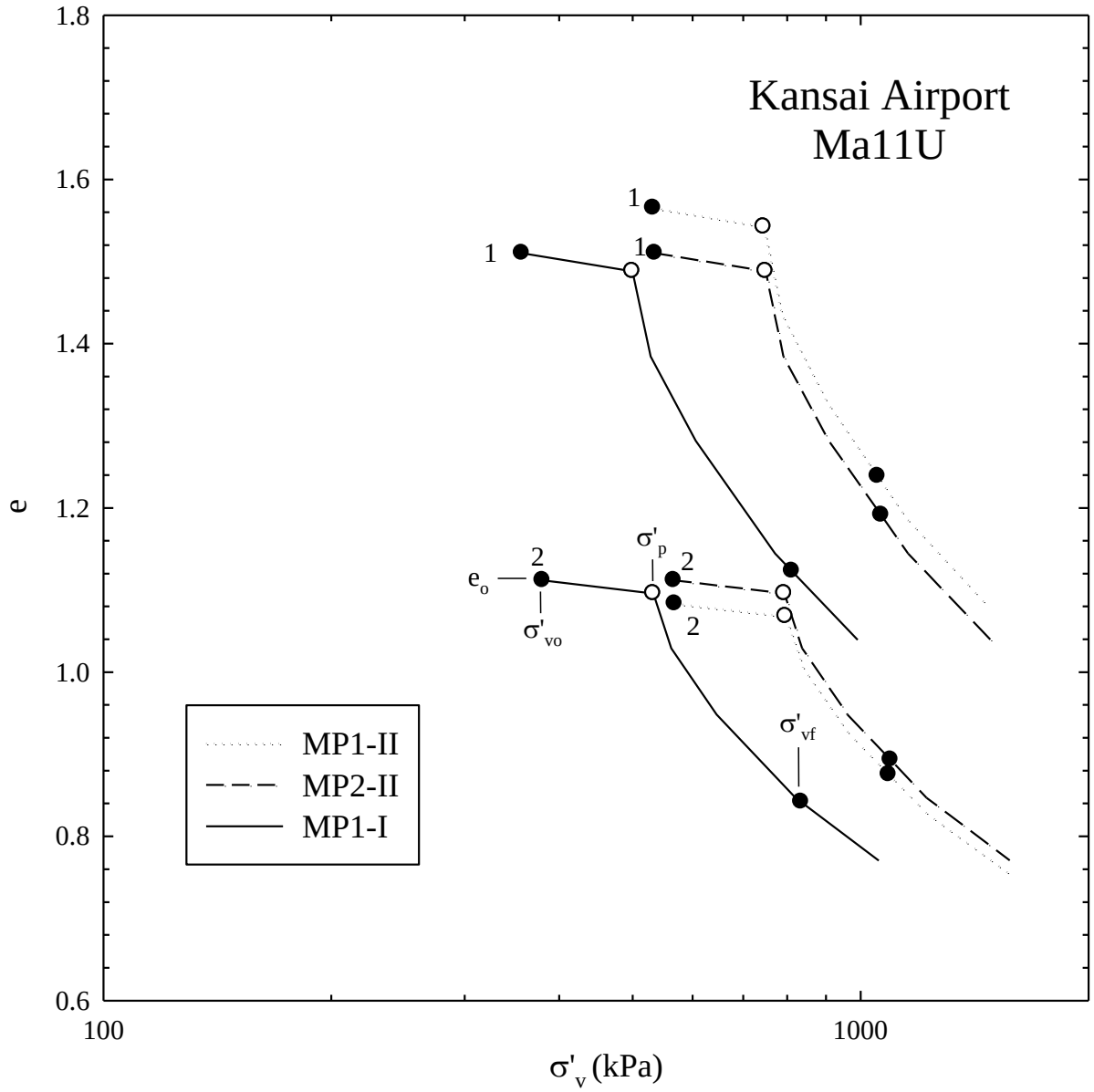

Figure 8-18 EOP e – log σ'_v relationships constructed for Ma11U. The numbers identify sublayers.

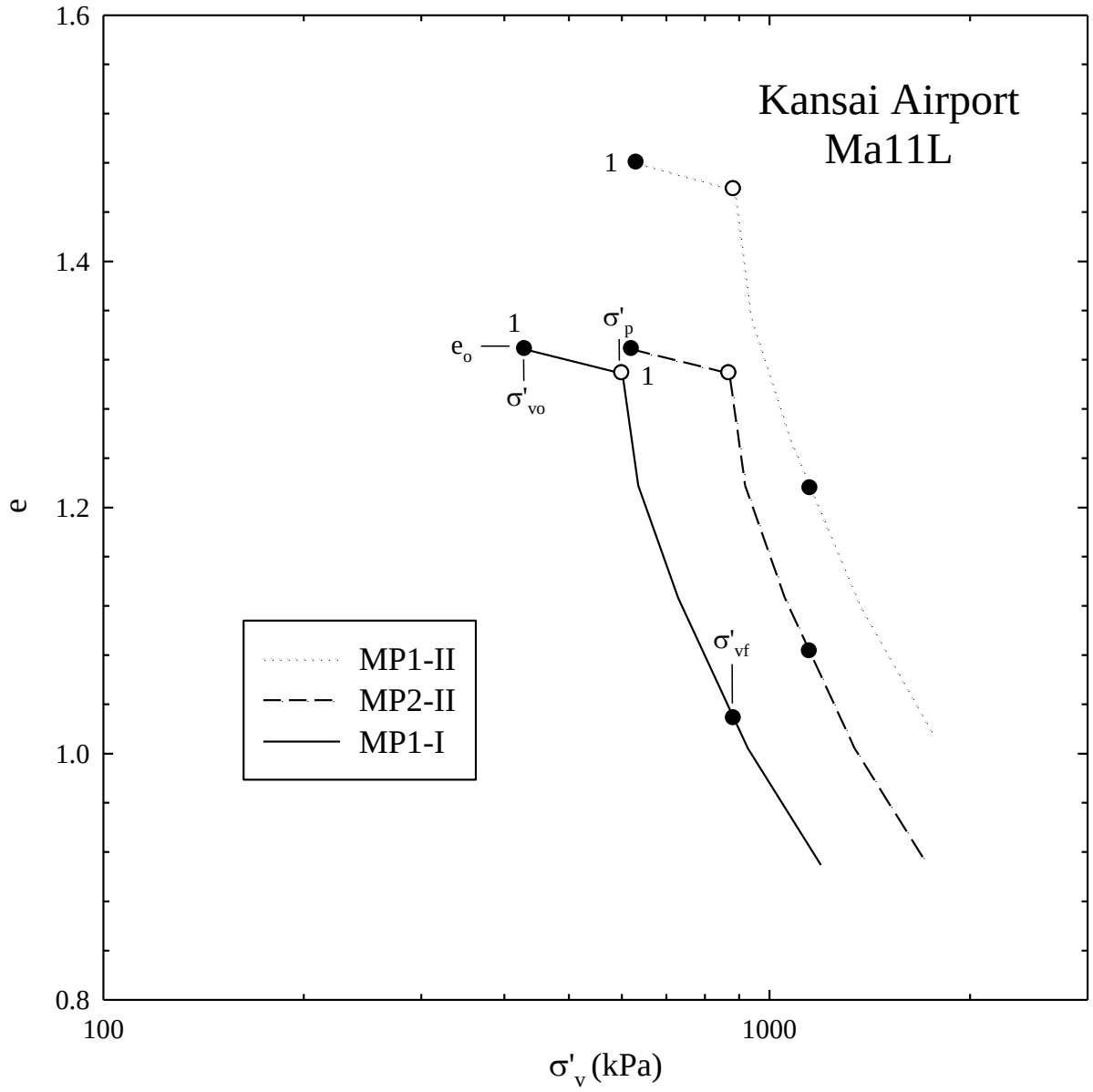

Figure 8-19 EOP e – log σ'_v relationships constructed for Ma11L. The numbers identify sublayers.

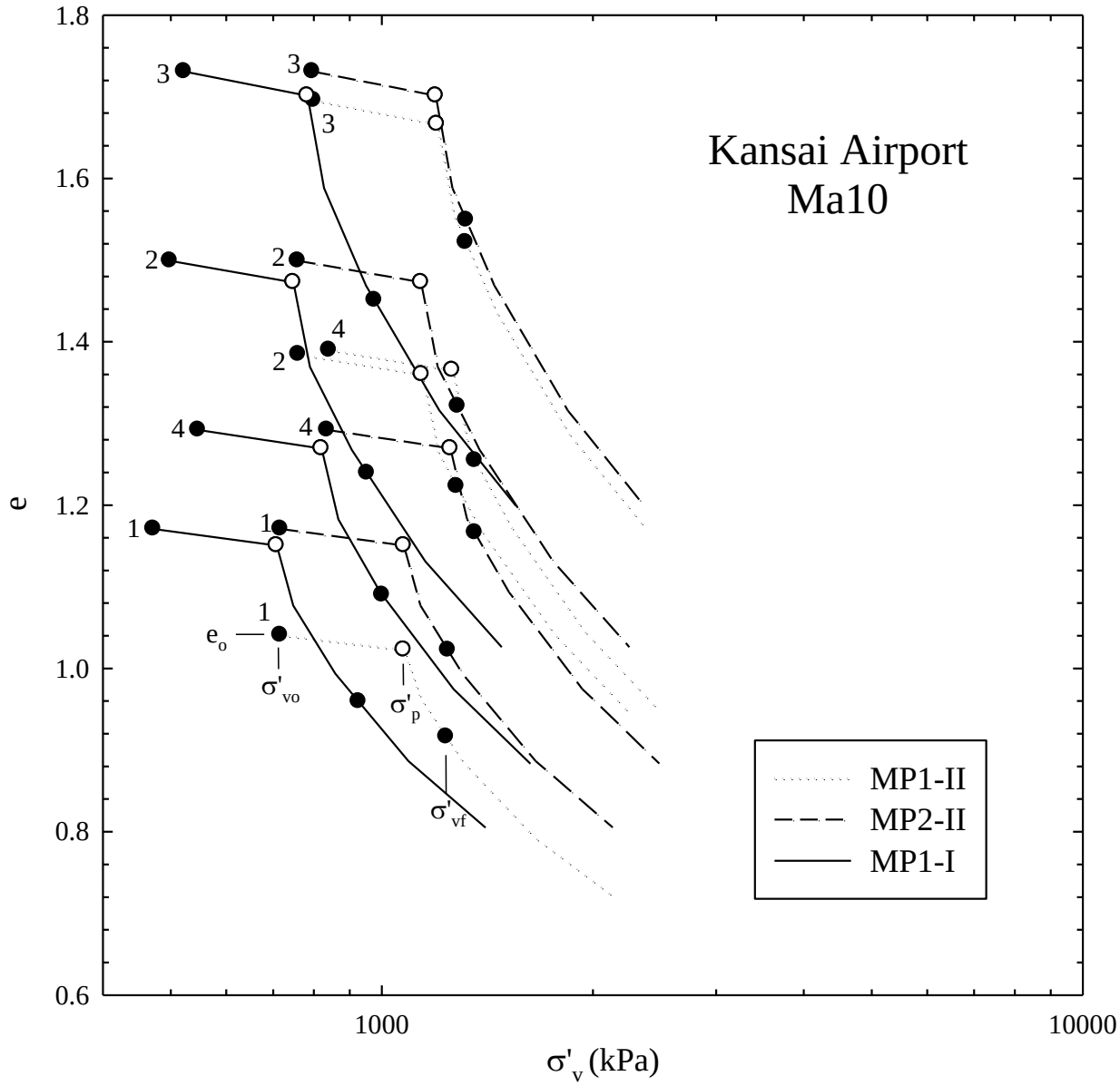

Figure 8-20 EOP e – log σ'_v relationships constructed for Ma10. The numbers identify sublayers.

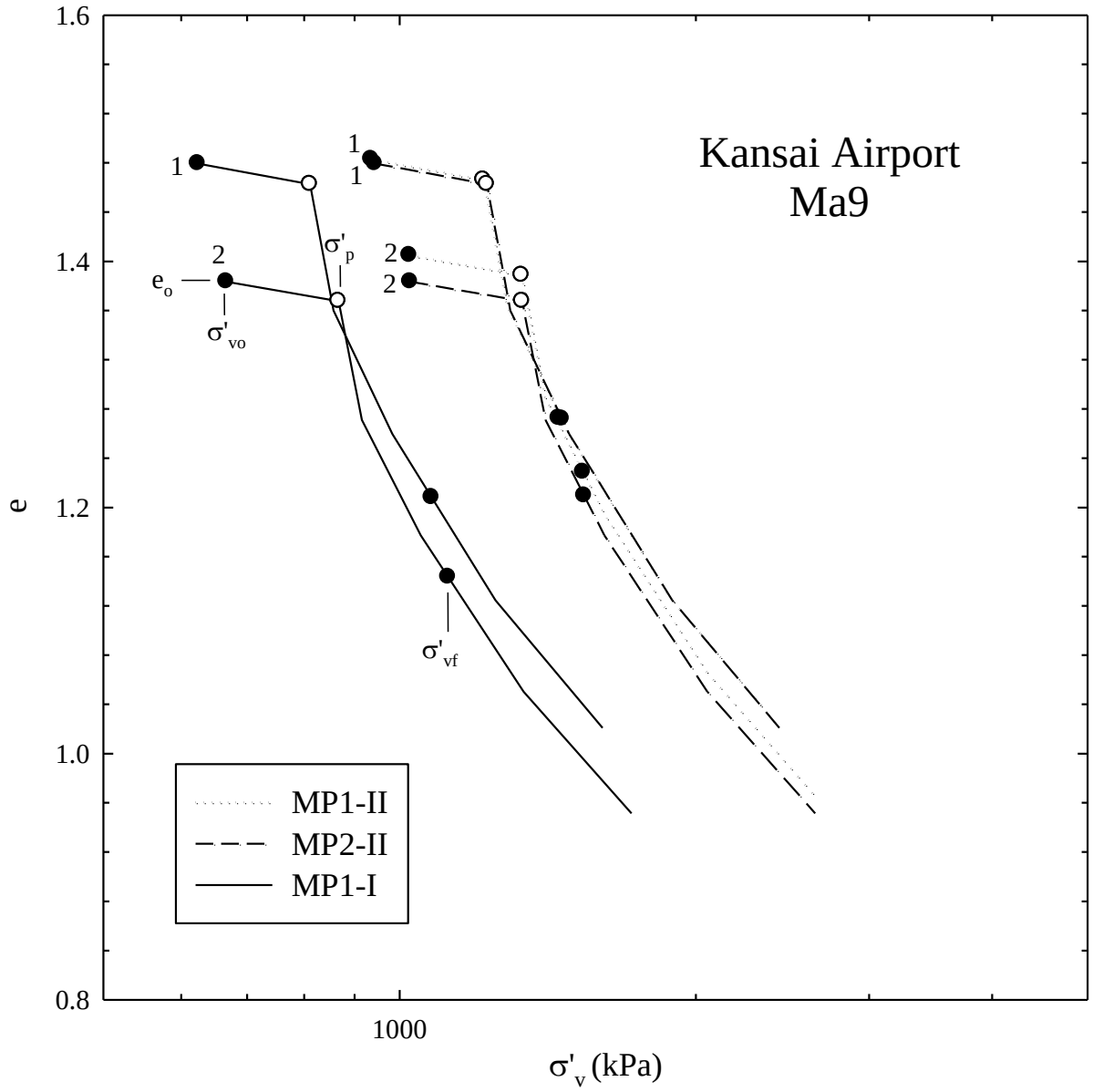

Figure 8-21 EOP e – log σ'_v relationships constructed for Ma9. The numbers identify sublayers.

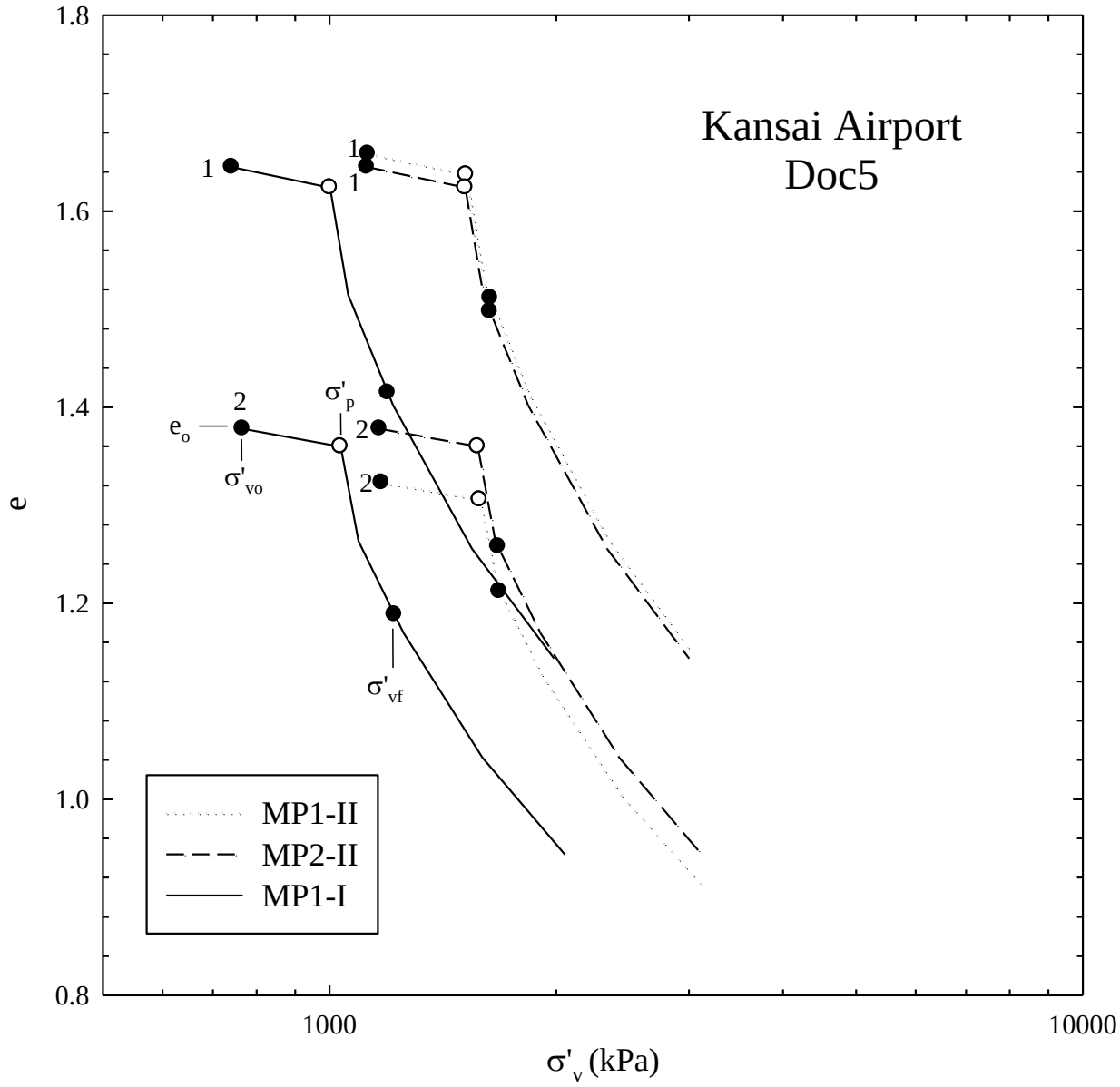

Figure 8-22 EOP e – log σ'_v relationships constructed for Doc5. The numbers identify sublayers.

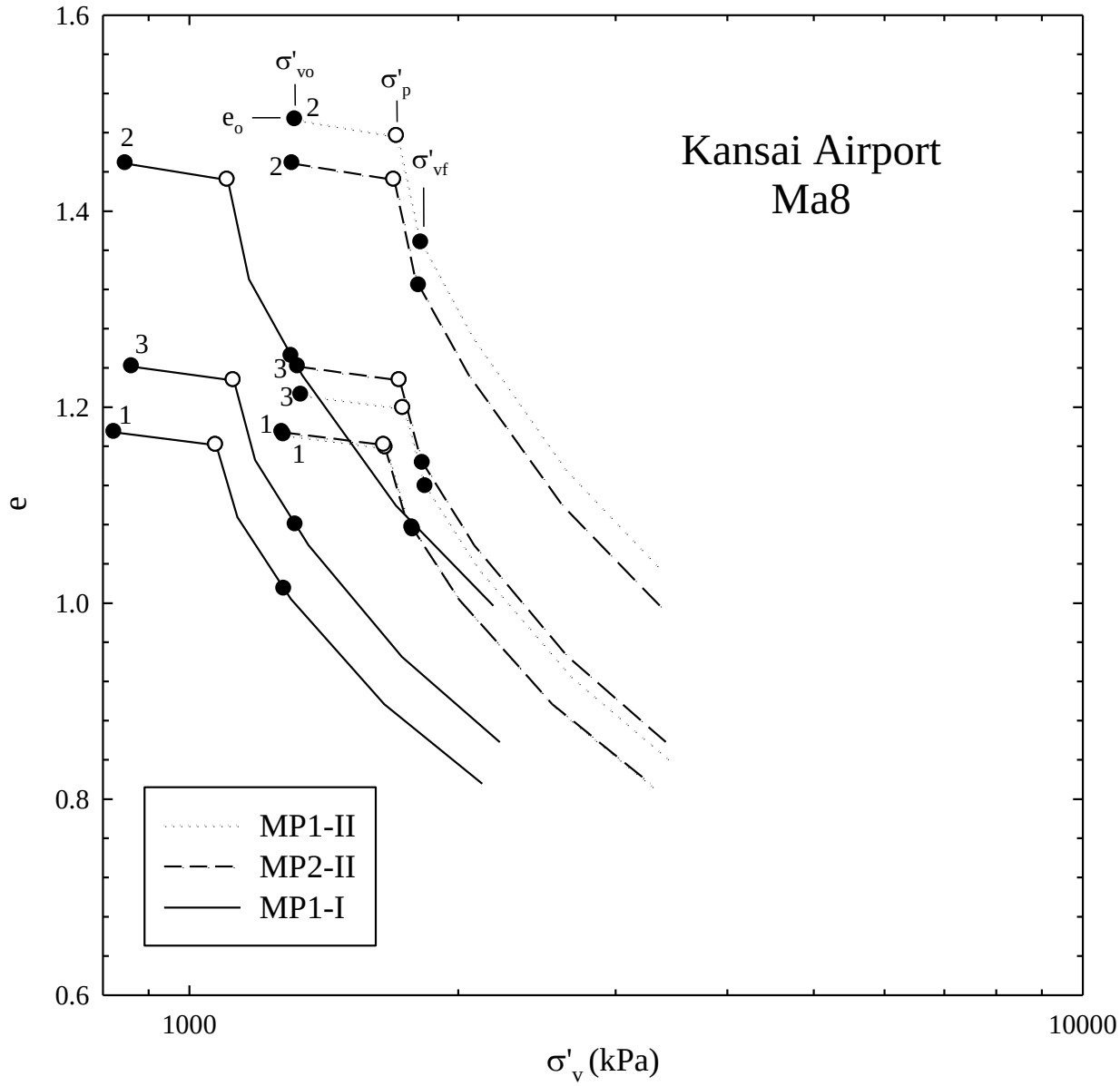

Figure 8-23 EOP e – log σ'_v relationships constructed for Ma8. The numbers identify sublayers.

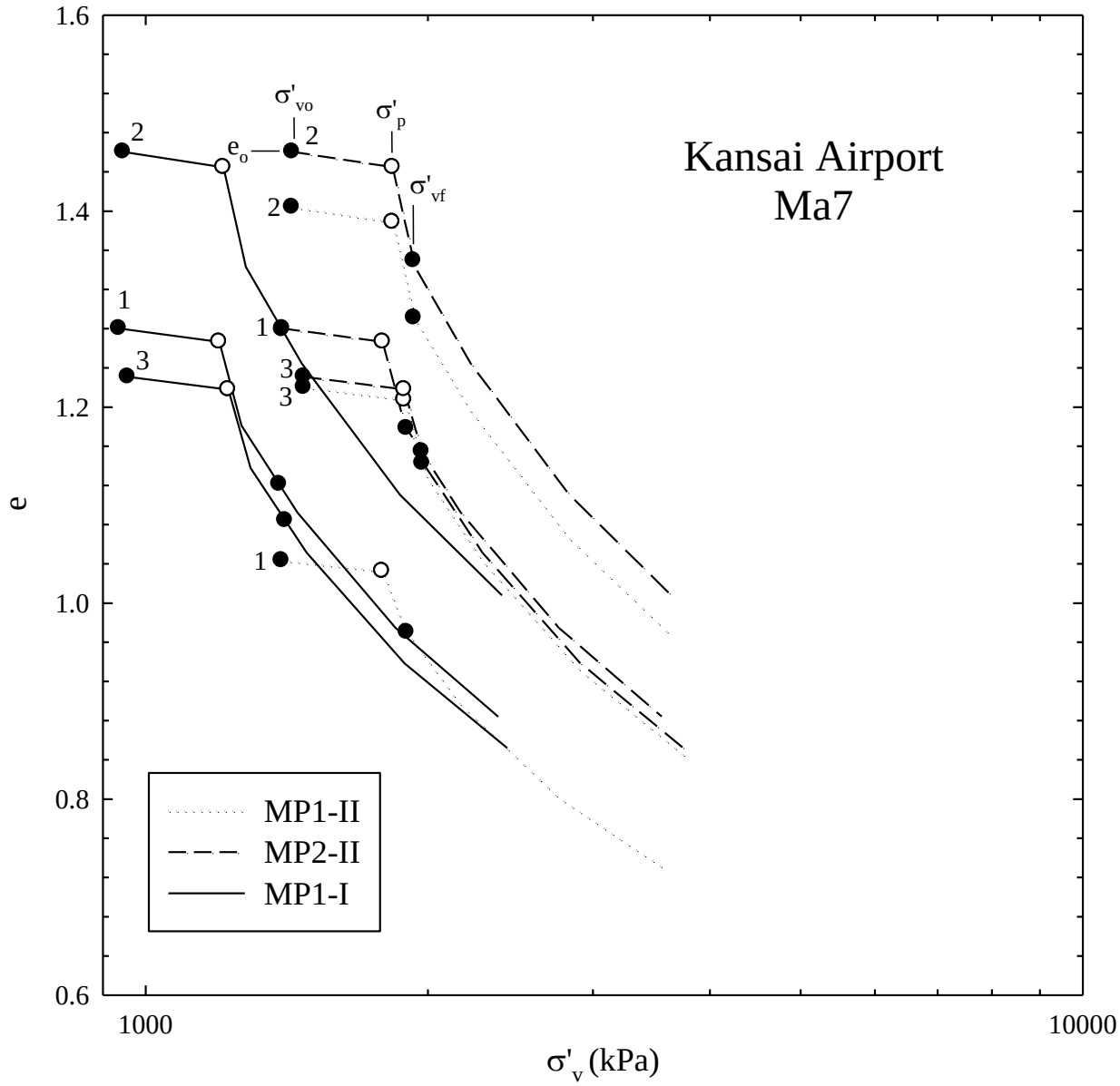

Figure 8-24 EOP e – log σ'_v relationships constructed for Ma7. The numbers identify sublayers.

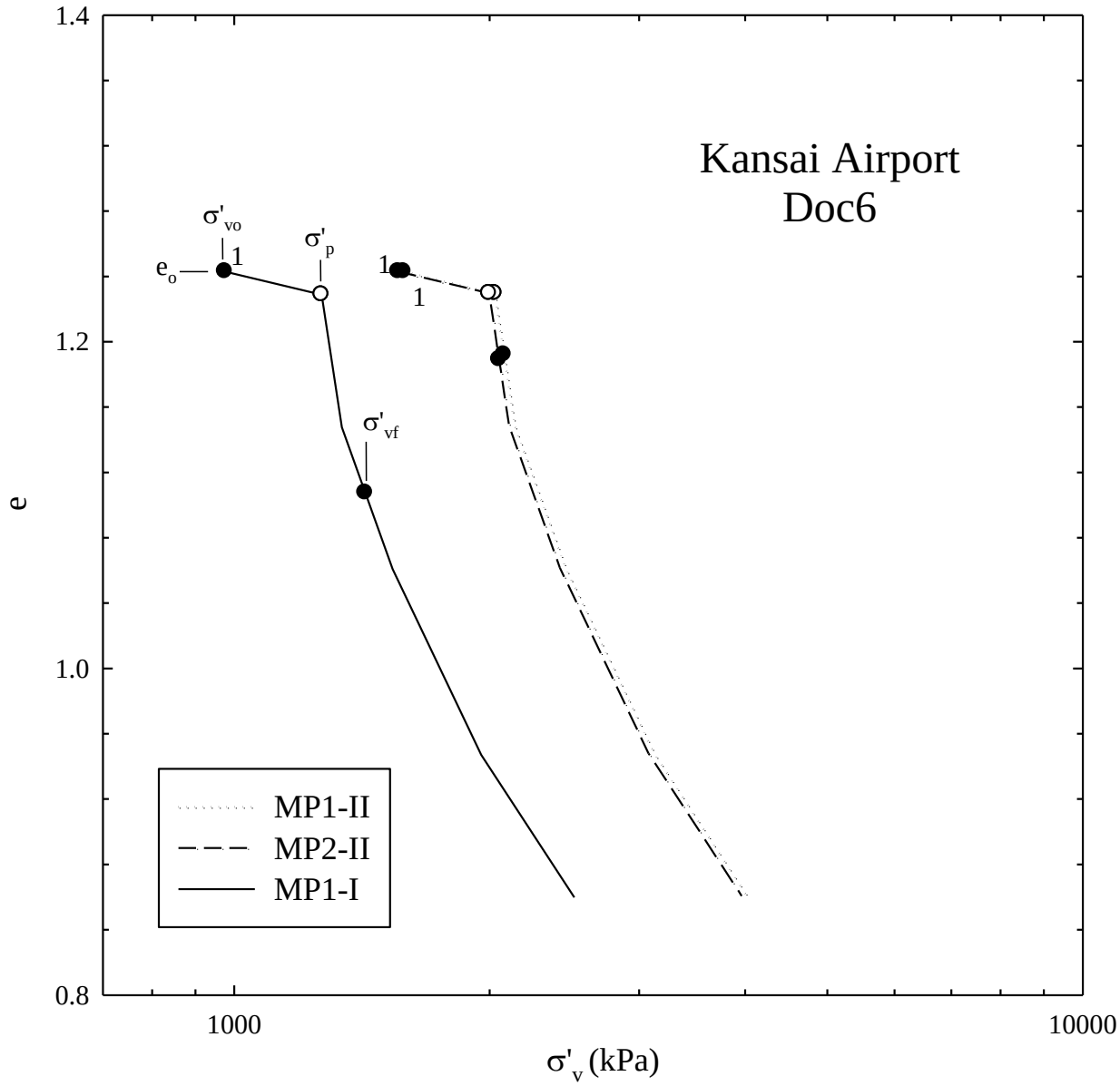

Figure 8-25 EOP e – log σ'_v relationships constructed for Doc6. The numbers identify sublayers.

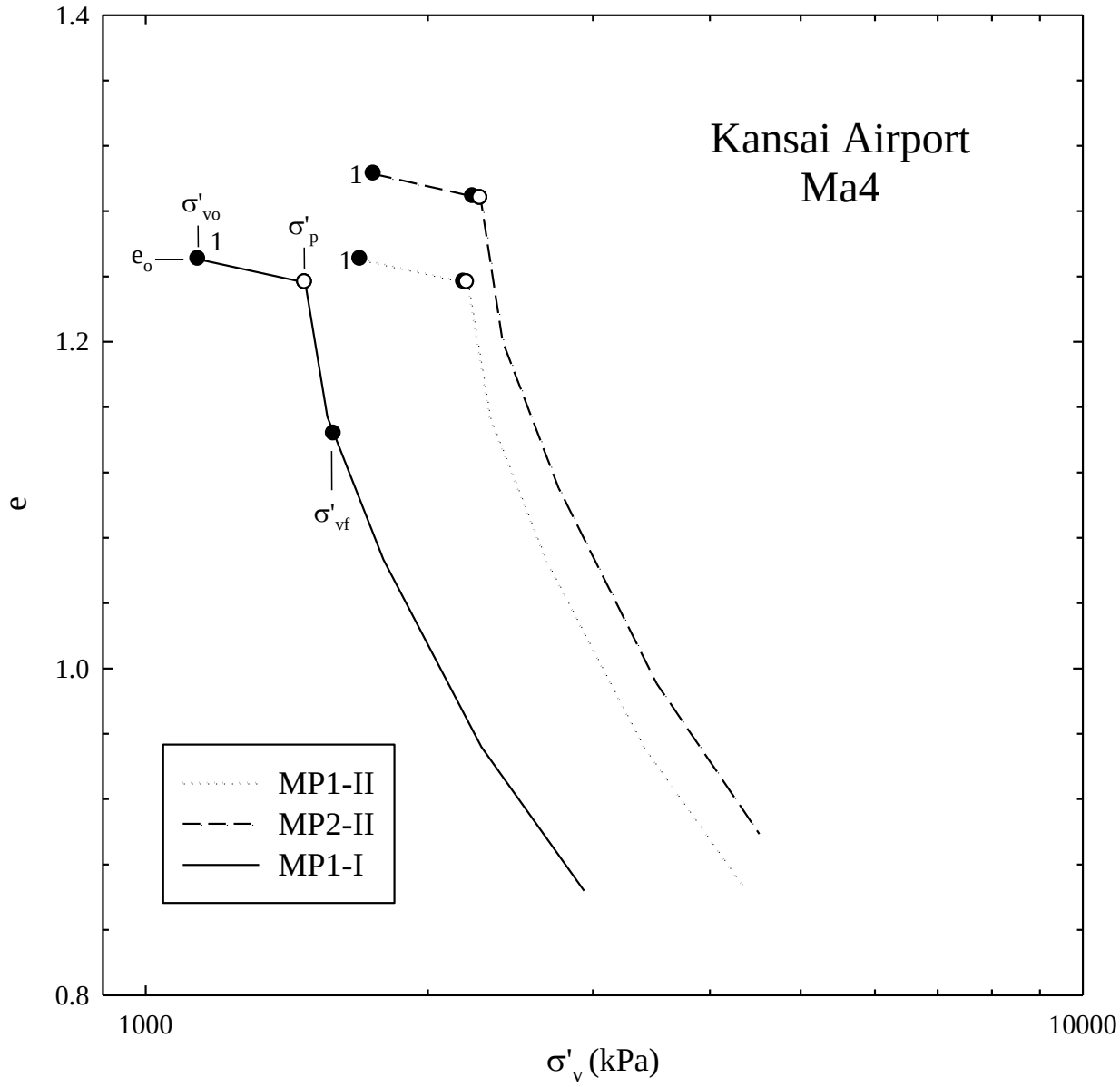

Figure 8-26 EOP e – log σ'_v relationships constructed for Ma4. The numbers identify sublayers.

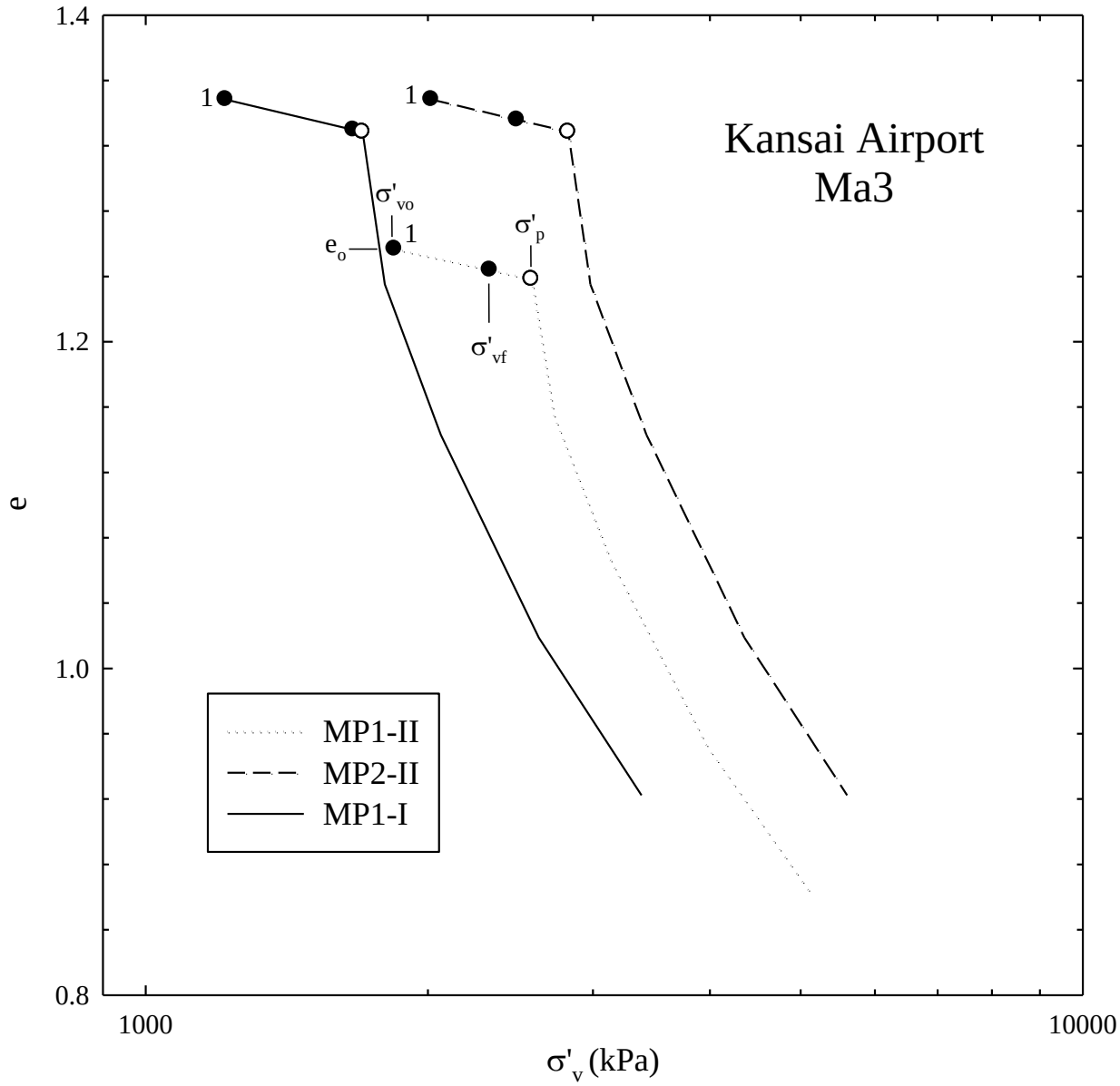

Figure 8-27 EOP e – log σ'_v relationships constructed for Ma3. The numbers identify sublayers.

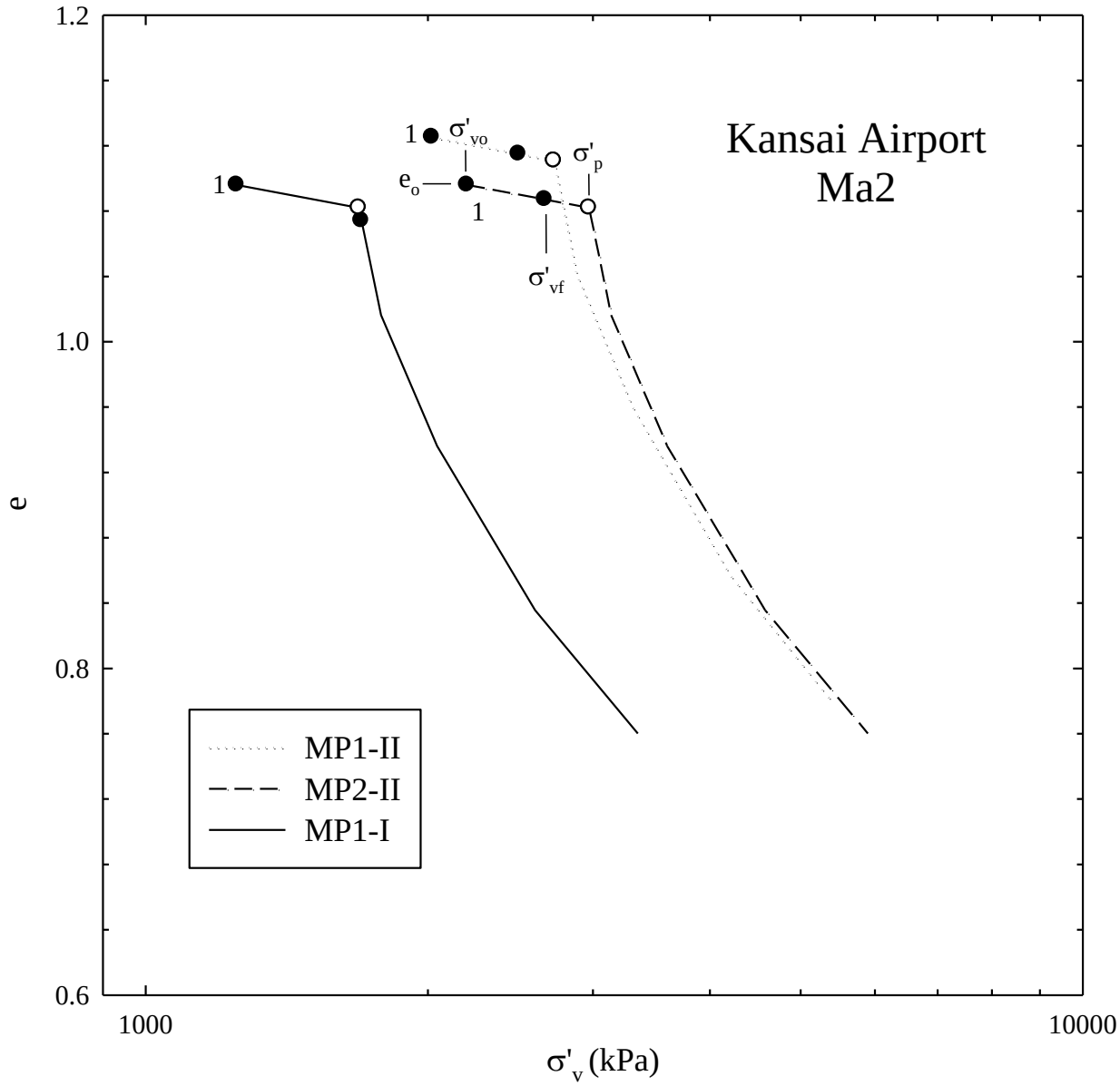

Figure 8-28 EOP e – log σ'_v relationships constructed for Ma2. The numbers identify sublayers.

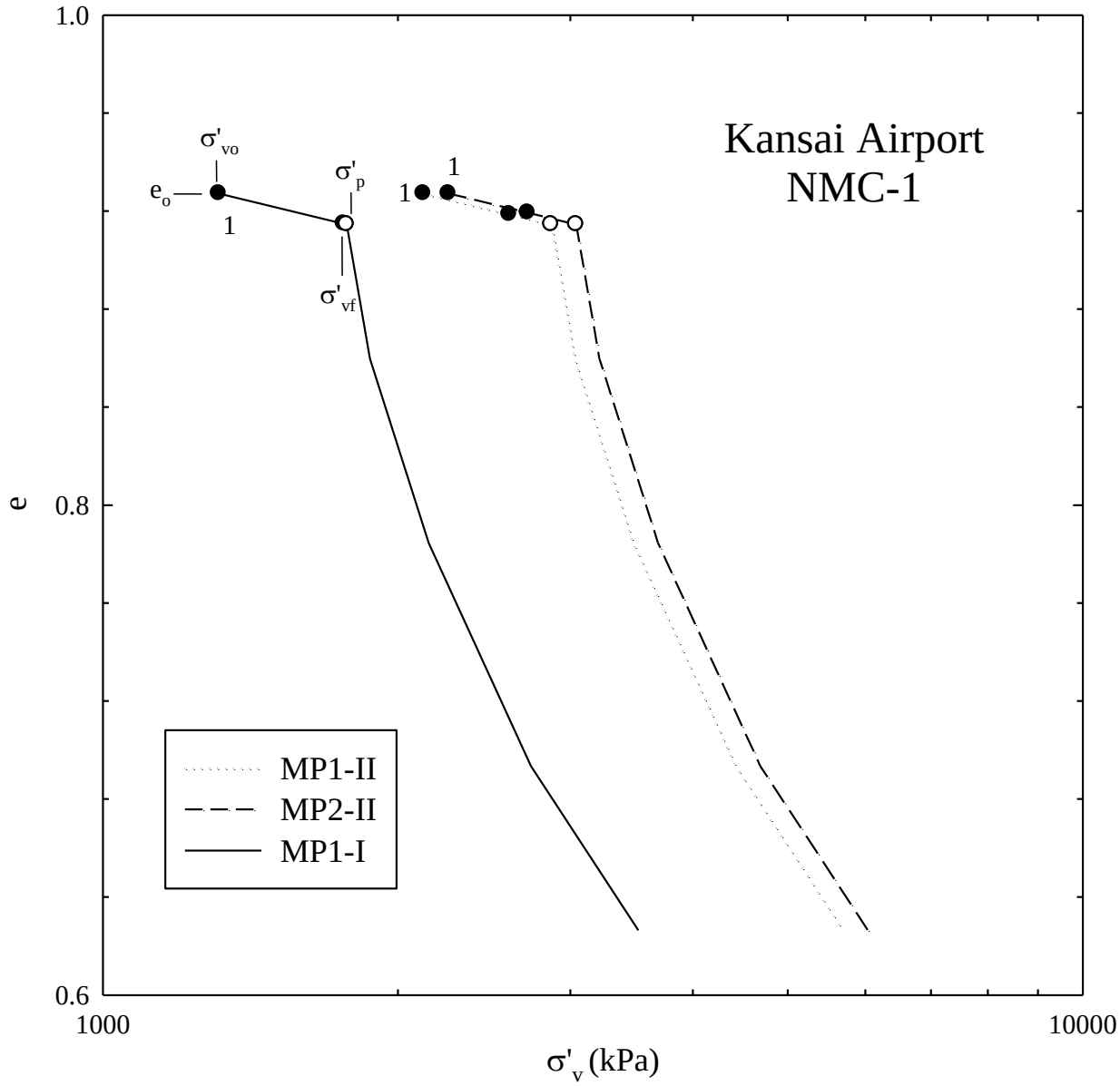

Figure 8-29 EOP e – log σ'_v relationships constructed for NMC-1. The numbers identify sublayers.

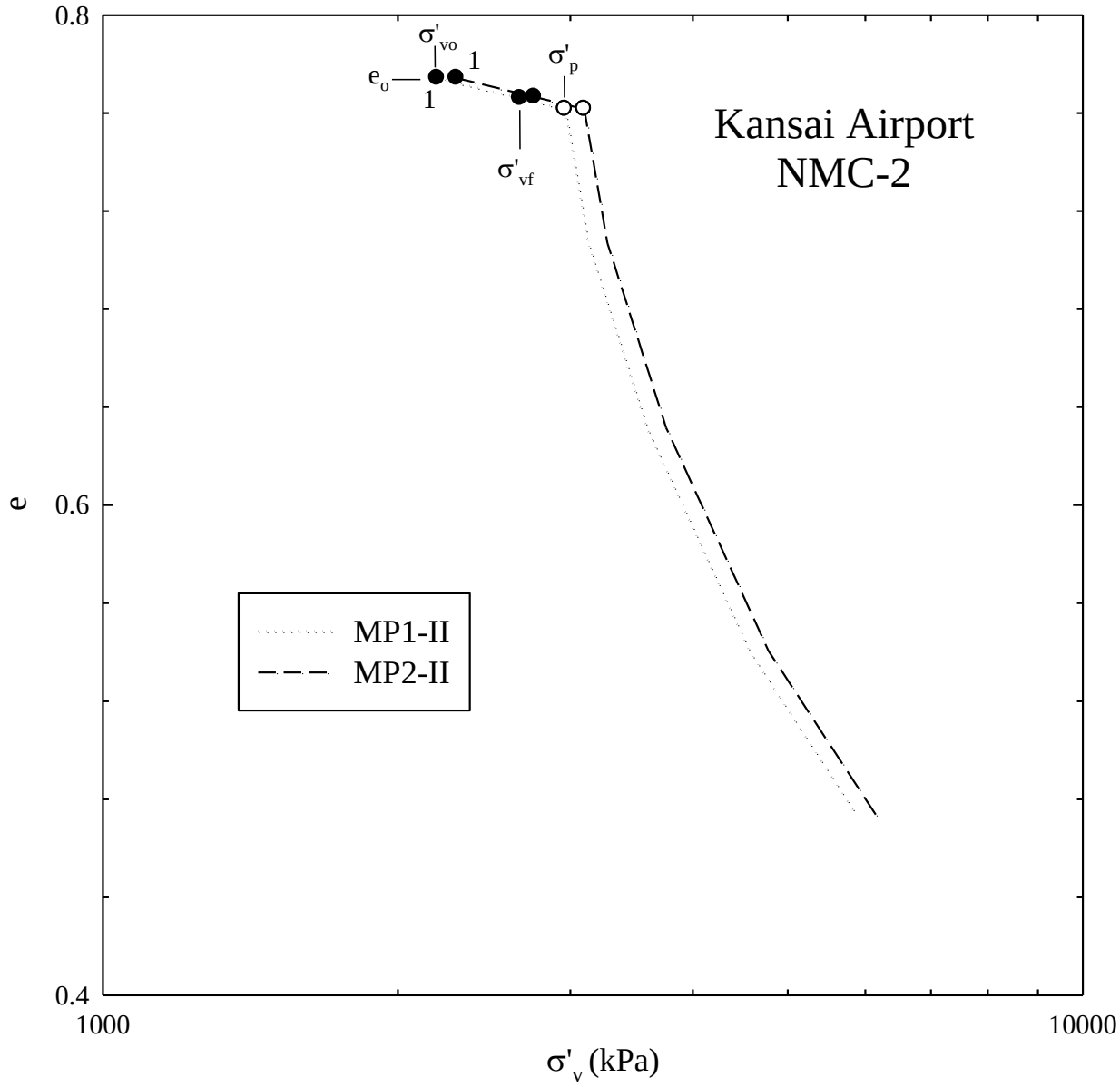

Figure 8-30 EOP e – log σ'_v relationships constructed for NMC-2. The numbers identify sublayers.

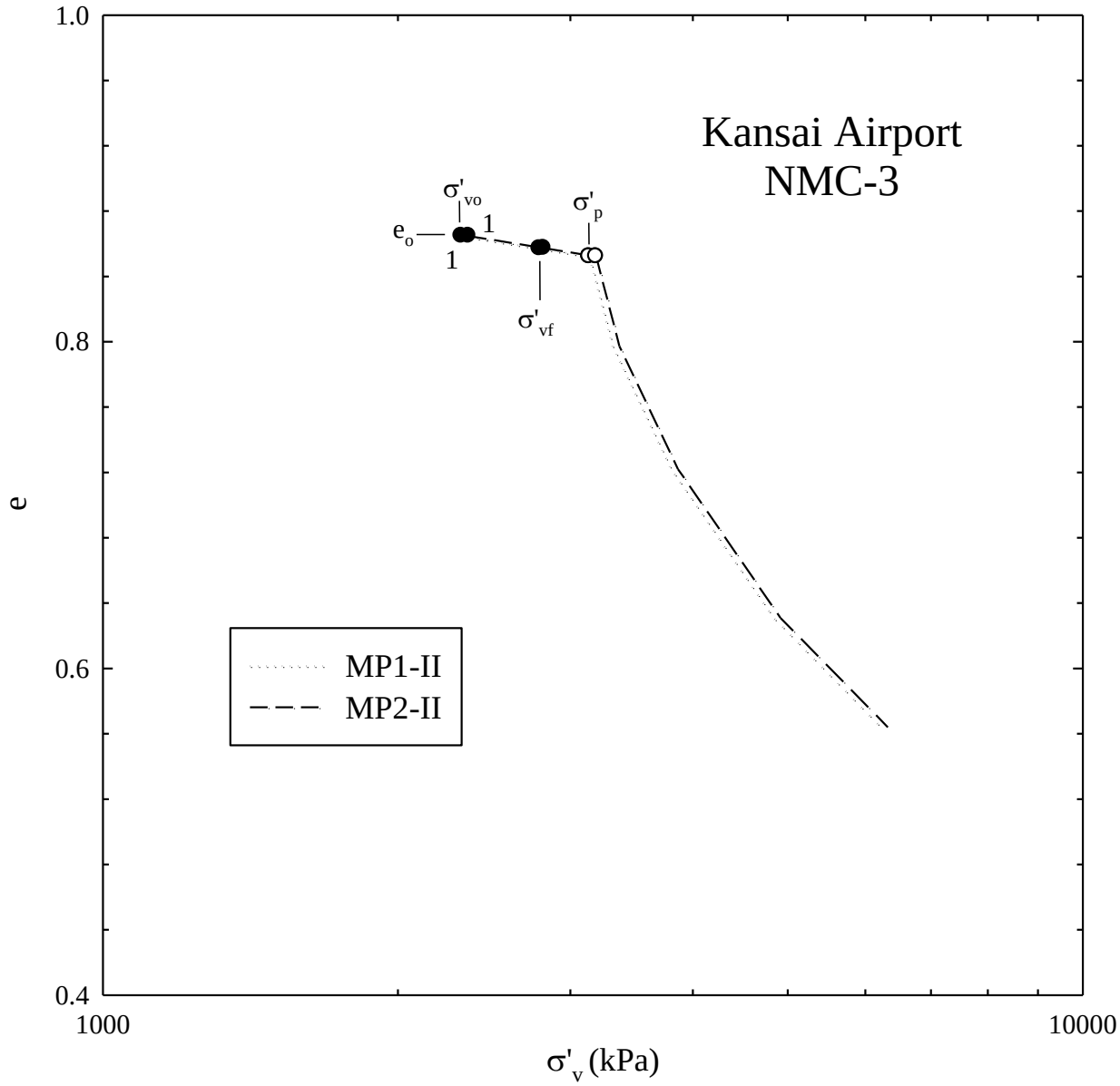

Figure 8-31 EOP e – log σ'_v relationships constructed for NMC-3. The numbers identify sublayers.

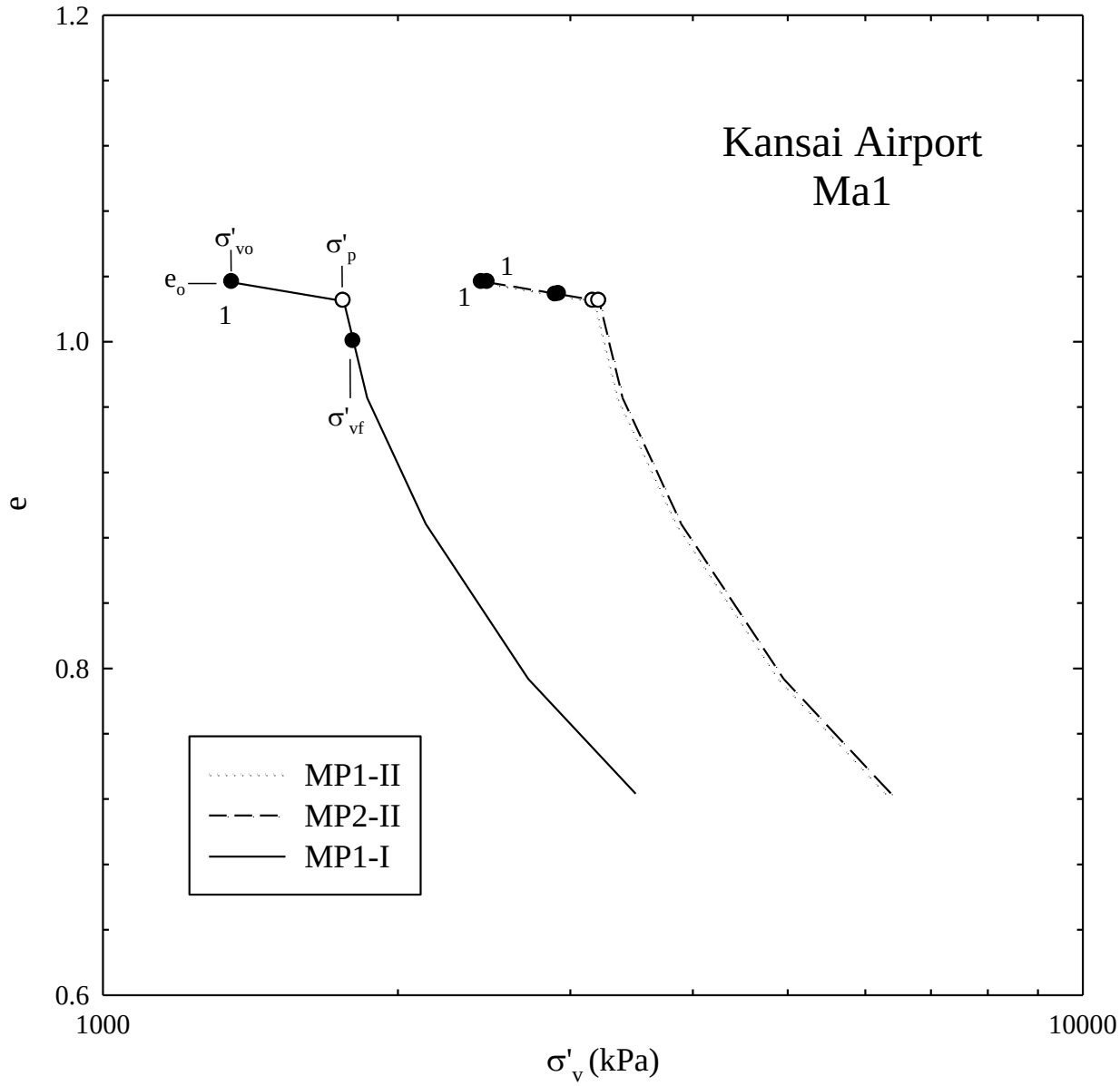

Figure 8-32 EOP e – log σ'_v relationships constructed for Ma1. The numbers identify sublayers.

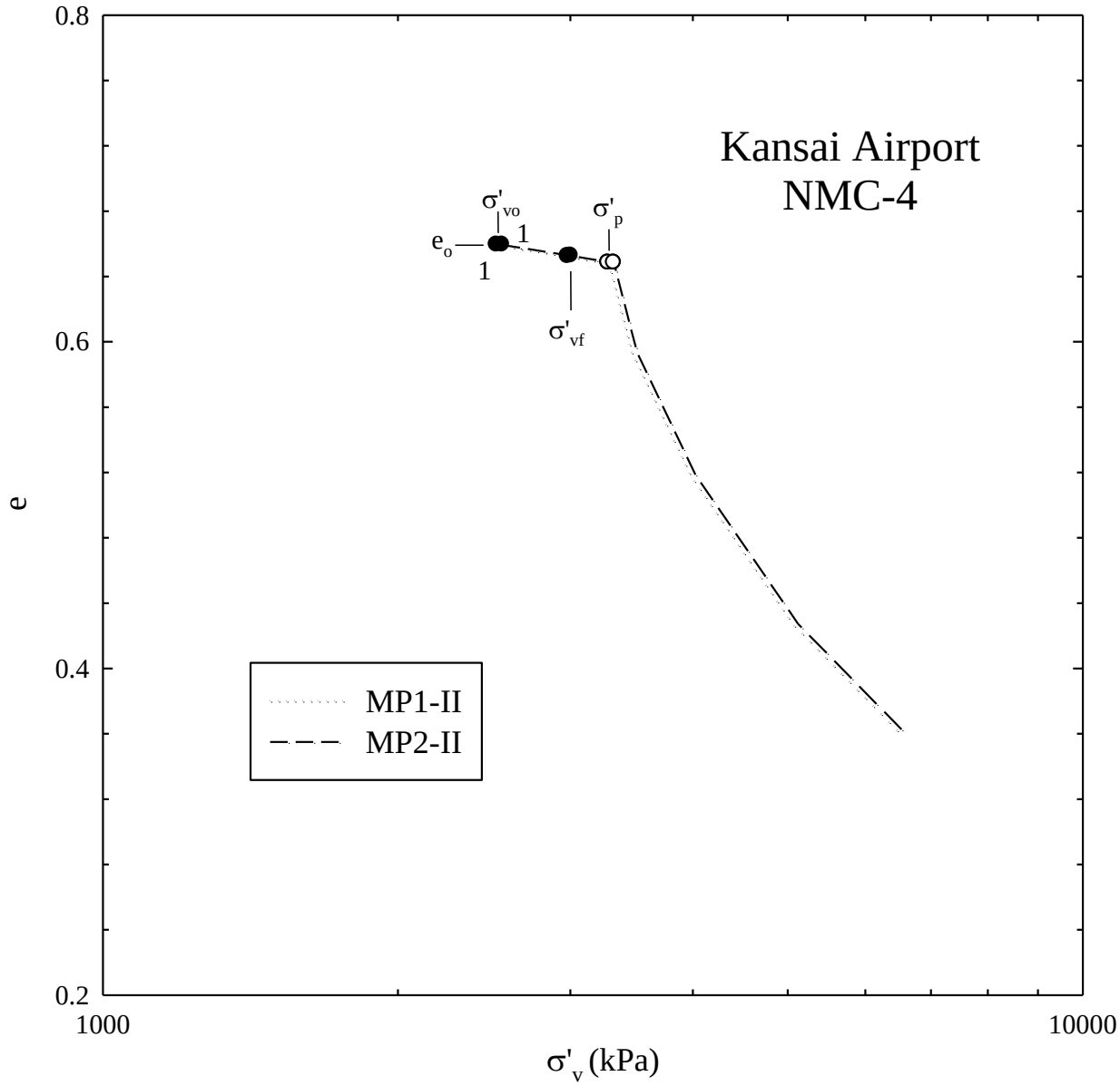

Figure 8-33 EOP e – log σ'_v relationships constructed for NMC-4. The numbers identify sublayers.

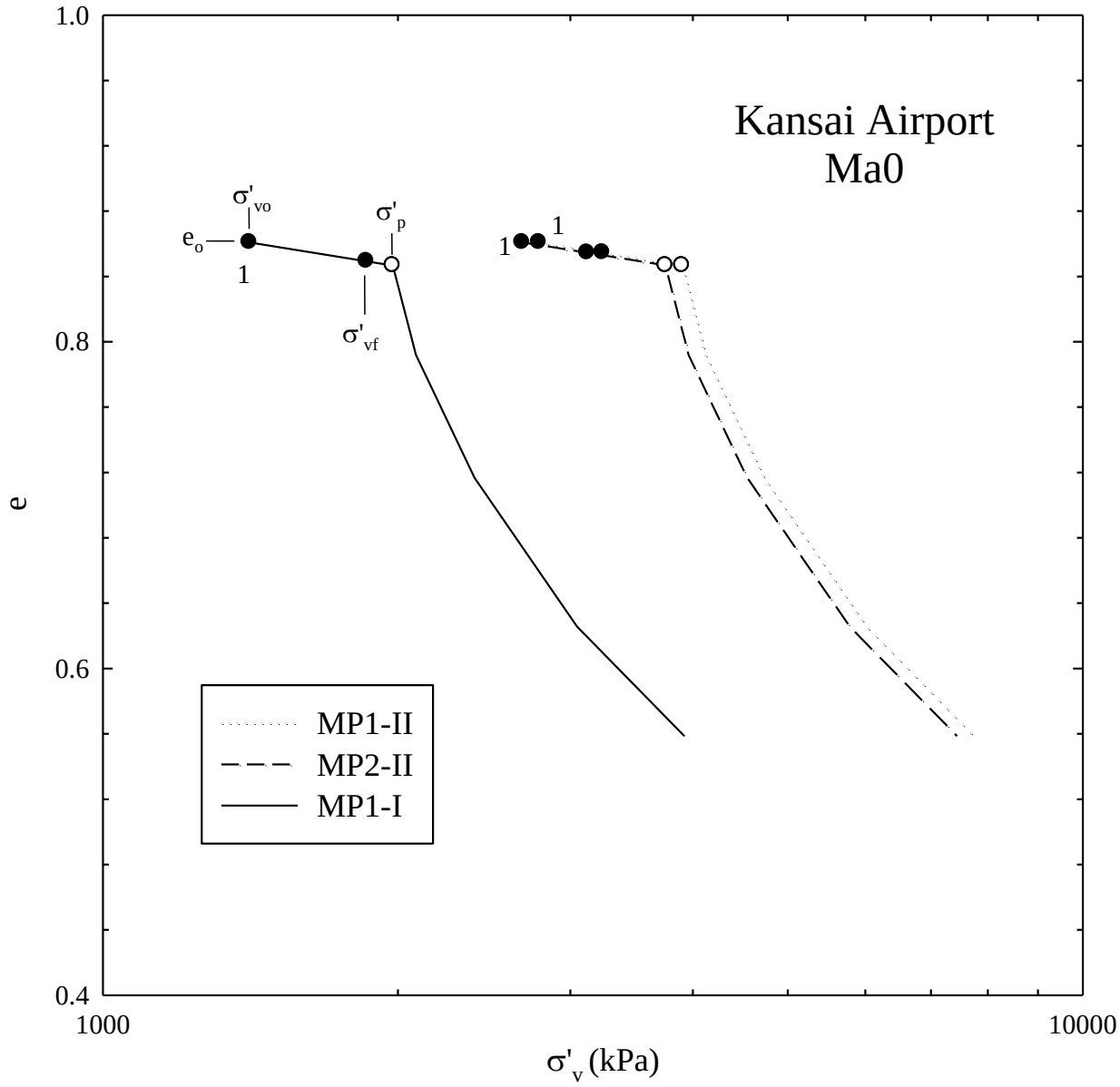

Figure 8-34 EOP e – log σ'_v relationships constructed for Ma0. The numbers identify sublayers.

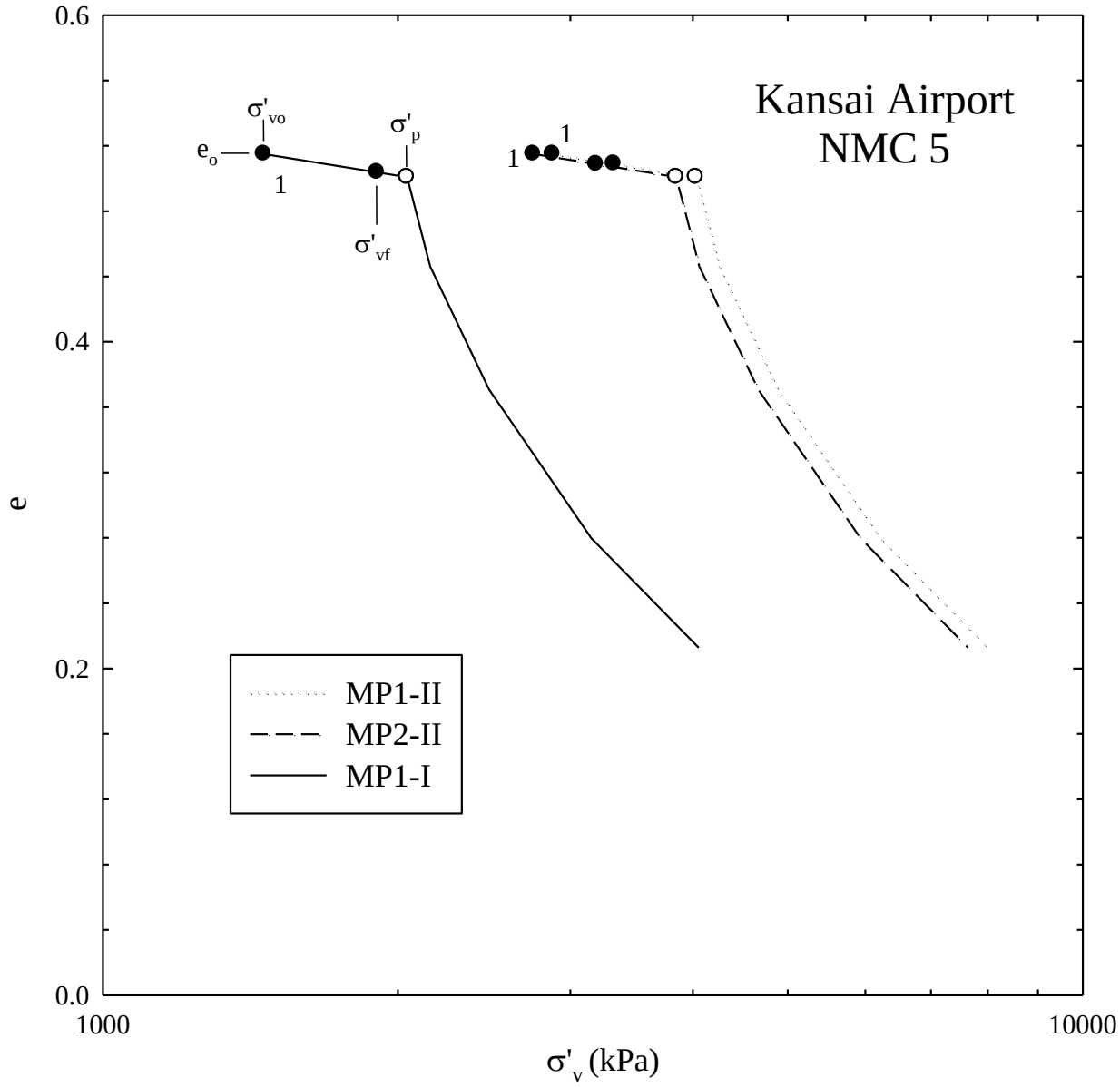

Figure 8-35 EOP e – log σ'_v relationships constructed for NMC-5. The numbers identify sublayers.

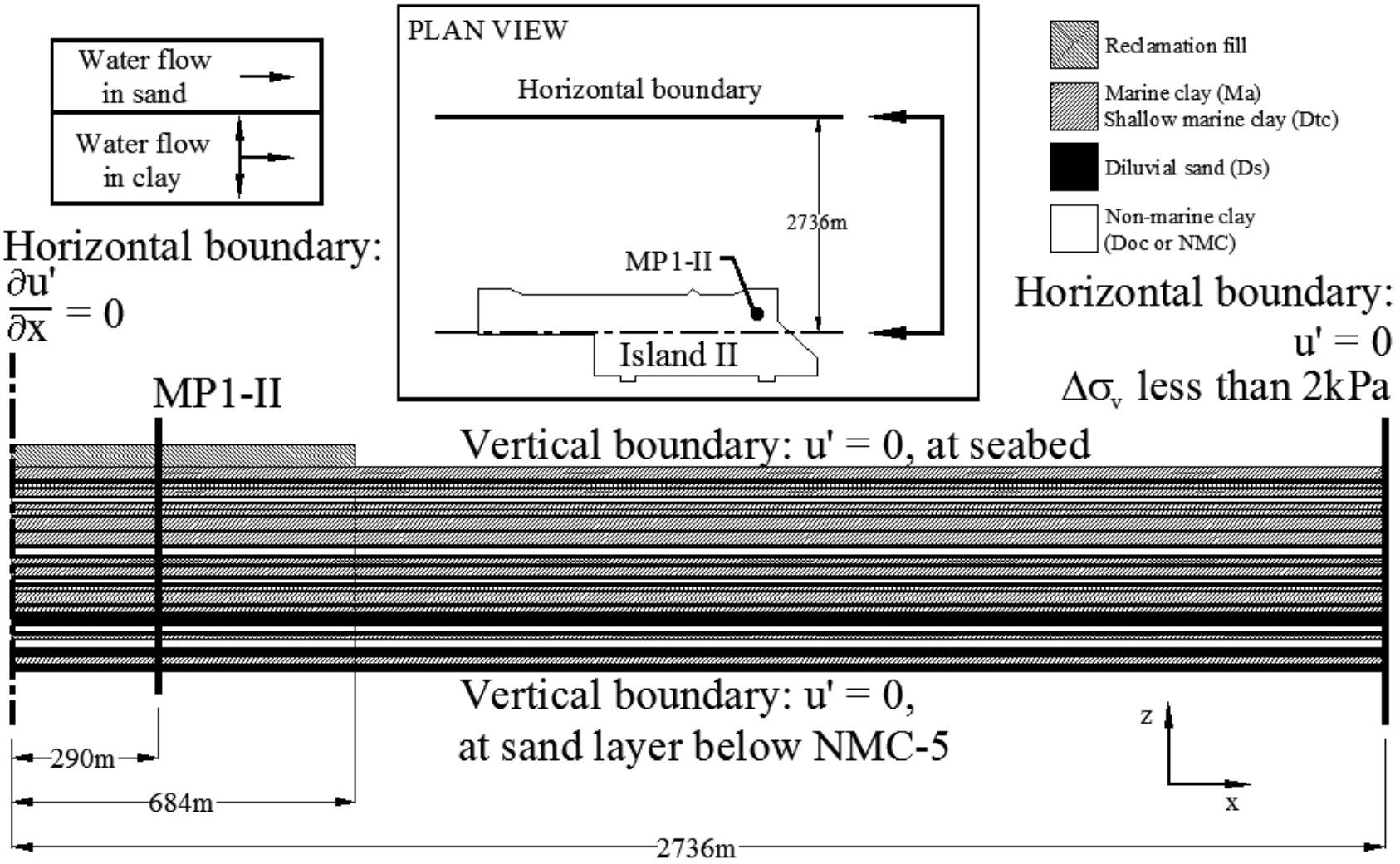

Figure 8-36 Setup for ILLICON analysis at MP1-II.

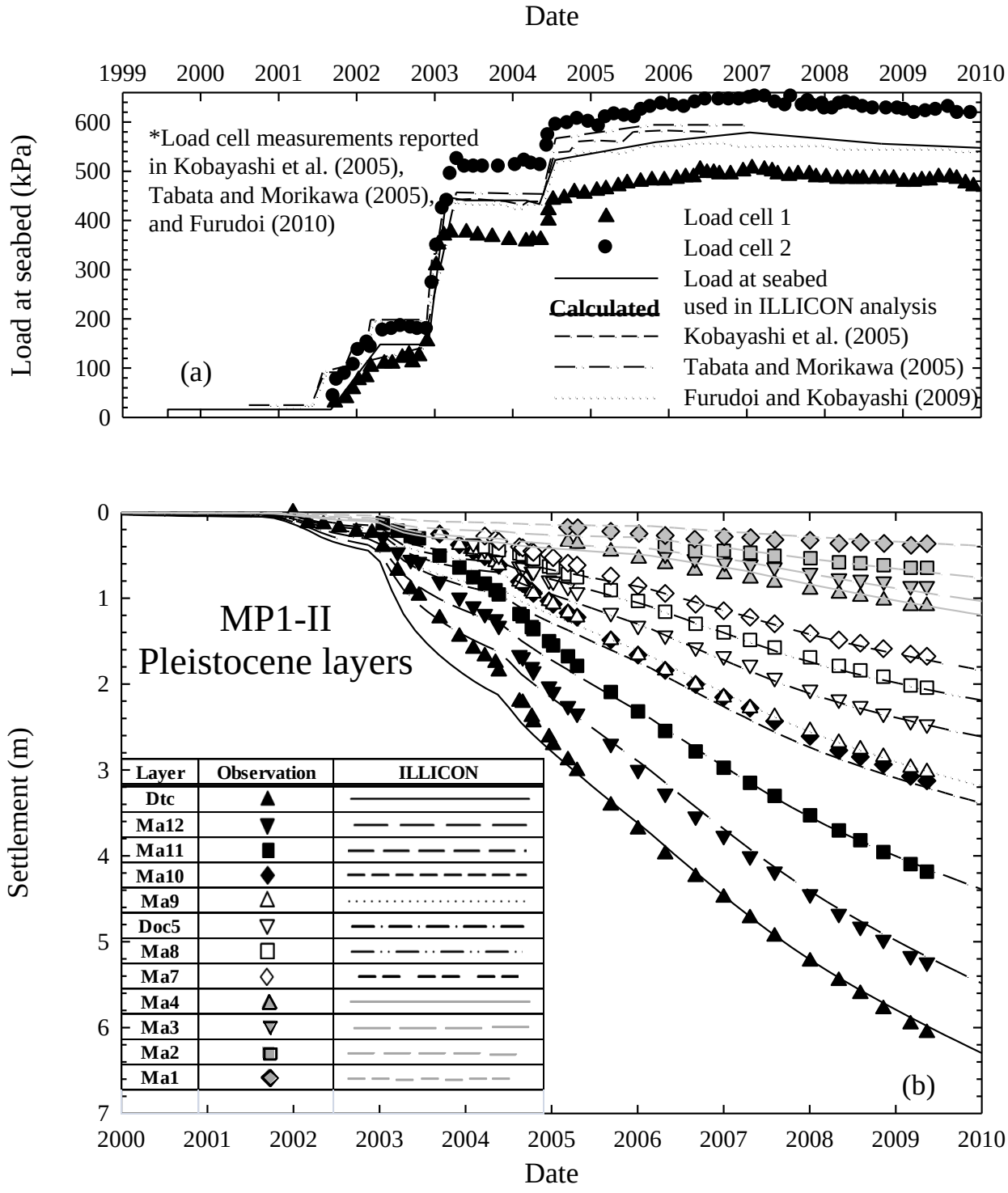

Figure 8-37 Observed (Furudoi and Kobayashi, 2009) and calculated settlement of Pleistocene layers at MP1-II.

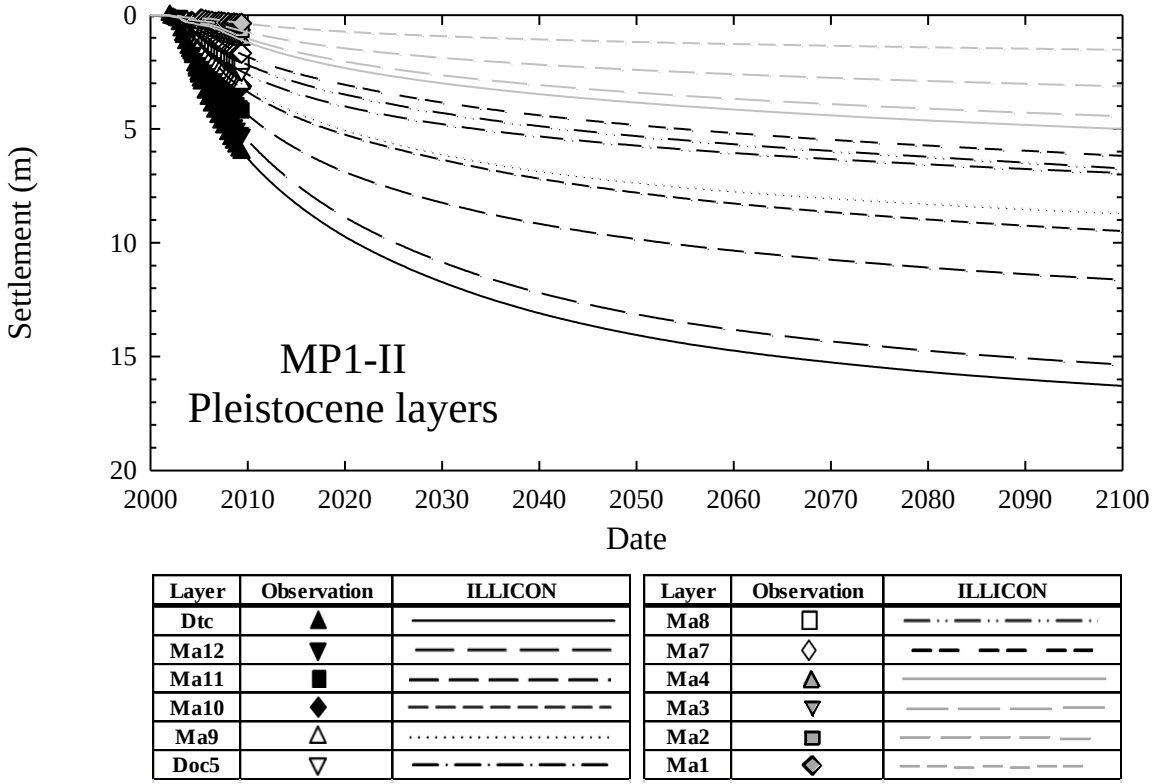

Figure 8-38 Long-term settlement of Pleistocene layers at MP1-II.

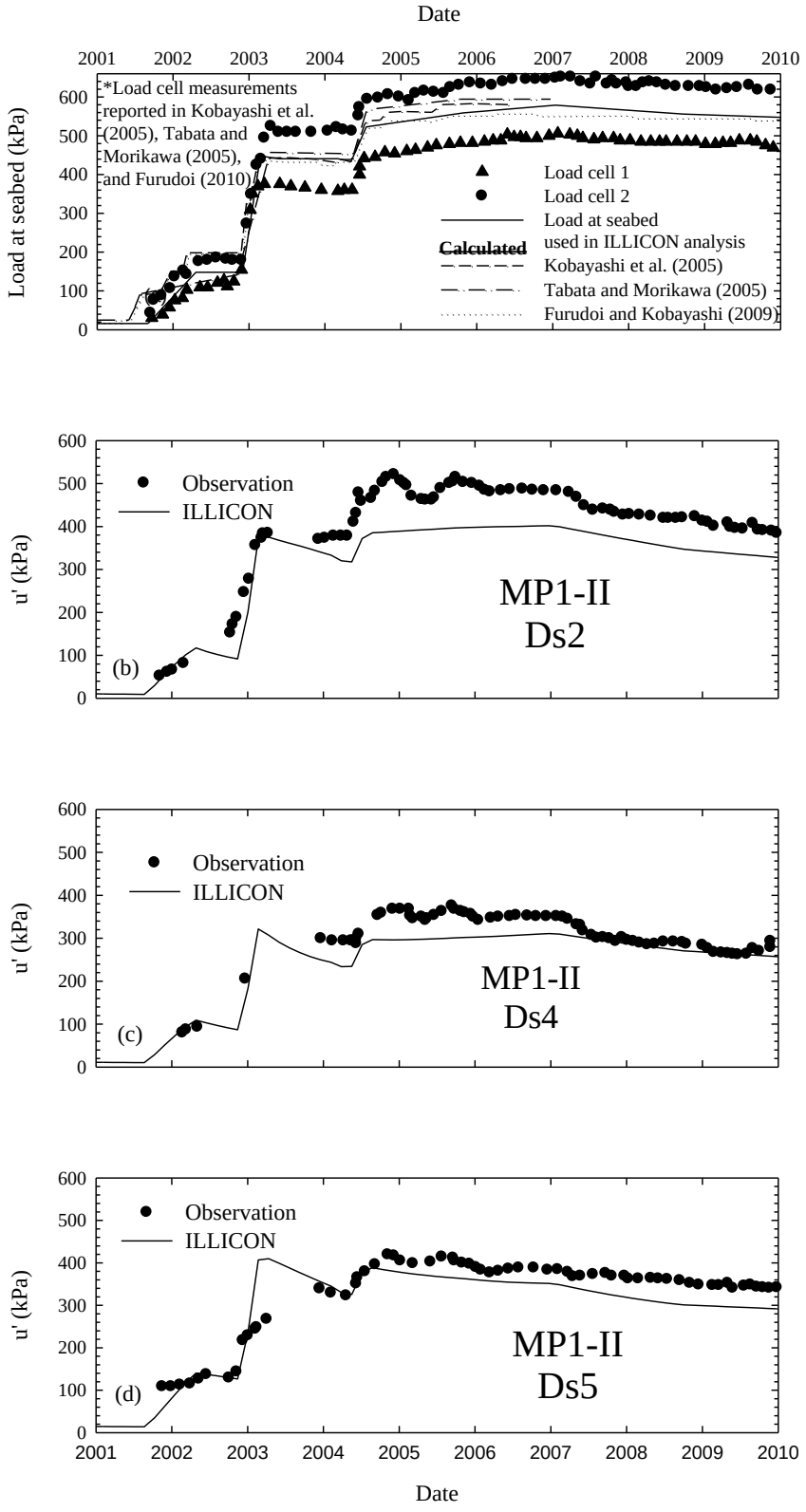

Figure 8-39 Observed (Furudoi, 2010) and calculated excess porewater pressures at MP1-II.

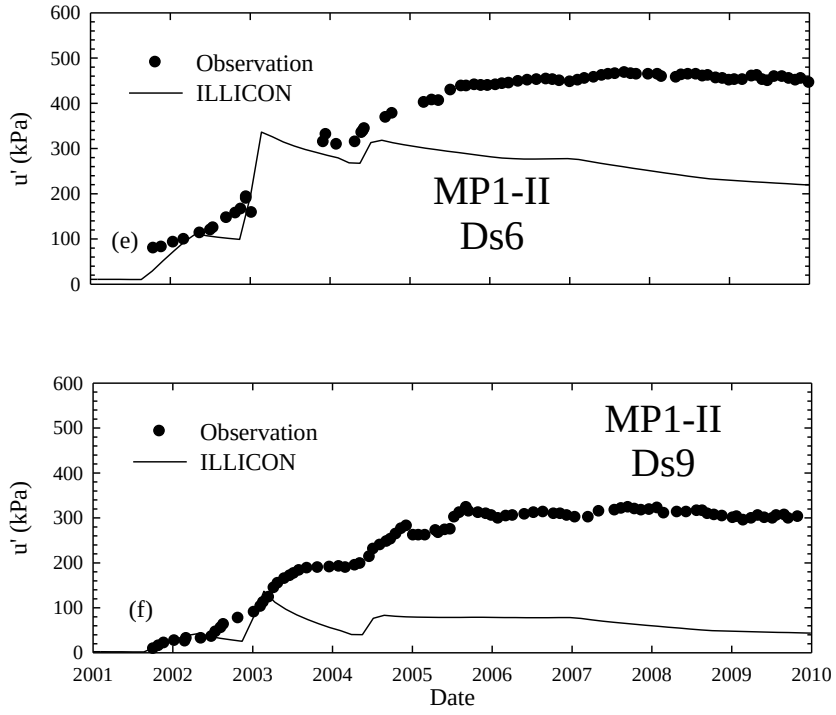

Figure 8-39 cont. Observed (Furudoi, 2010) and calculated excess porewater pressures at MP1-II.

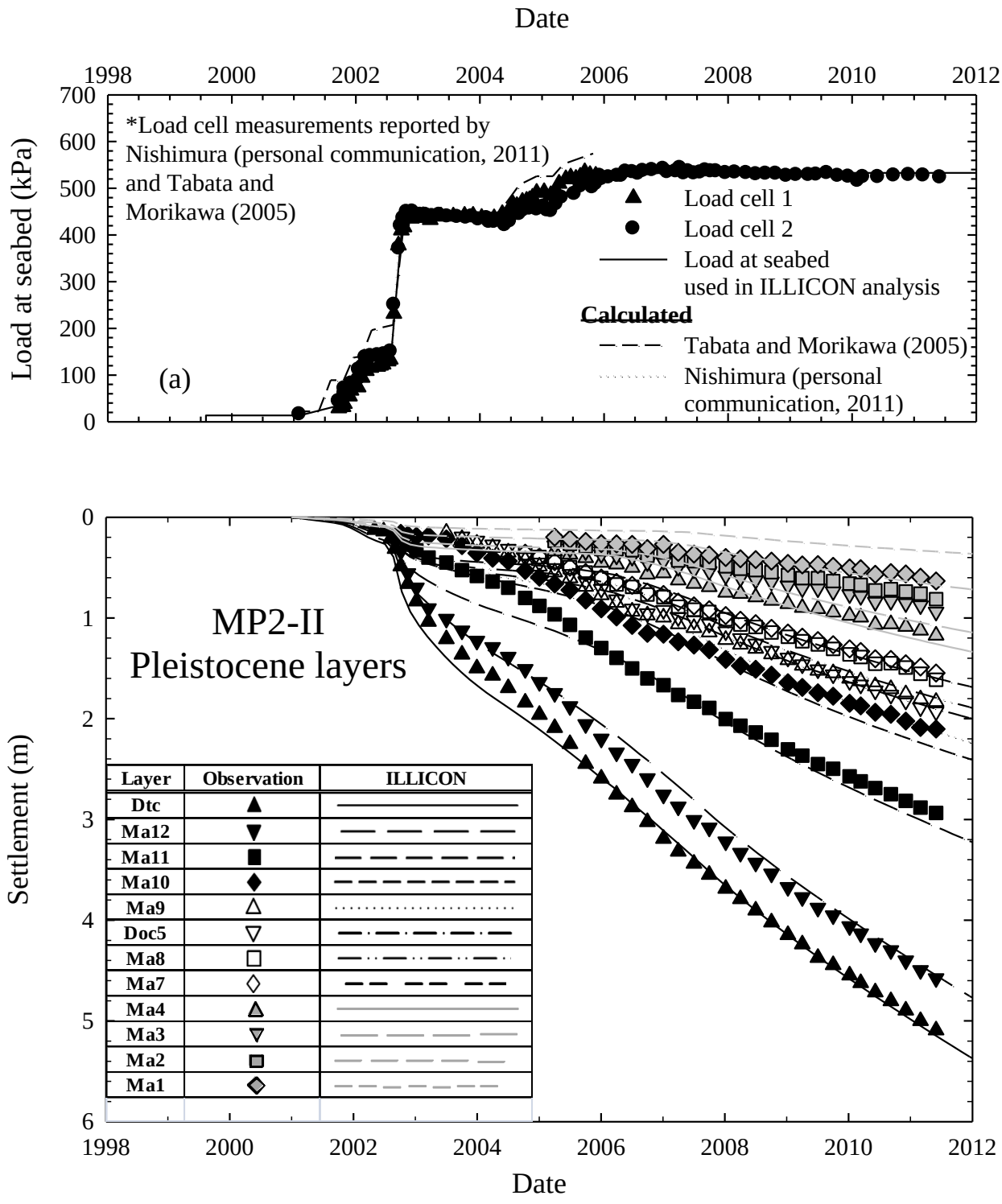

Figure 8-40 Observed (Nishimura, personal communication, 2011) and calculated settlement of Pleistocene layers at MP2-II.

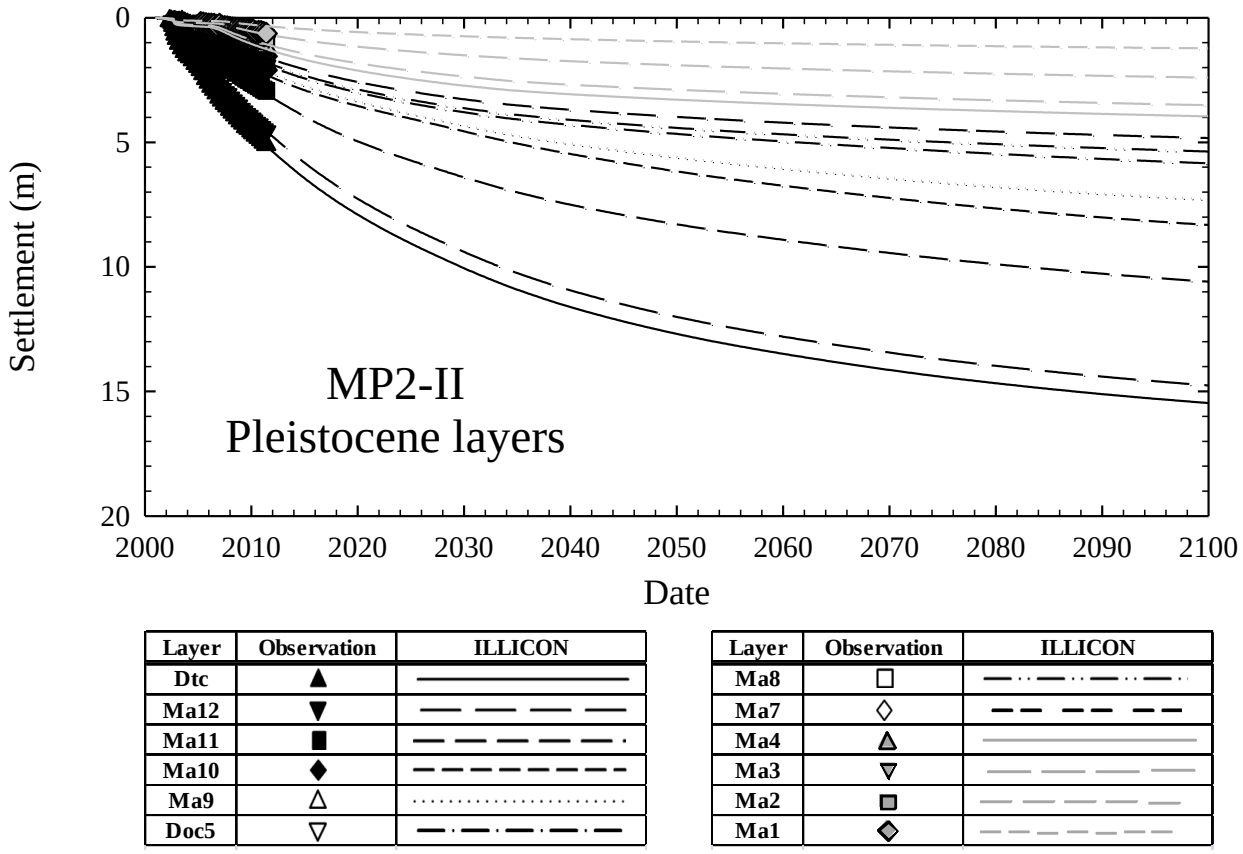

Figure 8-41 Long-term settlement of Pleistocene layers at MP2-II.

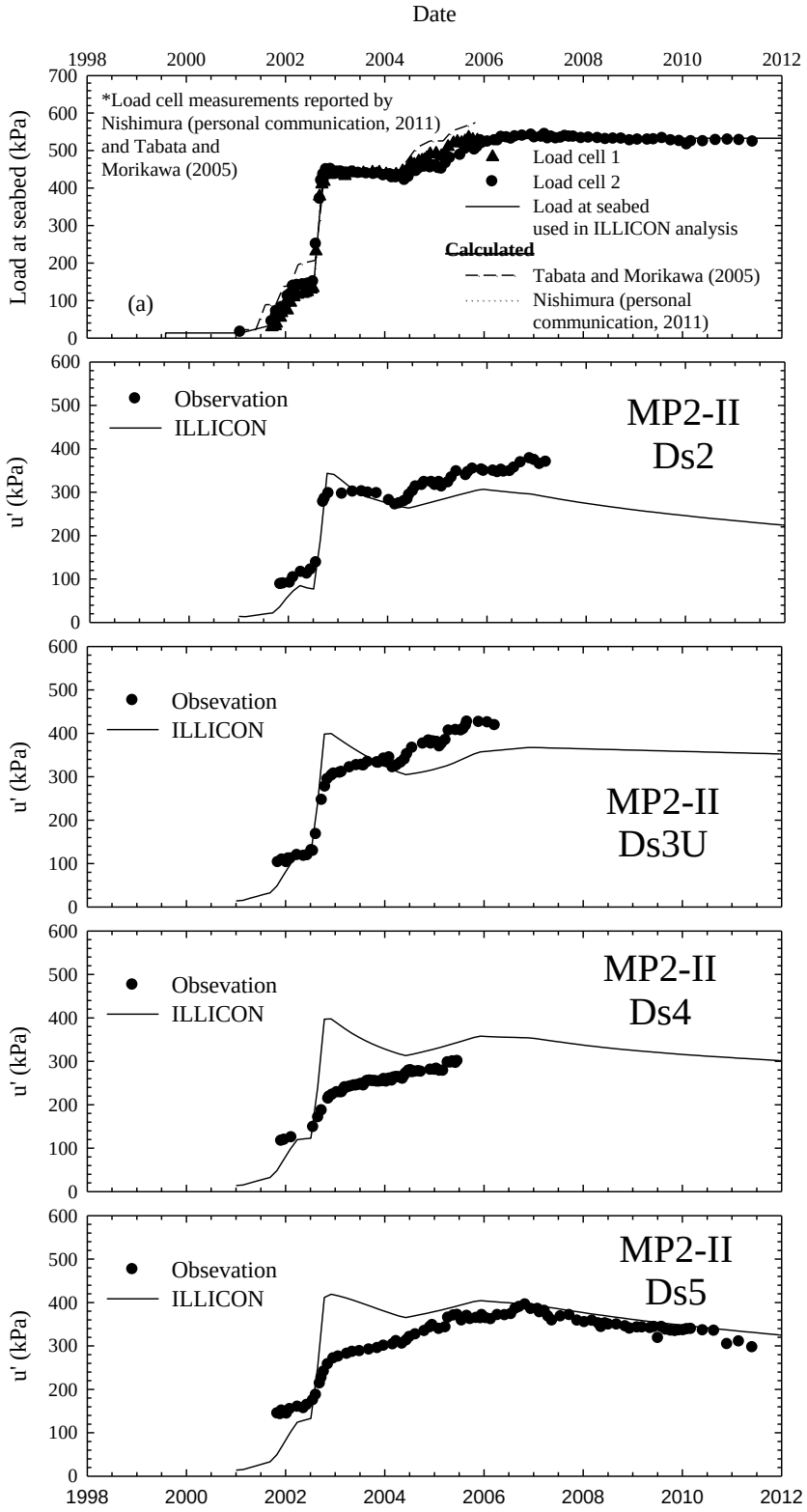

Figure 8-42 Observed (Tabata and Morikawa, 2005; Nishimura, personal communication, 2011) and calculated excess porewater pressures at MP2-II.

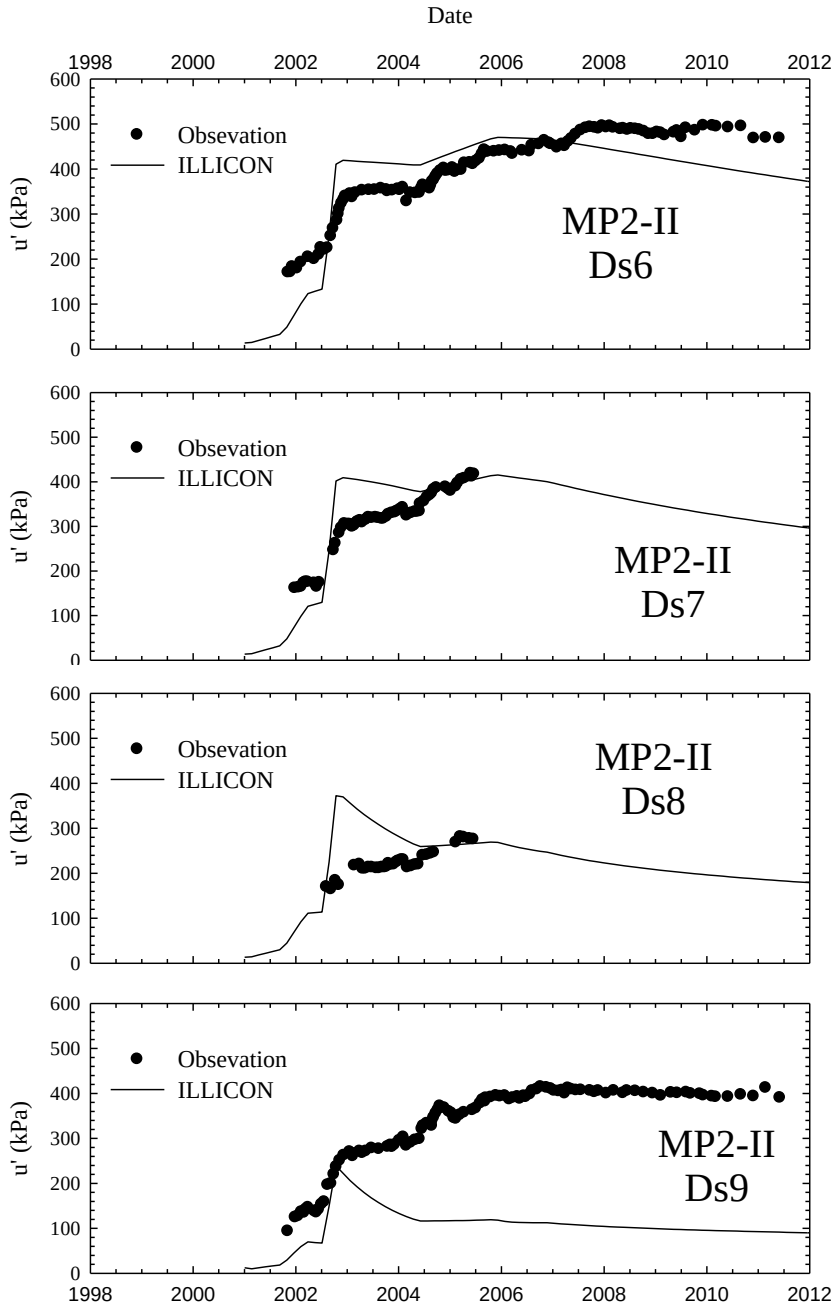

Figure 8-42 cont. Observed (Tabata and Morikawa, 2005; Nishimura, personal communication, 2011) and calculated excess porewater pressures at MP2-II.

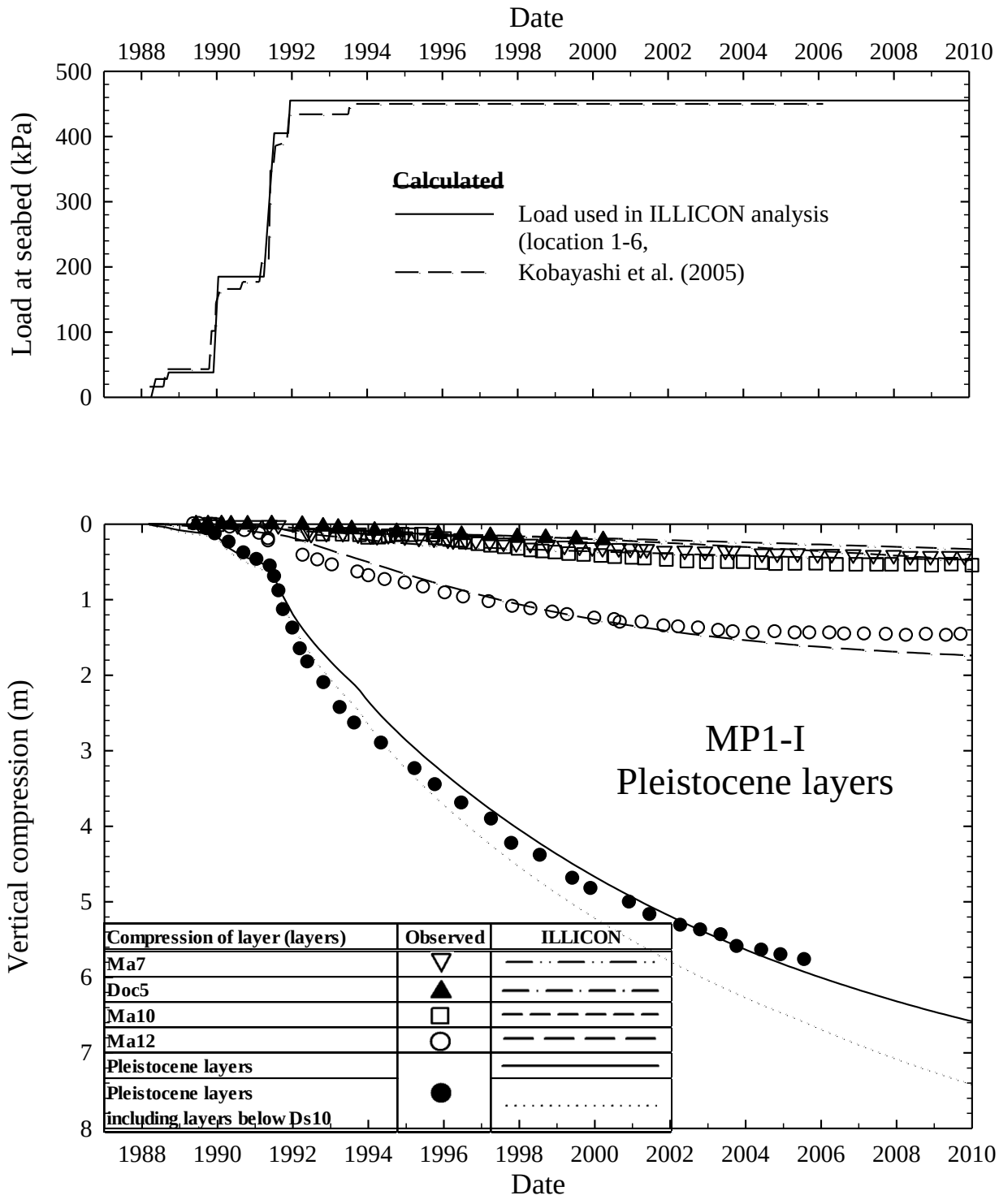

Figure 8-43 Observed (Kobayashi et al., 2005; Rocchi et al., 2007; Jeon et al., 2012) and calculated compression of Pleistocene layers at MP1-I.

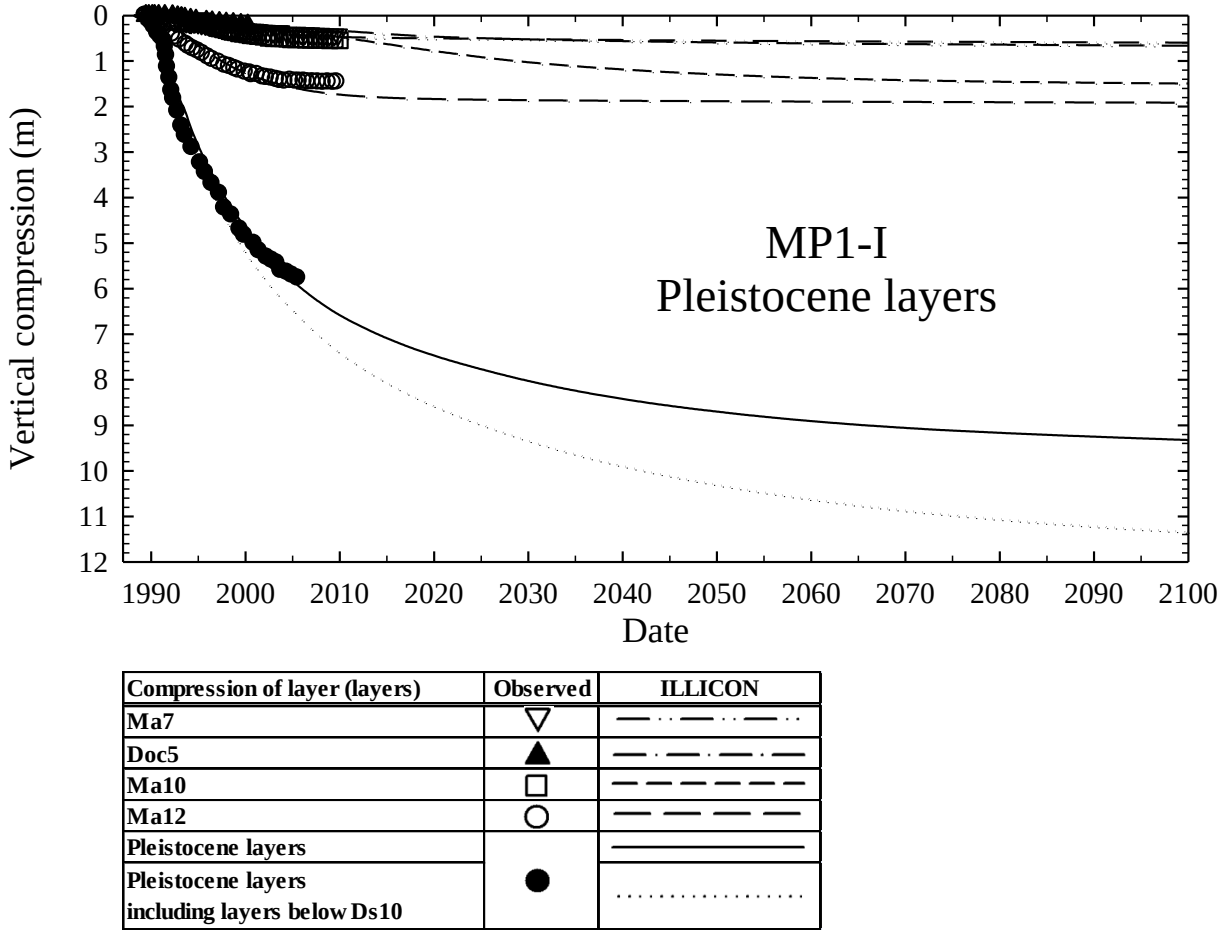

Figure 8-44 Long-term settlement of Pleistocene layers at MP1-I.

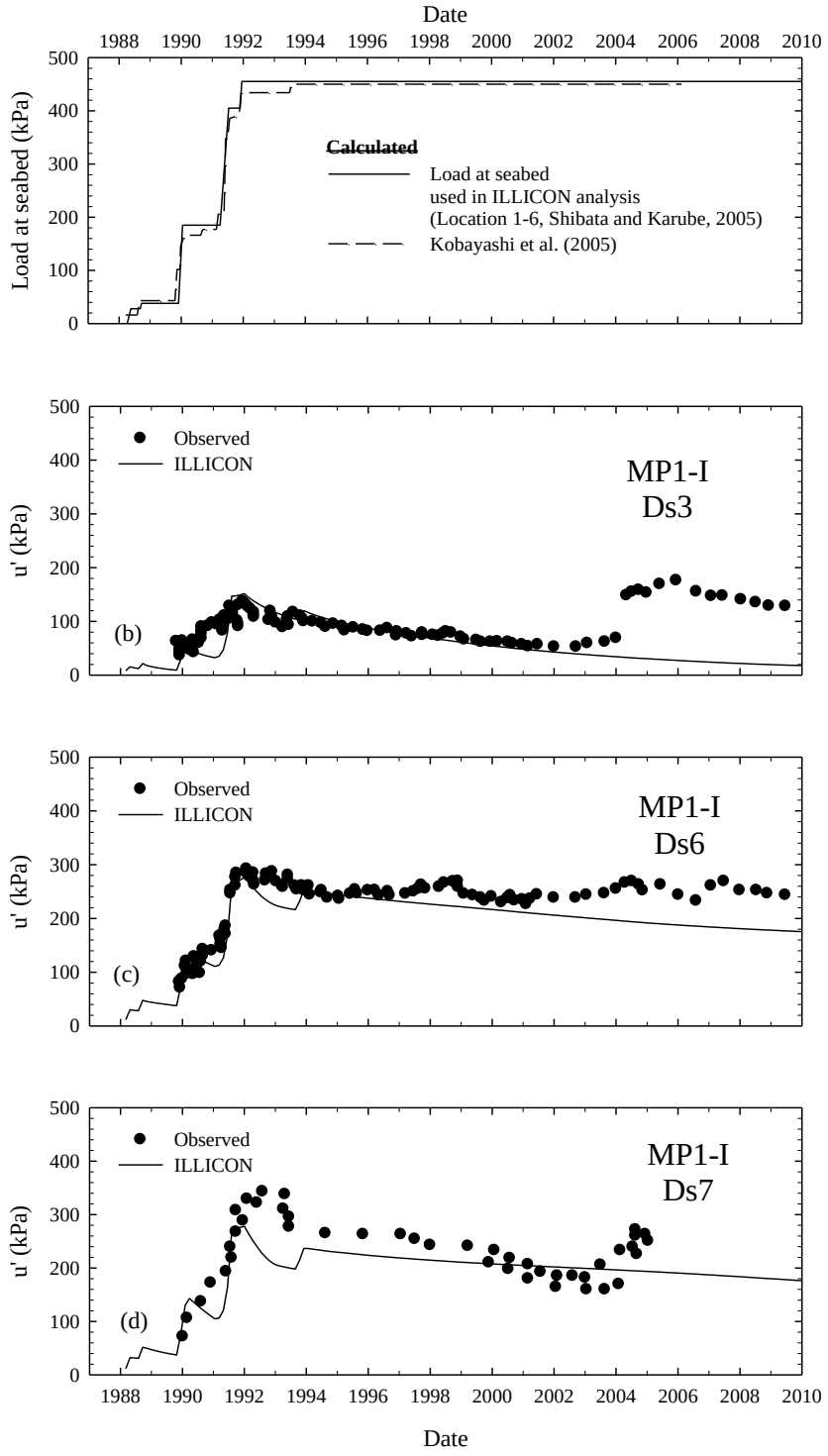

Figure 8-45 Observed (Kobayashi et al., 2005; Jeon et al., 2012) and calculated excess porewater pressures at MP1-I.

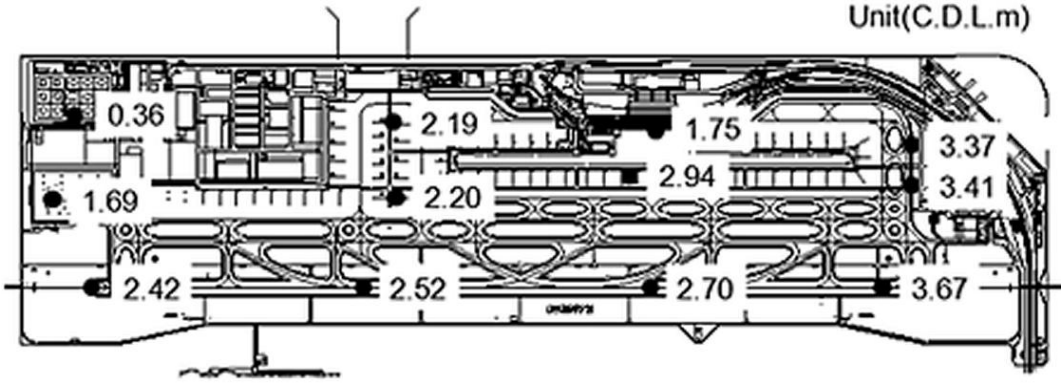

Figure 8-46 Elevations at various points on Island I referenced to Chart Datum Level (CDL) in December 2012 (NKIAC, 2012).

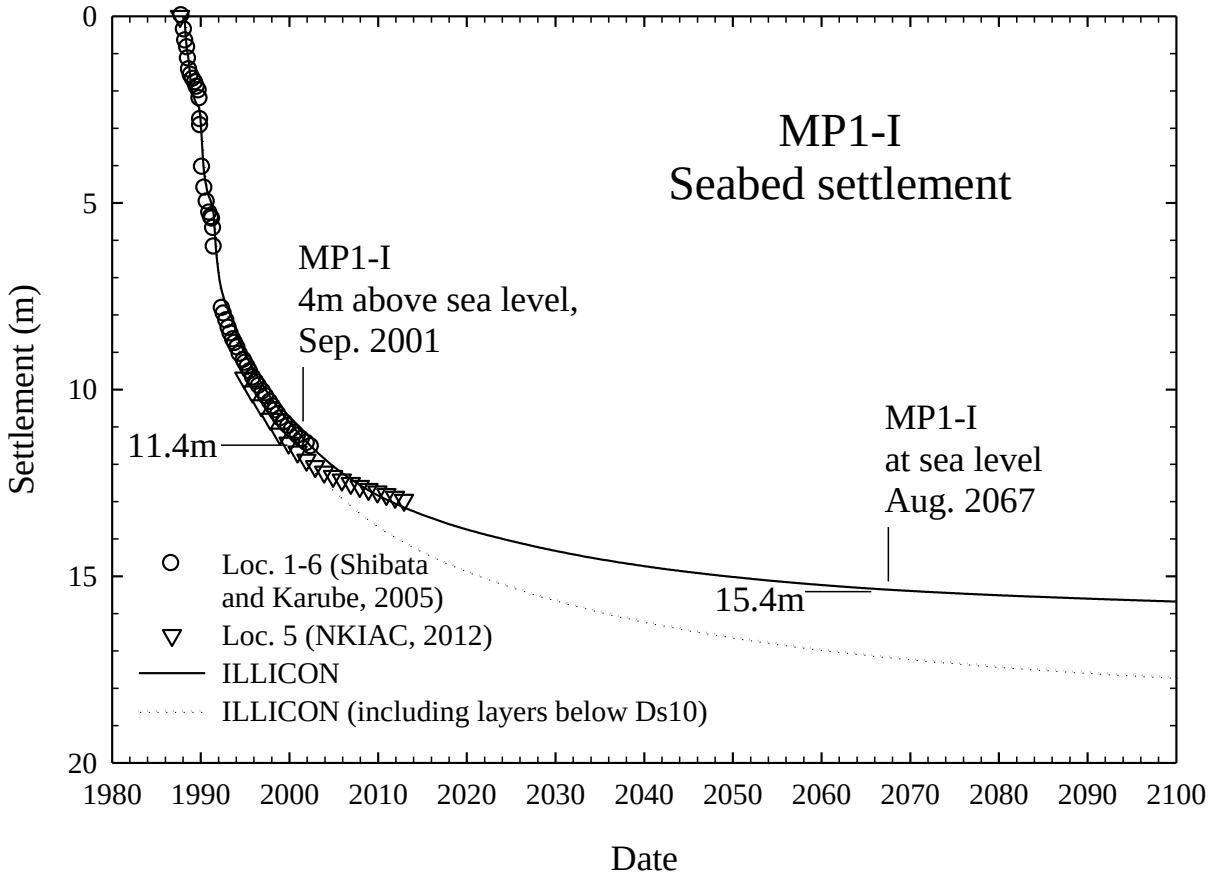

Figure 8-47 Seabed settlement at MP1-I, including compression of Holocene and Pleistocene layers.

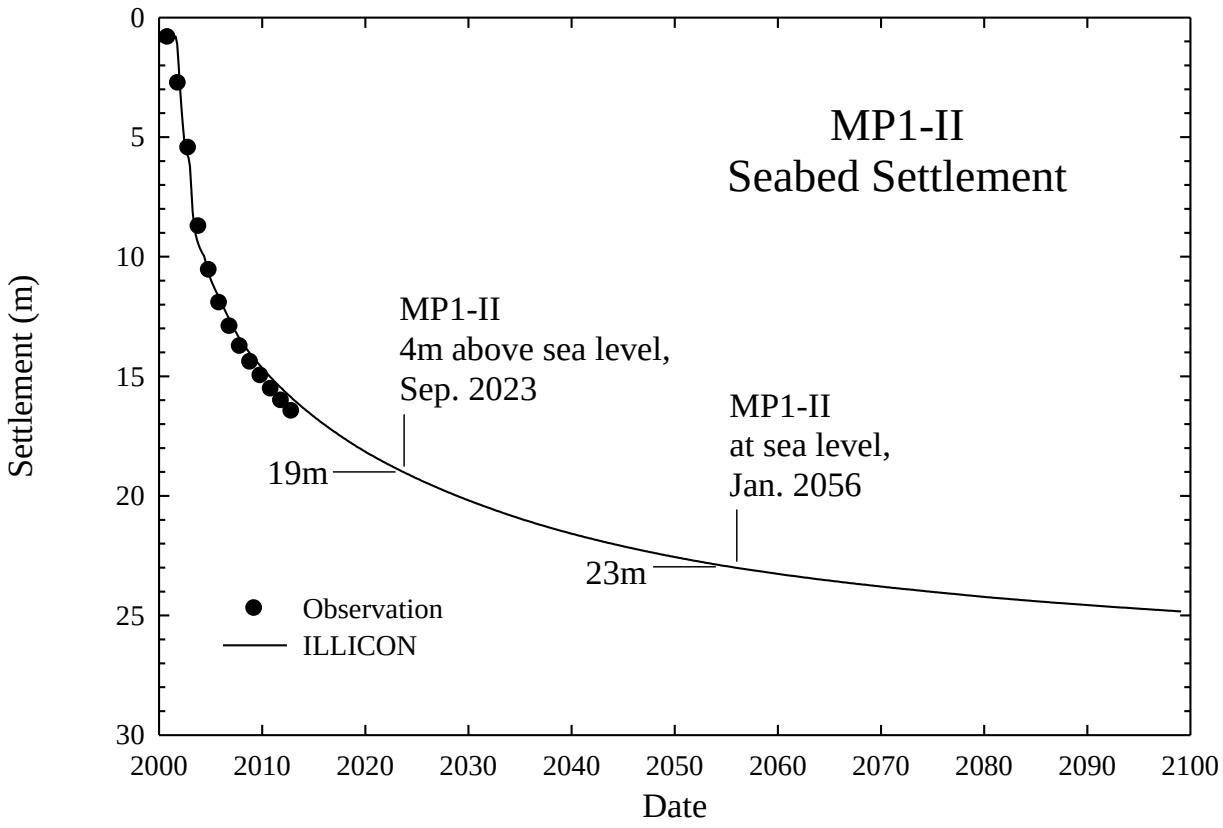

Figure 8-48 Seabed settlement at MP1-II, including compression of Holocene and Pleistocene layers.

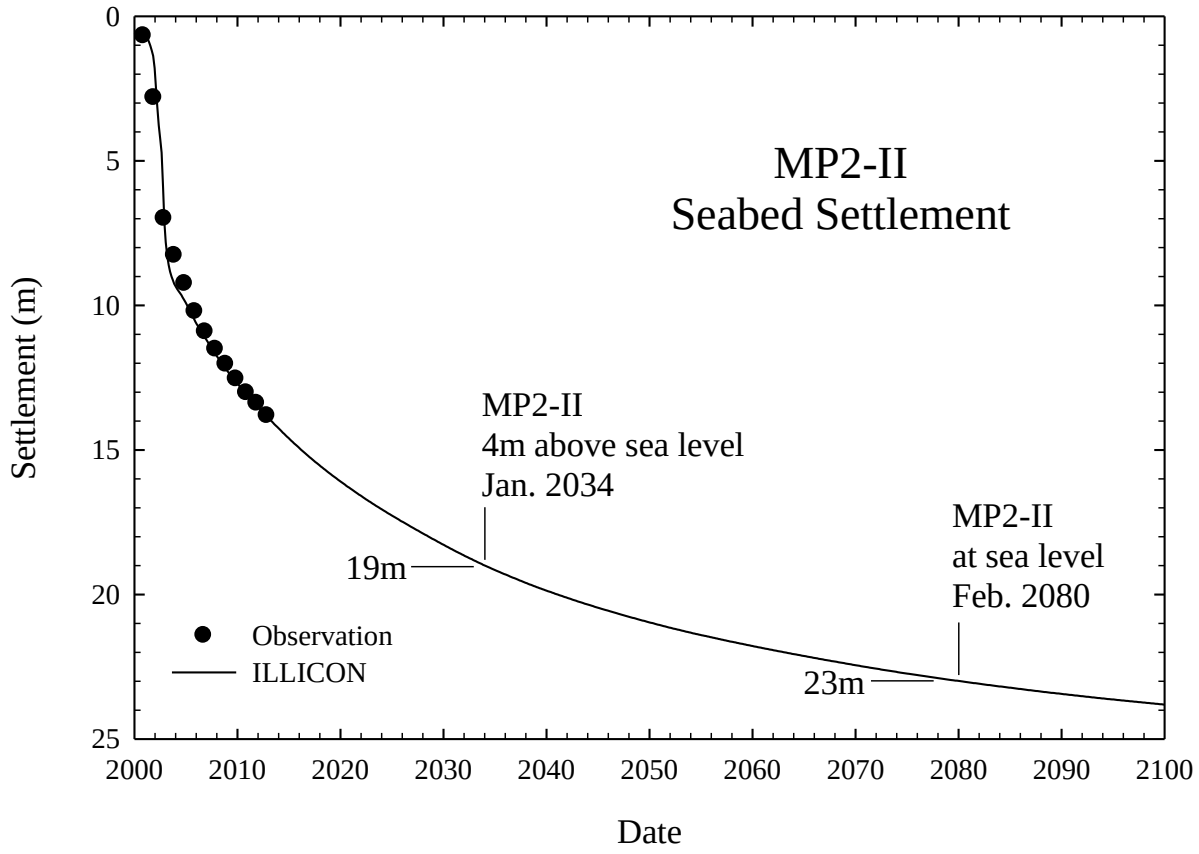

Figure 8-49 Seabed settlement at MP2-II, including compression of Holocene and Pleistocene layers.

CHAPTER 9 SUMMARY AND CONCLUSIONS

9.1 Summary

The Kansai International Airport Islands, located 5km off of the Senshu coast in Osaka Bay, Southwest Japan, were constructed as part of an effort to globalize the Kansai Region and to decentralize the Japanese economy from Tokyo (Sasaki et al., 1987; Rai, 1990; Takahashi and Kaneko, 1991). The project has been viewed as an engineering marvel. In fact, the American Society of Civil Engineers named Kansai International Airport one of the "Civil Engineering Monuments of the Millennium". However, as of December 2012, the average seabed settlement has exceeded 12.9m and 14.2m, respectively, for Airport Islands I and II (NKIAC, 2012). If settlements are too large the airport facilities will be out of service when waves overtop the seawall surrounding the islands. Eventually the islands could settle below sea level.

This project has received a lot of attention in geotechnical literature in part because of the scale of the project (Island I is 511ha and the seabed is approximately 18m below sea level and Island II is 545ha and the seabed is approximately 20m below sea level) and because of the availability of subsurface data as well as observations from settlement and porewater pressure instrumentation. At the forefront of the discussion regarding interpretation of field observations at the Kansai Airport site, is whether or not the uniqueness principle (Mesri and Choi, 1985b) can be applied to make settlement and porewater pressure predictions.

Some investigators (Hight and Leroueil, 2003; Mimura and Jang, 2005; Rocchi et al., 2006) have explicitly argued against application of the uniqueness principle to settlement and porewater predictions at the Kansai Airport site, while others (Imai et al., 2005; Oda et al., 2005; Tanaka, 2005) have made settlement calculations for the Kansai International Airport using rheological models that inherently assume that the compressibilities with respect to effective stress and with respect to time are separate, independent mechanisms contributing to consolidation.

Potentially misleading conclusions (e.g. Imai et al., 2005) regarding the secondary compression behavior of Osaka Bay clays have also been reached as a result of possible misinterpretation of laboratory oedometer tests as well as settlement observations at Kansai Airport.

This study includes a review of the geologic history of Osaka Bay as well as a careful

evaluation of the available subseabed data for 14 marine clay layers, 8 non-marine clay layers, and 20 sand layers that are contained within the up to 350m depth below seabed contributing to settlement of the Kansai Airport islands. Additionally, the reclamation process used to construct the airport islands and the instrumentation installed for settlement and porewater pressure observations were carefully examined as part of this study. Explicit finite difference techniques were developed within the ILLICON framework (Mesri and Rokhsar, 1974; Choi, 1982; Lo, 1991; Mesri et al., 1994) to facilitate settlement and porewater pressure calculations at the Kansai International Airport site. Settlement and porewater pressure calculations were performed at the Kansai International Airport Island I and Island II based on the assumption of uniqueness of end-of-primary void ratio – effective vertical stress relationship, together with the C_α/C_c law of compressibility to compute secondary compression.

9.1.1 Geologic history of Osaka Bay

A combination of north – south crustal movements that began in the middle Miocene Epoch and northwest – southeast crustal movements that began in the Pliocene Epoch were responsible for producing a chain of ellipsoidal basins, including Osaka Basin, in Southwest Japan (Huzita, 1962; Yamasaki and Nakada, 1996; Itoh et al., 2000; Inoue et al., 2003). The rise and fall of sea level over geologic time in conjunction with these crustal movements and associated basin formation are responsible for the subseabed profile and the lateral variation of thickness for individual layer formations within Osaka Bay.

The subseabed profile consists of an alternating sequence of marine clay and freshwater deposits. Marine clay layers correspond to warm global climates when sea levels were relatively high while non-marine clay and sand layers correspond to cold global climates when sea levels were relatively low (Ikebe et al., 1970; Itihara et al., 1975; Takatsugi and Hyodo, 1995; Yamasaki and Nakada, 1996; Biswas et al., 1999; Itoh et al., 2000, 2001; Takemura and Nakaseko, 2005). The correlation of marine and non-marine layers to climate has been confirmed by pollen analyses (Takatsugi and Hyodo, 1995) as well as oxygen isotope records (Takatsugi and Hyodo, 1995; Itoh et al., 2000; Inoue et al., 2003).

9.1.2 Subseabed data at the Kansai International Airport site

All available subseabed data, including vertical profiles of natural water content, Atterberg limits, particle size distribution, specific gravity of solids, and unit weight, as well as oedometer data, were evaluated as part of the ILLICON procedure for the settlement analyses of Kansai Airport Island I and Island II. These data were used to subdivide each geologic layer and a unique end-of-primary void ratio – effective vertical stress relationship was assigned to each sublayer.

Atterberg limit data presented in the literature (Maeda et al., 1990; Akai and Tanaka, 1999; Tanaka and Locat, 1999; Watabe et al., 2002; Tanaka et al., 2003; Tanaka et al., 2004; Imai et al., 2005) indicate that the majority of the fine grained soils underlying Kansai Airport are clays of high plasticity (CH), according to the Unified Soil Classification System.

The ratio of preconsolidation pressure to preconstruction effective overburden is generally less than 2 for Osaka Bay clays and can be explained by aging mechanisms alone (Mesri, 1997). Laboratory oedometer tests indicate that Osaka Bay Pleistocene clay specimens undergo a large, abrupt compression beyond σ'_p despite having a Specimen Quality Designation of C. One possible explanation for the large structural breakdown is leaching or diffusion during the geologic history (Mesri, 1997). The idea that leaching or diffusion has occurred in Osaka Bay seabed deposits is supported by the chloride content profile that rapidly decreases with depth (Tanaka et al., 2003).

Though there are not a lot of data specific to the Pleistocene sand layers, there have been qualitative reports in the literature indicating that many of the Pleistocene sand layers have relatively high fines content (Nakase, 1987; Kobayashi et al., 2005; Mimura and Jang, 2005). The high fines content of these Pleistocene sand layers implies relatively low values of permeability (as low as 10^{-7} m/s); therefore, low permeability and possible discontinuity of some Pleistocene sand layers have significantly impeded the progress of consolidation of the adjacent clay layers at the Kansai Airport site.

9.1.3 Construction of the Kansai International Airport Islands

Kansai Airport consists of two man-made Islands. Construction of the 511ha Island I began in 1987 and the Island I runway began operation in 1994. Construction of the 545ha Island

II began in 1999 and the Island II runway began operation in 2007. The construction of each airport island can generally be divided into four stages: installation of vertical drains in the Ma13 clay layer following placement of a sand blanket on the seabed, construction of the seawall, reclamation, and construction of airport facilities.

Over 400 million cubic meters of reclamation fill material was used to construct the airport islands. This reclamation fill was placed on a 15 to 24m Holocene marine clay layer through which over 2 million vertical sand drains were installed.

9.1.4 Instrumentation at the Kansai International Airport site

The majority of the instrumentation installed at the Kansai International Airport site was intended to monitor the progress of seabed settlement. Instrumentation used for the Kansai Airport project can generally be divided into three groups: instruments installed beneath the pilot work section of Island I, instruments installed at specific monitoring point locations at Island I and Island II, and instruments installed beneath the seawall and reclamation areas throughout the Kansai International Airport site.

Construction of the Pilot section began in November 1986, 2 months prior to start of reclamation for Island I, and consisted of a 500m long seawall section and a 6ha reclamation section. Construction and associated instrumentation of the pilot section was intended to improve settlement prediction for Ma13.

Layer by layer settlement and porewater pressure observations taken at the Airport Island I and Island II monitoring points were used to observe the progress of consolidation of the Pleistocene clay layers. Instrumentation was installed as deep as 350m below the seabed at the monitoring points (Shinohara, 2003; Tabata and Morikawa, 2005).

Additional instrumentation was installed below the seawall and reclamation areas throughout the Kansai Airport site. Twenty settlement gauges were installed beneath the seawall and 17 settlement gauges were installed beneath the reclamation area for Island I. Additionally, forty-three settlement gauges were installed beneath the seawall and fifty-four settlement gauges were installed beneath the reclamation area for Island II (Shinohara, 2003; KALD, 2005; Tabata and Morikawa, 2005; NKIAC, 2012). The observed seabed settlements at Island I range from 9.73m to 15.38m in December 2012, and the average seabed settlement for Island I was 12.92m

in December 2012. The observed seabed settlements for Island II range from 11.31m to 16.49m in December 2012, and the average seabed settlement for Island II was 14.25m in December 2012 (NKIAC, 2012).

9.1.5 Numerical modeling with ILLICON

The previous version of ILLICON was coded in Fortran 77 and had the capability of running two types of analyses: one-dimensional consolidation and consolidation with vertical drains (Mesri and Rokhsar, 1974; Choi, 1982; Lo, 1991). The previous version took the following into account:

- Any variation with depth of initial void ratio, initial coefficient of permeability, and initial or preconstruction effective vertical stress.
- For each sublayer, any shape for the EOP e – log σ'_v relationship.
- For each sublayer, any shape for the e – log k_v relationship.
- For each sublayer, the ratio of horizontal to vertical permeability (consolidation with vertical drains only).
- Compressibility with respect to time during the primary consolidation stage (see Section 7.4).
- Any variation with depth and time of vertical stress increase.
- Fully or partially penetrating vertical drains.
- Finite permeability (or well resistance) for vertical drains.
- Variable installation time for vertical drains.
- Smear zone adjacent to the vertical drain with EOP e – log σ'_v relationship for each sublayer independent of the adjacent undisturbed sublayer ($k_h/k_v = 1$ assumed within smear zone).

ILLICON was rebuilt using Microsoft Visual Studio 2010© to facilitate the settlement and porewater pressure calculations for the Kansai International Airport. A user-interface that provides graphical output was created as a Windows© Form Application and the computational core was coded using Microsoft Visual C++©. The current version of ILLICON retains the

capabilities listed above with the following additions:

- Capability to analyze consolidation with incompressible impeded drainage layers for the two-dimensional flow case and the axi-symmetric flow case.
  - For the two-dimensional flow case, a new hydrodynamic equation (Equation 7-15) was developed for the compressible clay layers and Equation 7-44 was developed to account for excess porewater pressure buildup in adjacent incompressible impeded drainage layers.
  - For the axi-symmetric flow case, the hydrodynamic equation previously used for the consolidation with vertical drains case (Equation 7-16) was employed for the compressible clay layers and Equation 7-53 was developed to account for excess porewater pressure buildup in adjacent incompressible impeded drainage layers.
- Capability to account for the decrease in load at the original ground surface resulting from settlement and associated submergence of fill material below the water table or below sea level.
- Capability to analyze cases involving vacuum consolidation.

9.2 Conclusions based on settlement analyses for the Kansai Airport project

The following is concluded based on computed and observed vertical compression of Ma13 at the Kansai International Airport site:

- The uniqueness principle satisfactorily explains the magnitude of vertical compression of Ma13 at MP1-II, MP2-II, CT, K-I, and MP1-I (see Figure 8-1 for location). Only the reclamation load at seabed and the thickness of Ma13 (and therefore σ'_{vo} and σ'_{vf} for each sublayer) varied from location to location for the settlement analyses (i.e. the same values of σ'_p / σ'_{vo} and C_c', and the same permeability relationships were applied at all five locations for the time rate of vertical compression calculations). End-of-primary compression ranges from 6.2m at MP1-I to 8.3m at MP1-II for the Ma13 clay layer.
- End-of-primary compression for Ma13 was reached soon after reclamation was completed for both Airport Island I and Airport Island II. Therefore, the majority of the

post-construction seabed settlement for the Kansai Airport Islands will result from settlement of the Pleistocene clay layers underlying Ma13.

The following is concluded from computed and observed settlement and excess porewater pressures at MP1-II and MP2-II:

- Settlement analyses of the Pleistocene layers at MP1-II and MP2-II indicate that settlement up to December 2012 from vertical compression of Pleistocene clay layers Dtc through Ma7 has been a result of primary consolidation. Large rates of observed settlement and high reported values of excess porewater pressure indicate that more settlement resulting from primary consolidation is expected for these Pleistocene clay layers at MP1-II and MP2-II. The calculated average degree of compression for Pleistocene clay layers Dtc through Ma7 is in the range of 12% to 71% at MP1-II and 5% to 52% at MP2-II for December 2012.
- Compression of the Pleistocene clay layers Dtc through Ma7 is impeded by adjacent sand layers. Equivalent permeabilities were back-calculated for the Pleistocene sand layers based on settlement and porewater pressure observations, and were determined to be in the range of $1x10^{-7}$ m/s to $8x10^{-4}$ m/s for the MP1-II and MP2-II analyses. These back-calculated equivalent permeabilities are consistent with values reported by Nakase (1987) as well as the values used in settlement analyses performed by Mimuran and Jang (2005) and Shibata and Karube (2005).
- Pleistocene clay layers below Ds10 at MP1-II and MP2-II have reached EOP consolidation and are presently undergoing secondary compression. These lower layers reach EOP consolidation relatively quickly (i.e. about 5 to 8 years after start of reclamation) because the post-construction final effective vertical stress resulting from reclamation load is less than the preconsolidation pressure.
- For Pleistocene clay layers at MP1-II and MP2-II with σ'_{vf}/σ'_{p} between 0.9 and 1.0, the C_{α}/C_{c} law of compressibility suggests large secondary compressions. The combined secondary compression of layers Ma4 through NMC-5 is computed to be 4.5m and 3.6m in the year 2100 at MP1-II and MP2-II, respectively.

- Seabed settlement is calculated to be 24.9m and 23.8m in the year 2100 at MP1-II and MP2-II, respectively.
- As part of the original design considerations, the surface elevation of the airport islands were to remain above +4m CDL to avoid the erosive action of waves overtopping the seawall (Arai, 1991). The surface elevation of MP1-II and MP2-II are expected to be at +4m CDL in September 2023 and January 2034, respectively.
- MP1-II and MP2-II are expected to be at sea level in January 2056 and February 2080, respectively.

The following is concluded from computed and observed settlement and excess porewater pressures at MP1-I:

- Settlement analysis of the Pleistocene clay layers at MP1-I indicate that settlement up to December 2012 has mainly been a result of primary consolidation. According to the ILLICON analysis, the Pleistocene clay layers underlying MP1-I reach EOP consolidation 18 to 91 years after the start of reclamation in 1987.
- Compression of the Pleistocene clay layers is impeded by adjacent sand layers. Equivalent permeabilities were back-calculated for the Pleistocene sand layers based on settlement and porewater pressure observation, and were determined to be in the range of $1x10^{-7}$ m/s to $1x10^{-4}$ m/s for the MP1-I analysis. These back-calculated equivalent permeabilities are consistent with values reported by Nakase (1987) as well as the values used in settlement analyses performed by Mimuran and Jang (2005) and Shibata and Karube (2005).
- Seabed settlement is calculated to be 15.7m in the year 2100 at MP1-I.
- Much of the surface elevation of Island I is already below +4m CDL.
- MP1-I is expected to be at sea level in August 2067, according to the time rate of settlement calculation using ILLICON.

The following general conclusion is reached based on the available subseabed data, information regarding reclamation load at seabed, and computed and observed settlements and porewater pressures for Airport Island I and Island II:

- The uniqueness principle together with the C_α/C_c law of compressibility sufficiently explains settlement and porewater pressure observations reported for the Kansai International Airport project.

REFERENCES

Akai, K. and Tanaka, Y. (1999). Settlement behaviour of an off-shore airport KIA. *Geotechnical Engineering for Transportation Infrastructure*. 1041-1046.

Akai, K., Nakaseko, K., Matsui, T., Kamon, M., Tanaka, Y., and Suwa, S. (1991). Geotechnical properties of marine clays in Osaka Bay. *GEO-COAST '91, Proceedings of the International Conference on Geotechnical Engineering for Coastal Development, Yokohama,* pp. 5-10.

Andresen, A. and Kolstad, P. (1979). The NGI 54-mm samplers for undisturbed sampling of clays and representative sampling of coarser materials. *Proc. Int. Symp. On Soil Sampling*, Singapore, pp. 1-9.

Arai, Y. (1991). Construction of an artificial offshore island for the Kansai International Airport. *GEO-COAST '91, Proceedings of the International Conference on Geotechnical Engineering for Coastal Development, Yokohama,* pp. 927-943.

Arai, Y., Oikawa, K., and Yamagata, N. (1991). Large-scale sand drain works for the Kansai International Airport Island. *GEO-COAST '91, Proceedings of the International Conference on Geotechnical Engineering for Coastal Development, Yokohama,* pp. 281-286.

Araki, H. and Hoes, O. (2008). Development of lowland areas (Capt. 7), *Urban Water in Japan,* Rutger de Graaf and Fransie Hooimeijer (Eds), Taylor & Francis.

Biswas, D.K., Hyodo, M., Taniguchi, Y., Kaneko, M., Katoh, S., Sato, H., Kinugasa, Y., and Mizuuno, K. (1999). Magnetostratigraphy of Plio-Pleistocene sediments in a 1700-m core from Osaka Bay, southwestern Japan and short geomagnetic events in the middle Matuyama and early Brunhes chrons. *Palaeogeogr. Palaeoclimatol. Palaeoecol.,* 148, 233-248.

Bjerrum, L. (1967). Engineering geology of Norwegian normally consolidated marine clays as related to settlements of buildings. *The Seventh Rankine Lecture, Geotechnique,* Vol. 17 (2), pp. 81-118.

Bjerrum, L., and Johannessen, I. J. (1960). Pore pressure resulting from pile driving. *Proc. Conference on Pore Pressure and Suction in Soils*, London, England, pp. 14-17.

Bradsher, Keith (1993, October 27). U.S Cancels a Plan to Begin Sanctions after Japan Acts. *The*

New York Times. Retrieved from http://www.nytimes.com

Burghignoli, A. and Vestroni, F. (1975). On the one-dimensional consolidation of clays, *Sessione special costruzioni su argille tenere, XII convegno nazionale di geotecnica*, Associazione Geotecnica Italiana, Cosenza 18-21 Sept. (Translated from Italian).

Champion, V. (1991). Bay of Plenty?. *Cargo Systems International*. Vol. 18 (8). pg. 63-65.

Choi, Y.K. (1982). "Consolidation behavior of natural clays." Ph.D. thesis, Univ. of Illinois at Urbana-Champaign, Urbana, Illinois.

Cook, R., Malkus, D., Plesha, M., and Witt, R. (2002). *Concepts and Applications of Finite Element Analysis*, 4th ed., New Jersey, John Wiley & Sons Inc., 722 pp.

Crawford, C. B. (1964). Interpretation of the consolidation test. *Journal of the Soil Mechanics and Foundation Division*, ASCE, Vol. 90 (SM5), pp. 87-102.

Crawford, C. B. (1965). The resistance of soil structure to consolidation. *Canadian Geotechnical Journal*, Vol. 2 (2), pp. 90-97.

Crawford, C. B. (1988). On the importance of rate of strain in the consolidation test. *Geotechnical Testing Journal*, GTJODJ, Vol. 11 (1), pp. 60-62.

Degago, S.A., Grimstad, G., Jostad, H.P., and Nordal, S. (2009). "The non-uniqueness of the end-of-primary (EOP) void ratio-effective stress relationship." *Proc. 17th Int. Conf. Soil Mech. Geotech. Engrg.*, Alexandria 1, 324-327.

Degago, S.A., Grimstad, G., Jostad, H.P., Nordal, S., and Olsson, M. (2011). "Use and misuse of isotache concept with respect to creep hypotheses A and B." *Géotechnique*, 61(10), 898-908.

Duncan, J., Rajot, J., and Perrone, V. (2005). Factors affecting magnitude of clay settlement. *Proceedings of the Symposium on Geotechnical Aspects of Kansai International Airport. Sept. 16 (Fri.) -17 (Sat.), 2005.*, 1-5.

Endo, H., Oikawa, K., and Komatsu, A. (1991). Settlement of diluvial clay layers caused by a large scale man-made island. *GEO-COAST '91, Proceedings of the International Conference on Geotechnical Engineering for Coastal Development, Yokohama,* pp. 177-182.

Fellenius, B. H., and Samson, L. (1976). Testing of drivability of concrete piles and disturbance to sensitive clays, *Canadian Geotechnical Journal*, Vol. 13, No. 2, pp. 139-160.

Feng, T. W. (1991). *Compressibility and permeability of natural soft clays and surcharging to*

reduce settlements, Thesis submitted to the University of Illinois at Urbana-Champaign, Urbana, Illinois.

Fujino, Y., Hashimoto, S., and Abe, M. (2005). Damage Analysis of Hanshin Expressway Viaducts during 1995 Kobe Earthquake. 1: Residual Inclination of Reinforced Concrete Piers. *Journal of Bridge Engineering, ASCE*. Vol. 10 (1). pp. 46-53.

Furudoi, T. (2010). The second phase construction of Kansai International Airport considering the large and long-term settlement of the clay deposits, *Soils and Foundations*, Vol. 50 (6), pp. 805-816.

Furudoi, T. and Kobayashi, M. (2009). Geotechnical issues and approach on Kansai International Airport Project – prediction and performance of settlement, *JSCE C*, Vol. 65 (4), pp. 998-1017.

Graham, J., Crooks, J. H. A., and Bell, A. L. (1983). Time effects on the stress-strain behavior of natural soft clays. *Geotechnique*, Vol. 33 (3) pp. 327-340.

Harmon, Craig (1961), Isotopic variations in meteoric waters, S*cience* 133, pp.1702-1703.

Hayashi, H., Marui, T., Taniguchi, N., Kayano, S. (2000). Restoration of Hanshin Expressway after Kobe/ Awaji Earthquake – challenge of 623 days before opening. *Cement and Concrete Composites*. Vol. 22. pp. 29-38.

Hazen, A. (1892). Physical properties of sands and gravels with reference to their use in filtration, *Rept. Mass State Board of Health*, p. 539.

Hight, D.W. and Leroueil, S. (2003). Characterization of soils for engineering purpose. *Characterisation and engineering properties of natural soils*. Vol. 1. pp. 255-362.

Holtz, R. D., and Holm, G. (1973). Excavation and sampling around some sand drains at Ska-Edeby, Sweden, *Proc. Nordic Geot. Meeting*, Trondheim, 1972, Norwegian Geotechnical Institute.

Huzita, K., (1962). Tectonic development of the median zone (Setouti) of southwest Japan since Miocene. J. Geosci. Osaka Univ. 6, 103-144.

Ikebe, N., Iwatsu, J., and Takenaka, J. (1970). Quaternary geology of Osaka with special reference to land subsidence. *J. Geosci. Osaka City Univ.* 13, 39-98.

Ikeda, K., Kusachi, K., Miyata, M., Kawasaki, K., Esakie, T., Hirota, A., and Ushiro, M. (2003). Osaka Port Yumeshima tunnel project. *Proceedings of the Nakase Memorial Symposium Yokosuka, Japan: Soft Ground Engineering in Coastal Areas, 28 November 2002*. A.A.

Balkema Publishers. 369-377.

Imai, G., Ohmukai, N., and Tanaka, H. (2005). An isotaches-type compression model for predicting long term consolidation of KIA clays. *Proceedings of the Symposium on Geotechnical Aspects of Kansai International Airport. Sept. 16 (Fri.) -17 (Sat.), 2005.*, 49-64.

Inoue, N., and Nakagawa, K., 2000. Modeling of the underground structure in the Osaka sedimentary basin based on geological interpretation of gravity anomalies and seismic profiles. *J. Geosci. Osaka City Univ.* 43, 97-110.

Inoue, N., Kitada, N., Itoh, Y., Takemura, K., and Nakagawa, K. (2003). Integrated study of high resolution geophysical and geological information of Osaka Bay, Southwest Japan. *Journal of Asian Earth Sciences*, 22, 1-11.

Ishida, S., Maenaka, K., and Yokoyama, T. (1969). Paleomagnetic chronology of volcanic ash of the Plio-Pleistocene series in Kinki district, Japan – the research of younger Cenozoic strata in Kinki district, Part 12. *J. Geol. Soc. Jpn.* 75, 183-197.

Itihara, M., Yoshikawa, S., Inoue, K., Hayashi, T., Tateishi, M., and Nakajima, K. (1975). Stratigraphy of the Plio-Pleistocene Osaka Group in Sennan-Senpoku area, south of Osaka, Japan – a standard stratigraphy of the Osaka Group. *Jour. Geosci.* 19, 1-29 (Osaka City University).

Itoh, Y., Takemura, K., Ishiyama, T., Tanaka, Y., and Iwaki, H. (2000). Basin formation at a contractional bend of a large transcurrent fault: Plio-Pleistocene subsidence of the Kobe and northern Osaka Basins, Japan. *Tectonophysics*, 321, 327-341.

Itoh, Y., Takemura, K., Kamata, H., (1998). History of basin formation and tectonic evolution at the termination of a large transcurrent fault system: deformation mode of central Kyushu, Japan. *Tectonophysics*, 284 135-150.

Itoh, Y., Takemura, K., Kawabata, D., Tanaka, Y., and Nakaseko, K. (2001). Quaternary tectonic warping and strata formation in the southern Osaka Basin inferred from reflection seismic interpretation and borehole sequence. *Jour. Asian Earth Sciences*, 20, 45-58.

Iwatani, F. (1991). Osaka Bay Phoenix Project. *Meeting of the United States – Japan Cooperative Program in Natural Resources (UJNR) Panel on Marine Facilities*. U.S Dept. of Commerce and National Oceanic and Atmospheric Administration. Vol. 17. pg. 360-367.

Jaluria, Y. and Torrance, K. (1986). *Computational Heat Transfer*. 1st ed., Hemispher Publishing Corporation, 366 pp.

Jamiolkowski, M., Ladd, C. C., Germaine, J., and Lancellota, R. (1985). New developments in field and laboratory testing of soils, *Proceedings, 11th ICSMFE,* San Francisco, Vol. 1, pp. 57-153.

Jang, W. Y., and Mimura, M. (2005). Effect of permeability and compressibility of sandwiched gravelly sand layers on subsequent settlement of Pleistocene deposits. *Soils and Foundations*, Vol. 45 (6), pp. 111-119.

Jang, W. Y., and Mimura, M. (2005). Effect of permeability and compressibility of permeable gravelly sand layers on long-term settlement of Pleistocene deposits. *Disaster Prevention Research Institute Annuals*, Kyoto University, Vol. 48B, pp. 383-393.

Jang, W. Y., and Mimura, M. (2003). Evaluation of time-dependent behavior of Osaka Pleistocene clay by elasto-viscoplastic finite element analysis. *Disaster Prevention Research Institute Annuals*, Kyoto University, Vol. 46B.

Japanese Industrial Standard (JIS) A 1204: Test method for particle size distribution of soils. Established 1950. Revised 2009.

Jeon, B., Mimura, M., and Saitsu, Y. (2012). Numerical assessment of the permeability for the Pleistocene sandy gravel deposits considering the subsurface stratigraphy of Kansai International Airport, *Annuals of Disas. Prev. Res. Inst.*, Kyoto Univ., No. 55 B, pp. 215-224.

Kagawa, T., Zhao, B., Miyakoshi, K., and Irikura, K. (2004). Modeling of 3D basin structures for seismic wave simulations based on available information on the target area: case study of the Osaka Basin, Japan. *Bulletin of the Seismological Society of America*. Vol. 94, No. 4, pp. 1353-1368.

Kanda, K., Suzuki, S., and Yamagata, N. (1991). Offshore investigation at the Kansai International Airport. *GEO-COAST '91, Proceedings of the International Conference on Geotechnical Engineering for Coastal Development, Yokohama*, pp. 33-38.

Kansai International Airport Co. Ltd. (KIAC) and Kansai International Airport Land Development Co. Ltd. (KALD). (2005). *Kansai International Airport: 2nd Phase Construction*. 30 pages.

Kansai International Airport Land Development Co. (KALD) (2005). *2nd Phase Construction in*

Progress: Final Stage of Reclamation and *Background of the Kansai International Airport: Environmentally-Friendly Air Traffic Gateway to the World* [DVD].

Kansai International Airport Land Development Company (KALD), Ltd. (2010). Retrieved July 2011, from http://www.kald.co.jp/SITE/contents/building/05/s_w/08.html

Khan, A.Q. (2010). "Ground improvement using vacuum preloading together with prefabricated vertical drains." Ph.D. thesis, Univ. of Illinois at Urbana-Champaign, Urbana, Illinois.

Kitazume, M., Miyajima, S., Hirose, M., Suzuki, S., Taki, M., and Hashizume, H. (2003). Interaction of two adjacent man-made islands on soft ground. *Proceedings of the Nakase Memorial Symposium Yokosuka, Japan: Soft Ground Engineering in Coastal Areas, 28 November 2002*. A.A. Balkema Publishers. 137-144.

Kobayashi, M., Furudoi, T., Suzuki, S., and Watabe, Y. (2005). Modeling of consolidation characteristics of clays for settlement prediction of Kansai International Airport. *Proceedings of the Symposium on Geotechnical Aspects of Kansai International Airport. Sept. 16 (Fri.) -17 (Sat.), 2005.*, 65-76.

Kobe Harborland. Retreived February 7, 2013 from: http://www.harborland.co.jp.

Kobe Ports and Harbors Office (2004). *The Development of Kobe Port*. Kobe Ports and Harbors Office, Kinki Regional Development Bureau, and Ministry of Land, Infrastructure, and Transport. 10 pages. Retrieved February 7, 2013 from http://www.pa.kkr.mlit.go.jp/kobeport/

Koushige, N., Karube, D., Honda, S., and Shigeno, T. (2003). An evaluation of the settlement of offshore man-made island improved with large scale preloading. *Soft Ground Engineering in Coastal Areas*. Tsuchida et al. (eds). pg. 127-135.

Ladd, C. C. (1971). Settlement analysis of cohesive soils. *Soil Publication 272*, Massachusetts Institute of Technology, Department of Civil Engineering, Cambridge, Mass., 92 pp.

Ladd, C. C., Foott, R., Ishihara, K., Schlosser, F., and Poulos, H.G. (1977). Stress-deformation and strength characteristics. *General Report, Proc. 9th Int. Conf. Soil Mech. Found. Engrg.*, 2, 421-494.

Larsson, R. and Sallfors, G. (1986). Automatic continuous consolidation testing in Sweden. *Consolidation of Soils*, STP 892, ASTM, pp. 299-328.

Leonards, G. A. (1980). Discussion: Strain rate behavior of Saint-Jean-Vianney clay. By Vaid

et al., *Canadian Geotechnical Journal*, Vol. 17 (2), pp. 461-462.

Leonards, G.A. (1972). Discussion, "Shallow foundations." *Proc. Spec. Conf. on Performance of Earth-Supported Structures*, ASCE, Lafayette, IN, 3, 169-173.

Leroueil, S. (1988), Recent developments in consolidation of natural clays, *Canadian Geotechnical Journal*, Vol. 25 (1), pp. 85-107.

Leroueil, S. (1994). Compression of clays: fundamental and practical aspects. *ASCE Conf. on Vertical and Horizontal Deformations of Foundations and Embankments*, College Station, TX, 1, 57-76.

Leroueil, S. (1995). Could it be that clays have no unique way of behaving during consolidation?. *Proc. Conf. Compression and Consolidation of Clayey Soils*, 2, 1039-1048.

Leroueil, S. and Tavenas, F. (1979). Discussion: Strain rate behavior of Saint-Jean-Vianney Clay, by Vaid et al., *Canadian Geotechnical Journal*, Vol. 16 (3), pp. 616-620.

Leroueil, S. Kabbaj, M., Tavenas, F., and Bouchard, R. (1985). Stress-strain-strain rate relation for the compressibility of sensitive natural clays, *Geotechnique*, Vol. 35 (2), pp. 159-180.

Leroueil, S., Samson, L., and Bozozuk, M. (1983). Laboratory and field determination of preconsolidation pressures at Gloucester. *Canadian Geotechnical Journal*, Vol. 20 (3), pp. 477-490.

Lo, D. O. K. (1991). *Soil Improvement by Vertical Drains*, Thesis submitted to the University of Illinois at Urbana-Champaign, Urbana, Illinois.

Lo, K. Y., and Stermac, A. G. (1965). Induced pore pressure during pile driving operations, *Proc. 6th International Conference on Soil Mechanics and Foundation Engineering*, Montreal, Quebec, Vol. 2, pp. 285-289.

Maeda, S., Higuchi, Y., and Furuichi, M. (1990). Large-scale sand drain works for the Kansai International Airport, Proc. Airports into the 21st Century (Hong Kong). pp. 485-496.

Matsui, T. (1994). Major onshore and offshore projects in Osaka Bay Area. *Proceedings of the Fourth International Offshore and Polar Engineering Conference*, Osaka, Japan. April 10-15. Vol. 1, pp. 8-17.

Matsui, T. and Sakagami, T. (1995). Fundamental consolidation behavior of aged clays in relation to geological history. *Compression and Consolidation of Clayey Soils: Proc. Symp on Compression and Consolidatin of Clayey Soils*, Hiroshima, Japan, 531-536.

Matsui, T., Oda, K., Mimura, M., Takeda, K., Yamamoto, K., Fujiwara, T., and Suwa, S. (2001).

Settlement behavior of Pleistocene marine clay deposits due to reclamation in Osaka Bay. In *Soft Soil Engineering*, edited by C. F. Lee, pp. 429-434 (Swets and Zeitlinger: Lisse).

Mesri, G. (1977). Discussion, "Stress-deformation and strength characteristics." *Proc. 9th Int. Conf. Soil Mech. Found. Engrg.*, Tokyo, 3, 354-355.

Mesri, G. (1986). Discussion, "Post-construction settlement of an expressway built on peat by precompression" by L. Samson. *Canadian Geotech. J.*, 23 (3), 403-407.

Mesri, G. (1987). Fourth Law of Soil Mechanics: A law of compressibility. *Proceedings, International Symposium on Goetechnical Engineering of Soft Soils*, Mexico City, Mexico, August.

Mesri, G. (1997). Aging of soils. Kersten Invited Lecture, *Geotech. Engrg. Conf. University of Minnesota, St. Paul, Minnesota*.

Mesri, G. (2001). "Primary compression and secondary compression." In *Soil behavior and soft ground construction*, (eds. J.T. Germain, T.C. Sheahan and R.V. Whitman), *Geotechnical Special Publication, ASCE*, 119, 122-166.

Mesri, G. and Choi, Y.K. (1985a). "Settlement analysis of embankments on soft clays," J. Geotech. Eng., ASCE, 111, No. 4, pp. 441-464.

Mesri, G. and Choi, Y.K. (1985b). "The uniqueness of the End-Of-Primary (EOP) void ratio-effective stress relationship," Proc. 11th Int. Conf. on Soil Mech. And Found. Eng., San Francisco, 2, pp. 587-590.

Mesri, G. and Godlewski, P.M. (1977). Time and stress compressibility interrelationship. *J. Geotech. Engrg.*, ASCE, May, 103(5), 417-430.

Mesri, G. and Godlewski, P.M. (1979). Closure: Time and stress compressibility interrelationship. *J. Geotech. Engrg.*, ASCE, Jan, 105(1), 106-113.

Mesri, G. and Lo, D.O.K. (1989). "Subsoil investigation: the weakest link in the analysis of test fills," The Art and Science of Geotechnical Engineering: At the Dawn of the Twenty-first Century, Englewood Cliffs, N.J., Prentice-Hall Inc., pp. 309-335.

Mesri, G. and Lo, D.O.K. (1991). Field performance of prefabricated vertical drains. *Proc. Int. Conf. on Geotech. Eng. for Coastal Development*, Yokohama, pp. 231-236

Mesri, G. and Olson, R. E. (1971). Consolidation characteristics of Montmorillonite. *Geotechnique*, 21 (4), pp. 341-353.

Mesri, G. and Castro, A. (1987). The Cα/Cc concept and Ko during secondary compression.

Journal of Geotechnical Engineering, ASCE, Vol. 113 (GT3), pp. 230-247.

Mesri, G. and Choi, Y. K. (1979). Discussion: Strain rate behavior of Saint-Jean-Vianney clay, by Vaid et al., *Canadian Geotechnical Journal*, Vol. 16 (4), pp. 831-834.

Mesri, G., and Choi, Y. K. (1984). Discussion: Time effects on the stress-strain behavior of natural soft clays, by Graham et al., *Geotechnique*, Vol. 34 (3), pp. 439-442.

Mesri, G., and Feng, T. W. (1986). Discussion: Stress-strain-strain rate relation for the compressibility of sensitive natural clays, by Leroueil et al., *Geotechnique*, Vol. 36 (2), pp. 283-290.

Mesri, G. and Feng, T. W. (2009). Discussion: The uniqueness of end-of-primary (EOP) void ratio – effective stress. *Proceedings of the 17th International Conference on Soil Mechanics and Geotechnical Engineering*. Alexandria, Egypt. pp. 3559-3561.

Mesri, G. and Feng, T. W. (2013). Consolidation of soils. *Geotechnical Special Publication, ASCE*.

Mesri, G., and Rokhsar, A. (1974). "Theory of consolidation for clays," *J. Geotech. Engrg.*, ASCE, Jan, 100(8), 889-904.

Mesri, G., Feng, T. W., Ali, S., and Hayat, T. M. (1994). Permeability characteristics of soft clays. *Proceedings, XIII ISSMFE Conference*, 2, pp. 187-192.

Mesri, G., Feng, T.W., and Shahien, M. (1995). Compressibility parameters during primary consolidation. Invited Special Lecure. *Int. Symp. Compression and Consolidation of Clayey Soils*, Hiroshima, Japan, May, Lectures and Reports Volume, 201-217.

Mesri, G. and Khan, A. Q. (2012). "Ground improvement using vacuum loading together with vertical drains," *J. Geotech. Engrg.*, ASCE, June, 138(6), 680-689.

Mesri, G., Lo, D.O.K. and Feng, T.W. (1994). "Settlement of embankments on soft clays". *Proc., Settlement '94, ASCE Specialty Conf., Geotech*. SP 40(1), 8–76.

Mesri, G., Rokhsar, A., and Bohor, B. F. (1975). Composition and compressibility of typical samples of Mexico City clay. *Geotechnique*, 25 (3), pp. 527-554.

Mesri, G., Stark, T. D., Ajlouni, M. A., and Chen, C. S. (1997). Secondary compression of peat with or without surcharging. *J. Geotech. Geoenv. Eng.*, Vol. 123 (5), pp. 411-421.

Mesri, G. and Vardhanabhuti, B. (2009). Compression of granular materials. *Can. Geotech. J.* Vol. 46. pp. 369-392.

Mikasa, M. and Ohnishi, H. (1981). Soil improvement by dewatering in Osaka South Port.

Proceedings of the Ninth ICSMFE: The Case History Volume. Tokyo. pg. 639-684.

Mimura, M. (2005). Evaluation of long-term settlement of the quasi-overconsolidated Pleistocene clay deposits in Osaka Port. *Proceedings of the Second Japan-U.S. Workshop on Testing, Modeling, and Simulation in Geomechanics*. Geotechnical Special Publication, no. 143, p 98-122, Geomechanics II: Testing, Modeling, and Simulation.

Mimura, M. and Jang, W. Y. (2004). Description of time-dependent behavior of quasi-overconsolidated Osaka Pleistocene clays using elasto-viscoplastic finite element analyses. *Soils and Foundations*, Vol. 44 (4), pp. 41-52.

Mimura, M. and Jang, W. Y. (2005). Verification of the elasto-viscoplastic approach assessing the long-term deformation of the quasi-overconsolidated Pleistocene clay deposits. *Soils and Foundations*, Vol. 45 (1), pp. 37-49.

Mimura, M. and Jang, W. Y. (2006). Numerical assessment for long-term settlement of the reclaimed pleistocene deposits. *Proceedings of the Second Japan-U.S. Workshop on Testing, Modeling, and Simulation in Geomechanics*. Geotechnical Special Publication, no 156, p 243-268, Geomechanics II: Testing, Modeling, and Simulation.

Mimura, M., and Jang, W. (2005). Long-term settlement of the Pleistocene deposits due to construction of KIA. *Proceedings of the Symposium on Geotechnical Aspects of Kansai International Airport. Sept. 16 (Fri.) -17 (Sat.), 2005.*, pg. 77-85.

Mimura, M., and Sumikura, Y. (2000). Deformation and excess pore water pressure of the Pleistocene marine deposits due to offshore reclamation. *Coastal Geotech. Engrg. in Practic; Proc. Int Symp*. Yokohama, Japan, 339-344.

Mimura, M., Shibata, T., Nozu, M., and Kitazawa, M. (1990). Deformation analysis of a reclaimed marine foundation subjected to land construction. *Soils and Foundations*, Vol. 30 (4), pp. 119-133.

Mimura, M., Takeda, K., Yamamoto, K., Fujiwara, T., and Jang, W. Y. (2003). Long-term settlement of the reclaimed quasi-overconsolidated Pleistocene clay deposits in Osaka Bay, *Soils and Foundations*, Vol. 43 (6), pp. 141-153.

Morin, P. Leroueil, S., and Samson, L. (1983). Preconsolidaiton pressure of champlain clays, Part I: In-situ determination. *Canadian Geotechnical Journal*, Vol. 20 (4), pp. 782-802.

Nakase, A. (1987). Kansai International Airport-Construction of Man-Made Island. *Proceedings of ISSMFE VHI Asian Regional Conference*. Vol. 2.

Nakase, A. (2003). Kansai International Airport-construction of man-made island. *Proceedings of the Nakase Memorial Symposium Yokosuka, Japan: Soft Ground Engineering in Coastal Areas, 28 November 2002*. A.A. Balkema Publishers. 21-35.

Nakaseko, K., Takemura, K., Nishiwaki, N., Nakagawa, Y., Furutani, M. and Yamauchi, M. (1984). Stratigraphy of the submarine strata at the Kansai International Airport in Osaka Bay off Senshu, central Japan. In: Nakaseko, K. (Ed.). *Report of the Calamity Science Institute, Japan*., 191-198.

New Kansai International Airport Co. (May 2012). Retrieved October 22, 2012, from: http://www.nkiac.co.jp

New Kansai International Airport Co. (NKIAC) (May 2012). Retrieved October 22, 2012, from: http://www.nkiac.co.jp

Newmark, N. M. (1942). Influence charts for computation of stresses in elastic foundations, *Univ. of Illinois Eng. Exp. Sta. Bull. 338*, 28 pp.

Oda, K., Tokida, K., Matsui, T., and Ono, M. (2005). Elasto-viscoplastic model for expressing strain rate dependency of creep behavior and its applicability to one-dimensional consolidation behavior of Pleistocene clays in Osaka Bay. *Proceedings of the Symposium on Geotechnical Aspects of Kansai International Airport. Sept. 16 (Fri.) -17 (Sat.), 2005.*, 41-48.

Ohmukai, N., Rito, F., and Mizukami, J. (2003). Estimation of the strain rate effect influenced to the consolidation characteristic of Osaka Bay Pleistocene clay. *Proceedings of the Nakase Memorial Symposium Yokosuka, Japan: Soft Ground Engineering in Coastal Areas, 28 November 2002*. A.A. Balkema Publishers. 79-84.

Okaichi T, Yanagi T (1997). Seto Inland Sea-historical background. In: Okaichi T, Yanagi T (eds) *Sustainable development in the Seto Inland Sea Japan from the viewpoint of fisheries*. Terra Scientific Publishing Company, Tokyo, pp 9–14.

Olson, R. (1977). Technical note: Consolidation under time dependent loading. *ASCE Journal of the Geotechnical Engineering Division*. 103 (1). pp. 55-60.

Osaka Municipal Government (2000). *Osaka and its technology*. No. 38. ISSN 0289-0798. 34 pages.

Ozisik, M. Necati. (1994). *Finite difference methods in heat transfer*. CRC Press, Boca Raton.

Peck, R. B., Hanson, W. E., and Thornburn, T. H. (1974). *Foundation Engineering*, 2nd Edition,

John Wiley, New York.

Port and Harbor Research Institution (PHRI) (1994). Osaka Port; convergence of the city and the sea. *Ports and Harbors*. Vol. 39 (3). pg. 32-34.

Rai, C. (1990). Osaka Bay Area Development Project. *Civil Engineering in Japan*. Vol. 29. pg. 68-77.

Raymond, G. P. (1969). Consolidation of deep deposits of homogeneous clay, *Geotechnique*, Vol. 19 (4), pp. 478-494.

Rocchi, G., Vaciago, G., Fontana, M., and Plebani, F. (2006). Enhanced prediction of settlement in structured clays with examples from Osaka Bay. *Geomechanics and Geoengineering: An International Journal*, Vol. 1, No. 3, pp. 217-237.

Rocchi, G., Vaciago, G., Fontana, M., and Plebani, F. (2007). Further insight into the behavior of Pleistocene Osaka clays at KIA Phase 1 island, *Geomechanics and Geoengineering: An International Journal*, Vol. 2, No. 3, pp. 159-173.

Roy, M., Blanchet, R., Tavenas, F., and La Rochelle, P. (1981). Behavior of a Sensitive Clay During Pile Driving, *Canadian Geotechnical Journal*, Vol. 18, No. 1, pp. 67-85.

Sallfors, G. (1975). *Preconsolidation pressure of soft high-plastic clays*. Ph.D. Thesis, Chalmers University of Technology, Gotenberg, Sweden.

Sasaki, S., Nakamura, Y., and Tokuhira, T. (1987). Long-term goals of Osaka Port Improvement Project. *Proceedings of the Fifth Symposium on Coastal and Ocean Management*. Seattle, Washington. Vol. 1. pg. 267-274.

Sekiguchi H, Aksornkoae S (2008) Environment problems in the coastal zone. In: Mimura N (ed) Asia-Pacific coasts and their management: states of environment. Springer, Dordrecht, p 65–171.

Shibata, T., and Karube, D. (2005). Settlement prediction of Kansai International Airport. *Proceedings of the Symposium on Geotechnical Aspects of Kansai International Airport. Sept. 16 (Fri.) -17 (Sat.), 2005.*, 87-96.

Shigeno, T., Honda, S., Koushige, N., and Fukui, M. (2003). Selection of soil improvement methods for reclaimed land and actual examples. *Soft Ground Engineering in Coastal Areas*. Tsuchida et al. (eds). pg. 169-178.

Shinohara, M. (2003). Settlement analysis and intelligent site management of the second-phase land reclamation works for Kansai International Airport. *Proceedings of the Nakase*

Memorial Symposium Yokosuka, Japan: Soft Ground Engineering in Coastal Areas, 28 November 2002. A.A. Balkema Publishers. 145-150.

Shiraishi, N. and Suzuki, S. (1995). Settlement management system for the construction of Kansai International Airport. *Compression and Consolidation of Clayey Soils*, Yoshikuni and Kusakabe (eds). Pp. 647-651.

Sims, Calvin (2001, July 29). Losses Mount at Kansai While the Airport Sinks. *The New York Times*. Retrieved from http://www.nytimes.com

Sterngold, James (1993, December 16). Osaka Journal; Pride and (Ouch!) Price: The $14 Billion Airport. *The New York Times*. Retrieved from http://www.nytimes.com

Suzuki, K., Yasuhara, K., and Fukusawa, T. (2003). A non-linear equation for the consolidation with vertical drain and its applications. *Proceedings of the Nakase Memorial Symposium Yokosuka, Japan: Soft Ground Engineering in Coastal Areas, 28 November 2002*. A.A. Balkema Publishers. 179-186.

Tabata, T. and Morikawa, Y. (2005). The second phase construction of Kansai International Airport considering the large and long-term settlement of the clay deposits. *Proceedings of the Symposium on Geotechnical Aspects of Kansai International Airport. Sept. 16 (Fri.) -17 (Sat.), 2005.*, 7-16.

Takahashi, M, and Kaneko, A. (1991). Toward and Enriched Waterfront. *Meeting of the United States – Japan Cooperative Program in Natural Resources (UJNR) Panel on Marine Facilities*. U.S Dept. of Commerce and National Oceanic and Atmospheric Administration. Vol. 17. pg. 433-440.

Takatsugi, K.O. and Hyodo, M. (1995). A geomagnetic excursion during the late Matuyama chron, the Osaka group, southwest Japan. *Earth and Planetary Science Letters*. 136, 511-524.

Takemura, K. and Nakaseko, K. (2005). Subsurface geology of Kansai International Airport, central Japan. *Proceedings of the Symposium on Geotechnical Aspects of Kansai International Airport. Sept. 16 (Fri.) -17 (Sat.), 2005.*, 17-22.

Talley, S. R., Smith, T., and Carpenter, M. (Executive Producers). (2000). *Super Structures of the World: The Kansai International Airport* [VHS]. Unapix Entertainment Inc. Seattle, Washington.

Tanaka, H. (2005). Consolidation behavior of natural soils around pc value – long term

consolidation test. *Soils and Foundations*. 45 (3). 83-95.

Tanaka, H. and Locat, J. (1999). A microstructural investigation of Osaka Bay clay: the impact of microfossils on its mechanical behavior. *Can. Geotech. J.*, 36, 493-508.

Tanaka, H., Kang, M., and Watabe, Y. (2004). Aging effects on consolidation properties – based on the site investigation of Osaka Pleistocene clays. *Soils and Foundations*. 44 (6), 39-51.

Tanaka, H., Rutoh, F., and Omukai, N. (2002). Quality of samples retrieved from great depth and its influence on consolidation properties. *Can. Geotech. J.*, 39.

Tanaka, H., Tanaka, M., Suzuki, S., and Sakagami, T. (2003). Development of a new cone penetrometer and its application to great depths of Pleistocene clays. *Soils and Foundations*. 43 (6), 51-61.

Tavenas, F. and Leroueil, S. (1977). Effects of stresses and time on yielding of clays. *Proceedings, 9th ICSMFE*, Tokyo, Vol. 1, pp. 319-326.

Tavenas, F., Jean, P., Leblond, P., and Leroueil, S. (1983b). The permeability of natural soft clays, Part II: Permeability characteristics, *Canadian Geotechnical Journal*, Vol. 20 (4), pp. 645-660.

Taylor, D. W. (1942). Research on the consolidation of clays. Publication from the Department of Civil and Sanitary Engineering, Massachusetts Institute of Technology, Serial No. 82.

Taylor, D.W., and Merchant, W. (1940). "A theory of clay consolidation accounting for secondary compression." J. Maths. and Physics, 19(3), pp. 167-185.

Terashi, M., and Juran, I. (2000). Ground improvement: state of the art. *International Conference on Geotechnical and Geological Engineering*. Melbourne. pp. 461-519.

Terzaghi, K., Peck, R.B., and Mesri, G. (1996). *Soil Mechanics in Engineering Practice*, Third Edition, John Wiley & Sons, New York.

Tsuchida, T. (2005). Structure due to cementation of Osaka Bay clay and its mathematical modeling. *Proceedings of the Symposium on Geotechnical Aspects of Kansai International Airport. Sept. 16 (Fri.) -17 (Sat.), 2005.*, 31-40.

Vadus, J. (1991). Ocean space utilization: Technology trends and future concepts. *Meeting of the United States – Japan Cooperative Program in Natural Resources (UJNR) Panel on Marine Facilities*. U.S Dept. of Commerce and National Oceanic and Atmospheric Administration. Vol. 17. pg. 312-328.

Vaid, Y. P., Robertson, P. K., and Campanella, R. G. (1979). Strain rate behavior of

Saint-Jean-Vianney clay. *Canadian Geotechnical Journal*, Vol. 16 (1), pp. 34-42.

Vaid, Y. P., Robertson, P. K., and Campanella, R. G. (1980). Reply: Strain rate behavior of Saint-Jean-Vianney clay. *Canadian Geotechnical Journal*, Vol. 18 (1), pp. 145-146.

Watabe, Y., and Tsuchida, T. (2001). Influence of stress release on sample quality of Pleistocene clay collected from large depth in Osaka Bay. *Soils and Foundations*. 41 (4), 17-24.

Watabe, Y., Tsuchida, T., and Adachi, K. (2002). Undrained shear strength of Pleistocene clay in Osaka Bay. *J. Geotech. and Geoenv. Engrg*. ASCE, March, 128(3), 216-226.

Watabe, Y., Udaka, K., and Morikawa, Y. (2008). Strain rate effect on long-term consolidation of Osaka Bay clay. *Soils and Foundations*. 48 (4), pp. 495-509.

Yamakawa, M. and Tsuruoka, T. (1996). Sand drain works for a large-scale man-made island. *Marine Georesources and Geotechnology*, 14, pp. 251-262.

Yamane, N. Fukasawa, T., and Mizukami, J. (2003). A new construction method for reclamation work in the Kansai International Airport second phase project. *Proceedings of the Nakase Memorial Symposium Yokosuka, Japan: Soft Ground Engineering in Coastal Areas, 28 November 2002*. A.A. Balkema Publishers. 201-204.

Yamasaki, T., and Nakada, M. (1996). Effects of Quaternary sea-level change on the subsidence of a sedimentary basin; a case study of the Osaka Bay sedimentary basin, Japan, *Tectonophysics*, Vol. 267, No. 1, pp. 229-238.

Yokokura, T., Kano, N., Yamaguchi, K., Miyazaki, T., Ikawa, T., Ohta, Y., Kawanaka, T., and Abe, S. (1998). Seismic profiling of deep geological structure in the Osaka Bay area. *Bull. Geol. Surv. Japan.*, 49, 571-590.

Yong, R., Mulligan, C., Fukue, M. (2007). *Geoenvironmental Sustainability*. Taylor and Francis Group, LLC, Boca Raton, FL. 387 pages.

APPENDIX A SETTLEMENT AND POREWATER PRESSURE PREDICTION AT OSAKA PORT USING THE ILLICON PROCEDURE

A.1 Introduction

Reclamation in the Osaka Port area began as early as the Edo Era (1600 to 1867) with reclaimed land on the delta of the Yodo and Yamato Rivers that was used primarily for rice cultivation (Mikasa and Ohnishi, 1981; Sasaki et al., 1987). Osaka Port was already a bustling port in the 17th and 18th centuries and it became an international trading port in 1868 (PHRI, 1994).

Reclamation projects constructed after World War II include urban facilities like residential areas, commercial areas, sites for research and development, and business centers in addition to port facilities (Matsui, 1994; Araki and Hoes, 2008). Reclaimed islands constructed after World War II include: Sakashima (also known as South Port) as well as Maishima, Yumeshima, and a relatively new island development on the offshore side of Yumeshima. Maishima, Yumeshima, and the new development make up the North Port.

Besides providing urban, port, and industrial facilities, the reclaimed islands in Osaka Port provide a site for waste disposal. Disposed materials used to construct the reclaimed islands include clays dredged for moorings and waterways, fill left over from construction work, incinerated domestic waste, and waste generated from public water and sewerage system facilities (Sasaki et al., 1987; Matsui, 1994, 2001; Osaka Municipal Government, 2000).

Figure A- 1 shows the most recent reclaimed islands in Osaka Port. The elevation of the seabed referenced to Osaka Peil (O.P.) is also shown (Mimura, 2005). Osaka Peil is the lowest tide observed in 1885 (Mikasa and Ohnishi, 1981). A settlement analyses was performed for the Holocene marine clay layer (Ma13) at Sakashima somewhere within Zone 3. Settlement analyses were also performed for the Pleistocene layers at locations S, M, and Y shown in Figure A- 1 for Sakashima, Maishima, and Yumeshima Islands, respectively.

A.2 Analysis for Holocene marine clay layer (Ma13) at South Port

Figure A- 2 shows w_p, w_l, w_o, CF, and σ'_p data for Ma13 at South Port prior to reclamation (Mikasa and Ohnishi, 1981). The CF data in Figure A- 2 most likely represent the percentage of particles with an equivalent spherical diameter less than 5 microns (JIS A 1204).

Preconsolidation pressure increases dramatically towards the bottom boundary of Ma13. Mikasa and Ohnishi (1981) explained that this is a result of pumping from the underlying sandy gravel layer in Western Osaka. The initial thickness (L_o) at the location where the settlement analysis was performed was 17.5m.

Construction of the 1002ha Sakishima began in 1958 (Matsui, 1994; Osaka Municipal Government, 2000; Mimura and Jang, 2005). Reclamation began in Zones 1 and 2 (see Figure A-1) where dredged marine clay was placed. Cardboard drains were installed in the dredged material, but not within the existing seabed (Ma13), and vacuum was not used at Zones 1 and 2. Later reclamation continued at the Middle Quay and South Quay where a sandy reclamation fill material was used. Vertical drains were installed in Ma13, and vacuum was not used at these locations either.

After placement of a 1.5m sand blanket in July 1963, from August 1963 to August 1964 forty centimeter diameter displacement type vertical sand drains were installed on a 3.55m square grid such that they partially penetrated Ma13 at Zone 3. The vertical sand drains were installed such that the elevation of the tip of the drain reached -18m O.P.; therefore, they penetrated 11.5m into Ma13 at the location where the settlement analysis was performed, leaving 6m from the tip of the drain to the bottom of Ma13 (Figure A- 3). The sand used for the sand blanket and vertical sand drains had D_{10} in the range of 0.05mm to 0.4mm and the coefficient of permeability of the sand blanket and vertical sand drains was reported equal to 10^{-4} to 10^{-5} m/s (Mikasa and Ohnishi, 1981).

One hundred eleven drain wells each equipped with a 2.2kW pump were installed at approximately 100m spacing within Zone 3. Settlement and porewater pressure instrumentation was also installed during drain well installation. Once the drain wells were installed, reclamation with dredged seabed material began in August 1965. Approximately 6 to 7 months later, after the dredged fill was placed to a thickness of approximately 2m, completely sealing the 1.5m sand blanket, operation of the vacuum pumps commenced. The pumps continued to operate until August 1969. However, half of the pumps malfunctioned as a result of cavitation and the remaining pumps maintained water level in the 1.5m sand blanket nearly at the elevation of the sand blanket itself (approximately 60kPa of vacuum applied at the location where settlement analysis was performed). Reclamation fill was placed through the end of 1970 (Mikasa and Ohnishi, 1981).

The settlement analysis was performed for the period from January 1966 through June 1968, soon after the end of settlement observation. Settlement observations were made using double-tube settlement gauges (see Chapter 6). The outer tube was installed in the sand blanket overlying Ma13 and the center tube was driven into the sandy gravel layer underlying Ma13. The double –tube settlement gauges were all eventually destroyed during placement of the dredged marine clay reclamation material. Figure A- 4 shows load at the seabed resulting from reclamation fill load, vacuum load, and combined vacuum and fill load. The fill load (32.6 kPa) was calculated assuming unit weight of the 1.5m sand blanket equal to 20 kN/m^3, unit weight of 5.5m of dredged clay fill material equal to 13.2 kN/m^3, and a hydrostatic reference porewater pressure condition from sea level (Mikasa and Ohnishi, 1981). The increase in effective vertical stress with depth resulting from application of vacuum load and reclamation fill load is shown in Figure A- 3.

Ma13 was divided into 5 sublayers based on the w_p, w_l, w_o, CF, and σ'_p data presented Figure A- 2. Table A- 1 shows representative values of e_o, σ'_{vo}, σ'_p, σ'_p/σ'_{vo}, k_{vo}, and C_k for each sublayer of Ma13. Initial void ratio was calculated assuming that the specific gravity of soil solids is 2.67 (Mikasa and Ohnishi, 1981). Preconstruction effective vertical stress was computed assuming unit weight equal to $15kN/m^3$ and a hydrostatic reference porewater pressure condition from sea level. Preconsolidation pressure was estimated based on the data reported in Figure A-2.

In the absence of direct permeability measurements, permeability values were assigned based on values reported in Tanaka et al. (2003) obtained from rate of compression observed in incremental loading oedometer tests, together with the Terzaghi consolidation theory, for Kansai Airport (Figure 4-33). Values of permeability that are computed this way are often smaller than directly measured values; therefore, k_{vo} values obtained from Figure 4-33 were increased by a factor of two (Mesri et al., 1994). The empirical relationship $C_k = 0.5e_o$ was employed to estimate change-in-permeability-index for subsequent settlement analyses (Tavenas et al., 1983b; Mesri et al., 1994).

Figure A- 5 shows the EOP e – log σ'_v relationships for each sublayer. The EOP e – log σ'_v relationships in the compression range were constructed using a single value of C_c reported in Mikasa and Ohnishi (1981) for each sublayer (note that for small values of $\sigma'_{vf}/\ \sigma'_p$ this is expected to somewhat underestimate primary compression). Recompression indices were

estimated assuming C_r/C_c equal to 0.1. Disturbance of the soil adjacent to the drain was incorporated in the settlement analysis by including a smear zone with a diameter equal to 80cm (two times the diameter of the vertical sand drains). A linear EOP e – log σ'_v relationship was assumed for the soil in the smear zone that is defined by the points (σ'_{vo}, e_o) and (σ'_{vf}, e_p), where e_p is the EOP void ratio corresponding to σ'_{vf}.

Computed and observed vertical compression of Ma13 is shown in Figure A- 6. The double tube settlement observations correspond to many different locations within Zone 3, and it is not clear which set of observations correspond to the location where the settlement analysis was performed. However, the ILLICON analysis is reasonable based on the available data for Ma13 at this location.

After reclamation of the dredged seabed material, an upper sand blanket was placed and 12cm diameter packed sand drains or 10cm wide cardboard drains were installed at 1 to 2m spacing such that they fully penetrated the dredged clay reclamation fill and formed a drainage connection to the sand blanket underlying the dredged clay fill. Then a sandy fill was placed on the upper sand blanket. Next, 11 kW pumps spaced 150m apart applied vacuum to the dredged clay layer at Zone 3. A similar construction technique was used at the North Quay (Mikasa and Ohnishi, 1981).

A.3 Analyses for Pleistocene marine clay layers at Osaka Port

Settlment analyses were performed for the Pleistocene layers at locations S, M, and Y shown in Figure A- 1 for Sakashima, Maishima, and Yumeshima Islands, respectively.

Construction of the 224ha Maishima and the 391ha Yumeshima began in 1972 and 1977, respectively (Matsui, 1994; Osaka Municipal Government, 2000; Mimura and Jang, 2005). Figure A- 1 shows that Maishima and Yumeshima are divided into four main sections separated by partition dikes. Section 1 of both islands consists of residues of incinerated domestic waste as well as waste generated from public water and sewerage system facilities. Sections 2 and 3 consist of surplus soil from construction sites as well as dredged soil from rivers and harbor areas. Section 4 of each island was constructed using soil from mountain blasting and surplus soil fill from construction sites. Waste materials were generally placed in 3m lifts with a 50cm thick soil cover. Dredged clay material was pumped directly to the site or carried via barge then pumped to the final location in sections 2 and 3 (Osaka Municipal Government, 2000).

In each case, prior to placement of reclaimed material, a sand blanket was placed followed by installation of vertical drains in Ma13. After placement of a clay cover that sealed the sand blanket, vacuum consolidation was used to improve Ma13. Whenever dredged seabed material was placed, an upper sand blanket was placed then plastic board vertical drains were installed. Next, pump wells were installed and vacuum consolidation was used to improve the dredged material (Osaka Municipal Government, 2000).

A.3.1 Subseabed condition

There are several important differences between the subseabed profile at Osaka Port and the subseabed profile at the Kansai Airport site. When sea levels receded intermittently throughout the Pleistocene Epoch subaerially exposing the ground where Kansai Airport is currently located, a flood plain environment existed and it is likely that the southern portion of Osaka Bay remained relatively far from sediment-carrying rivers. Therefore, when rain events caused the paleo-rivers to flood their banks and deposit sediment, only a small amount of clean sand, or no clean sand, was deposited at the location currently occupied by Kansai Airport. As a result, some of the sand layers that underlie Kansai Airport are thin and sometimes discontinuous with relatively high fines content. In contrast, the area currently occupied by Osaka Port has gravely sand layers that are thick and continuous with relatively low fines content (Mimura et al., 2003). The subseabed profile at Osaka Port is also unlike the subseabed profile at Kansai Airport because there are no substantial non-marine clay layers. Additionally, the marine clay layers Ma6 and Ma5, which are not present at the Kansai Airport site, are present at the Osaka Port site as evidenced by the boring OD-1 (see Figure 2-7).

Figure A- 7 shows the subseabed profiles at Locations S, M, and Y. Layer thicknesses from boring OD-1 (Figure A- 1) are shown for layers Ma8 and below for all three islands (Matsui et al., 2001).

Layers Ma12, Ma11U, Ma11L, Ma10, and Ma9 were subdivided based on values of e_o reported in the literature for Sakashima, Maishima, and Yumeshima Reclaimed Islands (Mimura and Jang, 2004, 2005). Figure A- 8, Figure A- 9, and Figure A- 10 show w_p and w_l, as well as the percentage of particles with an equivalent spherical diameter less than 5 microns for Pleistocene marine clay layers Ma12, Ma11U, Ma11L, and Ma10, respectively. The figures also include water content data that was taken sometime after a reclamation load was applied (Mimura et al.,

2003). While Mimura et al. (2003) do not specify the exact geographic location from which the samples for Atterberg limit and clay-size fraction data were taken; they indicate that the values are representative of the subseabed in Osaka Port. Vertical lines delineate average values of w_p, w_l, and % < 5μm for each sublayer.

Table A- 2 summarizes representative values of e_o, w_p, w_l, I_p and CF for each sublayer of Ma12, Ma11U, Ma11L, Ma10, and Ma9. Marine clay layer Ma9 was assigned representative values of w_p, w_l, and CF from available data at Kansai Airport (Akai and Tanaka, 1999; Imai et al., 2005; Tanaka and Locat, 1999; Tanaka et al., 2003; Tanaka et al., 2004; Watabe et al., 2002) because no data were available near Osaka Port.

Table A- 3 summarizes representative values of e_o, w_p, w_l, and CF for the Pleistocene marine clay layers below Ma9. The values were assigned based on data published for Kansai Airport (Akai and Tanaka, 1999; Imai et al., 2005; Tanaka and Locat, 1999; Tanaka et al., 2003; Tanaka et al., 2004; Watabe et al., 2002) because no data were available near Osaka Port.

A.3.2 EOP e – log σ′$_v$ relationships

Figure A- 12, Figure A- 13, and Figure A- 14 show σ'_{vo}, σ'_p, and σ'_{vf} with depth at Locations S, M, and Y, respectively. Preconstruction effective vertical stress and σ'_p were obtained from reported values in Mimura and Jang (2005) for Sakashima and Yumeshima Islands and from reported values in Mimura and Jang (2004) for Maishima Island. The final effective vertical stress was computed from the following equation:

$$\sigma'_{vf} = \sigma'_{vo} + \Delta\sigma_v \qquad (A-1)$$

where $\Delta\sigma_v$ is the increase in vertical stress calculated using the Boussinesq solution for a uniformly loaded circular area. The applied load on the seabed is approximately 265kPa at Sakashima, 225kPa at Maishima, and 260kPa at Yumeshima (Mimura and Jang, 2004; 2005). For all three islands, σ'_{vf} is greater than σ'_p for Ma12, Ma11U, and Ma11L, slightly less than or equal to σ'_p for Ma10 and Ma9, and significantly less than σ'_p for clay layers underlying Ma9.

To construct the EOP e – log σ'_v relationships for Pleisocene clay layers Ma12 through Ma9, first the point (σ'_{vo}, e_o) was defined. Then, the recompression curve from σ'_{vo} to σ'_p was constructed assuming C_r/C_c equal to 0.1. The compression indices were taken directly from Mimura and Jang (2005) for Sakashima and Yumeshima Islands and Mimura and Jang (2004)

for Maishima Island. In each case, Mimura and Jang (2004, 2005) report a single value of C_c for each sublayer. The oedometer tests available for Pleistocene layers at the Kansai Airport site (Figure 4-44) indicate that the EOP e – log σ'_v relationships at that location are highly non-linear beyond σ'_p; therefore, it is unlikely that a single value of C_c will accurately characterize the compressibility of the Pleistocene deposits at Osaka Port. This is a serious limitation to settlement analyses at Osaka Port. The C_c' data reported for the Kansai Airport project were not used at Osaka Port because the source material deposited at the Osaka Port site is not the same as the source material deposited at Kansai Airport. Additionally, the depositional environment, which is partly dictated by the velocity and volume of flow and proximity of sediment-carrying rivers to the Osaka Port site, is different than the Kansai Airport site.

Figure A- 15, Figure A- 16, Figure A- 17, Figure A- 18, and Figure A- 19 show EOP e – log σ'_v relationships for Ma12, Ma11U, Ma11L, Ma10, and Ma9, respectively. Table A- 4 shows C_r values used for Pleistocene clay layers Ma8 and below.

A.3.3 Coefficient of permeability of Pleistocene clay layers

In-situ coefficient of vertical permeability (k_{vo}) values reported in Mimura and Jang (2005) were used for settlement analyses at Sakashima and Yumeshima Islands, and k_{vo} values reported in Mimura and Jang (2004) were used for settlement analyses at Maishima Island. However, Mimura and Jang (2004, 2005) do not describe how they obtained the permeability values that they used for their analyses. Therefore, the following empirical equation together with representative values of e_o, w_p, w_l, and CF was used to check whether the magnitudes reported in Mimura and Jang (2004, 2005) are reasonable (Mesri et al., 1994):

$$k_{vo}(m/s) = C\left(\frac{e_o / CF}{A_c + 1}\right)^4 \qquad (A-2)$$

The clay-size fraction data used to develop Equation A-2 with C equal to 6.5e-11 (for k_{vo} in m/s) was taken as the percentage of particles with an equivalent spherical diameter less than 2μm (Mesri et al., 1994). However, the clay-size fraction data points shown in Figure A- 8 through Figure A- 11 represent the percentage of particles with an equivalent spherical diameter less than 5μm (JIS A 1204). Therefore, the CF values delineated in Figure A- 8 through Figure A- 11 were

reduced using the following equation:

$$[CF]_{\%<2\mu m} = \frac{[CF]_{\%<2\mu m}}{[CF]_{\%<5\mu m}} [CF]_{\%<5\mu m} \qquad (A-3)$$

with $\frac{[CF]_{\%<2\mu m}}{[CF]_{\%<5\mu m}}$ equal to 0.56 based on measurements of $[CF]_{\%<2\mu m}$ (Tanaka and Locat, 1999) and $[CF]_{\%<5\mu m}$ (Akai and Tanaka, 1999; Watabe et al., 2002) reported for the Kansai Airport site.

Table A- 5 shows k_{vo} values reported in Mimura and Jang (2004, 2005) and k_{vo} values calculated using Equation A-2 for each sublayer of Ma12, Ma11U, Ma11L, Ma10, and Ma9. The reported k_{vo} values are close to k_{vo} values calculated using Equation A-2 with a few exceptions. The bottom sublayer of Ma12 at Maishima and Yumeshima have reported k_{vo} values that are 2.5 times and 2.7 times larger than k_{vo} values computed from Equation A-2, respectively. Additionally, the top and bottom sublayers of Ma9 have reported k_{vo} values that are 3.8 times and 2.9 times larger than k_{vo} values computed from Equation A-2, respectively. Atterberg limit and CF values for Ma9 were obtained from data at the Kansai Airport site.

Table A- 6 k_{vo} values assigned to Pleistocene clay layers Ma8 and below. These values were taken from the analyses for Kansai Airport because no subsurface data was available for these layers at Osaka Port.

Permeability is commonly expressed as a function of void ratio. A widely-used permeability - void ratio relationship that is employed for settlement analyses is based on $C_k = \Delta e/\Delta \log k$ = constant where C_k is the change-in-permeability-index (Raymond, 1969; Mesri and Rokhsar, 1974; Burghignoly and Vestroni, 1975; Tavenas et al., 1983b). The change-in-permeability-index can be determined from routine oedometer tests or through direct permeability measurements. There were not sufficient oedometer test data or permeability measurements available at Osaka Port for determining C_k; therefore, the empirical relationship $C_k = 0.5e_o$ was employed for subsequent settlement analyses (Tavenas et al., 1983b; Mesri et al., 1994).

A.3.4 Coefficient of permeability of Pleistocene gravelly sand layers

Mimura and Jang (2003, 2004, 2005, 2006) describe the Pleistocene gravelly sand

layers that underlie Osaka Port as thick and continuous. Mimura and Jang (2006) made the following statement regarding the permeability of the gravelly sand layers:

> "…excess pore water pressure is scarcely generated in the gravelly sand layers due to large permeability of those layers ($k=2.16x10^{1}$ m/day)…"

Permeability values equal to $2.1x10^{1}$ m/day ($2.5x10^{-4}$ m/s) were also reported in Mimura and Jang (2005) for Pleistocene gravelly sand layers underlying Sakashima and Yumeshima Reclaimed Islands. Jang and Mimura (2005) varied the permeability of the Pleistocene gravelly sand layers in a series of finite element analyses and concluded that the calculated time rate of settlement at Maishima Reclaimed Isand remained unchanged when a permeability greater than or equal to 1 m/day ($1.16x10^{-5}$ m/s) was used.

Subsequent settlement analyses here assume that the excess porewater pressures within the gravelly sand layers below Ma13, below Ma9, and below Ma0 were equal to zero. Coefficient of permeability equal to $2.5x10^{-4}$ m/s together with Equation 7-53 were used to calculate the excess porewater pressure within the other gravelly sand layers.

A.3.5 Settlement analyses at Osaka Port

Double tube settlement gauges were installed at Sakashima, Location S. Settlement observations began in 1979 about 4 years after the completion of reclamation. Settlement of the Pleistocene layers and settlement of Ma11U was monitored (Mimura and Jang, 2003).

At Maishima Island, the settlement of the Pleistocene deposits was monitored by a double tube settlement gauge during first filling of dredged material. Later, during placement of a final sand blanket, differential settlement gauges were installed to measure vertical compression of layers below Ma10, Ma10, Ma11L, Ma11U and Ma12, and the Pleistocene layers, at Location M. Settlement records were interrupted due to damage of the gauges (Mimura and Jang, 2004).

Double tube settlement gauges and anchor rod settlement gauges were used at Yumeshima to monitor settlement of the Pleistocene layers at Location Y (Mimura and Jang, 2003).

Figure A- 20 shows the setup for the analysis at Maishima, Location M. The $\Delta\sigma_v$ was calculated using the Boussinesq solution for a uniformly loaded circular area. The diameter of the circle was selected such that the circular area is equal to the area of each island. Additionally,

the center of the uniformly loaded circular area coincides with the center of area for each reclaimed island. The initial thicknesses, compressibility relationships, and permeability relationships are assumed constant in the radial direction for each clay sublayer. The distance in the r direction from the centerline of Maishima to the freely draining radial boundary (2520m) was selected to be 1.5 times the diameter of the circular area (1680m). Water flow in the r direction within the sand layers was modeled according to Equation 7-53.

Secondary compression of the Pleistocene clay layers was computed using the C_α/C_c law of compressibility (Mesri and Godlewski, 1977, 1979) from the following equation:

$$S_\alpha = \frac{C_c}{1+e_o}\frac{C_\alpha}{C_c} L_o \log\frac{t}{t_p} \qquad (A-4)$$

where t_p is the time to end-of-primary consolidation. When σ'_{vf} / σ'_p was less than 0.9, then the C_c term in Equation A-4 was set equal to C_r. For σ'_{vf} / σ'_p greater than 0.9 the C_c term in Equation A-4 was set equal to C_c reported by Mimura and Jang (2004, 2005).

Figure A- 21 shows observed and calculated settlement for Location M at Maishima Island. The discrepancy between observed and calculated settlement demonstrates the serious limitation of using a single value of C_c for Pleistocene clay layers at Osaka Port. This is particularly problematic for Pleistocene clay layers Ma11L, Ma10, and Ma9 (σ'_{vf}/σ'_p for these layers is in the range of 0.96 to 1.13 wheras the reported C_c likely corresponds to a larger value of σ'_{vf}/σ'_p). For Pleistocene clay layers with final effective vertical stress slightly less than the preconsolidation pressure (e.g. Ma10 and Ma9), secondary compression is expected to be significant. This is because these layers reach EOP consolidation quickly, and because the C_α/C_c law of compressibility (Mesri and Godlewski, 1977, 1979) suggests that C_c used to calculate secondary compression in Equation A-4 is near the maximum C_c just beyond the preconsolidation pressure (unless of course a graphical procedure is used).

For Pleistocene clay layers with σ'_{vf} just beyond σ'_p, C_c' corresponding to σ'_v much greater than σ'_p is expected to underestimate EOP compression.

Figure A- 22 shows observed and calculated settlement for Location M using the C_c' data from Kansai Airport (Figure 4-44) to represent the compressibility of Pleistocene clay layers Ma11L, Ma10, and Ma9 beyond the preconsolidation pressure. There is better agreement for this case. However, as mentioned previously, the compressibility of the subseabed deposits at the Kansai Airport site is not necessarily representative of the compressibility of the subseabed

deposits at the Osaka Port site because the source material is different and because the depositional environment is different. For example, if C_c' data at the Kansai Airport site are used characterize the compressibility of Ma12, then calculated compression of Ma12 is greater than observed.

What is clear from Figure A- 21 and Figure A- 22, is that the compressibility of the Pleistocene marine clay deposits at Osaka Bay cannot be accurately characterized by a single value of C_c.

Figure A- 23 shows computed excess porewater pressure with depth for Pleistocene clay layers Ma12 through Ma9 at Location M. Excess porewater pressures in the gravelly sand layers calculated using Equation 7-53 with k_{eq} equal to 2.5x10-4 m/s (Mimura and Jang, 2005, 2006) remain relatively small, and therefore, do little to impede the progress of consolidation of the adjacent clay layers.

Computed and observed settlements for Location S and Location Y are shown in Figure A- 24 and Figure A- 25, respectively. Once again the discrepancy between computed and observed settlements at Location S is most likely the result of using a single value of C_c to characterize the compressibility of the Pleistocene clay layers beyond the preconsolidation pressure.

A.3.6 Concluding Remarks

Analyses of the Pleistocene layers at Osaka Port highlight the importance of careful interpretation of data including laboratory oedometer tests. A single value of compression index is not sufficient to describe the nonlinearity of the EOP e – log σ'_v relationships for Osaka Bay Pleistocene clays. The use of a single value of C_c is particularly detrimental when the final effective vertical stress is near the preconsolidation pressure. For these cases, the C_α/C_c law of compressibility suggests that C_c used to calculate secondary compression in Equation A-4 should be the maximum C_c just beyond the preconsolidation pressure for routine settlement calculations in the absence of the graphical method (Mesri and Godlewski, 1977, 1979). The use of C_c' data from the Kansai Airport site produced better agreement at Location M; however, most like the compressibility of the Pleistocene deposits at Kansai Airport is not representative of the compressibility of the Pleistocene deposits at Osaka Port because the source material and depositional environments are different.

Excess porewater pressures within the gravelly sand layers calculated using Equation 7-53, are small and do very little to impede the progress of consolidation of adjacent clay layers at the Osaka Port site.

A.4 Tables

Table A- 1 Representative values for Ma13.

Sublayer	Sublayer Thickness (m)	e_o	σ'_{vo} (kPa)	σ'_p (kPa)	σ'_p/σ'_{vo}	k_{vo} (m/s)	C_k
1	4.0	2.280	10.0	28.2	2.8	2.2E-08	1.1
2	4.0	2.223	30.0	53.0	1.8	8.8E-09	1.1
3	3.5	2.335	48.8	75.3	1.5	3.8E-09	1.2
4	3.0	2.443	65.0	161.0	2.5	1.8E-09	1.2
5	3.0	2.141	80.0	180.0	2.3	9.2E-10	1.1

Table A- 2 Representative values of e_o, w_p, w_ℓ, I_p and CF for Pleistocene clay layers Ma12, Ma11U, Ma11L, Ma10, and Ma9.

Layer	e_o			w_p[c] (%)	w_ℓ[c] (%)	I_p[c] (%)	% < 5μm[c]
	Sakashima[a]	Maishima[b]	Yumeshima[a]				
Ma12	2.20	2.34	2.22	40	112	71	57
	2.20	2.32	2.22	42	119	77	49
	1.65	1.63	1.70	27	68	40	56
	1.45	1.12	1.20	29	67	39	58
Ma11U	1.60	1.26	1.40	30	73	43	41
	1.20	1.04	1.20	30	73	43	48
	1.00	-	1.00	28	61	33	27
Ma11L	1.70	1.76	1.75	41	109	68	34
	1.30	1.51	1.38	32	81	49	45
	1.00	0.91	1.00	26	57	31	20
Ma10	1.60	1.45	1.60	44	107	63	56
	1.90	1.87	1.95	53	128	75	56
	2.20	2.21	2.20	60	140	80	56
	1.20	1.24	1.30	44	99	55	50
Ma9[d]	1.10	0.95	1.10	35	91	56	28
	1.50	1.37	1.50	35	91	56	28
	1.50	1.37	1.50	35	91	56	28
	1.80	1.61	1.80	34	90	56	39
	1.80	1.61	1.80	34	90	56	39
	1.50	1.15	1.50	34	90	56	39

a. Mimura and Jang (2005)

b. Mimura and Jang (2004)

c. Ma12, Ma11U, Ma11L, and Ma10 based on data reported in Mimura et al. (2003)
Ma9 based on data reported for Kansai Airport (Akai and Tanaka, 1999; Imai et al., 2005; Tanaka and Locat, 1999; Tanaka et al., 2003; Tanaka et al., 2004; Watabe et al., 2002)

Table A- 3 Representative values of e_o, w_p, w_ℓ, I_p and CF for Pleistocene clay layers below Ma9 based on data from Kansai Airport (Akai and Tanaka, 1999; Imai et al., 2005; Tanaka and Locat, 1999; Tanaka et al., 2003; Tanaka et al., 2004; Watabe et al., 2002).

Layer	**e_o**	**w_p (%)**	**w_ℓ (%)**	**I_p (%)**	**% < 2μm**
Ma8	1.17	31	83	51	33
	1.45	36	91	56	33
	1.24	32	60	28	33
Ma7	1.28	33	80	46	28
	1.46	37	96	59	29
	1.23	33	83	50	45
Ma6[a]	1.00	-	-	-	-
Ma5[a]	1.00	-	-	-	-
Ma4	1.30	34	87	53	30
Ma3	1.33	35	86	50	29
Ma2	1.10	31	82	51	28
Ma1	1.04	32	84	51	26
Ma0	0.86	25	63	38	14

a. No data available for layers Ma6 and Ma5.

Table A- 4 Recompression indices for Pleistocene clay layers Ma8 and below. Data from analyses at Kansai Airport (see Chapter 8).

Layer	C_r
Ma8	0.12
	0.15
	0.12
Ma7	0.13
	0.15
	0.12
Ma6	0.10
Ma5	0.10
Ma4	0.10
Ma3	0.13
Ma2	0.11
Ma1	0.10
Ma0	0.09

Table A- 5 Reported (Mimura and Jang, 2004, 2005) and calculated (Equation A2-2) k_{vo} values.

Layer	Sakashima		Maishima		Yumeshima	
	k_{vo}[a] (m/s)	k_{vo}[b] (m/s)	k_{vo}[a] (m/s)	k_{vo}[c] (m/s)	k_{vo}[a] (m/s)	k_{vo}[b] (m/s)
Ma12	1.3E-09	1.1E-09	1.7E-09	1.0E-09	1.4E-09	1.4E-09
	1.3E-09	1.1E-09	1.6E-09	1.0E-09	1.3E-09	1.4E-09
	1.8E-09	1.1E-09	1.8E-09	1.0E-09	2.1E-09	1.4E-09
	1.1E-09	1.1E-09	4.0E-10	1.0E-09	5.2E-10	1.4E-09
Ma11U	2.3E-09	3.2E-10	8.8E-10	7.0E-10	1.3E-09	2.7E-10
	7.3E-10	3.2E-10	5.8E-10	7.0E-10	7.3E-10	2.7E-10
	5.0E-10	3.2E-10	-	-	5.0E-10	2.7E-10
Ma11L	9.2E-10	2.3E-10	1.1E-09	6.0E-10	1.0E-09	2.7E-10
	6.1E-10	2.3E-10	1.1E-09	6.0E-10	7.8E-10	2.7E-10
	2.1E-09	2.3E-10	1.5E-09	6.0E-10	2.1E-09	2.7E-10
Ma10	5.5E-10	5.3E-10	3.7E-10	3.0E-10	5.5E-10	5.4E-10
	6.7E-10	5.3E-10	6.3E-10	3.0E-10	7.4E-10	5.4E-10
	1.0E-09	5.3E-10	1.0E-09	3.0E-10	1.0E-09	5.4E-10
	2.8E-10	5.3E-10	3.2E-10	3.0E-10	3.9E-10	5.4E-10
Ma9[d]	1.9E-10	3.4E-10	1.1E-10	4.0E-10	1.9E-10	3.4E-10
	6.6E-10	3.4E-10	4.6E-10	4.0E-10	6.6E-10	3.4E-10
	6.6E-10	3.4E-10	4.6E-10	4.0E-10	6.6E-10	3.4E-10
	8.4E-10	3.4E-10	5.4E-10	4.0E-10	8.4E-10	3.4E-10
	8.4E-10	3.4E-10	5.4E-10	4.0E-10	8.4E-10	3.4E-10
	4.0E-10	3.4E-10	1.4E-10	4.0E-10	4.0E-10	3.4E-10

a. Equation A2-2 (Mesri et al., 1994)

b. Mimura and Jang (2005)

c. Mimura and Jang (2004)

d. Data from Kansai Airport Islands used to obtain Atterburg limits (see chapter 4).

Table A- 6 k_{vo} values used for Pleistocene clay layers Ma8 and below at Osaka Port.

Layer	k_{vo} (m/s)
Ma8	2.4E-10
	4.6E-10
	1.1E-09
Ma7	5.6E-10
	4.9E-10
	1.8E-10
Ma6[a]	1.8E-10
Ma5[a]	1.8E-10
Ma4	3.8E-10
Ma3	5.5E-10
Ma2	2.4E-10
Ma1	2.1E-10
Ma0	4.8E-10

a. No data available for layers Ma6 and Ma5.

A.5 Figures

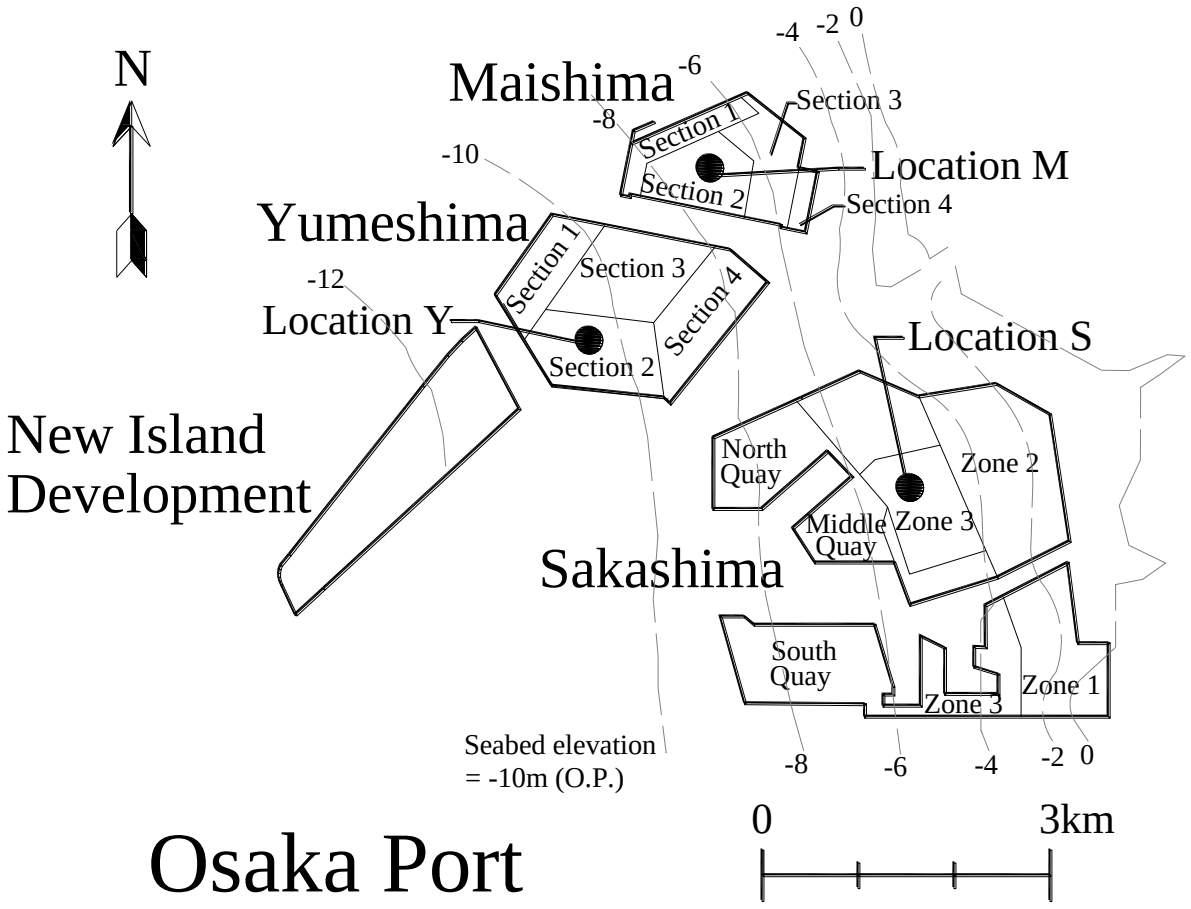

Figure A- 1 Reclamation projects in Osaka Port (Mikasa and Ohnishi, 1981; Mimura, 2005).

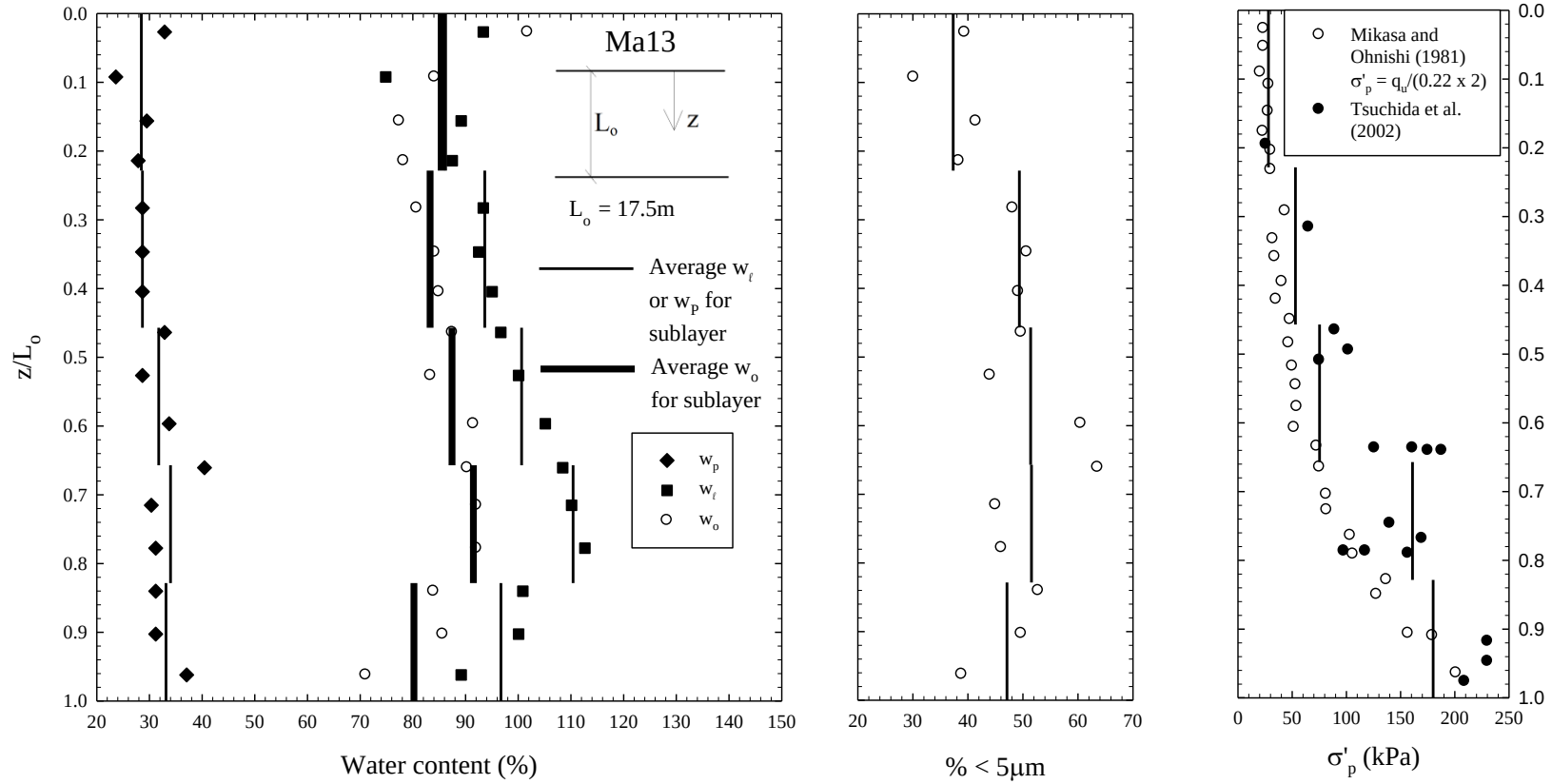

Figure A- 2 Data from Mikasa and Ohnishi (1981) and Tsuchida et al. (2002).

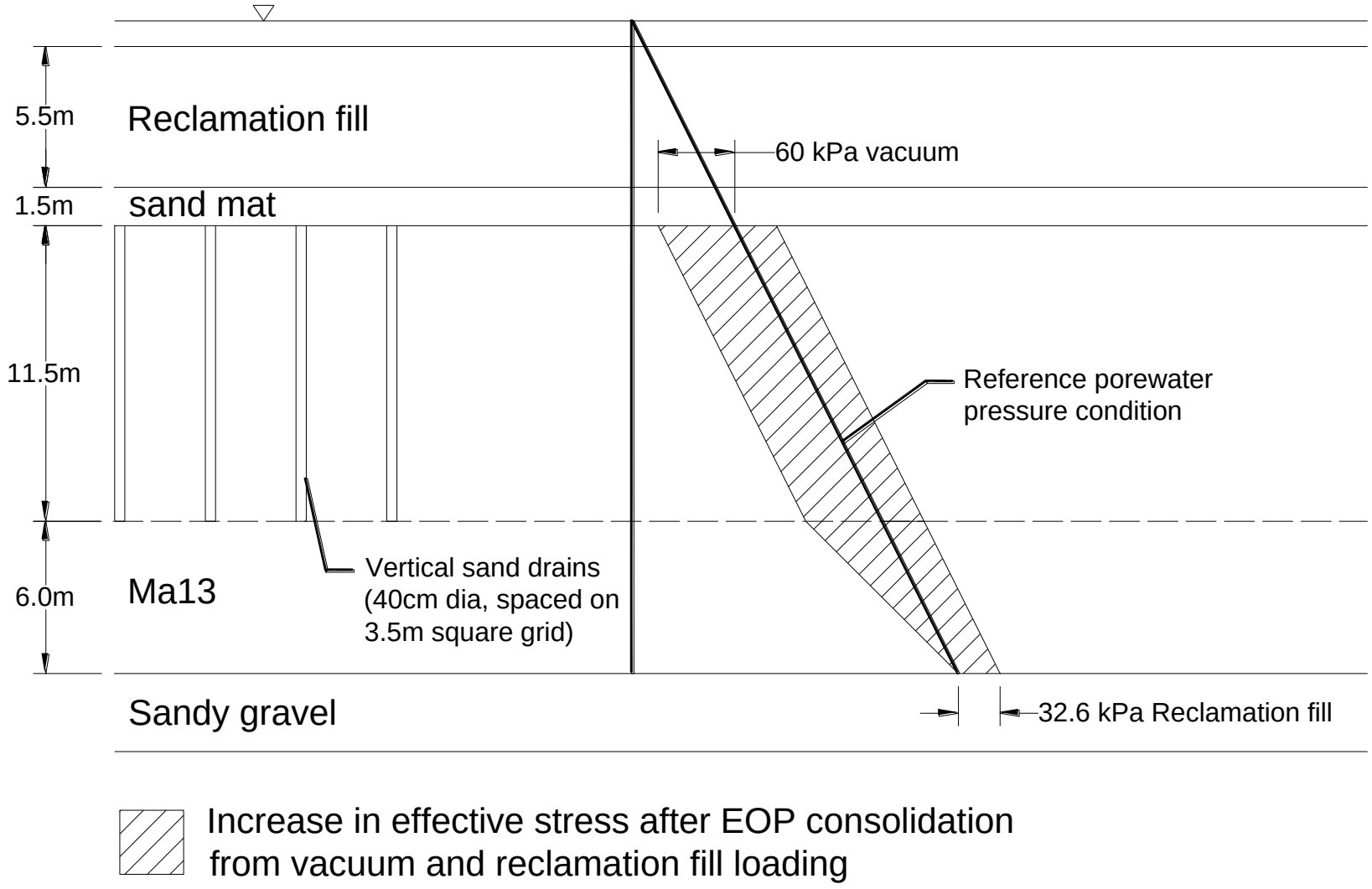

Figure A- 3 Increase in effective vertical stress with depth within Ma13 as a result of vacuum and fill loading at South Port (Mikasa and Ohnishi, 1981).

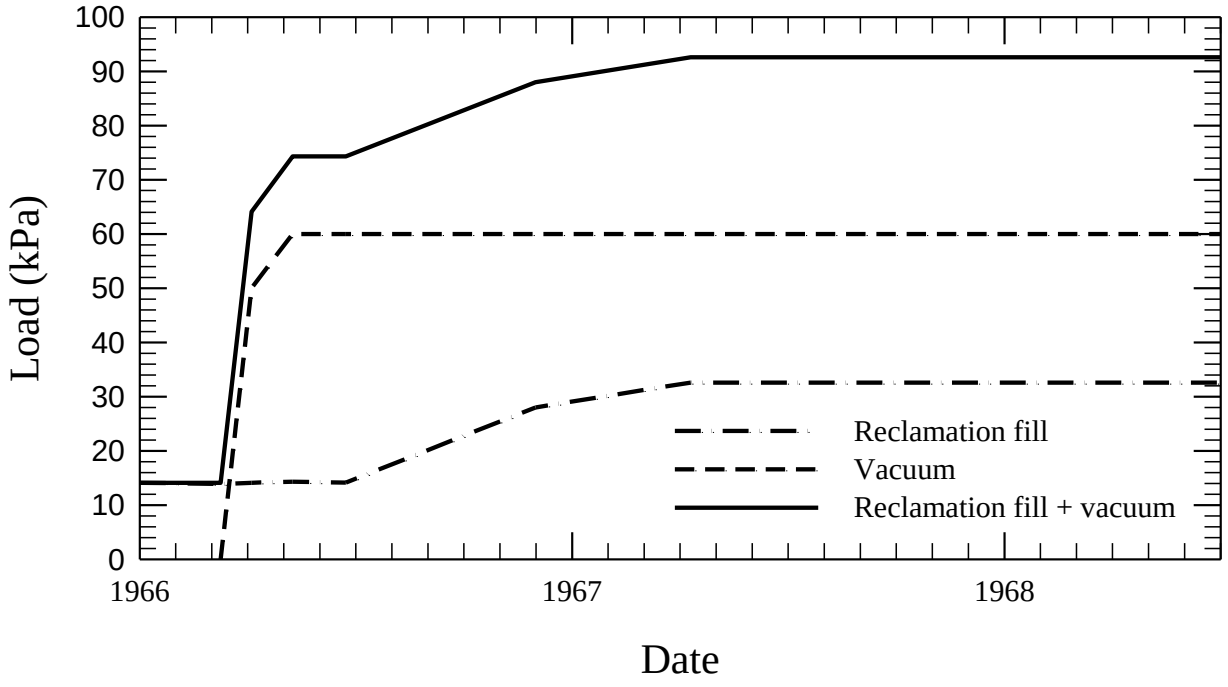

Figure A- 4 Vacuum and fill loading applied at seabed (Mikasa and Ohnishi, 1981).

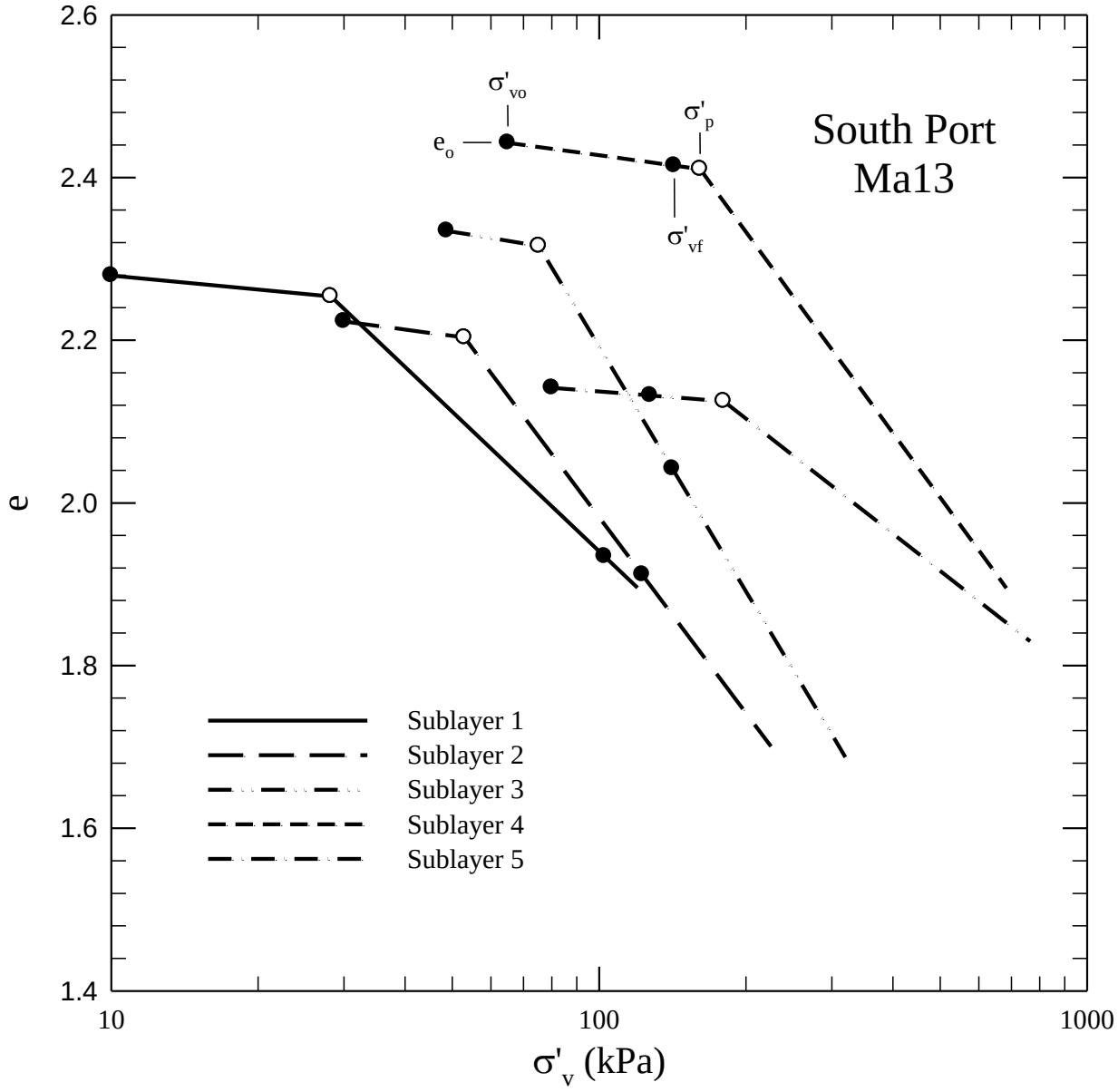

Figure A- 5 EOP e – log σ'_v relationships for Ma13 at South Port (Mikasa and Ohnishi, 1981).

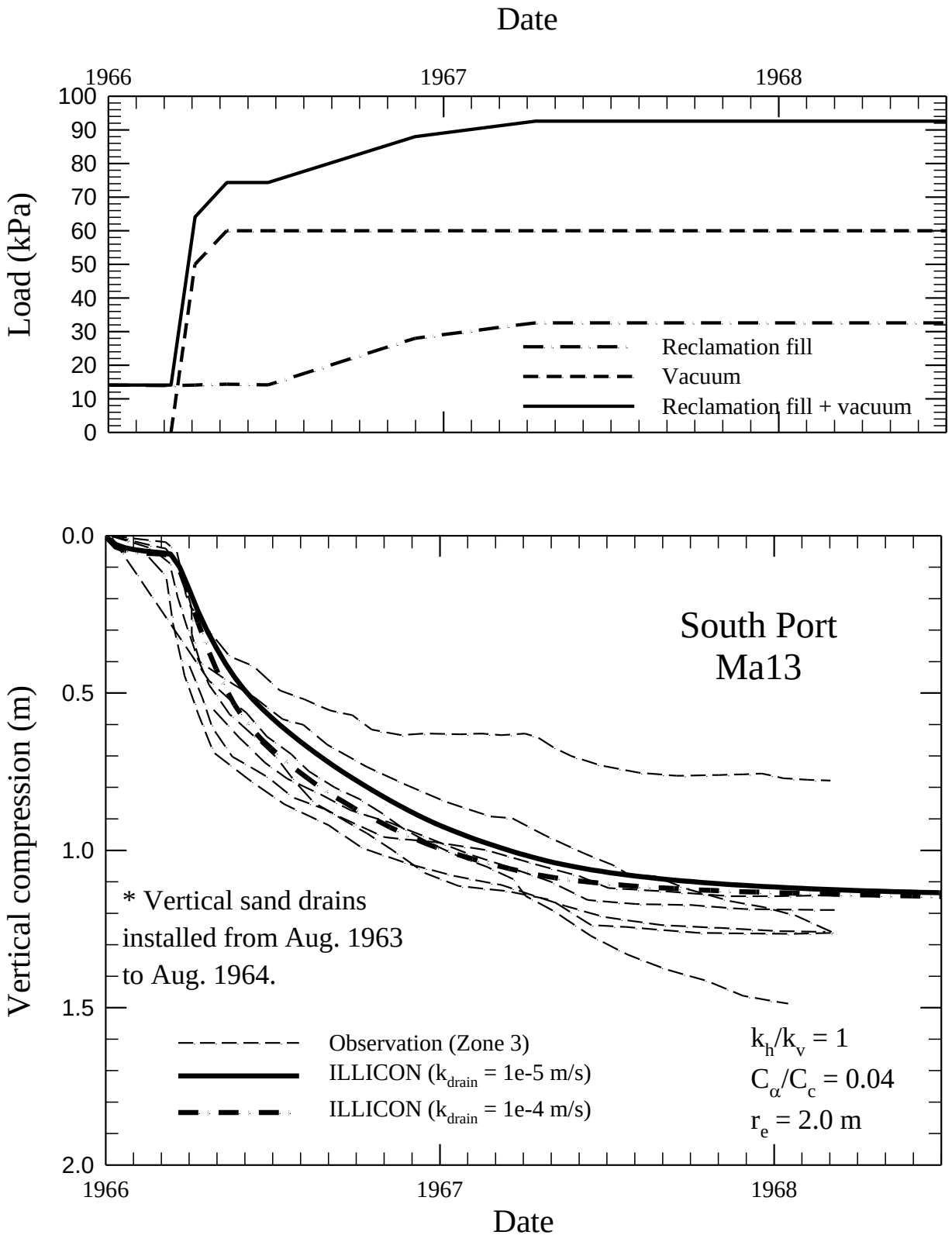

Figure A- 6 Computed and observed vertical compression of Ma13 at South Port.

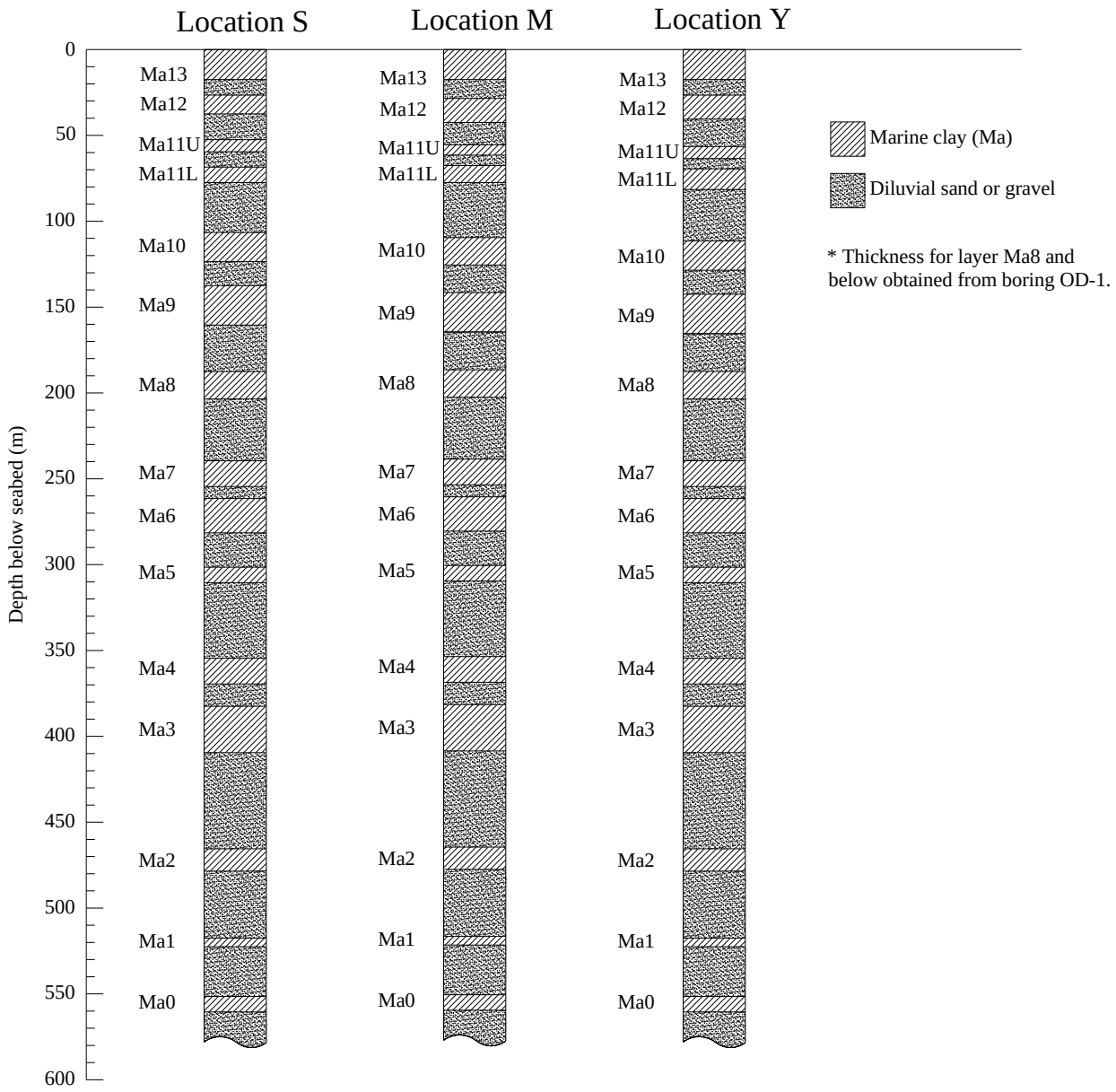

Figure A- 7 Subseabed profiles for Sakashima, Maishima, and Yumeshima (Matsui et al., 2001; Mimura and Jang, 2005; 2006).

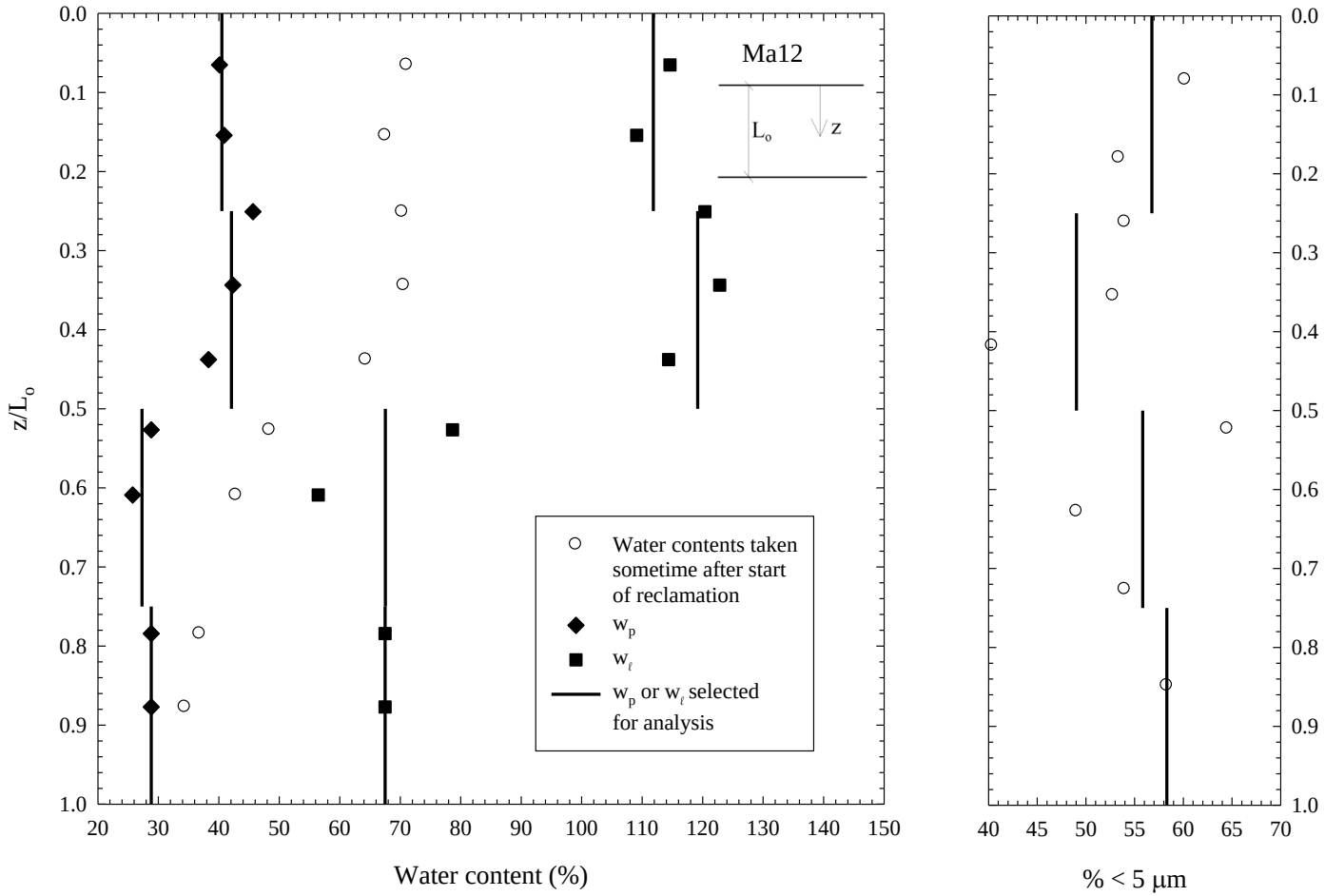

Figure A- 8 Atterberg limit and clay-size fraction data for Ma12. Data from Mimura et al. (2003).

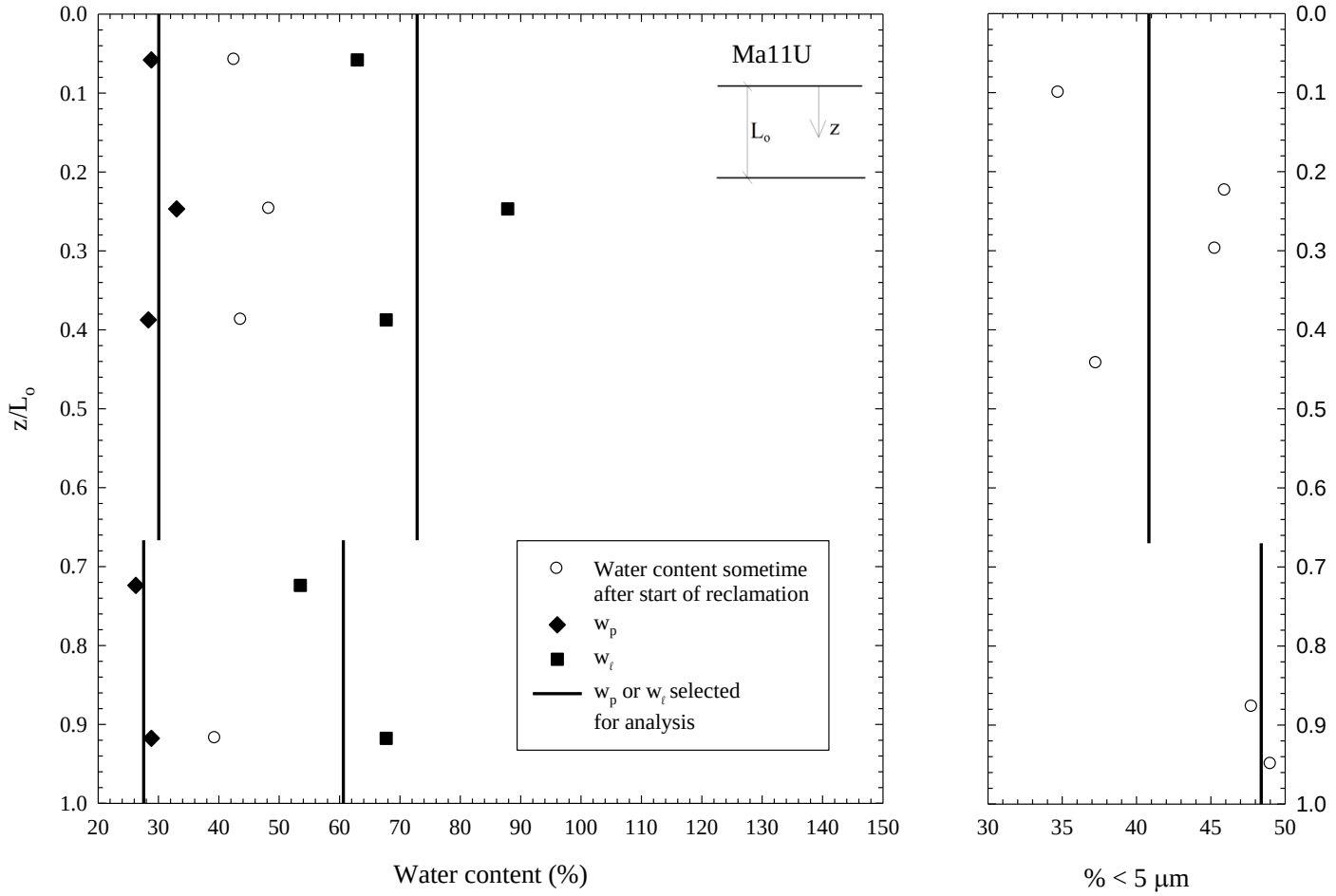

Figure A- 9 Atterberg limit and clay-size fraction data for Ma11U. Data from Mimura et al. (2003).

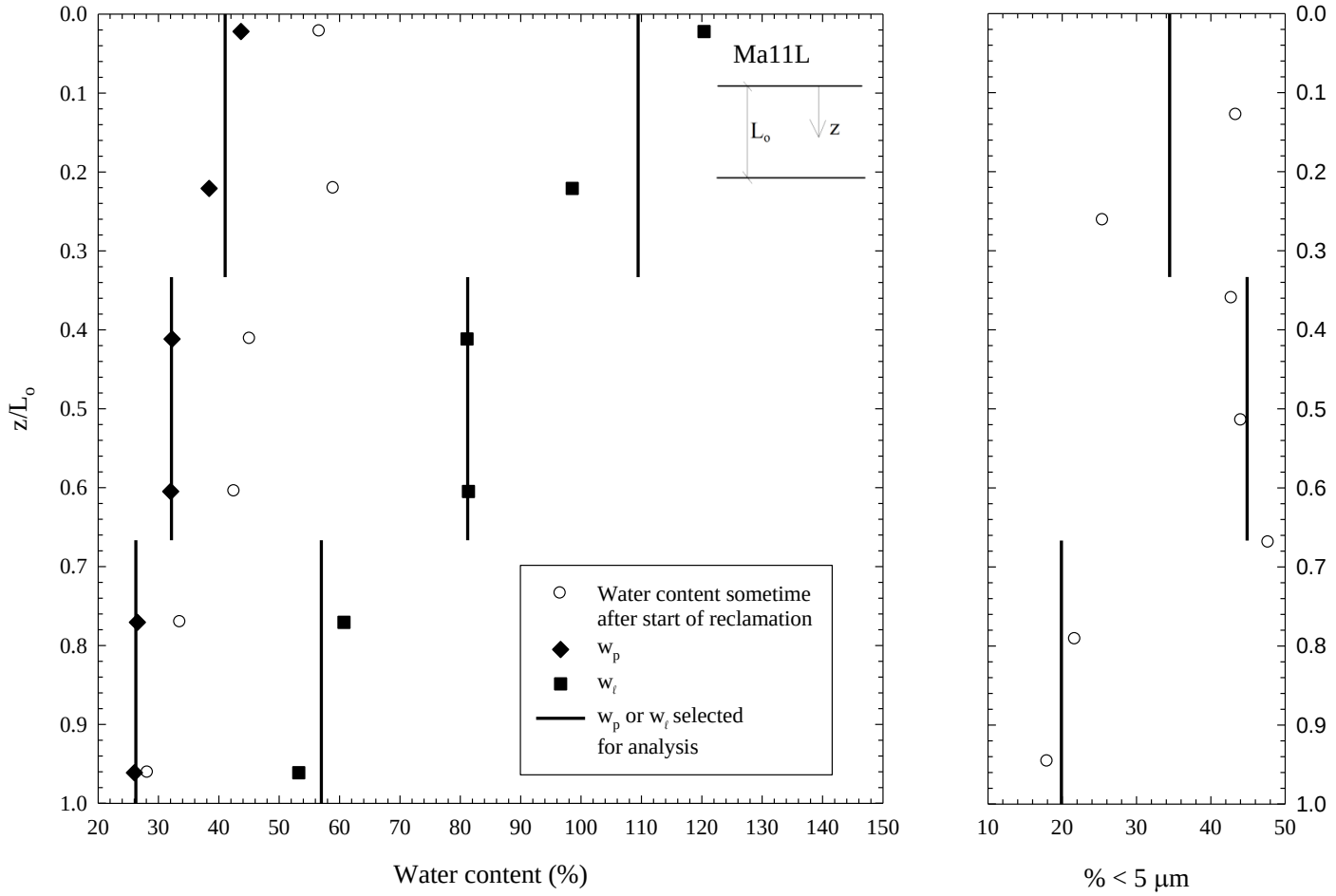

Figure A- 10 Atterberg limit and clay-size fraction data for Ma11L. Data from Mimura et al. (2003).

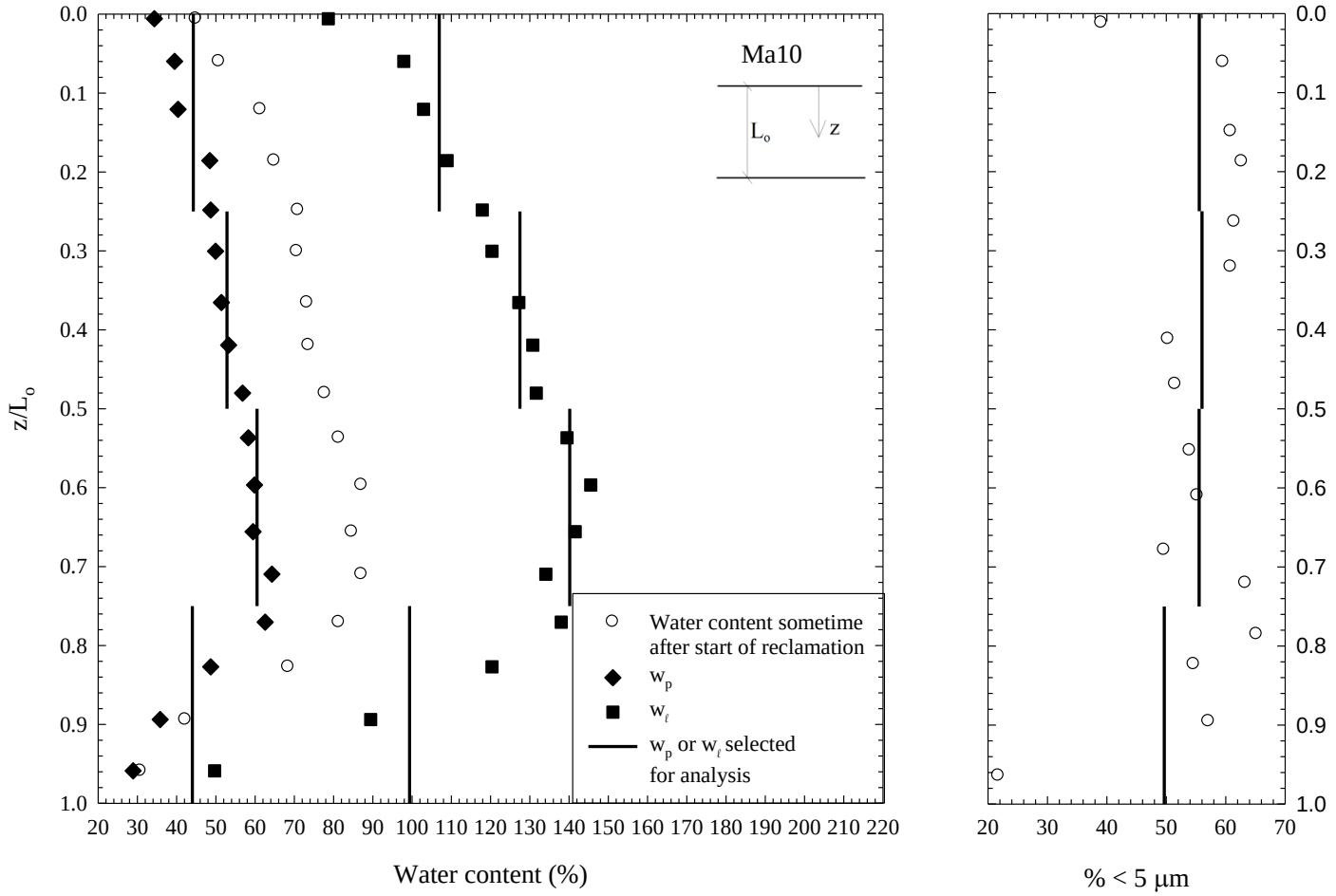

Figure A- 11Atterberg limit and clay-size fraction data for Ma10. Data from Mimura et al. (2003).

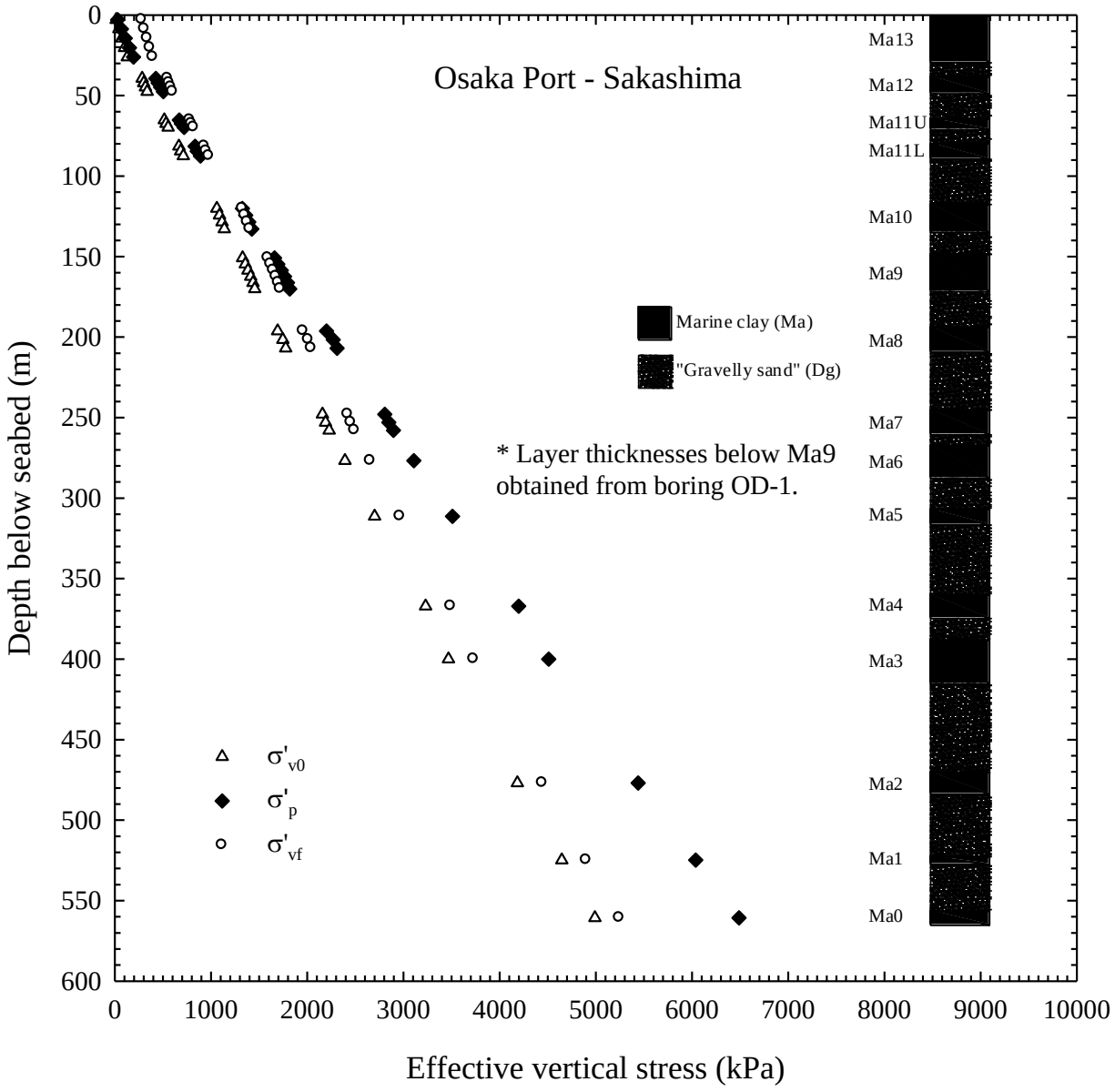

Figure A- 12 Preconstruction effective vertical stress (σ'_{vo}), preconsolidation pressure (σ'_{p}), and final effective vertical stress (σ'_{vf}) at Sakashima Island.

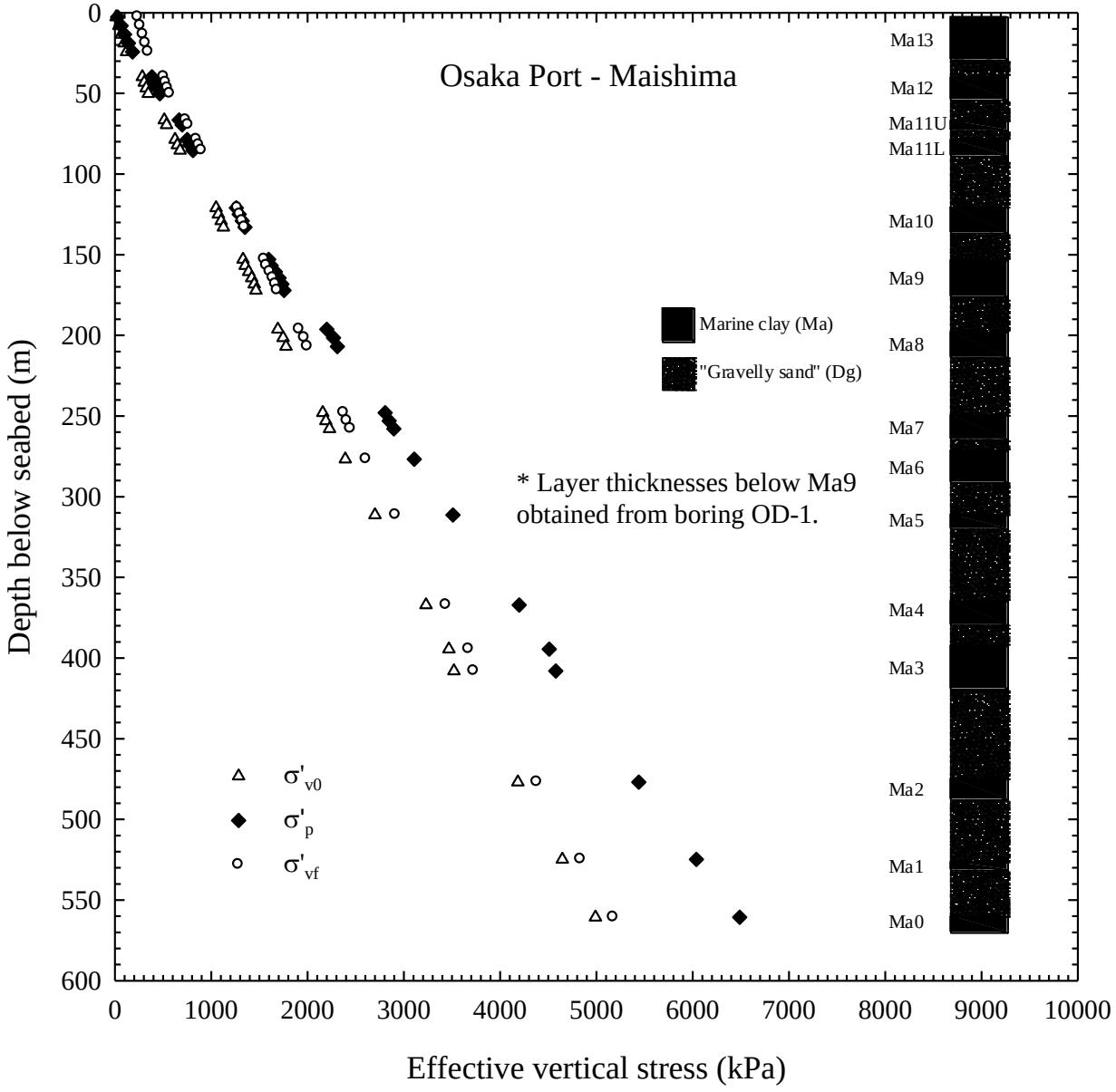

Figure A- 13 Preconstruction effective vertical stress (σ'_{vo}), preconsolidation pressure (σ'_{p}), and final effective vertical stress (σ'_{vf}) at Maishima Island**.**

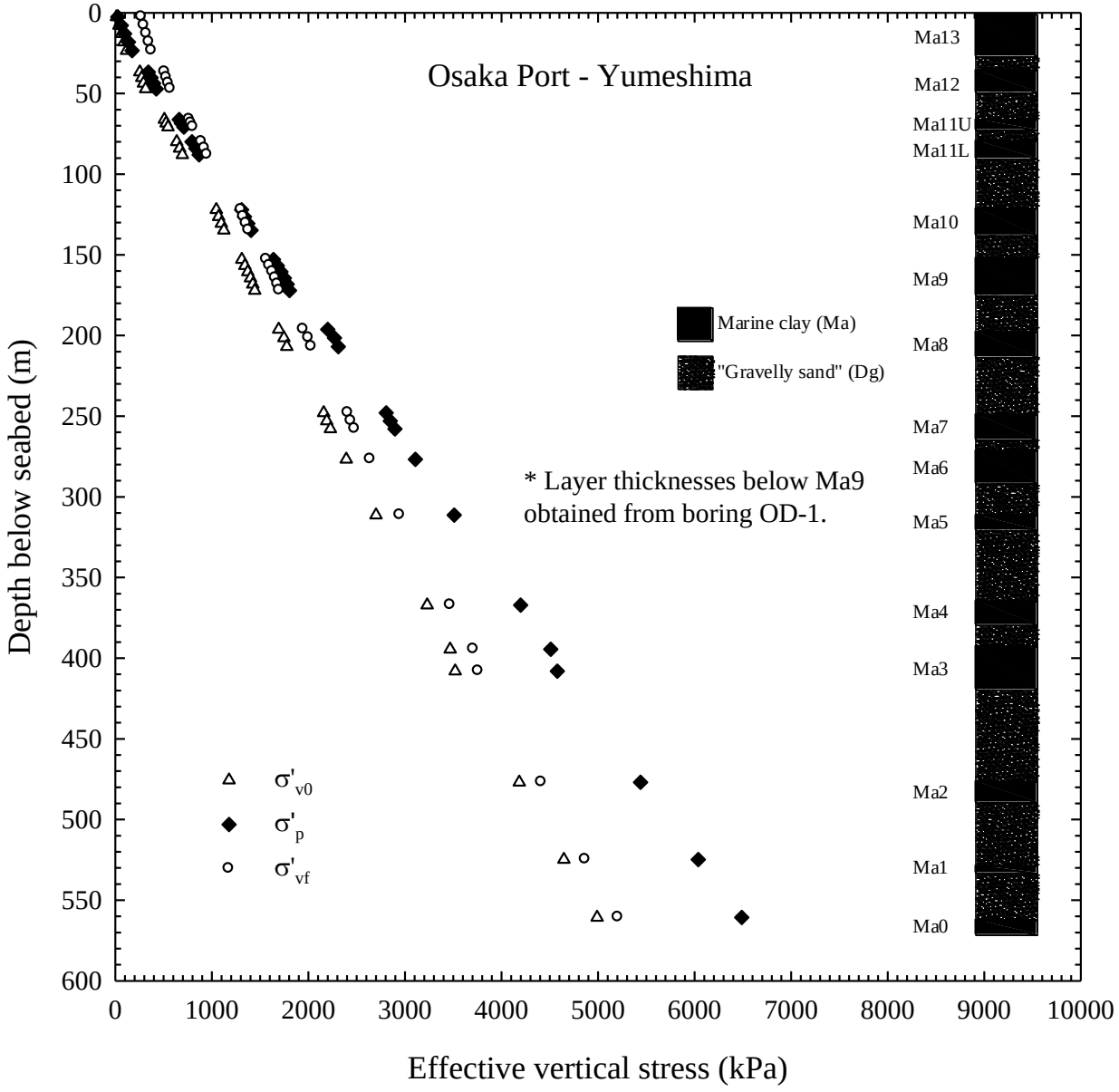

Figure A- 14 Preconstruction effective vertical stress (σ'_{vo}), preconsolidation pressure (σ'_{p}), and final effective vertical stress (σ'_{vf}) at Yumeshima Island.

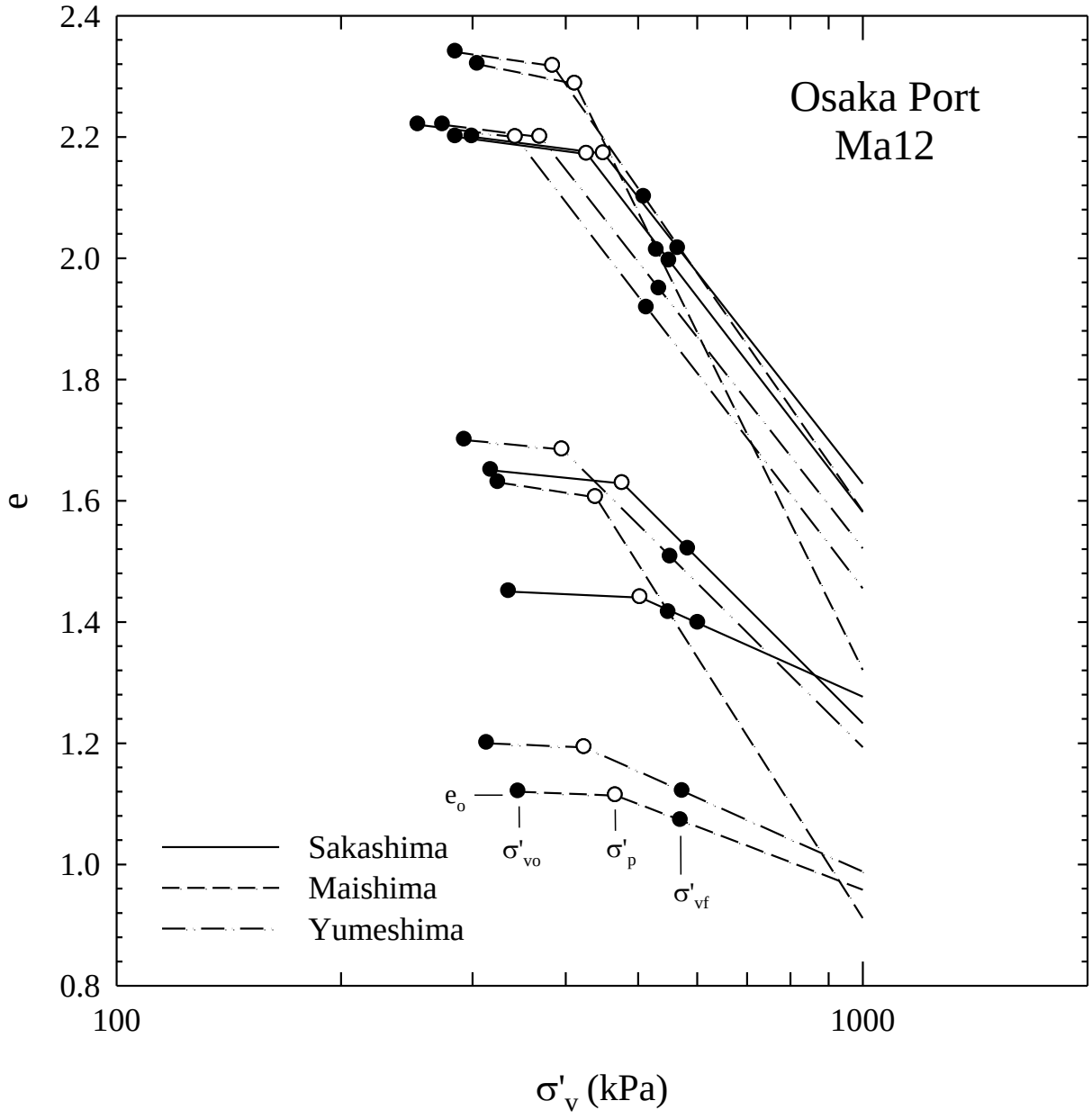

Figure A- 15EOP e – log σ'_v relationships for Osaka Port (Mimura and Jang, 2004, 2005).

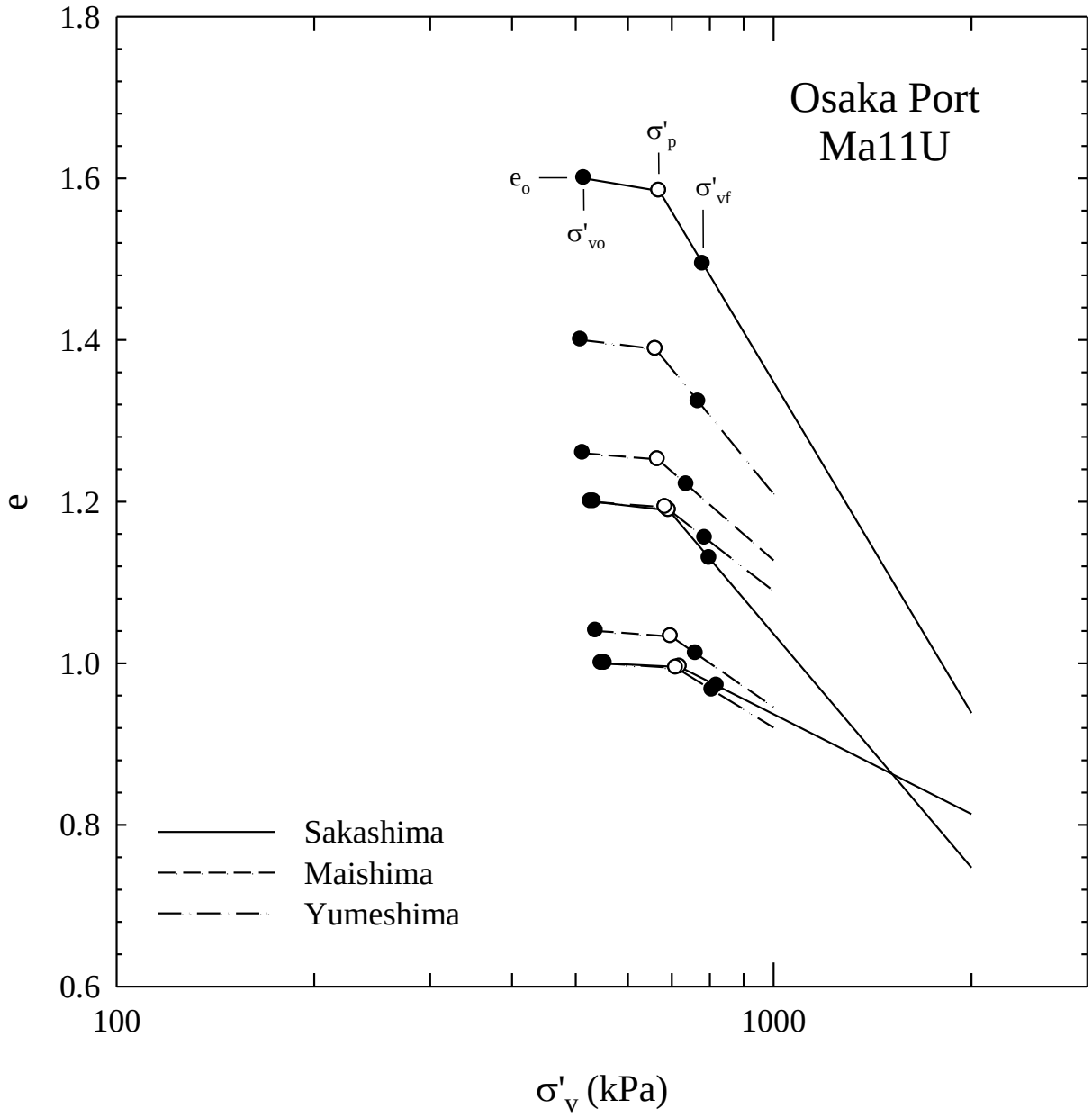

Figure A- 16EOP e – log σ'_v relationships for Osaka Port (Mimura and Jang, 2004, 2005).

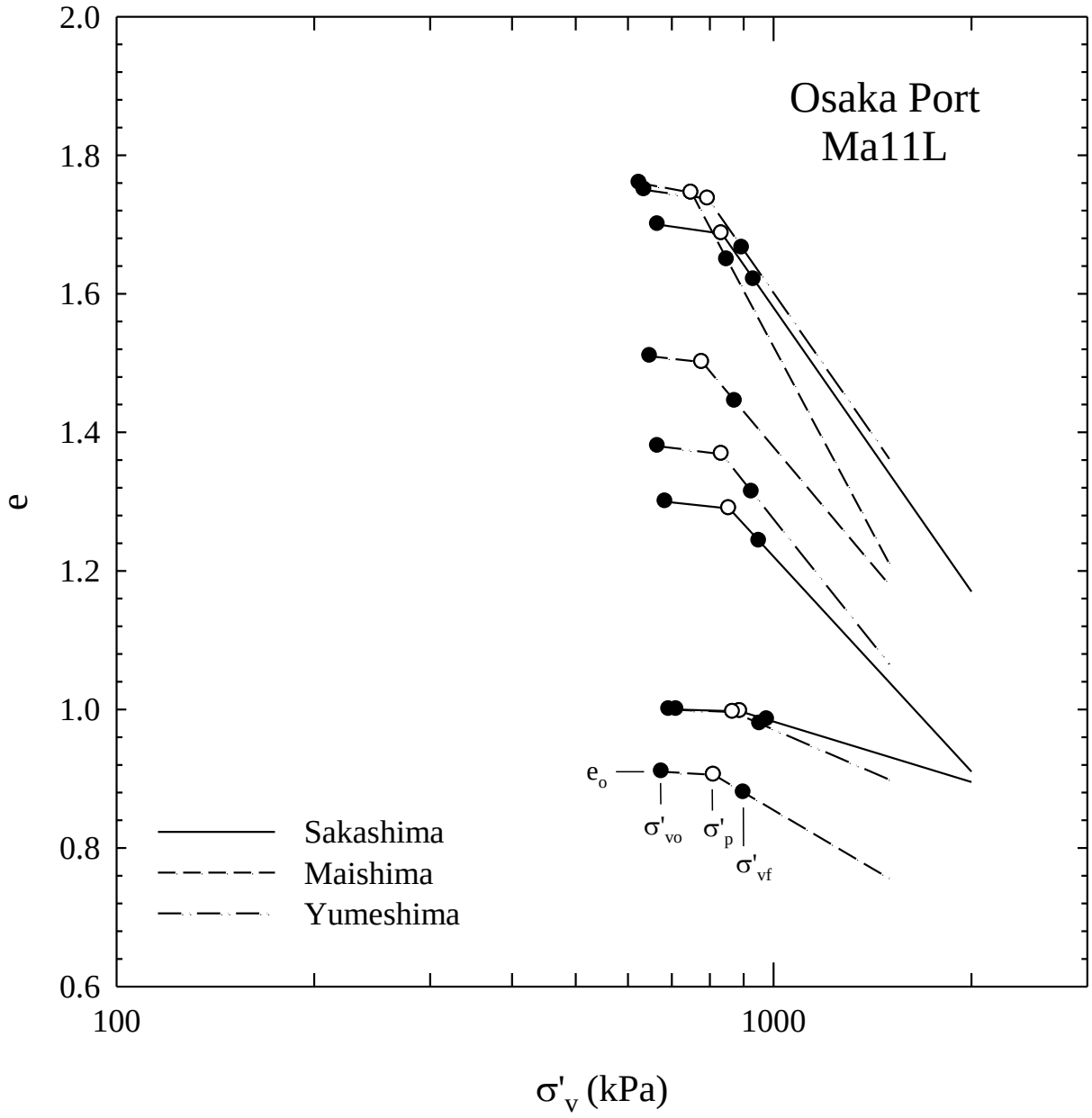

Figure A- 17EOP e – log σ'_v relationships for Osaka Port (Mimura and Jang, 2004, 2005).

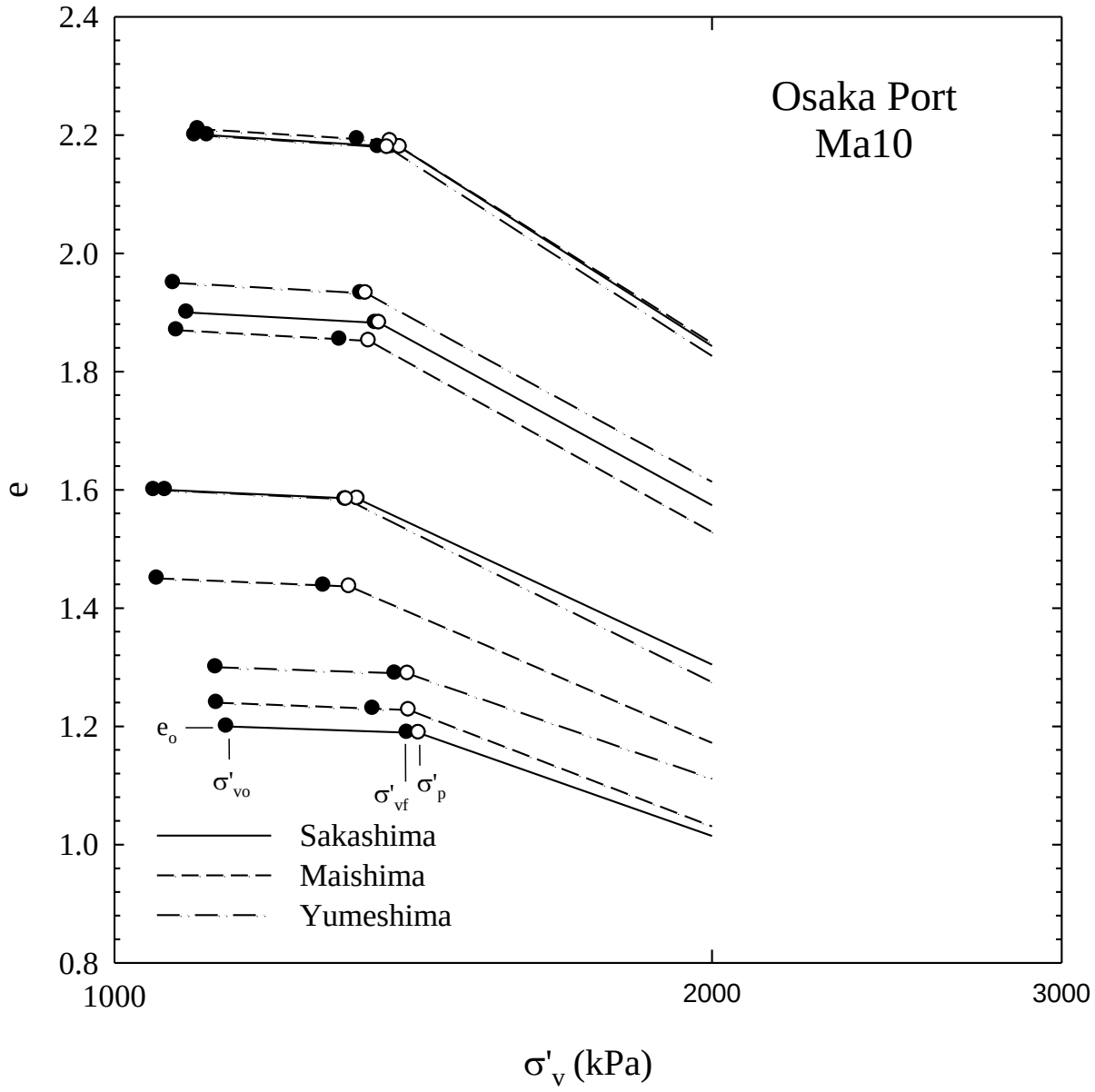

Figure A- 18EOP e – log σ'_v relationships for Osaka Port (Mimura and Jang, 2004, 2005).

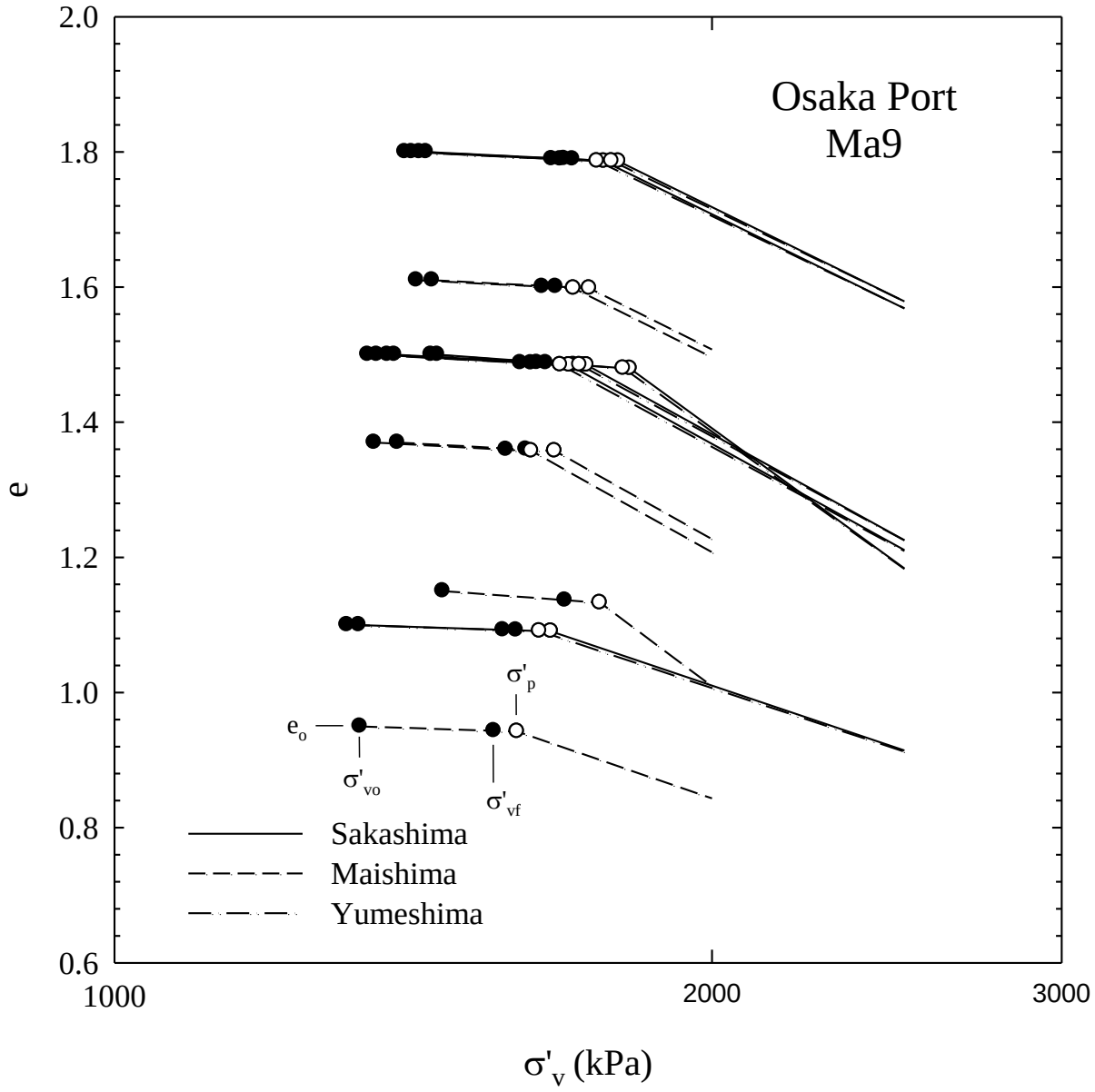

Figure A- 19EOP e – log σ'_v relationships for Osaka Port (Mimura and Jang, 2004, 2005).

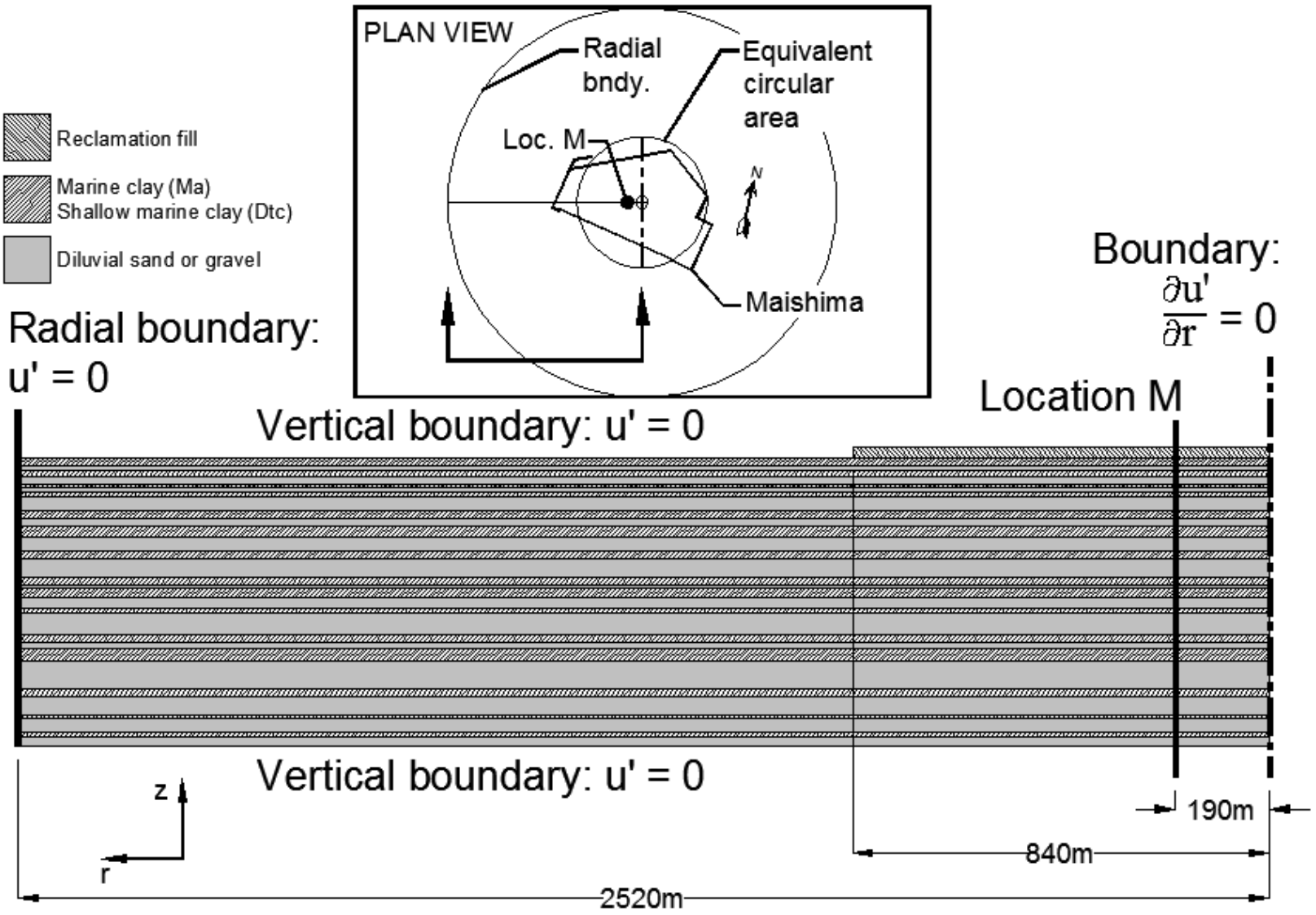

Figure A- 20 Setup for analysis at Maishima.

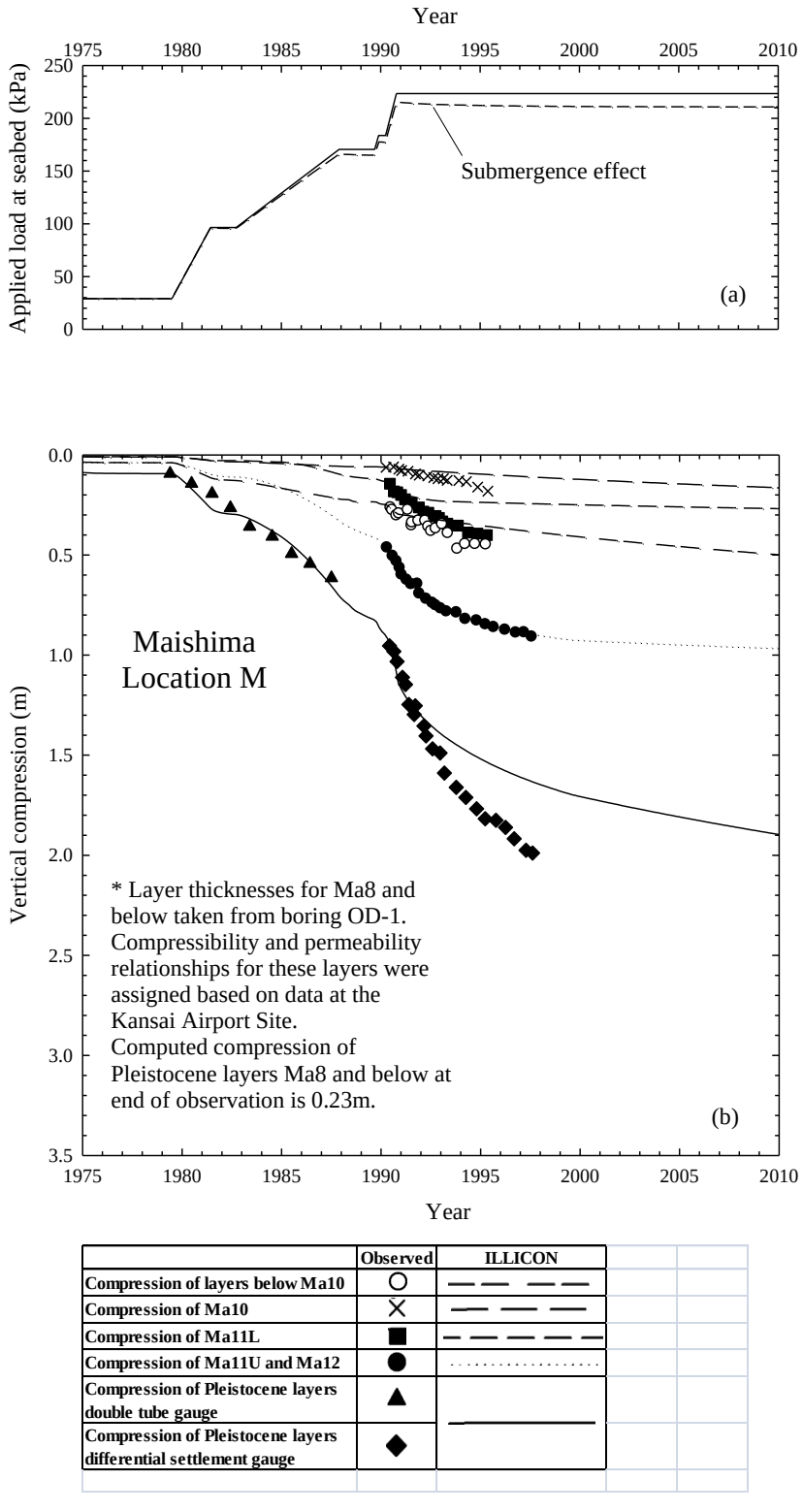

Figure A- 21 (a) Applied load at seabed versus time (Mimura and Jang, 2004). (b) Observed and calculated settlements and layer compressions for Location M at Maishima Island. Data from Mimura and Jang (2004).

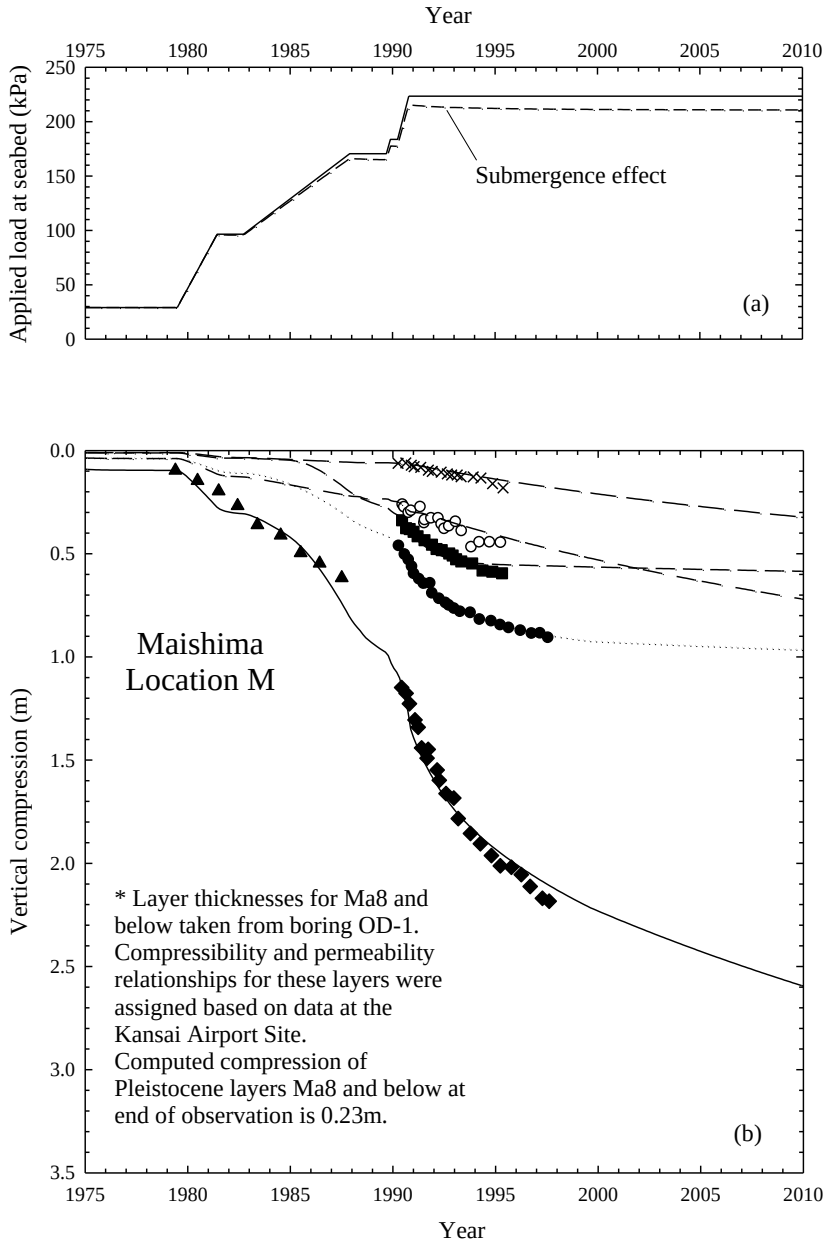

Figure A- 22 (a) Applied load at seabed versus time (Mimura and Jang, 2004). (b) Observed and calculated settlements and layer compressions for Location M. Data from Mimura and Jang (2004). Settlements calculated using C_c' data from Kansai Airport for Ma11L, Ma10, and Ma9.

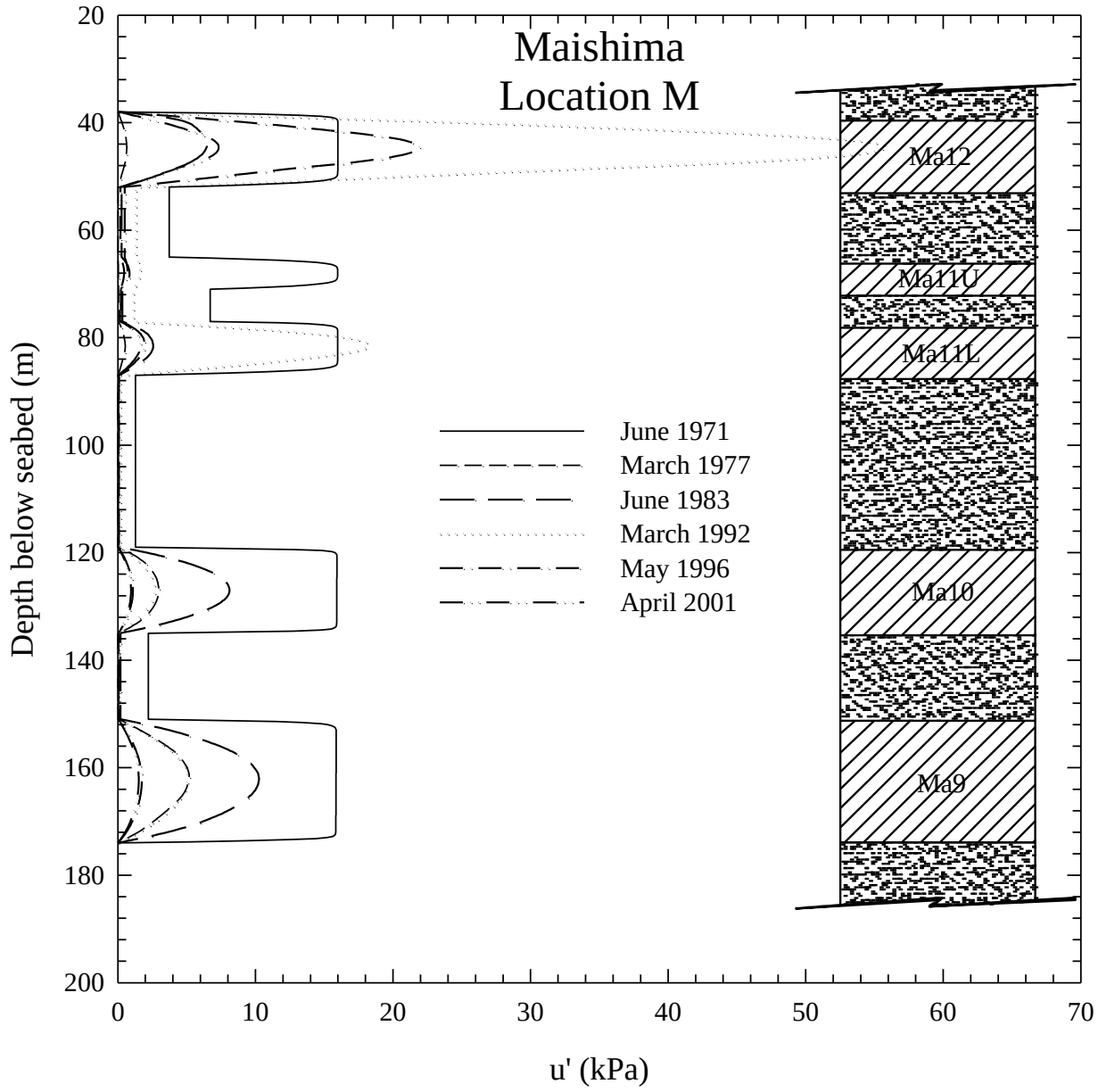

Figure A- 23Calculated excess porewater with depth at Maishima Location M.

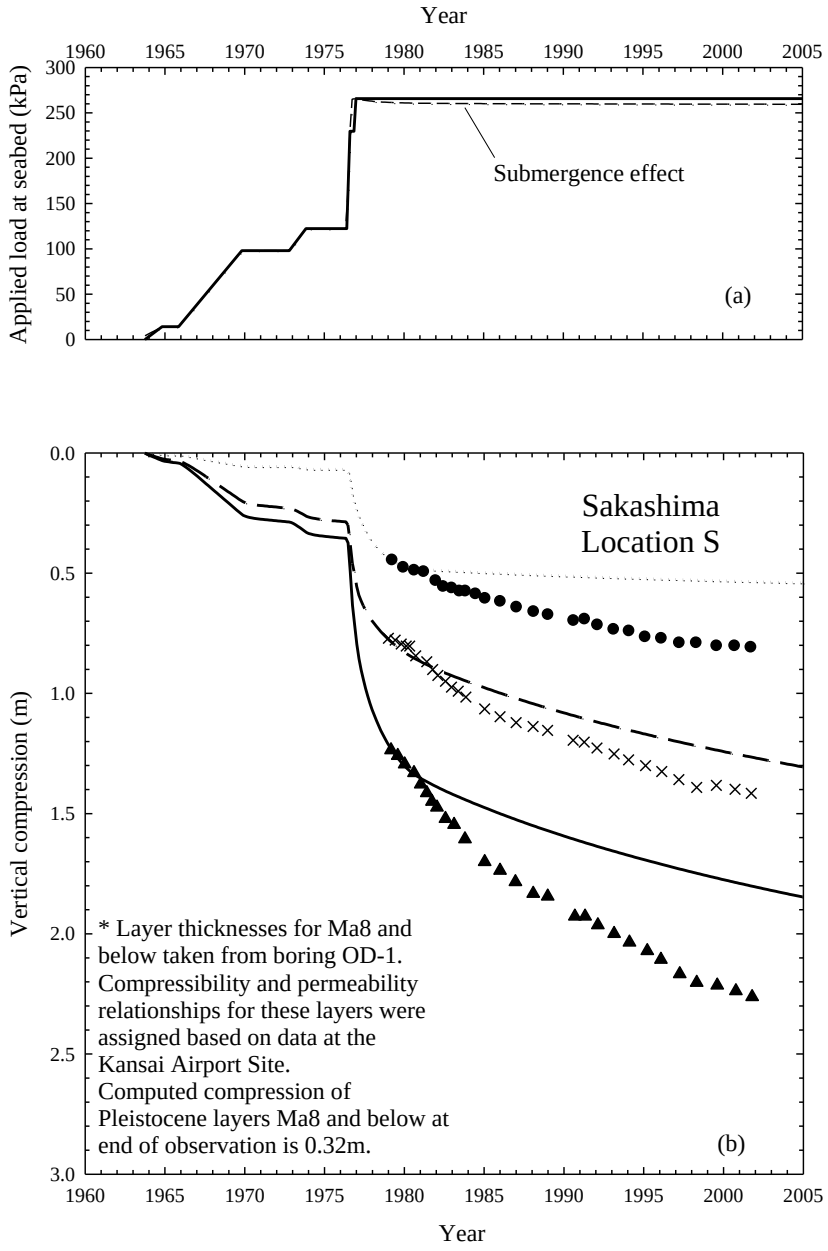

Figure A- 24 (a) Applied load at seabed versus time (Mimura and Jang, 2006). (b) Observed and calculated settlements and layer compressions for Sakashima Location S. Data from Mimura and Jang (2006).

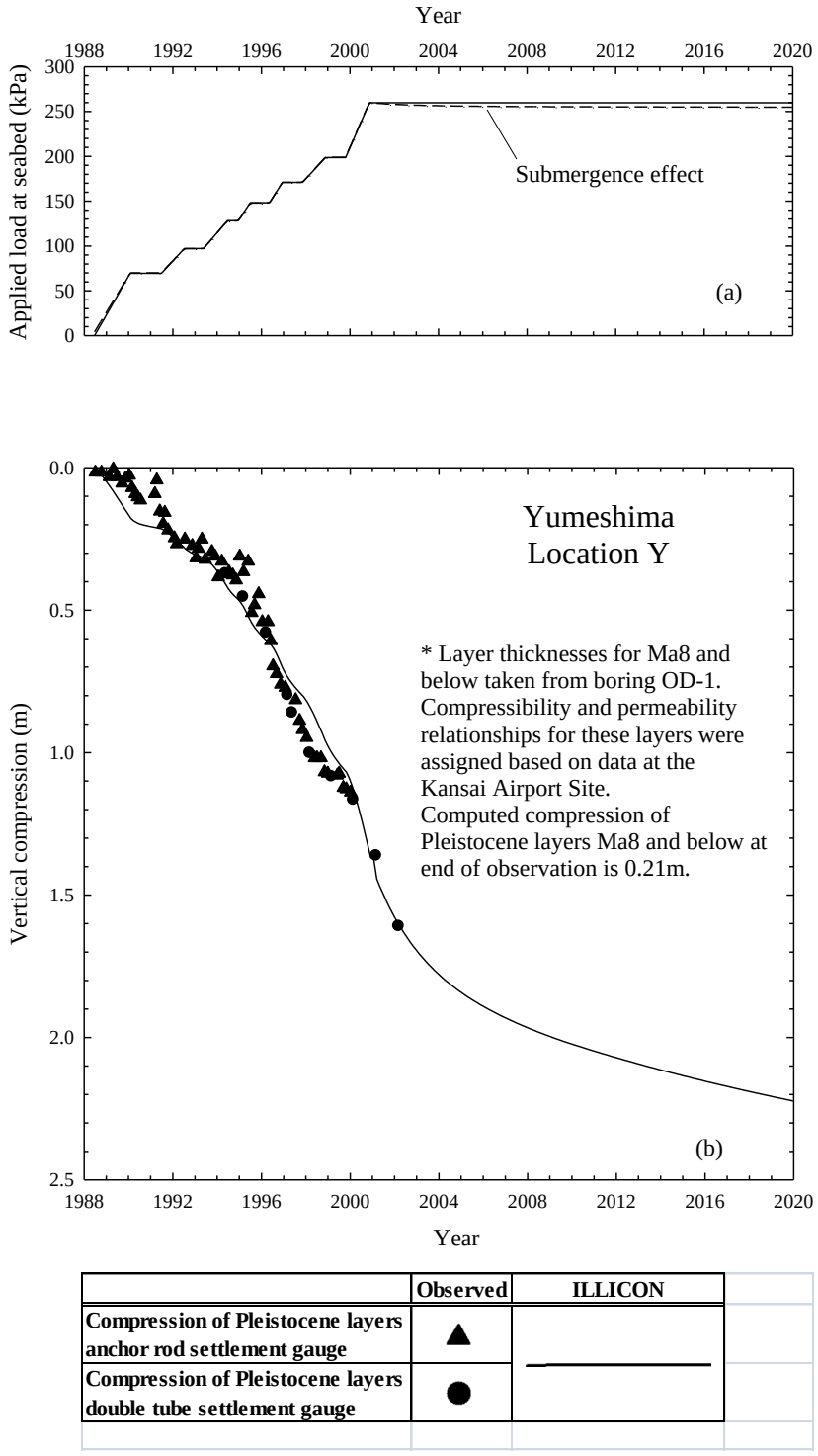

Figure A- 25 (a) Applied load at seabed versus time (Mimura and Jang, 2006). (b) Observed and calculated settlements and layer compressions for Yumeshima Location Y. Data from Mimura and Jang (2006).

APPENDIX B BACKCALCULATING c_h FROM SETTLEMENT OBSERVATIONS FOR MA13 AT THE KANSAI INTERNATIONAL AIRPORT

An attempt is made to develop a procedure for back-calculating horizontal coefficient of consolidation (c_h) of Ma13 from observed compression. During a large reclamation project, such as the Kansai Airport project, the value of c_h back-calculated using observation of compression at one location can be used for settlement analyses at other locations (e.g. c_h back-calculated at the pilot work section could have been used to make time rate of settlement predictions elsewhere at the Kansai Airport project). A relationship between average degree of consolidation (U) and time factor (T_h) for the case of equal strain, time-dependent loading (Figure B- 1) and vertical drains with smear zone is first developed (note: a U-T_h relationship was previously developed by R. Olson in 1977 for the case of equal strain, time-dependent loading and vertical drains without smear zone). Then the U-T_h relationship is used together with the Asaoka method (Asaoka, 1978, Mesri and Huvaj-Sarihan, 2009) and the inflection point method (Robinson, 1997; Mesri et al., 1999) to back-calculate c_h for Ma13.

The following integration is used to obtain u′ for the case of equal strain, time-dependent loading, and vertical drains with smear zone:

$$\int du' = \int \frac{dq}{F(n,s)} F_2 \exp\left(\frac{-2c_h(t-\tau)}{F(n,s)r_e^2}\right) d\tau \qquad (B-1)$$

where r is the radial distance from center of the drain, r_w is the radius to the edge of the drain, r_s is the radius to the edge of the smear zone, r_e is the radius of influence of the vertical drain in the surrounding soil, $n=r_e/r_w$, $s=r_s/r_w$, F(n,s) is defined as:

$$F(n,s) = \frac{n^2}{\left(n^2-s^2\right)} \ln\left(\frac{n}{s}\right) - \frac{3}{4} + \frac{s^2}{4n^2} + \frac{k_h}{k_s}\frac{\left(n^2-s^2\right)}{n^2}\ln(s) \qquad (B-2)$$

and F_2 is defined as:

$$F_2 = \ln\left(\frac{r}{r_s}\right) - \frac{\left(r^2-r_s^2\right)}{2r_e^2} + \frac{k_h}{k_s}\frac{\left(n^2-s^2\right)}{n^2}\ln(s) \qquad (B-3)$$

Integrating Equation B-1 for t less than construction time (t_c) yields:

$$u' = \frac{\Delta\sigma_{vc}F_2}{2T_{hc}}\left[1-\exp\left(\frac{-2T_h}{F(n,s)}\right)\right] \qquad (B-4)$$

where $\Delta\sigma_{vc}$ is shown in Figure B- 1, $T_h=c_h t/r_e^2$, and $T_{hc}=c_h t_c/r_e^2$.

Integrating Equation B-1 for t greater than the construction time (t_c) yields:

$$u' = \frac{\Delta\sigma_{vc} F_2}{2T_{hc}} \left[\exp\left(\frac{2T_{hc}}{F(n,s)} \right) - 1 \right] \exp\left(\frac{-2T_h}{F(n,s)} \right) \qquad (B-5)$$

The average degree of consolidation is defined by the following equation:

$$U = \frac{\int_0^{2\pi} \int_{r_s}^{r_e} \Delta\sigma_v r dr d\theta - \int_0^{2\pi} \int_{r_s}^{r_e} u' r dr d\theta}{\int_0^{2\pi} \int_{r_s}^{r_e} \Delta\sigma_{vc} r dr d\theta} \qquad (B-6)$$

where $\Delta\sigma_v$ is the applied stress at any time.

For t less than t_c:

$$U = \frac{T}{T_c} - \frac{F(n,s)}{2T_{hc}} \left[1 - \exp\left(\frac{-2T_h}{F(n,s)} \right) \right]$$

For t greater than t_c:

$$U = 1 - \frac{F(n,s)}{2T_{hc}} \left[\exp\left(\frac{2T_{hc}}{F(n,s)} \right) - 1 \right] \exp\left(\frac{-2T_h}{F(n,s)} \right) \qquad (B-7)$$

Figure B- 2 shows U versus $T_h/F(n,s)$ for a range of $T_{hc}/F(n,s)$.

It is useful to estimate excess porewater pressure and increase in effective stress if, for example, undrained strength stability analyses are to be carried out. Therefore, the average excess porewater pressure on a horizontal plane is determined from:

$$\bar{u}' = \frac{\int_0^{2\pi} \int_{r_s}^{r_e} u' r dr d\theta}{\int_0^{2\pi} \int_{r_s}^{r_e} r dr d\theta} \qquad (B-8)$$

For t less than t_c:

$$\bar{u}' = \frac{\Delta\sigma_{vc} F(n,s)}{2T_{hc}} \left[1 - \exp\left(\frac{-2T_h}{F(n,s)} \right) \right] \qquad (B-9)$$

For t greater than t_c:

$$\bar{u}' = \frac{\Delta\sigma_{vc} F(n,s)}{2T_{hc}} \left[\exp\left(\frac{2T_{hc}}{F(n,s)} \right) - 1 \right] \exp\left(\frac{-2T_h}{F(n,s)} \right) \qquad (B-10)$$

Figure B- 3 shows $\bar{u}'/\Delta\sigma_{vc}$ versus $T_h/F(n,s)$ for a range of $T_{hc}/F(n,s)$.

The Asaoka method (Asaoka, 1978; Mesri and Huvaj-Sarihan, 2009) is applied using the U-T_h relationship for t greater than t_c (Equation B-7). Considering settlements S_j and S_{j+1} at

elapsed times t_j and t_{j+1}, respectively:

$$S_j = S_{100}\left[1 - \frac{F(n,s)}{2T_{hc}}\left(\exp\left(\frac{2T_{hc}}{F(n,s)}\right) - 1\right)\exp\left(\frac{-2c_h t_j}{F(n,s)r_e^2}\right)\right] \quad (B-11)$$

$$S_{j+1} = S_{100}\left[1 - \frac{F(n,s)}{2T_{hc}}\left(\exp\left(\frac{2T_{hc}}{F(n,s)}\right) - 1\right)\exp\left(\frac{-2c_h t_{j+1}}{F(n,s)r_e^2}\right)\right] \quad (B-12)$$

Rewriting Equations B-11 and B-12, and dividing to obtain the slope of S_{j+1} versus S_j yields:

$$\beta = \frac{S_{100} - S_{j+1}}{S_{100} - S_j} = \exp\left(\frac{-2c_h}{F(n,s)r_e^2}\left(t_{j+1} - t_j\right)\right) \quad (B-13)$$

Simplifying and letting $t_{j+1} - t_j = \Delta t$:

$$\ln\beta = \frac{-2c_h \Delta t}{F(n,s)r_e^2} \quad (B-14)$$

Solving for c_h gives:

$$c_h = \frac{-r_e^2 F(n,s)\ln\beta}{2\Delta t} \quad (B-15)$$

The S_{j+1} versus S_j values were plotted for Ma13 at CT, K-I, and MP1-I as shown in Figure B- 4, Figure B- 5, and Figure B- 6, respectively. Horizontal coefficient of consolidation values determined from this method range from 2.5 to 7.4 m^2/year (average equal to 4.3 m^2/year).

The inflection point method (Robinson, 1997; Mesri et al., 1999) was also used to back-calculate c_h from observed compression of Ma13 at Kansai Airport. Equation B-7 was used together with the following equation:

$$\frac{d^2U}{d^2\log T_h} = \frac{\dfrac{d^2U}{dT_h^2} - \dfrac{dU}{d\log T_h}\dfrac{d^2\log T_h}{dT^2}}{\dfrac{d\log T_h}{dT_h}} = 0 \quad (B-16)$$

to solve for T_h at the inflection point of the U versus log T_h relationship. The time factor at the inflection point is:

$$T_h = \frac{F(n,s)}{2} \quad (B-17)$$

and therefore, c_h is calculated using the following equation:

$$c_h = \frac{r_e^2 F(n,s)}{2t} \qquad (B-18)$$

Time (t) in Equation B-18 is the elapsed time from initiation of the linearly increasing load to the time when the inflection point is visible on the deformation versus log of time plot.

This inflection point method was applied to portions of the compression versus time curves at CT, K-I, and MP1-I, as shown in Figure B- 7, Figure B- 8, and Figure B- 9, respectively. Using this method, the c_h values range from 3.9 to 5.2 m^2/year.

Table B- 1 summarizes c_h values calculated from the two methods described.

The oedometer data in Figure 4-45 together with the inflection point method (Robinson, 1997; Mesri et al., 1999) were used to back-calculate c_v for Ma13. Vertical coefficient of consolidation values equal to 2.2m^2/year, 3.7m^2/year, 2.7m^2/year, and 2.6m^2/year were back-calculated from the oedometer data. The average value of c_v from the oedometer tests (2.8 m^2/year) together with the average value of c_h from Table B- 1 (4.4m^2/year) suggest a permeability anisotropy approximately equal to 1.6 for Ma13 at the Kansai Airport site.

Permeability anisotropy was assumed equal to 1.0 for the settlement calculation presented in Chapter 8 for Ma13 at Kansai Airport. For comparison, the analysis at MP1-II was repeated using k_h/k_v equal to 1.6 and the results are presented in Figure B- 10. There is very little difference between the time rate of settlement calculations for k_h/k_v equal to 1.0 and k_h/k_v equal to 1.6 primarily because the rate of flow in the radial direction is controlled by the smear zone, within which k_h/k_v equal to 1.0 was assumed for the ILLICON analysis.

Table B- 1 Summary of c_h values obtained using two methods.

	Asaoka Method		Inflection Point Method c_h (m^2/yr)
Location	**β**	**c_h (m^2/yr)**	
CT	0.80	2.8	5.2
	0.82	2.5	
	0.68	4.8	
K-I	0.67	5.1	5.2
	0.71	4.4	
MP1-I	0.70	4.6	3.9
	0.80	2.8	
	0.56	7.4	
Average		**4.3**	**4.8**

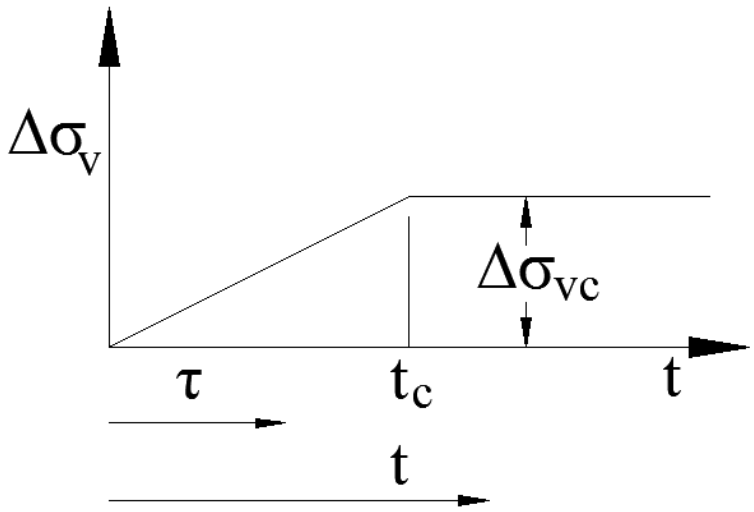

Figure B- 1 Definition of t_c and $\Delta\sigma_{vc}$ for time-dependent loading.

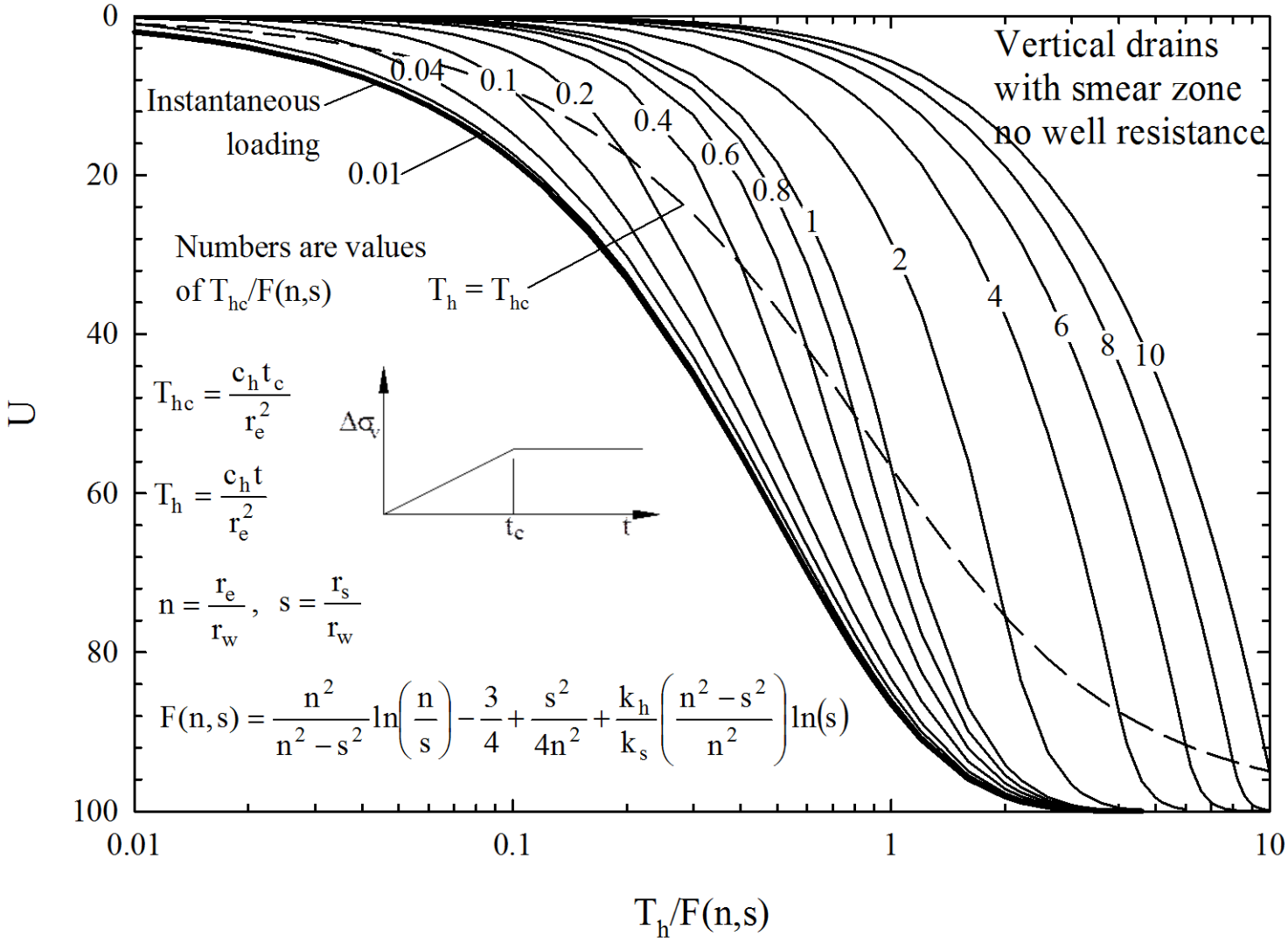

Figure B- 2 Average degree of consolidation for equal strain, time-dependent loading, and vertical drains with smear zone.

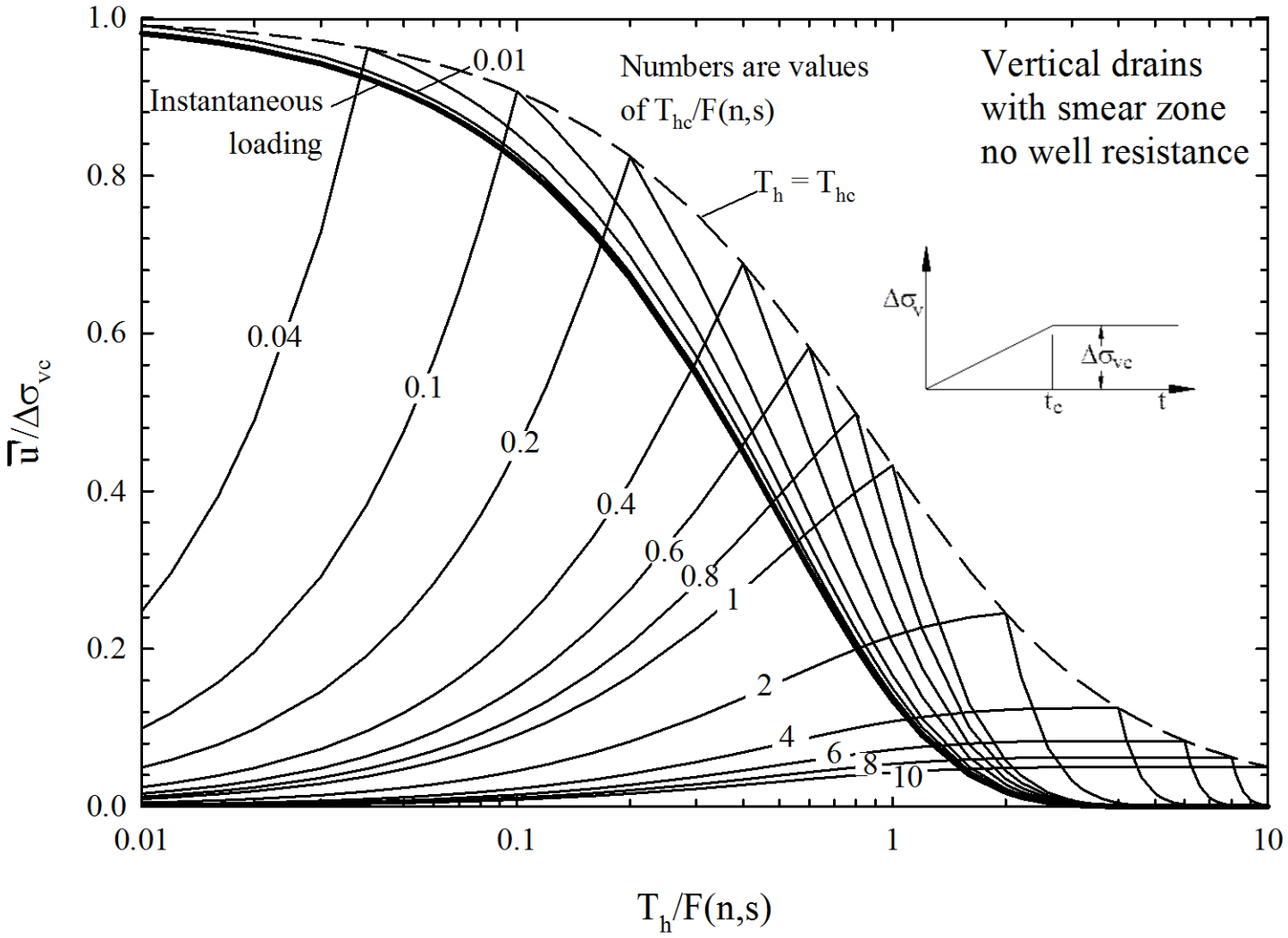

Figure B- 3 Relationship for average excess porewater pressure on a horizontal plane.

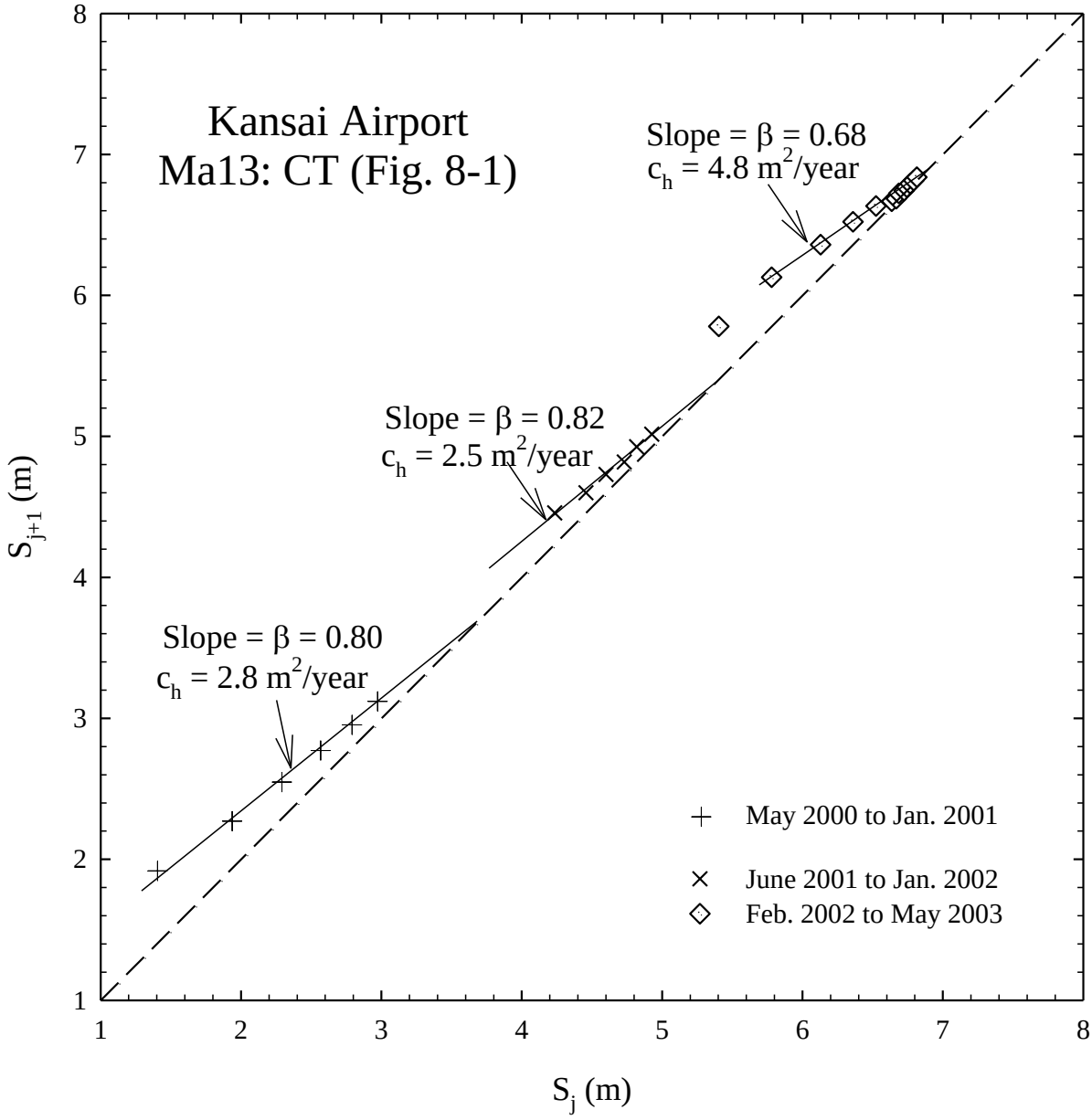

Figure B- 4 Asaoka's method applied to determine c_h.

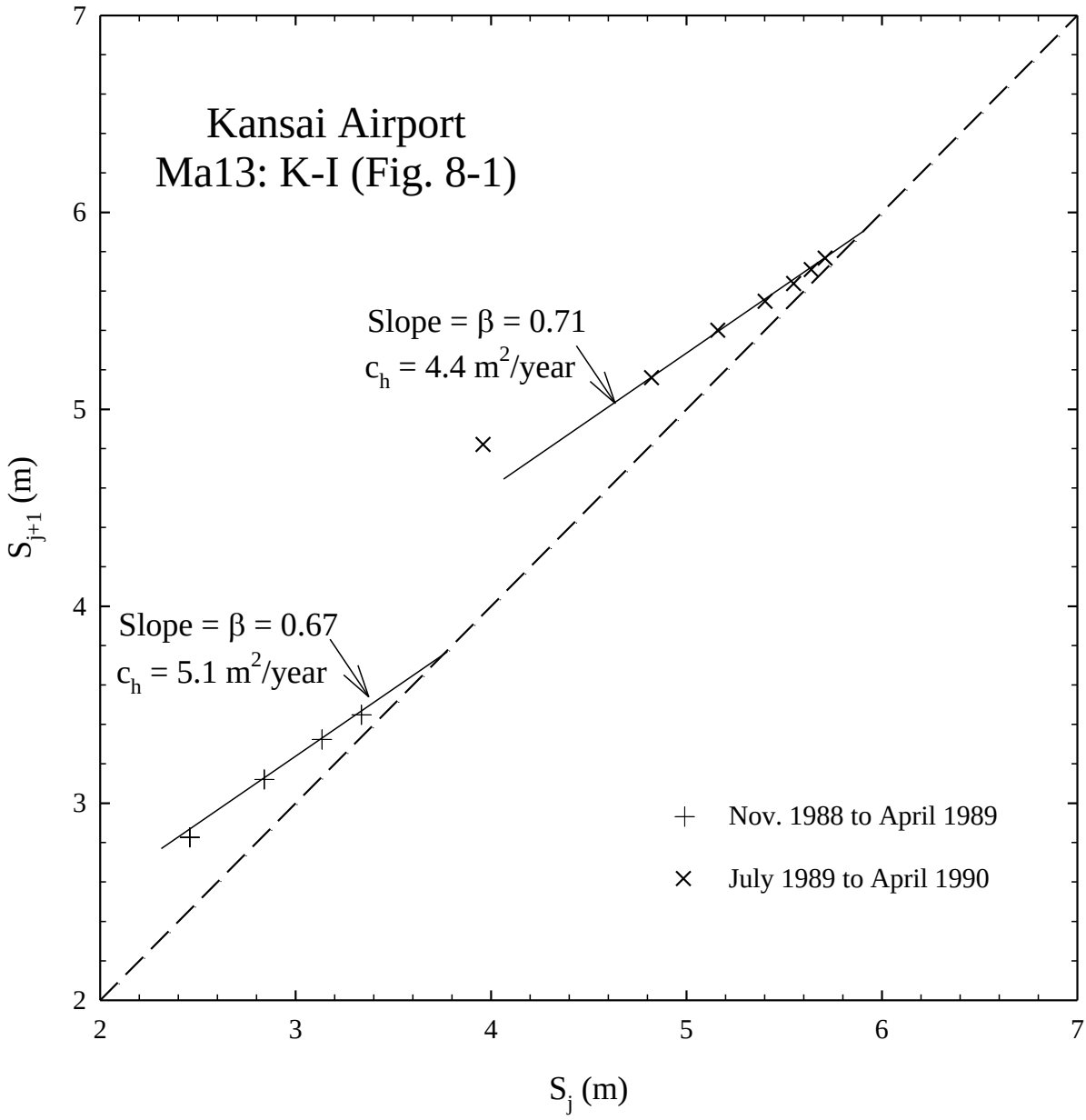

Figure B- 5 Asaoka's method applied to determine c_h.

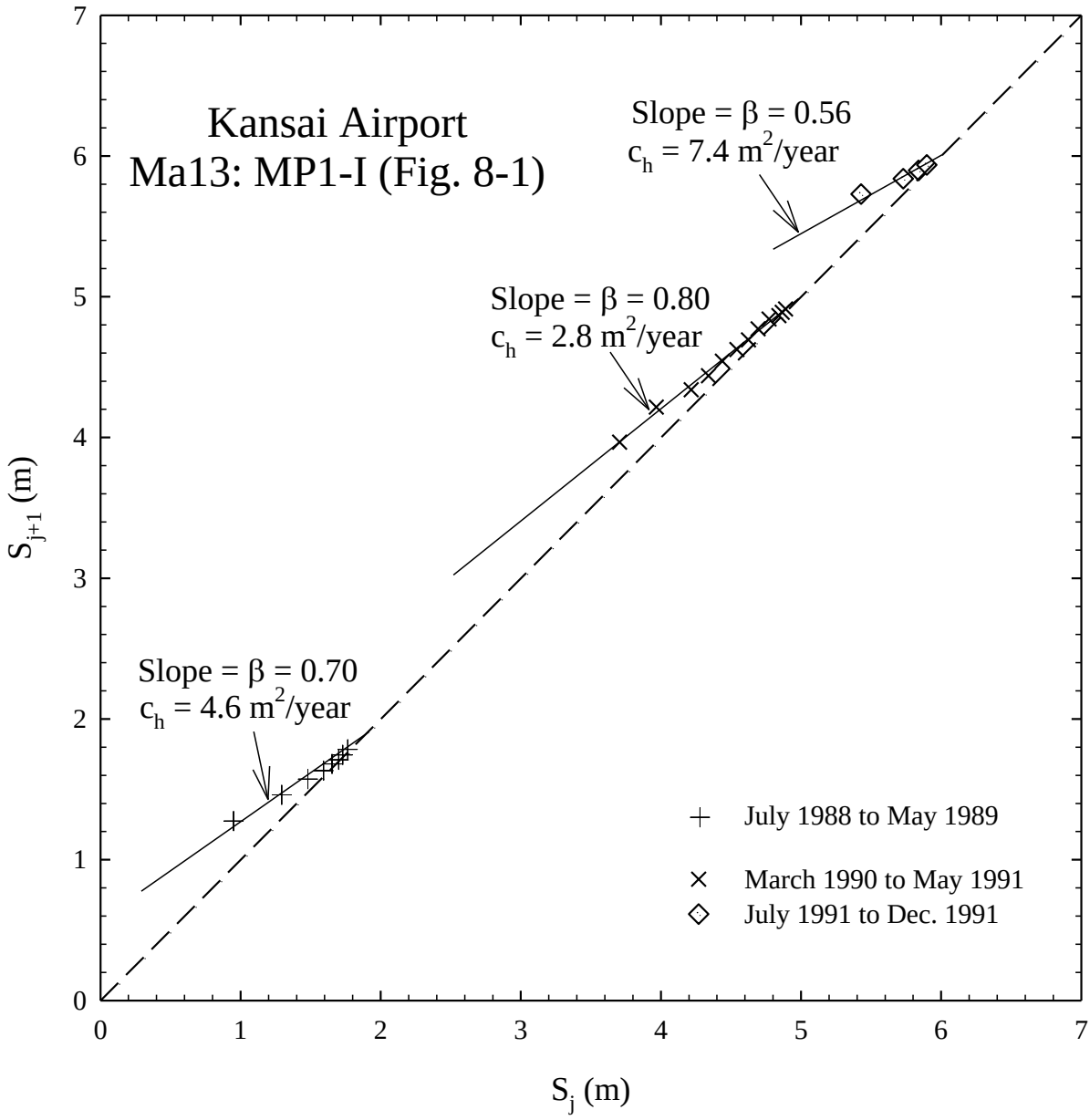

Figure B- 6 Asaoka's method applied to determine c_h.

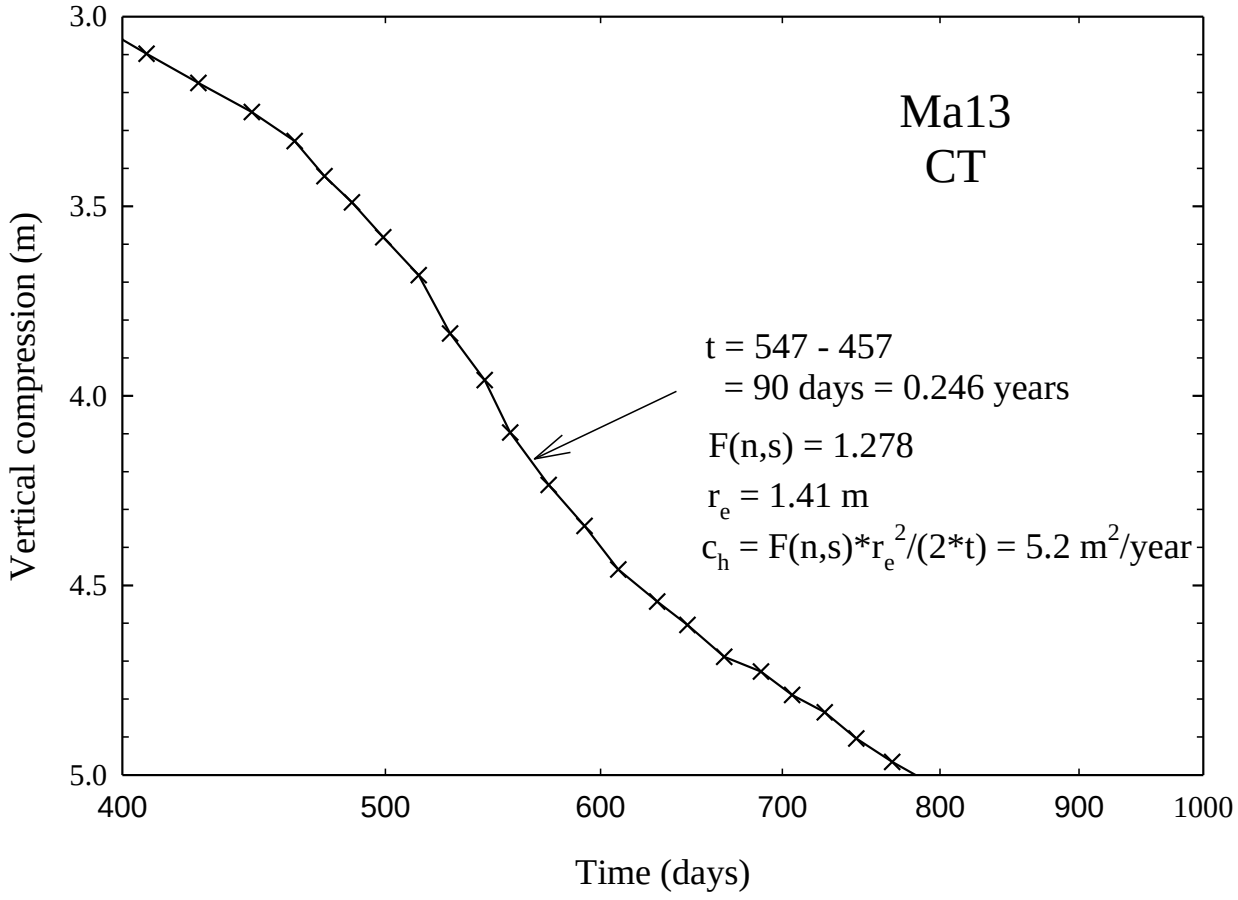

Figure B- 7 Inflection point method applied to determine c_h.

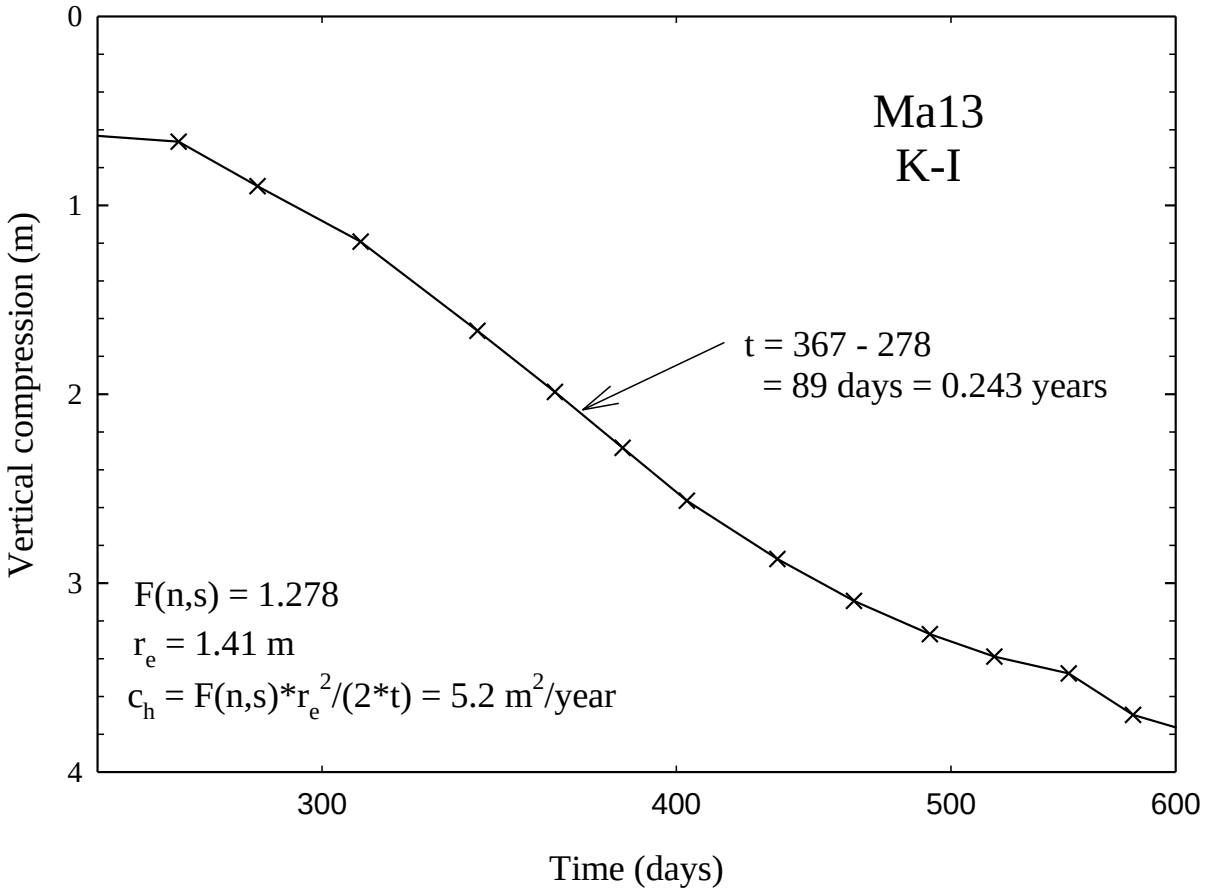

Figure B- 8 Inflection point method applied to determine c_h.

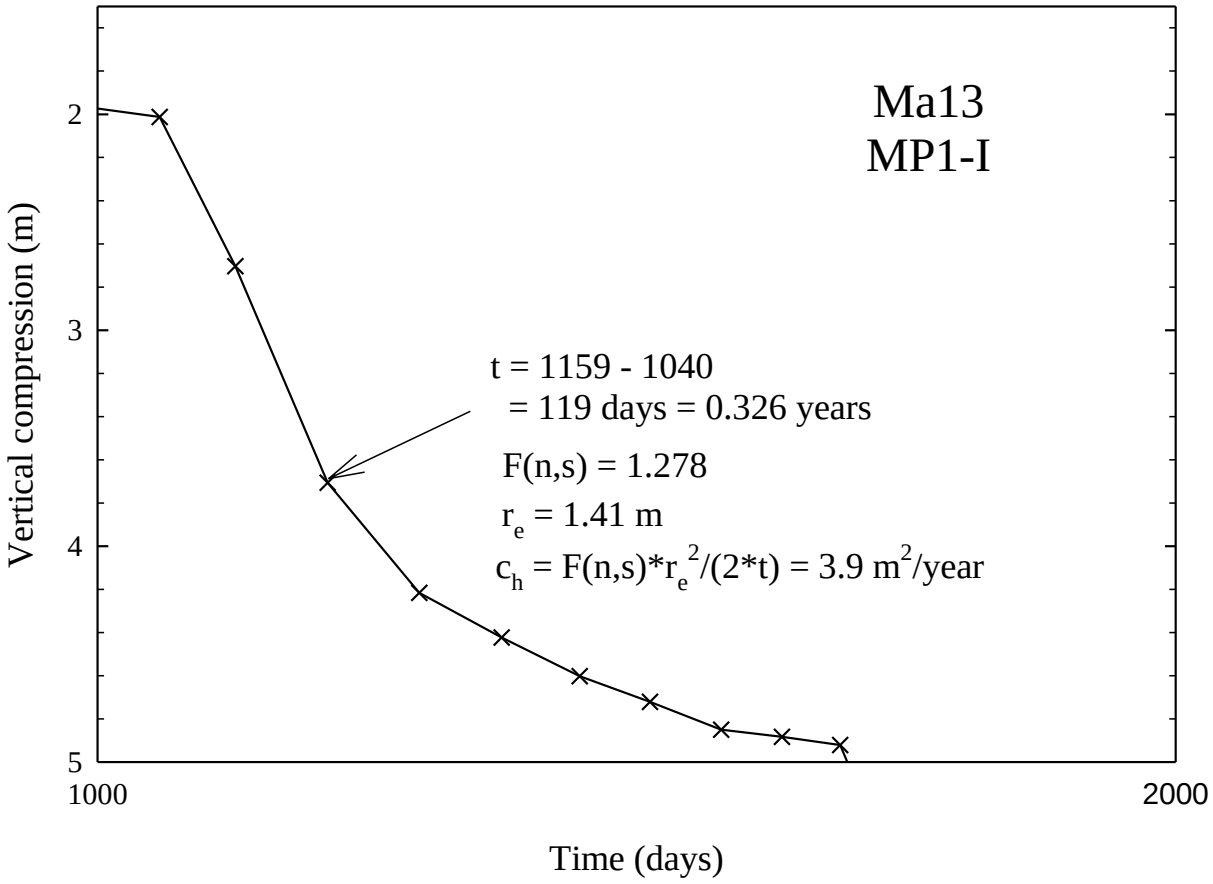

Figure B- 9 Inflection point method applied to determine c_h.

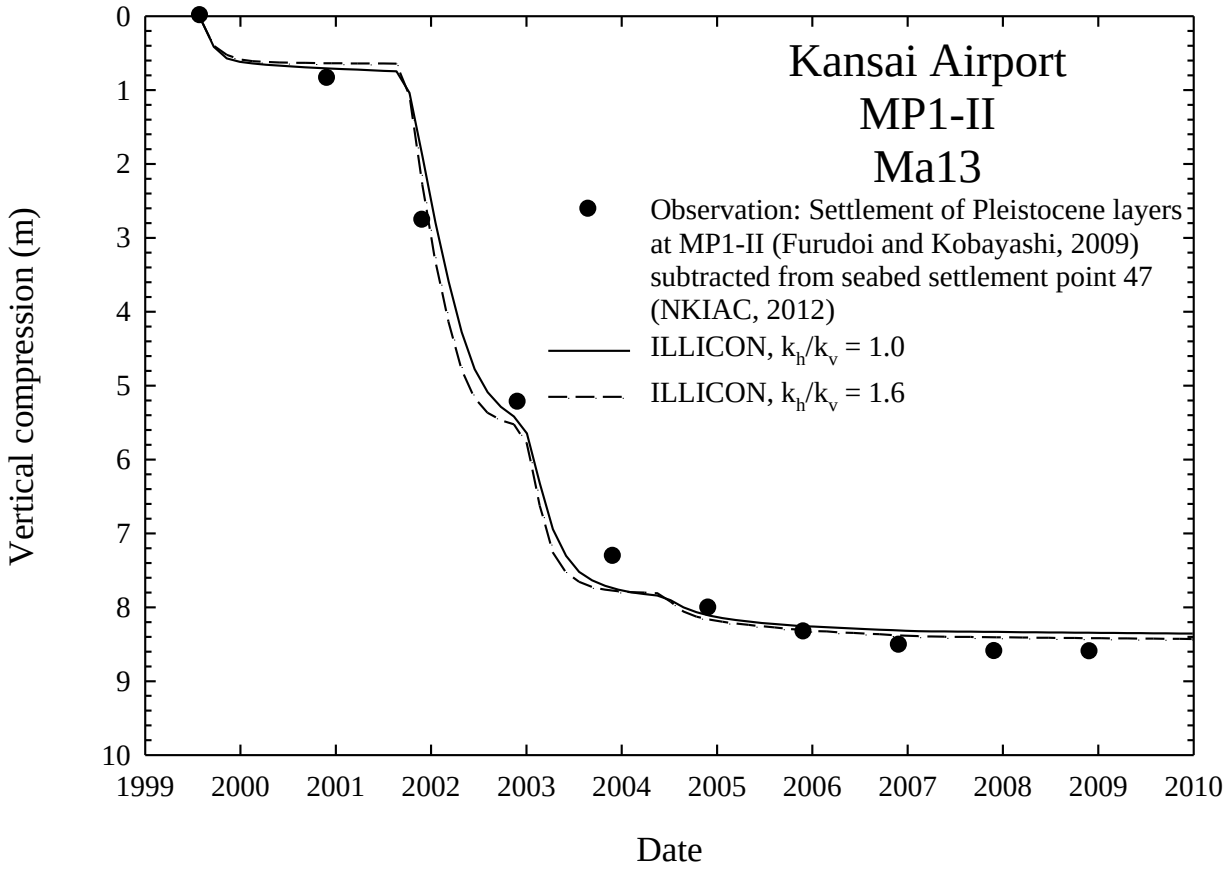

Figure B- 10 Observed and computed vertical compression for Ma13 at MP1-II.

APPENDIX C COMPRESSION OF GRANULAR SUBSEABED DEPOSITS AT MP1-II

An attempt is made here to estimate the vertical compression of the granular subseabed deposits to a depth of approximately 1500m (approximate depth to basement rock) at MP1-II. Because of a lack of published compressibility data for the granular soils in Osaka Bay, the compression indices were estimated based on the empirical data shown in Figure C- 1 (Mesri and Vardhanabhuti, 2009). The compression index for layer Ds1was estimated based on the Dr = 50% line (Assumption 1) and Dr = 100% line (Assumption 2) for clean quartz sand from Figure C- 1. Compression indices for layers Ds2, Ds3U, Ds3L, Ds4, Ds5, Ds6, Ds7, Ds8, Ds9, and Ds9'were estimated based on the upper line (Assumption 1) and lower line (Assumption 2) for quartz sands with 10% to 20% fines content from Figure C- 1. Compression indices for layer Ds10 and underlying granular materials were estimated based on the Dr = 100% line for clean quartz sand from Figure C- 1.

Table C- 1 summarizes the vertical compression of the granular subseabed deposits at MP1-II based on the two sets of assumptions for C_c described above. Unit weight data were obtained from Akai and Tanaka (1999). Data on specific gravity of solids was taken from Akai and Tanaka (1999) or a value of 2.65 was assumed. Initial void ratio was calculated from the following weight-volume relationship:

$$e = \frac{G_s - \gamma/\gamma_w}{\gamma/\gamma_w - 1} \qquad (C-1)$$

For the lowest layers an initial void ratio equal to 0.4 was assumed and the corresponding unit weight was calculated. The Dr = 100% line for clean quartz sand was used exclusively to estimate C_c for the lowest layers.

The calculated vertical compression of the granular subseabed deposits at MP1-II is 0.66m to 1.51m based on the assumptions described above. Therefore, the contribution to seabed settlement from the granular layers is expected to be small compared to the contribution to seabed settlement from clay layers. The seabed settlement resulting from compression of some of the granular layers, especially those below 395m is expected to occurring during reclamation, whereas other sand layers such as Ds2 and Ds5 will contribute to post-construction settlement.

Table C- 1 Vertical compression of granular subseabed deposits at MP1-II based on two sets of assumptions for C_c.

								Assumption 1		Assumption 2	
Layer	**Thickness (m)**	**mid-depth (m)**	**γ (kN/m^3)**	**G_s**	**e_o**	**σ'_{vo} (kPa)**	**σ'_{vf} (kPa)**	**C_c**	**Comp. (m)**	**C_c**	**Comp. (m)**
Ds1	9.8	29.0	22.2	2.63	0.29	188	767	0.015	0.070	0.006	0.027
Ds2	3.0	43.0	18.3	2.65	0.91	314	892	0.225	0.158	0.056	0.039
Ds3U	1.6	60.3	18.7	2.68	0.85	412	990	0.236	0.076	0.059	0.019
Ds3L	3.7	70.9	17.5	2.69	1.15	496	1073	0.242	0.138	0.062	0.035
Ds4	1.7	84.4	18.7	2.65	0.81	591	1166	0.249	0.068	0.066	0.018
Ds5	5.0	97.5	15.5	2.52	1.63	680	1254	0.257	0.129	0.069	0.035
Ds6	3.1	127.1	18.7	2.65	0.81	878	1447	0.265	0.099	0.075	0.028
Ds7	4.7	157.4	18.7	2.65	0.81	1088	1648	0.273	0.127	0.081	0.038
Ds8	5.4	178.0	18.7	2.70	0.87	1227	1782	0.277	0.130	0.085	0.040
Ds9	4.0	195.5	18.7	2.70	0.87	1360	1908	0.281	0.088	0.088	0.028
Ds9'	5.4	217.7	18.7	2.65	0.81	1525	2064	0.284	0.112	0.092	0.036
Ds10	5.3	233.6	19.3	2.72	0.78	1643	2177	0.009	0.003	0.009	0.003
Ds11	4.7	246.8	18.7	2.65	0.81	1743	2271	0.009	0.003	0.009	0.003
Ds12	7.2	274.1	18.7	2.65	0.81	1954	2470	0.009	0.004	0.009	0.004
Ds	6.0	291.0	18.7	2.65	0.81	2082	2589	0.009	0.003	0.009	0.003
Ds	4.4	301.3	18.7	2.65	0.81	2161	2664	0.010	0.002	0.010	0.002
Ds	8.9	312.1	18.7	2.65	0.81	2248	2746	0.010	0.004	0.010	0.004
Ds	4.7	329.7	18.7	2.65	0.81	2380	2869	0.010	0.002	0.010	0.002
Ds	18.8	367.7	18.7	2.65	0.81	2658	3130	0.011	0.008	0.011	0.008
Ds	4.3	392.9	18.7	2.65	0.81	2851	3312	0.011	0.002	0.011	0.002
From 395m below seabed to 1500m below seabed	1105	395 to 1500	21.8	2.65	0.40	3005 to 15,943	3460 to 16,168	0.011 to 0.037	0.284	0.011 to 0.037	0.284
								Σ	**1.51**	**Σ**	**0.66**

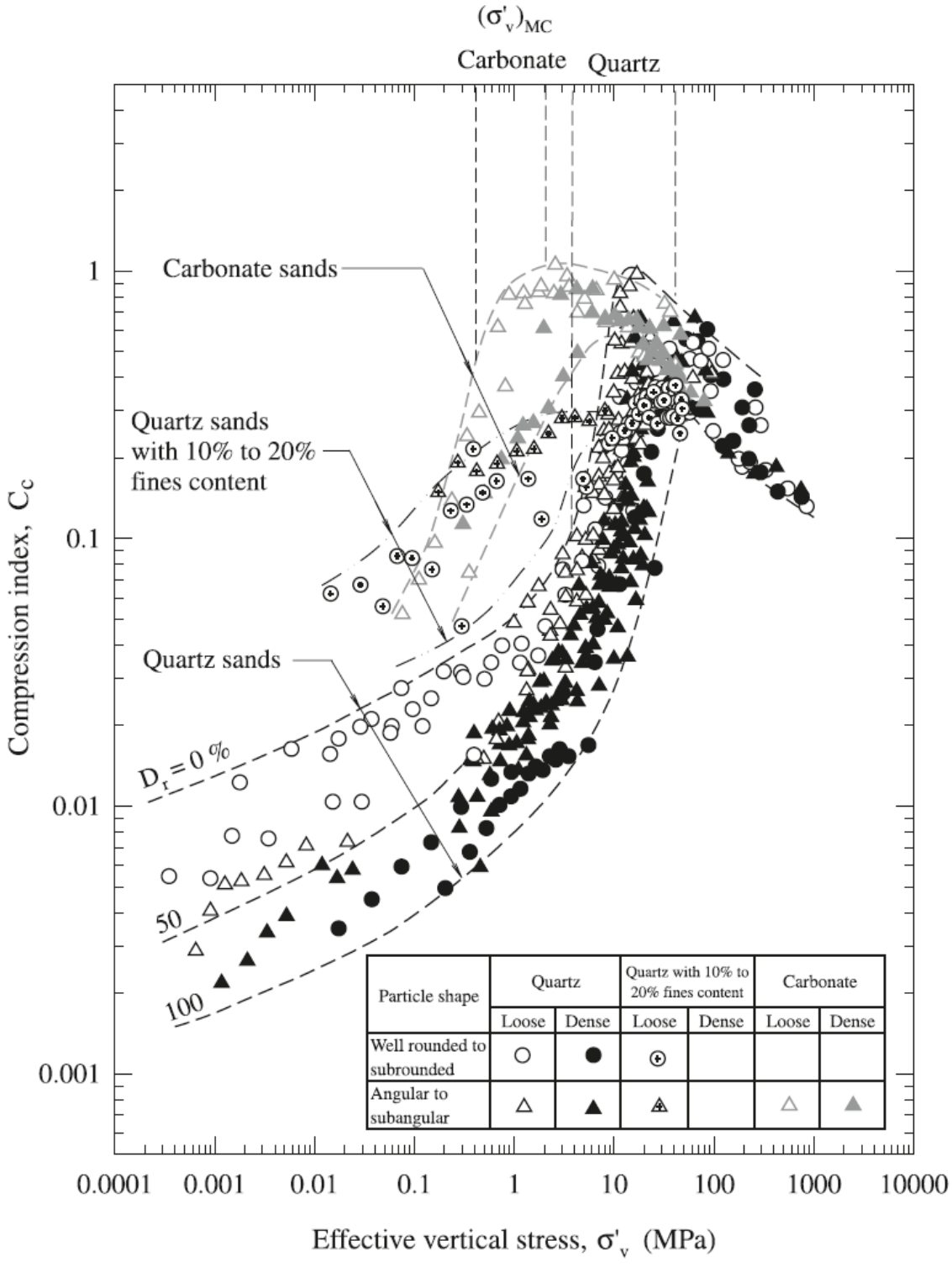

Figure C- 1 Data on C_c for sands (Mesri and Vardhanabhuti, 2009).